frontiers

Inorganic chemistry, polymer chemistry, and solid state chemistry editor's pick 2024

Edited by
Luís D. Carlos, Elena Vladimirovna Boldyreva and Pellegrino Musto

Published in
Frontiers in Chemistry

ISSN 2296-2646
ISBN 978-2-8325-5848-5
DOI 10.3389/978-2-8325-5848-5

About Frontiers

Frontiers is more than just an open access publisher of scholarly articles: it is a pioneering approach to the world of academia, radically improving the way scholarly research is managed. The grand vision of Frontiers is a world where all people have an equal opportunity to seek, share and generate knowledge. Frontiers provides immediate and permanent online open access to all its publications, but this alone is not enough to realize our grand goals.

Frontiers journal series

The Frontiers journal series is a multi-tier and interdisciplinary set of open-access, online journals, promising a paradigm shift from the current review, selection and dissemination processes in academic publishing. All Frontiers journals are driven by researchers for researchers; therefore, they constitute a service to the scholarly community. At the same time, the *Frontiers journal series* operates on a revolutionary invention, the tiered publishing system, initially addressing specific communities of scholars, and gradually climbing up to broader public understanding, thus serving the interests of the lay society, too.

Dedication to quality

Each Frontiers article is a landmark of the highest quality, thanks to genuinely collaborative interactions between authors and review editors, who include some of the world's best academicians. Research must be certified by peers before entering a stream of knowledge that may eventually reach the public - and shape society; therefore, Frontiers only applies the most rigorous and unbiased reviews. Frontiers revolutionizes research publishing by freely delivering the most outstanding research, evaluated with no bias from both the academic and social point of view. By applying the most advanced information technologies, Frontiers is catapulting scholarly publishing into a new generation.

Inorganic chemistry, polymer chemistry, and solid state chemistry editor's pick 2024

Topic editors

Luís D. Carlos — University of Aveiro, Portugal

Elena Vladimirovna Boldyreva — Novosibirsk State University, Russia

Pellegrino Musto — National Research Council (CNR), Italy

Citation

Carlos, L. D., Boldyreva, E. V., Musto, P., eds. (2025). *Inorganic chemistry, polymer chemistry, and solid state chemistry editor's pick 2024*. Lausanne: Frontiers Media SA. doi: 10.3389/978-2-8325-5848-5

We are pleased to introduce the collection Frontiers in Chemistry – Inorganic Chemistry, Polymer Chemistry, and Solid State Chemistry Editor's Pick 2024. This collection showcases the most well-received spontaneous articles from the past couple of years and has been specially handpicked by our Chief Editors.

The work presented here highlights the broad diversity of research performed across the sections and aims to put a spotlight on the main areas of interest. All research presented here displays strong advances in theory, experiment, and methodology with applications to compelling problems.

This collection aims to further support Frontiers' strong community by recognizing highly deserving authors.

Table of contents

frontiers | Frontiers in Chemistry

TYPE Editorial
PUBLISHED 30 January 2025
DOI 10.3389/fchem.2025.1562468

OPEN ACCESS

EDITED AND REVIEWED BY
Steve Suib,
University of Connecticut, United States

*CORRESPONDENCE
Luís D. Carlos,
lcarlos@ua.pt

RECEIVED 17 January 2025
ACCEPTED 20 January 2025
PUBLISHED 30 January 2025

CITATION
Carlos LD and Musto P (2025) Editorial: Inorganic chemistry, polymer chemistry, and solid state chemistry editor's pick 2024. *Front. Chem.* 13:1562468. doi: 10.3389/fchem.2025.1562468

Editorial: Inorganic chemistry, polymer chemistry, and solid state chemistry editor's pick 2024

Luís D. Carlos[1]* and Pellegrino Musto[2]

[1]Physics Department and CICECO-Aveiro Institute of Materials, University of Aveiro, Aveiro, Portugal, [2]Institute of Polymers, Composites and Biomaterials, National Research Council of Italy, Pozzuoli, Italy

KEYWORDS

1-butene polymerization, antimicrobial properties, MXene-polymer nanocomposites, sonophotocatalysis, radioactive isotopes

Editorial on the Research Topic
Inorganic chemistry, polymer chemistry, and solid state chemistry editor's pick 2024

We are pleased to introduce the Research Topic Inorganic Chemistry, Polymer Chemistry, and Solid State Chemistry Editor's Pick 2024, which features thirteen contributions, including ten Original Research articles, two Reviews, and one Perspective, authored by thirty-eight researchers from Algeria, Botswana, China, Iran, Italy, Egypt, Estonia, Ethiopia, France, Germany, Nepal, Pakistan, Saudi Arabia, Taiwan, Turkey, Slovenia, South Africa, Sweden, and the United States. This Research Topic highlights key advancements in experimental, theoretical, and *in silico* research on areas of significant interest for the three sections of the journal, aiming to strengthen the vibrant Frontiers community by recognizing highly meritorious contributions.

As follows, a summary of the scientific contributions is given.

Ali et al. employed advanced exfoliation techniques to produce kaolinite nano-silicate sheets with enhanced adsorption properties, demonstrating a superior surface area and safranin dye uptake, supported by thermodynamic and multi-molecular adsorption analyses.

Hameed et al. synthesized La^{3+}-doped $Co_{0.5}Zn_{0.5}LaxFe_{2-x}O_4$ spinel ferrites, demonstrating reduced bandgap and magnetization with increased doping. The materials show potential for microwave and energy storage applications.

Hemmami et al. extracted chitosan from Amanita phalloides, exhibiting excellent antimicrobial properties and water purification potential for pollutants like dyes and drugs, paving the way for eco-friendly applications.

Parajuli reviewed MXene-polymer nanocomposites for biomedical and environmental applications, emphasizing their potential in drug delivery, imaging, and water purification while addressing challenges like biocompatibility.

Khanmiri et al. investigated the leaching behavior of Na and Si in high-level nuclear waste borosilicate glass simulated from a 1000 MWe class PWR reactor, using response surface methodology. Statistical analysis confirmed the significance of pH, contact time, and temperature on leaching, with results consistent with prior studies, validating the applicability of the model.

Hazer et al. synthesized fully biodegradable amphiphilic copolymers from poly (3-hydroxybutyrate) and oligo (2-ethyl oxazoline), showcasing their promising biomedical applications through comprehensive structural characterization.

D'Anania et al. provided mechanistic insights into 1-butene polymerization using DFT simulations, revealing regioselectivity and termination reactions, with implications for designing advanced macromolecular architectures.

Shang uncovered a power-law relationship between neutrons and protons in stable and long-lived radioactive isotopes, offering predictive tools for exploring unknown isotopes.

Esakkimuthu et al. combined molecular dynamics and experimental analysis to study lignin-poly (lactic acid) composites, offering strategies to enhance compatibility by tuning molecular interactions.

Jõul et al. developed lignin-based organic aerogels and porous carbon aerogels, demonstrating tunable morphology and pore structures for tailored applications depending on lignin origin and formulation.

Mapukata et al. reviewed sonophotocatalysis as a promising water treatment technique, highlighting its enhanced efficiency and shorter reaction times. They discussed its mechanisms, commonly used catalysts, and synthesis pathways, along with applications in microbial disinfection and pollutant removal. Challenges, enhancement strategies, and future directions for large-scale implementation were critically analyzed to guide advancements in water treatment technology.

Alem et al. synthesized and characterized two Cr(III) complexes with 1,10-phenanthroline, metformin, and chrysin ligands. The complexes were evaluated for cytotoxicity, antibacterial, and antioxidant activities, with results indicating their potential as promising cytotoxic drug candidates.

Hao et al. synthesized four new U-Te-O compounds under high-temperature, high-pressure conditions: $K_2[(UO_2)(Te_2O_7)]$, $Mg[(UO_2)(TeO_3)_2]$, $Sr[(UO_2)(TeO_3)_2]$, and $Sr[(UO_2)(TeO_5)]$. These structures exhibit diverse uranium coordination and tellurium oxidation states. Architectures include 1D chains, 2D layers, and 3D frameworks, featuring edge-sharing polyhedra and tunnels formed by 6-membered rings. The study highlights the structural flexibility and synthetic potential of the U-Te-O system.

This Research Topic underscores the interdisciplinary nature of contemporary research and celebrates the diverse contributions advancing our understanding of these important fields.

Author contributions

LC: Conceptualization, Writing–original draft, Writing–review and editing. PM: Conceptualization, Writing–original draft, Writing–review and editing.

Funding

The author(s) declare that no financial support was received for the research, authorship, and/or publication of this article.

Acknowledgments

We are grateful to all of the authors who contributed to this Research Topic. We also express our appreciation to the reviewers who evaluated the manuscripts. Their professionalism and feedback were important in enhancing the quality and impact of all published works. Finally, we would like to sincerely thank the editorial staff of Frontiers in Chemistry for their support throughout the development and publication process of this Research Topic.

Conflict of interest

The authors declare that the research was conducted in the absence of any commercial or financial relationships that could be construed as a potential conflict of interest.

The author(s) declared that they were an editorial board member of Frontiers, at the time of submission. This had no impact on the peer review process and the final decision.

Generative AI statement

The author(s) declare that Generative AI was used in the creation of this manuscript. Improve of the text.

Publisher's note

frontiers | Frontiers in Chemistry

TYPE Original Research
PUBLISHED 10 March 2023
DOI 10.3389/fchem.2023.1152113

OPEN ACCESS

EDITED BY
Luiz Fernando Cappa De Oliveira,
Juiz de Fora Federal University, Brazil

REVIEWED BY
Renata Diniz,
Federal University of Minas Gerais, Brazil
Tyler Spano,
Oak Ridge National Laboratory (DOE), United States
Sergey Krivovichev,
Kola Science Centre (RAS), Russia

*CORRESPONDENCE
Evgeny V. Alekseev,
e.alekseev@fz-juelich.de

SPECIALTY SECTION
This article was submitted to Inorganic Chemistry, a section of the journal Frontiers in Chemistry

RECEIVED 27 January 2023
ACCEPTED 22 February 2023
PUBLISHED 10 March 2023

CITATION
Hao Y, Langer EM, Xiao B, Kegler P, Cao X, Hu K, Eichel R-A, Wang S and Alekseev EV (2023), Understanding of the structural chemistry in the uranium oxo-tellurium system under HT/HP conditions. *Front. Chem.* 11:1152113. doi: 10.3389/fchem.2023.1152113

Understanding of the structural chemistry in the uranium oxo-tellurium system under HT/HP conditions

Yucheng Hao[1], Eike M. Langer[2], Bin Xiao[2], Philip Kegler[2], Xin Cao[1], Kunhong Hu[1], Rüdiger-A. Eichel[3,4], Shuao Wang[5] and Evgeny V. Alekseev[3]*

[1]School of Energy Materials and Chemical Engineering, Hefei University, Hefei, China, [2]Institute of Energy and Climate Research (IEK-6), Forschungszentrum Jülich GmbH, Jülich, Germany, [3]Institute of Energy and Climate Research (IEK-9), Forschungszentrum Jülich GmbH, Jülich, Germany, [4]Institut für Materialien und Prozesse für Elektrochemische Energiespeicher-und Wandler, RWTH Aachen University, Aachen, Germany, [5]State Key Laboratory of Radiation Medicine and Protection, School for Radiological and Interdisciplinary Sciences (RAD-X) and Collaborative Innovation Center of Radiation Medicine of Jiangsu Higher Education Institutions, Soochow University, Suzhou, China

The study of phase formation in the U-Te-O systems with mono and divalent cations under high-temperature high-pressure (HT/HP) conditions has resulted in four new inorganic compounds: K_2 [(UO_2) (Te_2O_7)], Mg [(UO_2) $(TeO_3)_2$], Sr [(UO_2) $(TeO_3)_2$] and Sr [(UO_2) (TeO_5)]. Tellurium occurs as Te^{IV}, Te^{V}, and Te^{VI} in these phases which demonstrate the high chemical flexibility of the system. Uranium VI) adopts a variety of coordinations, namely, UO_6 in K_2 [(UO_2) (Te_2O_7)], UO_7 in Mg [(UO_2) $(TeO_3)_2$] and Sr [(UO_2) $(TeO_3)_2$], and UO_8 in Sr [(UO_2) (TeO_5)]. The structure of K_2 [(UO_2) (Te_2O_7)] is featured with one dimensional (1D) $[Te_2O_7]^{4-}$ chains along the *c*-axis. The Te_2O_7 chains are further linked by UO_6 polyhedra, forming the 3D $[(UO_2)$ $(Te_2O_7)]^{2-}$ anionic frameworks. In Mg [(UO_2) $(TeO_3)_2$], TeO_4 disphenoids share common corners with each other resulting in infinite 1D chains of $[(TeO_3)_2]^{4-}$ propagating along the *a*-axis. These chains link the uranyl bipyramids by edge sharing along two edges of the disphenoids, resulting in the 2D layered structure of $[(UO_2)$ $(Te_2O_6)]^{2-}$. The structure of Sr [(UO_2) $(TeO_3)_2$] is based on 1D chains of $[(UO_2)$ $(TeO_3)_2]_\infty^{2-}$ propagating into the *c*-axis. These chains are formed by edge-sharing uranyl bipyramids which are additionally fused together by two TeO_4 disphenoids, which also share two edges. The 3D framework structure of Sr [(UO_2) (TeO_5)] is composed of 1D $[TeO_5]^{4-}$ chains sharing edges with UO_7 bipyramids. Three tunnels based on 6-Membered rings (MRs) are propagating along [001] [010] and [100] directions. The HT/HP synthetic conditions for the preparation of single crystalline samples and their structural aspects are discussed in this work.

KEYWORDS

highpressure, uranium, tellurium, crystals, crystal structure, hightemperature

1 Introduction

The structural and chemical diversity of oxo-tellurium and uranium bearing phases has attracted researchers in the field of solid state and materials chemistry, especially in regard to the diverse oxidation states and coordination geometries that tellurium and uranium can adopt in oxo-based phases (Christy et al., 2016). In nature, a number of minerals within this family

have been reported: cliffordite [(UO_2) (Te_3O_7)] (Brandstatter, 1981), moctezumite ($PbUO_2(TeO_3)_2$) (Swihart et al., 1993), schmitterite ($(UO_2(TeO_3)$ (Meunier and Galy, 1973), and more recently markcooperite ($Pb_2(UO_2)TeO_6$) (Kampf et al., 2010). Besides the attention due to the diverse fundamental aspects of inorganic chemistry, the presence of tellurium within spent nuclear fuel and its corrosive capabilities also makes this thematic relevant for environmental issues (Kleykamp, 1985). Moctezumite and schmitterite, for example, are secondary minerals commonly observed in telluride-bearing ores (Swihart et al., 1993).

The predominant oxidation state of uranium in oxidizing conditions is U^{VI}. Hereby, uranium is present as almost linear trans dioxo-cations (UO_2^{2+}, the so called uranyl group) both in solid state as well as in solution. Within the solid state, the typical coordination environment surrounding the dioxo-cations is a bipyramid, in which the uranyl forms the central axis and additional four to six oxygen atoms occupy sites within the equatorial plane, leading to tetragonal, pentagonal or hexagonal bipyramids (Burns et al., 1997; Hao et al., 2016; Hao et al., 2017a; Hao et al., 2017b; Hao et al., 2018; Hao et al., 2020a; Hao et al., 2022).

Tellurium is typically present as Te^{IV} or Te^{VI} and hereby in form of oxo-anions, tellurites and tellurates, respectively. Te^{IV} is known to adopt several coordination environments, for example, pyramidal TeO_3, disphenoidal TeO_4 and square pyramidal TeO_5 (Balraj and Vidyasagar, 1999; Kim et al., 2007a; Kim et al., 2010). A further inter-connection *via* corner-sharing can lead to complex oxo-tellurium polymers (Lindqvist and Moret, 1973; Hafidi et al., 1986; Mao et al., 2008; Lin et al., 2013). In some compounds several coordination environments of Te can be found, for example, $NH_4ATe_4O_9{\cdot}2H_2O$ (A = Rb, Cs) in which all three coordination geometries of Te are present (Kim and Halasyamani, 2008). Additionally, the lone electron pairs in Te^{IV} have a strong influence on the diversity of Te-O coordination environments. The hexavalent Te (Te^{VI}) typically adopts trigonal bipyramidal, distorted octahedral or tetrahedral coordination in oxygen phases. A few ditellurates contain mixed valent tellurium, Te^{IV} and Te^{VI}, $ACuTe_2O_7$ (A = Sr, Ba, or Pb) and $BaMTe_2O_7$ (M = Mg or Zn) have been previously reported (Yeon et al., 2011; Yeon et al., 2012). Compared to Te^{IV} or Te^{VI}, which are more stable at ambient conditions, inorganic Te^{V} bearing phases were scarcely reported (Lindqvist and Moret, 1973; Hafidi et al., 1986; Balraj and Vidyasagar, 1999; Kim et al., 2007a; Mao et al., 2008; Kim et al., 2010; Lin et al., 2013).

The different structural units have a pronounced influence on the dimensionality of the resulting phases. In the presence of hexavalent uranium with uranyl groups, typically two-dimensional structures dominate (Burns et al., 1996; Burns et al., 1997). This is a direct consequence of oxo-anions typically only being able to condense perpendicular to the terminal uranyl group of the uranyl polyhedra (Burns et al., 1997; Hao et al., 2016; Hao et al., 2017a; Hao et al., 2017b; Hao et al., 2018; Hao et al., 2020; Hao et al., 2022). However, less than half of the currently known phases in uranyl oxo-tellurium system (15 of 32 found in the ICSD (Bergerhoff et al., 1987)), crystallize as two-dimensional structures. In this atypical formation of many one- and three-dimensional structures, the presence of the stereochemically active lone pair, plays a central role (Almond and Albrecht-Schmitt, 2002; Xiao et al., 2016a).

From a materials science point-of-view, studies on tellurium-based phases have been focused on the synthesis of non-centrosymmetric phases (NCS). These phases are of interest for potential applications in the fields of second harmonic generation (SHG) as well as ferro- and piezo-and pyroelectricity (Almond and Albrecht-Schmitt, 2002; Xiao et al., 2016a). This acentric behavior is also addressed by the presence of the aforementioned stereochemically active lone pairs present in Te^{IV}. This has resulted in rich results of NCS crystal structures in recent years (Chi et al., 2006; Kim et al., 2014). However, the presence of acentric tellurite groups does not necessarily need to result in NCS phases. The acentric units can order themselves to counteract a potential global NCS structure (Chi et al., 2006; Kim et al., 2007b; Kim et al., 2014).

We have recently systematically studied the A-U-Te-O (A = alkali and alkaline Earth metal) system under extreme conditions (HT/HP). Our goal is to further understand the different chemical behavior of actinide-tellurium oxo-phases from extreme conditions compared to conventional ones and to develop a methodology of how these phases crystallize under the extreme environment. As a result of this study, a series of quaternary oxide tellurium materials, K_2 $[(UO_2)$ $(Te_2O_7)]$, Mg $[(UO_2)$ $(TeO_3)_2]$, Sr $[(UO_2)$ $(TeO_3)_2]$ and Sr $[(UO_2)$ $(TeO_5)]$ have been prepared by the HT/HP solid state reaction method. In which, K_2 $[(UO_2)$ $(Te_2O_7)]$ is a very rare example of a Te^{V} bearing phase. The detailed HT/HP synthetic routes, high-temperature and high-pressure behavior, and topology of the structures are discussed.

2 Experimental section

Caution! *The $UO_2(NO_3)_2{\cdot}6H_2O$ used in this work contained natural uranium; nevertheless the standard precautions for handling radioactive materials must be followed. The γ-UO_3 was formed simply by heating the uranyl nitrate and analyzing it with powder XRD* (Engmann and De Wolff, 1963) *for its purity as we always use the γ-UO_3 as the initial compound in the HT/HP synthesis.*

2.1 Crystal growth

All the titled compounds were synthesized in the form of small single crystals using the high-temperature/high-pressure solid-state method. All the chemicals were obtained from commercial sources as analytically pure and used without further purification.

$K_2[(UO_2)$ $(Te_2O_7)]$. Uranium trioxide UO_3 (20.0 mg, 0.0699 mmol), KNO_3 (21.2 mg, 0.208 mmol), TeO_2 (22.3 mg, 0.140 mmol), and H_6TeO_6 (64.2 mg, 0.279 mmol) in a molar ratio of UO_3: KNO_3: TeO_2: H_6TeO_6 = 1 : 3: 2 : 4 were mixed together and finely ground. Then, the mixture was filled into a platinum capsule (outer diameter: 4 mm, wall thickness: 0.2 mm, length:7 mm). The capsule was sealed on both sides with an impulse micro welding device (Lampert PUK U4) and placed into the center of a 1/2-inch piston cylinder talc-pyrex assembly. After this, the capsule was inserted into a 6 mm diameter MgO spacer and positioned in the center of a tapered graphite furnace. The final run pressure of 3.5 GPa was applied within 30 min, then the temperature program was started. With a heating rate of 100 K min^{-1} the temperature was increased to the maximum temperature of 1173 K. After 1 h of annealing, the temperature was decreased to 570 K over a time period of 106 h (cooling rate 0.11 K min^{-1}). At 570 K, the experiment was automatically quenched to room temperature. After decompression for 20 min, the capsule was extracted out of the high-pressure assembly and broken. The product of yellow

TABLE 1 Crystallographic data for K_2 [(UO_2) (Te_2O_7)], Mg [(UO_2) $(TeO_3)_2$], Sr [(UO_2) $(TeO_3)_2$] and Sr [(UO_2) (TeO_5)].

Compound	K_2 [(UO_2) (Te_2O_7)]	Mg [(UO_2) $(TeO_3)_2$]	Sr [(UO_2) $(TeO_3)_2$]	Sr [(UO_2) (TeO_5)]
FW	1,428.62	645.53	708.84	565.24
Space group	*C2/c*	*Cmca*	*Pbam*	*Pbam*
a Å)	10.76408)	7.58644)	11.5299 (12)	12.53772)
b Å)	10.1671 (12)	11.51725)	7.89319)	12.45992)
c Å)	7.1707 (10)	7.51433)	4.03614)	7.57807 (16)
β (deg)	93.101 (10)	90	90	90
V (Å^3)	783.60 (15)	656.555)	367.316)	1,183.834)
Z	4	4	2	8
λ(Å)	0.71073	0.71073	0.71073	0.71073
F (000)	1,224	1,088	1,476	1955
D_c (g cm^{-3})	6.064	6.531	6.409	6.506
GOF on F^2	1.081	1.035	1.085	1.093
R_1	0.0201	0.0267	0.0393	0.0214
*w*R2	0.0561	0.0695	0.0900	0.0710
$R1 = \sum \|\|F_o\| - \|F_c\|\| / \sum \|F_o\|$, $wR2 = \left\{\sum w[(F_o)^2 - (F_c)^2]^2 / \sum w[(F_o)^2]^2\right\}^{1/2}$				

crystals were picked up for further analysis. The yield was impossible to be determined due to the similarity of broken glass pieces and obtained crystals.

Mg[(UO_2) $(TeO_3)_2$]. For the synthesis of Mg [(UO_2) $(TeO_3)_2$], UO_3 (20.0 mg, 0.0699 mmol), $Mg(NO_3)_2$ (20.7 mg, 0.140 mmol), TeO_2 (33.5 mg, 0.211 mmol), and H_6TeO_6 (16.1 mg, 0.070 mmol) were weighed with a molar ratio of 1:3:1:2 and subsequently thoroughly ground before being filled into platinum capsule. The operations of sealing the platinum capsule and opening it after the reactions are same as mentioned above for the synthesis of K_2 [(UO_2) (Te_2O_7)]. The pressure of 3.5 GPa was used within 30 min, then the temperature program was started. It was heated up to 1373 K with a heating rate of 100 K min^{-1}. After a holding time of 4 h at 1373 K, the temperature was decreased to 1173 K in 1h, and then cooled to 623 K over a time period of 90 h (cooling rate 0.10 K min^{-1}). At 623 K, the experiment was automatically quenched to room temperature. After decompression for 20 min, the capsule was extracted out of the high-pressure assembly and broken. The product containing small yellow crystals were picked up for further analysis.

Sr[(UO_2) $(TeO_3)_2$] and Sr[(UO_2) (TeO_5)]. Both phases co-precipitated using a finely ground mixture of UO_3 (30.0 mg, 0.105 mmol), $Sr(CO_3)$ (15.5 mg, 0.105 mmol), TeO_2 (16.7 mg, 0.105 mmol), and H_6TeO_6 (24.1 mg, 0.0.105 mmol) with a molar ratio of 1:1:1:1. The pressure of 3.5 GPa was applied within 30 min, then the temperature program was started. It was heated up to 1273 K with a heating rate of 100 K min^{-1}. After a holding time of 4 h at 1273 K, the temperature was cooled down to 1073 K in 1h, and then decreased to 573 K over a time period of 50 h (cooling rate 0.17 K min^{-1}). At 573 K, the experiment was automatically quenched to room temperature. After decompression for 20 min, the capsule was extracted out of the high-pressure assembly and broken. The product containing small yellow crystals together with colorless remains of the educts, mainly consisting of $SrCO_3$. The small yellow crystals were picked up for further analysis.

2.2 Crystallographic studies

Single crystal X-ray diffraction data for all four compounds were collected on an Agilent Technologies SuperNova diffractometer with Mo-Kα radiation (λ = 0.71073 Å) at room temperature. All data sets were corrected for Lorentz and polarization factors as well as for absorption by the multi-scan method (Sheldrick, 1998). The structures of all four compounds were solved by the direct method and refined by a full-matrix least-squares fitting on F^2 by SHELX (Almond and Albrecht-Schmitt, 2002; Xiao et al., 2016a). Their structures were checked for possible missing symmetry elements using PLATON with the ADDSYM algorithm, and no higher symmetry was found (Spek, 2001). Crystallographic data and structural refinements for all compounds are summarized in Table 1. More information of the important bond distances and angles of both compounds are listed in Supplementary Table S1. The crystal structures were deposited to the CCDC with the following numbers CSD2238172, CSD2238173, CSD2238174, CSD2238175 for the K_2 [(UO_2) (Te_2O_7)], Mg [(UO_2) $(TeO_3)_2$], Sr [(UO_2) $(TeO_3)_2$] and Sr [(UO_2) (TeO_5)], respectively.

2.3 Bond-valence analysis

As a semi-empirical method for the approximate determination of valence states, BVS of all atoms in both phases were calculated.

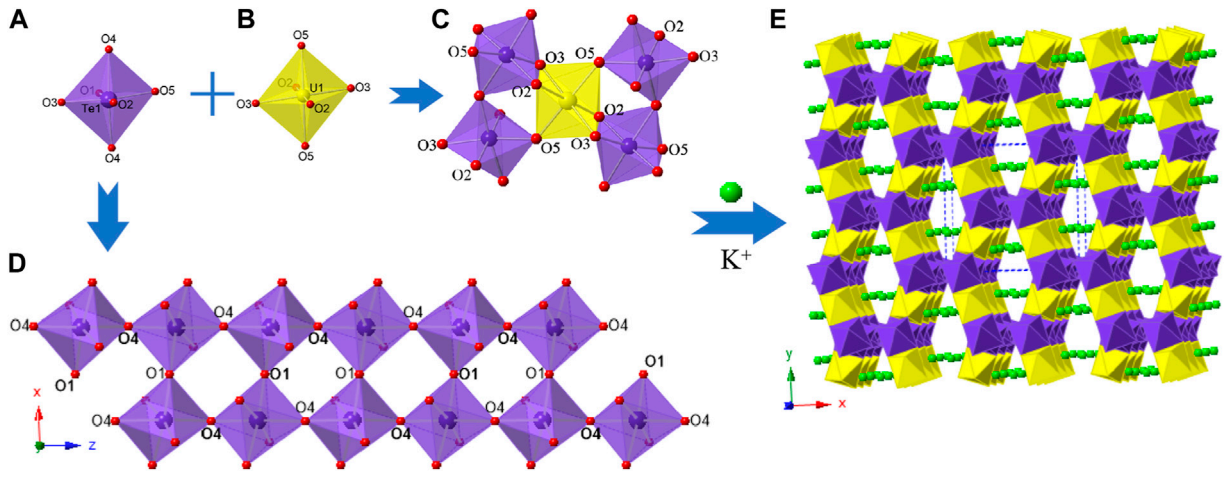

FIGURE 1
K_2 [(UO_2) (Te_2O_7)]: **(A)** TeO_6 polyhedron; **(B)** UO_6 polyhedron, **(C)** coordination environment for UO_6; **(D)** a Te_O double chain along the *c*-axis; and **(E)** view of the 3D structure along the *c*-axis. K atoms, TeO_6 polyhedra, UO_6 polyhedra, and O atoms are shown in green, purple, yellow and red, respectively.

The bond-valence parameters for U(VI)-O, K(I)-O, Mg(II)-O, Sr(II)-O, Te(IV)-O, Te(V)-O and Te(VI)-O were used according to Burns (Burns et al., 1997), Brese and O'Keeffe (Brown and Altermatt, 1985; Brese and O'Keeffe, 1991).

3 Results and discussion

3.1 Crystal growth

The investigation of the *A*-U-Te-O (*A* = alkali and alkaline Earth metal) system under extreme HT/HP conditions (3.5GPa, 1173–1373 K) yielded four novel compounds: K_2 [(UO_2) (Te_2O_7)], Mg [(UO_2) $(TeO_3)_2$], Sr [(UO_2) $(TeO_3)_2$] and Sr [(UO_2) (TeO_5)]. K_2 [(UO_2) (Te_2O_7)] was obtained through the usage of UO_3: KNO_3: TeO_2: H_6TeO_6 in a ratio of 1 : 3: 2 : 4. Although analytical-grade $Te^{IV}O_2$ and $H_6Te^{VI}O_6$ were used as an initial reagent, interestingly, tellurium occurs as Te^{V} with a 5+ oxidation state in K_2 [(UO_2) (Te_2O_7)]. We concluded that $Te^{IV}O_2$ and $H_6Te^{VI}O_6$ undergo an oxidation-reduction chemical reaction opposite to the disproportionation of Te^{V} under the extreme conditions (3.5GPa, 1173 K). Attempts were made to synthesize K_2 [(UO_2) (Te_2O_7)] through high temperature solid state reaction at ambient pressure, however this was unsuccessful. This suggests the high pressure is an essential factor for this redox reaction. For the synthesis of Mg [(UO_2) $(Te^{IV}O_3)_2$]: UO_3, $Mg(NO_3)_2$, TeO_2 and H_6TeO_6 were taken in molar ratios of 1 : 2: 3:1. Whereas both phases of Sr [(UO_2) $(Te^{IV}O_3)_2$] and Sr [(UO_2) $(Te^{VI}O_5)$] co-precipitated using a finely ground mixture of UO_3, $Sr(CO_3)$, TeO_2 and H_6TeO_6 with a molar ratio of 1:1:1:1. We presumed that the ratios of TeO_2 and H_6TeO_6 were used in the original reagents has also played a key role for the final oxidation states of tellurium in the compounds. The obtained materials have been found in the form of relatively small single crystals (up to 1 mm size). We presume that they grow up within so called self-flux which is usual for the materials crystallization from multicomponent high-temperature solid-state systems (Balraj and Vidyasagar, 1999; Kim et al., 2007a; Kim et al., 2010).

3.2 Crystal structures

3.2.1 Structure of K_2[(UO_2) (Te_2O_7)]

K_2 [(UO_2) (Te_2O_7)] crystallizes in the monoclinic space group *C*2/c. The structure of K_2 [(UO_2) (Te_2O_7)] can be described as a 3D open framework composed of uranium and tellurium polyhedra (Figure 1). Its framework is featured with 1D $[Te_2O_7]^{4-}$ double-chains, formed by a vertex (O4 and O1) sharing linkage along the *c*-axis (Figure 1D). These $[Te_2O_7]^{4-}$ double-chains are further connected by UO_6 polyhedra, forming the 3D $[(UO_2)$ $(Te_2O_7)]^{2-}$ anionic framework (Figure 1C; Figure 1E). Relatively large 1D tunnels with 10-MRs (10.167 Å ×5.540 Å) can be observed in the structure along the *c*-axis (Figure 2). K^+ cations fill the channels to balance the charge of the framework.

There is one crystallographically unique tellurium site Te (1), one uranium site U (1), one potassium site K (1) and five oxygen sites O (1)-O (5) in the structures of K_2 [(UO_2) (Te_2O_7)], respectively. Corner-shared TeO_6 octahedra form a one-dimensional double-chain along the *c*-axis, and these chains are further connected by UO_6 polyhedra along the *b*-axis, resulting in the 3D network (Figure 1E). The UO_6 pseudooctahedral coordination alternate between the Te-O double chains and are corner-shared (O5) to two TeO_6 octahedra and edge-shared (O2-O3) to two TeO_6 octahedra. The Te-O bond distances in TeO_6 octahedra range between 1.888(4) and 1.979(4) Å, whereas the U-O bond distances are in the range of [1.992(4)-2.031(4) Å]. Potassium cations are 10-oxygen coordinated and K-O bond distances range from 2.676(5) to 3.304(5) Å. All the bond angles and bond lengths in K_2 [(UO_2) (Te_2O_7)] are as shown in Supplementary Table S1. These bond lengths are comparable with previously reported works

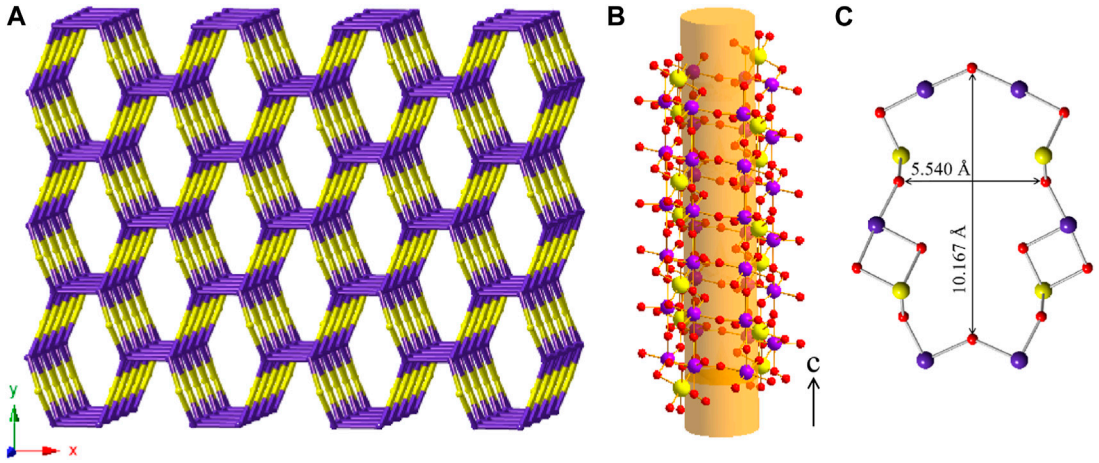

FIGURE 2
(A) View of the cation framework topology representation of K_2 [(UO_2) (Te_2O_7)] along the *c*-axis; **(B)** Side view of one 10-MRs tube along the [001] direction with ball-and-stick representation; **(C)** the pore size of a 10-MRs of the [$(UO_2)Te_2O_7$] tube. K, Te, U and O atoms are shown in green, purple, yellow and red, respectively.

(Almond and Albrecht-Schmitt, 2002; Chi et al., 2006; Kim et al., 2007b; Kim et al., 2014; Xiao et al., 2016a). From BVS calculations, the valences for U cations are suggested to be 6+ with values for the U1 at ca. 6.11. The valences for K cations are 1+ with BVS values for K1 at ca. 1.25.

It is noteworthy to compare the structure of K_2 [(UO_2) (Te_2O_7)] with the series of *A* [$CuTe_2O_7$] (A = Sr, Ba, or Pb) and Ba [MTe_2O_7] (*M* = Mg or Zn) (Yeon et al., 2011; Yeon et al., 2012), due to them having similar chemical composition with isovalent cations substituting UO_2^{2+} groups through divalent cations. Although K_2 [(UO_2) (Te_2O_7)], *A* [$CuTe_2O_7$] (A = Sr, Ba, or Pb) and Ba [MTe_2O_7] (*M* = Mg or Zn) have same stoichiometries, the structure of K_2 [(UO_2) (Te_2O_7)] is different from that series. In K_2 [(UO_2) (Te_2O_7)], Te atoms occur as Te^V as TeO_6 polyhedra, whereas in *A* [$CuTe_2O_7$] (A = Sr, Ba, or Pb) and Ba [MTe_2O_7] (*M* = Mg or Zn) they are mixed valent tellurium, Te^{4+} and Te^{6+}. $SrCuTe_2O_7$ and $PbCuTe_2O_7$ are isostructural, and their two-dimensional crystal structure consists of 2D layers based upon corner-sharing CuO_5 square pyramids, TeO_6 octahedra, and TeO_4 disphenoids. Ba*M*Te_2O_7 (*M* = Mg^{2+} and Zn^{2+}) are iso-structural with $BaCuTe_2O_7$, and exhibit a crystal structure composed of layers of corner-shared MO_5 (*M* = Mg^{2+} or Zn^{2+}) square pyramids, TeO_6 octahedra, and TeO_4 polyhedra. The $[MTe_2O_7]^{2-}$ anionic layers (*M* = Mg^{2+} and Zn^{2+}) stack along the *b*-axis, and are separated by Ba^{2+} cations. Comparing these phases we can presume that high-pressure conditions applied in our study not only condensed the final structures (from 2D towards 3D), but also influenced the redox stability of Te with stabilization of the rare Te^V cation.

In order to reveal the complex topological network of K_2 [(UO_2) (Te_2O_7)], we simplify the anionic uranyl tellurium framework $[(UO_2)Te_2O_7]^{2-}$, by removing the oxygen atoms, whilst the UO_6 and TeO_6 polyhedra were viewed as single nodes. As shown in Figure 2A, the simplified anionic net of K_2 [(UO_2) (Te_2O_7)] can be described as a 2-nodal net topological type with a point symbol of $\{3^2.4^2.5^2.6^3.7\}_2\{3^2.6^2.7^2\}$ (Blatov, 2006; Blatov et al., 2010; Alexandrov et al., 2011), which is a 4, 5-*c* net with stoichiometry (4-c) $(5\text{-c})_2$.

Natural tiling is an efficient approach to represent a network proposed by Blatov *et al.* (Blatov et al., 2007), which can be used for illustrating the channel system and cavities by tracing the colors of the tiles clearly as shown in Figure 3A. The framework of K_2 [(UO_2) (Te_2O_7)] is built from a novel composite building unit (*CBU*) $[10^2:6:4:3^2]$ (Figure 1B), with the 10-MR tunnels along the *c*-axis. Each $[10^2:6:4:3^2]$ *CBU* connects to four other neighboring ones, *via* their 10, 6, four or 3-MRs defining the 3D tiling network. Compared with the previously reported uranyl borates, phosphates and borophosphates system, the tilting network of this uranyl tellurium system is simpler with only one unique *CBU*. (Burns et al., 1997; Hao et al., 2016; Hao et al., 2017a; Hao et al., 2017b; Hao et al., 2018; Hao et al., 2020a; Hao et al., 2022), (Hao et al., 2013; Hao et al., 2014; Hao et al., 2020b), (Hao et al., 2020c; Hao et al., 2020d; Li et al., 2022) Similar situation is for the structure of Sr [(UO_2) (TeO_5)] (see below).

3.2.2 Structure of Mg[(UO_2) $(TeO_3)_2$]

Mg [(UO_2) $(TeO_3)_2$] crystallizes in the orthorhombic space group *Cmca*. Mg, U and Te occupy one crystallographically independent position each and for oxygen three crystallographically independent positions are occupied. As shown in Figure 4, Uranium is eight fold-coordinated by oxygen in bipyramidal fashion. The two oxygen positions located at the pyramid tops have a U-O bond length of 1.805(6) Å. Together with a bond angle of 180.0° between O-U-O along the central axis, these are typical values for a uranyl group. The equatorial oxygen atoms adopt bond-distances from 2.361(7) to 2.527(5) Å.

Tellurium is coordinated by four oxygen atoms resulting in disphenoidal symmetry. The electron lone pair points towards the top center of the disphenoid. The bond distances range from 1.881(4) to 2.042(3) Å. This coordination is found to be common within Te^{IV} structures (Balraj and Vidyasagar, 1999; Xiao et al., 2016b).

In Mg [(UO_2) $(TeO_3)_2$], TeO_4 disphenoids share common corners with each other resulting in infinite onedimensional

10.3389/fchem.2023.1152113

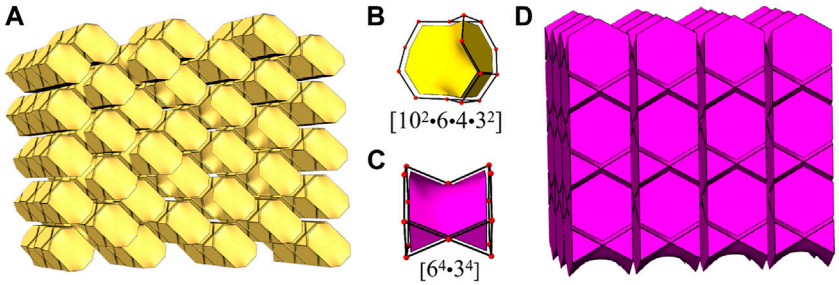

FIGURE 3
View of the channel systems in K_2 [(UO_2) (Te_2O_7)] **(A)** and Sr [(UO_2) (TeO_5)] **(D)** using natural tiling, new *CBU*s [$10^2?6?4?3^2$] **(B)** and [$6^4?3^4$] **(C)**.

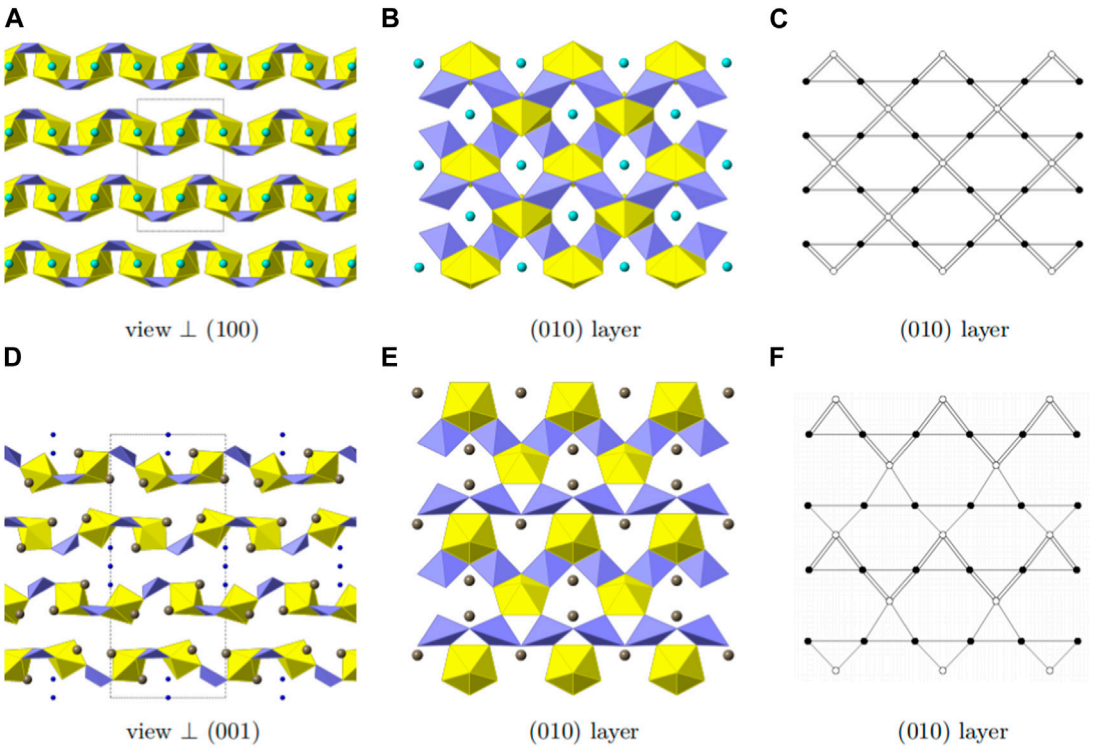

FIGURE 4
Structural and topologic depiction of Mg [(UO_2) $(TeO_3)_2$] **(A–C)** and in comparison Tl_3 ($(UO_2)_2$ $(Te_2O_5(OH))$ (Te_2O_6))?2(H_2O) **(D–E)**. In **(A)** and **(D)** a side view of the structure of the former and the latter can be seen. The unit-cell outline is shown in dashed-lines. In Mg [(UO_2) $(TeO_3)_2$], an *ABAB* ordering principle is visible whereas an *ABCDABCD* is found in Tl_3 ($(UO_2)_2$ $(Te_2O_5(OH))$ (Te_2O_6))·2(H_2O). In **(B)** and **(E)** a single (010) layer for both structures is shown and the according topology is depicted in **(C)** and **(F)**, respectively. UO_7 polyhedra are depicted in yellow, TeO_4 polyhedra in light purple, Mg in cyan, Tl in grey and water molecules in deep blue.

chains of $[(TeO_3)_2]^{4-}$ propagating along the a-axis. These chains link the uranyl bipyramids by edge sharing along two edges of the disphenoids. This results in two-dimensional sheets of [(UO_2) (Te_2O_6)]$^{2-}$ (Figure 4B). Within these sheets, four UO_8 hexagonal bipyramids and four TeO_4 disphenoids form a ring structure. This is well visible in the topologic description shown in Figure 4C.

Mg^{2+} are located within the rings of UO_8 and TeO_4 mentioned above. It is coordinated by six oxygen atoms in distances ranging from 2.051(5) to 2.284(6) Å leading to a rectangular bipyramid. Mg^{2+} acts as a counter charge for the [(UO_2) (Te_2O_6)]$^{2-}$ layers-resulting in a neutrally charged phase. Bond valence sum calculations for all positions (Mg~ 2.03, U~5.98, Te~4.06) yield values in accordance to the assumed oxidation states.

The layers found in Mg [(UO_2) $(TeO_3)_2$] most resemble the layers found in Tl_3 ($(UO_2)_2$ $(Te_2O_5(OH))$ (Te_2O_6))·2(H_2O) (Almond and Albrecht-Schmitt, 2002). The layers found in the latter are depicted in Figure 4E. Both structures possess one-dimensional chains of corner-sharing disphenoidal coordinated

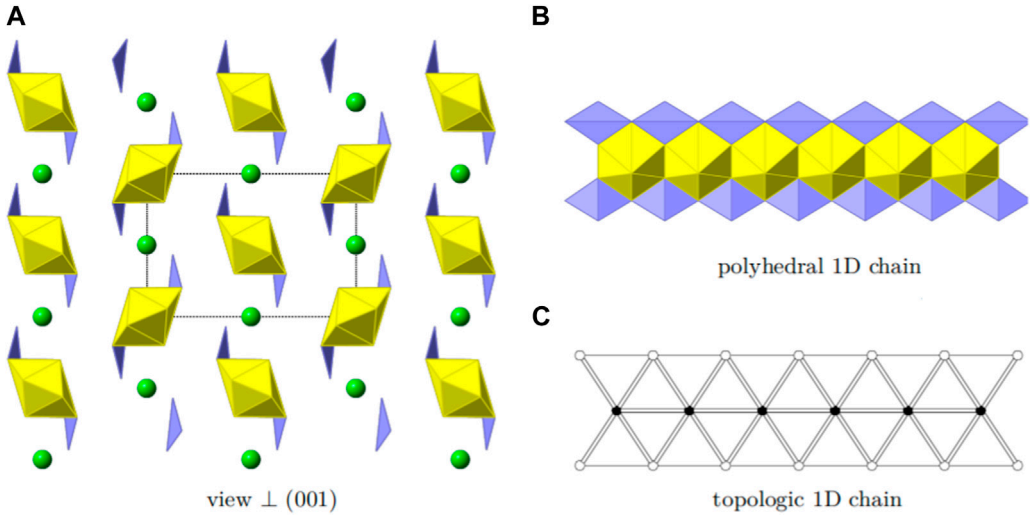

FIGURE 5
Structural and topologic depiction of Sr $[(UO_2)\ (TeO_3)_2]$. In **(A)** a side view of the structure can be seen. The unit-cell outline is shown in dashed-lines. In **(B)**, chains of $[(UO_2)\ (TeO_3)_2]^{2-}$ propagating into the [001] direction are shown. The according topology is depicted in **(C)**.

Te. Due to the presence of Mg^{2+} and Tl^{1+}, both structures are electro-neutral despite the charged layers. The essential difference between the two structures, arises from the presence of OH^- groups in Tl_3 $((UO_2)_2\ (Te_2O_5(OH))\ (Te_2O_6))\cdot 2(H_2O)$ in comparison to their absence in Mg $[(UO_2)\ (TeO_3)_2]$. In the former, two different chains of corner-sharing disphenoidal coordinated Te are present $[(Te_2O_5(OH)]^{3-}$ and $[(TeO_3)_2]^{4-}$. In Mg $[(UO_2)\ (TeO_3)_2]$ only chains of $[(TeO_3)_2]^{4-}$ are present. This leads to constant edge-sharing connections between tellurite disphenoids and uranyl bipyramids in Mg $[(UO_2)\ (TeO_3)_2]$, whereas edge-sharing connections are only found along the $[(TeO_3)_2]^{4-}$-chains in Tl_3 $((UO_2)_2\ (Te_2O_5(OH))\ (Te_2O_6))\cdot 2(H_2O)$ and corner-sharing positions along the $[(Te_2O_5(OH)]^{3-}$ chains. The difference of the resulting layers can also clearly be seen, whilst comparing the topology graphs for both structures. (Figures 4C,F).

Due to the different connections, the uranyl bipyramids in Tl_3 $((UO_2)_2\ (Te_2O_5(OH))\ (Te_2O_6))\cdot 2(H_2O)$ are only pentagonal whereas they are hexagonal in Mg $[(UO_2)\ (TeO_3)_2]$. This is the first report of hexagonal bipyramids in two-dimensional phases containing U and Te. Otherwise, these are only found in three-dimensional phases, such as within UTe_3O_9 (Galy and Meunier, 1971) or Na $[(UO_2)Te_6O_{13}(OH)]$ (Almond and Albrecht-Schmitt, 2002; Xiao et al., 2016a). It is also worth mentioning, that both phases have different packing orders of their layers. In Mg $[(UO_2)\ (TeO_3)_2]$ only two layers are stacked until the original layer is repeated (*ABAB* stacking), whereas four layers are necessary in Tl_3 $((UO_2)_2\ (Te_2O_5(OH))\ (Te_2O_6))\cdot 2(H_2O)$ (*ABCDABCD* stacking) (Figures 4A,D).

3.2.3 Structure of Sr$[(UO_2)\ (TeO_3)_2]$

Sr $[(UO_2)\ (TeO_3)_2]$ crystallizes in the orthorhombic space group *Pbam*. U, Sr and Te each are present on one independent position. As U and Sr lie on special positions (0.5, 0.5, 0.5 and 0.5, 0.0, 0.5, respectively) and Te lies on a general position in respect to *x* and *y* (0.2894, 0.2644, 0.0), the multiplicity results in a U:Te molar ratio of 1:2. Oxygen is present on four independent positions, each of them are general positions. The structure of Sr $[(UO_2)\ (TeO_3)_2]$ is depicted in Figure 5A.

Uranium is coordinated by two short-bonded actinyl oxygen with $\langle U\text{-}O_{yl}\rangle$ = 1.825 (13) Å and six equatorial oxygen ($\langle U\text{-}O_{eq}\rangle$ = 2.349(7) Å) forming hexagonal bipyramids and thus hexavalent U is present. BVS calculations are well in agreement with 6.21 *v. u.* Te is coordinated by four oxygen atoms forming a disphenoidal coordination polyhedron. This coordination is typical for tetravalent Te and BVS calculations yield 4.01 *v. u.*, supporting the assignment for tetravalent Te. The bonding distances range from 1.849 (13) to 2.102(4) Å. Eight oxygen positions surround Sr with bond distances of 2.525(7) to 3.029 (14) Å. Sr is predominantly stable as divalent Sr and a BVS of 2.09 *v. u.* is well in agreement with this.

The structure is based on one-dimensional chains of $[(UO_2)\ (TeO_3)_2]^{2-}$ propagating into the [001] direction. These chains are formed by edge-sharing uranyl bipyramids which are additionally fused together by two TeO_4 disphenoids, edge-sharing along two edges. Such a chain is depicted in Figure 5B. The according topology is shown in Figure 5C. The charge of the chains are compensated by the presence of the Sr^{2+} cations. The apparent additional void space is filled by the electron-lone pairs from the tetravalent Te. These are directed along the [010].

It is worth comparing the structures of chemical analogues Mg $[(UO_2)\ (TeO_3)_2]$ and Sr $[(UO_2)\ (TeO_3)_2]$. In Mg $[(UO_2)\ (TeO_3)_2]$, TeO_4 disphenoids share common corners with each other resulting in infinite 1D chains of $[(TeO_3)_2]^{4-}$ propagating along the *a*-axis. These chains link the uranyl bipyramids by edge sharing along two edges of the disphenoids, resulting in the 2D layered structure of $[(UO_2)\ (Te_2O_6)]^{2-}$. Mg^{2+} counter cations are located between the inter-layers to balance the anionic layered charge. The structure of Sr $[(UO_2)\ (TeO_3)_2]$ features a 1D chain structure $[(UO_2)\ (TeO_3)_2]^{2-}$, propagating into the *c*-axis. These chains are formed by edge-sharing uranyl bipyramids which are additionally fused together

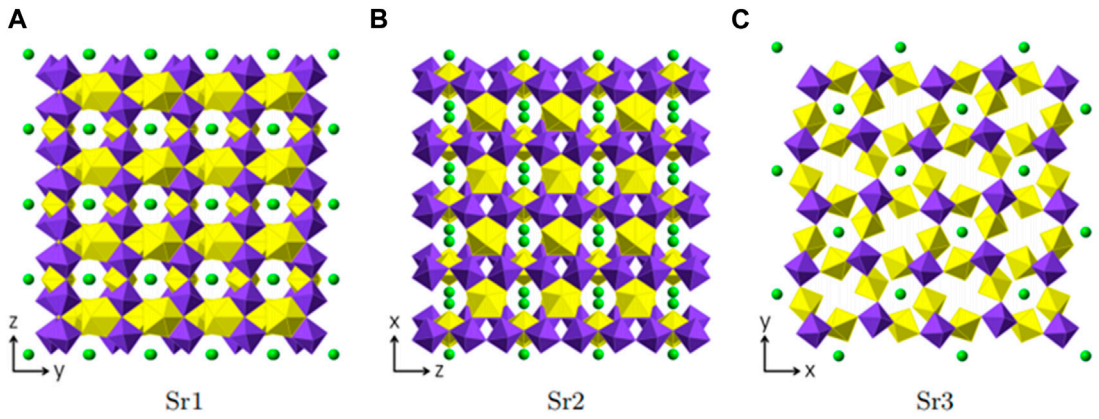

FIGURE 6
Sr positions within Sr [(UO_2) (TeO_5)] depicted in green. Each figure shows the complete uranyl tellurate framework with only the according Sr^{2+} positions depicted. **(A)** Srl -view ⊥[100], **(B)** Sr2-view⊥[010] and **(C)** Sr3-view⊥[001].

by two TeO_4 disphenoids, which also share two edges. We can see that with the counter cations radii increasing from Mg^{2+} to Sr^{2+} this results in the structure of materials changing from a 2D to a 1D structural type. In this case we can speak of a morphotropic transition within A^{II} [(UO_2) $(TeO_3)_2$] (A^{II}- alkali-earth elements).

3.2.4 Structure of Sr[(UO_2) (TeO_5)]

Sr [(UO_2) (TeO_5)] crystallizes in the orthorhombic space group *Pbam*. The crystallographic data is given in Table 1. It forms a 3D framework structure made up of UO_7 and TeO_6 polyhedra with Sr^{2+} cations filling the voids to achieve charge neutrality.

Two uranium positions are present within the structure and both have a typical bipyramidal pentagonal oxygen coordination of UO_7. The bond lengths of the uranyl oxygen positions are < U1-O_{yl}> = 1.81598) Å and <U2-O_{yl}> = 1.822(7) Å. This can be explained by the dense packing of the framework leading to a stronger coordination of the equatorial plane with average bond lengths of <U1-O_{eq}> = 2.353(7) Å and <U2-O_{eq}> = 2.357(1) Å, respectively. The closer coordination of the equatorial oxygen positions is charge compensated by the uranyl bonds. Both, $U1O_7$ and $U2O_7$, are not interconnected to each other, are however interlinked by octahedral TeO_6 units. The resulting framework is described in more detail below.

Te only adopts a single position and is coordinated by six oxygen atoms to form distorted octahedral polyhedra (Supplementary Figure S1). Hereby, two positions are slightly elongated (O1 and O4) with Te-O1 = 1.975(2) Å and Te-O4 = 1.980(2) Å. The other four positions range from 1.8805) Å to 1.9802) Å. Two TeO_6 polyhedra are interconnected by corner sharing of the O1 and O4 positions, leading to one-dimensional chains propagating in the [001] direction.

Three crystallographically independent Sr positions are present in Sr [(UO_2) (TeO_5)]. All three positions are shown in Figures 6A–C. Sr1 is located within [100] channels and coordinated tenfold by oxygen with distances ranging from 2.460(5) Å to 3.175(7) Å. Sr2 and Sr3 are eight-fold coordinated with distances ranging from 2.429(5) Å to 2.985(9) Å and 2.454(5) Å to 2.935(5) Å, respectively. Sr2 is located within [010] channels and Sr3 within [001] channels. To describe the framework structure of Sr [(UO_2) (TeO_5)], it is best to divide the structure into simpler one and two-dimensional units. This is shown in Figure 7. As already stated above, the structure is made up of infinite $[TeO_5]^{4-}$ chains. Two opposite edges of the TeO_6 octahedron are involved in edge-sharing with $U2O_7$ and $U1O_7$ bipyramids and the two remaining oxygen positions each corner-share with a $U1O_7$ and a $U2O_7$ (Supplementary Figure S1). The same framework topology can be found in Na_2 [(UO_2) (TeO_5)] (Almond and Albrecht-Schmitt, 2002; Xiao et al., 2016a).

Sr [(UO_2) (TeO_5)] has a multi-intersecting channel system as shown in Figure 8. Two 6-MRs channels exist along the *a*- and *b*-axis with diameters of ca. 6.6 Å × 4.7 Å and ca. 6.3 Å × 4.7 Å (distances are based on two opposite O atoms), respectively. (Figures 8B,C). Two 8-MRs channels is along the *c*-axis with diameters of ca. 6.5 Å × 5.7 Å and ca. 6.9 Å × 5.8 Å (Figures 8D,E). For the purpose of revealing the complex topological network of Sr [(UO_2) (TeO_5)], we also simplified the anionic uranyl tellurium framework [(UO_2) (TeO_5)]$^{2-}$, by removal of the oxygen anions, whilst the UO_7 and TeO_6 polyhedra were viewed as single nodes. As shown in Figure 8A, the simplified anionic net of Sr [(UO_2) (TeO_5)] can be described as a 2-nodal net topological type with a point symbol of $\{3^2.6^2.7^2\}\{3^4.4^2.6^4.7^5\}$; which is a 4, 6-*c* net with stoichiometry of (4-c) (6-c) (Brese and O'Keeffe, 1991; Blatov et al., 2010; Alexandrov et al., 2011). Natural tiling illustration of Sr [(UO_2) (TeO_5)] is shown in Figure 3D. The framework of Sr [(UO_2) (TeO_5)] is built from a novel *CBU* of $[6^4.3^4]$ (Figure 3C), with the 6-MR intersecting tunnels along the corresponding axis. Each $[6^4.3^4]$ *CBU* connects to eight other neighboring ones, *via* their six or 3-MRs window defining the 3D tiling network.

4 Conclusion

We have shown that by using extreme synthetic conditions (high-temperature high-pressure) novel single crystalline phases in the U-Te-O system can be obtained. Four new uranyl tellurium complex oxides obtained in this study, K_2 [(UO_2) (Te_2O_7)], Mg [(UO_2) $(TeO_3)_2$], Sr [(UO_2) $(TeO_3)_2$] and Sr [(UO_2) (TeO_5)], featured 1D-chain to 3D-framework structures. Surprisingly, tellurium is occurs as Te^V in one of the obtained materials, K_2 [(UO_2) (Te_2O_7)], which is a rare case in tellurium bearing inorganic phases. Under the same pressure (3.5 GPa)

10.3389/fchem.2023.1152113

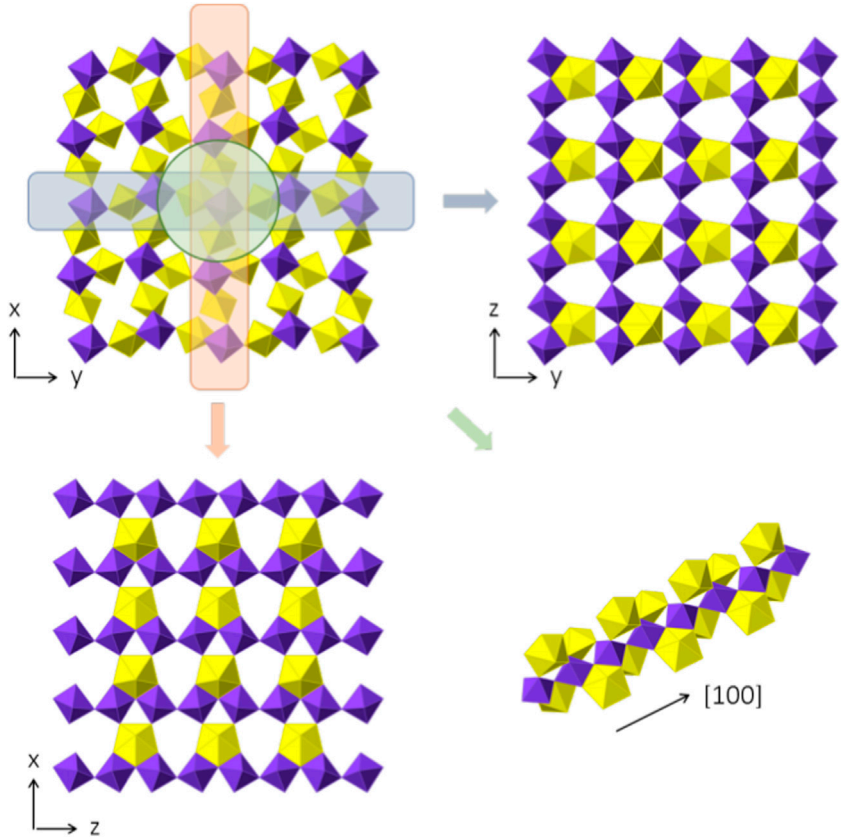

FIGURE 7
Framework composition of Sr [(UO_2) (TeO_5)]. In the top-left, the complete structure, omitting the Sr positions for clarity, which are positioned within the empty voids, is shown, perpendicular to [001]. Two-dimensional slices of the (100) and (010) plane are shown on the top right and the lower left. The layers are basically identical, despite the orientation. In the lower right, the infinite chain of $[TeO_5]^{4-}$ polyhedra is shown with the corner and edge sharing with UO_7 pentagonal bipyramids.

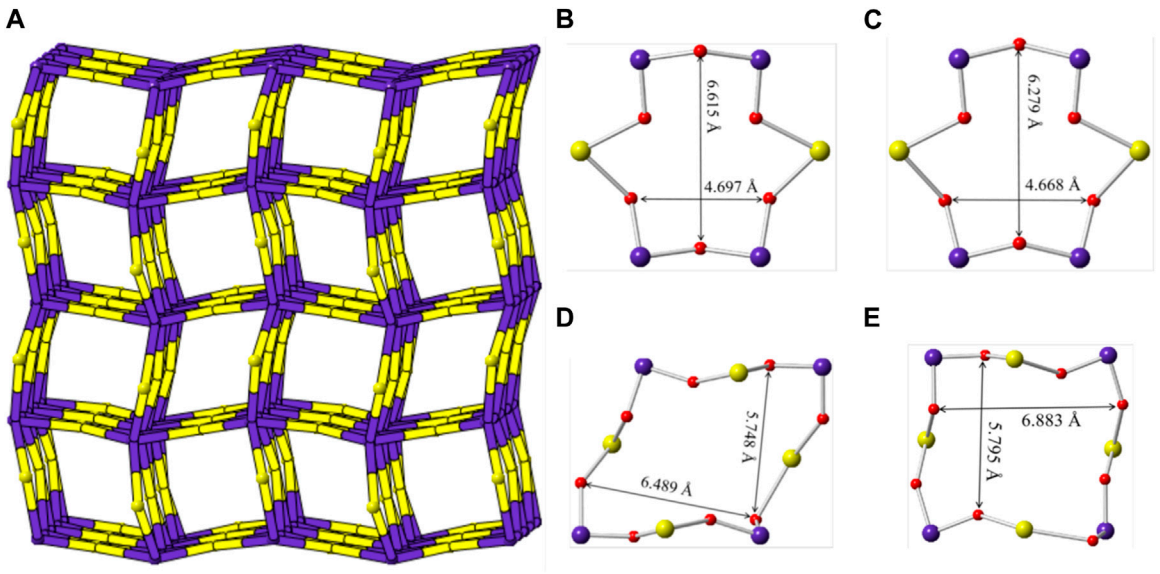

FIGURE 8
(A) View of the cation framework topology representation of Sr [(UO_2) (TeO_5)] along the *c*-axis; **(B–E)** the 6-MRs and 8-MRs pore size of the [(UO_2) (TeO_5)] tube along the *a*-, *b*- and *c*-axis. K, Te, U and O atoms are shown ain green, purple, yellow and red, respectively.

three novel alkaline Earth metal uranyl tellurites/tellurate, Mg [$(UO_2)(TeO_3)_2$], Sr [$(UO_2)(TeO_3)_2$] and Sr [$(UO_2)(TeO_5)$], were obtained. Mg [$(UO_2)(TeO_3)_2$] and Sr [$(UO_2)(TeO_3)_2$] have the same chemical formulas, but they are not iso-structures. This indicates that with the larger Sr^{2+}counter cation the dimensionality of the structure upon the ratio of U:Te = 1:2 decreases. It is noteworthy to consider the HT/HP role in generating these unique 1D to 3D structures, particularly in comparison to other actinide and non-actinide tellurium bearing compounds. Especially, HT/HP plays an important role in the stabilization of the less stable Te^{V} which we were not able to reproduce under normal conditions. This study further demonstrates how subtle adjustments to counter cations can reveal dramatic changes to structural type and topology. Further investigation ofthe *A*-U-Te-O system under similar synthetic conditions will lead towards obtaining different unique types of structures. This will help in achieving a deeper understanding of the influence of extreme conditions on the chemically complex tellurium bearing oxo-phases.

Data availability statement

The datasets presented in this study can be found in online repositories. The names of the repository/repositories and accession number(s) can be found below: https://www.ccdc.cam.ac.uk/structures/- CSD2238172, CSD2238173, CSD2238174, CSD2238175.

Author contributions

EVA performed design of the study, concept of the manuscript and structural and crystal chemical analysis; YH, EL, BX and PK performed HT/HP synthesis, XRD experiments and structural and crystal chemical analysis; XC, KH, R-A.E and SW participate in structural and crystal chemical analysis of the obtained materials, all authors participated in manuscript writing and correction.

Funding

EVA have been supported with DFG for the funding within the AL1527/3-1 project. YH is grateful to Natural Science Foundation of Anhui Province (2008085QB56), Hefei University Bilingual Course Construction Project (2021Yyykc02) and Anhui Province Postgraduate Education Quality Project (2022qyw/sysfkc042).

Conflict of interest

Authors EL, BX and PK were employed by Institute of Energy and Climate Research (IEK-6), Forschungszentrum Julich GmbH. Authors R-AE and EA were employed by Institute of Energy and Climate Research (IEK-9), Forschungszentrum Julich GmbH.

The remaining authors declare that the research was conducted in the absence of any commercial or financial relationships that could be construed as a potential conflict of interest.

Publisher's note

All claims expressed in this article are solely those of the authors and do not necessarily represent those of their affiliated organizations, or those of the publisher, the editors and the reviewers. Any product that may be evaluated in this article, or claim that may be made by its manufacturer, is not guaranteed or endorsed by the publisher.

Supplementary material

The Supplementary Material for this article can be found online at: https://www.frontiersin.org/articles/10.3389/fchem.2023.1152113/full#supplementary-material

References

Alexandrov, E. V., Blatov, V. A., Kochetkov, A. V., and Proserpio, D. M. (2011). Underlying nets in three-periodic coordination polymers: Topology, taxonomy and prediction from a computer-aided analysis of the cambridge structural database. *CrystEngComm* 13, 3947–3958. doi:10.1039/c0ce00636j

Almond, P. M., and Albrecht-Schmitt, T. E. (2002). Expanding the remarkable structural diversity of uranyl tellurites: Hydrothermal preparation and structures of $K[UO_2Te_2O_5(OH)]$, $Tl_3\{(UO_2)_2[Te_2O_5(OH)](Te_2O_6)\}.2H_2O$, β-$Tl_2[UO_2(TeO_3)_2]$ and $Sr_3[UO_2(TeO_3)_2](TeO_3)_2$. *Inorg. Chem.* 41, 5495–5501. doi:10.1021/ic025820m

Balraj, V., and Vidyasagar, K. (1999). Hydrothermal synthesis and characterization of novel one-dimensional tellurites of olybdenum(VI), $A_4Mo_6TeO_{22}{\cdot}2H_2O$ ($A = NH_4$, Rb. *Inorg. Chem.* 38, 1394–1400. doi:10.1021/ic980957r

Bergerhoff, G., Brown, I. D., and Allen, F. (1987). Crystallographic databases. *Int. Union Crystallogr. Chester* 360, 77–95.

Blatov, V. A., Delgado-Friedrichs, O., O'Keeffe, M., and Proserpio, D. M. (2007). Three-periodic nets and tilings: Natural tilings for nets. *Acta Crystallogr. A, Found. Crystallogr.* 63, 418–425. doi:10.1107/s0108767307038287

Blatov, V. A., O'Keeffe, M., and Proserpio, D. M. (2010). Vertex-face-point-Schläfli, and delaney-symbols in nets, polyhedra and tilings: Recommended terminology. *CrystEngComm* 12, 44–48. doi:10.1039/b910671e

Blatov, V. A. (2006). Multipurpose crystallochemical analysis with the program package TOPOS. *IUCr CompComm Newsl.* 7, 4–38.

Brandstatter, F. (1981). Non-stoichiometric, hydrothermally synthesized cliffordite. *Min. Pet.* 29, 1–8. doi:10.1007/bf01082811

Brese, N. E., and O'Keeffe, M. (1991). Bond-valence parameters for solids. *Acta Cryst.* B47, 192–197. doi:10.1107/s0108768190011041

Brown, I. D., and Altermatt, D. (1985). Bond-valence parameters obtained from a systematic analysis of the inorganic crystal structure database. *Acta Cryst.* B41, 244–247. doi:10.1107/s0108768185002063

Burns, P. C., Miller, M. L., and Ewing, R. C. (1996). U^{6+} minerals and inorganic phases: A comparison and hierarchy of crystal structures. *Can. Mineral.* 34, 845–880.

Burns, P. C., Ewing, R. C., and Hawthorne, F. C. (1997). The crystal chemistry of hexavalent uranium; polyhedron geometries, bond-valence parameters, and polymerization of polyhedra. *Can. Mineral.* 35, 1551–1570.

Chi, E. O., Ok, K. M., Porter, Y., and Halasyamani, P. S. (2006). $Na_2Te_9Mo_3O_{16}$: A new molybde-num tellurite with second-harmonic generating and pyroelectric properties. *Chem. Mat.* 18, 2070–2074. doi:10.1021/cm052614e

Christy, A. G., Mills, S. J., and Kampf, A. R. (2016). A review of the structural architecture of tellurium oxycompounds. *Mineral. Mag.* 80, 415–545. doi:10.1180/minmag.2016.080.093

Engmann, R. D., and De Wolff, P. M. (1963). The crystal structure of γ-UO_3. *Acta Cryst.* 16, 993–996. doi:10.1107/s0365110x63002656

Galy, J., and Meunier, G. (1971). A propos de la cliffordite UTe_3O_3. le systéme UO_3-TeO_2 700°C. structure cristalline de UTe_3O_9. *Acta Crystallogr. B Struct. Crystallogr. Cryst. Chem.* 27, 608–616. doi:10.1107/s0567740871002632

Hafidi, J. A., Peuzin, J. C., Couchaud, M., and Gay, J. C. (1986). Te_2O_5: Crystal growth and optical properties. *Mat. Res. Bull.* 21, 421–428. doi:10.1016/0025-5408(86)90007-3

Hao, Y. C., Hu, C. L., Xu, X., Kong, F., and Mao, J. G. (2013). $SrGe_2B_2O_8$ and $Sr_3Ge_2B_6O_{16}$: Novel strontium borogermanates with three-dimensional and layered anionic architectures. *Inorg. Chem.* 52, 13644–13650. doi:10.1021/ic402214p

Hao, Y. C., Xu, X., Kong, F., Song, J. L., and Mao, J. G. (2014). $PbCd_2B_6O_{12}$ and $EuZnB_5O_{10}$: Syntheses, crystal structures and characterizations of two new mixed metal borates. *CrystEngComm* 16, 7689–7695. doi:10.1039/c4ce00777h

Hao, Y., Klepov, V. V., Murphy, G. L., Modolo, G., Bosbach, D., Albrecht-Schmitt, T. E., et al. (2016). Influence of synthetic conditions on chemistry and structural properties of alkaline earth uranyl borates. *Cryst. Growth & Des.* 16, 5923–5931. doi:10.1021/acs.cgd.6b00978

Hao, Y., Kegler, P., Bosbach, D., Albrecht-Schmitt, T. E., Wang, S., and Alekseev, E. V. (2017). Divergent structural chemistry of uranyl borates obtained from solid state and hydrothermal conditions. *Cryst. Growth & Des.* 17, 5898–5907. doi:10.1021/acs.cgd.7b00997

Hao, Y., Murphy, G. L., Bosbach, D., Modolo, G., Albrecht-Schmitt, T. E., and Alekseev, E. V. (2017). Porous uranyl borophosphates with unique three-dimensional open-framework structures. *Inorg. Chem.* 56, 9311–9320. doi:10.1021/acs.inorgchem.7b01443

Hao, Y., Klepov, V. V., Kegler, P., Modolo, G., Bosbach, D., Albrecht-Schmitt, T. E., et al. (2018). Synthesis and study of the first zeolitic uranium borate. *Cryst. Growth & Des.* 18, 498–505. doi:10.1021/acs.cgd.7b01487

Hao, Y., Kegler, P., Albrecht-Schmitt, T. E., Wang, S., Dong, Q., and Alekseev, E. V. (2020). Two-dimensional uranyl borates: From conventional to extreme synthetic conditions. *Eur. J. Inorg. Chem.* 4, 407–416. doi:10.1002/ejic.201901239

Hao, Y., He, L., Ge, G., Zhang, Q., Luo, N., Huang, S., et al. (2020). $Mg_3Pt(BO_3)_2O_2$: The first platinum borate from the flux technique. *J. Solid State Chem.* 281, 121046. doi:10.1016/j.jssc.2019.121046

Hao, Y., Pan, Y., Lin, Y., He, L., Ge, G., Ruan, Y., et al. (2020). Highly porous aluminophosphates with unique three dimensional open framework structures from mild hydrothermal syntheses. *CrystEngComm* 22, 3070–3078. doi:10.1039/d0ce00075b

Hao, Y., Alekseev, E. V., Klepov, V. V., and Yu, N. (2020). Structural variations in complex sodium thorium arsenates. *Eur. J. Inorg. Chem.* 33, 3187–3193. doi:10.1002/ejic.202000492

Hao, Y., Murphy, G. L., Kegler, P., Li, Y., Kowalski, P. M., Blouin, S., et al. (2022). Understanding the role of flux, pressure and temperature on polymorphism in ThB_2O_5. *Dalton Trans.* 51, 13376–13385. doi:10.1039/d2dt01049f

Kampf, A. R., Mills, S. J., Housley, R. M., Marty, J., and Thorne, B. (2010). Lead-tellurium oxysalts from otto mountain near baker, California: IV. Markcooperite, $Pb(UO_2)Te^{6+}O_6$. The first natural uranyl tellurate. *Am. Mineral.* 95, 1554–1559. doi:10.2138/am.2010.3513

Kim, J. H., and Halasyamani, P. S. (2008). A rare multi-coordinate tellurite, $NH_4ATe_4O_9{\cdot}2H_2O$ (A= Rb or Cs): The occurrence of TeO_3, TeO_4, and TeO_5 polyhedra in the same material. *J. Solid State Chem.* 181, 2108–2112. doi:10.1016/j.jssc.2008.04.032

Kim, H., Cho, Y., Yun, H., and Do, J. (2007). Hydrothermal synthesis of a new vanadium tellurate (VI) with a novel chain structure: $(NH_4)_4\{[(VO_2)_2[Te_2O_8(OH)_2]\}2H_2O$. *Z. Anorg. Allg. Chem.* 633, 473–477. doi:10.1002/zaac.200600332

Kim, I. H., Back, J., and Halasyamani, P. S. (2007). $(NH_4)_2Te_2WO_3$: A new polar oxide with second-harmonic generating, ferroelectric, and pyroelectric properties. *Chem. Mater* 19, 5637–5641. doi:10.1021/cm7019334

Kim, M. K., Kim, S.-H., Chang, H.-Y., Halasyamani, P. S., and Ok, K. M. (2010). New noncen-trosymmetric tellurite phosphate material: Synthesis, characterization, and calculations of $Te_2O(PO_4)_2$. *Inorg. Chem.* 49, 7028–7034. doi:10.1021/ic100706n

Kim, Y. H., Lee, D. W., and Ok, K. M. (2014). Strong second harmonic generation (SHG) origi-nating from combined second-order Jahn-Teller (SOJT) distortive cations in a new non-centrosymmetric tellurite, $InNb(TeO_4)_2$. *Inorg. Chem.* 53, 5240–5245. doi:10.1021/ic5004337

Kleykamp, H. (1985). The chemical state of the fission products in oxide fuels. *J. Nucl. Mat.* 131, 221–246. doi:10.1016/0022-3115(85)90460-x

Li, X., Zhang, Y., Pan, Y., Hao, Y., Lin, Y., Li, H., et al. (2022). $Li_3[Al(PO_4)_2(H_2O)_{1.5}]$ and $Na[AlP_2O_7]$: From 2D layered polar to 3D centrosymmetric framework structures. *CrystEngComm* 24, 6917–6924. doi:10.1039/d2ce00994c

Lin, J., Diefenbach, K., Cross, J. N., Babo, I.-M., and Albrecht-Schmidt, T. E. (2013). Thermochromism, the alexandrite effect, and dynamic Jahn-Teller distortions in $Ho_2Cu(TeO_3)_2(SO_4)_2$. *Inorg. Chem.* 52, 13278–13281. doi:10.1021/ic402432q

Lindqvist, O., and Moret, J. (1973). The crystal structure of ditellurium pentoxide, Te_2O_5. *Acta Crystallogr. B Struct. Crystallogr. Cryst. Chem.* 29, 643–650. doi:10.1107/s0567740873003092

Mao, J. G., Jiang, H. L., and Kong, F. (2008). Structures and properties of functional metal selenites and tellurites. *Inorg. Chem.* 47, 8498–8510. doi:10.1021/ic8005629

Meunier, G., and Galy, J. (1973). Structure cristalline de la schmitterite synthétique $UTeO_5$. *Acta Crystallogr. B Struct. Crystallogr. Cryst. Chem.* 29, 1251–1255. doi:10.1107/s0567740873004334

Sheldrick, G. M. (1998). *SHELXTL, crystallographic software package, version 5.1*. Madison, WI: Bruker-AXS.

Spek, A. L. (2001). *Platon*. Utrecht, Netherlands: Utrecht University.

Swihart, G. H., Sen Gupta, P. K., Schlemper, E. O., Back, M. E., and Gaines, R. V. (1993). The crystal structure of moctezumite $[PbUO_2](TeO_3)_2$. *Am. Mineral.* 78, 830–839.

Xiao, B., Kegler, P., Bosbach, D., and Alekseev, E. V. (2016). Rich non-centrosymmetry in a Na-U- Te oxo-system achieved under extreme conditions. *Inorg. Chem.* 55, 4626–4635. doi:10.1021/acs.inorgchem.6b00440

Xiao, B., Kegler, P., Bosbach, D., and Alekseev, E. V. (2016). Investigation of reactivity and struc-ture formation in a K-Te-U oxo-system under high-temperature/high-pressure conditions. *Dalton Trans.* 45, 15225–15235. doi:10.1039/c6dt01350c

Yeon, J., Kim, S. H., Hayward, M. A., and Halasyamani, P. S. (2011). A" cation polarity control in $ACuTe_2O_7$ (A = Sr^{2+}, Ba^{2+}, or Pb^{2+}. *Inorg. Chem.* 50, 8663–8670. doi:10.1021/ic2012217

Yeon, J., Kim, S. H., Nguyen, S. D., Lee, H., and Halasyamani, P. S. (2012). Two new noncentrosymmetric (NCS) polar oxides: Syntheses, characterization, and structure–property relationships in $BaMTe_2O_7$ (M = Mg^{2+} or Zn^{2+}). *Inorg. Chem.* 51, 2662–2668. doi:10.1021/ic202602q

frontiers | Frontiers in Chemistry

TYPE Original Research
PUBLISHED 12 April 2023
DOI 10.3389/fchem.2023.1173604

OPEN ACCESS

EDITED BY
Arnold M. Guloy,
University of Houston, United States

REVIEWED BY
Ilkay Gumus,
Mersin University, Türkiye
Aurel Tabacaru,
Dunarea de Jos University, Romania

*CORRESPONDENCE
Mamaru Bitew Alem,
mamaru2005@gmail.com,
Tegene Desalegn,
tegened@yahoo.com,
Taye B. Demissie,
sene3095@gmail.com

SPECIALTY SECTION
This article was submitted to Inorganic Chemistry, a section of the journal *Frontiers in Chemistry*

RECEIVED 24 February 2023
ACCEPTED 24 March 2023
PUBLISHED 12 April 2023

CITATION
Alem MB, Desalegn T, Damena T, Bayle EA, Koobotse MO, Ngwira KJ, Ombito JO, Zachariah M and Demissie TB (2023), Organic–inorganic hybrid salt and mixed ligand Cr(III) complexes containing the natural flavonoid chrysin: Synthesis, characterization, computational, and biological studies.
Front. Chem. 11:1173604.
doi: 10.3389/fchem.2023.1173604

Organic–inorganic hybrid salt and mixed ligand Cr(III) complexes containing the natural flavonoid chrysin: Synthesis, characterization, computational, and biological studies

Mamaru Bitew Alem [1]*, Tegene Desalegn [1]*, Tadewos Damena [2], Enyew Alemayehu Bayle [3,4], Moses O. Koobotse [5], Kennedy J. Ngwira [6], Japheth O. Ombito [7], Matshediso Zachariah [5] and Taye B. Demissie [7]*

[1]Department of Applied Chemistry, Adama Science and Technology University, Adama, Ethiopia, [2]Department of Chemistry, Wachemo University, Hossana, Ethiopia, [3]Graduate Institute of Applied Science and Technology, National Taiwan University of Science and Technology, Taipei, Taiwan, [4]Department of Chemistry, Debre Markos University, Debre Markos, Ethiopia, [5]School of Allied Health Professions, University of Botswana, Gaborone, Botswana, [6]Molecular Sciences Institute, School of Chemistry, University of the Witwatersrand, Johannesburg, South Africa, [7]Department of Chemistry, University of Botswana, Gaborone, Botswana

Organic–inorganic hybrid salt and mixed ligand Cr(III) complexes (**Cr1** and **Cr2**) containing the natural flavonoid chrysin were synthesized. The metal complexes were characterized using UV-Vis, Fourier-transform infrared, MS, SEM-EDX, XRD, and molar conductance measurements. Based on experimental and DFT/TD-DFT calculations, octahedral geometries for the synthesized complexes were suggested. The powder XRD analysis confirms that the synthesized complexes were polycrystalline, with orthorhombic and monoclinic crystal systems having average crystallite sizes of 21.453 and 19.600 nm, percent crystallinities of 51% and 31.37%, and dislocation densities of 2.324×10^{-3} and 2.603×10^{-3} nm^{-2} for **Cr1** and **Cr2**, respectively. The complexes were subjected to cytotoxicity, antibacterial, and antioxidant studies. The *in vitro* biological studies were supported with quantum chemical and molecular docking computational studies. **Cr1** showed significant cytotoxicity to the MCF-7 cell line, with an IC_{50} value of 8.08 μM compared to 30.85 μM for **Cr2** and 18.62 μM for cisplatin. **Cr2** showed better antibacterial activity than **Cr1**. The higher E_{HOMO} (−5.959 eV) and dipole moment (10.838 Debye) values of **Cr2** obtained from the quantum chemical calculations support the observed *in vitro* antibacterial activities. The overall results indicated that **Cr1** is a promising cytotoxic drug candidate.

KEYWORDS

chrysin, Cr(III) complex, cytotoxicity, organic–inorganic hybrid salt, molecular docking, MCF-7

1 Introduction

Coordination compounds (CCs) have a more important place in chemistry as functional materials owing to their exceptional structural arrangements (Kilpin and Dyson, 2013; Renfrew, 2014). CCs have a wide range of applications, especially in medicine (diagnosis and treatment), biology, and therapeutics (Renfrew, 2014; Kasprzak et al., 2015; Boros et al., 2020; Karges et al., 2021; Damena et al., 2022; Olelewe and Awuah, 2023). As a result, interest in metal-based therapeutic agents is growing in the bioinorganic chemistry era due to the emergence of clinical trials with various mechanisms of action that could potentially provide new chemotherapeutic approaches to disease management (Boros et al., 2020; Damena et al., 2022; Scalese et al., 2022; Kacsir et al., 2023; Olelewe and Awuah, 2023). Numerous metal-based promising chemotherapeutic agents have been reported since the discovery of cisplatin for general oncology in 1978 (Kilpin and Dyson, 2013; Renfrew, 2014; Karges et al., 2021). However, anticancer agents from the first d-block elements series and essential abundant elements are not well explored (Chen et al., 2021). Chromium is among the ubiquitous metals considered to be biologically relevant (Vincent, 2004), both in animal feeding and human nutrition in its trivalent state (Dong et al., 2018). Chromium is believed to be involved in the metabolism of carbohydrates, lipids, and proteins mainly by increasing the efficiency of insulin (Vincent, 2004; Pechova and Pavlata, 2007; Kralovec et al., 2009).

Following the first suggestion that Cr(III) compounds could act as a nutritional enhancement to glucose metabolism in 1959 by Schwarz and Mertz (Pechova and Pavlata, 2007), there has been a search for Cr(III) supplements, with Cr(III)-picolinate being the oldest. Furthermore, *in vitro* and *in vivo* findings have shown that trivalent chromium, Cr(III), has biological benefits, such as enhancing the antioxidant enzyme defense system and facilitating insulin signaling or sensitivity (Anderson et al., 1997; Hao et al., 2011), suppressing free radical formation and inhibiting protein glycosylation (Dong et al., 2018), decreasing serum glucose levels (Pandey et al., 2012), lowering blood lipid levels (Anderson et al., 1997), reducing cholesterol and triglyceride levels in the blood (Wang et al., 2017), lowering glycated hemoglobin levels (El-Megharbel, 2015), and inhibiting α-glucosidase activity (Dong et al., 2018). However, the bioavailability and efficacy of Cr(III) are dependent on the ligands that chelate to chromium ions (Peng and Yang, 2015; Ulas et al., 2015) as the specific ligand environment around Cr(III) could affect the biological activity and bioavailability of chromium (Ahmad et al., 2012; Peng and Yang, 2015). However, organic–inorganic hybrid salts of chromium show promising applications as functional materials in various fields, such as catalysis, magnetism, medicine, cancer therapy, luminescence, conductivity, material science, and industrial applications (Ndong et al., 2020; Zare et al., 2021).

In this work, we designed an organic–inorganic hybrid salt consisting of a natural flavonoid chrysin and dichlorobis (1,10-phenanthroline)chromate (III) as Lewis base and acid, respectively, where $CrCl_3.6H_2O$ salt was used as a metal precursor. Moreover, metformin-coordinated Cr(III) complexes reportedly exhibit antibacterial activity and cytotoxicity. We previously reported the synthesis, antibacterial, and cytotoxicity profiles of Cu(II) complexes using 1,10-phenanthroline and the drugs metformin and ciprofloxacin (Alem et al., 2022), which showed the promising cytotoxicity profiles of Cu(II) mixed drug complexes against the MCF-7 human breast cancer cell line. Inspired by the previous findings and due to our interest in examining the innate cytotoxicity of Cr(III) against MCF-7, we synthesized and evaluated the biological activities of two metal complexes of Cr(III) using 1,10-phenanthroline, metformin, and chrysin ligands.

2 Materials and methods

2.1 Materials

All chemicals and reagents were of analytical grade and used without any treatment. 1,10-phenanthroline (BDH chemical Ltd., Poole, England), chrysin (Sigma Aldrich), chromium chloride hexahydrate ($CrCl_6.6H_2O$), dimethyl sulfoxide (DMSO), and dimethylformamide (DMF) were purchased from Loba Chemie Pvt. Ltd. (Mumbai, India). Triethylamine, $NaHCO_3$, Mueller–Hinton agar, methanol (MeOH), and diethyl ether were purchased from (Alpha Chemika, India). Ascorbic acid and 2,2-diphenyl-1-picrylhydrazyl (DPPH) were purchased from Sigma-Aldrich.

2.2 Synthesis

2.2.1 Synthesis of organic–inorganic hybrid salts of Cr(III)

A heteroleptic Cr(III)complex (**Cr1**) of 1,10-phenanthroline and an oxo ligand, chrysin (5,7-dihydroxy-2-phenyl-4H-chromen-4-one) was prepared as reported previously by Abebe and Hailemariam (2016) with minor modifications. In brief, 1 mmol of chrysin (0.254 g) was added to a mixture of 20 mL of methanol: ethanol solution (1:3 ratio) in the presence of a deprotonating agent, 1 mmol NaOH, and stirred for 20 min, resulting in a clear yellow solution. To this solution, 1 mmol of $CrCl_3.6H_2O$ (0.266 g) was added slowly and refluxed at 90°C in an oil bath. The resulting light green solution was refluxed for 1 h 20 min; then, 1 mmol of methanolic solution of 1,10-phenanthroline was added slowly. A drop of triethylamine was added to the reaction mixture to maintain the alkaline pH of the solution and the reflux was continued for an additional 6 h 40 min. The resulting brown solution was filtered and cooled. Next, 10 mL of diethyl ether was added to the filtrate and allowed to stand overnight. The resulting jelly-like brown precipitate was left to dry slowly at room temperature.

For **Cr2,** which consisted of metformin and oxo ligand, chrysin was prepared as reported by Lin et al. (Abd El-Halim et al., 2017) with minor modifications. Briefly, to the clear hot methanolic solution of metformin, 1 mmol of $CrCl_3.6H_2O$ (0.266 g) was added slowly and stirred, resulting in a faded green solution. To the reaction mixture, 1 mmol of chrysin (0.254 g) dissolved in a mixture of methanol:ethanol (1:3) was added in the presence of a deprotonating agent, 1 mmol NaOH. Triethylamine (1 mmol, 140 µL) was used to maintain the alkaline pH of the solution and the reaction was refluxed for an additional 8 h. The resulting greenish-brown solution was filtered, treated with diethyl ether, and allowed to stand for 2 weeks. A light green powder was obtained

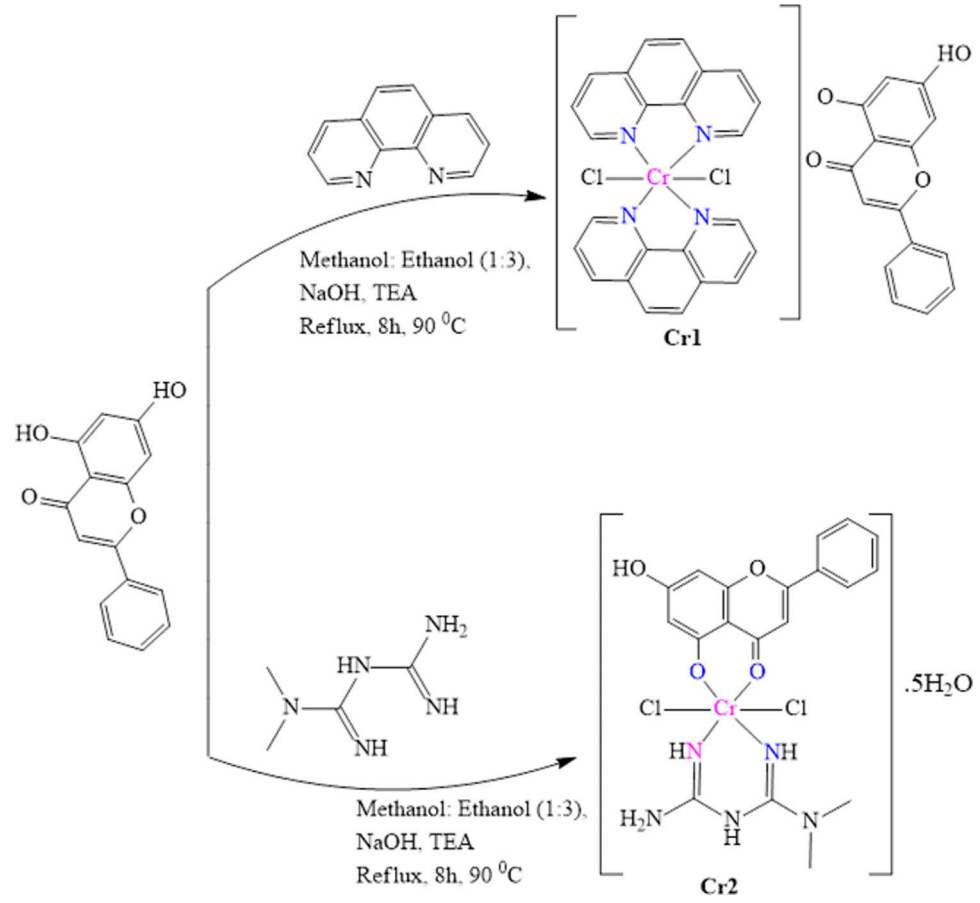

SCHEME 1
Schematic representation of the synthesis of **Cr(III)** complexes.

after the slow evaporation at room temperature. The overall synthesis scheme is presented in Scheme 1.

2.3 Instrumentation

Fourier-transform infrared (FTIR) spectroscopy was recorded from 4,000 to 400 cm^{-1} in KBr pellets on a PerkinElmer BX FTIR spectrometer. The UV-Vis spectra were recorded from 200–800 nm on an SM-1600 spectrophotometer using dilute solutions (1.0×10^{-4} M) of the test compounds. The thermogravimetric/differential thermal analyses (TGA/DTA) data were recorded from 25 to 800°C at a heating rate of 10°C/min under nitrogen-atmosphere (20 mL/min) on a Shimadzu DTG-60H thermal analyzer. X-ray diffraction (XRD-7000, Shimadzu Co., Japan) was used to determine the crystalline nature of the synthesized metal complexes. The diffraction was recorded with 2θ = 10 to 80 using CuKα (λ = 1.5406 Å) radiation at 40 kV and 30 mA (Holzwarth and Gibson, 2011). The inter-planar spacing (*d*), Miller indices (*hkl*), and lattice parameters (a, b, c, α, β, and γ) were estimated using QUALX2.0 (Altomare et al., 2015). SEM-EDX measurements were performed with a Joel JSM-6500F instrument (Joel, Tokyo, Japan). The high-resolution mass spectra were obtained with a Waters LCT Premier mass spectrometer using a sample concentration of 2 ng/μL with a capillary voltage of 2500 V and a desolvation temperature of 250°C using nitrogen gas at 250 L/h, Bruker APEX II CCD area detector diffractometer, with graphite monochromated Mo K3 radiation (50 kV, 30 mA) and temperature of measurement at 1732 K coupled with APEX 2 data collection software.

2.4 Biological activity studies

2.4.1 Cytotoxicity evaluation against the MCF-7 cell line

The cytotoxicities of the complexes (**Cr1** and **Cr2**) were evaluated using the 3-[4,5-dimethylthiazole-2-yl]-2,5-diphenyltetrazolium bromide (MTT) assay. The detailed cell culture conditions and procedure for the cytotoxicity assay were reported previously (Alem et al., 2022).

2.4.2 Antibacterial activity

The *in vitro* antibacterial activities of the metal complexes were evaluated against the Gram-positive (*Staphylococcus aureus*

(ATCC25923) and *Streptococcus* pyogenes (ATCC19615)) and Gram-negative (*Escherichia coli* (ATCC25922)) bacterial strains and *Pseudomonas aeruginosa* (ATCC27853) using the disk diffusion method in Mueller–Hinton agar (MHA) (Ommenya et al., 2020). All protocols and the negative and positive controls were similar to those reported previously (Lemilemu et al., 2021). Known concentrations (500 and 1,000 μM) of the metal complexes were prepared in DMSO. The analysis was conducted in triplicate, and the results were presented as a mean ± SD.

2.4.3 DPPH radical scavenging activity

The DPPH scavenging activities of the synthesized complexes (**Cr1** and **Cr2**) were evaluated as we described previously, with minor modifications (Lemilemu et al., 2021; Alem et al., 2022; Damena et al., 2023). The percent DPPH free radical scavenging activities of the synthesized complexes and the standard were calculated using Equation (1).

$$\%\ \text{DPPH radical scavenging activity} = \frac{Ac - As}{Ac} \times 100\%, \quad (1)$$

where A_c is the absorbance of the control and A_s is the absorbance of the sample.

2.5 Quantum chemical studies

Density functional theory (DFT) employing the B3LYP (Lee et al., 1988; Becke, 1993; Stephens et al., 1994) hybrid functional together with the 6–311++G (d, p) basis set (Krishnan et al., 1980) for atoms of the ligand and the Los Alamos National Laboratory 2-double-zeta (LanL2DZ) pseudopotential for the chromium atom (Hay and Wadt, 1985) were employed, respectively. Grimme's dispersion correction (Grimme, 2004) was employed to account for non-bonding interactions. Vibrational frequency calculations were used to ensure that the optimized geometries were real minima without imaginary frequencies. The time-dependent DFT (TD-DFT) was used to calculate the absorption energies. The calculated absorption spectra were red-shifted by 30 nm for better comparison with the corresponding experimental spectra. Quantum chemical descriptors calculation, frontier molecular orbital (FMO) visualization, and associated data were conducted as we previously reported (Alem et al., 2022; Damena et al., 2023).

2.6 Molecular docking studies

The molecular docking study against estrogen receptor alpha (ERα; PDB: 5G4) (Xie et al., 2017), *S. aureus* (PDB: 2w9h) (Heaslet et al., 2009), and *E. coli* (PDB: 6F86) (Narramore et al., 2019) proteins were performed using AutoDock 4.2.6 (Allouche, 2012). Docking protocols similar to our previous works (Bitew et al., 2021; Lemilemu et al., 2021; Alem et al., 2022) were used. Finally, the conformers with the lowest binding free energies were used to visualize the interactions between the active amino acids and the molecules using Discovery Studio software. Cisplatin and ciprofloxacin were used as positive controls to compare the docking results with the corresponding experimental results.

3 Results and discussion

3.1 Physicochemical properties

The designed complexes (Scheme 1) were synthesized at high yield with corresponding colors of brown and light green for **Cr1** and **Cr2**, respectively (Table 1). Solvents of varying polarity were used to evaluate the solubilities of the synthesized metal complexes. At room temperature, both complexes were soluble in the DMSO and DMF polar aprotic solvents, mildly soluble in the polar water solvents methanol and ethanol, and insoluble in dichloromethane, ethyl acetate, chloroform, and hexane.

3.2 Molar conductance analysis

Molar conductance analysis was performed to ascertain the electrolytic and non-electrolytic natures of the synthesized metal complexes. Their molar conductances for **Cr1** and **Cr2** were 53.90 and 104.40 Ω^{-1} mol^{-1} cm^2, respectively (Table 1). The results indicated that the 1:1 coordination sphere cation and anion ratio of **Cr1** had an electrolytic (ionic) nature (Ali et al., 2013). The higher molar conductance value for **Cr2** could be associated with the presence of water of crystallization and substitution of the two chlorides by the solvent molecules (Alem et al., 2022) (Scheme 2). To confirm the presence/absence of chloride ions in the ionization spheres of the **Cr1** and **Cr2** complexes, a chloride test was performed using 1 mol of $AgNO_3$ solution. A negative result for the expected white precipitate was obtained, inferring the absence of chloride ions in the ionization sphere. Hence, the geometries were proposed to be octahedral with molecular formulas of $[Cr(C_{12}H_8N_2)_2Cl_2](C_{15}H_9O_4)$ and $[C_{19}H_{20}Cl_2CuN_5O_4].5H_2O$, for **Cr1** and **Cr2**, respectively.

3.3 FTIR analysis

The FTIR experimental spectra of free chrysin showed characteristic vibrational peaks at 3,439–3,406 cm^{-1}, which were computationally identified as 3,698 cm^{-1} and 3,709 cm^{-1} for the fifth and seventh ν-OH of chrysin, respectively. Upon coordination with the Cr(III) center, the ν-OH vibration appeared at 3,399 and 3,404 cm^{-1} for **Cr1** and **Cr2**, respectively (Supplementary Figures S1, S2). The intensities of ν-OH of chrysin in **Cr1** (87% transmittance) and **Cr2** (85% transmittance) were relatively large compared to that for free chrysin (52%). This confirmed that only one of the hydroxyl groups participated in the bonding. Furthermore, the free chrysin vibrations (experimental/calculated) observed at 1,640/1,608 and 2,930/3,123 cm^{-1} occurred due to ν-C=O and ν-C-H stretching, respectively, similar to previous reports (Sundaraganesan et al., 2012). The ν-C=O vibrations shifted to 1,623 cm^{-1} for **Cr1** and 1,655 cm^{-1} for **Cr2**, confirming the change in free chrysin electron conjugation. The large vibrational frequency difference ($\Delta \sim 300\ cm^{-1}$) between the

TABLE 1 Physicochemical properties of the synthesized complexes.

Compound	Color	State	Mass (% yield)	M. pt (°C)	Conductivity ($\Omega^{-1}mol^{-1}cm^2$, 25 °C)
Cr1	Brown	Powder	0.584 g (83.908)	200–202	53.90
Cr2	Light green	Powder	0.484 g (81.344)	>220	104.40

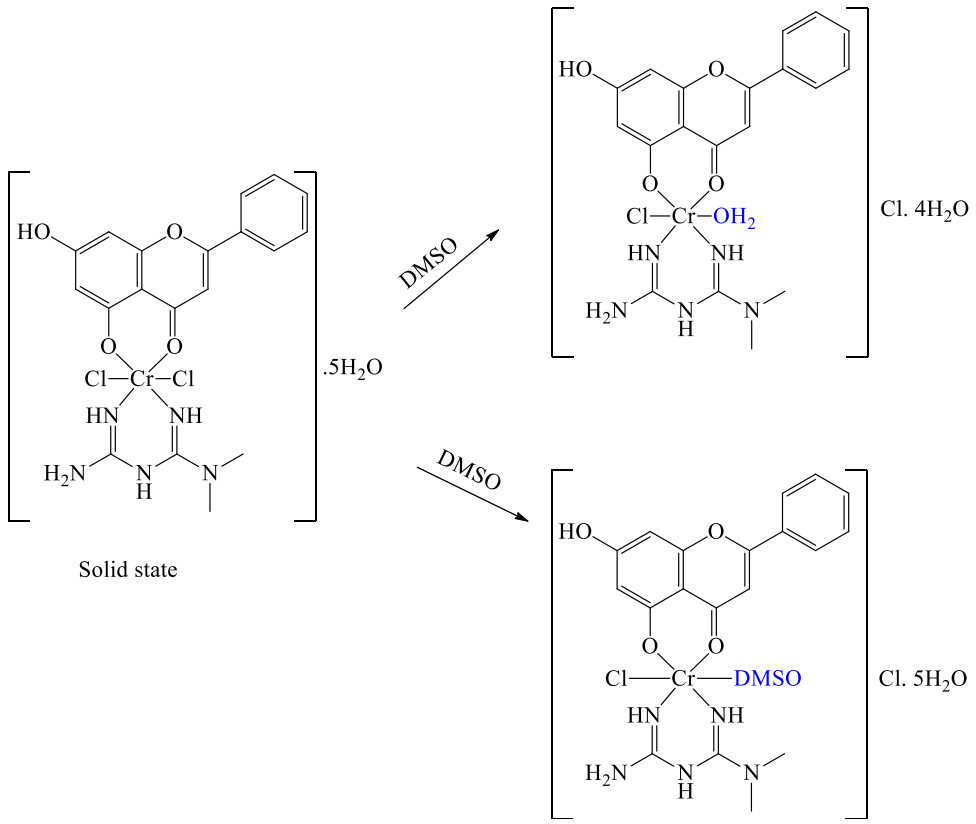

SCHEME 2
Proposed structures of the solid and solution forms of **Cr2**.

experimental and B3LYP calculated ν-OH could be due to the presence of an intermolecular hydrogen bond in the experimental measurement. In addition, the experimental/computational stretching vibrational bands of the 1,10-phenanthroline monohydrate ligand for ν-C=C (1,622/1,592 cm^{-1}) and ν-C=N (1,586/1,550 cm^{-1}) functional groups shifted to 1,630/1,608 and 1,521/1,429 cm^{-1}, respectively, in **Cr1,** with a decrease in intensity. The stretching vibrational bands of the ν-OH (3,430 cm^{-1}) associated with the water of crystallization of 1,10-phenanthroline were diminished following the metal-ligand coordination. The decreased intensity indicated the formation of a rigid and symmetric structure with the metal center (Abebe et al., 2020). In addition to the observed vibration frequency shifts, the formation of metal–ligand bonds was confirmed by the appearance of new vibrational bands (experimental/calculated) at 649/720 cm^{-1} for Cr-N bonds.

Metformin can be mainly characterized by its N–H stretching vibration, asymmetrical and symmetrical C-N vibrations, and NH_2 deformation, respectively, from 3,100 to 3,490, at 1,583–1,626, and 1,470–1,540 cm^{-1} in addition to other stretching and bending vibrations (Nakamoto, 2009; Villamizar-Delgado et al., 2020). In this study, these vibrational frequencies appeared at 3,429, 1,637, and 1,483–1,409 cm^{-1}. The participation of the nitrogen atom in the coordination with the metal center (**Cr2**) was evidenced by the changes in the intensity and vibrational frequency of the free metformin (Supplementary Figure S2). The formation of metal-ligand bonds was confirmed by the presence of peaks at 750 and 609 cm^{-1}, which corresponded to the formation of Cr–O and Cr–N bonds, respectively (Abbas et al., 2019).

3.4 UV-Vis analysis

The reported UV-Vis of chrysin spectra appear at 270 nm (intense) and 330 nm (less intense), which are associated with the

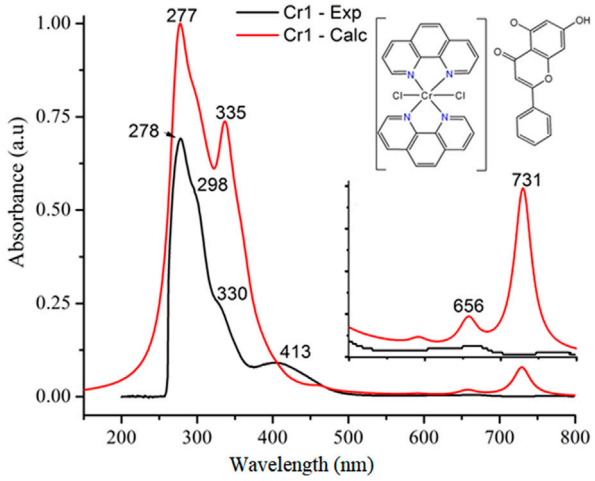

FIGURE 1
Experimental- (black) and TD-DFT-calculated (red) UV-Vis absorption spectra of **Cr1**.

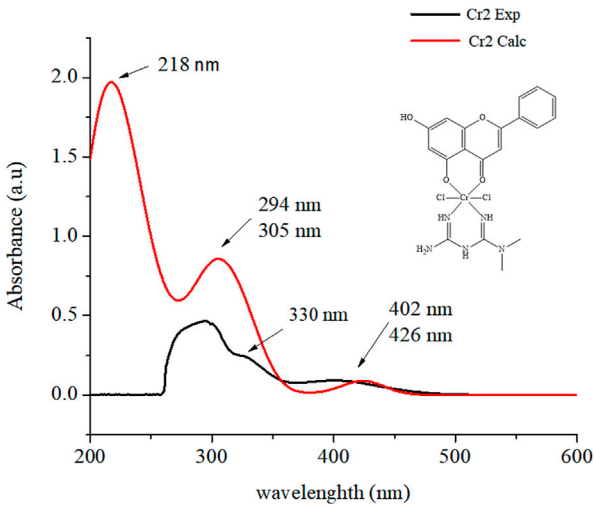

FIGURE 2
Experimental- (black) and TD-DFT-calculated (red) UV-Vis absorption spectrum of **Cr2**.

benzoyl system and cinnamoyl system in DMSO (Abd El-Halim et al., 2017). In this study, the UV-Vis/TD-DFT calculated absorption spectra of chrysin in DMSO appeared at 267/261 nm and 320/325 nm for π→π* transitions of the benzoyl and cinnamoyl systems, respectively, consistent with previous reports (Sundaraganesan et al., 2012; Halevas et al., 2021). The absorption spectra of the free ligand 1,10-phenanthroline (experimental/TD-DFT) showed absorption peaks at 228/226 nm and 263/258 nm, corresponding to n→π* (C=N) and π→π*(C=C) transitions, respectively (Tamiru et al., 2019; Alem et al., 2022). The obtained UV-Vis absorption spectrum of the ligands chrysin and 1,10-phenanthroline, and their metal complexes in DMSO together with their TD-DFT calculated results, are presented in Figure 1; Figure 2 and Supplementary Figures S3–S5 in the Supporting Material.

Following the reaction of Cr(III) with the ligands 1,10-phenanthroline and chrysin, bathochromic shifts to the benzoyl and cinnamoyl bands of chrysin were observed, whereas the bands of 1,10-phenanthroline were observed at a longer wavelength (278 nm). The broad peak of chrysin that appeared at 320/325 nm diminished with a slight bathochromic shift (330/335 nm for **Cr1** and 330 nm for **Cr2**), possibly due to the extension of the conjugated system due to complexation. New stronger absorption peaks appearing at 413 nm for **Cr1** (Figure 1) and at 404 nm for **Cr2** (Figure 2 and Supplementary Figure S5) were associated with ligand–ligand charge transfer (LLCT); i.e., the charge transfer between the ligands *via* a Cr(III) metal center (Vogler and Kunkely, 2007).

3.5 Mass spectrometric analysis

The mass spectrum of **Cr1** exhibited a peak at *m/z* = 738.109 to 741.114 (found = 735.070), which was attributed to the complex cation $[C_{39}H_{25}Cl_2CrN_4O_4]^+$, and a base peak at *m/z* = 516.077 (found = 514.040) associated with the coordination sphere and methanol ($M^+ + CH_3OH$], whereas a peak at *m/z* = 482.015 (found = 482.020) corresponded to the chemical entities in the coordination sphere, the Cr-metal center, two 1,10-phenanthroline and two chlorides $[M = C_{24}H_{16}Cl_2CrN_4]^+$, and an *m/z* value of 255.0653 (found = 254.060) corresponding to the ligand in the ionization sphere of the complex, which is a chrysin fragment $[C_{15}H_{10}O_4]$. The presence of *m*+4 peaks (peaks observed around *m/z* = 482.015 and 516.077) in the mass spectrum confirmed the coordination of two chlorides to the Cr-metal center. In **Cr2**, a molecular ion peak at *m/z* = 595.000 (found = 594.080) attributed to the complex $[C_{19}H_{30}Cl_2CrN_5O_9]$, a peak at *m/z* = 576.049 (found = 576.070), and a base peak at *m/z* = 558.039 (found = 558.060) were associated with $[C_{19}H_{28}Cl_2CrN_5O_8]$ and $[C_{19}H_{26}Cl_2CrN_5O_7]$ fragments, respectively. Two base peaks at *m/z* = 255.065 (found = 253.050) and *m/z* = 130.109 (found = 129.100) were associated with the chrysin ($C_{15}H_9O_4$) and metformin ($C_4H_{911}N_5$) ligands, respectively, confirming the coordination of the utilized ligands according to the designed complex (Scheme 1). Moreover, the presence of *m*+4 type peaks to the *m/z* peaks confirmed the coordination of two chlorides to the Cr(III) center (Supplementary Figures S6, S7 of the Supporting Material).

3.6 X-ray diffraction analysis

The XRD patterns of **Cr1** and **Cr2** mixed ligand complexes showed diffraction peaks in the range 2θ = 5°–80°, indicating the polycrystalline phases of the synthesized complexes (Supplementary Figure S9). The **Cr1** complex was an orthorhombic crystal system with spacing group P b c a and lattice parameters 16.2680 Å, 22.3369 Å, 24.0479 Å, 90°, 90°, and 90° for a, b, c, α, β, and γ, respectively. In contrast, **Cr2** followed a monoclinic crystal system and P 1 21/c 1 space group with lattice parameters 7.3135 Å, 7.6312 Å, 20.5697, Å, 90°, 99.462°, and 90°, respectively for a, b, c, α, β, and γ.

TABLE 2 Temperature range values for decomposition and corresponding weight loss values.

	Decomposition temp. (°C)	Mass loss (%)		DTG_{max} (°C)	Interpretation
		Obsd	Calcd		
Cr1	51–213	7.21	7.19	126	Loss due to water molecules
	295–590	41.63	41.60	465	Loss due to $C_{15}H_8O_3$ + 2Cl groups
Cr2	55–267	9.11	9.80	243	Loss due to water molecules
	275–411	11.76	11.74	400	Release of the chlorine moiety
	420–524	24.42	24.40	441	Decomposition of $C_4H_{11}N_5$ + OH^- organic moiety

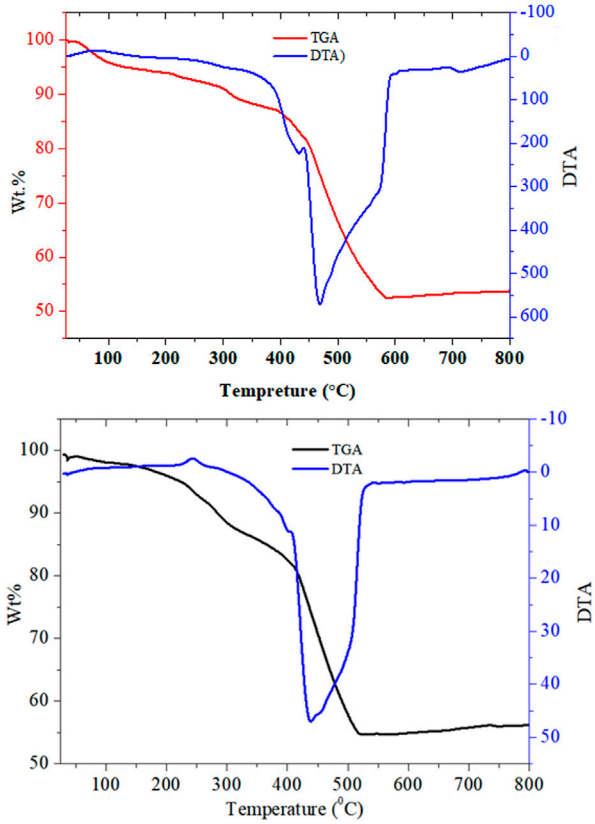

FIGURE 3
TGA/DTA graphical presentations of the **Cr1** (top) and **Cr2** (bottom) complexes.

The average crystallite sizes of the complexes were calculated according to the Debye–Scherrer equation (Holzwarth and Gibson, 2011). The average crystalline sizes of the complexes were 21.453 and 19.600 nm, respectively, for **Cr1** and **Cr2**. The percent crystalline index of the complexes was calculated using Equation (2).

$$\text{Crystalline Index } (CI) = \frac{Ac}{Ac + Aa} \times 100\%, \quad (2)$$

where *Ac* is the area of crystalline and *Aa* is the area of the amorphous part of the materials.

Accordingly, the synthesized Cr(III) mixed ligand complexes showed 66.51% and 31.37% crystallinity for **Cr1** and **Cr2,** respectively. The numbers of dislocation lines per unit area of the crystal and dislocation density (δ*) of the complexes were calculated from their relation to the average crystalline size (D) of the complexes (El-Sonbati et al., 2019; El-Sonbati et al., 2021) using Equation (3).

$$\text{Dislocation density } (\delta*) = \frac{1}{D^2}. \quad (3)$$

The calculated dislocation density values were 2.324×10^{-3} and 2.603×10^{-3} nm^{-2} for **Cr1** and **Cr2** complexes, respectively, representing a crystalline material with relatively less dislocation density and less irregularity within the structure. Previous research work by El-Sonbati et al. (2021) reported dislocation densities ranging from 3.00×10^{-4}–2.10×10^{-3} nm^{-2} for Cu(II), Ni(II), Mn(II), and UO_2II) mixed ligand polycrystalline complexes.

3.7 Thermogravimetric analysis

The thermal stabilities of the **Cr1** and **Cr2** complexes were identified based on the thermogravimetric curves in the temperature range between 25°C and 800°C (Table 2; Figure 3). The **Cr1** complex thermally decomposed into two main degradation steps: *i)* from 51.2°C to 213.2°C (DTG_{max} = 126°C), the weight loss was 7.21% (calcd. 7.20%), corresponding to the release of water molecules, *ii)* from 295.2°C to 590.4°C (DTG_{max} = 465°C) due to $C_{15}H_8O_3$ + 2Cl groups with a total weight loss of 41.63% (calcd. 41.60%) (Ndong et al., 2020).

The **Cr2** complex thermally decomposed into three main degradation steps: *i)* from 55.56°C to 267.41°C (DTG_{max} = 243°C), the weight loss was 9.11% (calcd. 9.10%), corresponding to the release of water molecules; *ii)* from 275.57°C to 411.07°C (DTG_{max} = 400°C), associated with the decomposition of the two chlorine moiety, with a total weight loss of 11.76% (calcd. 11.73%); *iii)* from 420°C to 524°C (DTG_{max} = 441°C) and a weight loss of 24.42% (calcd 24.40%), corresponding to the decomposition of $C_4H_{11}N_5$ + OH organic moiety with the final residue of chromium oxide (Ndong et al., 2020).

3.8 SEM-EDX analysis

The elemental compositions of the reported complexes (**Cr1** and **Cr2**) were obtained from energy-dispersive X-ray (EDX) analysis.

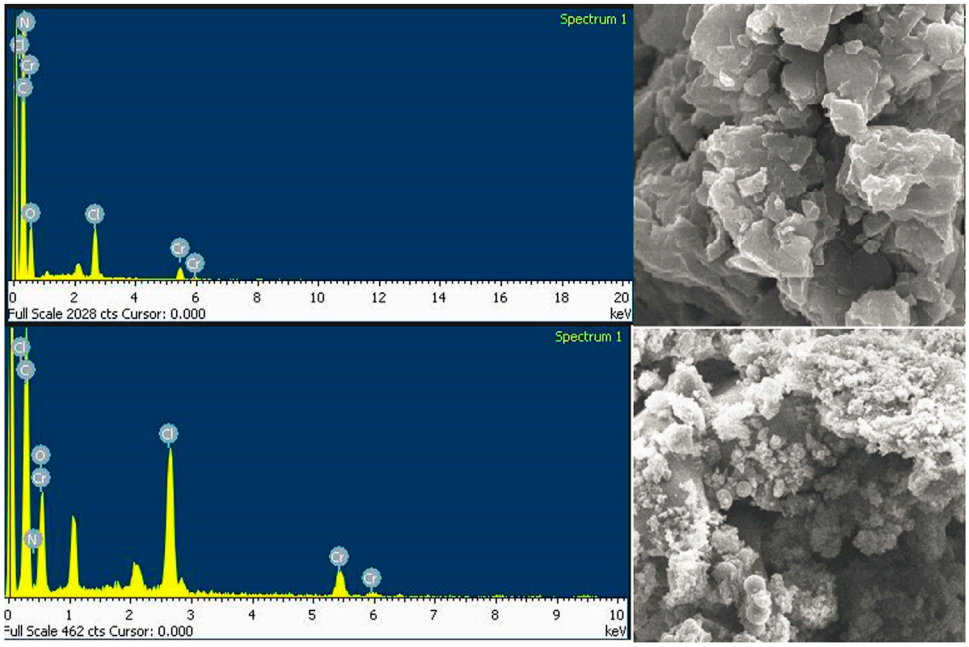

FIGURE 4
SEM-EDX images of the **Cr1** (top) and **Cr2** (bottom) complexes.

TABLE 3 Quantum chemical descriptors of the ligands and Cr(III) complexes: band gap (eV), electronegativity (eV), electronic chemical potential (eV), global chemical hardness (eV), global softness (σ = eV^{-1}), global electrophilicity index (eV), nucleophilicity index (eV^{-1}), and dipole moment (Debye).

Cpd	HOMO	LUMO	E_g	χ	μ	H	Σ	Ω	Nu	Dipole moment
Met	−6.440	−0.452	5.988	3.446	−3.446	2.994	0.167	1.983	0.504	5.752
Phen	−6.690	−1.935	4.755	4.313	−4.313	2.377	0.210	3.912	0.256	5.192
Cry	−6.555	−2.152	4.403	4.353	−4.353	2.202	0.227	4.304	0.232	7.884
Cr1	−4.989	−2.380	2.609	3.684	−3.684	1.304	0.383	5.203	0.192	0.062
Cr2	−5.959	−2.508	3.451	4.234	−4.234	1.725	0.290	5.194	0.193	10.838

Met, metformin; Phen, 1,10-phenanthroline; Cry, chrysin.

The SEM image of the synthesized complexes showed agglomerated particles and the presence of non-uniform-sized small grains. The EDX spectra of **Cr1** and **Cr2** showed characteristic signals for carbon, nitrogen, oxygen, chlorine, and chromium, which were associated with the atoms present in the ligands and the metal center, confirming the presence of the complexes waving the CHCrNOCl chemical composition of the complexes (Figure 4).

3.9 Quantum chemical analysis

Quantum chemical descriptors vital for correlating the energy, structure, and reactivity characteristics of the synthesized Cr(III) complexes were calculated from the frontier molecular orbitals (FMOs) HOMO, and LUMO (Table 3. The reactivities of the ligands and the synthesized complexes were determined using the highest occupied molecular orbital (HOMO) and lowest unoccupied molecular orbital (LUMO) band gap energy. The HOMO and LUMO eigenvalues and band gap energy are strongly associated with biological activities such as antibacterial, cytotoxicity, and antioxidant activities (Alem et al., 2022; Damena et al., 2023). The band gap energy (eV) of the ligands and their metal complexes were 5.988, 4.403, 2.609, and 3.452 eV, respectively, for metformin (Met), chrysin (Cry), **Cr1**, and **Cr2**. The metal complexes showed decreased band gap energy supported by increased global softness (Table 3), inferring the biological significance of the synthesized metal complexes relative to the ligands alone. The higher eigenvalue of the HOMO (−5.959 eV) and high dipole moment (10.838 Debye) of **Cr2** were major contributors to its better *in vitro* antibacterial activity (*vide supra*).

According to the hard–soft–acid–base (HSAB) theory, hard acids prefer to coordinate with hard bases and soft acids with soft bases (Ismael et al., 2020; Alem et al., 2022). Hence, DNA, enzymes, and

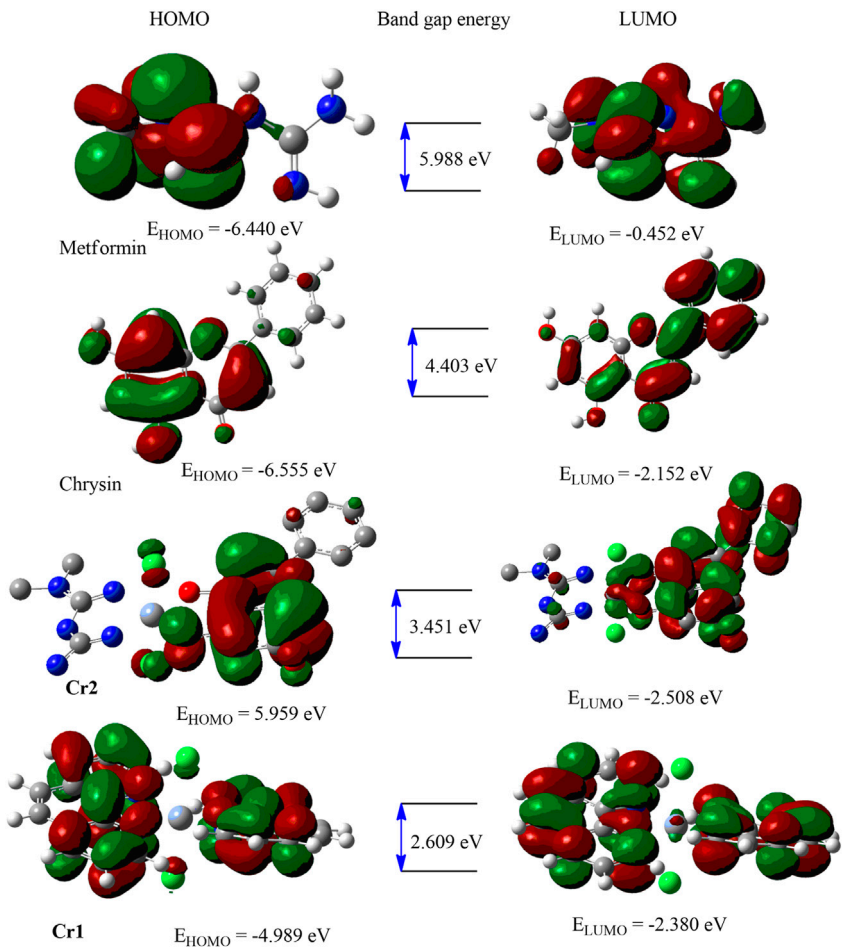

FIGURE 5
HOMO–LUMO distributions of the ligands and metal complexes.

proteins are soft biological molecules targeted for drug discovery. The small band gap energy together with large softness owing to the synthesized metal complexes make them promising therapeutic agents.

Chemical potential (μ) is the tendency of an electron to leave a stable system. A negative chemical potential indicates that a stable complex that does not spontaneously decompose into its constituent element is stable, whereas hardness (η) measures the resistance to changes in the distribution of electrons within a molecule. It is characterized by compounds with large HOMO–LUMO gaps possessing less reactivity (Choudhary et al., 2019). In this study, metal complexes showed negative chemical potentials (μ) of −3.684 and −4.234 eV, respectively, for **Cr1** and **Cr2**, inferring that **Cr2** followed a stable system.

3.10 Frontier molecular orbital (FMO) analysis

The B3LYP-calculated HOMO–LUMO distributions of the ligands and the corresponding metal complexes (**Cr1** and **Cr2**) are presented in Figure 5 and Supplementary Figure S8. In **Cr1**, the uniform distribution of the HOMO–LUMO confirmed the presence of ligand–ligand charge transfer *via* the Cr(III) metal center. This dominant charge transfer masked the expected d→d electronic transition. In the **Cr2** complex, the HOMO–LUMO isodensity showed the concentration of the HOMO on chrysin and LUMO on the chrysin and metal center, inferring the possible intra-ligand and ligand-to-metal charge transfer.

3.11 Biological activity evaluation

3.11.1 Cytotoxicity evaluation against MCF-7 cells

Cr(III) complexes have been used as efficient cancer therapeutic agents both *in vivo* and *in vitro via* the reactive oxygen species (ROS) generation mechanism (Chen et al., 2021). In contrast, flavonoid (Renfrew, 2014; Kasprzak et al., 2015) and 1,10-phenanthroline-based metal complexes cause cytotoxicity in cancer cells (Bravo-Gómez et al., 2009; Ruiz-Azuara and Bravo-Gomez, 2010; Buchtík et al., 2012; Reina et al., 2021). A low incidence of cancer has been reported among patients with diabetes treated with metformin (Abdelrahman et al., 2021), suggesting that metformin reduces cancer risk. Some of the proposed mechanisms of anticancer

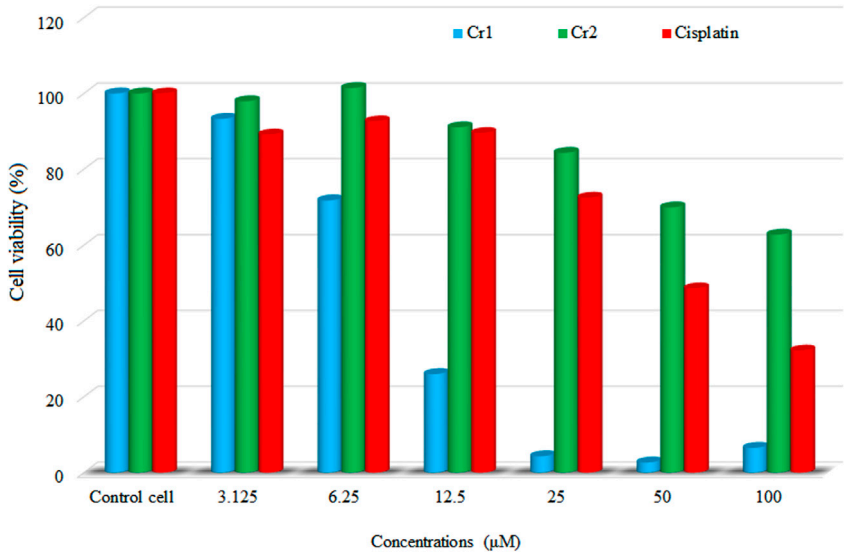

FIGURE 6
Cell viability profile of the synthesized complexes against MCF-7 cells.

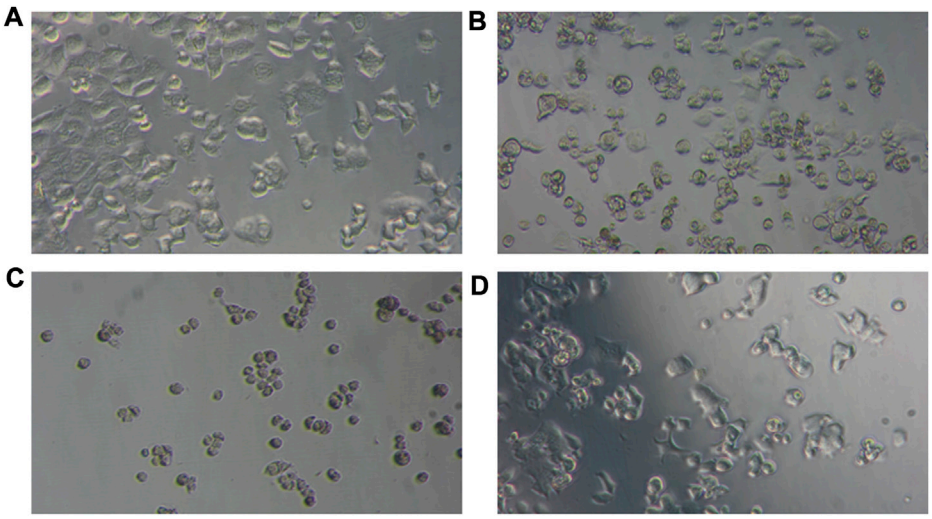

FIGURE 7
Photomicrographs of the cellular morphology of **(A)** untreated MCF-7 and the changes induced by **(B)** cisplatin, **(C) Cr1**, and **(D) Cr2** using 50 μM.

activity of metformin are based on its ability to form an adduct with glutathione and interactions with mitochondrial copper ions (Abdelrahman et al., 2021). The viability of the MCF-7 cell line was evaluated by MTT assay with six concentrations of test compounds in triplicate (Figure 6 and Supplementary Table S1).

In this study, a natural flavonoid, chrysin, and metformin coordinated Cr(III) complexes were synthesized and subjected to cytotoxicity evaluation against the human breast adenocarcinoma cancer cell line (MCF-7) at a range of concentrations (3.125–100 μM). Although both complexes showed promising cytotoxicity results, the **Cr1** complex showed better cytotoxic activity, with an IC_{50} value of 8.08 μM compared to **Cr2** (IC_{50} = 30.85 μM) and cisplatin (IC_{50} = 18.62 μM). A lower cell viability indicates a higher cytotoxic potential of the test compound (Ramasamy et al., 2022); i.e., a test compound is considered cytotoxic for vitality percentage <70% and non-cytotoxic for values >70% (Cannella et al., 2019; Ismael et al., 2020; Ramasamy et al., 2022). Therefore, the reported Cr(III)-based compounds in this study

TABLE 4 Molecular docking scores and the corresponding prominent residual amino acid interactions of the complexes against estrogen receptor alpha (ERα; PDB: 5G4).

Cpds	Rmsd	Binding energy (kcal/mol)	Inhibition constant (K_i) (μM)	H-bonding	van der Waals	π–alkyl/π–ion
Cr1	1.14	−6.83	9.93	-	Phe 445, Gly 390, Ile 386, Leu 387, Trp 360, and Asn 359	Met 357, His 356, Arg 363, Lys 449, Arg 394, and Glu 323
Cr2	1.35	−6.26	22.99	-	Phe 445, Gly 390, Ile 386, Leu 387, Trp 360, and Asn 359	Arg 390, Lys 449, Glu 357, Arg 363, His 356, and Met 357
Cisplatin	0.39	−6.32	23.42	Ser 468 and Asp 374	Lys 467	Thr 371 and Glu 471

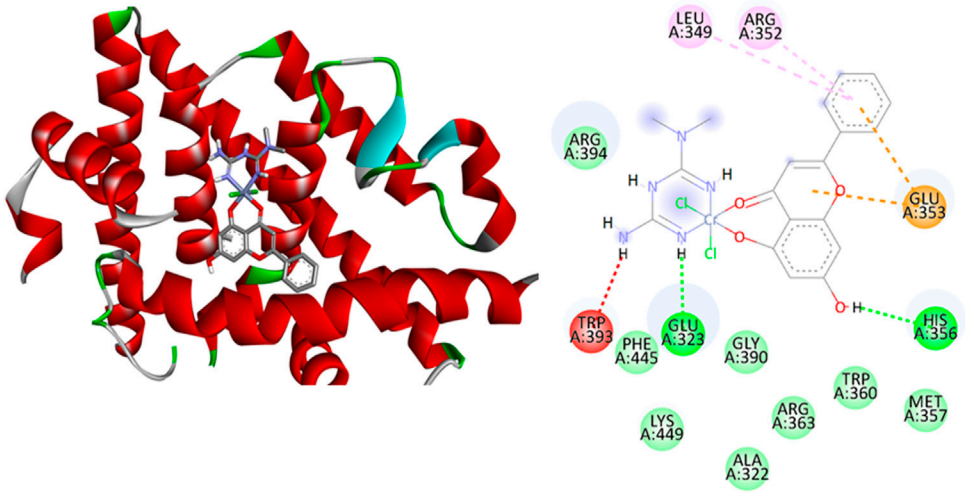

FIGURE 8
Binding interactions of **Cr2** against estrogen receptor alpha (ERα; PDB: 5G4).

are considered cytotoxic with IC_{50} values in the range of those previously reported (Bravo-Gómez et al., 2009; Alem et al., 2022). Comparing the ligand composition of the complexes, **Cr1** with 1,10-phenanthroline showed enhanced bioactivity consistent with the previously reported 1,10-phenanthroline-based cytotoxic metal complexes (Bravo-Gómez et al., 2009; Buchtík et al., 2012; Nunes et al., 2020; Reina et al., 2021). The cellular morphology of the microscopic images of the MCF-7 cells (untreated) and treated with 50 μM **Cr1**, **Cr2**, and cisplatin for 24 h is provided in Figures 7A–D.

MCF-7 cells are characterized by their epithelial-like cell morphology with irregular and polygonal shapes (Andiappan et al., 2018; Razak et al., 2019). This morphology was observed in untreated MCF-Cells (Figure 7A). However, after treatment with 50 μM **Cr1**, **Cr2**, and cisplatin for 24 h, the morphology changed, with the cells appearing round to oval in shape, while the cell density was also reduced. The effect was more pronounced for the **Cr1** complex even at lower concentrations (12.5 μM). Generally, the microscopic and cell viability results obtained from this work demonstrated that the reported metal complexes are cytotoxic, as reported for other metal complexes (Andiappan et al., 2018; Razak et al., 2019; Nunes et al., 2020; Alem et al., 2022).

3.11.2 Molecular docking analysis against estrogen receptor alpha

The 2D and 3D interaction of the synthesized complexes (**Cr1** and **Cr2**) with estrogen receptor alpha (ERα; PDB:5G4) residual amino acids together with a binding affinity (kcal/mol) and the inhibition constant (Ki) parameters are given in Table 4; Figure 8 and Supplementary Figure S10 of the Supporting Material. **Cr1** demonstrated a binding energy and an inhibition constant of −6.83 kcal/mol and 9.93 μM, respectively, with a total of 14 van der Waals (Phe 445, Gly 390, Ile 386, Leu 387, Trp 360, and Asn 359) and π–alkyl/π–ion (Met 357, His 356, Arg 363, Lys 449, Arg 394, Glu 353, Glu 323, and His 356) interactions (Figure 8). **Cr2** showed two hydrogen bonding (Glu 323 and His 356), 16 van der Waals (Arg 394, Phe 445, Lys 449, Gly 390, Ala 322, Arg 263, and Met 357), and π–alkyl/π–ion (Arg 394, Lee 349, Arg 352, Glu 353, Glu 353, Glu 323, Glu 323, Trp 393, and Trp 393) interactions. Arg 394, Glu 353, Leu 387, and Leu 391 are the most important active site amino acids of ERα that participate in hydrogen bonding and π–alkyl interactions (Pang et al., 2018). The synthesized complexes showed interaction with three of the amino acids (Arg 394, Glu 353, and Leu 387), with high interactions for **Cr1**. The obtained residual amino acid interactions showed that the number

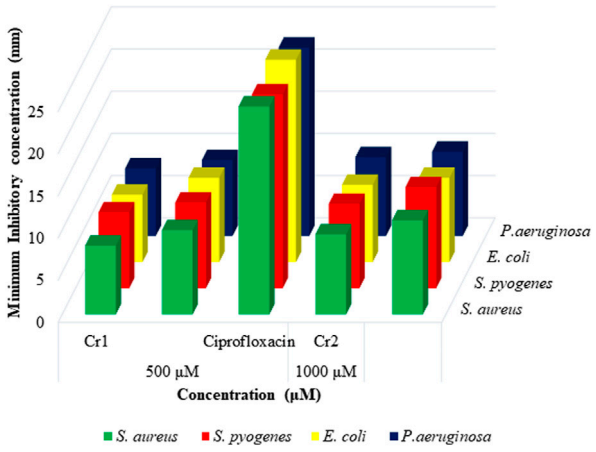

FIGURE 9
Antibacterial activity evaluation graph for **Cr1** and **Cr2** complexes.

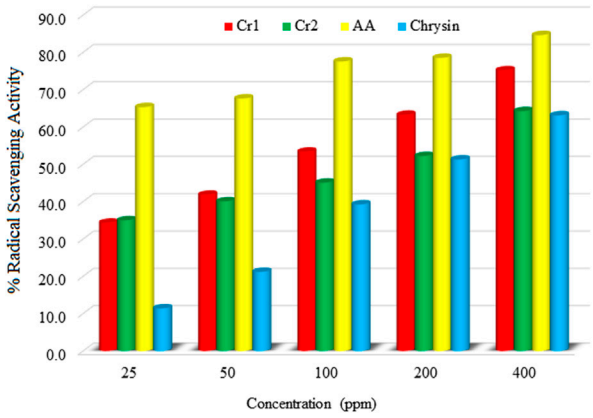

FIGURE 11
Antioxidant profiles of the synthesized metal complexes (**Cr1** and **Cr2**).

of interactions affected the binding affinity and *Ki*. The results further showed that the **Cr1** > Cisplatin > **Cr2,** in line with the cytotoxicity activity of the complexes.

3.12 Antimicrobial activity studies

All synthesized complexes showed minimum inhibition zones ranging from 8.00 to 12.00 mm, inferring that the complexes were active against the tested bacterial strains (Supplementary Table S2), as cultured bacteria with halos >7 mm were considered susceptible to the tested complex (Alam et al., 2010; Allouche, 2012; Omolo et al., 2014). However, a high difference between the MIZ of the complexes and the control, ciprofloxacin, was observed (Figure 9).

3.12.1 Molecular docking analysis against *Staphylococcus aureus* and *Escherichia coli*

Molecular docking studies fundamentally define the binding modes of ligand interaction at the active site of the protein (Kouser et al., 2022). In this study, the synthesized Cr(III)-centered mixed ligand complexes were subjected to molecular docking studies against bacterial strains on which the complexes showed better *in vitro* antibacterial activity. The binding interactions with the complexes showed that **Cr2** created hydrogen bonding interactions with Leu 5 and Phe 92 amino acid residues (Supplementary Tables S2, S4 and Figure 10). Moreover, it created 14 interactions, nine of which were van de Waals (Leu 54, Asp 27, Val 31, Thr 46, Val 6, Phe 98, Trp 22, Ser 49, and Gln 19) and five of which were π–alkyl/π–ion (Leu 28, Leu 20, Ala 7, Ile 4, and Ile 50) with a binding energy and inhibition constant of −8.82 kcal/mol and 0.30 µM, respectively. The presence of a greater number of interactions, high binding energy, and small inhibition constant of **Cr2** against *S. aureus* make this

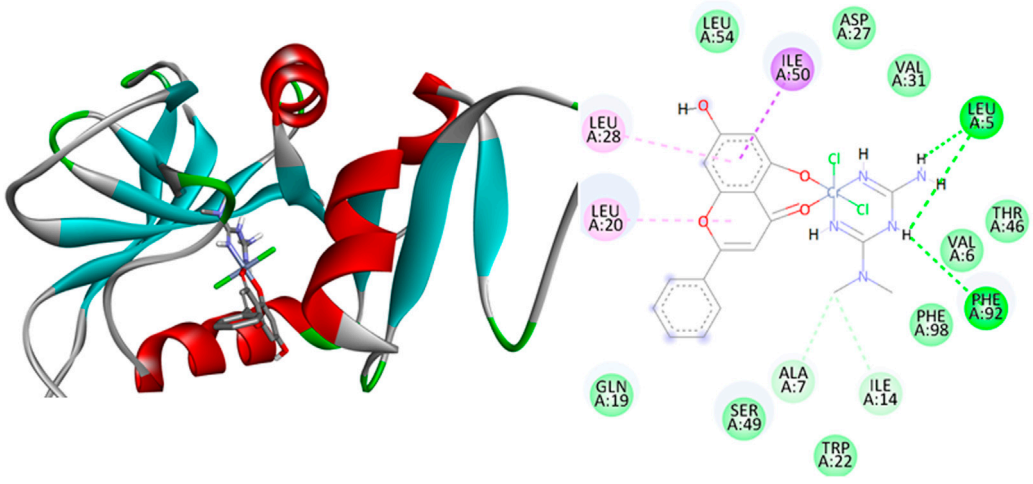

FIGURE 10
Binding interactions of **Cr2** against *Staphylococcus aureus* (PDB: 2w9h).

complex show better *in vitro* antibacterial activity compared to **Cr1** (Supplementary Table S3 and Supplementary Figure S11). Similarly, the docking study of **Cr2** against *E. coli* protein showed high binding energy (−7.51 kcal/mol), minimum inhibition constant (2.78 μM), two hydrogen bonds (Gly 77 and Asn 46), eight van der Waals interactions (Val 44, Thr 165, Gly 75, Glu 50, Pro 79, Asp 49, Ile 94, and Met 166), and seven π–alkyl/π–ion interactions (Gly 77, Val 167, Val 43, Ala 47, Asp 73, Val 71, and Asn 46 amino acid residues) (Supplementary Table S4 and Figure 10, Supplementary Figure S11–S14). The obtained results in all types of bacterial strains are consistent with the minimum zone of inhibition obtained in the *in vitro* evaluations of the antibacterial activity.

3.12.2 DPPH radical scavenging activity analysis

The graphical presentation of the free radical scavenging activity of the free ligand chrysin and the synthesized complexes (**Cr1** and **Cr2**) were evaluated using a DPPH assay (Figure 11. Higher antioxidant activities (34.370%–75.179% DPPH free radical scavenging) of the metal complexes than the free ligand (11.398%–63.118%) were observed. The extended conjugation because of the metal coordination to the ligands might have enhanced the proton transfer process observed in the increased antioxidant activity of the metal complexes over the free ligand chrysin. The antioxidant activity against DPPH free radical scavenging followed the order AA > **Cr1** > **Cr2** > chrysin with percent radical scavenging activities of 84.624, 75.179, 64.245, and 63.118% for AA, **Cr1**, **Cr2**, and chrysin, respectively, at 400 ppm.

4 Conclusion

Organic–inorganic hybrid salts of Cr(III) complexes containing the natural flavonoid chrysin were synthesized. Spectroscopic (FTIR and UV/Vis), microscopic (SEM-EDX), thermogravimetric (TGA/DTA), mass spectrometric, pXRD, and molar conductance measurements were used to characterize the synthesized complexes. The coordinations of the ligands to the metal ions were confirmed using FTIR and UV/Vis spectral data. A molar conductance study was used to confirm the ionic/non-ionic nature of the complexes. The molecular weights of the metal complexes were confirmed by mass spectrometry. SEM-EDX was used to confirm the composition of the elements in the synthesized metal complexes. The pXRD patterns of the complexes in their powder showed polycrystalline natures with crystalline average sizes of 21.453 and 19.600 nm, for **Cr1** and **Cr2**, respectively. Biologically, **Cr1** showed significant cytotoxicity against the MCF-7 cell line, with an IC_{50} value of 8.08 μM compared to **Cr2** (IC_{50} = 30.85 μM) and cisplatin (IC_{50} = 18.62 μM). The overall results showed that the Cr(III) complexes reported in this study are promising cytotoxic drug candidates. However, further *in vivo* cytotoxicity studies against the MCF-7 cell line and toxicity studies are recommended.

Data availability statement

The datasets presented in this study can be found in online repositories. The names of the repository/repositories and accession number(s) can be found in the article/Supplementary Material.

Author contributions

Experimental: MBA, TeD, TBD, EAB, and MOK. Data analysis: MBA, TaD, TeD, and TBD. Methodology: MBA, TeD, and TBD. Original draft writing: MBA, TBD, and TeD. Writing—review and editing: MBA, TaD, TeD, TBD, JOO, MOK, EAB, KJN, and MZ.

Acknowledgments

The authors thank Adama Science and Technology University and the University of Botswana for technical and material support. Computational resources were supplied by MetaCentrum under the project ‘e-Infrastructure CZ’ (e-INFRA CZ ID: 90140) supported by the Ministry of Education, Youth and Sports of the Czech Republic. The authors thank Associate Professor Claire Perks (University of Bristol, United Kingdom) for providing MCF-7 breast cancer cells, as well as Kgomotso Modo for her technical assistance.

Conflict of interest

The authors declare that the research was conducted in the absence of any commercial or financial relationships that could be construed as a potential conflict of interest.

Publisher’s note

All claims expressed in this article are solely those of the authors and do not necessarily represent those of their affiliated organizations, or those of the publisher, the editors, and the reviewers. Any product that may be evaluated in this article, or claim that may be made by its manufacturer, is not guaranteed or endorsed by the publisher.

Supplementary material

The Supplementary Material for this article can be found online at: https://www.frontiersin.org/articles/10.3389/fchem.2023.1173604/full#supplementary-material

References

Abbas, B. F., Kamel, B. A., and Khamais, W. M. (2019). Preparation, diagnosis, biological activity, and theoretical studies of some mixed drug complexes. *Sci. World J.* 2019, 8962923. doi:10.1155/2019/8962923

Abd El-Halim, H. F., Mohamed, G. G., and Khalil, E. A. M. (2017). Synthesis, spectral, thermal and biological studies of mixed ligand complexes with newly prepared Schiff base and 1,10-phenanthroline ligands. *J. Mol. Struct.* 1146, 153–163. doi:10.1016/j.molstruc.2017.05.092

Abdelrahman, S., Alghrably, M., Campagna, M., Hauser, C. A. E., Jaremko, M., and Lachowicz, J. I. (2021). Metal complex formation and anticancer activity of Cu(I) and Cu(II) complexes with metformin. *Molecules* 26, 4730. doi:10.3390/molecules26164730

Abebe, A., Bayeh, Y., Belay, M., Gebretsadik, T., Thomas, M., and Linert, W. (2020). Mono and binuclear cobalt(II) mixed ligand complexes containing 1,10-phenanthroline and adenine using 1,3-diaminopropane as a spacer: Synthesis, characterization, and antibacterial activity investigations. *Future J. Pharm. Sci.* 6, 1–9. doi:10.1186/s43094-020-00030-4

Abebe, A., and Hailemariam, T. (2016). Synthesis and assessment of antibacterial activities of ruthenium(III) mixed ligand complexes containing 1,10-Phenan-troline and guanide. *Bioinorganic Chem. Appl.* 2016, 1–9. doi:10.1155/2016/3607924

Ahmad, S., Hamid, F., Hamid, M., Wattoo, S., Sarwar, S., and Nawaz, A. (2012). Spectrophotometric study of stability constants of cimetidine–Ni(II) complex at different temperatures. *Arabian J. Chem.* 5, 309–314. doi:10.1016/j.arabjc.2010.09.009

Alam, M., Yasmin, M., Nessa, J., and Ahsan, C. (2010). Antibacterial activity of chloroform and ethanol extracts of black cumin seeds (Nigella sativa) against multi-drug resistant human pathogens under laboratory conditions. *J. Med. Plants Res.* 4, 1901–1905. doi:10.5897/JMPR10.324

Alem, M., Damena, T., Desalegn, T., Koobotse, M., Eswaramoorthy, R., Ngwira, K., et al. (2022). Cytotoxic mixed-ligand complexes of Cu(II): A combined experimental and computational study. *Front. Chem.* 10, 1028957. doi:10.3389/fchem.2022.1028957

Ali, I., Wani, W. A., and Saleem, K. (2013). Empirical formulae to molecular structures of metal complexes by molar conductance. *Synthesis React. Inorg. metal-organic, nano-metal Chem.* 43, 1162–1170. doi:10.1080/15533174.2012.756898

Allouche, A.-r. (2012). Gabedit-A graphical user interface for computational chemistry softwares. *J. Comput. Chem.* 32, 174–182. doi:10.1002/jcc.21600

Altomare, A., Corriero, N., Cuocci, C., Falcicchio, A., Moliterni, A., and Rizzi, R. (2015). *QUALX2.0*: A qualitative phase analysis software using the freely available database POW_COD. *J. Appl. Crystallogr.* 48, 598–603. doi:10.1107/s1600576715002319

Anderson, R. A., Cheng, N., Bryden, N. A., Polansky, M. M., Cheng, N., Chi, J., et al. (1997). Elevated intakes of supplemental chromium improve glucose and insulin variables in individuals with type 2 diabetes. *Diabetes* 46, 1786–1791. doi:10.2337/diabetes.46.11.1786

Andiappan, K., Sanmugam, A., Deivanayagam, E., Karuppasamy, K., Kim, H.-S., and Vikraman, D. (2018). *In vitro* cytotoxicity activity of novel Schiff base ligand-lanthanide complexes. *Sci. Rep.* 8, 3054. doi:10.1038/s41598-018-21366-1

Becke, A. D. (1993). Density-functional thermochemistry III. The role of exact exchange. *J. Chem. Phys.* 98, 5648–5652. doi:10.1063/1.464913

Bitew, M., Desalegn, T., Demissie, T. B., Belayneh, A., Endale, M., and Eswaramoorthy, R. (2021). Pharmacokinetics and drug-likeness of antidiabetic flavonoids: Molecular docking and DFT study. *Plos One* 16, e0260853. doi:10.1371/journal.pone.0260853

Boros, E., Dyson, P. J., and Gasser, G. (2020). Classification of metal-based drugs according to their mechanisms of action. *Chem* 6, 41–60. doi:10.1016/j.chempr.2019.10.013

Bravo-Gómez, M. E., García-Ramos, J. C., Gracia-Mora, I., and Ruiz-Azuara, L. (2009). Antiproliferative activity and QSAR study of copper(II) mixed chelate [Cu(N–N)(acetylacetonato)]NO3 and [Cu(N–N)(glycinato)]NO3 complexes, (Casiopeínas®). *J. Inorg. Biochem.* 103, 299–309. doi:10.1016/j.jinorgbio.2008.10.006

Buchtík, R., Trávníček, Z., and Vančo, J. (2012). *In vitro* cytotoxicity, DNA cleavage and SOD-mimic activity of copper(II) mixed-ligand quinolinonato complexes. *J. Inorg. Biochem.* 116, 163–171. doi:10.1016/j.jinorgbio.2012.07.009

Cannella, V., Altomare, R., Chiaramonte, G., Di Bella, S., Mira, F., Russotto, L., et al. (2019). Cytotoxicity evaluation of endodontic pins on L929 cell line. *BioMed Res. Int.* 2019, 3469525. doi:10.1155/2019/3469525

Chen, M., Huang, X., Shi, H., Lai, J., Ma, L., Lau, T.-C., et al. (2021). Cr(V)–Cr(III) *in-situ* transition promotes ROS generation to achieve efficient cancer therapy. *Biomaterials* 276, 120991. doi:10.1016/j.biomaterials.2021.120991

Choudhary, V., Bhatt, A., Dash, D., and Sharma, N. (2019). DFT calculations on molecular structures, HOMO–LUMO study, reactivity descriptors and spectral analyses of newly synthesized diorganotin(IV) 2-chloridophenylacetohydroxamate complexes. *J. Comput. Chem.* 40, 2354–2363. doi:10.1002/jcc.26012

Damena, T., Alem, M. B., Zeleke, D., Demissie, T. B., and Desalegn, T. (2023). Synthesis and computational studies of novel cobalt(II) and oxovanadium(IV) complexes of quinoline carbaldehyde derivative ligand for antibacterial and antioxidant applications. *J. Mol. Struct.* 1280, 134994. doi:10.1016/j.molstruc.2023.134994

Damena, T., Zeleke, D., Desalegn, T., Demissie, B. T., and Eswaramoorthy, R. (2022). Synthesis, characterization, and biological activities of novel vanadium(IV) and cobalt(II) complexes. *ACS Omega* 7, 4389–4404. doi:10.1021/acsomega.1c06205

Dong, J., Wang, N. N., Yao, Z. J., Zhang, L., Cheng, Y., Ouyang, D., et al. (2018). ADMETlab: A platform for systematic ADMET evaluation based on a comprehensively collected ADMET database. *J. Cheminformatics* 10, 1–11. doi:10.1186/s13321-018-0283-x

El-Megharbel, S. (2015). Synthesis, characterization and antidiabetic activity of chromium (III) metformin complex. *J. Microb. Biochem. Technol.* 7, 65–75. doi:10.4172/1948-5948.1000184

El-Sonbati, A., Omar, N., Abou-Dobara, M., Diab, M., El-Mogazy, M., Morgan, S. M., et al. (2021). Structural, molecular docking computational studies and *in-vitro* evidence for antibacterial activity of mixed ligand complexes. *J. Mol. Struct.* 1239, 130481. doi:10.1016/j.molstruc.2021.130481

El-Sonbati, A. Z., Diab, M. A., Eldesoky, A. M., Morgan, S. M., and Salem, O. L. (2019). Polymer complexes. LXXVI. Synthesis, characterization, CT-DNA binding, molecular docking and thermal studies of sulfoxine polymer complexes. *Appl. Organomet. Chem.* 33, e4839. doi:10.1002/aoc.4839

Grimme, S. (2004). *Reviews in computational chemistry volume, 20*. United States: Wiley, 153–218.

Halevas, E., Mavroidi, B., Pelecanou, M., and Hatzidimitriou, A. G. (2021). Structurally characterized zinc complexes of flavonoids chrysin and quercetin with antioxidant potential. *Inorganica Chim. Acta* 523, 120407. doi:10.1016/j.ica.2021.120407

Hao, C., Hao, J., Wang, W., Han, Z., Li, G., Zhang, L., et al. (2011). Insulin sensitizing effects of oligomannuronate-chromium (III) complexes in C2C12 skeletal muscle cells. *PLoS One* 6, e24598. doi:10.1371/journal.pone.0024598

Hay, P. J., and Wadt, W. R. (1985). *Ab initio* effective core potentials for molecular calculations. Potentials for K to Au including the outermost core orbitals. *J. Chem. Phys.* 82, 299–310. doi:10.1063/1.448975

Heaslet, H., Harris, M., Fahnoe, K., Sarver, R., Putz, H., Chang, J., et al. (2009). Structural comparison of chromosomal and exogenous dihydrofolate reductase from*Staphylococcus aureus*in complex with the potent inhibitor trimethoprim. *Proteins Struct. Funct. Bioinforma.* 76, 706–717. doi:10.1002/prot.22383

Holzwarth, U., and Gibson, N. (2011). The Scherrer equation versus the 'Debye-Scherrer equation'. *Nat. Nanotechnol.* 6, 534. doi:10.1038/nnano.2011.145

Ismael, M., Abdel-Mawgoud, A. M. M., Rabia, M. K., and Abdou, A. (2020). Design and synthesis of three Fe(III) mixed-ligand complexes: Exploration of their biological and phenoxazinone synthase-like activities. *Inorganica Chim. Acta* 505, 119443. doi:10.1016/j.ica.2020.119443

Kacsir, I., Sipos, A., Kiss, T., Major, E., Bajusz, N., Tóth, E., et al. (2023). Half sandwich-type osmium, ruthenium, iridium and rhodium complexes with bidentate glycosyl heterocyclic ligands induce cytostasis in platinum-resistant ovarian cancer cells and bacteriostasis in Gram-positive multiresistant bacteria. *Front. Chem.* 11, 1086267. doi:10.3389/fchem.2023.1086267

Karges, J., Stokes, R. W., and Cohen, S. M. (2021). Metal complexes for therapeutic applications. *Trends Chem.* 3, 523–534. doi:10.1016/j.trechm.2021.03.006

Kasprzak, M. M., Erxleben, A., and Ochocki, J. (2015). Properties and applications of flavonoid metal complexes. *Rsc Adv.* 5, 45853–45877. doi:10.1039/c5ra05069c

Kilpin, K. J., and Dyson, P. J. (2013). Enzyme inhibition by metal complexes: Concepts, strategies and applications. *Chem. Sci.* 4, 1410–1419. doi:10.1039/c3sc22349c

Kouser, S., Joythi, M., Begum, A. B., Asha, M., Al-Ostoot, F. H., Lakshmeesha, D., et al. (2022). Molecular docking, synthesis and antimicrobial evaluation of metal complexes with Schiff base. *Results Chem.* 5, 100650. doi:10.1016/j.rechem.2022.100650

Kralovec, J. A., Potvin, M. A., Wright, J. H., Watson, L. V., Ewart, H. S., Curtis, J. M., et al. (2009). Chromium(III)–docosahexaenoic acid complex: Synthesis and characterization. *J. Funct. Foods* 1, 291–297. doi:10.1016/j.jff.2009.06.001

Krishnan, R., Binkley, J. S., Seeger, R., and Pople, J. A. (1980). Self-consistent molecular orbital methods. XX. A basis set for correlated wave functions. *J. Chem. Phys.* 72, 650–654. doi:10.1063/1.438955

Lee, C., Yang, W., and Parr, R. G. (1988). Development of the Colle-Salvetti correlation-energy formula into a functional of the electron density. *Phys. Rev. B* 37, 785–789. doi:10.1103/physrevb.37.785

Lemilemu, F., Bitew, M., Demissie, T. B., Eswaramoorthy, R., and Endale, M. (2021). Synthesis, antibacterial and antioxidant activities of thiazole-based schiff base derivatives: A combined experimental and computational study. *BMC Chem.* 15, 67. doi:10.1186/s13065-021-00791-w

Nakamoto, K. (2009). *Infrared and Raman spectra of inorganic and coordination compounds, part B: Applications in coordination, organometallic, and bioinorganic chemistry*. United States: John Wiley & Sons.

Narramore, S., Stevenson, C. E., Maxwell, A., Lawson, D. M., and Fishwick, C. W. (2019). New insights into the binding mode of pyridine-3-carboxamide inhibitors of *E. coli* DNA gyrase. *Bioorg. Med. Chem.* 27, 3546–3550. doi:10.1016/j.bmc.2019.06.015

Ndong, P. R., Signé, M., Kenfack, P. T., Mbiangué, Y. A., Bebga, G., and Wenger, E. (2020). A novel chromium(III) hybrid salt, triethylammonium trans-diaquabis(oxalato-κ2O1,O2) chromate(III), (C6H16N)[Cr(C2O4)2(H2O)2]: Synthesis, spectroscopic studies, thermal behavior and crystal structure. *Open J. Inorg. Chem.* 10, 39–51. doi:10.4236/ojic.2020.104005

Nunes, P., Correia, I., Marques, F., Matos, A. P., Dos Santos, M. M., Azevedo, C. G., et al. (2020). Copper complexes with 1,10-phenanthroline derivatives: Underlying factors affecting their cytotoxicity. *Inorg. Chem.* 59, 9116–9134. doi:10.1021/acs.inorgchem.0c00925

Olelewe, C., and Awuah, S. G. (2023). Mitochondria as a target of third row transition metal-based anticancer complexes. *Curr. Opin. Chem. Biol.* 72, 102235. doi:10.1016/j.cbpa.2022.102235

Ommenya, F., Nyawade, E., Andala, D., and Kinyua, J. (2020). Synthesis, characterization and antibacterial activity of schiff base, 4-chloro-2-{(E)-[(4-Fluorophenyl)imino]methyl}phenol metal (II) complexes. *J. Chem.* 2020, 1745236. doi:10.1155/2020/1745236

Omolo, J. O., Mayaka, R. K., Njue, A. W., Adongo, J. O., and Matofari, J. (2014). Antimicrobial activity of the seed crude extracts of Triumfettarhomboidea (Tiliaceae). *Sci. J. Microbiol.* 2014, 1–5. doi:10.7237/sjmb/249

Pandey, G., Jain, G. C., and Mathur, N. (2012). Therapeutic potential of metals in managing diabetes mellitus: A review. *J. Mol. Pathophysiol.* 1, 63–76. doi:10.5455/jmp.20120410105457

Pang, X., Fu, W., Wang, J., Kang, D., Xu, L., Zhao, Y., et al. (2018). Identification of estrogen receptor α antagonists from natural products via *in vitro* and in silico approaches. *Oxidative Med. Cell. Longev.* 2018, 6040149. doi:10.1155/2018/6040149

Pechova, A., and Pavlata, L. (2007). Chromium as an essential nutrient: A review. *Veterinarni Medicina-Praha* 52, 1–18. doi:10.17221/2010-vetmed

Peng, M., and Yang, X. (2015). Controlling diabetes by chromium complexes: The role of the ligands. *J. Inorg. Biochem.* 146, 97–103. doi:10.1016/j.jinorgbio.2015.01.002

Ramasamy, S., Muthusamy, S., Nagarajan, S., Nath, A. V., Savarimuthu, J. S., Jayaprakash, J., et al. (2022). Fabrication of collagen with polyhexamethylene biguanide: A potential scaffold for infected wounds. *J. Biomed. Mater. Res. Part B Appl. Biomaterials* 110, 535–546. doi:10.1002/jbm.b.34933

Razak, N. A., Abu, N., Ho, W. Y., Zamberi, N. R., Tan, S. W., Alitheen, N. B., et al. (2019). Cytotoxicity of eupatorin in MCF-7 and MDA-MB-231 human breast cancer cells via cell cycle arrest, anti-angiogenesis and induction of apoptosis. *Sci. Rep.* 9, 1514. doi:10.1038/s41598-018-37796-w

Reina, M., Hernández-Ayala, L. F., Bravo-Gómez, M. E., Gómez, V., and Ruiz-Azuara, L. (2021). Second generation of Casiopeinas®: A joint experimental and theoretical study. *Inorganica Chim. Acta* 517, 120201. doi:10.1016/j.ica.2020.120201

Renfrew, A. K. (2014). Transition metal complexes with bioactive ligands: Mechanisms for selective ligand release and applications for drug delivery. *Metallomics* 6, 1324–1335. doi:10.1039/c4mt00069b

Ruiz-Azuara, L., and Bravo-Gomez, M. E. (2010). Copper compounds in cancer chemotherapy. *Curr. Med. Chem.* 17, 3606–3615. doi:10.2174/092986710793213751

Scalese, G., Kostenkova, K., Crans, D. C., and Gambino, D. (2022). Metallomics and other omics approaches in antiparasitic metal-based drug research. *Curr. Opin. Chem. Biol.* 67, 102127. doi:10.1016/j.cbpa.2022.102127

Stephens, P. J., Devlin, F. J., Chabalowski, C. F., and Frisch, M. J. (1994). *Ab initio* calculation of vibrational absorption and circular dichroism spectra using density functional force fields. *J. Phys. Chem.* 98, 11623–11627. doi:10.1021/j100096a001

Sundaraganesan, N., Mariappan, G., and Manoharan, S. (2012). Molecular structure and vibrational spectroscopic studies of Chrysin using HF and Density Functional Theory. *Spectrochimica Acta Part A Mol. Biomol. Spectrosc.* 87, 67–76. doi:10.1016/j.saa.2011.11.011

Tamiru, G., Abebe, A., Abebe, M., and Liyew, M. (2019). Synthesis, structural investigation and biological application of new mono- and binuclear cobalt (II) mixed-ligand complexes containing 1,10-phenanthroline, acetamide and ethylenediamine. *Ethiop. J. Sci. Technol.* 12, 69–91. doi:10.4314/ejst.v12i1.4

Ulas, M., Orhan, C., Tuzcu, M., Ozercan, I. H., Sahin, N., Gencoglu, H., et al. (2015). Anti-diabetic potential of chromium histidinate in diabetic retinopathy rats. *BMC complementary Altern. Med.* 15, 16. doi:10.1186/s12906-015-0537-3

Villamizar-Delgado, S., Porras-Osorio, L. M., Pineros, O., Ellena, J., Balcazar, N., Varela-Miranda, R. E., et al. (2020). Biguanide–transition metals complexes as potential drug for hyperglycemia treatment. *RSC Adv.* 10, 22856–22863. doi:10.1039/d0ra04059b

Vincent, J. B. (2004). Recent advances in the nutritional biochemistry of trivalent chromium. *Proc. Nutr. Soc.* 63, 41–47. doi:10.1079/pns2003315

Vogler, A., and Kunkely, H. (2007). Ligand-to-ligand and intraligand charge transfer and their relation to charge transfer interactions in organic zwitterions. *Coord. Chem. Rev.* 251, 577–583. doi:10.1016/j.ccr.2006.04.015

Wang, C., Chen, Z., Pan, Y., Gao, X., and Chen, H. (2017). Anti-diabetic effects of Inonotus obliquus polysaccharides-chromium (III) complex in type 2 diabetic mice and its sub-acute toxicity evaluation in normal mice. *Food Chem. Toxicol.* 108, 498–509. doi:10.1016/j.fct.2017.01.007

Xie, M., Zhao, H., Liu, Q., Zhu, Y., Yin, F., Liang, Y., et al. (2017). Structural basis of inhibition of erα-coactivator interaction by high-affinity N-terminus isoaspartic acid tethered helical peptides. *J. Med. Chem.* 60, 8731–8740. doi:10.1021/acs.jmedchem.7b00732

Zare, A., Monfared, F., and Sajadikhah, S. S. (2021). Synthesis and characterization of a novel organic–inorganic hybrid salt and its application as a highly effectual Brønsted–Lewis acidic catalyst for the production of N,N′-alkylidene bisamides. *Appl. Organomet. Chem.* 35, e6046. doi:10.1002/aoc.6046

frontiers | Frontiers in Chemistry

TYPE Review
PUBLISHED 23 August 2023
DOI 10.3389/fchem.2023.1252191

OPEN ACCESS

EDITED BY
Gcina Mamba,
University of South Africa, South Africa

REVIEWED BY
Mohamed Bayati,
University of Missouri System,
United States
Fulai Zhao,
Tianjin University, China

*CORRESPONDENCE
Sivuyisiwe Mapukata,
sivuyisiwem@mintek.co.za
Bulelwa Ntsendwana,
bulelwan@mintek.co.za

RECEIVED 03 July 2023
ACCEPTED 11 August 2023
PUBLISHED 23 August 2023

CITATION
Mapukata S, Ntsendwana B, Mokhena T and Sikhwivhilu L (2023), Advances on sonophotocatalysis as a water and wastewater treatment technique: efficiency, challenges and process optimisation.
Front. Chem. 11:1252191.
doi: 10.3389/fchem.2023.1252191

Advances on sonophotocatalysis as a water and wastewater treatment technique: efficiency, challenges and process optimisation

Sivuyisiwe Mapukata[1]*, Bulelwa Ntsendwana[1]*, Teboho Mokhena[1] and Lucky Sikhwivhilu[1,2]

[1]Nanotechnology Innovation Centre (NIC), Advanced Materials Division, Mintek, Johannesburg, South Africa, [2]Department of Chemistry, Faculty of Science, Engineering and Agriculture, University of Venda, Thohoyandou, South Africa

Due to water shortage and increased water pollution, various methods are being explored to improve water quality by treating contaminants. Sonophotocatalysis is a combination of two individual water treatment processes i.e., photocatalysis and sonocatalysis. With advantages including shorter reaction times and enhanced activity, this technique shows possible futuristic applications as an efficient water treatment technology. Herein, background insight on sonophotocatalysis as a water and wastewater treatment technique as well as the general mechanism of activity is explained. The commonly used catalysts for sonophotocatalytic applications as well as their synthesis pathways are also briefly discussed. Additionally, the utilisation of sonophotocatalysis for the disinfection of various microbial species as well as treatment of wastewater pollutants including organic (dyes, pharmaceuticals and pesticides) and inorganic species (heavy metals) is deliberated. This review also gives a critical analysis of the efficiency, enhancement strategies as well as challenges and outlooks in this field. It is thus intended to give insight to researchers in the context of facilitating future developments in the field of water treatment, and advancing sonophotocatalysis towards large-scale implementation and commercialization.

KEYWORDS

sonophotocatalysis, sonocatalysis, photocatalysis, wastewater treatment, semiconductors

1 Introduction

Water reclamation and reuse is rapidly gaining attention worldwide due to the heightened water scarcity as a result of industrialisation, climate change and poor resource management (Englande et al., 2015). Access to safe drinking water is therefore becoming an ever-increasing problem in an expanding global economy and increasing population (Boretti and Rosa, 2019). Repercussions of the water shortage include ecosystem degradation, health complications and overall destruction of livelihood (Mishra et al., 2021).

Different techniques have been explored for treating wastewater and enhancing water security, such as flocculation, coagulation, adsorption, ultrafiltration, biodegradation, and reverse osmosis processes (Barakat and Schmidt, 2010; Moghaddam et al., 2010; Park and Hu, 2010; Aneyo et al., 2016; Kryuchkova et al., 2021; Sibiya et al., 2021). However, most of

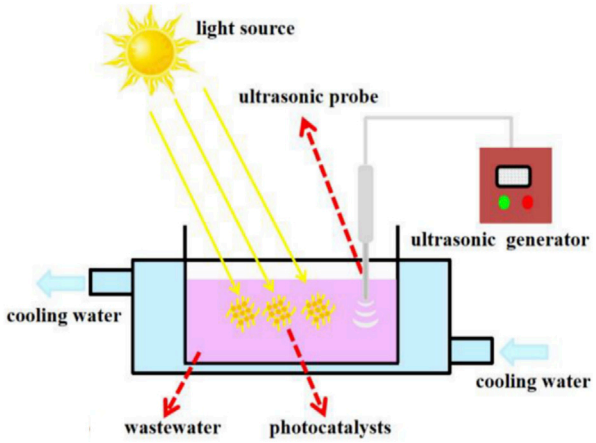

FIGURE 1
Schematic diagram of the sonophotocatalytic reactor. Reprinted with permission from (Zhang et al., 2021).

these methods are not cost effective and have several drawbacks such as the inability to achieve total mineralization of the pollutants as well as long treatment times (Al-Tohamy et al., 2022). Additionally, treatment methods like reverse osmosis generate water that is devoid of useful minerals (Sharma and Bhattacharya, 2017).

Advanced oxidation processes (AOPs) have thus been investigated as efficient methods for the degradation of water pollutants as they rely on the generation of highly reactive radicals which generally mineralise contaminants into CO_2 and H_2O (Kaswan and Kaur, 2023). Photocatalysis is generally the most commonly implemented AOP due to its outstanding pollutant degradation capability for a wide range of contaminants (ul Haq et al., 2022). The photocatalysis process is based on the exposure of a photocatalyst to light, leading to the generation of highly reactive oxygen species (ROS), including radicals and peroxides, which break down pollutants and eliminate microorganisms from an aqueous environment (Zhu and Wang, 2017). However, photocatalysis is limited to treating highly transparent wastewater to ensure that the photocatalysts get sufficient light exposure (Wang et al., 2022). Sonocatalytic degradation on the other hand uses ultrasound to generate highly reactive radicals that efficiently degrade a range of pollutants (Eren and Ince, 2010; Wang and Cheng, 2023a). This technology has gained attention because it does not require any pre-treatment of the effluent and it has a stronger penetration ability than light in the catalytic degradation of pollutants (Wang et al., 2017). These two processes can either be implemented separately or concurrently i.e., sonophotocatalysis, which is based on the synergistic interaction of the two individual processes and is therefore a more effective and versatile technique (Wang and Cheng, 2023b). Using a reactor such as that shown in Figure 1 (Zhang et al., 2021), sonophotocatalysis generates clean water upon treatment of wastewater in the presence of a catalyst, which is exposed to both ultrasound and light irradiation.

This review is thus intended to give insight on sonophotocalysis as a water and wastewater treatment technique. Advances that have been achieved in the utilisation of sonophotocatalysis in the disinfection of various microbial species as well as treatment of wastewater pollutants including organic (dyes, pharmaceuticals and pesticides) and inorganic species (heavy metals) are critically analysed. With the aim of contributing to future developments in the field of sonophotocatalytic wastewater treatment, a critical analysis of the efficiency, enhancement strategies as well as challenges and outlooks in this field are also deliberated.

2 Sonophotocatalysis mechanism

The mechanisms of activity of sonocatalysis and photocatalysis as well as their synergistic interaction in sonophotocatalysis are detailed below.

2.1 Sonocatalysis

Sonocatalysis is a process that uses a photoactive material in the presence of ultrasonic irradiation but without the presence of light irradiation. Sonocatalytic degradation technology is highly efficient and operable due to the strong penetration of ultrasound waves in the pollutants during the degradation process (Xu et al., 2023a). Semiconductor materials such as TiO_2 have been employed for the sonocatalytic degradation of textile wastewater as shown in Figure 2 (Song et al., 2018). This process is largely based on the phenomenon of acoustic cavitation, which is defined as the growth and collapse of pre-existing microbubbles under the influence of an ultrasonic field in liquids. The formation of bubbles is due to the strong decline in local instantaneous pressure induced by strong ultrasound or by some hydrodynamic motion (Mondal et al., 2021; Liu et al., 2023). Under optimum conditions, the bubbles are likely to collapse very violently due to their inherent spherical geometry and the inertia of the surrounding liquid.

At the end of the violent bubble collapse, temperature and pressure inside the bubble significantly increase to more than 4000 K and 300 bar (1 bar = 105 Pa = 0.987 atm), respectively (Yasui, 2021; Xu et al., 2023b). This leads to the formation of reactive species as well as light emission known as sonoluminescence (SL), usually in the presence of a photoactive semiconductor material (Qiu et al., 2018). If the energy of light from sonoluminescence is greater than the band gap of the semiconductor, it causes it to be excited, resulting in the formation of electron-hole pairs (e^-/h^+), thereby producing hydroxyl ($HO^\bullet$) and superoxide ($O_2\bullet$-) radicals at the valance and conduction bands, respectively (Thiemann et al., 2017). Additionally, the generated high temperature can possibly provoke the thermal excitation of the semiconductor material, leading to the generation of e^-/h^+ pairs by thermal catalysis as well (de Andrade et al., 2021).

The generation of all of these ROS active in sonocatalysis is shown using the equations below:

$$H_2O + \text{ultrasound} + \text{catalyst} \rightarrow HO^\bullet + H^\bullet \quad (1)$$

$$HO^\bullet + H^\bullet \rightarrow H_2O_2 \quad (2)$$

$$H^\bullet + O_2 \rightarrow HO_2^\bullet \quad (3)$$

$$HO^\bullet + {}^\bullet OH \rightarrow H_2O_2 \quad (4)$$

$$HO_2^\bullet + HO_2^\bullet \rightarrow H_2O_2 + O_2 \quad (5)$$

$$H_2O + {}^\bullet OH \rightarrow H_2O_2 + H^\bullet \quad (6)$$

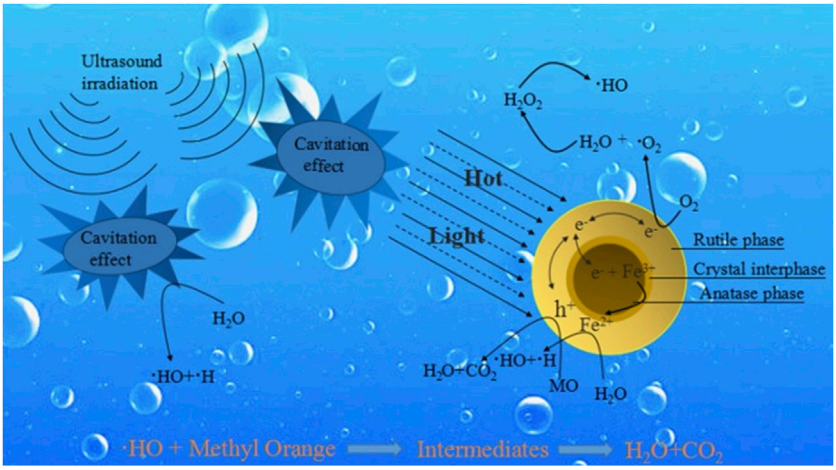

FIGURE 2
Schematic overview of the sonocatalytic degradation mechanism. Reprinted with permission from (Song et al., 2018).

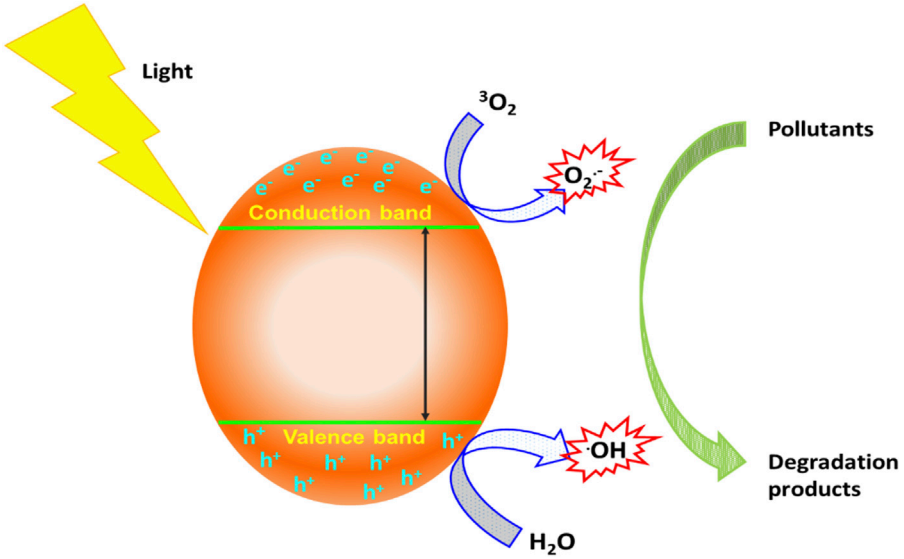

FIGURE 3
Schematic overview of a semiconductor-mediated photocatalytic treatment process.

The formation of these highly reactive species has allowed the use of sonocatalytic processes in highly contaminated water. Thus, the process is efficient to treat wastewater or effluents containing an array of organic pollutants amongst others.

2.2 Photocatalysis

The photocatalysis process generally involves reduction and oxidation responses on the surface of photocatalyst material (Tahir et al., 2021). A schematic overview of photocatalytic degradation process is depicted in Figure 3.

Briefly, the absorption of light (photon energy higher than the band gap of the photocatalyst) by a photocatalyst creates holes (h^+) on the valence band and electrons (e^-) on the conduction band (Navidpour et al., 2023). The photo-created e^-/h^+ pairs mediate the formation of species, like $HO^•$ and $O_2^{•-}$ from atmospheric oxygen and moisture (Fotiou et al., 2014). These species have been reported to have the potential to oxidize and break down organic pollutants, poisonous gas, and eliminate microorganisms from an aqueous environment (Zhao et al., 2020; Xu, 2021). Additionally, the photocatalytic process can also generate hydroperoxyl ($HO_2^•$) radicals which can aid the degradation of inorganic compounds present in industrial wastewater.

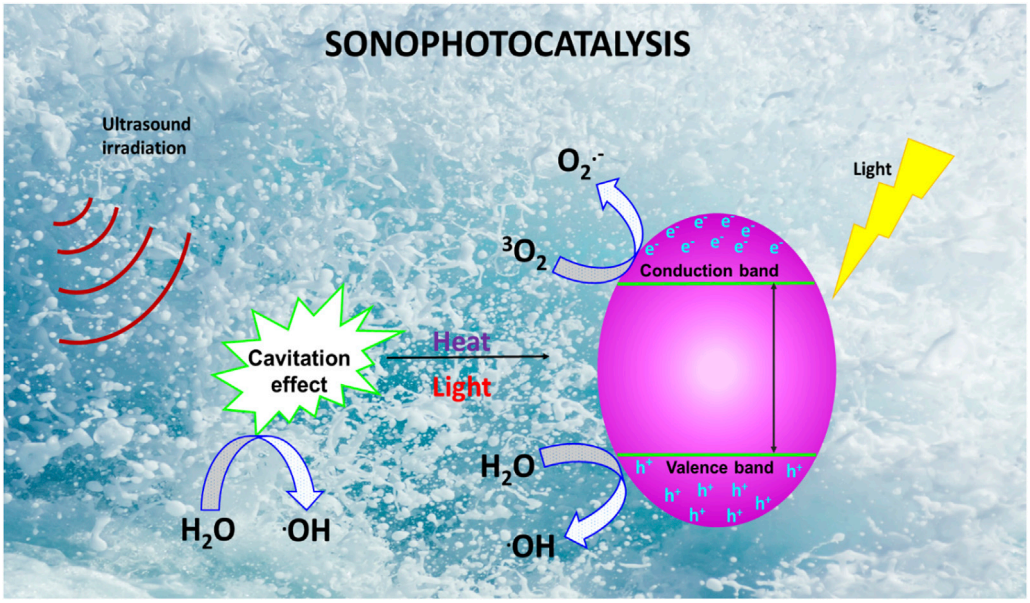

FIGURE 4
Schematic overview of a sonophotocatalytic treatment process.

The generation of all of these ROS is shown on the equations below:

$$\text{Semiconductor} + h\upsilon \rightarrow \text{Semiconductor}\left(h^+_{VB} + e^-_{CB}\right) \quad (7)$$

$$h^+_{VB} + e^-_{CB} \rightarrow \text{heat} \quad (8)$$

$$OH^- + h^+_{VB} \rightarrow HO^\bullet \quad (9)$$

$$H_2O + h^+_{VB} \rightarrow HO^\bullet + H^+ \quad (10)$$

$$HO^\bullet + HO^\bullet \rightarrow H_2O_2 \quad (11)$$

$$e^-_{CB} + H^+ + O_2 \rightarrow {}^\bullet HO_2 \quad (12)$$

$${}^\bullet HO_2 + {}^\bullet HO_2 \rightarrow O_2 + H_2O_2 \quad (13)$$

$$O_2 + e^-_{CB} \rightarrow O_2^{\bullet-} \quad (14)$$

$$O_2^{\bullet-} + H^+ + {}^\bullet HO_2 \rightarrow O_2 + H_2O_2 \quad (15)$$

$$H_2O_2 + e^-_{CB} \rightarrow HO^\bullet + OH^- \quad (16)$$

$$H_2O_2 + HO^\bullet \rightarrow H_2O + {}^\bullet HO_2 \quad (17)$$

The high recombination rate of e^-/h^+ pairs in the photocatalyst, as well as agglomeration result in loss of photocatalytic efficiency (Hayati et al., 2020). The combination of photocatalysis with sonocatalysis, however deals with these hindrances and results in highly efficient water treatment systems, hence, sonophotocatalysis is a more efficient water treatment technique (Wang and Cheng, 2023b).

2.3 Sonophotocatalysis

Sonophotocatalysis generally entails the combination of light, ultrasound and a catalyst that work synergistically to accelerate the production of ROS, which are highly destructive against water pollutants (Malika and Sonawane, 2022). A schematic overview of sonophotocatalytic degradation process is depicted in Figure 4. Briefly, upon irradiation of a catalyst with ultrasonic waves, sonoluminescence results due to cavitation in the aqueous solution, causing pyrolysis of water molecules and generating highly reactive radicals (Wang and Cheng, 2023b). Additionally, light generated from sonoluminescence can excite the catalyst, leading to the formation of e^-/h^+ pairs and subsequently ROS generation (de Andrade et al., 2021). Irradiation of the catalyst's surface with light increases the generation of ROS as the h^+ in the valence band react with water molecules adsorbed on the catalyst surface to generate $HO^\bullet$, while the e^-generated in the conduction band react with dissolved oxygen to generate $O_2^{\bullet-}$, $HO^\bullet$, and H_2O_2 (Hanifehpour and Joo, 2018). These active species react with pollutants to generate different degradation intermediates and even mineralization products (H_2O and CO_2).

Therefore, while the use of light facilitates the degradation of pollutants through the generation of photo-induced ROS, ultrasonication enhance this process by stimulating the production of $HO^\bullet$ and assisting in reducing the recombination of photogenerated e^-/h^+ pairs (Torres et al., 2008). Ultrasonication also helps with de-aggregation of the catalyst, which enhances its surface area and promotes mass transfer of pollutants between the liquid phase and the catalyst surface (Panda and Manickam, 2017). Moreover, combination of sono- and photocatalysis allows for efficient degradation of both hydrophobic and hydrophilic organic pollutants (Al-Musawi et al., 2021).

In addition to the irradiation sources (light and ultrasound), the overall efficiency of a sonophotocatalytic process also depends on the type of material (sonophotocatalysts) and their efficiency in generating sufficient ROS. Therefore, suitable sonophotocatalysts must exhibit the ability to respond to light and ultrasound irradiation while maintaining good chemical and photo-stability, good electronic properties and efficiency, as well as negligible toxicity and low cost. Semiconductor materials are commonly implemented due to their vital role in lowering the energy barrier

TABLE 1 Commonly used semiconductor materials and their respective band gap energies.

Semiconductor	Band gap energies (eV)	Ref
TiO_2 (anatase)	3.20	Dette et al. (2014)
ZnS	3.60	D'Amico et al. (2017)
ZnO	3.37	Djurišić et al. (2012)
SnO_2	3.60	Doyan et al. (2021)
WO_3	2.60–3.00	González-Borrero et al. (2010)
CdO	2.20	Przeździecka et al. (2021)
CuO	1.2–2.6	Xu et al. (2018)
MgO	5.0–7.8	Badar et al. (2012)
CdS	2.42	Dalhat et al. (2022)
Bi_2O_3	3.34	Nurmalasari et al. (2020)

for the formation of cavitation bubbles during the sonocatalysis process, while their light-harvesting capacity reveals the population of photogenerated e^-/h^+ pairs during the photocatalysis process (Wang and Cheng, 2023b).

Selection of these semiconductors depends on their band gap energies (the minimum energy that is required to excite an e^- into the conduction band) which measures photoactivation potentials as shown in Table 1 (Dette et al., 2014; D'Amico et al., 2017; Djurišić et al., 2012; Doyan et al., 2021; González-Borrero et al., 2010; Przeździecka et al., 2021; Xu et al., 2018; Badar et al., 2012; Dalhat et al., 2022; Nurmalasari et al., 2020). Since most of them have large band gap energies (>2 eV), they are mainly activated using UV light. This does limit their real life applications as the UV regime is only a small fraction of the Sun's energy (<10%) (Wang et al., 2016).

Various methods have been employed for the fabrication of these semiconductor sonophotocatalysts, some of the most common being; co-precipitation (El-Sawy et al., 2022), hydrothermal (Kumaresan et al., 2020), sol-gel (Leroy et al., 2020; Norabadi et al., 2020) sonochemical (Anandan and Ashokkumar, 2009) and the solvothermal (Rashid et al., 2023) method. The focus of this review is to showcase the advances that have been made in the application of sonophotocatalysis in water and wastewater treatment, thus these synthesis methods are not detailed.

3 Water and wastewater treatment applications

A considerable amount of research has gone into the development of sustainable water treatment techniques and technologies capable of improving the quality of water. The inaccessibility of drinkable water is a critical issue, especially in regions where conventional drinking water treatment systems fail to eradicate toxic waste consisting of aquatic pathogens, metal ions and industrial waste (Ahmed and Haider, 2018). The use of sonophotocatalysis as a possible water and wastewater treatment technique for the most common of these pollutants i.e., organics, microbes and metals has been extensively studied and explored as discussed next.

3.1 Degradation of persistent organic pollutants

Due to increased industrialisation and mass production of various products, countless toxic organic chemicals are readily discharged into water bodies, including pharmaceuticals and personal care products (PPCPs), dyes as well as pesticides (Rauf and Ashraf, 2009; Awfa et al., 2018; Fang et al., 2018). Polluted water with refractory organics is difficult to recycle and reuse (Zhang et al., 2020). In addition to sonophotocatalysis, several other treatment technologies [e.g., biodegradation, catalysis, coagulation and adsorption (Patsoura et al., 2007; Le Borgne et al., 2008; Wang et al., 2020; Xiao et al., 2021)] have been applied in the treatment of these hazardous pollutants. However, due to its high treatment efficiency, advances on the use of sonophotocatalysis as a treatment technique for these different organic pollutants is elaborated below.

3.1.1 Neutral, cationic and anionic dyes

Textile industries are the major contributors to water and general environmental pollution as they release undesirable dye effluents (Yaseen and Scholz, 2019). Conventional wastewater treatment methods (physical, chemical and biological) demonstrate several limitations in the elimination of dyes, including low removal efficiencies towards non-biodegradable and refractory organic dyes as well as lengthy treatment times (Crini and Lichtfouse, 2019). These traditional methods are also not very destructive, and usually work by changing the dyes to another form and therefore cause the formation of secondary pollutants. A plethora of research has thus been conducted on the use of sonophotocatalysis as an alternative treatment method for wastewaters containing dyes as listed in Table 2 (Vinu and Madras, 2009; Paramarta and Saleh, 2018; Lops et al., 2019; Razaghi et al., 2021; Al-Hawary et al., 2023; Kucukcongar et al., 2023).

Al-Hawary et al. (2023) depicted the mechanism of sonophotocatalytic treatment of dyes, using acid red 14 (AR14) as a model pollutant as shown in Figure 5. They reported that the AR14 dye removal can be achieved in solution and catalyst surface through sonolysis and sonocatalytic processes. They also reported that the combination of ultrasound and light radiation was highly efficient as it enhanced the formation of e^-/h^+ pairs in the valence and conduction bands of particles resulting in increased ROS generation. Their research findings also showed that the removal efficiency of AR14 increased with increasing operating parameters such as nanoparticle content, ultrasound frequency, and radiation power, while it decreased with increasing the initial pH and initial concentration of AR14 (Al-Hawary et al., 2023).

Just as with photocatalysis, the degradation efficiency in the sonophotocatalysis process can be influenced by the morphology of materials used, since photosensitization occurs on the surface of the semiconductor. To prove this, Lops et al. (2019) synthesized five zinc oxide catalyst powders with different morphologies and sizes i.e., Desert Roses (DRs), Multipods (MPs), Microwires (MWs),

TABLE 2 Common organic pollutants treated using sonophotocatalysis and their respective treatment materials and conditions.

Type of organic pollutant	Pollutant name	Material	Preparation method	Catalyst loading (gL^{-1})	Treatment conditions		Treatment efficiency (%)	Ref
					Ultrasound power (W)	Light		
Dyes	Acid Red 14	Fe_3O_4@SiO_2/PAEDTC@MIL-101 (Fe)	—	0.5	36.0	36.0 W	100	Al-Hawary et al. (2023)
	Rhodamine B	ZnO	Sol-gel	0.5	1.00	150 W/m^2	100	Lops et al. (2019)
	Methylene Blue	Fe_3O_4/SnO_2/NGP	Sol-gel and Co-precipitation	0.3	—	40.0 W	100	Paramarta and Saleh (2018)
	Orange G, Remazol Brilliant Blue R, Alizarin Red S, Methyl Blue, and Indigo Carmine	TiO_2	Solution combustion	1.0	36.0	80.0 W	—	Vinu and Madras (2009)
	Reactive Red 195	Ag/TiO_2 and Ag/TiO_2/Fe_3O_4	Co-precipitation	0.1	—	27 W	96 (UVA) 98 (visible)	Kucukcongar et al. (2023)
	Rhodamine B	$CuFe_2F_8(H_2O)_2$ and Au/$CuFe_2F_8(H_2O)_2$	Solvothermal	0.02	130	—	82.22	Razaghi et al. (2021)
Pharmaceuticals	Tetracycline	Ca doped ZnO	Sol-gel	0.5	100	1.6 W	100	Bembibre et al. (2022)
	Ofloxacin	TiO_2	Commercial	1.0	8.4	3.16 W/m^2	98.3	Hapeshi et al. (2013)
	Tetracycline and Ciprofloxacin	Cu_2O/MoS_2/rGO	Microwave and Hummer	0.3	120	150 W	100 and 94.0	Selvamani et al. (2021)
	Tetracycline	Au/B-TiO_2/rGO	Hydrothermal	0.25	600	300 W	100	Vinesh et al. (2019)
	Acetaminophen and Amoxicillin	Mn-doped TiO_2	Ultrasound	0.10	500	160 W/m^2	26 and 53	Khani et al. (2019)
Pesticides	Diazinon	Fe doped TiO_2	Hydrothermal	0.4	100	32.4 MW/cm^2	85.0	Tabasideh et al. (2017)
	Benomyl	TiO_2	Commercial	1–3	190	6.53 mW/cm^2	—	Park (2009)
	Flonicamid	CuO, ZnO and TiO_2	Commercial	CuO – 1.0 ZnO - 0.75 TiO_2 - 0.75	100	125 W	CuO – 86.89 ZnO – 91.53 TiO_2 – 98.36	Ayare and Gogate (2020)
	Isoproturon	TiO_2	Commercial	0.1	50	160 W/m^2	100	Schieppati et al. (2019)

Nanoparticles (NPs) and Nanowires (NWs) for the sonophotocatalytic treatment of the cationic Rhodamine B (RhB) dye. They found that the sonophotocatalytic degradation in the presence of DRs microparticles showed the greatest efficiency. The synthesized materials also demonstrated a good stability over repeated cycles of dye treatment (Lops et al., 2019).

Researchers including Paramarta and Saleh (2023) evaluated the efficiency of the sonophotocatalytic degradation. They used Fe_3O_4/SnO_2 composite, deposited onto nanographene platelets (NGPs) using co-precipitation and ultrasound assisted methods. The catalyst reusability tests revealed that the Fe_3O_4/SnO_2/NGP (10wt%) composite could be repeatedly used up to four times without any significant change in the sonocatalytic and sonophotocatalytic activity using cationic Methylene Blue dye as a model pollutant (Paramarta and Saleh, 2018).

Vinu and Madras (2009) studied the sonophotocatalytic degradation of various anionic dyes (Orange G, Remazol Brilliant Blue R, Alizarin Red S, Methyl Blue, and Indigo Carmine) using solution combustion synthesized TiO_2 (CS TiO_2) and commercial Degussa P-25 TiO_2 (DP-25). The rate of sonophotocatalytic degradation of all the dyes and the reduction of total organic

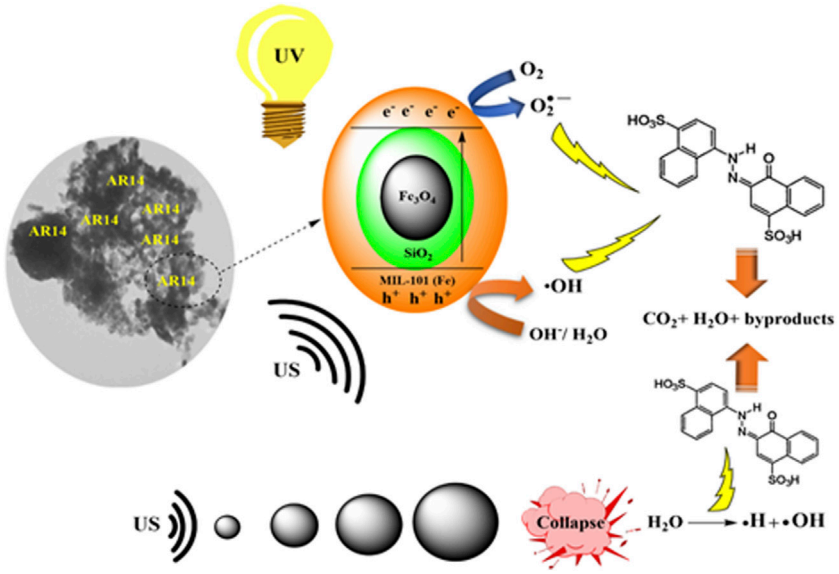

FIGURE 5
A schematic illustration of decomposition of AR14 under the sonophotocatalysis process. Reprinted with permission from (Al-Hawary et al., 2023).

carbon was higher compared to the individual photo- and sonocatalytic processes (Vinu and Madras, 2009).

Kucukcongar et al. (2023) investigated the removal efficiency of the neutral reactive red 195 (RR195) dye by photocatalytic and sonophotocatalytic processes under UV-A and visible irradiation using Ag/TiO_2 and Ag/TiO_2/Fe_3O_4 nanocomposites. Removal of RR195 dye under visible irradiation for 120 min using Ag/TiO_2/Fe_3O_4 was determined as the best with 92% and 96% efficiency for photocatalytic and sonophotocatalytic processes, respectively. They also found that the percentage of RR195 removal under UV-A and visible light decreased with the increase in initial dye concentration and pH values and increased with the increase in light power (Kucukcongar et al., 2023).

Lastly, Razaghi et al. (2021) prepared a stable, mixed-anion sonophotocatalyst $CuFe_2F_8(H_2O)_2$ oxyfluoride with narrow band-gap based Au-NPs sensitizer and sacrificial electron mediator for degradation of RhB in aqueous media. The study was the first example of stable degradation of an organic dye driven by visible light coupled with ultrasound wave excitation using an oxyfluoride. They also tested the durability and reusability of the samples for five consecutive cycles under illumination by visible light and ultrasound waves. They found that the sample activities decrease slightly after each repeat reaction cycle under the same experimental conditions, attributing it to a reduction in the active sites of the catalysts, after several sonophotocatalytic degradations (Razaghi et al., 2021).

3.1.2 Pharmaceuticals

Pharmaceuticals and personal care products (PPCPs) constitute one of the largest groups of emerging pollutants as they pertain to medications and therapeutic drugs, cosmetics and other personal hygiene products that promote the general health and wellbeing of humans and animals (Reyes et al., 2021). Research efforts around pharmaceutical agents are however more prominent as most of them last long in the aquatic environment due to lipophilicity, so their cytotoxic effects are chronic rather than acute, even at low concentrations (Zare et al., 2022).

Pharmaceutical agents in drinking water predominantly come from two different sources i.e., production processes of the pharmaceutical industry as well as the common use of pharmaceutical compounds resulting in their presence in urban and farm wastewaters (Gadipelly et al., 2014). Antibiotics are one of the most prominent groups of pharmaceuticals as they are commonly used in human infections, veterinary medicine, and agriculture. The presence of antibiotics has thus been detected in surface waters, ground water aquifers, and even in drinking water in a range of nanogram/L to microgram/L (Sodhi et al., 2021). They are generally released into the environment by various pathways, such as the pharmaceutical industry's wastewater, wastewater treatment plants, hospitals, as well as human and animal elimination (Samal et al., 2022). This issue leads to the generation of antibiotic-resistant genes (ARGs) and antibiotic-resistant bacteria (ARBs), which accelerate the spread of antibiotic resistance, causing a threat to human health and ecological systems (Serwecińska, 2020).

It has been reported that conventional treatments are not capable of efficiently removing pharmaceuticals as they are predominantly water-soluble and neither volatile nor biodegradable (Abdurahman et al., 2021). As listed in Table 2 (Hapeshi et al., 2013; Khani et al., 2019; Vinesh et al., 2019; Karim and Shriwastav, 2021; Selvamani et al., 2021; Bembibre et al., 2022), numerous researchers have thus explored sonophotocatalysis as a possible treatment alternative for the removal of antibiotics in particular, due to their alarming long-term effects.

Karim and Shriwastav (2021) evaluated the efficacy of photocatalytic, sonocatalytic, and sonophotocatalytic oxidation processes for the degradation of amoxicillin using visible light with nitrogen doped TiO_2 (N–TiO_2) nanoparticles as the catalyst. At optimal conditions, maximum degradation efficiencies of 27%

and 31% were reported for photocatalysis and sonocatalysis, respectively. The combination of ultrasound and visible light in the presence of N–TiO_2 enhanced the degradation of amoxicillin due to the reduced bandgap of the catalyst, enhanced cavitation effect, sonoluminescence phenomenon, and improved mass transfer of pollutants, consequently a higher degradation efficiency of 37% was reported for sonophotocatalysis (Karim and Shriwastav, 2021).

Bembibre et al. (2022) investigated the sonophotocatalytic mineralization of tetracycline-based antibiotics using Ca-doped ZnO under LED visible light irradiation. The effects of pH, Ca doping, light and ultrasound intensity were systematically investigated. The ZnO-based catalyst with 2 at% of Ca dopant exhibited the best sonophotocatalytic performance in mineralizing tetracyclines with excellent reusability and minimal sonophotocorrosion i.e., ≤ 1% of catalyst (Bembibre et al., 2022).

Hapeshi et al. (2013) studied the extent of the degradation of ofloxacin in secondary treated effluents by means of sonolysis, photocatalysis, sonocatalysis and sonophotocatalysis using TiO_2. Various parameters affecting the treatment efficiency including TiO_2 loading, solution pH, sparging gas, addition of H_2O_2, and ultrasound acoustic power were investigated. Sonophotocatalysis was generally faster than the respective individual processes presumably due to the enhanced formation of reactive radicals. It was found that an increase in acoustic intensity was proportional to an increased efficiency of the sonophotocatalytic degradation of ofloxacin. Twenty transformation products were then proposed as a result of the sonophotocatalytic process (Hapeshi et al., 2013).

Selvamani et al. (2021) prepared a ternary Cu_2O/MoS_2/rGO composite, synthesized by the microwave method, for the sonophotocatalytic degradation of tetracycline and ciprofloxacin. The composite demonstrated a synergic sonophotocatalytic degradation of tetracycline (20 mg/L) and ciprofloxacin (10 mg/L) antibiotics with high efficiency of 100% and 94% within a short duration of 10 and 75 min, respectively. They further elucidated that the synergic effect of degradation is due to the spontaneous production of $HO^{\bullet}$ and $O_2^{\bullet-}$ radicals favouring free e^- to actively participate in the degradation process (Selvamani et al., 2021).

Vinesh et al. (2019) reported on the incorporation of e^- deficient boron atoms along with Au doped TiO_2 in the presence of rGO support for the sonophotocatalytic degradation of tetracycline using visible light illumination. They found the individual effect of photocatalysis and sonocatalysis for the degradation of tetracycline to be 45% and 12%, respectively, whereas complete degradation (100%) was achieved with 1.3 folds synergistic effect for sonophotocatalysis in 1 h. The enhanced degradation activity was mainly attributed to combined effect of rapid e^-/h^+ pair separation facilitated by e^- deficient B-atoms and rGO support and physical forces of ultrasound as well (Vinesh et al., 2019).

Khani et al. (2019) reported on the synthesis of Mn-doped TiO_2 by ultrasound for the sonophotocatalytic degradation of acetaminophen and amoxicillin. They found that the ultrasound synthesized samples had a higher brookite content and wider distribution of the band-gaps, in the 1.6–1.91 eV range, while traditional ones ranged from 1.72 to 1.8 eV. The catalysts synthesized with ultrasound were also up to 50% more active than the traditional samples. Interestingly, as shown in Figure 6, their results also showed that amoxicillin decomposed more easily than acetaminophen due to its different molecular properties (pKa and polar surface area). The maximum AMO degradation achieved was 53% with the catalyst with the smallest band-gap (1.6 eV) and the highest surface area (158 $m^2\ g^{-1}$), whereas the maximum APAP degradation was 26% with the catalyst with the band-gap of (1.7 eV) and the surface area of (132 $m^2\ g^{-1}$) (Khani et al., 2019).

3.1.3 Pesticides (herbicides, fungicides and insecticides)

Although pesticides are recognised as reagents for protecting crops against harmful pests, their runoff from agricultural fields into water bodies has detrimental health effects to aquatic organisms and humans (Syafrudin et al., 2021). This is attributed to their ability to interfere with the normal functioning of a large number of species including human beings and animals (Shefali et al., 2021). They can pose severe health risks upon ingestion i.e., they have potential as carcinogenic agents as well as endocrine disruptors (Damalas and Eleftherohorinos, 2011). These pesticides are usually categorized depending on the kind of pest they regulate, i.e., insecticides are used for controlling insects, herbicides for weeds and fungicides are used for controlling fungi. Ideally, they should be toxic to the target organisms but that is not always the case as they leach into water bodies easily. Hence as listed in Table 2 (Park, 2009; Tabasideh et al., 2017; Schieppati et al., 2019; Ayare and Gogate, 2020), numerous researchers have explored sonophotocatalysis as a promising treatment method for the different types of pesticides relative to other treatment methods i.e., photocatalysis and sonocatalysis.

Tabasideh et al. (2017) conducted a comparative study on the sonocatalytic, photocatalytic, and sonophotocatalytic degradation of diazinon (insecticide) using iron-doped TiO_2 nanoparticles. They found sonophotocatalysis to be a better treatment method for diazinon than sonocatalysis and photocatalysis. Their results also revealed that the degradation of diazinon increased with the increase of the concentration of catalyst and Fe doping concentration in all three cases (sonocatalytic, photocatalytic, and sonophotocatalytic), while the degradation efficiency decreased with the increase of initial diazinon concentration and pH (Tabasideh et al., 2017).

Park (2009) reported on the degradation of benomyl (fungicide) by a sonophotocatalytic and photocatalytic system for comparison. Under the optimal conditions, i.e., initial benomyl concentration was 3.2 mg L^{-1} and the concentration of TiO_2 was 2 g L^{-1}, degradation rates from the sonophotocatalytic system were about 1.5 times higher than those from the photocatalytic system (Park, 2009).

Ayare and Gogate (2020) reported on the efficacy of sonocatalytic, photocatalytic and sonophotocatalytic oxidation of flonicamid (insecticide) solution using various catalysts (CuO, ZnO, and TiO_2). Sonophotocatalysis treatment was found to be the most effective treatment approach for mineralization of flonicamid solution using the different catalysts. The proposed mechanisms showed enhanced generation of oxidizing species, accelerating the formation of cavities and enhancing the catalytic activity at the catalyst surface (Ayare and Gogate, 2020).

Schieppati et al. (2019) studied the individual, additive and synergistic degradation action of photolysis, sonolysis, sonophotolysis, and sonophotocatalysis against isoproturon (herbicide) by varying catalyst loading and/or ultrasound power for the last three techniques. With 0.1 gL^{-1} catalyst, photocatalysis

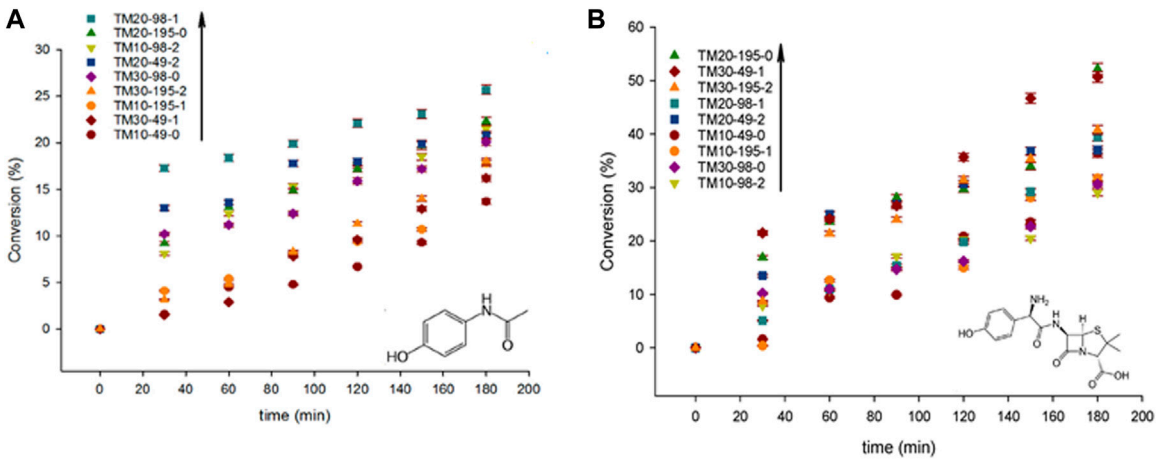

FIGURE 6
(A) acetaminophen and **(B)** amoxicillin degradation with various Mn-doped TiO_2 catalysts; error within ± 2%. Reprinted with permission from (Khani et al., 2019).

and sonophotopcatalysis completely degraded isoproturon within 240 and 60 min, respectively (>99% conversion). Sonophotocatalysis was also found to break isoproturon down into smaller molecules than photocatalysis alone (Schieppati et al., 2019).

3.2 Heavy metal treatment

The treatment of heavy metals in wastewater has proven to be a challenge that requires attention, as heavy metals are major wastewater pollutants that are not biodegradable, are toxic in the human body and can accumulate in the ecosystem (Vidu et al., 2020). Typical industrial methods employed in wastewater treatment, such as adsorption, chemical precipitation, ion exchange, ozonation and biological methods cannot efficiently reduce the metal concentration in water to within the regulatory standards effectively. This is because there is a considerable number of heavy metals in water that are complexed with organic chelating agents that come from textile, nuclear, and electroplating sources (Gao and Meng, 2021). Research on the sonophotocatalytic treatment of heavy metals is also very limited and is an area worth advancing, as the little work that's been done has yielded promising results which demonstrate feasibility of this technique.

For instance, Chen et al. (2021) prepared zirconium–porphyrin metal–organic frameworks (MOFs) for the visible-light-driven sonophotocatalytic reduction of toxic Cr(VI) to Cr(III) in water. They found that the catalysts exhibited enhanced activities for Cr(VI) reduction compared with the photocatalytic process. Using fluorescence and UV–vis absorption spectra measurements, they were also able to deduce that the sonophotocatalytic process promotes the transfer of photoinduced electrons from the catalyst to Cr(VI), hence enhancement in the catalytic performance (Chen et al., 2021).

Chen et al. (2022) also prepared titanium–porphyrin MOFs and used them as visible-light-driven catalysts for the sonophotocatalytic reduction of Cr(VI). All the catalysts presented higher efficiency in the reduction of Cr(VI) to Cr(III) in aqueous solution when sonophotocatalytic treatment was employed than in photocatalysis. Sonophotocatalytic experiments and electron paramagnetic resonance measurement proved that the Ti-oxo chain units and porphyrin ligand in the structures of the catalysts existed as catalytic active centers for sonophotocatalytic reduction of Cr(VI). They also reported that photoluminescence and UV absorption spectra revealed that the synergy between photocatalysis and sonocatalysis strengthened the migration of photogenerated e^- from the catalyst to Cr(VI), which improved the activities of catalysts (Chen et al., 2022).

3.3 Microbial disinfection

The disinfection of water is useful for the elimination of the pathogens that are responsible for waterborne diseases (Liu et al., 2021). Traditional disinfection methods typically entail the use of chlorine or other oxidative chemicals in water. There is however growing concern over the formation of harmful disinfection byproducts during chlorine- or chemical-based disinfection, which has heightened the need to develop alternative processes for water disinfection (Qiu et al., 2020).

Although still at its infancy stages, sonophotocatalysis has been explored as a viable method for the treatment of microbes, especially bacteria. The combined effects of ultrasonication and photocatalysis in microbes is depicted in Figure 7. The physical or mechanical consequences of ultrasound cavitation (such as shock waves and shear pressures) cause the mechanical rupturing of cell membranes and lead to cellular lysis (Dai et al., 2020). Additionally, the generated ROS from both sonocatalytic and photoinduced chemical reactions result in the damage of DNA and other intercellular components and they are then ejected from the cell due to cytoplasmic material leakage (Moradi et al., 2022).

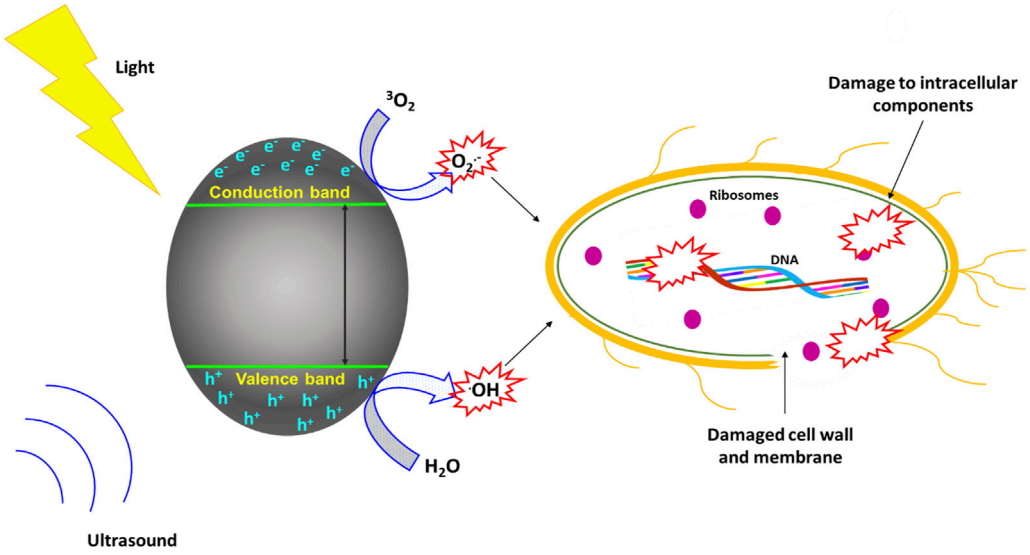

FIGURE 7
Mechanism of sonophotocatalytic treatment of microbes.

Rahman et al. (2020) reported on the sonophotocatalytic treatment of *Salmonella Typhimurium* using Fe-doped ZnO nanoparticles (ZnO:Fe) wherein complete disinfection of the targeted bacteria was achieved within 45 min. The efficiency of ZnO:Fe nanoparticles was found to be higher than that of conventional sonophotocatalysts (ZnO and TiO_2). Their investigations also indicated that the $HO^{\bullet}$ and $O_2^{\bullet-}$ radicals could have been the key ROS interfering with the oxido-reductase protein system of the bacteria and hence hindered its metabolic activity. Additionally, they reported that the treatment process did not result in any process resistance, making it a good candidate for water disinfection (Rahman et al., 2023).

Mukherjee et al. (2022) reported on the efficiency of sonophotocatalysis in eradicating multi-drug resistant *Klebsiella pneumonia*. Hydrothermally synthesized CdS nanorods were applied as the sonophotocatalysts under blue light irradiation from a LED source in combination with low frequency ultrasonication for the complete disinfection of the coliform bacteria. Various reaction parameters including light intensity, sonication power, and catalyst dose were found to affect the disinfection capability. Following optimisation, the disinfection strategy was able to handle 106 CFU/mL of *K. pneumonia* efficiently in 20 min. The sonophotocatalyst demonstrated good reusability and stability. They elucidated that sonophotocatalysis is a viable disinfection technology which utilises the release of ROS and mechanical shear to induce bacterial disinfection (Mukherjee et al., 2022).

Drosou et al. (2010) reported on the efficacy of heterogeneous photocatalysis and sonophotocatalysis induced by UV-A irradiation and low frequency (24–80 kHz) ultrasound irradiation in the presence of TiO_2 and peracetic acid (PAA) as an additional disinfectant to inactivate *Escherichia coli* in water. PAA-assisted UV-A/TiO_2 photocatalysis generally led to nearly complete bacterial inactivation in 10–20 min of contact time with the extent of inactivation depending on the photocatalyst type and loading (in the range 100–500 mg L^{-1}) and PAA concentration (in the range 0.5–2 mg L^{-1}). PAA-assisted UV-A/TiO_2 sonophotocatalysis however showed complete bacterial inactivation with shorter treatment times and lower PAA doses and was therefore reported as the most efficient treatment technique (Drosou et al., 2010).

4 Efficiency and enhancement strategies

From the reported findings of several researchers, it can be deduced that sonophotocatalysis has greater efficiency in the treatment of water pollutants at different conditions relative to photocatalysis and sonocatalysis. The high ROS generation efficiency in sonophotocatalytic treatment contributes to the versatility of the process i.e., treatment of a range of water pollutants. Additionally, sonophotocatalysis eliminates some of the main disadvantages observed in each individual technique including high costs, sluggish activity, and prolonged reaction times (Moradi et al., 2022). The synergy between the ultrasound and light irradiation moreover causes an enhanced photocatalyst activity due to the ultrasonic separation of photocatalyst particles, which in turn increases the surface area of the photocatalyst for increased exposure to light (Yetim and Tekin, 2017). Furthermore, ultrasound can be used as an irradiation source to induce sonocatalytic activity in the photocatalysts even if light radiation is blocked because of trapping of the photocatalyst in the pores of its support (Joseph et al., 2009). Lastly, ultrasound helps in catalyst cleaning and regeneration (Moradi et al., 2022). This possibly increases the available active sites and thus enhances the light absorption and catalyst reusability efficiency. As discussed next, various strategies have been employed for enhancing the efficiency of sonophotocatalysis, either by modifying the sonophotocatalysts or the sonophotocatalytic process itself.

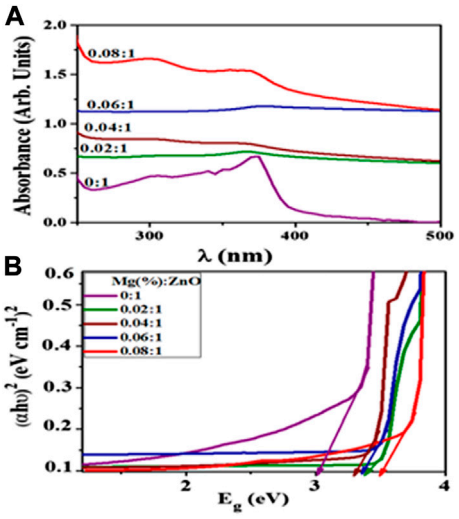

FIGURE 8
(A) Absorption spectra and **(B)** Tauc plots of samples of Mg-doped ZnO. Reprinted with permission from (Ikram et al., 2021).

4.1 Sonophotocatalyst modification

One of the prevalent strategies employed for further enhancing the efficiency of sonophocatalytic treatment of water pollutants is the modification of the sonophotocatalysts. Modification of properties such as physical, electronic and magnetic properties in nanometer scale help with enhancement the sonophotocatalytic activity. This can be achieved by various methods including; doping the sonophotocatalysts with metals or non-metals (Tabasideh et al., 2017; Rajoriya et al., 2019). The dopants help increasing the absorption band width into the visible region as well as reducing the hole–electron recombination (Chakma and Moholkar, 2015). This corroborates with Paul et al. (2017) who evaluated the sonophotocatalytic efficiency of pure and Ag doped flower-like hierarchical molybdenum oxide nanorods for the degradation of Methylene Blue dye under diffused sunlight. They found that the optical band gap energy decreased with Ag doping while the degradation efficiency was increased (Paul et al., 2017).

Anomalies do occur though, for instance, Ikram et al. (2021) prepared various concentrations of Mg-doped ZnO nanorods which they applied in the photocatalytic, sonocatalytic and sonophotocatalytic degradation of a mixture of Methylene Blue and ciprofloxacin. As shown in Figure 8A, they observed a shift in absorption upon doping which they attributed to oxygen deficiency, particle size effect and grain structure defects. They extracted values from Figure 8A to calculate optical band gap (E.g.,) of ZnO (using Tauc plots), which increased from 3.32 to 3.72 eV with increased Mg doping (Figure 8B). They explained the blueshift in E.g., based on the Burstein–Moss effect phenomenon. They explained that in the metal oxide method, particle size reduction can result in a blueshift of the band gap due to the quantum confinement effect (QCE). They further elaborated that doping may also affect local symmetry and generate lattice defect centers that change the structure of the band and induce significant shifts in optical properties. Nonetheless, the experimental results however showed improved degradation performance by Mg-doped ZnO nanorods relative to the bare ones (Ikram et al., 2021).

Another promising strategy for enhancing sonophotocatalysis is by coupling the nanoscale semiconductor sonophotocatalyst with another lower band gap semiconductor i.e., creating heterojunctions (Zhang et al., 2021). The close contact of semiconductors with different Fermi levels leads to the formation of an internal electric field. This electric field can direct the movement of electrons and holes through the interfacial zone (Moradi et al., 2022). For instance, Guo et al. (2021) investigated the influence of the heterojunction by comparing the sonophotocatalytic capabilities of ZnO and ZnO/ZnS core–shell nanorod arrays in the degradation of Methylene Blue. As depicted in Figure 9, they observed that the nanorods with the heterojunction i.e., ZnO/ZnS core–shell had a higher degradation efficiency (45.4%) than ZnO (25.1%). They also studied the morphological influence in the heterojunctions by comparing ZnO/ZnS nanorods and ZnO/ZnS nanotubes which further showed that the latter had a higher capability of 63.3%. They ascribed the improvement to the coupling effect of the enhanced piezoelectric field and the reduced migration distance, which suppresses the recombination of photoexcited e^-/h^+ pairs while transforming the morphology from nanorod to nanotube (Guo et al., 2021).

The sonophotocatalysts can also be modified by dye photosensitisation i.e., conjugation of the semiconductor sonophotocatalyst to a dye (Kaur and Singh, 2007; Mkhondwane et al., 2023a). This results in composite materials with two light absorbers, wherein the dye absorbs visible light, which is beneficial as most of the solar irradiation is in the visible region. The synergistic interaction of a dye with a semiconductor photocatalyst is depicted in Figure 10. The excited dye causes an influx of electrons in the conduction band of the semiconductor, thereby enhancing the generation of ROS which can then decompose a range of pollutants. Moreover, ultrasonic cavitation may cause the pyrolysis of water molecules in contact with the surface of the sonophotocatalyst, thereby further enhancing the generation of ROS (de Andrade et al., 2021).

Mkhondwane et al. (2023) investigated the use of two Zn phthalocyanines as photosensitisers for TiO_2 fibers in sonocatalytic, photocatalytic, and sonophotocatalytic degradation of Rhodamine 6G. They found that the ZnPc functionalized fibers displayed higher activity than their corresponding bare ZnPc analogous. Additionally, the sonophotocatalytic process displayed higher degradation aptitude than sonocatalytic and photocatalytic processes (Mkhondwane et al., 2023b). Moreover, Hakki and Allahyari (2022) prepared Bi_2O_3-ZnO photocatalysts with various amounts of copper phthalocyanine as a photosensitiser for the sonophotocatalytic degradation of Methyl Orange dye. They compared the sonophotocatalytic degradation of Methyl Orange under simulated solar light with sole photocatalysis and sonolysis, and the results showed that the sonophotacatalytic degradation was the most efficient (Hakki and Allahyari, 2022).

4.2 Process modification

The alteration and optimisation of the actual sonophotocatalytic process can also drastically improve the wastewater treatment results. For instance, using gases (N_2, Ar, O_2) to purge the

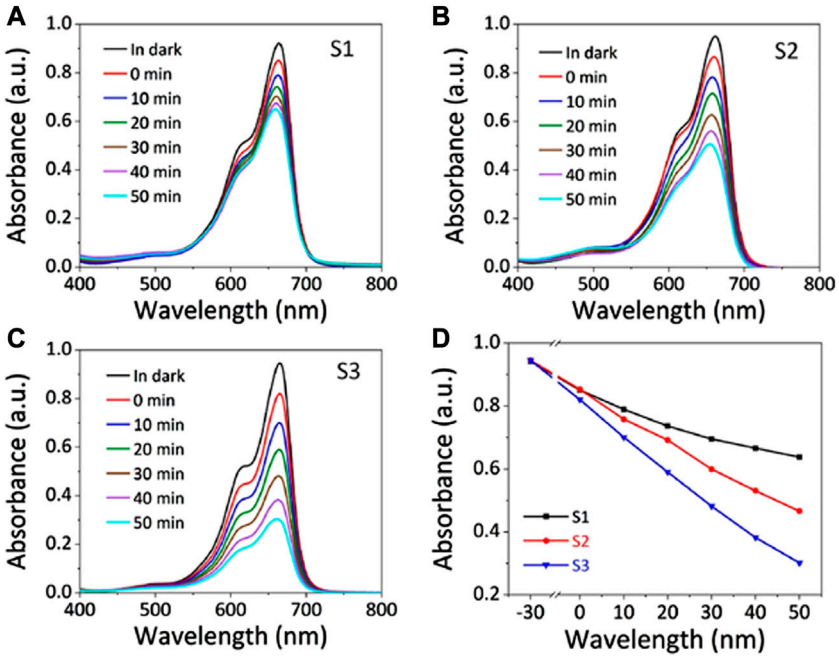

FIGURE 9
Sonophotocatalytic capabilities of the three samples. **(A–C)** Absorption curves of methylene blue sonophotocatalyzed by **(A)** ZnO nanorods, **(B)** ZnO/ZnS nanorods, and **(C)** ZnO/ZnS nanotubes. **(D)** Sonophotocatalytic degradation rates of the three samples. Reprinted with permission from (Guo et al., 2021).

sonophotocatalytic reaction enhances the performance of the system by generating high-potential bubble formation sites. This then results in an increased rate of cavitation and greatly influences the amount of produced H_2O_2, which can actively participate in and contribute to the pollutant degradation process (Moradi et al., 2022).

The addition of oxidation agents (O_3 and H_2O_2) has also been reported to enhance sonophotocatalytic efficiency (Joseph et al., 2009; Sathishkumar et al., 2016). The addition of H_2O_2 can cause the release of a large number of free and adsorbed radicals in the medium and it can act as an electron trap to suppress e^-/h^+ recombination (Moradi et al., 2022). For instance, Wei et al. (2021) observed an enhancement in the sonophotocatalytic performance of H_2O_2-assisted titania based system for degradation of Acid Orange 7 (Wei et al., 2021). Ozonation on the other hand can be utilised to enhance the production of reactive species either alone or in combination with ultrasound and or light irradiation (Kohantorabi et al., 2022).

Lastly, Fe-containing catalysts integrated with light and ultrasound improve the pollutant removal efficiency due to enhanced synergistic interaction in a process called sono-photo-Fenton catalysis (Moradi et al., 2020; Qi et al., 2020). The reaction of ferrous ions with *in situ* produced H_2O_2 during sonophotocatalytic reactions provides free additional radicals that facilitate the degradation of dissolved contaminants (Moradi et al., 2022). Unfortunately, the catalyst can suffer from poisoning during the oxidation process, due to the adsorption of reaction intermediates on its surface, thereby leading to a progressively inactive surface (Zhong et al., 2011). Segura et al. (2009) investigated the sono- and photo-Fenton processes separately as well as the combined systems (sono-photo-Fenton) in order to evaluate of possible beneficial effects on the use of coupled systems in the degradation of phenol. They observed enhanced activity for the sequentially-integrated sono–photo-Fenton process which resulted in a total phenol degradation and ca. 90% TOC reduction. They attributed the effective degradation of the sequential sono–photo-Fenton process to the benefits of ultrasound for the partial degradation of amenable aromatic compounds towards further oxidized by-products along with the fragmentation of catalyst to finer particles that produces more activity in photo-Fenton systems (Segura et al., 2009).

5 Challenges and future prospects

The majority of research conducted on sonophotocatalysis utilises UV-active materials (Taghizadeh and Abdollahi, 2011; Dinesh et al., 2015; Asgari et al., 2020), although some researchers have employed various modification methods to enhance the visible light absorption efficiency of the reported catalysts (Neppolian et al., 2011; Aziz et al., 2023). Research therefore needs to be conducted on the use of stable sonophotocatalysts with absorption in the Vis and NIR regions of the spectra so as to maximise utilisation of the sunlight. These include but are not limited to hematite and tungsten trioxide.

Many researchers have also reported on the anatase polymorph of TiO_2 as the best catalyst for the photocatalytic treatment water pollutants relative to the rutile (Zhang et al., 2014; Theerthagiri et al., 2016). A comparative study on sonophotocatalysis using different TiO_2 polymorphs at similar conditions therefore needs to be conducted to elucidate the best polymorph for sonophotocatalytic treatment.

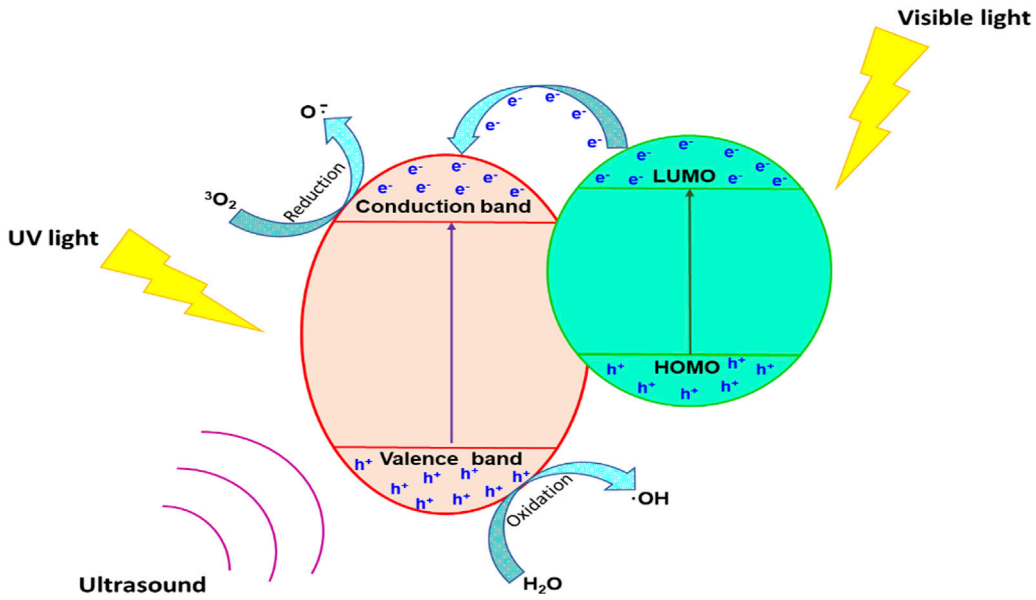

FIGURE 10
The mechanism of synergistic interaction of dye photosensitised semiconductor sonophotocatalysts.

Catalyst regeneration and reusability is another important aspect to wastewater treatment so as to prevent further contamination as a result of the catalyst (Argyle and Bartholomew, 2015; Taufik et al., 2016; Obaideen et al., 2022). Hence extensive research needs to be conducted on the sonophotocatalytic properties of retrievable materials including magnetic nanoparticles, films and fibers. The potential risks associated with the sonophotocatalytic process also need to be studied, including the possible generation of toxic byproducts and their potential release (and impact thereof) into the environment.

Research findings have depicted that the pollutant removal efficiency using sonophotocatalytic treatment is dependent on a range of parameters including pH, light source and power, ultrasound frequency and catalytic loading (Camacho-Alvarado et al., 2017; Yentür and Dükkancı, 2021). Moreover, a range of contaminants are likely to coexist in wastewater and not a single kind as most research tends to focus. This therefore suggests that interactions between different kinds of pollutants would complicate the sonophotocatalytic degradation process. Future studies are hence needed to evaluate the potential adverse effects of complex water systems with a range of pollutants, under different operating conditions. The application and optimization of sonophotocatalysis in environmental remediation also needs to be broadened to other resistant and toxic contaminants such as personal care products, oil, as well as other microbes like viruses and fungi.

Additionally, extensive research needs to be conducted on the influence of the sonophotocatalytic process on the stability of the catalysts at different conditions. This is a precaution to prevent the potential release (and impact thereof) of the sonophotocatalyst into the environment. Ideally, the process should not damage the catalyst's physical and/or chemical structure, alter the morphology or disintegrate binary or ternary composites.

Lastly, although sonophotocatalytic treatment of water contaminants has been proven to be efficient, large scale up processes would not be economically viable without optimising the required facilities including suitable reactors as well as process operation and maintenance. Furthermore, the process requires electrical energy for generation of the ultrasounds which is a costly exercise.

6 Conclusion

Sonophotocatalysis has proven to be a highly efficient wastewater treatment process as it often shows higher removal rates and shorter reaction times when compared to its individual treatments i.e., sonocatalysis and photocatalysis. The ultrasound has a synergistic interaction with the light irradiation as it continuously cleans the catalytic surface and resolves problems related to catalyst opacity and porosity. Additionally, sonophotocatalysis eliminates the resistance in mass transfer between the liquid phase and the catalyst surface, eradicates catalyst fouling and promotes the generation of more free radicals ($HO^{\bullet}$, $O_2^{\bullet-}$) for enhanced activity.

Features including the sonophotocatalysts (type, durability, stability, reusability) and treatment processes (irradiation intensity, scalability, reactor setup) are pivotal to the success of the sonophotocatalytic process. It can however be enhanced by sonophotocatalyst modification (doping, heterojunctions and dye photosensitisation) or process optimization (addition of gases, oxidants or ferrous agents).

Although the sonophotocatalytic treatment of dyes, pesticides, pharmaceuticals, heavy meatls and bacteria has been reported,

research still needs to be conducted on the use of sonophotocatalysis in other pollutants like oils, personal care products, viruses and fungi, as well as complex water with a range of pollutants.

This review has thus shed light on the different water treatment applications that have been studied using sonophotocatalysis as well as the areas that need further exploration. It has also shed light on various aspects that still need to be considered and optimised to enhance the efficiency, real-life feasibility, largescale operation and commercial viability of sonophotocatalysis as a wastewater treatment technique.

Author contributions

SM: Conceptualization, Formal analysis, Writing, Reviewing and Editing. BN: Formal analysis, Writing, Reviewing, Proof-reading and Editing. TM: Proof-reading and Editing. LS: Proof-reading and Editing. All authors contributed to the article and approved the submitted version.

Funding

This work was supported by Nanotechnology Innovation Centre/Department of Science and Innovation of South Africa.

Conflict of interest

Authors SM, BN, TM, and LS were employed by the company Mintek.

Publisher's note

All claims expressed in this article are solely those of the authors and do not necessarily represent those of their affiliated organizations, or those of the publisher, the editors and the reviewers. Any product that may be evaluated in this article, or claim that may be made by its manufacturer, is not guaranteed or endorsed by the publisher.

References

Abdurahman, M. H., Abdullah, A. Z., and Shoparwe, N. F. (2021). A comprehensive review on sonocatalytic, photocatalytic, and sonophotocatalytic processes for the degradation of antibiotics in water: synergistic mechanism and degradation pathway. *Chem. Eng. J.* 413, 127412. doi:10.1016/j.cej.2020.127412

Ahmed, S. N., and Haider, W. (2018). Heterogeneous photocatalysis and its potential applications in water and wastewater treatment: a review. *Nanotechnology* 29, 342001. doi:10.1088/1361-6528/aac6ea

Al-Hawary, S. I. S., Rahimpoor, R., Rahmani, A., Romero-Parra, R. M., Ramírez-Coronel, A. A., Alhachami, F. R., et al. (2023). Enhanced sonophotocatalytic degradation of acid red 14 using Fe_3O_4@SiO_2/PAEDTC@MIL-101 (Fe) based on metal-organic framework. *Catalysts* 13, 411. doi:10.3390/catal13020411

Al-Musawi, T. J., Rajiv, P., Mengelizadeh, N., Mohammed, I. A., and Balarak, D. (2021). Development of sonophotocatalytic process for degradation of acid orange 7 dye by using titanium dioxide nanoparticles/graphene oxide nanocomposite as a catalyst. *J. Environ. Manage.* 292, 112777. doi:10.1016/j.jenvman.2021.112777

Al-Tohamy, R., Ali, S. S., Li, F., Okasha, K. M., Mahmoud, Y. A. G., Elsamahy, T., et al. (2022). A critical review on the treatment of dye-containing wastewater: ecotoxicological and health concerns of textile dyes and possible remediation approaches for environmental safety. *Ecotoxicol. Environ. Saf.* 231, 113160. doi:10.1016/j.ecoenv.2021.113160

Anandan, S., and Ashokkumar, M. (2009). Sonochemical synthesis of Au-TiO_2 nanoparticles for the sonophotocatalytic degradation of organic pollutants in aqueous environment. *Ultrason. Sonochem.* 16, 316–320. doi:10.1016/j.ultsonch.2008.10.010

Aneyo, I. A., Doherty, F. V., Adebesin, O. A., and Hammed, M. O. (2016). Biodegradation of pollutants in waste water from pharmaceutical, textile and local dye effluent in lagos, Nigeria. *J. Health Pollut.* 6, 34–42. doi:10.5696/2156-9614-6.12.34

Argyle, M. D., and Bartholomew, C. H. (2015). Heterogeneous catalyst deactivation and regeneration: a review. *Catalysts* 5, 145–269. doi:10.3390/catal5010145

Asgari, G., Shabanloo, A., Salari, M., and Eslami, F. (2020). Sonophotocatalytic treatment of AB113 dye and real textile wastewater using ZnO/persulfate: modeling by response surface methodology and artificial neural network. *Environ. Res.* 184, 109367. doi:10.1016/j.envres.2020.109367

Awfa, D., Ateia, M., Fujii, M., Johnson, M. S., and Yoshimura, C. (2018). Photodegradation of pharmaceuticals and personal care products in water treatment using carbonaceous-TiO_2 composites: a critical review of recent literature. *Water Res.* 142, 26–45. doi:10.1016/j.watres.2018.05.036

Ayare, S. D., and Gogate, P. R. (2020). Sonochemical, photocatalytic and sonophotocatalytic oxidation of flonicamid pesticide solution using different catalysts. *Chem. Eng. Process. Process Intensif.* 154, 108040. doi:10.1016/j.cep.2020.108040

Aziz, N., Rasool, S., Ullah, T., Khitab, F., Halim, S. A., Bawazeer, S., et al. (2023). Sonophotocatalytic degradation of fast yellow AB and Remazol brilliant violet-5R by using Ag-impregnated ZnO as a photocatalyst. *ACS Omega* 8, 18509–18515. doi:10.1021/acsomega.3c00171

Badar, N., Chayed, N. F., Rusdi, R., Kamarudin, N., and Kamarulzaman, N. (2012). Band gap energies of magnesium oxide nanomaterials synthesized by the sol-gel method. *Adv. Mat. Res.* 545, 157–160. doi:10.4028/www.scientific.net/amr.545.157

Barakat, M. A., and Schmidt, E. (2010). Polymer-enhanced ultrafiltration process for heavy metals removal from industrial wastewater. *Desalination* 256, 90–93. doi:10.1016/j.desal.2010.02.008

Bembibre, A., Benamara, M., Hjiri, M., Gómez, E., Alamri, H. R., Dhahri, R., et al. (2022). Visible-light driven sonophotocatalytic removal of tetracycline using Ca-doped ZnO nanoparticles. *Chem. Eng. J.* 427, 132006. doi:10.1016/j.cej.2021.132006

Boretti, A., and Rosa, L. (2019). Reassessing the projections of the world water development report. *NPJ Clean. Water* 2, 15. doi:10.1038/s41545-019-0039-9

Camacho-Alvarado, C., Castillo-Araiza, C. O., and Ruiz-Martinez, R. S. (2017). Degradation and mineralization of a cationic dye by a sequential photo-sono catalytic process. *Int. J. Chem. React. Eng.* 15, 20170078. doi:10.1515/ijcre-2017-0078

Chakma, S., and Moholkar, V. S. (2015). Investigation in mechanistic issues of sonocatalysis and sonophotocatalysis using pure and doped photocatalysts. *Ultrason. Sonochem.* 22, 287–299. doi:10.1016/j.ultsonch.2014.06.008

Chen, D., Jin, Z., and Xing, H. (2022). Titanium–porphyrin metal–organic frameworks as visible-light-driven catalysts for highly efficient sonophotocatalytic reduction of Cr(VI). *Langmuir* 38, 12292–12299. doi:10.1021/acs.langmuir.2c01932

Chen, D., Liu, W., Guo, Z., Jin, Z., Li, B., and Xing, H. (2021). Visible-light-driven sonophotocatalysis for the rapid reduction of aqueous Cr(VI) based on zirconium–porphyrin metal–organic frameworks with csq topology. *Inorg. Chem.* 60, 18133–18140. doi:10.1021/acs.inorgchem.1c02739

Crini, G., and Lichtfouse, E. (2019). Advantages and disadvantages of techniques used for wastewater treatment. *Environ. Chem. Lett.* 17, 145–155. doi:10.1007/s10311-018-0785-9

Dai, J., Bai, M., Li, C., Cui, H., and Lin, L. (2020). Advances in the mechanism of different antibacterial strategies based on ultrasound technique for controlling bacterial contamination in food industry. *Trends Food Sci.* 105, 211–222. doi:10.1016/j.tifs.2020.09.016

Dalhat, M. H., and Ahmad, A. (2022). "Removal of pesticides from water and wastewater by solar-driven photocatalysis," in *Development in wastewater treatment research and processes*. Editors M. Shah, S. Rodriguez-Couto, and J. Biswas (Amsterdam, Netherlands: Elsevier), 435–458.

Damalas, C. A., and Eleftherohorinos, I. G. (2011). Pesticide exposure, safety issues, and risk assessment indicators. *Int. J. Environ. Res. Public Health.* 8, 1402–1419. doi:10.3390/ijerph8051402

D'Amico, P., Calzolari, A., Ruini, A., and Catellani, A. (2017). New energy with ZnS: novel applications for a standard transparent compound. *Sci. Rep.* 7, 16805. doi:10.1038/s41598-017-17156-w

de Andrade, F. V., Augusti, R., and de Lima, G. M. (2021). Ultrasound for the remediation of contaminated waters with persistent organic pollutants: a short review. *Ultrason. Sonochem.* 78, 105719. doi:10.1016/j.ultsonch.2021.105719

Dette, C., Pérez-Osorio, M. A., Kley, C. S., Punke, P., Patrick, C. E., Jacobson, P., et al. (2014). TiO_2 anatase with a bandgap in the visible region. *Nano Lett.* 14, 6533–6538. doi:10.1021/nl503131s

Dinesh, G. K., Anandan, S., and Sivasankar, T. (2015). Sonophotocatalytic treatment of Bismarck Brown G dye and real textile effluent using synthesized novel Fe(0)-doped TiO2 catalyst. *RSC Adv.* 5, 10440–10451. doi:10.1039/c4ra07685k

Djurišić, A. B., Chen, X., Leung, Y. H., and Ching Ng, A. M. (2012). ZnO nanostructures: growth, properties and applications. *J. Mat. Chem.* 22, 6526–6535. doi:10.1039/c2jm15548f

Doyan, A., Susilawati, Muliyadi L., Hakim, S., Munandar, H., and Taufik, M. (2021). The effect of dopant material to optical properties: energy band gap Tin Oxide thin film. *J. Phys. Conf. Ser.* 1816, 012114. doi:10.1088/1742-6596/1816/1/012114

Drosou, C., Coz, A., Xekoukoulotakis, N. P., Moya, A., Vergara, Y., and Mantzavinos, D. (2010). Peracetic acid-enhanced photocatalytic and sonophotocatalytic inactivation of *E. coli* in aqueous suspensions. *J. Chem. Technol. Biotechnol.* 85, 1049–1053. doi:10.1002/jctb.2396

El-Sawy, A. M., Salem, M. A., Salem, I. A., Hydara, M. M., and Zaki, A. B. (2022). Sonophotocatalytic degradation of malachite green in aqueous solution using six competitive metal oxides as a benchmark. *Photochem. Photobiol. Sci.* 22, 579–594. doi:10.1007/s43630-022-00336-7

Englande, A. J., Krenkel, P., and Shamas, J. (2015). "Wastewater treatment &water reclamation," in *Reference module in earth systems and environmental sciences*. Editor S. Elias (Amsterdam, Netherlands: Elsevier), 1–32.

Eren, Z., and Ince, N. H. (2010). Sonolytic and sonocatalytic degradation of azo dyes by low and high frequency ultrasound. *J. Hazard Mat.* 177, 1019–1024. doi:10.1016/j.jhazmat.2010.01.021

Fang, H., Zhang, H., Han, L., Mei, J., Ge, Q., Long, Z., et al. (2018). Exploring bacterial communities and biodegradation genes in activated sludge from pesticide wastewater treatment plants via metagenomic analysis. *Environ. Pollut.* 243, 1206–1216. doi:10.1016/j.envpol.2018.09.080

Fotiou, T., Triantis, T. M., Kaloudis, T., Papaconstantinou, E., and Hiskia, A. (2014). Photocatalytic degradation of water taste and odour compounds in the presence of polyoxometalates and TiO_2: intermediates and degradation pathways. *J. Photochem. Photobiol. A Chem.* 286, 1–9. doi:10.1016/j.jphotochem.2014.04.013

Gadipelly, C., Pérez-González, A., Yadav, G. D., Ortiz, I., Ibáñez, R., Rathod, V. K., et al. (2014). Pharmaceutical industry wastewater: review of the technologies for water treatment and reuse. *Ind. Eng. Chem. Res.* 53, 11571–11592. doi:10.1021/ie501210j

Gao, X., and Meng, X. (2021). Photocatalysis for heavy metal treatment: a review. *Processes* 9, 1729. doi:10.3390/pr9101729

González-Borrero, P. P., Sato, F., Medina, A. N., Baesso, M. L., Bento, A. C., Baldissera, G., et al. (2010). Optical band-gap determination of nanostructured WO_3 film. *Appl. Phys. Lett.* 96, 061909. doi:10.1063/1.3313945

Guo, L., Chen, Y., Ren, Z., Li, X., Zhang, Q., Wu, J., et al. (2021). Morphology engineering of type-II heterojunction nanoarrays for improved sonophotocatalytic capability. *Ultrason. Sonochem.* 81, 105849. doi:10.1016/j.ultsonch.2021.105849

Hakki, H. K., and Allahyari, S. (2022). Sonophotocatalytic treatment of wastewater using simulated solar light-driven Bi_2O_3-ZnO nanophotocatalyst sensitized with copper phthalocyanine. *Mat. Chem. Phys.* 288, 126355. doi:10.1016/j.matchemphys.2022.126355

Hanifehpour, Y., and Joo, S. W. (2018). Synthesis, characterization and sonophotocatalytic degradation of an azo dye on Europium doped cadmium selenide nanoparticles. *Nanochem. Res.* 3, 178–188. doi:10.22036/NCR.2018.02.007

Hapeshi, E., Fotiou, I., and Fatta-Kassinos, D. (2013). Sonophotocatalytic treatment of ofloxacin in secondary treated effluent and elucidation of its transformation products. *Chem. Eng. J.* 224, 96–105. doi:10.1016/j.cej.2012.11.048

Hayati, F., Isari, A. A., Anvaripour, B., Fattahi, M., and Kakavandi, B. (2020). Ultrasound-assisted photocatalytic degradation of sulfadiazine using MgO@CNT heterojunction composite: effective factors, pathway and biodegradability studies. *Chem. Eng. J.* 381, 122636. doi:10.1016/j.cej.2019.122636

Ikram, M., Aslam, S., Haider, A., Naz, S., Ul-Hamid, A., Shahzadi, A., et al. (2021). Doping of Mg on ZnO nanorods demonstrated improved photocatalytic degradation and antimicrobial potential with molecular docking analysis. *Nanoscale Res. Lett.* 16, 78–16. doi:10.1186/s11671-021-03537-8

Joseph, C. G., Puma, L. G., Bono, A., and Krishnaiah, D. (2009). Sonophotocatalysis in advanced oxidation process: a short review. *Ultrason. Sonochem.* 16, 583–589. doi:10.1016/j.ultsonch.2009.02.002

Karim, A. V., and Shriwastav, A. (2021). Degradation of amoxicillin with sono, photo, and sonophotocatalytic oxidation under low-frequency ultrasound and visible light. *Environ. Res.* 200, 111515. doi:10.1016/j.envres.2021.111515

Kaswan, V., and Kaur, H. A. (2023). A comparative study of advanced oxidation processes for wastewater treatment. *Water Pract. Technol.* 18, 1233–1254. doi:10.2166/wpt.2023.061

Kaur, S., and Singh, V. (2007). Visible light induced sonophotocatalytic degradation of Reactive Red dye 198 using dye sensitized TiO_2. *Ultrason. Sonochem.* 14, 531–537. doi:10.1016/j.ultsonch.2006.09.015

Khani, Z., Schieppati, D., Bianchi, C. L., and Boffito, D. C. (2019). The sonophotocatalytic degradation of pharmaceuticals in water by MnOx-TiO_2 systems with tuned band-gaps. *Catalysts* 9, 949. doi:10.3390/catal9110949

Kohantorabi, M., Moussavi, G., Oulego, P., and Giannakis, S. (2022). Heterogeneous catalytic ozonation and peroxone-mediated removal of Acetaminophen using natural and modified hematite-rich soil, as efficient and environmentally friendly catalysts. *Appl. Catal. B* 301, 120786. doi:10.1016/j.apcatb.2021.120786

Kryuchkova, M., Batasheva, S., Akhatova, F., Babaev, V., Buzyurova, D., Vikulina, A., et al. (2021). Pharmaceuticals removal by adsorption with montmorillonite nanoclay. *Int. J. Mol. Sci.* 22, 9670. doi:10.3390/ijms22189670

Kucukcongar, S., Alwindawi, A. G. J., Turkyilmaz, M., and Ozaytekin, I. (2023). Reactive dye removal by photocatalysis and sonophotocatalysis processes using Ag/TiO_2/Fe_3O_4 nanocomposite. *Water Air Soil Pollut.* 234, 103. doi:10.1007/s11270-023-06136-8

Kumaresan, N., Sinthiya, M. M. A., Kumar, M. P., Ravichandran, S., Babu, R. R., Sethuraman, K., et al. (2020). Investigation on the photocatalytic and sonophotocatalytic activities of {002} facets of ZnO nanoparticles synthesized through template/surfactant-free hydrothermal method at different temperatures and time durations. *J. Mat. Sci. Mat. Electron.* 31, 13817–13837. doi:10.1007/s10854-020-03942-2

Le Borgne, S., Paniagua, D., and Vazquez-Duhalt, R. (2008). Biodegradation of organic pollutants by halophilic bacteria and archaea. *J. Mol. Microbiol. Biotechnol.* 15, 74–92. doi:10.1159/000121323

Leroy, S., Blach, J. F., Huvé, M., Léger, B., Kania, N., Henninot, J. F., et al. (2020). Photocatalytic and sonophotocatalytic degradation of rhodamine B by nano-sized $La_2Ti_2O_7$ oxides synthesized with sol-gel method. *J. Photochem. Photobiol. A Chem.* 401, 112767. doi:10.1016/j.jphotochem.2020.112767

Liu, N., Ming, J., Sharma, A., Sun, X., Kawazoe, N., Chen, G., et al. (2021). Sustainable photocatalytic disinfection of four representative pathogenic bacteria isolated from real water environment by immobilized TiO_2-based composite and its mechanism. *Chem. Eng. J.* 426, 131217. doi:10.1016/j.cej.2021.131217

Liu, Y. C., Liu, X., Wang, X., Li, Z. H., Chen, C. L., and Xiang, Z. (2023). Hybrid persulfate/sonocatalysis for degradation of acid orange 7 in the presence of Ag_2O/$CuWO_4$ composite: operating parameters and sonocatalytic mechanism. *J. Clean. Prod.* 394, 136287. doi:10.1016/j.jclepro.2023.136287

Lops, C., Ancona, A., Di Cesare, K., Dumontel, B., Garino, N., Canavese, G., et al. (2019). Sonophotocatalytic degradation mechanisms of Rhodamine B dye via radicals generation by micro- and nano-particles of ZnO. *Appl. Catal. B* 243, 629–640. doi:10.1016/j.apcatb.2018.10.078

Malika, M., and Sonawane, S. S. (2022). The sono-photocatalytic performance of a Fe_2O_3 coated TiO_2 based hybrid nanofluid under visible light via RSM. *Colloids Surf. A Physicochem. Eng. Asp.* 641, 128545. doi:10.1016/j.colsurfa.2022.128545

Mishra, B. K., Kumar, P., Saraswat, C., Chakraborty, S., and Gautam, A. (2021). Water security in a changing environment: concept, challenges and solutions. *Water* 2, 490. doi:10.3390/w13040490

Mkhondwane, S. T., Mgidlana, S., Openda, Y. I., Nene, L., and Nyokong, T. (2023b). Photosono catalytic degradation of an organic pollutant using phthalocyanine supported on electrospun nanofibers. *SSRN* 2023. doi:10.2139/ssrn.4412777

Mkhondwane, S. T., Mgidlana, S., Openda, Y. I., Nene, L., and Nyokong, T. (2023a). Phthalocyanine sensitized electrospun TiO_2 nanofibers for degradation of Rhodamine 6G: the comparison between photo-sono-and photosono-catalytic degradation processes. *SSRN*. 2023 doi:10.2139/ssrn.4348843

Moghaddam, S. S., Moghaddam, A. M. R., and Arami, M. (2010). Coagulation/flocculation process for dye removal using sludge from water treatment plant: optimization through response surface methodology. *J. Hazard. Mat.* 175, 651–657. doi:10.1016/j.jhazmat.2009.10.058

Mondal, J., Lakkaraju, R., Ghosh, P., and Ashokkumar, M. (2021). Acoustic cavitation-induced shear: a mini-review. *Biophys. Rev.* 13, 1229–1243. doi:10.1007/s12551-021-00896-5

Moradi, M., Elahinia, A., Vasseghian, Y., Dragoi, E. N., Omidi, F., and Mousavi Khaneghah, A. (2020). A review on pollutants removal by Sono-photo -Fenton processes. *J. Environ. Chem. Eng.* 8, 104330. doi:10.1016/j.jece.2020.104330

Moradi, S., Rodriguez-Seco, C., Hayati, F., and Ma, D. (2022). Sonophotocatalysis with photoactive nanomaterials for wastewater treatment and bacteria disinfection. *ACS Nanosci. Au* 3, 103–129. doi:10.1021/acsnanoscienceau.2c00058

Mukherjee, A., Das, S., and Ahn, Y. H. (2022). Sono-photocatalytic disinfection of high strength multi-drug resistant Klebsiella pneumonia in presence of blue LED-active CdS nanorods. *J. Environ. Chem. Eng.* 10, 108460. doi:10.1016/j.jece.2022.108460

Navidpour, A. H., Abbasi, S., Li, D., Mojiri, A., and Zhou, J. L. (2023). Investigation of advanced oxidation process in the presence of TiO2 semiconductor as photocatalyst: property, principle, kinetic analysis, and photocatalytic activity. *Catalysts* 13, 232. doi:10.3390/catal13020232

Neppolian, B., Ciceri, L., Bianchi, C. L., Grieser, F., and Ashokkumar, M. (2011). Sonophotocatalytic degradation of 4-chlorophenol using Bi_2O_3/$TiZrO_4$ as a visible light

responsive photocatalyst. *Ultrason. Sonochem.* 18, 135–139. doi:10.1016/j.ultsonch.2010.04.002

Norabadi, E., Ashrafi, S. D., Kamani, H., and Jahantiq, A. (2020). Degradation of 2,6-dichlorophenol by Fe-doped TiO_2 Sonophotocatalytic process: kinetic study, intermediate product, degradation pathway. *Int. J. Environ. Anal. Chem.* 102, 7720–7735. doi:10.1080/03067319.2020.1837122

Nurmalasari, N., Yulizar, Y., and Apriandanu, D. O. B. (2020). Bi_2O_3 nanoparticles: synthesis, characterizations, and photocatalytic activity. *IOP Conf. Ser. Mat. Sci. Eng.* 763, 012036. doi:10.1088/1757-899x/763/1/012036

Obaideen, K., Shehata, N., Sayed, E. T., Abdelkareem, M. A., Mahmoud, M. S., and Olabi, A. G. (2022). The role of wastewater treatment in achieving sustainable development goals (SDGs) and sustainability guideline. *Energy Nexus* 7, 100112. doi:10.1016/j.nexus.2022.100112

Panda, D., and Manickam, S. (2017). Recent advancements in the sonophotocatalysis (SPC) and doped-sonophotocatalysis (DSPC) for the treatment of recalcitrant hazardous organic water pollutants. *Ultras. Sonochem.* 36, 481–496. doi:10.1016/j.ultsonch.2016.12.022

Paramarta, V., and Saleh, R. (2018). Wastewater treatment by sonocatalysis and sonophotocatalysis using Fe_3O_4/SnO_2 composite supported on nanographene platelets. *AIP Conf. Proc.* 2023, 020013. doi:10.1063/1.5064010

Park, J. H. (2009). Photochemical degradation and toxicity reduction of methyl 1-[(butylamino)carbonyl]-1H-benzimidazol-2-ylcarbamate in agricultural wastewater: comparative study of photocatalysis and sonophotocatalysis. *Desalination* 249, 480–485. doi:10.1016/j.desal.2009.01.018

Park, S. K., and Hu, J. Y. (2010). Assessment of the extent of bacterial growth in reverse osmosis system for improving drinking water quality. *J. Environ. Sci. Health A Tox. Hazard Subst. Environ. Eng.* 45, 968–977. doi:10.1080/10934521003772386

Patsoura, A., Kondarides, D. I., and Verykios, X. E. (2007). Photocatalytic degradation of organic pollutants with simultaneous production of hydrogen. *Catal. Today* 124, 94–102. doi:10.1016/j.cattod.2007.03.028

Paul, M., Dhanasekar, M., and Bhat, S. V. (2017). Silver doped h-MoO_3 nanorods for sonophotocatalytic degradation of organic pollutants in ambient sunlight. *Appl. Surf. Sci.* 418, 113–118. doi:10.1016/j.apsusc.2016.12.031

Przeździecka, E., Strąk, P., Wierzbicka, A., Adhikari, A., Lysak, A., Sybilski, P., et al. (2021). The band-gap studies of short-period CdO/MgO superlattices. *Nanoscale Res. Lett.* 16, 59. doi:10.1186/s11671-021-03517-y

Qi, L., Lu, W., Tian, G., Sun, Y., Han, J., and Xu, L. (2020). Enhancement of sono-fenton by p25-mediated visible light photocatalysis: analysis of synergistic effect and influence of emerging contaminant properties. *Catalysts* 10, 1297–1313. doi:10.3390/catal10111297

Qiu, H., Fang, S., Huang, G., and Bi, J. (2020). A novel application of In2S3 for visible-light-driven photocatalytic inactivation of bacteria: kinetics, stability, toxicity and mechanism. *Environ. Res.* 190, 110018. doi:10.1016/j.envres.2020.110018

Qiu, P., Park, B., Choi, J., Thokchom, B., Pandit, A. B., and Khim, J. (2018). A review on heterogeneous sonocatalyst for treatment of organic pollutants in aqueous phase based on catalytic mechanism. *Ultrason. Sonochem.* 45, 29–49. doi:10.1016/j.ultsonch.2018.03.003

Rahman, A. P. H., Misra, A. J., Panda, S., Das, B., Bhol, P., Mohanty, P. S., et al. (2023). Sonophotocatalysis-mediated morphological transition modulates virulence and antibiotic resistance in: *salmonella Typhimurium*. *Environ. Sci. Water Res. Technol.* 6, 1917–1930. doi:10.1039/d0ew00224k

Rajoriya, S., Bargole, S., George, S., Saharan, V. K., Gogate, P. R., and Pandit, A. B. (2019). Synthesis and characterization of samarium and nitrogen doped TiO_2 photocatalysts for photo-degradation of 4-acetamidophenol in combination with hydrodynamic and acoustic cavitation. *Sep. Purif. Technol.* 209, 254–269. doi:10.1016/j.seppur.2018.07.036

Rashid, J., Ahsan, A., Xu, M., Savina, I., and Rehman, F. (2023). Synthesis of cerium oxide embedded perovskite type bismuth ferrite nanocomposites for sonophotocatalysis of aqueous micropollutant ibuprofen. *RSC Adv.* 13, 2574–2586. doi:10.1039/d2ra07509a

Rauf, M. A., and Ashraf, S. S. (2009). Fundamental principles and application of heterogeneous photocatalytic degradation of dyes in solution. *Chem. Eng. J.* 151, 10–18. doi:10.1016/j.cej.2009.02.026

Razaghi, P., Dashtian, K., Yousefi, F., Karimi, R., and Ghaedi, M. (2021). Gold anchoring to $CuFe_2F_8(H_2O)_2$ oxyfluoride for robust sono-photodegradation of Rhodamine-B. *J. Clean. Prod.* 313, 127916. doi:10.1016/j.jclepro.2021.127916

Reyes, N. J. D. G., Geronimo, F. K. F., Yano, K. A. V., Guerra, H. B., and Kim, L. H. (2021). Pharmaceutical and personal care products in different matrices: occurrence, pathways, and treatment processes. *Water* 13, 1159. doi:10.3390/w13091159

Samal, K., Mahapatra, S., and Ali, M. H. (2022). Pharmaceutical wastewater as Emerging Contaminants (EC): treatment technologies, impact on environment and human health. *Energy Nexus* 6, 100076. doi:10.1016/j.nexus.2022.100076

Sathishkumar, P., Mangalaraja, R. V., and Anandan, S. (2016). "Sonophotocatalytic mineralization of environmental contaminants present in aqueous solutions," in *Handbook of ultrasonics and sonochemistry*. Editor M. Ashokkumar (Berlin, Germany: Springer), 673–710.

Schieppati, D., Galli, F., Peyot, M. L., Yargeau, V., Bianchi, C. L., and Boffito, D. C. (2019). An ultrasound-assisted photocatalytic treatment to remove an herbicidal pollutant from wastewaters. *Ultrason. Sonochem.* 54, 302–310. doi:10.1016/j.ultsonch.2019.01.027

Segura, Y., Molina, R., Martínez, F., and Melero, J. A. (2009). Integrated heterogeneous sono-photo Fenton processes for the degradation of phenolic aqueous solutions. *Ultrason. Sonochem.* 16, 417–424. doi:10.1016/j.ultsonch.2008.10.004

Selvamani, P. S., Vijaya, J. J., Kennedy, L. J., Mustafa, A., Bououdina, M., Sophia, P. J., et al. (2021). Synergic effect of Cu_2O/MoS_2/rGO for the sonophotocatalytic degradation of tetracycline and ciprofloxacin antibiotics. *Ceram. Int.* 47, 4226–4237. doi:10.1016/j.ceramint.2020.09.301

Serwecińska, L. (2020). Antimicrobials and antibiotic-resistant bacteria: a risk to the environment and to public health. *Water* 12, 3313. doi:10.3390/w12123313

Sharma, S., and Bhattacharya, A. (2017). Drinking water contamination and treatment techniques. *Appl. Water Sci.* 7, 1043–1067. doi:10.1007/s13201-016-0455-7

Shefali, K. R., Sankhla, M. S., Kumar, R., and Sonone, S. S. (2021). Impact of pesticide toxicity in aquatic environment. *Biointerface Res. Appl. Chem.* 11, 10131–10140. doi:10.33263/BRIAC113.1013110140

Sibiya, N. P., Rathilal, S., and Tetteh, E. K. (2021). Coagulation treatment of wastewater: kinetics and natural coagulant evaluation. *Molecules* 26, 698. doi:10.3390/molecules26030698

Sodhi, K. K., Kumar, M., Balan, B., Dhaulaniya, A. S., Shree, P., Sharma, N., et al. (2021). Perspectives on the antibiotic contamination, resistance, metabolomics, and systemic remediation. *SN Appl. Sci.* 3, 269. doi:10.1007/s42452-020-04003-3

Song, S., Hao, C., Zhang, X., Zhang, Q., and Sun, R. (2018). Sonocatalytic degradation of methyl orange in aqueous solution using Fe-doped TiO_2 nanoparticles under mechanical agitation. *Open Chem.* 16, 1283–1296. doi:10.1515/chem-2018-0137

Syafrudin, M., Kristanti, R. A., Yuniarto, A., Hadibarata, T., Rhee, J., Al-Onazi, W. A., et al. (2021). Pesticides in drinking water-a review. *Int. J. Environ. Res. Public Health* 18, 468–515. doi:10.3390/ijerph18020468

Tabasideh, S., Maleki, A., Shahmoradi, B., Ghahremani, E., and McKay, G. (2017). Sonophotocatalytic degradation of diazinon in aqueous solution using iron-doped TiO_2 nanoparticles. *Sep. Purif. Technol.* 189, 186–192. doi:10.1016/j.seppur.2017.07.065

Taghizadeh, M. T., and Abdollahi, R. (2011). Sonolytic, sonocatalytic and sonophotocatalytic degradation of chitosan in the presence of TiO_2 nanoparticles. *Ultrason. Sonochem.* 18, 149–157. doi:10.1016/j.ultsonch.2010.04.004

Tahir, M. B., Sohaib, M., Sagir, M., and Rafique, M. (2021). "Role of Nanotechnology in photocatalysis," in *Encyclopedia of smart materials*. Editor M. Rafique (Amsterdam, Netherlands: Elsevier). 578–89.

Taufik, A., Tju, H., and Saleh, R. (2016). Comparison of catalytic activities for sonocatalytic, photocatalytic and sonophotocatalytic degradation of methylene blue in the presence of magnetic Fe_3O_4/CuO/ZnO nanocomposites. *J. Phys. Conf. Ser.* 710, 012004. doi:10.1088/1742-6596/710/1/012004

Theerthagiri, J., Senthil, R. A., Thirumalai, D., and Madhavan, J. (2016). "Sonophotocatalytic degradation of organic pollutants using nanomaterials," in *Handbook of ultrasonics and sonochemistry*. Editor M. Ashokkumar (Berlin, Germany: Springer), 553–586.

Thiemann, A., Holsteyns, F., Cairós, C., and Mettin, R. (2017). Sonoluminescence and dynamics of cavitation bubble populations in sulfuric acid. *Ultrason. Sonochem.* 34, 663–676. doi:10.1016/j.ultsonch.2016.06.013

Torres, R. A., Nieto, J. I., Combet, E., Pétrier, C., and Pulgarin, C. (2008). Influence of TiO_2 concentration on the synergistic effect between photocatalysis and high-frequency ultrasound for organic pollutant mineralization in water. *Appl. Catal. B* 80, 168–175. doi:10.1016/j.apcatb.2007.11.013

ul Haq, A., Saeed, M., Khan, S. G., and Ibrahim, M. (2022). "Photocatalytic applications of titanium dioxide (TiO_2)," in *Titanium dioxide - advances and applications*. Editor H. M. Ali (London, UK: IntechOpen).

Vidu, R., Matei, E., Predescu, A. M., Alhalaili, B., Pantilimon, C., Tarcea, C., et al. (2020). Removal of heavy metals from wastewaters: a challenge from current treatment methods to Nanotechnology applications. *Toxics* 8, 101. doi:10.3390/toxics8040101

Vinesh, V., Shaheer, A. R. M., and Neppolian, B. (2019). Reduced graphene oxide (rGO) supported electron deficient B-doped TiO_2 (Au/B-TiO_2/rGO) nanocomposite: an efficient visible light sonophotocatalyst for the degradation of Tetracycline (TC). *Ultrason. Sonochem.* 50, 302–310. doi:10.1016/j.ultsonch.2018.09.030

Vinu, R., and Madras, G. (2009). Kinetics of sonophotocatalytic degradation of anionic dyes with nano-TiO_2. *Environ. Sci. Technol.* 43, 473–479. doi:10.1021/es8025648

Wang, G., and Cheng, H. (2023b). Application of photocatalysis and sonocatalysis for treatment of organic dye wastewater and the synergistic effect of ultrasound and light. *Molecules* 28, 3706. doi:10.3390/molecules28093706

Wang, G., and Cheng, H. (2023a). Facile synthesis of a novel recyclable dual Z-scheme $WO_3/NiFe_2O_4$/BiOBr composite with broad-spectrum response and enhanced sonocatalytic performance for levofloxacin removal in aqueous solution. *Chem. Eng. J.* 461, 141941. doi:10.1016/j.cej.2023.141941

Wang, G., Huang, Y., Li, G., Zhang, H., Wang, Y., Li, B., et al. (2017). Preparation of a novel sonocatalyst, Au/$NiGa_2O_4$-Au-Bi_2O_3 nanocomposite, and application in sonocatalytic degradation of organic pollutants. *Ultrason. Sonochem.* 38, 335–346. doi:10.1016/j.ultsonch.2017.03.031

Wang, W., Liu, Y., Yu, S., Wen, X., and Wu, D. (2022). Highly efficient solar-light-driven photocatalytic degradation of pollutants in petroleum refinery wastewater on hierarchically-structured copper sulfide (CuS) hollow nanocatalysts. *Sep. Purif. Technol.* 284, 120254. doi:10.1016/j.seppur.2021.120254

Wang, Y., Pan, T., Yu, Y., Wu, Y., Pan, Y., and Yang, X. (2020). A novel peroxymonosulfate (PMS)-enhanced iron coagulation process for simultaneous removal of trace organic pollutants in water. *Water Res.* 185, 116136. doi:10.1016/j.watres.2020.116136

Wang, Y., Sun, C., Zhao, X., Cui, B., Zeng, Z., Wang, A., et al. (2016). The application of nano-TiO_2 photo semiconductors in agriculture. *Nanoscale Res. Lett.* 11, 529. doi:10.1186/s11671-016-1721-1

Wei, H., Rahaman, M. H., Zhao, J., Li, D., and Zhai, J. (2021). Hydrogen peroxide enhanced sonophotocatalytic degradation of acid orange 7 in aqueous solution: optimization by box–behnken design. *J. Chem. Technol. Biotechnol.* 96, 2647–2658. doi:10.1002/jctb.6809

Xiao, W., Jiang, X., Liu, X., Zhou, W., Garba, Z. N., Lawan, I., et al. (2021). Adsorption of organic dyes from wastewater by metal-doped porous carbon materials. *J. Clean. Prod.* 284, 124773. doi:10.1016/j.jclepro.2020.124773

Xu, L., An, H. L., Liu, N. P., Wang, S. H., Ju, W. T., Wang, Y., et al. (2023b). Construction and characterization of ternary BiOBr/Bi/$CoWO_4$ composites and study on sonocatalysis degradation of tetracycline. *Compos. B Eng.* 263, 110870. doi:10.1016/j.compositesb.2023.110870

Xu, L., Wu, X. Q., Li, C. Y., Liu, N. P., An, H. L., Ju, W. T., et al. (2023a). Sonocatalytic degradation of tetracycline by BiOBr/$FeWO_4$ nanomaterials and enhancement of sonocatalytic effect. *J. Clean. Prod.* 394, 136275. doi:10.1016/j.jclepro.2023.136275

Xu, L., Zheng, G., Pei, S., and Wang, J. (2018). Investigation of optical bandgap variation and photoluminescence behavior in nanocrystalline CuO thin films. *Optik* 158, 382–390. doi:10.1016/j.ijleo.2017.12.138

Xu, Y. J. (2021). Promises and challenges in photocatalysis. *Front. Catal.* 1, 1–3. doi:10.3389/fctls.2021.708319

Yaseen, D. A., and Scholz, M. (2019). Textile dye wastewater characteristics and constituents of synthetic effluents: a critical review. *Int. J. Environ. Sci. Technol.* 16, 1193–1226. doi:10.1007/s13762-018-2130-z

Yasui, K. (2021). Multibubble sonoluminescence from a theoretical perspective. *Molecules* 26, 4624. doi:10.3390/molecules26154624

Yentür, G., and Dükkancı, M. (2021). Synergistic effect of sonication on photocatalytic oxidation of pharmaceutical drug carbamazepine. *Ultrason. Sonochem.* 78, 105749. doi:10.1016/j.ultsonch.2021.105749

Yetim, T., and Tekin, T. (2017). A kinetic study on photocatalytic and sonophotocatalytic degradation of textile dyes. *Period. Polytech. Chem. Eng.* 61, 102–108. doi:10.3311/PPch.8535

Zare, E. N., Fallah, Z., Le, V. T., Doan, V. D., Mudhoo, A., Joo, S. W., et al. (2022). Remediation of pharmaceuticals from contaminated water by molecularly imprinted polymers: a review. *Environ. Chem. Lett.* 20, 2629–2664. doi:10.1007/s10311-022-01439-4

Zhang, J., Zhou, P., Liu, J., and Yu, J. (2014). New understanding of the difference of photocatalytic activity among anatase, rutile and brookite TiO_2. *Phys. Chem. Chem. Phys.* 16, 20382–20386. doi:10.1039/c4cp02201g

Zhang, J., Zhao, W., Pan, J., and Tang, R. (2021). The sono-photocatalytic performance of PAN/g-C_3N_4/CdS nanofibers heterojunction. *Materials* 14, 5959. doi:10.3390/ma14205959

Zhang, S., Li, B., Wang, X., Zhao, G., Hu, B., Lu, Z., et al. (2020). Recent developments of two-dimensional graphene-based composites in visible-light photocatalysis for eliminating persistent organic pollutants from wastewater. *Chem. Eng. J.* 390, 124642. doi:10.1016/j.cej.2020.124642

Zhao, F., Feng, Y., Wang, Y., Zhang, X., Liang, X., Li, Z., et al. (2020). Two-dimensional gersiloxenes with tunable bandgap for photocatalytic H_2 evolution and CO_2 photoreduction to CO. *Nat. Commun.* 11, 1443–1513. doi:10.1038/s41467-020-15262-4

Zhong, X., Royer, S., Zhang, H., Huang, Q., Xiang, L., Valange, S., et al. (2011). Mesoporous silica iron-doped as stable and efficient heterogeneous catalyst for the degradation of C.I. Acid Orange 7 using sono–photo-Fenton process. *Sep. Purif. Technol.* 80, 163–171. doi:10.1016/j.seppur.2011.04.024

Zhu, S., and Wang, D. (2017). Photocatalysis: basic principles, diverse forms of implementations and emerging scientific opportunities. *Adv. Energy Mat.* 7, 1700841. doi:10.1002/aenm.201700841

frontiers | Frontiers in Chemistry

TYPE Original Research
PUBLISHED 08 January 2024
DOI 10.3389/fchem.2023.1326454

OPEN ACCESS

EDITED BY
Tong Han,
Royal Institute of Technology, Sweden

REVIEWED BY
Liangcai Wang,
Nanjing Forestry University, China
Adam Ekielski,
Warsaw University of Life Sciences, Poland

*CORRESPONDENCE
Mihkel Koel,
mihkel.koel@taltech.ee

RECEIVED 23 October 2023
ACCEPTED 15 December 2023
PUBLISHED 08 January 2024

CITATION
Jõul P, Järvik O, Lees H, Kallavus U, Koel M and Lukk T (2024), Preparation and characterization of lignin-derived carbon aerogels.
Front. Chem. 11:1326454.
doi: 10.3389/fchem.2023.1326454

Preparation and characterization of lignin-derived carbon aerogels

Piia Jõul[1], Oliver Järvik[2], Heidi Lees[2], Urve Kallavus[3], Mihkel Koel[1]* and Tiit Lukk[1]

[1]Department of Chemistry and Biotechnology, Tallinn University of Technology, Tallinn, Estonia, [2]Department of Energy Technology, Tallinn University of Technology, Tallinn, Estonia, [3]Department of Mechanical and Industrial Engineering, Tallinn University of Technology, Tallinn, Estonia

Lignin is considered a valuable renewable resource for building new chemicals and materials, particularly resins and polymers. The aromatic nature of lignin suggests a synthetic route for synthesizing organic aerogels (AGs) similar to the aqueous polycondensation of resorcinol with formaldehyde (FA). The structure and reactivity of lignin largely depend on the severity of the isolation method used, which challenges the development of new organic and carbon materials. Resorcinol aerogels are considered a source of porous carbon material, while lignin-based aerogels also possess great potential for the development of carbon materials, having a high carbon yield with a high specific surface area and microporosity. In the present study, the birch hydrolysis lignin and organosolv lignin extracted from pine were used to prepare AGs with formaldehyde, with the addition of 5-methylresorcinol in the range of 75%–25%, yielding monolithic mesoporous aerogels with a relatively high specific surface area of up to 343.4 m^2/g. The obtained lignin-based AGs were further used as raw materials for the preparation of porous carbon aerogels (CAs) under well-controlled pyrolysis conditions with the morphology, especially porosity and the specific surface area, being dependent on the origin of lignin and its content in the starting material.

KEYWORDS

aerogels, carbon aerogels, lignin, resorcinol–formaldehyde gels, supercritical drying, pyrolysis

Introduction

For many applications, it is important to have a porous material with a well-defined and uniform structure with a specific surface area, pore structure, and pore size that can be tuned according to the needs of a particular application; in such cases, both organic and carbon aerogels (AGs and CAs) possess very good potential to provide this kind of materials (Estevez et al., 2017; Qiang et al., 2017; Li et al., 2019). Most carbon products are obtained by heating coal (to give coke), natural gas (to give carbon black), or other carbonaceous materials of plant or animal origin (to give charcoal at elevated temperatures). Nowadays, more attention is being paid to using biomass as a source of porous materials not because of using renewable raw materials but because it can provide more diverse porous materials with tuneable properties in an economical way.

Lignin comprises 10%–25% of the total renewable lignocellulosic biomass, and it is the most abundant natural source of aromatics (Ragauskas et al., 2014; Dessbesell et al., 2020). Three primary phenylpropanoid monomer units, namely, syringyl-(S), guaiacyl-(G), and *p*-coumaryl-(H), constitute the basis for providing a good starting platform for a wide range of chemicals (Panga et al., 2017; Suota et al., 2021). The effective extraction or separation of

lignin with a stable structure and high purity from biomass is an important step for further valorization. For that, the bond rupture to separate lignin from carbohydrates and its partial depolymerization to make lignin extractable are required, resulting in its solubilization in a proper solvent for further processing (Sun et al., 2018).

Lignin is largely available from the papermaking industry processes like kraft pulping, sulfite pulping, and soda pulping. Other methods, such as hydrolysis/fractionation using hot water, dilute acid, and alkaline and organic solvents, are being utilized on a smaller scale (Zakzeski et al., 2010; Zhao and Abu-Omar, 2021). In active research, the focus is on using enzymes and developing biorefinery processes (Bornscheuer et al., 2014; Fabbri et al., 2023). For environmentally friendlier processes, soda pulping and organosolv (OS) extraction can be proposed, where the lignin obtained is sulfur-free. However, in all these areas, lignin is considered a waste with a very low industrial value, except as fuel for particular industries.

The phenolic nature of lignins makes them potential replacements for phenol/resorcinol in a multitude of industrial applications. A synthetic route of producing AGs by the aqueous polycondensation of resorcinol (1,3-dihydroxybenzene) with formaldehyde (FA) was proposed by Pekala (1989). When lignin contains a free phenolic hydroxyl group and abundant vacant *ortho*- or *para*-sites, it can react with FA to yield polymeric gels. The first attempts at making lignin–phenol–formaldehyde resins were already reported 20 years ago (Effendi et al., 2008; Chen et al., 2011; Grishechko et al., 2013). Various drying processes, such as drying with supercritical CO_2, drying in ambient conditions, and freeze-drying, were used, producing AGs, xerogels, and cryogels, respectively.

The different amounts of the primary phenylpropanoid monomer units in lignin provide different lignin reactivities. It should be noted that H-type units possess more than one active site, offering the potential to create highly cross-linked structures. In the G-type units, one *ortho*-position is already occupied by a methoxyl group, whereas in the S-type units, both are occupied. The H- and G-units are able to react with FA to synthesize lignin-based resins, while the S-unit (no active site is present) is not. In this regard, softwood lignins, which contain mainly G-units, are a better choice for lignin-based resin synthesis than hardwood lignins, which contain S- and some H-units. Spectroscopic methods like infrared spectroscopy (IR) and nuclear magnetic resonance (NMR) are important means that characterize the particular lignin structure prior to material development (Brudin and Schoenmakers, 2010; Singh et al., 2023).

In addition to the different origins, the structure and reactivity of lignins largely depend on the severity of the isolation method used, which must be considered for any desired application. This is one of the greatest challenges for the development of new materials (Titton Dias et al., 2017; Boarino and Klok, 2023). Alkali and AG lignins with a higher number of G-units, free *ortho*-position, and moderate molecular weight are better candidates for the synthesis of 100% lignin-based resins (Raj et al., 2020). Therefore, due to the nature of the reaction between lignin and FA, the structure of lignin is more important than its molecular weight and polydispersity in the synthesis of lignin-based AGs. Although lignins are less reactive toward the addition/substitution reactions due to the lack of reactive sites, the replacement of phenol with lignin would be economically highly advantageous as the phenolic resins are used in many industrial applications such as in the automotive field, computing, aerospace, and construction, as well in the manufacture of engineered wood products (Upton and Kasko, 2016; Gao et al., 2021).

In different developments, phenolic resins and resorcinol AGs are considered useful sources for porous carbon materials, having some distinct advantages such as high carbon yield and high microporosity of the carbonized materials, even without any activation (Jõul et al., 2018; Li et al., 2019; Jõul et al., 2021). The same tendency has also been observed for lignin-derived materials (Xua et al., 2018; Barra et al., 2022; Wu et al., 2022). Thermal treatment and carbonization of lignin-based resins are attractive topics for the research on porous carbons and carbon fibers (Ren et al., 2021). The thermal degradation of lignin is a complex process because of the variety of structural units with different decomposition pathways, including competitive and/or consecutive reactions. The thermal decomposition process of lignin in the temperature range of 20°C–900°C is divided into several distinctive steps with different degradation products and complex changes in the material structure (Talabia et al., 2020; Huang et al., 2022). It is generally believed that the pyrolysis of lignin mainly occurs via free radical reactions (Ma et al., 2023). In the molecular structure of lignin, the oxygen bridge bonds connecting phenyl-propane units and side chains are easily broken when heated. Active free radicals containing benzene rings are formed, and these can easily react with other molecules or free radicals to generate macromolecules with more stable structures, eventually forming biochar at higher temperatures (Chen et al., 2022). These conclusions were drawn from studies on thermal properties, including thermal stability, and thermal degradation kinetics of lignin (Wang et al., 2022). The pyrolysis process of lignin is dominated by the condensation reaction and degradation and rearranging of smaller structural units within it. In the third stage of lignin pyrolysis above 500°C, the aromatic ring-opening, condensation reactions and the formation of char occur (Ren et al., 2021). With the increasing pyrolysis temperature, the rapid decomposition of the biomass and the release of volatiles lead to the formation of pores in the resulting biochar (Chen et al., 2022). There are discussions about the direct use of biomass for carbon materials, and they also point toward the high variability and complicated control of pyrolysis of the material (Matveeva and Bronstein, 2022). Different studies indicate that pyrolysis conditions have a notable impact on the carbon material morphology, and high heating rates lead to the plastic deformation of particles (i.e., melting), resulting in smooth surfaces and large cavities (Cetin et al., 2005; Choi et al., 2022). It has been reported that the porosity and high surface area of lignin-based CAs are generated by the simultaneous pyrolysis and KOH activation of lignin-based organic AGs (Xua et al., 2018). Therefore, a careful study of the structural components of lignin, its various sources, surface area, pore size, and pore distribution is essential for understanding the post-pyrolysis behavior of the obtained carbon materials (Mehta et al., 2020).

Considering the above-mentioned aspects of lignins, including their chemical nature and the resulting behavior, the aim of this work is to continue the studies on the synthesis of lignin-based AGs using different raw materials and the use of these organic porous

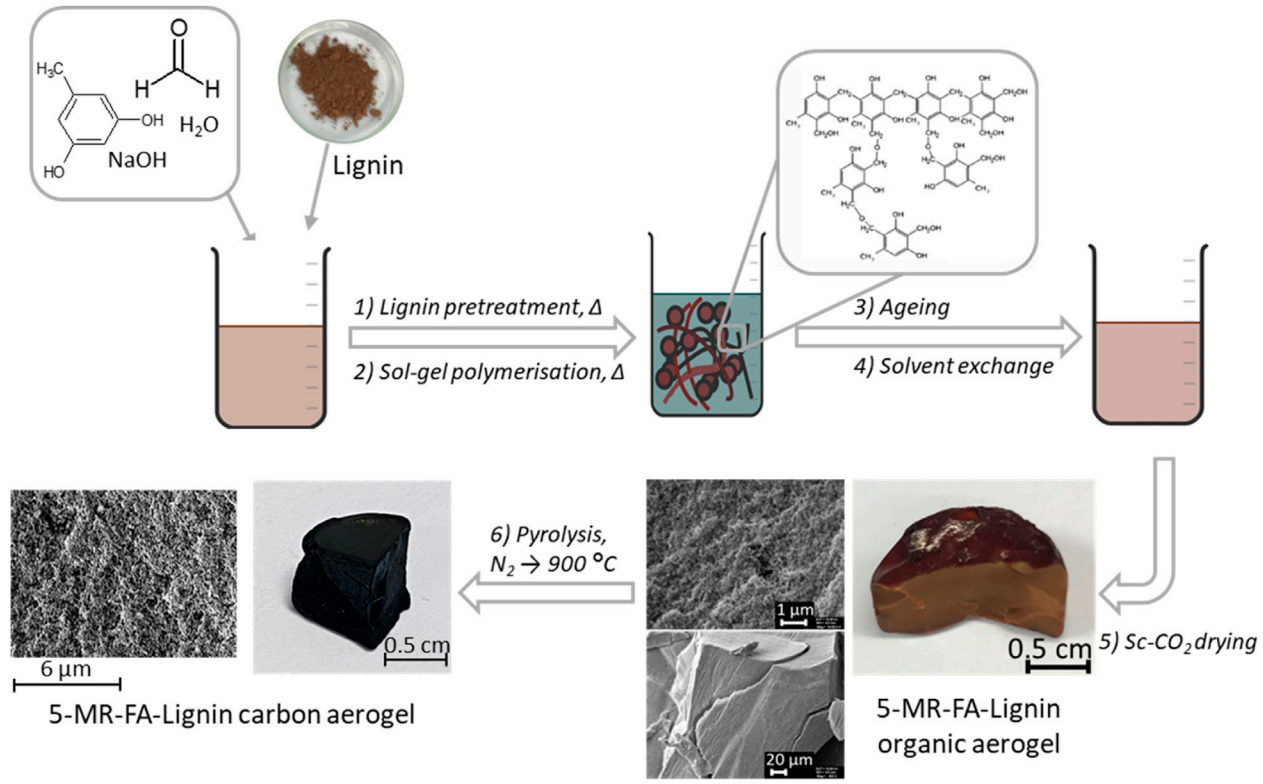

FIGURE 1
Process of CA preparation.

materials to develop a reliable process for porous CA formation, including a thorough characterization of the materials obtained.

Materials and methods

Chemicals

Ethanol, dioxane, hydrochloric acid, acetic acid, sodium hydroxide, sulfuric acid, the FA solution (37 wt% in H_2O), and the sodium carbonate powder (≥99.0%) were purchased from Sigma-Aldrich (Germany). All the chemicals were of analytical grade and were used as received. Deionized water from a Milli-Q water purification system (Millipore S.A.S., Molsheim, France) was used throughout the study. 5-Methylresorcinol (5-MR) with a reported purity of >99% was provided by AS VKG (Estonia).

Raw materials and the methodology of the preparation of aerogel

Two types of lignin were used in this project: hydrolysis lignin from birch trees and OS lignin obtained from pine trees. Fibenol OÜ (Estonia) provided the birch hydrolysis lignin. Pine timber sawdust for OS lignin was provided by the Laboratory of Wood Technology (Tallinn University of Technology). All the raw materials were dried in a convection oven at 50°C to 8% moisture, followed by grinding to a fine powder and storing in plastic bags at room temperature. The AG isolation of lignin with ethanol and dioxane from this biomass was performed according to the process described in Jõul et al. (2022).

The lignins were used to prepare the lignin-5-MR-FA AGs via the sol–gel polycondensation process, according to the procedure described in a previous paper by Jõul et al. (2022). The process is shown in Figure 1. Shortly, the procedure started with lignin homogenization in ultrapure water at 85°C with 0.09% NaOH (wt% based on lignin), and the pH of the mixture was close to 10. After that, the water solution of 5-MR and FA was added to the cooled mixture of lignin and homogenized by mixing on a vortex. The reaction mixtures were chosen so that 25%–75% of 5-MR was replaced with a particular type of lignin. The mixture was kept at 85°C to allow gelation for 1–3 h. The gels were let to age in 1% acetic acid for 12 h. Before supercritical drying, the solvent was exchanged for acetone. The gels were dried by dynamic supercritical CO_2 drying (100 bar, 1.5 h, 25°C; 120 bar, 2.5 h, 45°C). For this purpose, a supercritical extraction system—a 100-mL double-clamp autoclave (NWA Analytische Meßgeräte GmbH, Germany)—was used. Samples under the study are listed in Table 1.

To obtain CAs, pyrolysis was carried out in the N_2 atmosphere using an MTF 12/38/400 pyrolysis oven (Carbolite Gero, England). The optimization of the pyrolysis temperature program for conducting carbonization was performed using different process steps and heating rates. Finally, throughout the research, the following temperature program was applied: from 25°C to 300°C at a rate of 10°C/min (held for 10 min), 300°C–550°C at 10°C/min

TABLE 1 Samples under study and the parameters of the prepared AGs.

Organic aerogel (AG)		Carbon aerogel (CA)	Comment
	Amount of 5-MR replaced by lignin, %	Carbonization—25°C–950°C, N_2	Precursors, lignin type
AG-5-MR-FA	0	CA-5-MR-FA	Pure 5-MR-FA
AG-HL-75	75	CA-HL-75	Hydrolysis lignin, birch
AG-HL-50	50	CA-HL-50	Hydrolysis lignin, birch
AG-HL-25	25	CA-HL-25	Hydrolysis lignin, birch
AG-EOL-Pine	75	CA-EOL-Pine	Ethanol organosolv lignin, pine
AG-DOL-Pine	75	CA-DOL-Pine	Dioxane organosolv lignin, pine

AGs and CAs were analyzed for morphological characteristics and thermal decomposition.

TABLE 2 Structural data on the studied AGs.

Organic aerogel (AG)				Carbon aerogel (CA)			
	S_{BET}, m^2/g	Total pore volume, cm^3/g^a	Average pore diameter, nm		S_{BET}, m^2/g	Total pore volume, cm^3/g^a	Average pore diameter, nm
AG-5-MR-FA	224.3	1.72	30.6	CA-5-MR-FA	501.2	0.36	2.85
AG-HL-75	299.5	1.39	18.6	CA-HL-75	108.9	0.24	8.89
AG-HL-50	343.4	1.04	20.7	CA-HL-50	254.3	0.36	17.0
AG-HL-25	244.6	0.62	16.0	CA-HL-25	434.9	0.65	18.3
AG-EOL-Pine	424.1	0.94	8.9	CA-EOL-Pine	20.9	0.04	7.36
AG-DOL-Pine	393.2	1.13	11.47	CA-DOL-Pine	345.7	0.29	3.36

[a]Total pore volume at $P/P_0 = 0.99$ (cm3/g).

(held for 10 min), and finally, increased to 900°C at 10°C/min (held for 60 min). After pyrolysis, the furnace was allowed to cool to room temperature in the N_2 atmosphere.

Characterization of the materials' morphology

The pore structures of the AG samples were investigated by the N_2 adsorption–desorption method at 77 K with the QuantaChrome autosorb iQ apparatus in the relative pressure range of 0.005–0.995. Prior to analysis, the AG powder was degassed at 105°C for 24 h to remove surface impurities and moisture. The specific surface area (S_{BET}) was calculated by applying the Brunauer–Emmett–Teller (BET) method, and the total pore volume was determined by the volume of N_2 adsorbed at a relative pressure of 0.99. The pore size distribution was determined using the density functional theory (DFT). The data are presented in Table 2.

Scanning electron microscopic (SEM) images were generated to characterize the morphology of the resulting AGs. The surface morphology of both AGs and CAs was examined with a high-resolution scanning electron microscope Zeiss EVO MA 15 SEM at an accelerating voltage of 10 kV. For imaging, pieces of AG samples were fractured into smaller parts to open the internal structure and view the particles' close morphology. The fractured pieces were attached with a double-sided adhesive tape to the stub and coated with the Ag/Pd conductive layer in the Fine Coat Ion Sputter JFC-1100.

The ground samples of AGs were spotted on a diamond crystal and analyzed on an IRTracer-100 FTIR spectrophotometer (Shimadzu, Japan) in the attenuated total reflection (ATR) mode. The spectra were recorded over the 750–4,000 cm^{-1} range by averaging 20 scans at a maximum resolution of 2 cm^{-1} and analyzed using LabSolutions software (Thermo Fisher Scientific).

The micro-Raman spectra were recorded using a Horiba LabRam HR800 spectrometer and a 532-nm Nd-YAG laser focused on the sample with a spot size of approximately 5 μm.

Thermal analysis of materials

The thermogravimetric analysis (TGA) of the AG samples was performed using a NETZSCH STA 449 *F3* Jupiter® thermal analyzer.

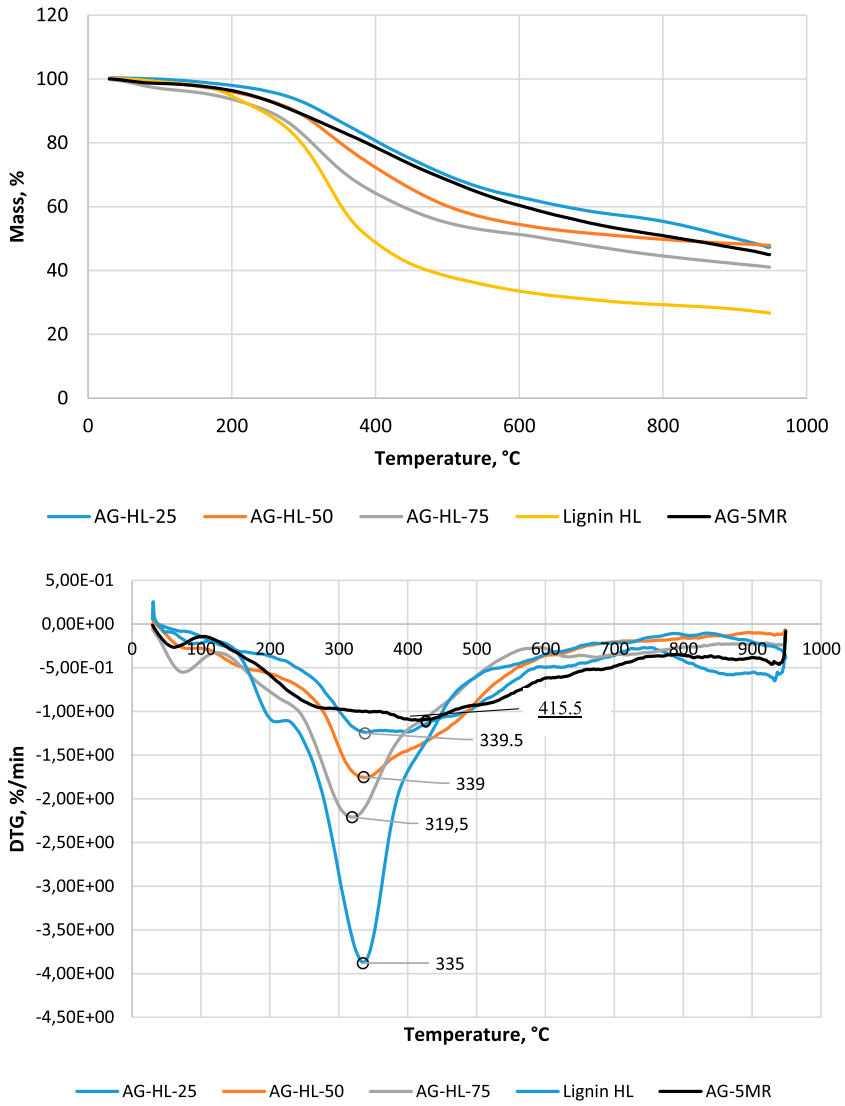

FIGURE 2
TGA and DTG of AG samples with different contents of hydrolysis lignin. For comparison, data on pure lignin (lignin-HL) and 5-methylresorcinol–formaldehyde aerogel (AG-5-MR-FA) have been added.

For analysis, high-purity N_2 (99.999%) was used. Approximately 5 mg of the previously homogenized material was weighed into Al_2O_3 crucibles without lids. The heating rate of 10°C/min was applied. Parallel measurements were run, and these showed excellent reproducibility (differences between mass change steps <2%).

Results and discussion

Thermogravimetric analysis

The thermal degradation of lignin is a complex process because the materials have many components with different decomposition pathways, including competitive and/or consecutive reactions.

In the pyrolysis/carbonization process of AGs between 50°C and 950°C, three stages can be distinctly distinguished, which are very similar to those of the pyrolysis of lignin or resorcinol AGs: the first step begins from the start to 150°C, with a weight loss of about 5% corresponding to the evaporation of water and residual organic precursors. The second step consists in the main smooth degradation between 200°C and 500°C, with a weight loss of 50% centered around 350°C. At this stage, the evolution of a high amount of gases also means the occurrence of substantial chemical changes. The third step after 500°C is related to the slow carbonization with a highly insignificant evolution of volatiles and with almost no mass loss up to 950°C. Three similar stages have been proposed earlier, except the third one, char formation, which is considered to start at above 450°C. At that stage, the recombination and coupling reactions can occur within the particles and the condensation reaction of degradation products takes place (Yu et al., 2021).

The first step was to study the different lignin types. The TGA and derivative thermogravimetric DTG result with AGs prepared using different types of lignin is shown in Supplementary Figure

S1. The amount of lignin was, in all cases, 75% of the aromatic part of the AG. There are quite different degradation maxima (320°C for AG-HL-75, 381°C for AG-EOL-pine, and 388°C for AG-DOL-pine), suggesting different degradation pathways. AGs from AG lignins exhibit close maximum degradation temperatures, which are almost 65°C higher than in the case of hydrolysis lignin. The final product forming 25–45 wt% of the initial weight is carbonaceous material (25% for AG-EOL-pine, 35% for AG-DOL-pine, and 45% for AG-HL-75). Here, the effect of different origins of lignin is seen.

Further studies were carried out on aerogels with different lignin contents—25%, 50%, and 75%. The lignin used was birch hydrolysis lignin. The experiments show that the lignin content can be increased to 80% to obtain a stable composite aerogel. Figure 2 shows the thermal analysis data for AGs with different lignin contents. The TGA curves show a fairly general degradation characteristic of resorcinol–formaldehyde AGs (Maldonado-Hodar et al., 1999).

The differences are more obvious on the DTG curves. The difference is in the weight loss peak temperature, which is 415°C for AG-5-MR-FA and in the range of 320°C–339°C for lignin-based AGs, depending on the content of lignin. From the DTG curve, one can follow two degradation processes: one is related to the degradation of lignin structure units (the 320°C–339°C range), and the other is related to the resorcinol structure degradation (above 425°C). The lower temperature of degradation maxima points to the weaker bonds in the lignin in the AG matrix. Virtual DTG curve decomposition could give an idea of the thermal reactions during the pyrolysis of the investigated materials (figures in the Supplementary Material). Here, the simplest approach with Gaussian curves was performed by varying the peak temperature, peak height, and peak number to match the measured DTG. The results are presented in the Supplementary Material. Two different ranges are seen in the reactions related to the degradation of the material—for lignin with the tip temperature in the range of 330–335°C and degradation of 5-MR part in the range of 425°C–430°C. However, the decomposition of the pure 5-MR-FA aerogel DTG curve gives a much more complicated picture of the thermal degradation of the resorcinol–formaldehyde material. For pure lignin degradation, this virtual decomposition also follows the following three main stages: low-temperature range of 200°C–280°C with two peaks, intensive degradation with the maximum at 338°C, and carbonization at higher temperatures >600°C.

The higher mass of the residual for AG-5-MR-FA compared to lignin AGs indicates that the content of the volatiles in lignin is higher compared to that in 5-MR. At above 600°C, the decarbonylation of alkyl side chains takes place along with a substantial reduction in the functional groups and the aromatic condensation reactions occurring to cause the aromatic polycondensation, leading to the formation of amorphous carbon (Brebu and Vasile, 2010). These volatiles participate in the char formation reactions at higher temperatures. This reaction fills the porous carbon structures from the resorcinol–formaldehyde carbonization, resulting in an amorphous-like non-porous structure and a very dense carbonaceous material. The pyrolysis process in terms of weight loss is very similar for all samples, which provides evidence of the similarity of the process for resorcinol-based and lignin-based materials.

FTIR analysis

Fourier-transform infrared spectroscopy (FTIR) analysis shows the main differences in the structure of AG-5-MR-FA and lignin-based AGs (Figure 3). In the FTIR spectra of the lignin-based AGs, a peak at 1,505.47 cm^{-1} (stretching vibrations in the aromatic structure C=C) and peaks at 2,842.16 cm^{-1} and 2,928.96 cm^{-1} (symmetric and asymmetric stretching vibrations of C–H related to methyl and methylene) are observed, while their intensity is increased in the spectra of AGs, which have a higher content of lignin. The same tendency was observed for the phenolic hydroxyl groups (1,215.17 cm^{-1}).

Raman analysis

Raman spectroscopy of the materials studied provides some additional information, especially on CAs. The spectra of the CA show two broad and strongly overlapping peaks with intensity maxima at 1,336 cm^{-1} (D-band) and 1,593 cm^{-1} (G-band) and with similar intensities. This structure and the Raman spectra of the CA can be interpreted as highly disordered graphitic structures. The G-band is always present in all carbon and graphitic materials, and the D-band is associated with imperfections or loss of hexagonal symmetry in the carbon structure (Gunko et al., 2013). The spectra of the AGs are not very characteristic, and it is difficult to draw serious conclusions about the structure (figure in the Supplementary Material).

Morphology of aerogels

S_{BET} and porosity were determined by the N_2 adsorption/desorption technique, which allows the calculation of average pore sizes and the distribution, as well as the S_{BET} of the material. Data on the porosity of AGs, both organic and carbon, are presented in Table 2. No difference was found in the carbon samples prepared using different temperature programs.

Hydrolysis lignin-based organic AGs show a relatively high S_{BET}, which is close to that of AG-5-MR-FA. AG lignin-based organic AGs (AG-EOL-pine and AG-DOL-pine) have an even higher S_{BET} compared to that of AG-5-MR-FA. The differences in CAs are more evident, especially in the case of CA lignins, which is indicative of the highly different behavior of the materials during the carbonization process. The organic AGs from hydrolysis lignin do not exhibit a very high S_{BET}, and the decrease in S_{BET} during carbonization is not very high either. The reason for this can be related to pore formation during carbonization—the total pore volume is substantially lower, and the pore diameters are smaller. The resulting material is harder and denser compared to the CA derived from 5-MR-FA. Therefore, it can be observed that S_{BET} decreases with a higher HL content. However, there is a significant difference between EOL-pine- and DOL-pine-based CAs. After the pyrolysis procedure, the S_{BET} value of the former is more than 15 times higher, while the total pore volume is much lower.

The N_2 adsorption–desorption isotherms of the prepared AGs (lignin-based, in which 25% and 50% of the 5-MR were replaced by lignin and related CAs, respectively) are shown in Figure 4. The

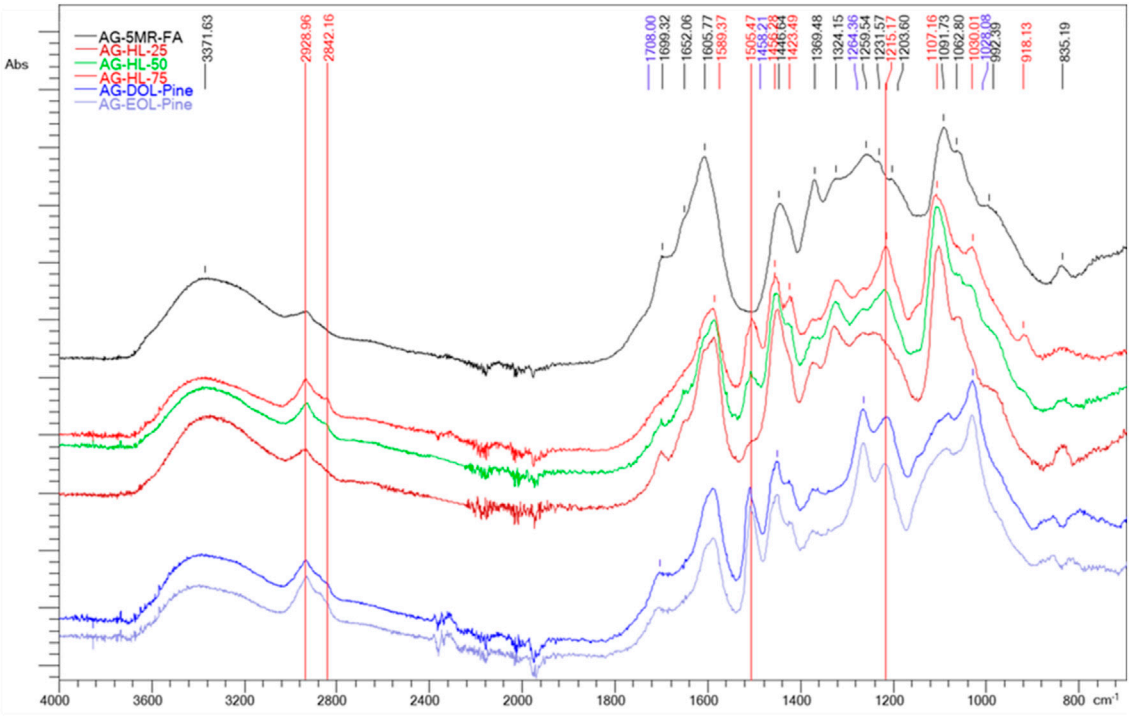

FIGURE 3
ATR-FTIR spectra of lignin-based and 5-MR-FA aerogels.

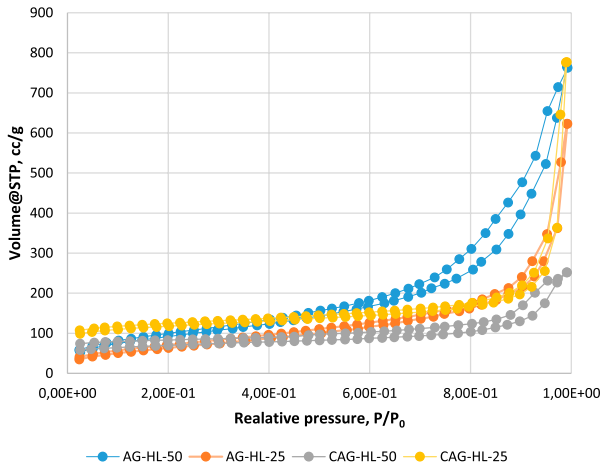

FIGURE 4
N_2 absorption curves for lignin-containing AGs and related CAs.

Supplementary Material presents the pore size distribution for these aerogels (Supplementary Figures S13, S14).

According to the IUPAC classification, the obtained N_2 adsorption/desorption isotherms for AGs are characteristic of mesoporous adsorbents, where the adsorption hysteresis is clearly seen and can provide information about the texture (e.g., pore size distribution, pore geometry, and connectivity) of the mesoporous material.

The initial region of the isotherms at low P/P_0, which indicates the presence of micropores in addition to mesopores in the gel structure, is very similar in the case of all the samples and is not characteristic of these AGs specifically. It is well known that organic resorcinol–FA AGs do not have microporosity in their structure. Hysteresis loops for gels in the P/P_0 range of 0.2–1.0 reveal that mesoporosity is dominant in their structures.

From a previous study, it became clear that AG-5-MR-FA exhibits a network structure composed of agglomerates of uniform spherical particles (Peikolainen et al., 2012). The addition of lignin into the structure of AG tends to induce some disordering, leading to a partial opening of the network structure. This observation can also be extended to CAs.

SEM analysis

SEM pictures of organic AGs confirm the similarity between AGs having a uniform structured tenuous network of clustered nanopores of sizes approximately 10–30 nm and CAs having those of approximately 3–18 nm.

As demonstrated by 31P-NMR quantitative analysis in a previous publication by Jõul et al. (2022), a significantly higher amount of aromatic OH groups was found after the dioxane AG extraction than when using ethanol. This did not significantly affect the properties of organic AGs (Supplementary Figure S2), but if these organic AGs are compared with CAs (Supplementary Figure S3), it can be said that differences in the morphology of CA-DOL-pine and CA-EOL-pine are caused by changes in the molecular structure of AGs during the pyrolysis procedure.

Replacing 25% of 5-MR with lignin creates light and porous CAs, while AG prepared from materials with 50% of lignin content

already gives a solid and dense monolith and that with 75% gives a hard solid monolith with needle crystals on the surface (Supplementary Figures S4, S5).

For comparison, Supplementary Figure S6 shows AG-5-MR-FA and its carbonized form CA-5-MR-FA, which is a light and fragile CA.

Based on the previous knowledge of CA-5-MR-FA, it can be expected that replacing 5-MR with lignin creates AGs with adjustable S_{BET} and a certain amount of micro-, macro-, and meso-pores and also enables easy structural modification with other elements (N and S) and metals.

Conclusion

The present study shows that the extraction processes of the pine AG lignin and the birch hydrolysis lignin generated the material with a high reactivity to form a gel with FA. It was possible to produce FA AGs from lignin with the addition of 5-MR (25%–75%). The additional pretreatment of the precursor lignin with NaOH allows increasing its solubility, which, thus, enhances the gelation process. The commercially available hydrolysis lignin is a material that has good reactivity to form gels with 5-MR and FA, yielding monolithic mesoporous AGs with a relatively high S_{BET} of up to 343.4 m^2/g. Supercritical CO_2 drying is superior and provides stable AGs. The obtained lignin-based organic AGs were used as the raw material for porous CAs, but the pyrolyzed organic AGs with a high lignin content did not exhibit as outstanding porous properties as 5-MR-FA-based CAs. The search for some kind of lignin pretreatment is needed to guide the lignin pyrolysis toward a monolithic carbonization process.

For exploration of potential future trends in the case of lignin-based AGs, particularly for carbon materials, further investigation of lignin pyrolysis is necessary to get correlations between the lignin structure and the resulting morphology of the carbon material.

Data availability statement

The original contributions presented in the study are included in the article/Supplementary Material; further inquiries can be directed to the corresponding author.

Author contributions

PJ: data curation, formal analysis, investigation, methodology, resources, validation, visualization, and writing–review and editing. OJ: conceptualization, data curation, funding acquisition, investigation, methodology, resources, supervision, validation, and writing–review and editing. HL: conceptualization, data curation, formal analysis, investigation, methodology, resources, validation, visualization, and writing–review and editing. UK: data curation, formal analysis, investigation, methodology, validation, visualization, and writing–review and editing. MK: conceptualization, methodology, project administration, supervision, validation, writing–original draft, and writing–review and editing. TL: conceptualization, funding acquisition, methodology, resources, supervision, validation, and writing–review and editing.

Funding

The authors declare financial support was received for the research, authorship, and/or publication of this article. This study was supported by ERDF and Estonian Research Council via project RESTA11 and via Grant PRG1784. The authors declare that this study received chemicals from Fibenol OÜ and VKG AS. The funders were not involved in the study design, collection, analysis, interpretation of data, the writing of this article, or the decision to submit it for publication. This publication is based upon work from COST Action "Advanced Engineering of aeroGels for Environment and Life Sciences" (AERoGELS, ref. CA18125), supported by COST (European Cooperation in Science and Technology).

Conflict of interest

The authors declare that the research was conducted in the absence of any commercial or financial relationships that could be construed as a potential conflict of interest.

Publisher's note

Supplementary material

The Supplementary Material for this article can be found online at: https://www.frontiersin.org/articles/10.3389/fchem.2023.1326454/full#supplementary-material

References

Barra, A., Nunes, C., Ruiz-Hitzky, E., and Ferreira, P. (2022). Green carbon nanostructures for functional composite materials. *Int. J. Mol. Sci.* 23, 1848. doi:10.3390/ijms23031848

Boarino, A., and Klok, H.-A. (2023). Opportunities and challenges for lignin valorization in food packaging, antimicrobial, and agricultural applications. *Biomacromolecules* 24, 1065–1077. doi:10.1021/acs.biomac.2c01385

Bornscheuer, U., Buchholz, K., and Seibel, J. (2014). Enzymatic degradation of (Ligno) cellulose *A J. Ger. Chem. Soc* 53, 41, 10876–10893. doi:10.1002/anie.201309953

Brebu, M., and Vasile, C. (2010). Thermal degradation of lignin—a Review. *Cellul. Chem. Technol.* 44, 353–363.

Brudin, S., and Schoenmakers, P. (2010). Analytical methodology for sulfonated lignins. *J.Separation Sci.* 33 (3), 439–452. doi:10.1002/jssc.200900691

Cetin, E., Gupta, R., and Moghtaderi, B. (2005). Effect of pyrolysis pressure and heating rate on radiata pine char structure and apparent gasification reactivity. *Fuel* 84, 1328–1334. doi:10.1016/j.fuel.2004.07.016

Chen, D., Cen, K., Zhuang, X., Gan, Z., Zhou, J., Zhang, Y., et al. (2022). Insight into biomass pyrolysis mechanism based on cellulose, hemicellulose, and lignin: evolution of volatiles and kinetics, elucidation of reaction pathways, and characterization of gas, biochar and bio-oil. *Combust. Flame* 242, 112142. doi:10.1016/j.combustflame.2022.112142

Chen, F., Xu, M., Wang, L., and Li, J. (2011). Preparation and characterization of organic aerogels from a lignin-resorcinol- formaldehyde copolymer. *BioResources* 6 (2), 1262–1272. doi:10.15376/biores.6.2.1262-1272

Choi, J.-H., Kim, J.-H., Lee, S. Y., Jang, S.-K., Kwak, H. W., Kim, H., et al. (2022). Thermoplasticity reinforcement of ethanol organosolv lignin to improve compatibility in PLA-based ligno-bioplastics: focusing on the structural characteristics of lignin. *Int. J. Biol. Macromol.* 209B, 1638–1647. doi:10.1016/j.ijbiomac.2022.04.090

Dessbesell, L., Paleologou, M., Leitch, M., Pulkki, R., and Xu, C. (2020). Global lignin supply overview and kraft lignin potential as an alternative for petroleum-based polymers. *Renew. Sustain. Energy Rev.* 123, 109768. doi:10.1016/j.rser.2020.109768

Effendi, A., Gerhauser, H., and Bridgwater, A. V. (2008). Production of renewable phenolic resins by thermochemical conversion of biomass: a review. *Renew.Sustain. Energy Rev.* 12, 2092–2116. doi:10.1016/j.rser.2007.04.008

Estevez, L., Prabhakaran, V., Garcia, A. L., Shin, Y., Tao, J., Schwarz, A. M., et al. (2017). Hierarchically porous graphitic carbon with simultaneously HighSurface area and colossal pore volume engineered via ice templating. *ACS Nano* 11, 11047–11055. doi:10.1021/acsnano.7b05085

Fabbri, F., Bischof, S., Mayr, S., Gritsch, S., Jimenez Bartolome, M., Schwaiger, N., et al. (2023). The biomodified lignin platform: a review. *Polymers* 15, 1694. doi:10.3390/polym15071694

Gao, Z., Lang, X., Chen, S., and Zhao, C. (2021). Mini-review on the synthesis of lignin-based phenolic resin. *Energy fuels* 35, 18385–18395. doi:10.1021/acs.energyfuels.1c03177

Grishechko, L. I., Amaral-Labat, G. I., Szczurek, A., Fierro, V., Kuznetsov, B. N., and Celzard, A. (2013). Lignin–phenol–formaldehyde aerogels and cryogels. *Microporous Mesoporous Mater.* 168, 19–29. doi:10.1016/j.micromeso.2012.09.024

Gunko, V. M., Bogatyrov, V. M., Turov, V. V., Leboda, R., Skubiszewska-Zieba, J., and Urubkov, I. V. (2013). Structural features of resorcinol–formaldehyde resin chars and interfacial behavior of water co-adsorbed with low-molecular weight organics. *App. Surf. Sci.* 283, 683–693. doi:10.1016/j.apsusc.2013.06.165

Huang, X., Yin, H., Zhang, H., Mei, N., and Mu, L. (2022). Pyrolysis characteristics, gas products, volatiles, and thermo–kinetics of industrial lignin via TG/DTG–FTIR/MS and in–situ Py–PI–TOF/MS. *Energy* 259, 125062. doi:10.1016/j.energy.2022.125062

Jõul, P., Ho, T. T., Kallavus, U., Konist, A., Leiman, K., Salm, O.-S., et al. (2022). Characterization of organosolv lignins and their application in the preparation of aerogels. *Materials* 15, 2861. doi:10.3390/ma15082861

Jõul, P., Vaher, M., and Kuhtinskaja, M. (2018). Evaluation of carbon aerogel-based solid-phase extraction sorbent for the analysis of sulfur mustard degradation products in environmental water samples. *Chemosphere* 198, 460–468. doi:10.1016/j.chemosphere.2018.01.157

Jõul, P., Vaher, M., and Kuhtinskaja, M. (2021). Carbon aerogel-based solid-phase microextraction coating for the analysis of organophosphorus pesticides. *Anal. Methods* 13 (1), 69–76. doi:10.1039/D0AY02002H

Li, Z., Wang, L., Li, Y., Feng, Y., and Feng, W. (2019). Carbon-based functional nanomaterials: preparation, properties and Applications. *Comp. Sci.& Tech.* 179, 10–40. doi:10.1016/j.compscitech.2019.04.028

Ma, L., Syed-Hassan, S. S. A., Tong, Y., Xiong, Z., Chen, Y., Xu, J., et al. (2023). Interactions of cellulose- and lignin-derived radicals during pyrolysis: an in-situ Electron Paramagnetic Resonance (EPR) study. *Fuel Process. Technol.* 239, 107536. doi:10.1016/j.fuproc.2022.107536

Maldonado-Hodar, F. J., Ferro-Garcıa, M. A., Rivera-Utrilla, J., and Moreno-Castilla, C. (1999). Synthesis and textural characteristics of organic aerogels, transition-metal-containing organic aerogels and their carbonized derivatives. *Carbon* 37, 1199–1205. doi:10.1016/S0008-6223(98)00314-5

Matveeva, G. V., and Bronstein, L. M. (2022). From renewable biomass to nanomaterials: does biomass origin matter? *Prog. Mat. Sci.* 130, 100999. doi:10.1016/j.pmatsci.2022.100999

Mehta, S., Jha, S., and Liang, H. (2020). Lignocellulose materials for supercapacitor and battery electrodes: a review. *Renew. Sustain. Energy Rev.* 134, 110345. doi:10.1016/j.rser.2020.110345

Panga, B., Yanga, S., Fanga, W., Yuana, T.-Q., Argyropoulosb, D. S., and Sun, R.-C. (2017). Structure-property relationships for technical lignins for the production of lignin-phenol-formaldehyde resins. *Industrial Crops Prod.* 108, 316–326. doi:10.1016/j.indcrop.2017.07.009

Peikolainen, A.-L., Volobujeva, O., Aav, R., Uibu, M., and Koel, M. (2012). Organic acid catalyzed synthesis of 5-methylresorcinol based organic aerogels in acetonitrile. *J.Porous Mat.* 19 (2), 189–194. doi:10.1007/s10934-011-9459-8

Pekala, R. W. (1989). US patent. *U. S. Pat.* 4, 804.

Qiang, Z., Xia, Y., Xia, X., and Vogt, B. D. (2017). Generalized synthesis of a family of highly heteroatom-doped ordered mesoporous carbons. *Chem. Mat.* 29, 10178–10186. doi:10.1021/acs.chemmater.7b04061

Ragauskas, A. J., Beckham, G. T., Biddy, M. J., Chandra, R., Chen, F., Davis, M. F., et al. (2014). Lignin valorization: improving lignin processing in the biorefinery. *Science*, 344. doi:10.1126/science.1246843

Raj, A., Devendra, L. P., and Sukumaran, R. K. (2020). Comparative evaluation of laccase mediated oxidized and unoxidized lignin of sugarcane bagasse for the synthesis of lignin-based formaldehyde resin. *Industrial Crops Prod.* 150, 112385. doi:10.1016/j.indcrop.2020.112385

Ren, Y., Xie, J., He, X., Shi, R., and Liu, C. (2021). Preparation of lignin-based high-ortho thermoplastic phenolic resins and fibers. *Molecules* 26, 3993. doi:10.3390/molecules26133993

Singh, S. S., Lim, L.-T., and Manickavasagan, A. (2023). Imaging and spectroscopic techniques for microstructural and compositional analysis of lignocellulosic materials: a review. *Biomass Convers. Biorefinery* 13, 499–517. doi:10.1007/s13399-020-01075-4

Sun, Z., Fridrich, B., de Santi, A., Elangovan, S., and Barta, K. (2018). Bright side of lignin depolymerization: toward new platform chemicals. *Chem. Rev.* 118, 614–678. doi:10.1021/acs.chemrev.7b00588

Suota, M. J., da Silva, T. A., Zawadzki, S. F., Sassaki, G. L., Hansel, F. A., Paleologou, M., et al. (2021). Chemical and structural characterization of hardwood and softwood LignoForce™ lignins. *Industrial Crops Prod.* 173, 114138. doi:10.1016/j.indcrop.2021.114138

Talabia, S. I., da Luza, A. P., Pandolfellia, V. C., Limac, V. H., Botaroc, V. R., and de Almeida Lucasa, A. (2020). Graphitization of lignin-phenol-formaldehyde resins. *Mater. Res.* 23, 2, e20190686. doi:10.1590/1980-5373-MR-2019-0686

Titton Dias, O. A., Negrão, D. R., Gonçalves, D. F. C., Cesarino, I., and Leão, A. L. (2017). Recent approaches and futuretrends for lignin-based materials. *Mol. Cryst. Liq. Cryst.* 655 (1), 204–223. doi:10.1080/15421406.2017.1360713

Upton, B. M., and Kasko, A. M. (2016). Strategies for the conversion of lignin to high-value polymeric materials: review and perspective. *Chem. Rev.* 116, 2275–2306. doi:10.1021/acs.chemrev.5b00345

Wang, J., Hou, S., Shen, Z., Wen, J., and Qi, C. (2022). Thermal characteristics and simulation of enzymatic lignin isolated from Chinese fir and birch. *Forests* 13, 914. doi:10.3390/f13060914

Wu, C.-W., Li, P.-H., Wei, Y.-M., Yang, C., and Wu, W.-J. (2022). Review on the preparation and application of lignin-based carbon aerogels. *RSC Adv.* 12, 10755. doi:10.1039/D2RA01402E

Xua, J., Zhoua, X., Chena, M., Shia, S., and Cao, Y. (2018). Preparing hierarchical porous carbon aerogels based on enzymatic hydrolysis lignin through ambient drying for supercapacitor electrodes. *Microporous Mesoporous Mater.* 265, 258–265. doi:10.1016/j.micromeso.2018.02.024

Yu, J., Wang, D., and Sun, L. (2021). The pyrolysis of lignin: pathway and interaction studies. *Fuel* 290, 120078. doi:10.1016/j.fuel.2020.120078

Zakzeski, J., Bruijnincx, P. C. A., Jongerius, A. L., and Weckhuysen, B. M. (2010). The catalytic valorization of lignin for the production of renewable chemicals. *Chem. Rev.* 110, 3552–3599. doi:10.1021/cr900354u

Zhao, S., and Abu-Omar, M. M. (2021). Materials based on technical bulk lignin. *ACS Sustain. Chem. Eng.* 9, 1477–1493. doi:10.1021/acssuschemeng.0c08882

frontiers | Frontiers in Chemistry

TYPE Original Research
PUBLISHED 08 February 2024
DOI 10.3389/fchem.2024.1347147

OPEN ACCESS

EDITED BY
Rajkumar Patel,
Yonsei University, Republic of Korea

REVIEWED BY
Pavel Nikishau,
University of Alabama at Birmingham, United States
Nabendu B. Pramanik,
Institute of Chemical Technology, India

*CORRESPONDENCE
Esakkiammal Sudha Esakkimuthu,
sudha.esakkimuthu@innorenew.eu
Veerapandian Ponnuchamy,
veerapandian.ponnuchamy@innorenew.eu
Mika H. Sipponen,
mika.sipponen@mmk.su.se

†PRESENT ADDRESSES
Veerapandian Ponnuchamy, Department of Mechanical Engineering, Eindhoven University of Technology, Eindhoven, Netherlands
David DeVallance, College of Science and Technology, Commonwealth University of Pennsylvania, Lock Haven, PA, United States

‡These authors have contributed equally to this work

RECEIVED 30 November 2023
ACCEPTED 26 January 2024
PUBLISHED 08 February 2024

CITATION
Esakkimuthu ES, Ponnuchamy V, Sipponen MH and DeVallance D (2024), Elucidating intermolecular forces to improve compatibility of kraft lignin in poly(lactic acid).
Front. Chem. 12:1347147.
doi: 10.3389/fchem.2024.1347147

Elucidating intermolecular forces to improve compatibility of kraft lignin in poly(lactic acid)

Esakkiammal Sudha Esakkimuthu[1,2*‡], Veerapandian Ponnuchamy[1,3*†‡], Mika H. Sipponen[2,4*] and David DeVallance[1,5†]

[1]InnoRenew CoE, Izola, Slovenia, [2]Department of Materials and Environmental Chemistry, Stockholm University, Stockholm, Sweden, [3]Andrej Marušič Institute, University of Primorska, Koper, Slovenia, [4]Wallenberg Wood Science Center, Department of Materials and Environmental Chemistry, Stockholm University, Stockholm, Sweden, [5]Faculty of Mathematics, Natural Sciences and Information Technologies, University of Primorska, Koper, Slovenia

Owing to its abundant supply from renewable resources, lignin has emerged as a promising functional filler for the development of sustainable composite materials. However, achieving good interfacial compatibility between lignin and synthetic polymers, particularly poly (lactic acid) (PLA), remains a fundamental challenge. To advance the development of high-performance bio-based composites incorporating lignin and PLA, our study has scrutinized to unravel the nuances of interfacial binding interactions with the lignin and PLA composite system. Molecular level and experimental examinations were employed to decipher fundamental mechanisms governing and demonstrating the interfacial adhesion. We synthesized casted films of lignin/PLA and acetylated lignin/PLA at varying weight percentages of lignin (5%, 10%, and 20%) and comprehensively investigated their physicochemical and mechanical properties. The inclusion of acetylated lignin in the composites resulted in improved mechanical strength and Young's modulus, while the glass transition temperature and melting point were reduced compared to neat PLA. Systematic variations in these properties revealed distinct compatibility behaviors between unmodified lignin and acetylated lignin when incorporated into PLA. Molecular dynamics (MD) simulation results elucidated that the observed changes in material properties were primarily attributed to the acetylation of lignin. Acetylated lignin exhibited lower Coulombic interaction energy and higher van der Waals forces, indicating a stronger affinity to PLA and a reduced propensity for intermolecular aggregation compared to unmodified lignin. Our findings highlight the critical role of controlling intermolecular interactions and lignin aggregation to develop PLA composites with predictable performance for new applications, such as functional packaging materials.

KEYWORDS

lignin, poly - (lactic acid), composites, molecular dynamics simulations, hydrogen bonding, mechanical properties

1 Introduction

Lignocellulosic biomass is a complex and highly heterogeneous composite material of polysaccharides (cellulose and hemicellulose) and aromatic biopolymer (lignin) (Cai et al., 2017). Among these components, lignin is an undervalued by-product and energy source through combustion in lignocellulosic biorefineries such as chemical pulp mills. Lignin macromolecules originate from the radical polymerization of one or more of the so-called monolignols (Schoenherr et al., 2017). A major body of research has been conducted to find ways to utilize lignin for value-added applications. One of the directions is to use lignin as a functional filler in polymer composites (Duval and Lawoko, 2014; Upton and Kasko, 2016; Wang et al., 2016).

Incorporation of lignin in the polymer matrix can enhance thermal, mechanical, UV-protective, and radical scavenging properties of the polymers such as polyethylene, polypropylene, poly (lactic acid) (PLA), and poly (ε-caprolactone) (Thakur et al., 2014). Among them, PLA is of particular interest as an industrially compostable polyester derived from biotechnologically produced lactic acid (Garlotta, 2001; Lim et al., 2008; Rasal et al., 2010). It has been applied for several applications including food packaging, single-use items, medical applications, etc., (Jem and Tan, 2020). In 2019, 190,000 tons annually of PLA were reported to be produced (Masutani and Kimura, 2014; Dubey et al., 2017; Jem and Tan, 2020). However, the selling cost of PLA is relatively high, about 5140 US$/per ton (Ratshoshi et al., 2021) and despite its appropriate mechanical strength, PLA exhibits poor UV shielding character when used in food packaging applications. These issues disfavor PLA in comparison with aromatic polymers such as polyethylene terephthalate (PET) and polystyrene (PS) (van den Oever et al., 2017).

The blending of lignin in PLA decreases the total cost and enhances the UV barrier properties (Shankar et al., 2015; Sakai et al., 2018; Rukmanikrishnan et al., 2020; Hararak et al., 2021; Črešnar et al., 2021; Makri et al., 2022). However, direct utilization of lignin as a filler in PLA often leads to poor compatibility between the contrastive polymers. An underlying reason suggested for this incompatibility is the intermolecular aggregation of lignin in the PLA polymer. Such aggregation phenomena should be minimized in order to enhance compatibility along with thermal and mechanical properties. Simultaneously, the interaction between lignin and PLA ought to be enhanced. In such instances, chemical modification of lignin, mainly acetylation has been proposed to improve compatibility and thermal stability compared to unmodified lignin in PLA(Gordobil et al., 2014; Kim et al., 2017; Li et al., 2017; Park et al., 2019; Johansson et al., 2023).

Numerous experimental investigations have centered around incorporating diverse chemical modifications of lignin, utilizing various methods to augment the compatibility of lignin within the PLA matrix (Daassi et al., 2023; Zaidi et al., 2023). The complex interplay within these lignin-based PLA composites can be enabled through the application of advanced computational modeling techniques. Through computational simulations, we aim to unravel the intermolecular forces that control the interfacial behavior of these composites. This computational exploration governs the compatibility and structural integrity of the composite system, thereby bridging the gap between experimental observations and a comprehensive mechanistic understanding.

Molecular dynamics (MD) simulation method accounts for important interactions and allow the prediction of mechanical properties. Despite their utility to understand and predicting properties of various pure PLA (Farazin and Mohammadimehr, 2022) and PLA-based composites with different materials such as hydroxyapatite, graphene, amorphous cellulose and wood cell wall constituents (Zhang et al., 2009; Zhou et al., 2013; Hasheminejad and Montazeri, 2020; Ren et al., 2021; Ren et al., 2023). It is crucial to emphasize that the existing literature lacks substantial evidence derived from the combination of experimental findings and theoretical atomistic modeling concerning lignin within the PLA matrix. To the best of our knowledge, this study marks the first time into the investigation of both lignin and acetylated lignin in conjunction with PLA through comprehensive molecular dynamics (MD) simulations.

In the present work, we have prepared lignin/PLA (LIG/PLA) and acetylated lignin/PLA (aLIG/PLA) composites using a casting method with three different weight percentages of lignin (5%, 10%, and 20%) in the PLA matrix. The composites were systematically characterized for mechanical (tensile strength, Young's modulus) and thermal (glass transition temperature) properties. Furthermore, the MD approach was employed to investigate the composites to provide significant insights into the intermolecular interactions. The MD simulations provided means to decipher the experimental results based on the physicochemical, dynamic, and mechanical properties such as radial distribution function, hydrogen bonding, mean square displacement, Young's modulus, and glass transition temperature. Overall, the combination of experimental and modelling methods provided a comprehensive view of the features that determine the extent that lignin aggregates in PLA composites.

2 Materials and methods

Kraft softwood lignin (UPM BioPiva 395) was purchased from UPM biochemicals with an average molecular weight of 6,000 g/mol and less than 2% of ash content. Polylactic acid (PLA) pellets, namely, Inzea F38 were purchased from the Nurel biopolymers and contained 70% biobased content with a density of 1.23 g/cm^3 and a melt flow index of 1.8 g/10 min and was measured with ISO 1133. Acetic anhydride (reagent grade, ≥99% purity) and Pyridine (reagent grade, anhydrous, 99.8%) were purchased from Sigma-Aldrich.

2.1 Lignin modification using acetylation

Kraft lignin (5 g, dry basis) was mixed with 15 mL of acetic anhydride and 50 mL of pyridine mixture (3:10 ratio). The reaction mixture was stirred at room temperature for 18 h. Then, the product was precipitated in ice-cold distilled water (1 L) and filtered through cellulose membrane filters. The precipitate was washed with distilled water several times to remove the unreacted reagents and dried in the oven at 40°C (Esakkimuthu et al., 2022b).

2.2 Lignin/PLA and modified lignin/PLA composites preparation

Lignin/PLA (LIG/PLA) and Acetylated lignin/PLA (aLIG/PLA) films were prepared using a solvent casting process using chloroform as a solvent. The total amount of dry substance in the composite films was kept constant at 2 g. PLA was used as a matrix, and different weight percentages (5%, 10%, and 20%) of lignin and acetylated lignin were added as fillers. PLA was stirred in 20 mL of chloroform at room temperature until complete dissolution followed by the addition of lignin and stirred for another 2 h before casting. The stirred solution mixtures were casted onto the 10 cm diameter glass Petri dish and dried at room temperature for 24 h. Then, the residual chloroform was removed using the vacuum drying process. The produced composite films resulted in a thickness of 200±50 µm. It is crucial to emphasize that we sourced PLA from Nurel Biopolymers and subsequently fabricated PLA films using a solvent casting process. Therefore, the term "Neat PLA" refers to the pure PLA obtained from the solvent casting procedure, without addition of any lignin materials.

2.3 Fourier transform infrared spectroscopy (FTIR)

FTIR analysis of kraft and acetylated kraft lignin was performed on a PerkinElmer spectrophotometer. The absorbance spectra of the samples were collected in the range of 4,000–400 cm^{-1} in the attenuated total reflectance mode and a total of 64 scans with a resolution of 4 cm^{-1} were collected in transmission mode.

2.4 Thermogravimetric analysis (TGA)

The thermal stability of LIG and aLIG samples were analyzed in Platinum pans using a Waters TA Instrument™ TGA 5500. The instrument was temperature calibrated using Nickel as calibrant. The samples (5–10 mg) were tested in a temperature range from 40°C to 800°C with a heating rate of 10°C min^{-1} under a nitrogen atmosphere with a flow rate of 25 mL min^{-1}.

2.5 Differential scanning calorimetry (DSC) analysis

DSC measurements of LIG/PLA and aLIG/PLA biocomposites were performed with TA Waters Instruments, New Castle, DE, United States using Tzero Aluminum pans with Indium as reference material by applying cell constant/temperature calibration method under a nitrogen atmosphere with a temperature range of −25°C–210°C at a heating rate of 10°C min^{-1} with a flow rate of 25 mL min^{-1}. Glass transition temperature (T_g), and melting temperature (T_m) were calculated from the recorded thermograms.

2.6 Mechanical test

The mechanical performance of neat PLA and PLA with LIG and aLIG composites was evaluated using a universal Testing Machine (Instron 4,204, United States) equipped with a 100 N load cell. Casted samples (5 mm width and 0.3 mm thickness) were tested according to the ISO 527–2 standard crosshead speed of 5 mm min^{-1} and an initial grip separation of 25 mm. Force and displacement were measured and recorded in the measurement environment of 50% RH at 23°C. Young's modulus (E) was determined from the slope in the initial linear region of the stress-strain curve. A minimum of seven composite specimens were measured to calculate Young's modulus, tensile strength, and elongation at break values.

2.7 Scanning electron microscopy (SEM)

The morphology of PLA-lignin composite specimens was examined using a field-emission scanning electron microscope (FE-SEM; Zeiss Sigma VP, Germany). Fractured surfaces from the tensile test were affixed to carbon tape to investigate surface morphological features. Subsequently, the samples underwent gold sputter-coating for 60 s at 10 mA. Micrographs of the surfaces were captured at an accelerating voltage of 5 kV using a secondary electron detector.

2.8 Molecular dynamics simulations

Due to its natural variability and heterogeneity at the molecular level, no universal structure for lignin exists to represent lignin for molecular dynamics. We have chosen a lignin model proposed by Vermass et al. (2019) which originally depicts softwood lignin. The selected model is shown in Figure 1C and the corresponding structure is composed of 6-G units and 1-P unit and contains 1 (β-O-4), 2 (5–5), 1 (4-O-5), and 2 (β −1) linkages with a total molecular weight of 1.2 kDa (unmodified lignin). In the case of acetylated lignin structure, the hydroxyl groups present in the phenyl rings and aliphatic chains were modified into corresponding acetylated lignin.

For MD simulations, the bonded and non-bonded (intermolecular) interactions are accounted by CHARMM force fields, and we used an excellent graphical interphase platform, CHARMM-GUI to build all lignin structures such as lignin (LIG) and acetylated lignin (aLIG) and PLA polymer for the simulations. In the case of PLA polymer, there are 50 repeating units or degrees of polymerization (DP = 50) used. No tacticity was considered in this study for PLA. Initially, separate simulation boxes were constructed for each system (LIG/PLA and aLIG/PLA) with three different weight percentages of lignin, such as 5%, 10%, and 20% with respect to PLA. The systems investigated in this study are presented in Table 1. It is important to validate the force field potential before performing extensive MD simulations to minimize the issues related to the representation of the systems. Therefore, we have conducted benchmark simulations for LIG and PLA materials separately and computed the density of the system from the simulations (at 298.15 K), and compared them with experimental data. The simulated density values for LIG and PLA were found to be 1,202 and 1,178 kg m^{-3}, respectively. In the case of LIG system, various experimental density values are proposed (Ehrnrooth, 1984; Cotterill et al., 1996; Michelsen and Foss, 1996), ranging from

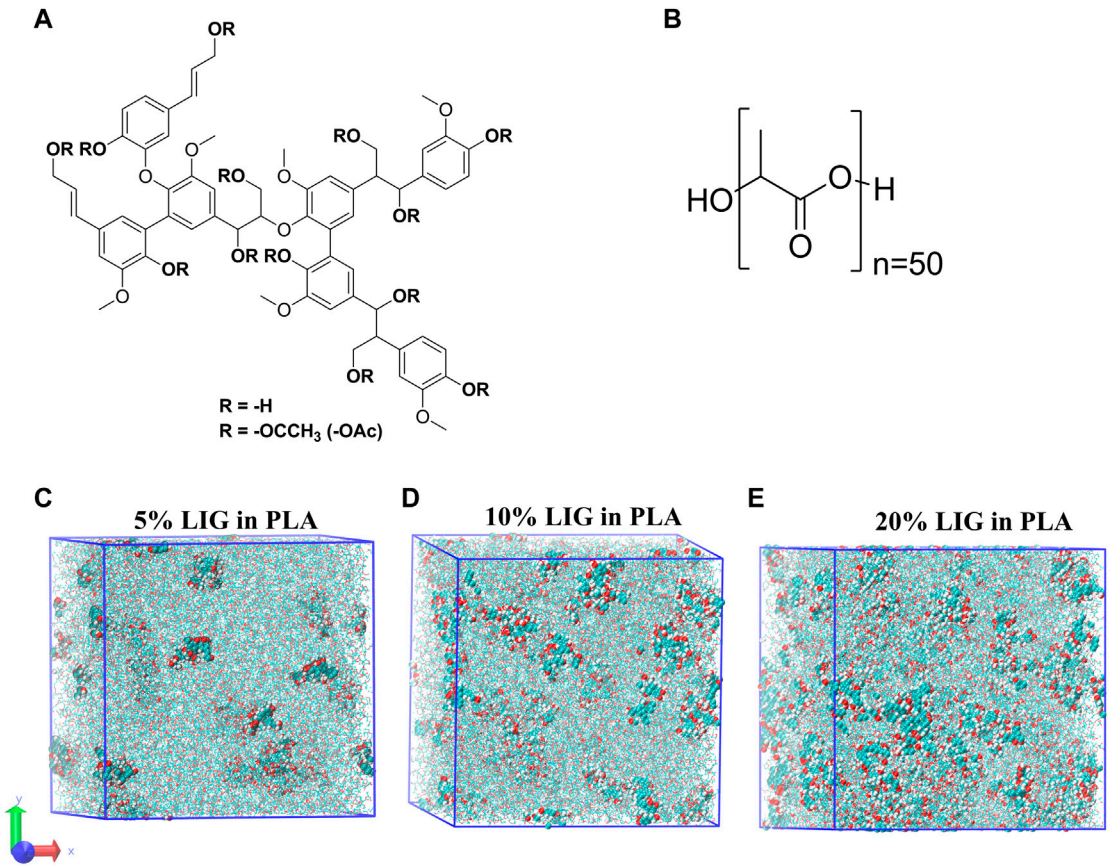

FIGURE 1
Molecular models used for MD calculations: **(A)** MD–Lignin model with acetyl (R = -OAc) substitution, **(B)** MD–PLA model with a degree of polymerization of 50, and **(C–E)** represent the equilibrated MD systems of lignin at 5%, 10% and 20% in PLA, respectively.

TABLE 1 The investigated systems containing the number of PLA, LIG, and aLIG with the corresponding composition, final density, and size of the simulation box (standard deviation in the parenthesis).

Systems	wt% of lignin	No. of lignin molecules	PLA	Final density (kg m^{-3})	Final box size (nm) x = y = z
PLA		0	255	1.178 (0.004)	10.9 (0.01)
LIG/PLA	5	42	255	1.181 (0.004)	11.1 (0.01)
	10	87	255	1.183 (0.003)	11.3 (0.01)
	20	198	255	1.188 (0.003)	11.7 (0.01)
aLIG/PLA	5	27	255	1.178 (0.003)	11.1 (0.01)
	10	58	255	1.179 (0.003)	11.3 (0.01)
	20	134	255	1.178 (0.002)	11.7 (0.01)

1,280 to 1,500 kg m^{-3}. While for the PLA case, the experimental density is about 1,240 kg m^{-3} (Bhasney et al., 2019). These simulated values are consistent with experimental values and indicate that the employed potential is sufficient to represent the models. All MD simulations in this study were performed with GPU-supported GROMACS version of 2022.2 (Van Der Spoel et al., 2005; Abraham et al., 2015).

Each system presented in Table 1 was prepared with a cubic box size range from 17 to 20 nm based on the number of lignin molecules. For instance, the large box size of 20 nm was used as a starting dimension for 20 wt% of lignin. After randomly placing the lignin molecule in the simulation box, a linear PLA polymer configuration with DP = 50 was packed and followed by minimizing the box using the steepest descent algorithm to ensure no unfavorable impacts in the system. Equilibration simulation was carried out at 298.15 K for 3 ns in order to relax the entire system into a more appropriate state. The present work considered the random distribution of polymers such as lignin and PLA. Therefore,

mixing the components toward attaining a highly mixed state was necessary to assure no void present in the simulation box. In such a case, a 3 ns run was performed at constant isotropic stress and temperature of 0.5 MPa and 600 K, respectively. The applied stress has been removed for the subsequent 3 ns run with 1 bar pressure at the same temperature of 600 K. After stress removal, there were two different simulations carried out, (i) cooling of the system from 600 K to 0 K to calculate glass transition temperature (T_g) by decreasing the temperature at 0.1 K/ps and (ii) a production NPT (constant number of particles, constant pressure, and constant temperature) run of 15 ns at 298.15 K with 1 bar pressure. All the simulations were performed at 1 fs timestep, and pressure and temperature coupling were applied at every 1.0 ps and 2.0 ps, respectively. The pressure was controlled by the Parrinello-Rahman method. After production run calculations, the simulations were further continued by applying deformation with respect to three axes separately. Figures 1E–G depicts the simulation systems after the production run from 5%, 10%, and 20% of lignin in the PLA matrix. All the examined systems were deformed at a constant strain rate of $5 \times 10^8\ s^{-1}$ with zero pressure and compressibility in a given axis under NPT conditions. The stress value of a system was calculated by averaging the stress value obtained from the x, y, and *z*-axis.

In this work, we have prepared PLA-matrix composites with softwood kraft lignin and its acetylated counterpart. The composite films prepared by solvent casting method were subjected to experimental characterization complemented with MD simulation studies. In the following, we first present the experimental results as a ground for reflecting the information obtained from the computational method.

3 Results

3.1 FT-IR

Since the fundamental approach in this work was to systematically compare softwood kraft lignin and corresponding acetylated lignin in PLA composites we decided to begin with validation of the conversion of the hydroxyl groups. The acetylation reaction of lignin was confirmed by FT-IR analysis and the spectra of unmodified lignin (LIG) and acetylated lignin (aLIG) are shown in Figure 2. We have mainly investigated the -OH stretching frequency peak observed for lignin at 3,450 cm^{-1} as it should diminish due to the acetylation. In the case of unmodified lignin, this particular peak exhibited a broad intensity whereas, after acetylation of lignin, it was almost flattened which indicated the substitution of hydroxyl groups of the lignin. Acetylated lignin showed the ester peak at 1,740 cm^{-1}, C-H bond stretching peak at 1,380 cm^{-1} and acetyl group stretching peak at 1,202 cm^{-1} which are assigned to the non-conjugated carbonyl bonds of acetylated lignin. Absorbance changes were related to the degree of acetylation by measuring the height of the -OH stretching band at 3,300 cm^{-1} and normalized with the height of the C-C of aromatic skeletal vibration at 1,510 cm^{-1} which was taken as a reference (Saralegi et al., 2013; Gordobil et al., 2015). Hydroxyl group conversion (α) was calculated from Eq. 1, which provides the acetylation reaction achieved a conversion rate of 92%.

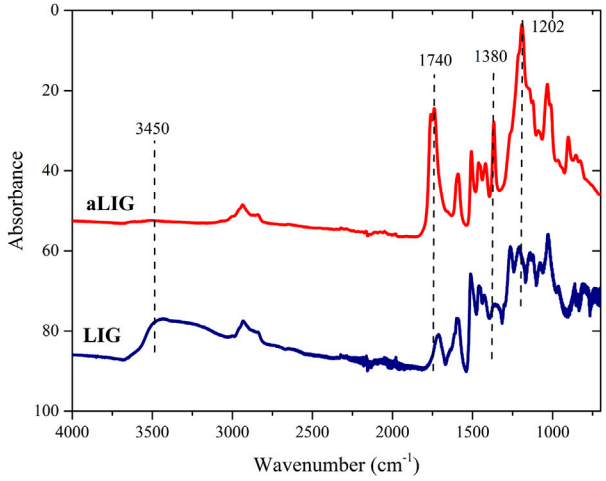

FIGURE 2
FT-IR spectra of crude Kraft lignin (LIG) and acetylated lignin (aLIG).

$$\alpha = 1 - \left[\frac{\left(\frac{H_{OH}}{H_{ref}}\right)_t}{\left(\frac{H_{OH}}{H_{ref}}\right)_0}\right] \times 100 \quad (1)$$

3.2 Mechanical properties

The presence of lignin in the PLA matrix can significantly alter its mechanical properties. We used tensile strength testing to obtain characteristic mechanical features of pristine PLA, LIG/PLA, and aLIG/PLA (Figure 3). In all the cases, pristine PLA showed better mechanical performance than the composites with lignin incorporated. It is interesting to see that the tensile strength and Young's modulus were drastically reduced upon the addition of LIG and aLIG in PLA. We repeated the analysis and obtained the same results. The processing method employed for composites preparation (i.e., casting method) and plasticization effect might cause such significant changes in the mechanical properties. Comparing the composites such as LIG/PLA and aLIG/PLA showed that aLIG/PLA exhibited improved mechanical properties in terms of Young's modulus and tensile strength. We hypothesize that the reason is that the unmodified lignin tends to aggregate in the dissolved PLA during the composite preparation, while acetylation reduces the aggregation effect and enhances the compatibility with the PLA. These findings are in line with prior observations by different authors (Gordobil et al., 2014; Kim et al., 2017).

3.3 Thermogravimetric analysis

In addition to mechanical properties, another essential property of PLA composites is their thermal behavior which determines usability in many practical applications. Thermogravimetric analysis was performed to study the effect of lignin on the thermal degradation characteristics of PLA in the nitrogen

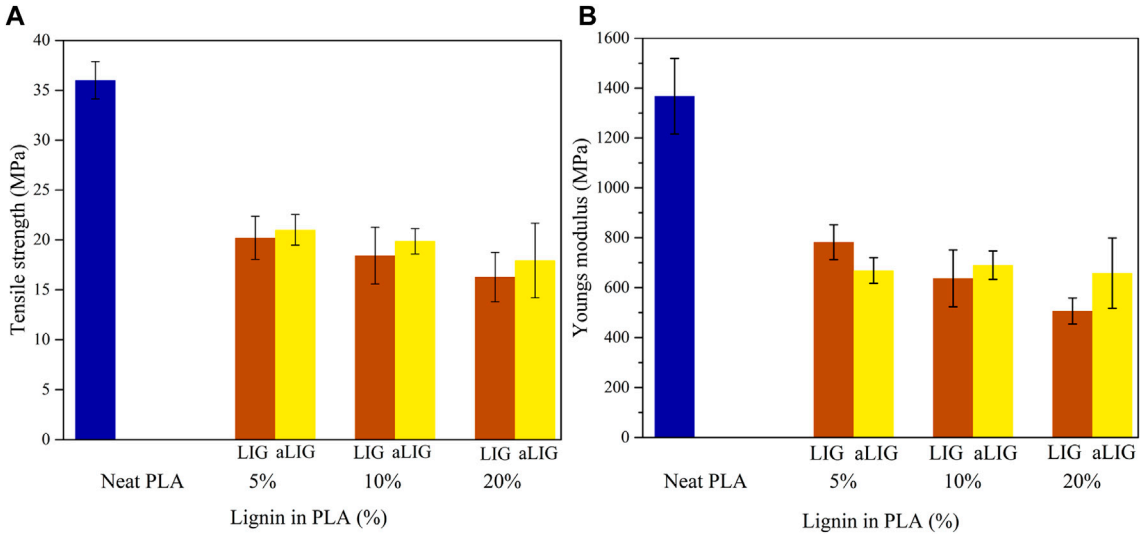

FIGURE 3
Mechanical properties of LIG/PLA and aLIG/PLA, **(A)** Tensile strength, and **(B)** Young's modulus.

atmosphere. Between 100°C and 150°C (Figure 4A), neat PLA lost around 5% of weight due to the residual amount of chloroform present from the casting process. Thermal degradation characteristics of neat PLA compared with the LIG/PLA and aLIG/PLA in Table 2. The results showed that increasing the weight proportion of kraft lignin systematically increased the thermal stability of the PLA composites. The 10% of LIG/PLA started to degrade at the higher temperature of 306°C compared to the neat PLA at around 293°C. There was a tradeoff between the thermal stability and lignin content of aLIG/PLA composites. At the lowest lignin content (5%), the thermal stability was up to 296°C while at the lignin content of 10% the thermal degradation onset temperature occurred earlier (270°C) than that of neat PLA (293°C). The results concluded that a lower weight percentage of derivatized lignin addition improved the thermal stability whereas, at a higher percentage, the possibility of lignin-lignin interaction was relatively high which results in a strong tendency to form aggregates. Therefore, it is crucial to understand the underlying reason behind the interaction between lignin-lignin and lignin-PLA in order to support the experimental findings and to further elucidate additional key properties. Such interaction mechanisms can be studied by a bottom-up approach, called computational modelling to investigate the materials at the atomic scale.

3.4 Differential scanning calorimetry (DSC) analysis

DSC analysis was carried out to investigate the thermal characteristics of pristine PLA, lignin-PLA (LIG/PLA), and acetylated lignin-PLA (aLIG/PLA) (5, 10, and 20%) films. The obtained results from first and heating scans are shown in Figures 4B, C, and the glass transition temperature (T_g) peak temperature (T_p), and melting peak (T_m) values are shown in Table 2. Kraft lignin showed a T_g value of 147.4°C, whereas acetylated lignin showed a T_g of 117.0°C. The difference in the T_g values of the underivatized and acetylated lignin could be due to the reason that unmodified lignin molecules are held together by strong intermolecular hydrogen bonding, van der Waals, and hydrophobic interactions, whereas the acetylation decreased the intermolecular forces between lignin molecules results in increased excluded volume and chain extension that would promote attractive interactions with PLA (Chung et al., 2013; Cachet et al., 2014; Gordobil et al., 2015).

Pure PLA cast films showed a T_g of 46.3°C and T_m of 148.5°C (Sharma et al., 2019), and the T_{cc} peak was absent with the addition of lignin and acetylated lignin, there was no significant change observed in T_g. At a higher percentage of lignin addition, the T_g value shifted to a lower temperature which is attributed to increased molecular mobility of the chain induced by the plasticizing effect of the lignin. The cooling crystallization behavior of PLA disappeared with the addition of lignin and acetylated lignin. Also, a reduction in the T_m value was observed due to the amorphous characteristics of the lignin. The T_g values of all films increased during the second heating scan, and there was no significant difference observed between the films. Similarly, the T_m values followed a similar trend, with the melting temperature increasing during the second heating scan. It is also noted that in the cases of increased composition of aLIG in PLA (10% and 20% cases), no Tm peak was observed. The absence of a melting peak during the second scan can indicate that acetylation may lead to increased miscibility with PLA, suppressing and affecting the crystallization behavior.

3.5 Morphology analysis of the composite films

Scanning electron microscopy (SEM) analysis provides the distribution of the lignin in the PLA polymer matrix and the tensile fractured LIG/PLA and aLIG/PLA specimens' surface was analyzed. Neat PLA and a higher weight percentage (10%) of LIG and aLIG incorporated PLA are shown in Figure 5. The neat PLA

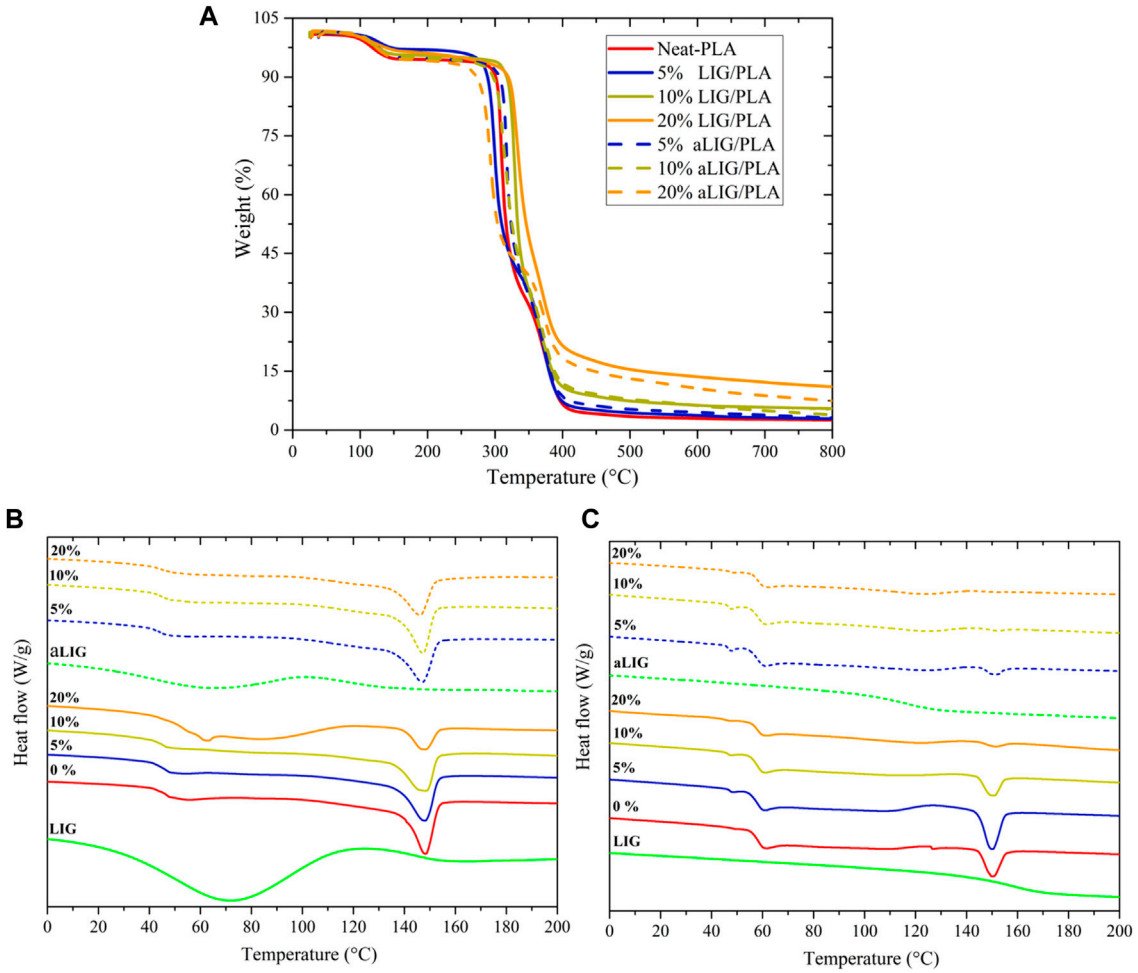

FIGURE 4
(A) Thermogravimetric curves of Neat PLA, LIG/PLA and aLIG/PLA, and **(B,C)** DSC scan curves of first heating and second heating scan: *Continuous lines*–PLA + *X* % of LIG and *Dashed lines*–PLA + *X* % of aLIG. (*X* is 5%, 10%, and 20%).

TABLE 2 Thermal (TGA) and DSC properties of neat PLA, LIG/PLA and aLIG/PLA composites. T_{max}–Maximum temperature from TGA, and T_g–glass transition temperature, and T_m–melting temperatures from the first heating and second heating scan.

	TGA		DSC—First scan		DSC—Second scan	
	T_{max} (°C)	Residue at 800 °C (%)	T_g (°C)	T_m (°C)	T_g (°C)	T_m (°C)
Neat PLA	323	2.8	46.3	148.5	58.0	150.1
5% LIG/PLA	304	2.9	45.1	148.3	57.2	150.1
10% LIG/PLA	326	5.5	44.9	148.7	57.3	150.4
20% LIG/PLA	338	11.0	43.5	148.0	57.4	151.2
5% aLIG/PLA	322	1.7	44.1	147.4	57.3	151.3
10% aLIG/PLA	311	3.9	46.6	147.4	57.1	-
20% aLIG/PLA	291	7.5	44.9	146.4	58.1	-

surface was found to be smoother compared to the lignin-incorporated specimen (Figure 5). With 10% LIG addition results showed that the formation of voids and indication of a rough surface influenced Young's modulus results. The tensile test results indicated that the addition of 10% of LIG in PLA decreased the tensile strength of the composite due to a lack of compatibility. On the other hand, the SEM image of 10% aLIG in PLA improved ductility (Figure 5). The small size particles of aLIG in the PLA acted

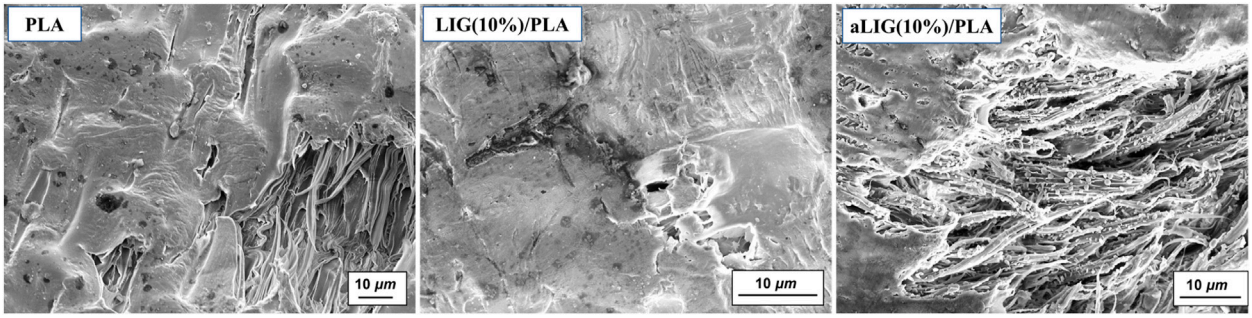

FIGURE 5
SEM micrographs of neat PLA, LIG/PLA (10%), and aLIG/PLA(10%).

as a plasticizer to hold together the PLA matrix and eventually improved the compatibility and enhanced the mechanical strength compared to unmodified lignin.

3.6 Molecular dynamics (MD) simulation results

3.6.1 The prediction of glass transition temperature (T_g)

The glass transition temperature (T_g) is an important thermal property of polymeric materials that describes the transition of amorphous polymer from the glassy state to the rubbery state. As such, the T_g also provides fundamental information on the thermal performance of the polymer system. T_g is usually calculated from the cooling stage, and thus we studied the cooling simulation from 600 to 0 K within 6 ns. During the simulation, the energy file was written every 1 ps and the density of PLA was calculated at each temperature. As shown in Figure 6A density values increase with decreasing temperature, and at a certain temperature value, the transition from a rubbery state to a glassy state (i.e., where T_g is calculated) can be seen. However, past research indicated that the T_g value could vary significantly concerning the density points from linear fitting. The authors performed T_g calculation for several compounds and obtained different T_g values for the same compounds by considering different fitting temperature points (Lin et al., 2021).

Nevertheless, the bulk of the literature points out that the T_g range can be calculated from the mean square displacement (MSD) calculations by performing additional MD simulations with different temperatures. With increasing temperature, the MSD gradually increases, but the MSD curve shifts drastically when the transition occurs in the system from a glassy state to a rubbery state due to the large motion of molecules in the rubbery state (Figure 6B). This is demonstrated by T_g which typically considered in the range between lower and higher temperature values. These MSD calculations greatly support the accurate prediction of the T_g range in the density calculation method. For instance, as shown in Figure 6B in the case of 5% LIG/PLA, the MSD values increase significantly from 350 to 360 K which indicates the range of glass transition temperature, T_g, and finally, the fitted density values show a final T_g value, around 359.61 K from Figure 6A. The fitted T_g values associated to pure PLA, LIG/PLA and aLIG/PLA composites using these two methods (density fitting and MSD calculation), are presented in Table 3.

From Table 3, the T_g value for pure PLA was found to be 359.5 K (~86.4°C) and the addition of 5% LIG in the PLA matrix increases the T_g temperature of the composites. Nevertheless, the incorporation of 5% aLIG (acetylated) in the PLA matrix lowers the T_g value. The decreasing T_g value for aLIG/PLA composites indicated that the esterification reaction (acetylation) on the hydroxyl group substitution significantly reduces the hydrogen bonds and agglomeration, and leads to a lower T_g value compared to LIG/PLA. Increasing the wt% of both LIG and aLIG with PLA enhances the T_g, of which 10% of aLIG almost exhibits a similar value to the T_g value of PLA. Finally, 20% of both modified and unmodified lignin showed higher T_g values. It should be noted that the calculated T_g values of all systems in Table 3 are overestimated compared to experimental values presented in Table 2. As the T_g is not a true first-order phase transition, this discrepancy cannot be ruled out due to different cooling conditions applied during experiments. Furthermore, a recent prediction from Lin et al., proposed T_g values for various amorphous systems and the obtained T_g value exhibited an error value of around 20.5°C. Therefore, considering the predicted value of pure PLA is 359.5 K (86.4°C) which is consistent with the values obtained from our experimental value of 46.29°C and literature values of around 60°C by taking into account with the error, around 20.5°C (Kim et al., 2017; Esakkimuthu et al., 2022a). Moreover, the trend observed from the simulation for all T_g values associated with the different wt% can be correlated directly to the experiments.

3.6.2 Fractional free volume

The fractional free volume (FFV) defines the intermolecular space dispersed in the system, like in the form of an empty area or hole to enable the molecules' motion. The FFV is normally calculated from the relation of occupied volume V_0 and free volume V_f, and therefore, FFV = $V_f/(V_0 + V_f)$. The FFV is calculated by inserting a probe radius of 0 nm and the determined FFV is known as true free volume. The obtained FFV results shown in Figure 7A indicated that all LIG/PLA composites exhibited lower FFV than compared corresponding aLIG/PLA systems. The inclusion of an acetyl side chain in the hydroxyl group is expected to increase the distance between PLA and acetylated lignin polymers. The higher content of LIG (20%) in

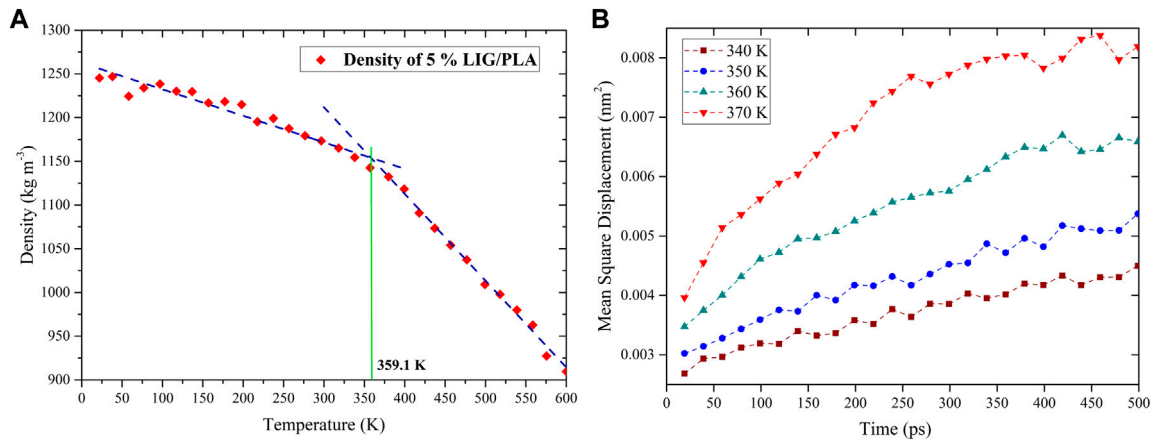

FIGURE 6
T_g calculation from, **(A)** linear fitting of the density-temperature curve, and **(B)** mean-square displacement simulation with different temperatures.

TABLE 3 The glass transition temperature of polymer composites was obtained from the density fitting method and mean square displacement method.

	T_g by density fitting method (K)	T_g by MSD curve method (K)
Pure PLA	359.5	350–360
5% LIG/PLA	359.1	350–360
10% LIG/PLA	358.1	350–360
20% LIG/PLA	365.8	360–370
5% aLIG/PLA	350.5	340–350
10% aLIG/PLA	352.2	340–350
20% aLIG/PLA	364.3	350–360

PLA presented the lowest FFV, which indicated that the motion of PLA is majorly restricted due to hydroxyl groups present in LIG polymer.

3.6.3 Mechanical properties: Young's modulus

Young's modulus is used to account for the elastic mechanical properties of LIG/PLA and aLIG/PLA composites. As described in the method section, a constant strain rate of 5×10^8 s^{-1} was applied in the model system and we performed an elongation up to 20% of the original length, in which an initial 4% of strain was taken into account to determine Young's modulus. The calculated Young's modulus values correspond to the average of three axes (x, y and z) due to the fact of heterogeneity of composites. The average Young's modulus was calculated, and the results are shown in Figure 7B. The addition of low wt% (5%) of LIG and aLIG in the PLA matrix resulted in a similar Young's modulus as for neat PLA, and increasing the wt% of both LIG and aLIG increases the modulus values. The Young's modulus obtained from MD simulations was overestimated, about 41.1% for PLA than experimental values (shown in Figure 3B). Various reasons can be associated with such a difference, including the strain rate applied in MD, the polymer chain lengths considered for the MD study and the composite processing techniques used for PLA synthesis. On the other hand, the MD method precited Young's modulus for LIG/PLA and aLIG/PLA composites showed almost three times higher than the values obtained from experiments. The mechanical properties calculation with the MD method indicated that the incorporation of lignin or acetylated lignin showed a minor impact on Young's modulus, while experimental data presented in Figure 3, showed a clear difference between various composites.

3.6.4 Interaction energy

A short-range interaction between lignin and PLA polymers was calculated to quantify the binding interaction by taking van der Waals interaction (Lennard-Jones: LJ) and coulomb interaction energy terms. These energy values were averaged with respect to one lignin (LIG and aLIG) to compare both systems. The obtained results shown in Figure 8 revealed that the total interaction energy of aLIG exceeded that of unmodified lignin (LIG). However, it is interesting to see that Lennard-Jones short range interaction energies were higher in the case of aLIG/PLA contributing to the elevated total interaction energies of acetylated lignins with PLA. On the other hand, Coulomb energy was more dominant in the case of LIG/PLA than aLIG/PLA. It is indicated that the hydroxyl groups present in LIG majorly increases the binding with PLA polymer, which significantly decreases upon modifying the hydroxyl groups with acetylation.

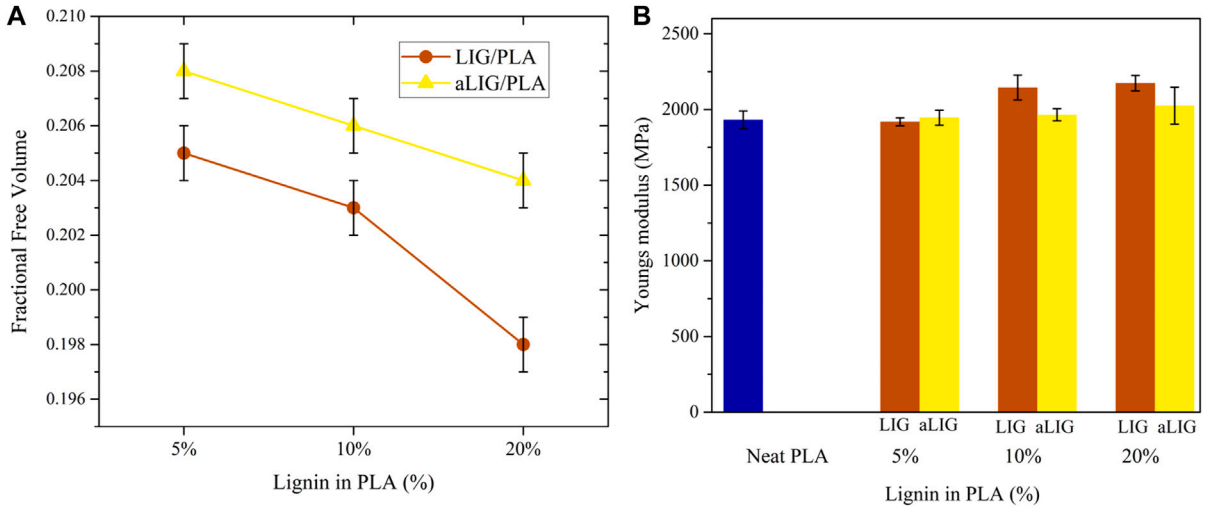

FIGURE 7
(A) The fractional free volume (FFV) of LIG/PLA and aLIG/PLA, and **(B)** The Youngs modulus values of LIG/PLA and aLIG/PLA based composites with different weight %.

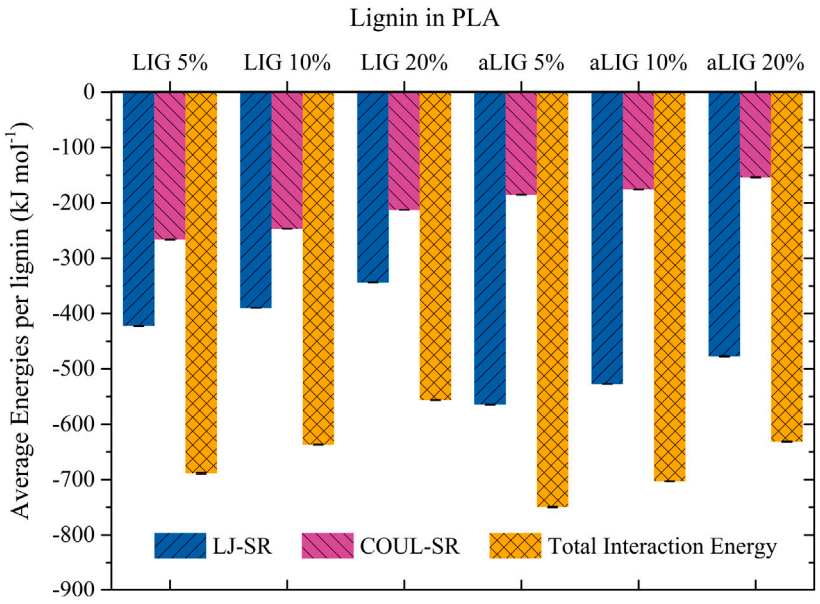

FIGURE 8
The Lennard-Jones (van der Waals) energy, Coulombic energy, and total interaction energies of LIG and aLIG with PLA at different compositions.

3.6.5 Hydrogen bond analysis

The average number of hydrogen bonds between LIG/PLA and aLIG/PLA was calculated by considering the criteria of the cut-off distance of 3.5 Å and an angle of 30°, and the results are presented in Figure 9. In the case of LIG/PLA systems, the average number of H-bonds was significantly higher compared to aLIG/PLA systems which is due to the fact that aLIG composites contain only the carboxylic acids as donor groups. In contrast, the abundant hydroxyl groups present in the unmodified LIG molecules possess both donor (-H) and acceptor (-O). Therefore, LIG tends to form a higher number of hydrogen bonds, with PLA and acetylation, markedly reduces the possibility of hydrogen bonding with PLA. At higher lignin content the number of hydrogen bonds in both LIG/PLA and aLIG/PLA decreases as the combination of LIG-LIG and aLIG-aLIG increases other intermolecular interactions at the cost of hydrogen bonding. The distance associated with the hydrogen bond formation was evaluated, and the distance distribution is shown in Figure 9B. The acetyl groups in aLIG tend to make a shorter hydrogen bond (about 0.268 nm or 2.68 Å) than LIG/PLA composites, about 0.28 nm or 2.8 Å, which may be due to the acetylation reduced ionic repulsion between the lignin molecules the lignin polymer.

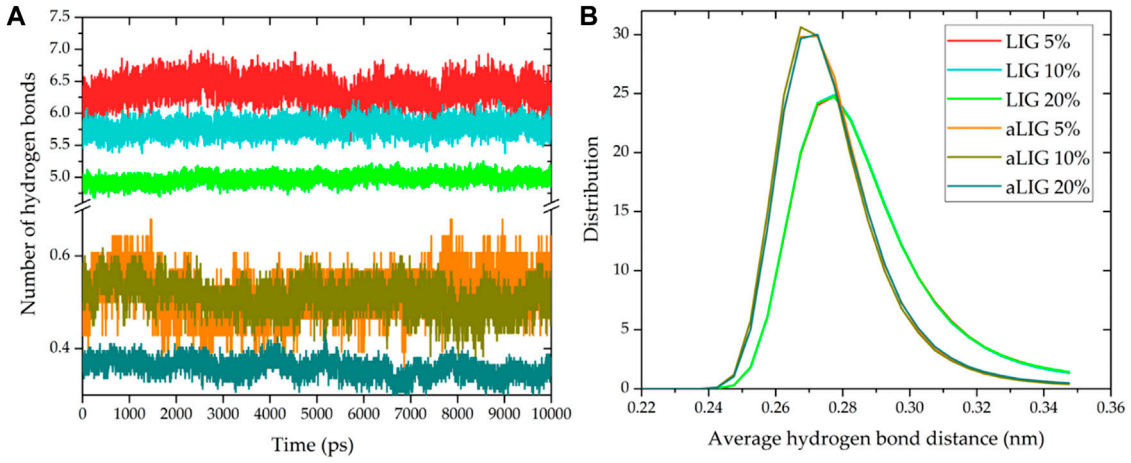

FIGURE 9
Hydrogen bonding characteristics of LIG/PLA and aLIG/PLA systems, **(A)** the average number of hydrogen bonds **(B)** the distance distribution of hydrogen bond formation.

3.6.6 Radial distribution function

The radial distribution function (RDF) provides a detailed insight into understanding the molecular arrangements of atoms or molecules in the system. The RDFs of LIG/PLA and aLIG/PLA were calculated and shown in Figure 10. As seen in Figure 10, the typical distance between oxygen in unmodified lignin (LIG) and hydrogen attached to oxygen in PLA was found to be 1.9 Å. The g(r) distribution decreased at higher content of LIG in PLA due to the increasing contacts of LIG-LIG that dominated over those of LIG-PLA. Similarly, the average distance of the center of mass of aromatic rings (Ar) with carbonyl oxygen (O=C) and methyl group (CH_3) in PLA was calculated, and the results showed that Ar-O_C exhibited a shorter distance than Ar-CH_3, due to the fact of strong interaction of polar groups (O=C) than non-polar group (CH_3). In the case of aLIG/PLA (Figures 10C, D), the calculated distance distribution between the carbonyl oxygen from the acetyl group in lignin and the hydroxyl group in PLA exhibited a similar distance, about 1.8 Å in all examined weight percentages. This correlation indicated that acetylation of lignin not only increases the chain length but also reduces the distance of interaction with hydroxyl groups in PLA compared to the case of LIG/PLA, thereby enhancing compatibility. The distance between the aromatic ring and carbonyl oxygen in PLA averaged 3.6 Å. In the case of aromatic ring–methyl group, the average distance was 4.2 Å. Changing the weight % in aLIG/PLA was found to have a minimal effect on the hydrogen bonding distance.

4 Discussion

Our combined experimental characterization and computational modelling results have provided new insights into the compatibility of lignin in polylactic acid composites. The the experimental results indicated that acetylation may enhance the plasticity and motion of acetylated lignin in PLA, which moderately decreases the glass transition temperature.

Molecular dynamics (MD) simulations overestimated the glass transition temperatures and Young's moduli for all systems studied due to their sensitivity to various parameters and fitting methods employed. In contrast to the modelling results, indicating no marked changes in Youngs's moduli, our experimental results showed that the addition of lignin or acetylated lignin to PLA leads to a drastic decrement in Young's moduli of the composites.

We obtained a Young's modulus value of 1,400 MPa for PLA, which is lower than our previously proposed value of approximately 2,100 MPa (Esakkimuthu et al., 2022a). It has been noted that the mechanical properties of composites are significantly influenced by the processing methods employed during fabrication. In this study, the solvent casting method was used, which tends to result in lower tensile strength and Young's moduli compared to other methods such as extrusion molding, injection molding, and compression molding (Raj et al., 2021). Surprisingly, both the tensile strength and Young's moduli values of the composites decreased to one half of those of PLA, contradicting values reported in the literature (Kim et al., 2017). This drastic change could be attributed to the plasticization effect and inferior compatibility of lignin and its counterpart with PLA. We observed a lower Tg (46.3°C) value in the present study compared to our previously reported value of 60.3°C (Esakkimuthu et al., 2022a). The differences in thermal properties between the neat PLA and LIG/PLA composite obtained in current study by solvent casting method could be attributed to several factors, including, (i) process method, in which extrusion method is conducted at high-temperature and high shear conditions, (ii) orientation of polymer chains in the composites, in which solvent casting exhibited lower degree of molecular orientation than extrusion, and (iii) Solvent casting, being a milder process, might preserve the chemical structure better than extrusion method which may induce higher possible chemical interactions or reactions. However, our results for the predicted glass transition temperatures of both LIG/PLA and aLIG/PLA are consistent and show a similar trend compared to earlier results (Kim et al., 2017). It should be noted that incorporating a higher weight percentage of lignin (40%) in PLA resulted in increased brittleness, making it impractical to consider the corresponding mechanical properties in this study.

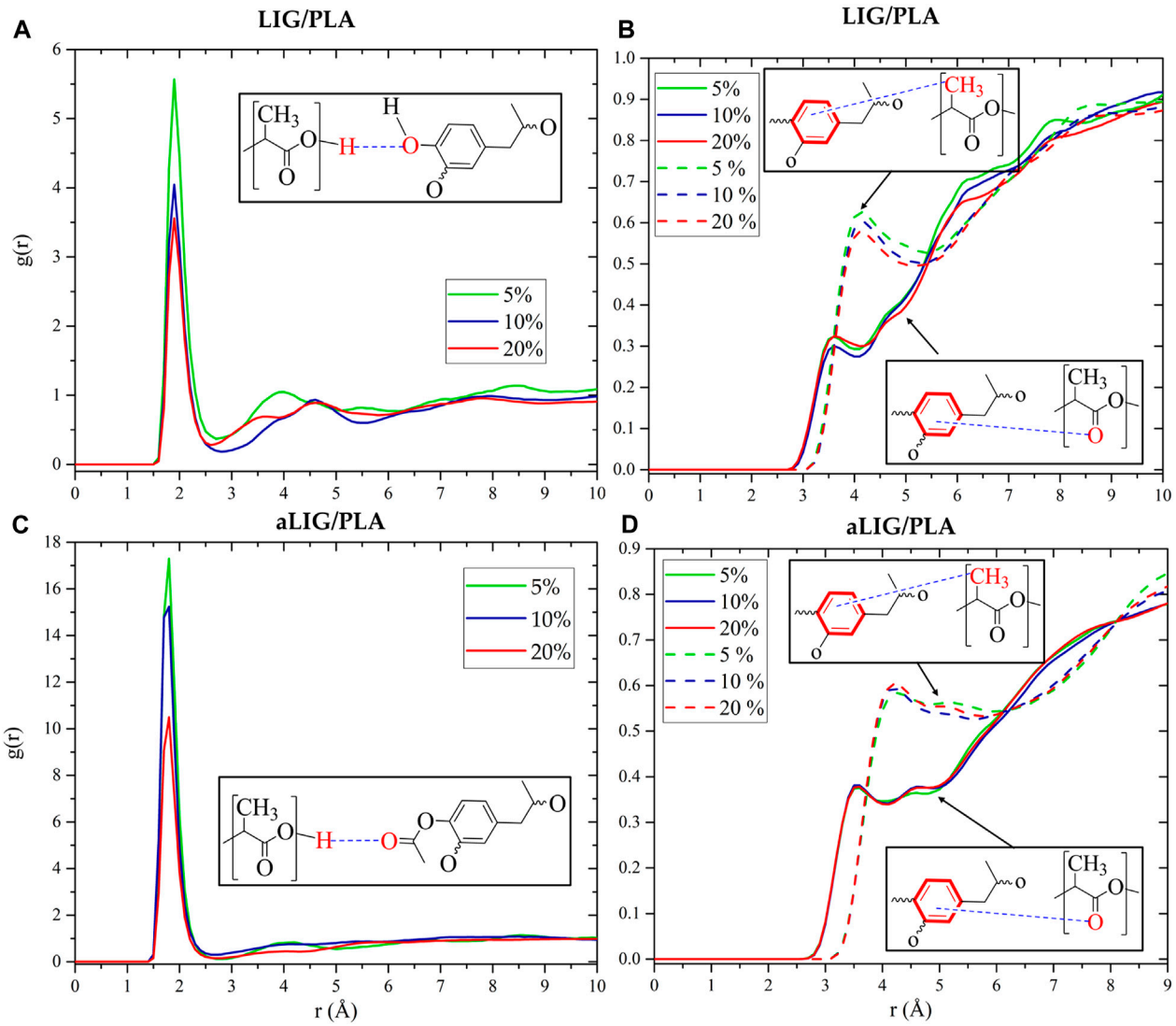

FIGURE 10
Radial distribution function between different atoms in LIG/PLA **(A,B)** systems, and aLIG/PLA **(C,D)** systems.

It is essential to highlight additional properties wherein acetylated lignin demonstrates notable enhancements, including improved water permeability, surface wettability, and water solubility. As reported by Kim et al. (2017), the combination of acetylated lignin with PLA exhibited a lower water vapor transmission rate compared to unmodified lignin. Similarly, Johansson et al. (2023) observed a significant delay in moisture absorbance for acetylated lignin over 28 days, and Kim et al. (2023) noted the maintenance of contact angles from water droplet experiments. The acetylation reaction primarily blocks hydroxyl groups in lignin, increasing hydrophobicity and consequently reducing lignin's interaction with water.

MD simulations conducted at the bulk scale revealed that aLIG/PLA-based composites exhibited a larger free volume compared to LIG/PLA, indicating that the increased side chains in lignin enhance plasticity. Similarly, interaction energy calculations demonstrated that electrostatic interactions played a significant role in LIG, likely due to the presence of hydroxyl groups, while such interactions were lower in aLIG/PLA systems. The modification of lignin with acetylation led to a significant reduction in the number of hydrogen bonds, which may explain the decreased aggregation of modified lignin compared to unmodified lignin. Therefore, the comprehensive analyses including the hydrogen bonding, interaction energy and free volume prediction by MD elucidated the underlying origin of intermolecular forces within the composite system. The results associated to MD are in good agreement with the experimental results of this work.

It is noted that the Young's modulus obtained from the MD simulations aligns with previous literature results where composites were prepared using the extrusion method (Gordobil et al., 2014; Esakkimuthu et al., 2022a). There are disparities between the mechanical properties obtained from MD simulations and experimental values in the present study. Such differences can be attributed to several factors, such as: (i) MD simulations operate at

the molecular scale and on nanosecond timescales; in contrast, experimental testing measures macroscopic properties over longer durations, (ii) MD simulations depend on the reliability of force fields and parameters used. The limitations in predicting dynamic and complex behaviors, especially arising from structurally heterogeneous lignin molecules, contribute to differences between simulated and experimental outcomes, (iii) experiments consider various external factors that might not be fully accounted for in simulations, such as impurities, processing conditions, and structural variations, and (iv) aggregations in polymer composites may occur on longer time scales, posing challenges in capturing them within the simulation timeframe. However, it is important to acknowledge that no aggregation was observed during the MD simulations, as the lignin molecules were randomly distributed within the PLA matrix. In contrast, experimental processes may exhibit apparent aggregation. Furthermore, the present MD simulation focused on investigating the interfacial interactions between lignin and PLA, as they predominantly influence the properties of the composites.

5 Conclusion

Intermolecular interactions play a vital role in lignin-lignin and lignin-PLA systems, and understanding these interactions is crucial for utilizing composites in various value-added applications, including packaging. Therefore, this study employed a combined approach of experimental and computational modeling to elucidate the fundamental properties of lignin/PLA composites. Solvent-casted lignin/PLA and acetylated lignin/PLA composites with different weight percentages of lignin (5%, 10%, and 20%) were investigated. Mechanical characterization revealed that acetylation of lignin improved both the tensile strength and Young's modulus of the corresponding composites. The glass transition temperature of the composites moderately decreased with 5% and 10% weight fraction of acetylated lignin, whereas no significant effect was observed with the unmodified lignin at similar lignin contents. To investigate the underlying reasons for these differences, computational modeling methods such as molecular dynamics (MD) were employed and compared with experimental results. The MD results indicated that acetylation of lignin decreases the T_g and Young's modulus of aLIG/PLA compared to LIG/PLA. However, the obtained MD results for T_g and Young's modulus of pure PLA, LIG/PLA, and aLIG/PLA were found to be overestimated compared to experimental findings. The interaction energy results showed that aLIG exhibited higher van der Waals forces and lower Columbic interaction with PLA compared to unmodified lignin. Additionally, a higher fractional free volume was observed for aLIG. One possible reason is that acetylated lignin significantly reduces the number of hydrogen bonds, which are central to understanding the aggregation of lignin in the PLA matrix. Overall, this combined study involving experiments and computational modeling provided new insights into the compatibility of lignin with PLA, which can be further enhanced by tailoring modifications for PLA-based composite materials. However, further studies are suggested to evaluate the contribution of hydrophobic interactions to the total energy of interaction between esterified lignin and PLA.

Data availability statement

The raw data supporting the conclusions of this article will be made available by the authors, without undue reservation.

Author contributions

EE: Conceptualization, Data curation, Formal Analysis, Funding acquisition, Methodology, Resources, Validation, Writing–original draft. VP: Conceptualization, Data curation, Formal Analysis, Methodology, Resources, Software, Validation, Visualization, Writing–original draft. MS: Supervision, Writing–review and editing. DV: Supervision, Writing–review and editing.

Funding

The author(s) declare financial support was received for the research, authorship, and/or publication of this article. The authors gratefully acknowledge the European Commission for funding the InnoRenew project [H2020 WIDESPREAD-2-Teaming grant number 739574] and the Republic of Slovenia [investment funding from the Republic of Slovenia and the European Regional Development Fund]. EE acknowledges Horizon 2020, the EU Framework Programme for Research and Innovation [Marie Sklodowska-Curie Actions grant number 101031402]. MS acknowledges Swedish Foundation for Strategic Research (SSF) for financial support (grant number FFL21-006).

Acknowledgments

Part of molecular dynamics calculations were performed with high-performance computing and VP acknowledges the HPC RIVR consortium (www.hpc-rivr.si) and EuroHPC JU (eurohpc-ju.europa.eu) for funding this research by providing computing resources of the HPC system Vega at the Institute of Information Science (www.izum.si).

Conflict of interest

The authors declare that the research was conducted in the absence of any commercial or financial relationships that could be construed as a potential conflict of interest.

Publisher's note

References

Abraham, M. J., Murtola, T., Schulz, R., Páll, S., Smith, J. C., Hess, B., et al. (2015). GROMACS: high performance molecular simulations through multi-level parallelism from laptops to supercomputers. *SoftwareX* 1 (2), 19–25. doi:10.1016/j.softx.2015.06.001

Bhasney, S. M., Bhagabati, P., Kumar, A., and Katiyar, V. (2019). Morphology and crystalline characteristics of polylactic acid [PLA]/linear low density polyethylene [LLDPE]/microcrystalline cellulose [MCC] fiber composite. *Compos. Sci. Technol.* 171, 54–61. doi:10.1016/j.compscitech.2018.11.028

Cachet, N., Camy, S., Benjelloun-Mlayah, B., Condoret, J.-S., and Delmas, M. (2014). Esterification of organosolv lignin under supercritical conditions. *Industrial Crops Prod.* 58, 287–297. doi:10.1016/j.indcrop.2014.03.039

Cai, J., He, Y., Yu, X., Banks, S. W., Yang, Y., Zhang, X., et al. (2017). Review of physicochemical properties and analytical characterization of lignocellulosic biomass. *Renew. Sustain. Energy Rev.* 76, 309–322. doi:10.1016/j.rser.2017.03.072

Chung, Y.-L., Olsson, J. V., Li, R. J., Frank, C. W., Waymouth, R. M., Billington, S. L., et al. (2013). A renewable lignin–lactide copolymer and application in biobased composites. *ACS Sustain. Chem. Eng.* 1, 1231–1238. doi:10.1021/sc4000835

Cotterill, J. V., Wilkins, R. M., and da Silva, F. T. (1996). Controlled release of diuron from granules based on a lignin matrix system. *J. Control. Release* 40, 133–142. doi:10.1016/0168-3659(95)00188-3

Črešnar, K. P., Klonos, P. A., Zamboulis, A., Terzopoulou, Z., Xanthopoulou, E., Papadopoulos, L., et al. (2021). Structure-Properties relationships in renewable composites based on polylactide filled with Tannin and Kraft Lignin - crystallization and molecular mobility. *Thermochim. Acta* 703, 178998. doi:10.1016/j.tca.2021.178998

Daassi, R., Durand, K., Rodrigue, D., and Stevanovic, T. (2023). Optimization of the electrospray process to produce lignin nanoparticles for PLA-based food packaging. *Polymers* 15, 2973. doi:10.3390/polym15132973

Dubey, S. P., Thakur, V. K., Krishnaswamy, S., Abhyankar, H. A., Marchante, V., and Brighton, J. L. (2017). Progress in environmental-friendly polymer nanocomposite material from PLA: synthesis, processing and applications. *Vacuum* 146, 655–663. doi:10.1016/j.vacuum.2017.07.009

Duval, A., and Lawoko, M. (2014). A review on lignin-based polymeric, micro- and nano-structured materials. *React. Funct. Polym.* 85, 78–96. doi:10.1016/j.reactfunctpolym.2014.09.017

Ehrnrooth, E. M. L. (1984). Change in pulp fibre density with acid-chlorite delignification. *J. Wood Chem. Technol.* 4, 91–109. doi:10.1080/02773818408062285

Esakkimuthu, E. S., DeVallance, D., Pylypchuk, I., Moreno, A., and Sipponen, M. H. (2022a). Multifunctional lignin-poly (lactic acid) biocomposites for packaging applications. *Front. Bioeng. Biotechnol.* 10, 1025076. doi:10.3389/fbioe.2022.1025076

Esakkimuthu, E. S., Marlin, N., Brochier-Salon, M.-C., and Mortha, G. (2022b). Application of a universal calibration method for true molar mass determination of fluoro-derivatized technical lignins by size-exclusion chromatography. *AppliedChem* 2, 30–47. doi:10.3390/appliedchem2010002

Farazin, A., and Mohammadimehr, M. (2022). Effect of different parameters on the tensile properties of printed Polylactic acid samples by FDM: experimental design tested with MDs simulation. *Int. J. Adv. Manuf. Technol.* 118, 103–118. doi:10.1007/s00170-021-07330-w

Garlotta, D. (2001). A literature review of poly(lactic acid). *J. Polym. Environ.* 9, 63–84. doi:10.1023/A:1020200822435

Gordobil, O., Delucis, R., Egüés, I., and Labidi, J. (2015). Kraft lignin as filler in PLA to improve ductility and thermal properties. *Industrial Crops Prod.* 72, 46–53. doi:10.1016/j.indcrop.2015.01.055

Gordobil, O., Egüés, I., Llano-Ponte, R., and Labidi, J. (2014). Physicochemical properties of PLA lignin blends. *Polym. Degrad. Stab.* 108, 330–338. doi:10.1016/j.polymdegradstab.2014.01.002

Hararak, B., Winotapun, C., Inyai, J., Wannid, P., and Prahsarn, C. (2021). Production of UV-shielded spherical lignin particles as multifunctional bio-additives for polyvinyl alcohol composite films. *J. Nanopart Res.* 23, 193. doi:10.1007/s11051-021-05308-z

Hasheminejad, K., and Montazeri, A. (2020). Enhanced interfacial characteristics in PLA/graphene composites through numerically-designed interface treatment. *Appl. Surf. Sci.* 502, 144150. doi:10.1016/j.apsusc.2019.144150

Jem, K. J., and Tan, B. (2020). The development and challenges of poly (lactic acid) and poly (glycolic acid). *Adv. Industrial Eng. Polym. Res.* 3, 60–70. doi:10.1016/j.aiepr.2020.01.002

Johansson, M., Skrifvars, M., Kadi, N., and Dhakal, H. N. (2023). Effect of lignin acetylation on the mechanical properties of lignin-poly-lactic acid biocomposites for advanced applications. *Industrial Crops Prod.* 202, 117049. doi:10.1016/j.indcrop.2023.117049

Kim, J., Bang, J., Park, S., Jung, M., Jung, S., Yun, H., et al. (2023). Enhanced barrier properties of biodegradable PBAT/acetylated lignin films. *Sustain. Mater. Technol.* 37, e00686. doi:10.1016/j.susmat.2023.e00686

Kim, Y., Suhr, J., Seo, H.-W., Sun, H., Kim, S., Park, I.-K., et al. (2017). All biomass and UV protective composite composed of compatibilized lignin and poly (Lactic-acid). *Sci. Rep.* 7, 43596. doi:10.1038/srep43596

Li, J., Wang, M., She, D., and Zhao, Y. (2017). Structural functionalization of industrial softwood kraft lignin for simple dip-coating of urea as highly efficient nitrogen fertilizer. *Industrial Crops Prod.* 109, 255–265. doi:10.1016/j.indcrop.2017.08.011

Lim, L.-T., Auras, R., and Rubino, M. (2008). Processing technologies for poly(lactic acid). *Prog. Polym. Sci.* 33, 820–852. doi:10.1016/j.progpolymsci.2008.05.004

Lin, K.-H., Paterson, L., May, F., and Andrienko, D. (2021). Glass transition temperature prediction of disordered molecular solids. *npj Comput. Mater* 7, 179–187. doi:10.1038/s41524-021-00647-w

Makri, S. P., Xanthopoulou, E., Klonos, P. A., Grigoropoulos, A., Kyritsis, A., Tsachouridis, K., et al. (2022). Effect of micro- and nano-lignin on the thermal, mechanical, and antioxidant properties of biobased PLA–lignin composite films. *Polymers* 14, 5274. doi:10.3390/polym14235274

Masutani, K., and Kimura, Y. (2014). *Chapter 1 PLA synthesis. From the monomer to the polymer*. United Kingdom: Royal Society of Chemistry, 1–36. doi:10.1039/9781782624806-00001

Michelsen, F. A., and Foss, B. A. (1996). A comprehensive mechanistic model of a continuous Kamyr digester. *Appl. Math. Model.* 20, 523–533. doi:10.1016/0307-904X(95)00171-F

Park, S. Y., Kim, J.-Y., Youn, H. J., and Choi, J. W. (2019). Utilization of lignin fractions in UV resistant lignin-PLA biocomposites via lignin-lactide grafting. *Int. J. Biol. Macromol.* 138, 1029–1034. doi:10.1016/j.ijbiomac.2019.07.157

Raj, S. S., Kannan, T. K., Kathiresan, M., Balachandar, K., and Krishnakumar, S. (2021). Why not stir casting for polymer composites? Investigations on poly lactic acid based wood plastic composite. *Mater. Today Proc.* 45, 862–868. doi:10.1016/j.matpr.2020.02.926

Rasal, R. M., Janorkar, A. V., and Hirt, D. E. (2010). Poly(lactic acid) modifications. *Prog. Polym. Sci.* 35, 338–356. doi:10.1016/j.progpolymsci.2009.12.003

Ratshoshi, B. K., Farzad, S., and Görgens, J. F. (2021). Techno-economic assessment of polylactic acid and polybutylene succinate production in an integrated sugarcane biorefinery. *Biofuels, Bioprod. Biorefining* 15, 1871–1887. doi:10.1002/bbb.2287

Ren, Z., Guo, R., Zhou, X., Bi, H., Jia, X., Xu, M., et al. (2021). Effect of amorphous cellulose on the deformation behavior of cellulose composites: molecular dynamics simulation. *RSC Adv.* 11, 19967–19977. doi:10.1039/D1RA02625A

Ren, Z., Sun, H., Zhou, X., Chi, X., Bi, H., Ji, T., et al. (2023). Insights from molecular dynamics simulations for interfacial effects between polylactic acid and wood cell wall constituents. *Compos. Part A Appl. Sci. Manuf.* 164, 107310. doi:10.1016/j.compositesa.2022.107310

Rukmanikrishnan, B., Ramalingam, S., Rajasekharan, S. K., Lee, J., and Lee, J. (2020). Binary and ternary sustainable composites of gellan gum, hydroxyethyl cellulose and lignin for food packaging applications: biocompatibility, antioxidant activity, UV and water barrier properties. *Int. J. Biol. Macromol.* 153, 55–62. doi:10.1016/j.ijbiomac.2020.03.016

Sakai, H., Kuroda, K., Muroyama, S., Tsukegi, T., Kakuchi, R., Takada, K., et al. (2018). Alkylated alkali lignin for compatibilizing agents of carbon fiber-reinforced plastics with polypropylene. *Polym. J.* 50, 281–284. doi:10.1038/s41428-017-0009-3

Saralegi, A., Rueda, L., Fernández-d'Arlas, B., Mondragon, I., Eceiza, A., and Corcuera, M. A. (2013). Thermoplastic polyurethanes from renewable resources: effect of soft segment chemical structure and molecular weight on morphology and final properties. *Polym. Int.* 62, 106–115. doi:10.1002/pi.4330

Schoenherr, S., Ebrahimi, M., and Czermak, P. (2017). *Lignin degradation processes and the purification of valuable products*. IntechOpen. doi:10.5772/intechopen.71210

Shankar, S., Reddy, J. P., and Rhim, J.-W. (2015). Effect of lignin on water vapor barrier, mechanical, and structural properties of agar/lignin composite films. *Int. J. Biol. Macromol.* 81, 267–273. doi:10.1016/j.ijbiomac.2015.08.015

Sharma, S., Singh, A. A., Majumdar, A., and Butola, B. S. (2019). Tailoring the mechanical and thermal properties of polylactic acid-based bionanocomposite films using halloysite nanotubes and polyethylene glycol by solvent casting process. *J. Mater Sci.* 54, 8971–8983. doi:10.1007/s10853-019-03521-9

Thakur, V. K., Thakur, M. K., Raghavan, P., and Kessler, M. R. (2014). Progress in green polymer composites from lignin for multifunctional applications: a review. *ACS Sustain. Chem. Eng.* 2, 1072–1092. doi:10.1021/sc500087z

Upton, B. M., and Kasko, A. M. (2016). Strategies for the conversion of lignin to high-value polymeric materials: review and perspective. *Chem. Rev.* 116, 2275–2306. doi:10.1021/acs.chemrev.5b00345

van den Oever, M., Molenveld, K., van der Zee, M., and Bos, H. (2017). *Bio-based and biodegradable plastics: facts and figures: focus on food packaging in The Netherlands*. Netherlands: Wageningen Food and Biobased Research. doi:10.18174/408350

Van Der Spoel, D., Lindahl, E., Hess, B., Groenhof, G., Mark, A. E., and Berendsen, H. J. C. (2005). GROMACS: fast, flexible, and free. *J. Comput. Chem.* 26, 1701–1718. doi:10.1002/jcc.20291

Vermaas, J. V., Dellon, L. D., Broadbelt, L. J., Beckham, G. T., and Crowley, M. F. (2019). Automated transformation of lignin topologies into atomic structures with LigninBuilder. *ACS Sustain. Chem. Eng.* 7, 3443–3453. doi:10.1021/acssuschemeng.8b05665

Wang, C., Kelley, S. S., and Venditti, R. A. (2016). Lignin-based thermoplastic materials. *ChemSusChem* 9, 770–783. doi:10.1002/cssc.201501531

Zaidi, S. A. S., Kwan, C. E., Mohan, D., Harun, S., Luthfi, A. A. I., and Sajab, M. S. (2023). Evaluating the stability of PLA-lignin filament produced by bench-top extruder for sustainable 3D printing. *Materials* 16, 1793. doi:10.3390/ma16051793

Zhang, H., Lu, X., Leng, Y., Fang, L., Qu, S., Feng, B., et al. (2009). Molecular dynamics simulations on the interaction between polymers and hydroxyapatite with and without coupling agents. *Acta Biomater.* 5, 1169–1181. doi:10.1016/j.actbio.2008.11.014

Zhou, S.-Q., Cheng, X.-C., Jin, Y.-L., Wu, J., and Zhao, D.-S. (2013). Molecular dynamics simulation on interacting and mechanical properties of polylactic acid and attapulgite(100) surface. *J. Appl. Polym. Sci.* 128, 3043–3049. doi:10.1002/app.38492

frontiers | Frontiers in Chemistry

TYPE Perspective
PUBLISHED 12 February 2024
DOI 10.3389/fchem.2024.1057928

OPEN ACCESS

EDITED BY
Zoltan Kovacs,
University of Texas Southwestern Medical Center, United States

REVIEWED BY
Valeriia Starovoitova,
International Atomic Energy Agency, Austria
Zoltan Szucs,
Institute for Nuclear Research, Hungary

*CORRESPONDENCE
Haitao Shang,
htshang.research@gmail.com

RECEIVED 30 September 2022
ACCEPTED 09 January 2024
PUBLISHED 12 February 2024

CITATION
Shang H (2024), Probing long-lived radioactive isotopes on the double-logarithmic Segrè chart.
Front. Chem. 12:1057928.
doi: 10.3389/fchem.2024.1057928

Probing long-lived radioactive isotopes on the double-logarithmic Segrè chart

Haitao Shang *

Institute of Ecology and Evolution, University of Oregon, Eugene, OR, United States

Isotopes have been widely applied in a variety of scientific subjects; many aspects of isotopes, however, remain not well understood. In this study, I investigate the relation between the number of neutrons (N) and the number of protons (Z) in stable isotopes of non-radioactive elements and long-lived isotopes of radioactive elements at the double-linear scale (conventional Segrè chart) and the double-logarithmic scale. Statistical analyses show that N is a power-law function of Z for these isotopes: $N = 0.73 \times Z^{1.16}$. This power-law relation provides better predictions for the numbers of neutrons in stable isotopes of non-radioactive elements and long-lived isotopes of radioactive elements than the linear relation on the conventional Segrè chart. The power-law pattern reveled here offers empirical guidance for probing long-lived isotopes of unknown radioactive elements.

KEYWORDS

non-radioactive elements, radioactive elements, stable isotopes, long-lived isotopes, unknown isotopes, power laws, double-logarithmic scale, Segrè chart

1 Introduction

Isotopes are variants of elements that possess the same number of protons but differ in the number of neutrons (De Groot, 2004; Ellam, 2016). Several hundred isotopes have been detected in natural environments on Earth, while thousands of other isotopes are continuously created in various areas in the universe (White, 2014; McSween Jr and Huss, 2022). Since the first discovery by Frederick Soddy in 1913 (Soddy, 1913), isotopes have been widely applied in different subjects. For example, ecologists use isotopic signatures to study the exchanges of materials between life and environments (Michener and Lajtha, 2008), biologists investigate metabolic processes on the basis of intermolecular and intramolecular isotopic effects (Kohen and Limbach, 2005), and geochemists use the fingerprints that isotopes left in sedimentary records to reconstruct the evolutionary trajectories of life and environments on the ancient Earth (White, 2014).

Isotopes are classified into two categories according to their stability: stable and radioactive isotopes. Stable isotopes of one element do not transform into other elements under natural conditions, while radioactive isotopes decay to other elements after certain time periods with specific half-lives (De Groot, 2004; Ellam, 2016). Among the known 118 elements on the periodic table, 80 of them have one or more stable isotopes and are called as non-radioactive elements (De Groot, 2004; Ellam, 2016). This non-radioactive category includes the elements with atomic number (Z) less than 83 except for two elements that have no stable isotopes (i.e., technetium with $Z = 43$ and promethium with $Z = 61$) (De Groot, 2004; Ellam, 2016). In contrast, nature creates neutrons and protons in an asymmetric manner in the nuclei of elements with atomic number larger than 83; these

elements are also referred to as radioactive elements (Blatt and Weisskopf, 1991; Thomson, 2013). As the imbalance between neutrons and protons of a nucleus grows, its stability decreases; in this case, decay offers an chance for the nucleus to re-establish a balance between its neutrons and protons (Blatt and Weisskopf, 1991; Thomson, 2013). While radioactive elements eventually decay into other elements, their long-lived isotopes may have rather extended lifespans (Blatt and Weisskopf, 1991; Thomson, 2013). For example, the half life of ^{209}Bi, an isotope of the radioactive element bismuth, is 2.01×10^{19} years, which is 1.5×10^{9} times greater than the age of the universe (De Groot, 2004; Ellam, 2016).

Combining protons and neutrons in an arbitrary way does not necessarily generates a stable nucleus. A nucleus is unbounded when it is outside the valley of stability, which is defined by the neutron drip line and proton drip line (Hansen, 1993; Thoennessen, 2004). Substantial efforts have been dedicated to exploring the principles and mechanisms for the stability of isotopes. Since Myers, Światecki, Viola Jr., and Seaborg predicted that nuclei of superheavy elements occupy a region called as stability island on the Segrè chart (a plot arranging nuclides by proton number Z and neutron number N at the double-linear scale) (Myers and Swiatecki, 1966; Viola Jr and Seaborg, 1966), the concept of the "island of stability" has been a dominant paradigm in the study of superheavy nuclei. A variety of intriguing properties in the island of stability have been revealed. For example, it was discovered in the late 1940s that nuclei possessing a magic number (2, 8, 20, 28, 50, 82, or 126) of protons or neutrons exhibit much higher stability than other nuclei; this phenomenon then became the basis of the nuclear shell model (Wigner, 1937; Mayer, 1948; Haxel et al., 1949; Kanungo et al., 2002).

Here, I investigate the relation between N and Z in stable isotopes of non-radioactive elements and long-lived isotopes of radioactive elements at double-linear and double-logarithmic scales and show that N is a power-law function of Z in these isotopes. The power law refers to a functional relation between two variables in which one variable changes as a power of the other. On a double-logarithmic plot, the power law appears as a straight line, implying that the underlying regularity of this relation is independent of the specific scales one investigates (Clauset et al., 2009; Alstott et al., 2014). Statistical analyses in this work demonstrate that the power-law relation on the double-logarithmic Segrè chart provides more accurate predictions for N than the linear relation obtained on the conventional double-linear Segrè chart. These results offer new insights into the future searching for the long-lived isotopes of unknown radioactive elements.

2 Data and methods

The dataset on isotopes is from Nubase 2020 (Kondev et al., 2021). Except for technetium and promethium, each non-radioactive element has one or more stable isotopes; the numbers of neutrons in these isotopes usually are close to one another. For each non-radioactive element, I calculate the average number of neutrons in its stable isotopes and denote this mean value by $\bar{N}$. On the other hand, the lifespans of a radioactive element's isotopes often vary across a large range. For each radioactive element, I take the isotope with the longest lifespan as the representative long-lived isotope and denote the number of neutrons in this representative isotope by N_{rad}. For simplicity, I henceforth use N to denote $\bar{N}$ or N_{rad}.

To investigate the relation between N and Z, I first divide the plot of N versus Z into two regions (Figure 1): (1) non-radioactive elements ($\bar{N}$ versus Z) and (2) radioactive elements (N_{rad} versus Z). I then apply linear regression to fit the data in region (1) and region (2) at the double-linear (Figure 1A) and double-logarithmic (Figure 1B) scales; blue and green lines in Figure 1 show the best-fitting lines in region (1) and region (2), respectively. The lines obtained at the double-linear scale (Figure 1A) are conventional linear regression lines, while the lines obtained at the double-logarithmic scale (Figure 1B) are referred to as power laws. The details of power-law analyses are described in Alstott et al. (2014) and Clauset et al. (2009). Moreover, to compare the effectiveness of predictions by the fitting formulas obtained using data in both regions (1) and (2) to that obtained only based on data in an individual region (1) or (2), I fit the data in both regions at the double-linear (Figure 1A) and double-logarithmic (Figure 1B) scales; red lines in Figure 1 show the best-fitting lines for all data in both regions (1) and (2). The magnified plots for Figures 1A, B are presented in Figure 2 and Figure 3, respectively.

To evaluate the goodness of fit of the fitting formulas, I calculate the coefficients of determination (R^2's) and perform the Kolmogorov-Smirnov (KS) test (Massey Jr, 1951) and Cramér-von Mises (CM) two-sample test (Anderson, 1962). The metric R^2 measures the fraction of variations in a dependent variable that can be explained by a fitting function; a larger value of R^2 indicates a better fitting and therefore a more reliable model (Freund and Wilson, 2003). The KS statistic is defined as $\sup|M_{\mathrm{m}} - M_{\mathrm{d}}|$, which measures the largest distance between the cumulative distribution functions (CDFs) of a distribution that best fits the data (M_{m}) and the data themselves (M_{d}) (Massey Jr, 1951). The CM test is defined as $\frac{A\times B}{(A+B)^2}[\sum_{a=0}^{A}(M_{\mathrm{m}}(x_a) - M_{\mathrm{d}}(x_a))^2 + \sum_{b=0}^{B}(M_{\mathrm{m}}(x'_b) - M_{\mathrm{d}}(x'_b))^2]$, where $\{x_a\}_{a=0}^{A}$ and $\{x'_b\}_{b=0}^{B}$ are samples independently drawn from two distributions with CDFs M_{m} and M_{d}, respectively (Anderson, 1962). To perform the KS and CM tests, I set the null hypothesis and two-sided alternative as H_0: $M_{\mathrm{m}} = M_{\mathrm{d}}$ and H_1: $M_{\mathrm{m}} \neq M_{\mathrm{d}}$, respectively. The critical p-value for these tests is set to 0.05; $p > 0.05$ suggests that a function fits the data well while $p \leq 0.05$ suggests that a function does not adequately describes the data. To compare the effectiveness of predictions by the fitting formulas obtained at the double-linear and double-logarithmic scales, I calculate the average relative errors (AREs) and root mean square errors (RMSEs) for the predicted values of these fitting formulas; a smaller value of ARE or RMSE indicates a better model.

3 Results

Figures 1A, B show the linear regression for $\bar{N}$ or N_{rad} versus Z at the double-linear and double-logarithmic scales, respectively. Region (1) in these two panels presents the dataset on stable isotopes of non-radioactive elements (blue circles) and the linear regression line (blue line) for these data, while region (2) illustrates the dataset on long-lived isotopes of radioactive elements (green circles) and the linear regression line (green line) for these data. The

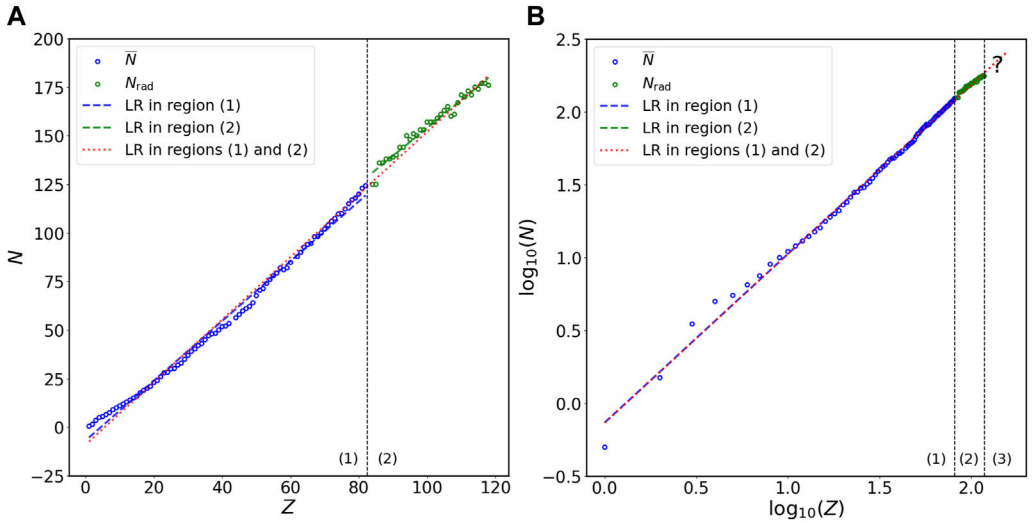

FIGURE 1
Relation of N versus Z in stable isotopes of non-radioactive elements and long-lived isotopes of radioactive elements at the **(A)** double-linear and **(B)** double-logarithmic scales. The N on the vertical axis represents either $\bar{N}$ (in region (1)) or N_{rad} (in regions (2) and (3)). Region (1) in panel **(A)** or **(B)** is for $\bar{N}$ versus Z in stable isotopes of non-radioactive elements (blue circles), region (2) in panel **(A)** or **(B)** is for N_{rad} versus Z in long-lived isotopes of radioactive elements (green circles), and region (3) in panel **(B)** is for long-lived isotopes of unknown radioactive elements. Blue line in region (1) of panel **(A)** or **(B)** is the linear regression (LR) for stable isotopes of non-radioactive elements (blue circles) at the linear or logarithmic scale, respectively. Green line in region (2) of **(A)** or **(B)** is the LR for long-lived isotopes of radioactive elements (green circles) at the linear or logarithmic scale, respectively. Red line in regions (1) and (2) of panel **(A)** or **(B)** is the LR for both stable isotopes of non-radioactive elements and long-lived isotopes of radioactive elements at the linear or logarithmic scale, respectively. Red line (with question mark) in region (3) of panel **(B)** represents the predictions for N values of long-lived isotopes of unknown radioactive elements. The results of statistical analyses are presented in Tables 1, 2. The magnified plots for panels **(A)** and **(B)** are presented in Figures 2, 3, respectively.

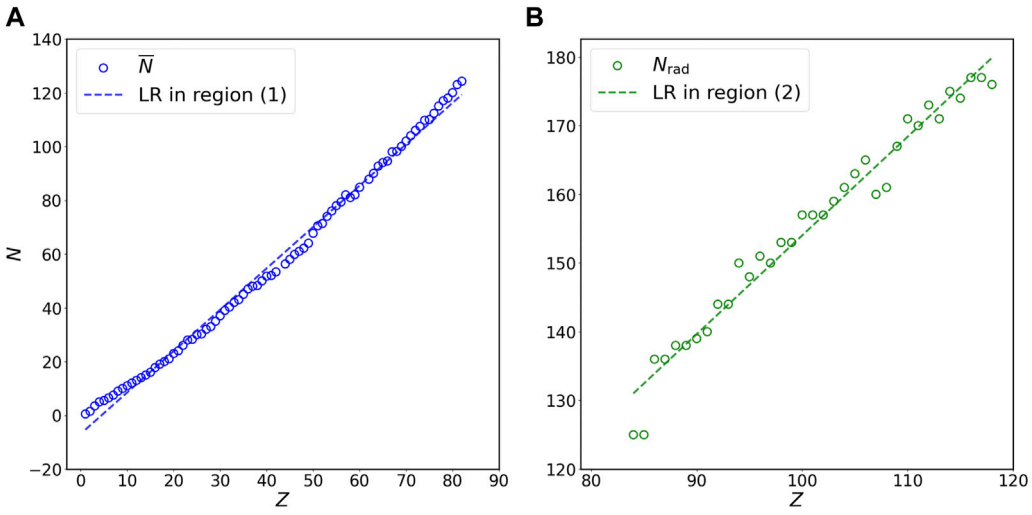

FIGURE 2
Relation of N versus Z for **(A)** stable isotopes of non-radioactive elements (blue circles) and **(B)** long-lived isotopes of radioactive elements (green circles) at the double-linear scale. Panels **(A)** and **(B)** in this figure are the magnification of region (1) and region (2) in Figure 1A, respectively. The N on the vertical axis represents $\bar{N}$ for panel **(A)** and N_{rad} for panel **(B)** in this figure. Blue and green lines are the linear regression (LR) for stable isotopes of non-radioactive elements (blue circles) and long-lived isotopes of radioactive elements (green circles), respectively, at the double-linear scale. The results of statistical analyses are presented in Tables 1, 2.

magnified plots for Figures 1A, B are illustrated in Figure 2 and Figure 3, respectively. The mathematical expressions for linear regression of the dataset on stable isotopes of non-radioactive elements (i.e., $\bar{N}$ versus Z) at the double-linear (Figure 2A) and double-logarithmic (Figure 3A) scales are $N = 1.54 \times Z - 6.86$ and $N = 0.74 \times Z^{1.15}$, respectively. For the dataset on long-lived isotopes of radioactive elements (i.e., N_{rad} versus Z), the mathematical expressions for linear regression at the double-linear (Figure 2B)

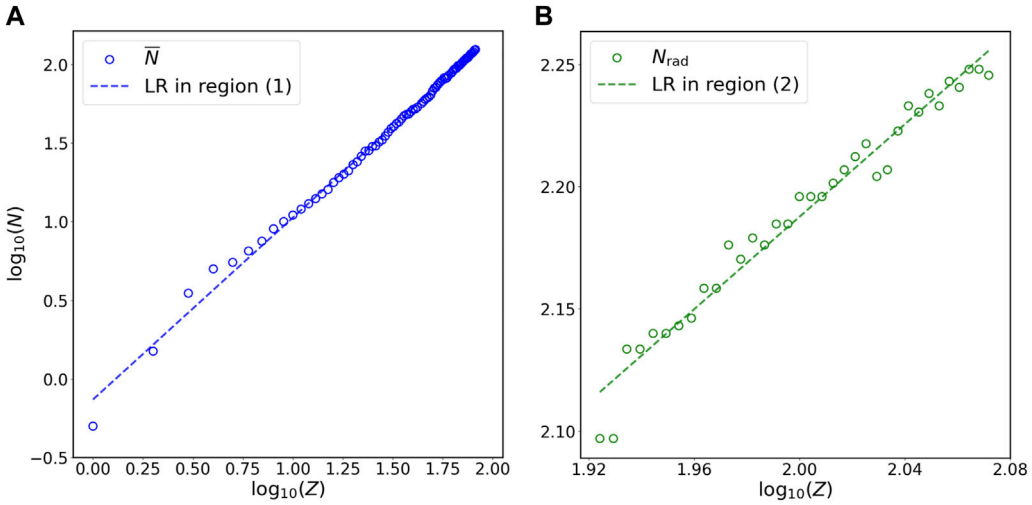

FIGURE 3
Relation of N versus Z for **(A)** stable isotopes of non-radioactive elements (blue circles) and **(B)** long-lived isotopes of radioactive elements (green circles) at the double-logarithmic scale. Panels **(A)** and **(B)** in this figure are the magnification of region (1) and region (2) in Figure 1B, respectively. The N on the vertical axis represents $\bar{N}$ for panel **(A)** and N_{rad} for panel **(B)** in this figure. Blue and green lines are the linear regression (LR) for stable isotopes of non-radioactive elements (blue circles) and long-lived isotopes of radioactive elements (green circles), respectively, at the double-logarithmic scale. The results of statistical analyses are presented in Tables 1, 2.

TABLE 1 Coefficients of determination (R^2's), p-values of the Kolmogorov-Smirnov test (p_{KS}'s), and p-values of the Cramér-von Mises two-sample test (p_{CM}'s) of the best-fitting formulas obtained in region (1), region (2), and both regions (1) and (2) in Figure 1 at the double-linear (Figure 1A) and double-logarithmic (Figure 1B) scales. Region (1) and region (2) in Figure 1A correspond to panel (A) and panel (B) in Figure 2, respectively; region (1) and region (2) in Figure 1B correspond to panel (A) and panel (B) in Figure 3, respectively.

Region in Figure 1	Panel in Figure 2 or Figure 3	Scale	Best-fitting line	Best-fitting formula	R^2	p_{KS}	p_{CM}
Region (1) in Figure 1A	Figure 2A	Linear	Blue	$N = 1.54 \times Z - 6.86$	0.94	0.99	0.98
Region (1) in Figure 1B	Figure 3A	Logarithmic	Blue	$N = 0.74 \times Z^{1.15}$	0.99	1.00	1.00
Region (2) in Figure 1A	Figure 2B	Linear	Green	$N = 1.44 \times Z + 10.29$	0.96	0.98	0.99
Region (2) in Figure 1B	Figure 3B	Logarithmic	Green	$N = 1.97 \times Z^{0.95}$	0.98	0.99	0.99
Regions (1) & (2) in Figure 1A	—	Linear	Red	$N = 1.61 \times Z - 9.01$	0.98	0.99	0.99
Regions (1) & (2) in Figure 1B	—	Logarithmic	Red	$N = 0.73 \times Z^{1.16}$	0.99	0.99	1.00

and double-logarithmic (Figure 3B) scales are $N = 1.44 \times Z + 10.29$ and $N = 1.97 \times Z^{0.95}$, respectively. To evaluate how well these mathematical formulas fit the datasets, I calculate the coefficient of determination (R^2) and perform the KS and CM tests (Section 2); the statistical results are summarized in Table 1. All R^2 values are close to 1 and all p-values for the KS and CM tests are much greater than the critical value 0.05, indicating that all formulas presented in Table 1 fit the data in specific regions extraordinarily well.

To test the effectiveness of predictions by the mathematical expressions in Table 1, I first use the fitting formulas for the dataset on stable isotopes of non-radioactive elements (i.e., $\bar{N}$ versus Z) at the double-linear (Figure 2A) and double-logarithmic (Figure 3A) scales to predict the values of $\bar{N}$ and N_{rad}. The AREs and RMSEs of these predictions are presented in Table 2, which shows that switching from the fitting formula obtained at the double-linear scale ($N = 1.54 \times Z - 6.86$) to the fitting formula obtained at the double-logarithmic scale ($N = 0.74 \times Z^{1.15}$) reduces the AREs of the predictions for $\bar{N}$ by 86%, N_{rad} by 39%, and both $\bar{N}$ and N_{rad} by 84%, and reduces the RMSEs of the predictions for $\bar{N}$ by 56%, N_{rad} by 41%, and both $\bar{N}$ and N_{rad} by 42%. These results suggest that the power law offers more accurate predictions for N than the linear relation obtained at the double-linear scale. To further justify this implication, I use the linear regression formulas for the dataset on long-lived isotopes of radioactive elements (i.e., N_{rad} versus Z) at the double-linear scale (Figure 2B) and the double-logarithmic scale (Figure 3B) to predict the values of $\bar{N}$ and N_{rad}. When using the power law ($N = 1.97 \times Z^{0.95}$) instead of the linear relation ($N = 1.44 \times Z + 10.29$), the AREs of the predictions for $\bar{N}$, N_{rad}, and both $\bar{N}$ and N_{rad} decrease by 62%, 13%, and 62%, respectively; the RMSEs of the predictions for $\bar{N}$, N_{rad}, and both $\bar{N}$ and N_{rad} decrease by 26%, 5%, and 25%, respectively (Table 2). These results also imply that the power law provides better predictions for N than the linear relation obtained at the double-linear scale.

TABLE 2 Average relative errors (AREs) and root mean square errors (RMSEs) of the predictions for N by the best-fitting formulas obtained in region (1), region (2), and both regions (1) and (2) in Figure 1 at the double-linear (Figure 1A) and double-logarithmic (Figure 1B) scales. The statistical results in the specific regions in Figure 1 from which the best-fitting formulas in this table are obtained is presented in Table 1. Region (1) and region (2) in Figure 1A correspond to panel (A) and panel (B) in Figure 2, respectively; region (1) and region (2) in Figure 1B correspond to panel (A) and panel (B) in Figure 3, respectively. The percentages in parentheses show how much the AREs or RMSEs of predictions for N in specific regions change when switching from linear relations to power laws; downward arrows indicate decreases.

Best-fitting formula	ARE of predictions in region (1)	ARE of predictions in region (2)	ARE of predictions in regions (1) & (2)	RMSE of predictions in region (1)	RMSE of predictions in region (2)	RMSE of predictions in regions (1) & (2)
$N = 1.54 \times Z - 6.86$	29.61% (↓ 86%)	4.54% (↓ 39%)	21.98% (↓ 84%)	2.82 (↓ 56%)	7.47 (↓ 41%)	4.75 (↓ 42%)
$N = 0.74 \times Z^{1.15}$	4.01%	2.52%	3.56%	1.25	4.43	2.74
$N = 1.44 \times Z + 10.29$	87.02% (↓ 62%)	1.43% (↓ 13%)	60.91% (↓ 62%)	13.51 (↓ 26%)	2.55 (↓ 5%)	11.36 (↓ 25%)
$N = 1.97 \times Z^{0.95}$	33.01%	1.24%	23.34%	9.98	2.43	8.46
$N = 1.61 \times Z - 9.01$	39.35% (↓ 90%)	2.37% (↓ 11%)	28.43% (↓ 88%)	3.39 (↓ 59%)	4.34 (↓ 17%)	3.46 (↓ 23%)
$N = 0.73 \times Z^{1.16}$	3.97%	2.11%	3.52%	1.39	3.61	2.65

To predict the N values of long-lived isotopes of unknown radioactive elements [region (3) in Figure 1B], I calculate the power-law formula between N and Z using all data [both regions (1) and (2) in Figure 1B] at the double-logarithmic scale; the relation of N versus Z for all data at the double-linear scale [both regions (1) and (2) in Figure 1A] is also computed for comparison. The AREs of the predictions for $\bar{N}$, N_{rad}, and both $\bar{N}$ and N_{rad} obtained using the power law ($N = 0.73 \times Z^{1.16}$) are 90%, 11%, and 88% lower, respectively, than the linear relation at the double-linear scale ($N = 1.61 \times Z - 9.01$), and the RMSEs of the predictions for $\bar{N}$, N_{rad}, and both $\bar{N}$ and N_{rad} obtained using the power law are 59%, 17%, and 23% lower, respectively, than the linear relation (Table 2). These results again support the above conclusion that the predictions for N by power laws are more accurate than those by linear relations obtained on the Segrè chart.

4 Discussion

As quantum systems, nuclei's behaviors can be depicted with the nonrelativistic Schrödinger equation (Olavo, 1999; Schleich et al., 2013); within nuclei, how triple quarks gather to form protons and neutrons can be interpreted by quantum chromodynamics (QCD) (Marciano and Pagels, 1978; Greiner et al., 2007; Group et al., 2022). However, it is well known that describing the features of isotopes does not need to explicitly include quarks in theoretical models; instead, having protons and neutrons in these models is sufficient to predict a variety of properties of isotopes (Blatt and Weisskopf, 1991; Thomson, 2013). For example, the mass of a nucleus can be estimated from its number of protons and neutrons using the Weizsäcker mass formula (Weizsäcker, 1935), which is a refined form of the liquid drop model for the binding energy of nuclei (Gamow, 1930). Moreover, neutrons also affect the stability of nuclei and isotopes' decay (Mueller and Sherrill, 1993; Pfützner et al., 2012). In a stable nucleus, valence neutrons are well bound; the corresponding wavefunction decays rapidly when the valence neutron is outside the limit of stability (Blatt and Weisskopf, 1991; Mueller and Sherrill, 1993). In contrast, within an unstable nucleus, valence neutrons are loosely bound and live in the classically forbidden region; the corresponding wavefunction possesses a long tail (Blatt and Weisskopf, 1991; Mueller and Sherrill, 1993). For a specific element (with a fixed number of protons), the lifespans of its isotopes are influenced by the number of neutrons (Thomson, 2013; Martin and Shaw, 2017). Therefore, the number of neutrons offers a window through which to predict the long-lived isotopes of unknown radioactive elements.

Statistical analyses in this study show that power laws exist between the number of neutrons and the number of protons in both stable isotopes of non-radioactive elements and long-lived isotopes of radioactive elements. Power laws have been identified in a variety of natural systems, such as the evolutionary processes of life over geological time scales (Raup, 1986; Shang, 2024), the distributions of amino acids and expressed genes in various organisms and tissues (Furusawa and Kaneko, 2003; Mora and Bialek, 2011), and the degradation rate versus age of organic matter in ecosystems (Middelburg, 1989; Shang, 2023). However, the specific reasons for many observed power-law patterns are not well understood (Clauset et al., 2009; Alstott et al., 2014). Similarly, why the coefficient and exponent in the power-law relation between N and Z (Figure 1B, Figure 3; Table 1) take those specific values remain unknown. Moreover, the underlying physical mechanisms responsible for the emergence of these power laws may not be readily interpreted by our current knowledge of nucleons. It is well known that the binding energy of a nucleus derives from the strong interaction, which is described by QCD (Marciano and Pagels, 1978; Greiner et al., 2007; Group et al., 2022). Nevertheless, the (low-energy) QCD is not at the stage where we can use it to obtain comprehensive understating of nucleons (Marciano and Pagels, 1978; Greiner et al., 2007; Group et al., 2022). From the perspective of statistical mechanics, power laws are usually attributed to self-organized criticality, a concept that was originally suggested by Bak, Tang, and Wiesenfeld (Bak et al., 1987). Self-organized criticality refers to the phenomenon that the internal interactions of a system organize itself into states where power laws appear (Bak et al., 1987, 1988). However, studies have shown that power-law patterns are an emergent property of self-organized criticality and do not necessarily originate from the latter (Solow, 2005; Clauset et al.,

2009; Marković and Gros, 2014). Whether the power-law pattern observed in this study (Figure 1B, Figure 3; Table 1) originates from certain mechanisms related to self-organized criticality in nuclei requires further investigation.

The power laws shown in this work provide better prediction for the number of neutrons in stable isotopes of non-radioactive elements or long-lived isotopes of radioactive elements than the linear relation on the Segrè chart (Tables 1, 2). The power law, $N = 0.73 \times Z^{1.16}$, which is obtained using all data (i.e., both $\bar{N}$ and N_{rad} versus Z) at the double-logarithmic scale (Table 2), therefore, may be applied to predict N values of long-lived isotopes of unknown radioactive elements with $Z \geq 119$ [region (3) in Figure 1B]. For example, with this mathematical formula, one may expect that the mean number of neutrons in long-lived isotopes of the unknown radioactive element with $Z = 120$ would be about 188; the region surrounding this point, (120, 188), on the plot of N versus Z at the double-logarithmic scale would be the island of stability for the isotopes of this unknown radioactive element. However, one should note that predicting the maximum number of neutrons that can exist in a stable/long-lived nucleus, which has been recognized as a difficult task for *ab initio* many-body theories (Ring and Schuck, 2004; Hergert, 2020), is beyond the ability of the power-law relation presented in this work.

Studies have suggested that the neutron-proton asymmetry significantly influences the stability of a nucleus; as the value of Z increases, the stability of a nucleus decreases due to the growth of Coulomb repulsion (Blatt and Weisskopf, 1991; Martin and Shaw, 2017). This implies that the power-law pattern presented here probably will disappear when Z exceeds a certain large, critical value. Actually, power laws observed in natural systems often vanish at some critical points (Schroeder, 2009; Bak, 2013). Although this appears daunting, no available clue shows that the disappearance of the power-law pattern occurs immediately when $Z \geq 119$. Therefore, the mathematical formula, $N = 0.73 \times Z^{1.16}$, may still provide empirical guidance for probing the long-lived isotopes of unknown radioactive elements. Future discovery of new radioactive elements will offer further validation for the predictive ability of the power-law relation revealed in this study.

Data availability statement

The original contributions presented in the study are included in the article/Supplementary Material, further inquiries can be directed to the corresponding author.

Author contributions

HS conceived the project, performed the analysis, and wrote the manuscript.

Acknowledgments

I thank editor Zoltan Kovacs for securing reviewers and Valeriia Starovoitova and Zoltan Szucs for thoughtful and constructive comments on the manuscript. I am grateful for the financial support from the Open Access Article Processing Charge Award Fund of the University of Oregon Libraries.

Conflict of interest

The author declares that the research was conducted in the absence of any commercial or financial relationships that could be construed as a potential conflict of interest.

Publisher's note

All claims expressed in this article are solely those of the authors and do not necessarily represent those of their affiliated organizations, or those of the publisher, the editors and the reviewers. Any product that may be evaluated in this article, or claim that may be made by its manufacturer, is not guaranteed or endorsed by the publisher.

References

Alstott, J., Bullmore, E., and Plenz, D. (2014). Powerlaw: a Python package for analysis of heavy-tailed distributions. *PloS One* 9 (1), e85777. doi:10.1371/journal.pone.0085777

Anderson, T. W. (1962). On the distribution of the two-sample Cramér-von Mises criterion. *Ann. Math. Statistics* 33, 1148–1159. doi:10.1214/aoms/1177704477

Bak, P. (2013). *How nature works: the science of self-organized criticality*. Cham: Springer Science & Business Media.

Bak, P., Tang, C., and Wiesenfeld, K. (1987). Self-organized criticality: an explanation of the 1/*f* noise. *Phys. Rev. Lett.* 59 (4), 381–384. doi:10.1103/physrevlett.59.381

Bak, P., Tang, C., and Wiesenfeld, K. (1988). Self-organized criticality. *Phys. Rev. A* 38 (1), 364–374. doi:10.1103/physreva.38.364

Blatt, J. M., and Weisskopf, V. F. (1991). *Theoretical nuclear physics*. Massachusetts, United States: Courier Corporation.

Clauset, A., Shalizi, C. R., and Newman, M. E. (2009). Power-law distributions in empirical data. *SIAM Rev.* 51 (4), 661–703. doi:10.1137/070710111

De Groot, P. A. (2004). *Handbook of stable isotope analytical techniques, volume 1*. Amsterdam, Netherlands: Elsevier.

Ellam, R. (2016). *Isotopes: a very short introduction*. Times New Roman: Oxford University Press.

Freund, R. J., and Wilson, W. J. (2003). *Statistical methods*. Amsterdam, Netherlands: Elsevier.

Furusawa, C., and Kaneko, K. (2003). Zipf's law in gene expression. *Phys. Rev. Lett.* 90 (8), 088102. doi:10.1103/physrevlett.90.088102

Gamow, G. (1930). Mass defect curve and nuclear constitution. *Proc. R. Soc. Lond. Ser. A, Contain. Pap. a Math. Phys. Character* 126 (803), 632–644. doi:10.1098/rspa.1930.0032

Greiner, W., Schramm, S., and Stein, E. (2007). *Quantum chromodynamics*. Cham: Springer Science & Business Media.

Group, P. D., Workman, R., Burkert, V., Crede, V., Klempt, E., Thoma, U., et al. (2022). Review of particle physics. *Prog. Theor. Exp. Phys.* 2022 (8), 083C01. doi:10.1093/ptep/ptac097

Hansen, P. (1993). Nuclear structure at the drip lines. *Nucl. Phys. A* 553, 89–106. doi:10.1016/0375-9474(93)90617-7

Haxel, O., Jensen, J. H. D., and Suess, H. E. (1949). On the "magic numbers" in nuclear structure. *Phys. Rev.* 75 (11), 1766. doi:10.1103/physrev.75.1766.2

Hergert, H. (2020). A guided tour of *ab initio* nuclear many-body theory. *Front. Phys.* 8, 379. doi:10.3389/fphy.2020.00379

Kanungo, R., Tanihata, I., and Ozawa, A. (2002). Observation of new neutron and proton magic numbers. *Phys. Lett. B* 528 (1-2), 58–64. doi:10.1016/s0370-2693(02)01206-6

Kohen, A., and Limbach, H. H. (2005). *Isotope effects in chemistry and biology*. Florida, United States: CRC Press.

Kondev, F., Wang, M., Huang, W., Naimi, S., and Audi, G. (2021). The NUBASE2020 evaluation of nuclear physics properties. *Chin. Phys. C* 45 (3), 030001. doi:10.1088/1674-1137/abddae

Marciano, W., and Pagels, H. (1978). Quantum chromodynamics. *Phys. Rep.* 36 (3), 137–276. doi:10.1016/0370-1573(78)90208-9

Marković, D., and Gros, C. (2014). Power laws and self-organized criticality in theory and nature. *Phys. Rep.* 536 (2), 41–74. doi:10.1016/j.physrep.2013.11.002

Martin, B. R., and Shaw, G. (2017). *Particle physics*. New Jersey, United States: John Wiley & Sons.

Massey, F. J., Jr (1951). The Kolmogorov-Smirnov test for goodness of fit. *J. Am. Stat. Assoc.* 46 (253), 68–78. doi:10.1080/01621459.1951.10500769

Mayer, M. G. (1948). On closed shells in nuclei. *Phys. Rev.* 74 (3), 235–239. doi:10.1103/physrev.74.235

McSween, H., Jr, and Huss, G. (2022). *Cosmochemistry*. Cambridge: Cambridge University Press.

Michener, R., and Lajtha, K. (2008). *Stable isotopes in ecology and environmental science*. New Jersey, United States: John Wiley & Sons.

Middelburg, J. J. (1989). A simple rate model for organic matter decomposition in marine sediments. *Geochimica Cosmochimica Acta* 53 (7), 1577–1581. doi:10.1016/0016-7037(89)90239-1

Mora, T., and Bialek, W. (2011). Are biological systems poised at criticality? *J. Stat. Phys.* 144, 268–302. doi:10.1007/s10955-011-0229-4

Mueller, A. C., and Sherrill, B. M. (1993). Nuclei at the limits of particle stability. *Annu. Rev. Nucl. Part. Sci.* 43 (1), 529–583. doi:10.1146/annurev.ns.43.120193.002525

Myers, W. D., and Swiatecki, W. J. (1966). Nuclear masses and deformations. *Nucl. Phys.* 81 (1), 1–60. doi:10.1016/0029-5582(66)90639-0

Olavo, L. (1999). Foundations of quantum mechanics: non-relativistic theory. *Phys. A Stat. Mech. its Appl.* 262 (1-2), 197–214. doi:10.1016/s0378-4371(98)00395-1

Pfützner, M., Karny, M., Grigorenko, L., and Riisager, K. (2012). Radioactive decays at limits of nuclear stability. *Rev. Mod. Phys.* 84 (2), 567–619. doi:10.1103/revmodphys.84.567

Raup, D. M. (1986). Biological extinction in Earth history. *Science* 231 (4745), 1528–1533. doi:10.1126/science.11542058

Ring, P., and Schuck, P. (2004). *The nuclear many-body problem*. Cham: Springer Science & Business Media.

Schleich, W. P., Greenberger, D. M., Kobe, D. H., and Scully, M. O. (2013). Schrödinger equation revisited. *Proc. Natl. Acad. Sci.* 110 (14), 5374–5379. doi:10.1073/pnas.1302475110

Schroeder, M. (2009). *Fractals, chaos, power laws: minutes from an infinite paradise*. Massachusetts, United States: Courier Corporation.

Shang, H. (2023). A generic hierarchical model of organic matter degradation and preservation in aquatic systems. *Commun. Earth Environ.* 4 (16), 16. doi:10.1038/s43247-022-00667-4

Shang, H. (2024). Scaling laws in the evolutionary processes of marine animals over the last 540 million years. *Geosystems Geoenvironment* 3 (1), 100242. doi:10.1016/j.geogeo.2023.100242

Soddy, F. (1913). Intra-atomic charge. *Nature* 92 (2301), 399–400. doi:10.1038/092399c0

Solow, A. R. (2005). Power laws without complexity. *Ecol. Lett.* 8 (4), 361–363. doi:10.1111/j.1461-0248.2005.00738.x

Thoennessen, M. (2004). Reaching the limits of nuclear stability. *Rep. Prog. Phys.* 67 (7), 1187–1232. doi:10.1088/0034-4885/67/7/r04

Thomson, M. (2013). *Modern particle physics*. Cambridge: Cambridge University Press.

Viola, V., Jr, and Seaborg, G. (1966). Nuclear systematics of the heavy elements — II Lifetimes for alpha, beta and spontaneous fission decay. *J. Inorg. Nucl. Chem.* 28 (3), 741–761. doi:10.1016/0022-1902(66)80412-8

Weizsäcker, C. v. (1935). Zur theorie der kernmassen. *Z. für Phys.* 96 (7-8), 431–458. doi:10.1007/BF01337700

White, W. M. (2014). *Isotope geochemistry*. New Jersey, United States: John Wiley & Sons.

Wigner, E. (1937). On the consequences of the symmetry of the nuclear Hamiltonian on the spectroscopy of nuclei. *Phys. Rev.* 51 (2), 106–119. doi:10.1103/physrev.51.106

frontiers | Frontiers in Chemistry

TYPE Original Research
PUBLISHED 13 March 2024
DOI 10.3389/fchem.2024.1377740

OPEN ACCESS

EDITED BY
Virendra Kumar Gupta,
Reliance Industries, India

REVIEWED BY
Pavel Nikishau,
University of Alabama at Birmingham, United States
Ketan Patel,
Central Salt & Marine Chemicals Research Institute (CSIR), India

*CORRESPONDENCE
Giovanni Talarico,
talarico@unina.it

RECEIVED 28 January 2024
ACCEPTED 28 February 2024
PUBLISHED 13 March 2024

CITATION
D'Anania O, De Rosa C and Talarico G (2024), Mechanistic insights on 1-butene polymerization catalyzed by homogeneous single-site catalysts: a DFT computational study.
Front. Chem. 12:1377740.
doi: 10.3389/fchem.2024.1377740

Mechanistic insights on 1-butene polymerization catalyzed by homogeneous single-site catalysts: a DFT computational study

Olga D'Anania[1,2,3], Claudio De Rosa[2] and Giovanni Talarico[1,2]*

[1]Scuola Superiore Meridionale, Napoli, Italy, [2]Dipartimento di Scienze Chimiche, Università degli Studi di Napoli Federico II, Napoli, Italy, [3]Scuola Normale Superiore, Pisa, Italy

Isotactic poly (1-butene) (iPB) is an interesting semi-crystalline thermoplastic material characterized by notable physical and mechanical attributes encompassing superior creep and stress resistance, elevated toughness, stiffness, and thermal endurance. These distinctive features position iPB as a viable candidate for specific applications; however, its widespread utilization is hindered by certain inherent limitations. Indeed, iPB manifests an intricate polymorphic behavior, and the gradual and spontaneous transition of the kinetically favored form II to the thermodynamically favored form I during aging introduces alterations to the material's properties. Despite its potential, the attainment of iPB with an exceedingly high molecular mass remains elusive, particularly when employing homogeneous catalysts renowned for their efficacy in propene polymerization. In this study we analyze the mechanistic aspects governing 1-butene polymerization by using DFT calculations modelling the regioselectivity of 1-butene insertions and the termination reactions occurring after primary (1,2) and secondary (2,1) insertions. Finally, the isomerization pathways leading to the formation of 4,1 units in iPB samples synthesized by homogenous catalysts is also discussed. All these aspects, furnish a mechanistic picture of the main drawbacks of an "old" but still interesting material.

KEYWORDS

olefin polymerization, DFT calculations, stereoselective polymerization, 1-butene polymerization, transition metal catalysis

Introduction

Polyolefins can be regarded as the most important class of polymeric materials produced by industries, accounting for more than half of the total weight of the globally produced polymers (Olabisi, 2016; Sauter et al., 2017; Talarico et al., 2019). Indeed, they are well-suited for a broad spectrum of applications that cover practically every aspect of our everyday lives (Hutley and Ouederni, 2016). Among these, polyethylene (PE) and polypropylene (PP) occupy the largest market share (Makaryan and Sedov, 2020). However, there exist other noteworthy α-olefin-based materials with peculiar characteristics. Notably, isotactic poly (1-butene) (iPB), a semi-crystalline thermoplastic material synthesized commercially using Ziegler-Natta catalysts (Natta et al., 1955), exhibits several remarkable physical and mechanical properties surpassing those of PE and PP. iPB's commendable attributes, including superior creep and stress resistance, high toughness,

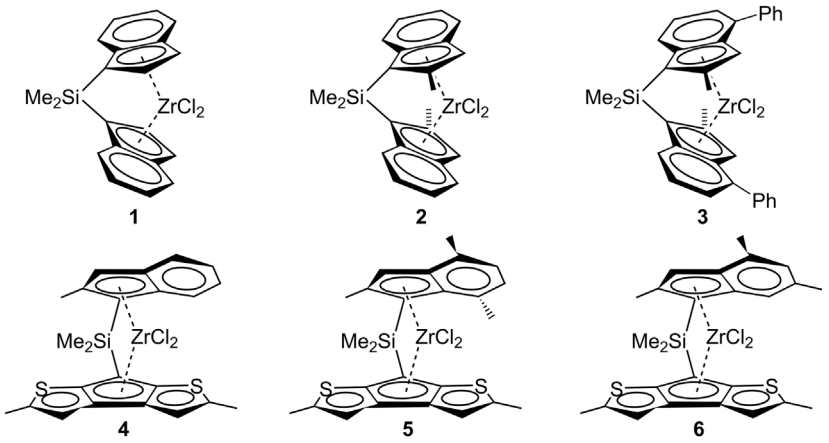

CHART 1
C_2- and C_1-symmetric metallocene systems employed for 1-butene polymerization.

stiffness, and tear strength (Luciani et al., 1988), position it as the material of choice for diverse applications ranging from hot water pipes to pressurized tanks and food packaging. However, its widespread industrial use is constrained by certain drawbacks, primarily associated with its complex polymorphic behavior.

Upon crystallization from the melt, iPB adopts the kinetically favored form II (Turner-Jones, 1963; Petraccone et al., 1976), gradually and spontaneously transforming into the thermodynamically favored form I at room temperature (Natta et al., 1960; De Rosa et al., 2009a; De Rosa et al., 2009b). These distinct crystalline forms possess disparate intrinsic properties (density, melting point, etc.), impacting material characteristics, particularly mechanical performance (Nakamura et al., 1999).

Effective control of the form II-form I transformation rate holds importance from both academic and industrial perspectives (Qiao et al., 2016; Tashiro et al., 2016). Substantial efforts have been dedicated to addressing this challenge, such as the introduction of defects in the iPB main chain through comonomeric units (Gianotti and Capizzi, 1969; De Rosa et al., 2019; De Rosa et al., 2020a) or stereoerrors (Schaffhauser, 1967; De Rosa et al., 2014). Another challenge lies in the realm of homogeneous catalysis, where certain complexes known for their efficacy in propene polymerization exhibit disparate behavior when applied to 1-butene polymerization, particularly concerning molecular weight capability.

Illustratively, the C_2-symmetric $Me_2Si(Ind)_2ZrCl_2$ metallocene system **1** (Chart 1) yields iPB with a low molecular weight (M_v = 16,000, at a polymerization temperature of 50°C) in the case of 1-butene polymerization (Resconi et al., 2006). Similarly, substituted C_2-symmetric metallocenes, like $Me_2Si(2\text{-Me-Ind})_2ZrCl_2$ (system **2**) and $Me_2Si(2\text{-Me-4-Ph-Ind})_2ZrCl_2$ (system **3**), known for improved propene polymerization performance, do not exhibit equivalent efficacy in 1-butene polymerization (M_v = 381,100 at a polymerization temperature of 50°C for system **2** and M_v = 111,000 at a polymerization temperature of 70°C for system **3**).

Notwithstanding, Resconi and coworkers reported instances of fully regioselective 1-butene polymerization by using heterocycle C_1-metallocene systems (Chart 1, systems **4**–**6**) that yield high molecular weight iPB (Resconi et al., 2006).

Numerous investigations have underscored the notable influence of regioerrors (or 2,1 insertions) on the propagation rate in propene polymerization (Busico et al., 1998; Correa et al., 2007). Indeed, due to the difficulties encountered by the monomer insertion into a secondary growing chain, a low reactive "dormant site" is formed (Jüngling et al., 1995; Landis et al., 2004; Busico et al., 2005). The study by Resconi et al. (2006) suggests that regioirregular insertions can exert a profound impact on 1-butene polymerization, influencing the balance between propagation and termination reactions.

It is noteworthy that 1-butene polymerization is a multifaceted process characterized by side mechanisms that give rise to a distinctive polymer microstructure, differing in several aspects from that of polypropylene. First, the analysis of ^{13}C NMR spectra indicates that the majority of metallocene catalysts allow the occasional incorporation of 2,1 units in the polypropylene main chain (Resconi et al., 2000). Notably, in the case of iPB samples, the presence of 2,1 units has exclusively been identified at chain ends, with none detected in the main chain (Busico et al., 1995).

Second, the microstructure of polypropylene samples obtained by metallocenes may be characterized by the presence of 3,1 units, resulting from an isomerization of the 2,1 units (Resconi, 1999). In contrast, the presence of 3,1 units has not been observed for iPB. Instead, various studies have consistently reported the detection of 4,1-units (Busico et al., 1995; Borriello et al., 1997), attributed to the isomerization of the 2,1 unit.

Finally, the isomerization path of 2,1 butene units remains uncertain, with two proposed mechanisms: a stepwise mechanism and a concerted mechanism (Busico et al., 1995). The stepwise mechanism (Scheme 1A) involves a sequence of β-H transfer to the metal, the formation of a double bond at the chain end, rotation of the olefin, and re-insertion into the metal-hydrogen bond. This process leads to the formation of a 3,1-unit intermediate, and the steps are reiterated, ultimately yielding the 4,1-unit product. In addition to this proposed mechanism, as 3,1 units have never been detected, a concerted mechanism (Scheme 1B) has also been suggested. The concerted mechanism involves a single transition state (TS) and directly produces the 4,1 unit from the 2,1-last inserted butene unit.

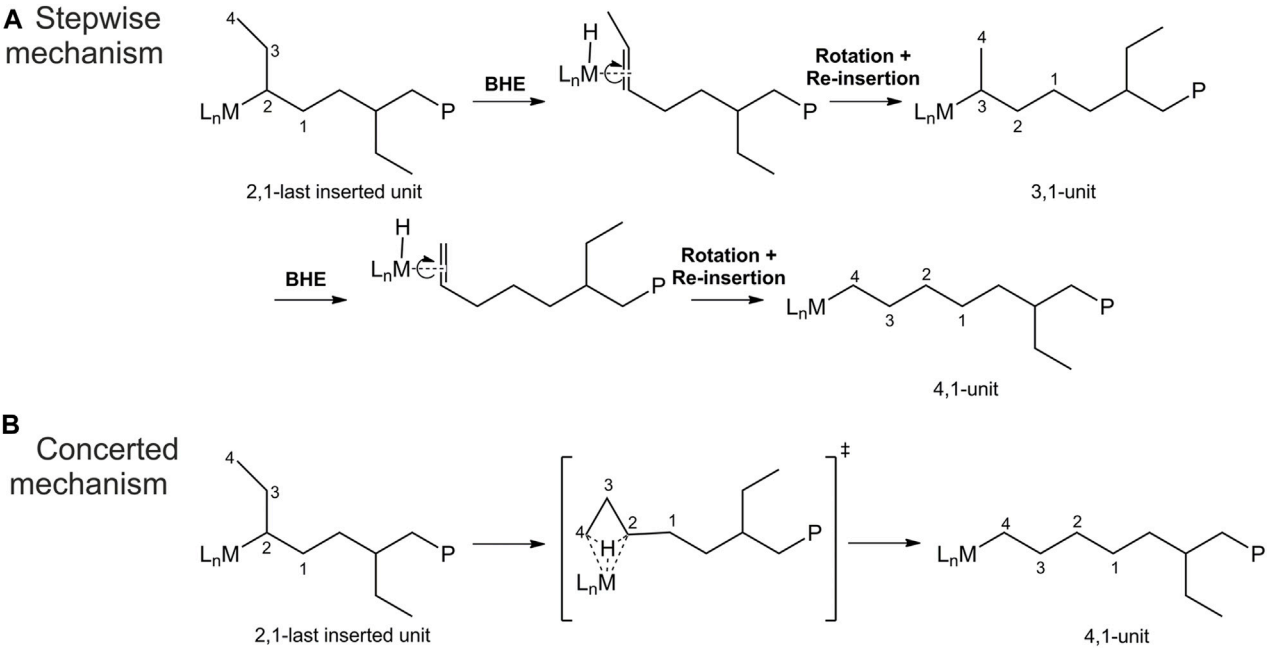

SCHEME 1
Mechanisms for the stepwise **(A)** and concerted **(B)** isomerization of 2,1-last inserted butene units leading to 4,1 units.

While propene polymerization has been extensively investigated in various aspects, including stereoselectivity (Corradini et al., 1979; Corradini et al., 2004; Busico et al., 2006), regioselectivity (Busico et al., 1998; Talarico et al., 2003; Busico et al., 2004; Correa et al., 2007), competition between propagation and termination reactions (Talarico et al., 2002; Talarico and Budzelaar, 2006; Caporaso et al., 2010), and isomerization mechanisms (Busico and Cipullo, 1995; Pilme et al., 2007), a comprehensive theoretical exploration focused on the mechanistic aspects of 1-butene polymerization is notably absent. To address this gap, we embarked on an in-depth analysis of 1-butene polymerization through the application of density functional theory (DFT) calculations.

The limited outcomes observed for iPB samples produced by C_2-symmetric metallocene catalysts, particularly in terms of molecular weight, have been systematically investigated. This elucidation involves an examination of the stereoselectivity and regioselectivity in 1-butene polymerization, the termination reactions following primary (1,2) and secondary (2,1) insertions, and an exploration of both stepwise and concerted isomerization pathways leading to 4,1 units in the iPB main chain.

For the sake of simplicity, DFT calculations have been carried out on the prototype C_2-symmetric *ansa*-metallocene system **1**, although the obtained results are easily extended to other types of C_2-symmetric metallocene catalysts.

Computational details

The structures of the transition states (TSs) and intermediates have been optimized by using the Gaussian16 set of programs (Frisch et al., 2016) and the B3LYP hybrid Generalized Gradient Approximation (GGA) functional (Becke, 1988; Lee et al., 1988) combined with two layers of basis set has been selected. The standard polarized split-valence basis set of Ahlrichs and co-workers (SVP) (Schäfer et al., 1992) has been used for H, C, and Si, meanwhile the LANL2DZ basis and Effective Core Potential (ECP) (Hay and Wadt, 1985) have been employed for the metal centre. The nature of the stationary points has been determined by performing a vibrational analysis and by checking the presence of zero or only one imaginary frequency for intermediates or TSs, respectively. This analysis has been also used for the computation of zero-point energies and thermal (enthalpy and entropy) corrections (298.15 K, 1 bar). Refined electronic energies have been obtained by performing single point calculations with B3LYP functional and a larger TZVP basis set for H, C, and Si (Weigend et al., 2003) and the SDD basis augmented with a f function with exponent 0.5 and pseudopotential (Wadt and Hay, 1985) for Zr. The dispersion corrections (EmpiricalDispersion = D3) (Grimme et al., 2010) and solvation contribution (toluene) through the Polarizable Continuum Model (PCM) (Cossi et al., 1996) have been added. These refined electronic energies have been added to the thermal corrections computed at the SVP/LANL2DZ to obtain the ΔG hereafter reported. This computational approach has been already tested in the olefin polymerization catalysis and found to be viable (Falivene et al., 2015; Falivene et al., 2018). In the following we define: the stereoselectivity ΔE ($\Delta G^{\#}_{stereo}$) as the electronic (Gibbs energy) difference between the favored TSs for 1,2 insertions with different enantiofaces; the regioselectivity ΔE ($\Delta G^{\#}_{regio}$) as the electronic (Gibbs energy) difference between the favored TSs for 1,2 and 2,1 monomer insertions; the competition between propagation and termination reactions ΔE ($\Delta G^{\#}_{T\text{-}P}$) as the electronic (Gibbs energy) between the favored α-olefin insertion (ΔG_P) and the lower β-H transfer to the monomer (ΔG_T). Positive values of $\Delta G^{\#}_{T\text{-}P}$ indicate that propagation is favored over

TABLE 1 Calculated ΔE $(\Delta G)^{\#}$ in kcal/mol for stereoselectivity, regioselectivity and competition between termination and propagation reactions for propene and 1-butene polymerization promoted by system 1.

Monomer	Chain	ΔE $(\Delta G)^{\#}_{stereo}$ [a]	ΔE $(\Delta G)^{\#}_{regio}$ [a]	ΔE $(\Delta G)^{\#}_{T\text{-}P}$ [b]
Propene	Primary	4.2 (4.4) kcal/mol	3.3 (3.1) kcal/mol	6.7 (4.4) kcal/mol
	Secondary	1.4 (0.6) kcal/mol	2.1 (1.3) kcal/mol	2.6 (0.6) kcal/mol
1-Butene	Primary	4.7 (3.8) kcal/mol	3.1 (2.7) kcal/mol	7.1 (4.6) kcal/mol
	Secondary	0.0 (0.1) kcal/mol	1.3 (0.5) kcal/mol	−0.4 (−2.7) kcal/mol

[a]The ΔE $(\Delta G)^{\#}_{stereo}$ and ΔE $(\Delta G^{\#})_{regio}$ values are calculated with respect to the favored monomer enantioface TSs.
[b]The ΔE $(\Delta G)^{\#}_{T\text{-}P}$ values are obtained by comparing the most stable TS for BHT (as reported in the main text) with the favored monomer enantioface insertion TS into the growing polymer chain.

termination. For 1-butene polymerization, calculations have been performed by employing a -$CH_2CH(CH_2CH_3)CH_2CH_2CH_3$ group in order to reproduce the primary growing chain, instead the secondary chain, formed by a 2,1-last inserted butene unit, is simulated by a -$CH(CH_2CH_3)CH_2CH_2CH_2CH_3$ group. For propene polymerization, instead, calculations with ^{i}Bu group simulating the primary growing chain and a ^{s}Bu group simulating a secondary chain with the 2,1-last inserted propene unit have been used.

Results and discussion

The results of DFT calculations on the mechanistic aspects of 1-butene polymerization promoted by catalyst **1** are summarized in Table 1, including data obtained from propene polymerization for comparative analysis.

The calculated stereoselectivities on a primary growing chain reveal a remarkable similarity between propene and 1-butene as indicated by the ΔE $(\Delta G)^{\#}_{stereo}$ values in Table 1 (Mercandelli et al., 2007). This congruence aligns with the established concept that stereocontrol originates from the chiral orientation of the growing chain, as elucidated by (Corradini et al., 2004). The TS structures, depicted in Supplementary Figure S1, show the stabilization of the chiral conformation of the polymer chain and DFT calculation highlights the pivotal role of α-agostic interaction in enhancing the stability of the chiral arrangement for both propene and 1-butene monomers (Talarico and Budzelaar, 2016). Furthermore, the utilization of a secondary growing chain results in a substantial loss of stereoselectivity, consistent with the proposed model. The close resemblance between the TS structures for propene and 1-butene in this context (Supplementary Figure S2) is indicative of Gibbs energies approaching zero (0.6 kcal/mol for propene and 0.1 kcal/mol for 1-butene).

DFT calculations of the regioselectivity observed in the polymerization of propene and 1-butene, is still emphasizing the similarity between the two monomers (Ratanasak et al., 2021). The ΔE $(\Delta G)^{\#}_{regio}$ values in Table 1 underscore the consistent regioselectivity in both cases. It is well-established that 2,1 insertions are unlikely to occur in α-olefin polymerization catalyzed by metallocene catalysts, attributed to electronic and steric factors, (Correa et al., 2007). The energetic profiles of the TS structures for propene and 1-butene on a primary chain, as depicted in Supplementary Figure S3, exhibit striking similarities. A nuanced analysis of regioselectivity with a secondary chain reveals a smaller variation for propene (1.3 kcal/mol) compared to almost complete loss for 1-butene (0.5 kcal/mol), as illustrated in Supplementary Figure S4. Moving from a primary to a secondary chain results in a substantial decrease in regioselectivity, measuring 1.8 kcal/mol for propene and 2.2 kcal/mol for 1-butene. The impact of the secondary chain is more pronounced in 1-butene polymerization, where the more encumbered ethyl group interacts with the 2,1-last inserted unit (Supplementary Figure S4).

Overall, the calculated values for ΔE $(\Delta G)^{\#}_{stereo}$ and ΔE $(\Delta G)^{\#}_{regio}$ of Table 1 with primary and/or secondary growing chain still did not account for the peculiarity of the 1-butene polymerization kinetics as well as the microstructures reported experimentally for the two α-olefins highlighted in the Introduction. So, we decided to investigate the termination reactions and their energetic comparison with the propagation steps.

Our initial analysis involves a comparison of the preferred TSs for propagation and termination reactions, considering the active species with a primary chain derived from a 1,2-last inserted unit. The chain release can occur via two types of β-hydrogen transfers: β-H transfer to the monomer (BHT) and β-hydrogen elimination (BHE), where a β-H is transferred from the growing polymer chain to the metal (Cavallo and Guerra, 1996). For system **1** the BHT plays a fundamental role in lowering the molecular weight of the obtained polymer. As a matter of fact, modifications of the ligand framework by adding a Me substituent at the position 2 of the indenyl group destabilize the spatially demanding 6-centers TS of the BHT with respect to the 4-centers TS of the propagation and samples characterized by higher molecular weight are obtained (Stehling et al., 1994). Therefore, the free energies of the preferred TSs with propene and 1-butene insertion into a primary growing polymer chain (Figures 1A, C) and their favoured TSs for the termination via BHT from a primary chain (Figures 1B, D), are compared (Laine et al., 2010). The calculated ΔE $(\Delta G)^{\#}_{T\text{-}P}$ reported in Table 1 show that the TS for BHT is higher in free energy than for propagation and still the propene ($\Delta G^{\#}_{T\text{-}P}$ = 4.4. kcal/mol) and 1-butene ($\Delta G^{\#}_{T\text{-}P}$ = 4.6 kcal/mol) results predict homopolymers with similar molecular mass if termination reaction occurs by a primary growing chain.

Taking into account that, as already mentioned in the introduction section, more regioselective metallocene complexes seem to lead to iPB characterized by higher molecular weight (Resconi et al., 2006), we hyphotesized a direct correlation between the occurrence of regioerrors and molecular mass so we extended our study to the analysis of species bearing a secondary chain, formed by a 2,1-last inserted unit.

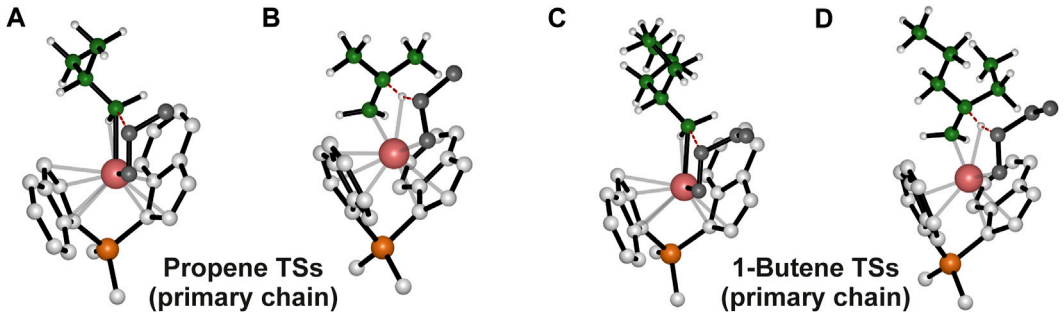

FIGURE 1
DFT optimized structures of the preferred propene **(A)** and 1-butene **(C)** insertion into a primary growing polymer chain TSs and the β-H transfer from the primary chain to propene **(B)** and 1-butene **(D)** monomers TSs. The hydrogen atoms belonging to the monomer and the ligand are omitted for simplicity. The growing polymer chain and the monomer are represented in green and grey, respectively.

It is important to highlight that termination reactions occurring in the presence of a 2,1-last inserted unit lead to a much more complicated *scenario* with respect to the case of a primary growing chain. In fact, for a secondary chain, there are two β-hydrogens prone to be transferred to the monomer (BHT) or to the metal (BHE) belonging to two different methylene groups, the one of the main chain and the other of the side ethyl group. Moreover, both BHT and BHE give an internal double bond, which can be *cis* or *trans* in configuration (Scheme 2).

The most relevant BHT and BHE TS structures for 1-butene polymerization are reported in Supplementary Figures S5, S6, and their electronic (Gibbs) energies values are reported in Supplementary Tables S1, S2.

Interestingly, we found that the ΔE $(\Delta G)^{\#}_{T\text{-}P}$ for propene polymerization by a secondary chain is still positive (2.6 (0.6) kcal/mol, Table 1) favoring the propagation (Figure 2A) over the termination (Figure 2B) (Caporaso et al., 2010). The calculated ΔE $(\Delta G)^{\#}_{T\text{-}P}$ for 1-butene changes dramatically and the insertion (Figure 2C) is highly disfavored with respect to the termination (Figure 2D) with a $(\Delta G)^{\#}_{T\text{-}P}$ = −2.7 kcal//mol. The preferred BHT corresponds to the β-H transfer from the methylene of the main chain to the 1,2 1-butene (Figure 2D) and it is the most stable among the analyzed BHT TSs since both the alkyl groups linked to the forming double C-C bond are oriented in the less hindered area of the ligand framework. Furthermore, this TS leads to the formation of a *cis*-3,4-pentenyl chain end group, which has been experimentally observed through ^{13}C NMR spectra analysis (Resconi et al., 2006).

Therefore, it can be stated that when a 1-butene regioirregular unit is inserted, the termination step is favored over propagation. Catalysts that are not fully regioselective give low molecular weight iPB, due to the synergistic effect of a destabilized 1-butene insertion (monomer-chain interaction) and a stabilized termination TSs.

In fact, it is noteworthy that β-H transfer from a primary growing chain TS, which is higher in energy than the respective propagation TS, is characterized by a disfavoring interaction between the monomer and the side ethyl group (Figure 1D), instead no destabilizing interactions are present in the TS in which the β-H is transferred from a secondary chain. Hence, differently from what happens with 1-butene, 2,1 propene units can be incorporated in the main chain and high molecular weight polymers are obtained also by employing catalysts not fully regioselective.

Concerning the TSs for the BHE reactions, we found that the most stable TS is the one reported in Figure 3A, which corresponds to a β-H transfer from the ethyl side group to the metal. It should yield a *trans*-2,3-pentenyl chain end group, which, however, has never been detected experimentally. In fact, they can be considered as the starting point for the stepwise isomerization mechanism leading to 4,1 units in the iPB main chain.

As already mentioned in the introduction section, the isomerization mechanism is still uncertain and both a stepwise and a concerted mechanism have been proposed (Busico et al., 1995). DFT calculations have been employed to evaluate both the mechanisms. Figure 4 reports the energy profiles where the pathway for the stepwise isomerization mechanism is represented in black, and the concerted one is shown in red. Let us first discuss the stepwise mechanism. The reference point (INT1) is the catalyst which bears a secondary growing polymer chain stabilized by a β-agostic interaction between the metal and the H atom of the methylene belonging to the ethyl side group. INT1 evolves into the TS determining the first BHE of the reaction pathway: the H involved in the β-agostic is transferred to the Zr atom, an extra β-agostic interaction contributes to the stabilization of the TS. The *trans* configuration of the growing chain yields an intermediate (INT2) showing a *trans* 2,3 C=C bond (INT2). At this point, a 180° rotation of the olefin around the metal center occurs. The TS for this rotation (TS ROT1) was found to be the highest energy TS of the whole isomerization path, thus being the rate determining step (rds). It is destabilized by the unfavorable orientation of the olefin, indeed both the alkyl groups (Me and *n*-Butyl groups) linked to the C=C bond point towards the indenyl ligands. TS ROT1 leads to INT2a, which is about 1 kcal/mol higher in energy with respect to the previous intermediate. The reaction proceeds with the reinsertion of the rotated olefin into the Zr-H bond (TS INS1) and the formation of INT3 intermediate. INT3 corresponds to a 3,1 unit and shows a β-agostic interaction between a hydrogen from the methyl group and the metal atom. It evolves in the TS BHE2 by the H transfer to the metal center and into the formation of a terminal double bond (INT4). Also in this case, an additional β-agostic interaction enables the stabilization of the TS. Again, the rotation of the formed double

10.3389/fchem.2024.1377740

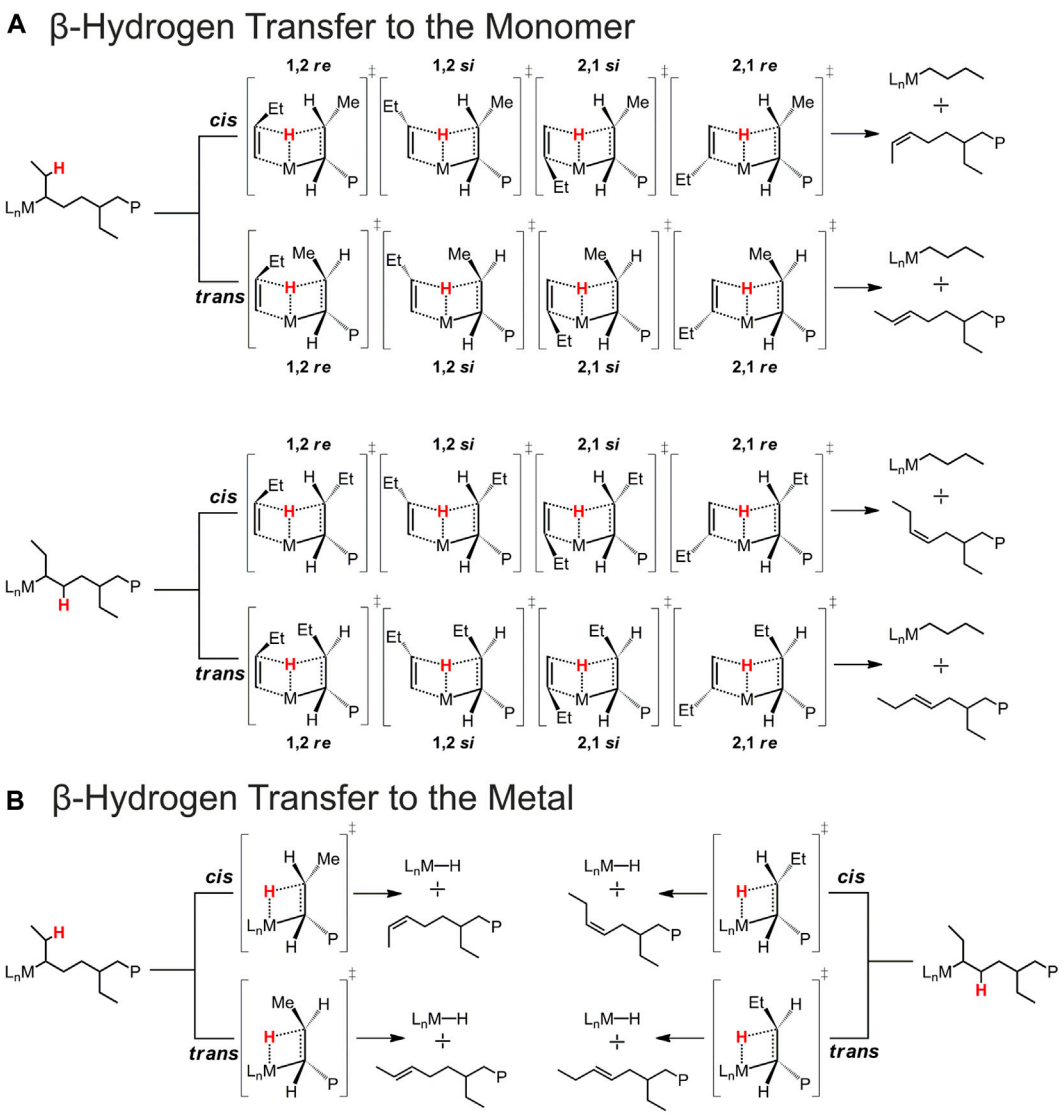

SCHEME 2
Schematic representation of the possible BHT and BHE TSs occurring after a 2,1 1-butene insertion leading to different chain end groups. **(A)** β-Hydrogen transfer to the monomer. **(B)** β-Hydrogen transfer to the metal.

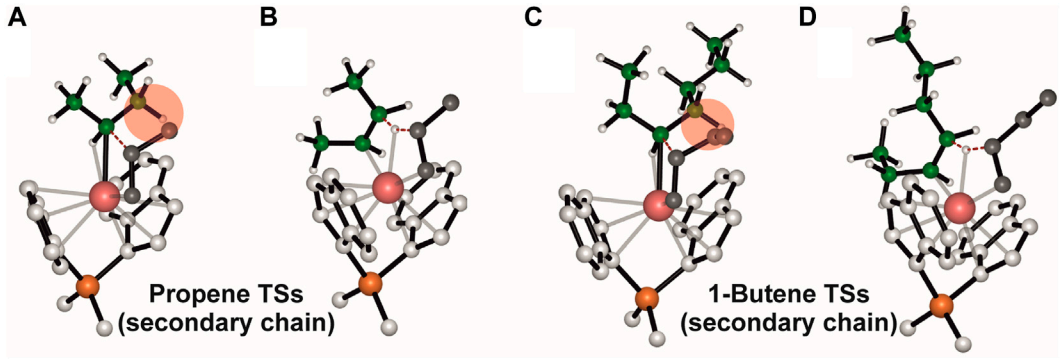

FIGURE 2
DFT optimized structures of the "right" propene **(A)** and 1-butene **(C)** enantioface insertion into a secondary growing polymer chain TSs and the β-H transfer from the secondary chain to (1,2) propene **(B)** and 1-butene **(D)** TSs. The hydrogen atoms belonging to the monomer and the ligand are omitted for simplicity. The growing polymer chain and the monomer are represented in green and grey, respectively.

10.3389/fchem.2024.1377740

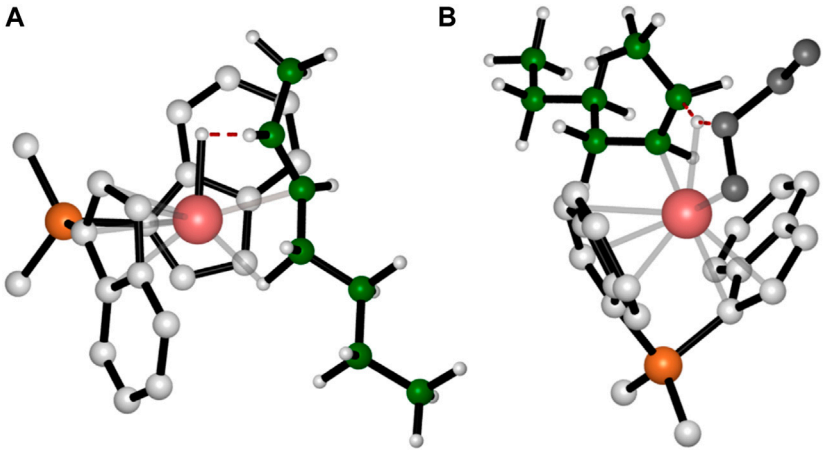

FIGURE 3
DFT optimized structures of the favorite TSs for BHE **(A)** and BHT **(B)** occurring after the epimerization of the secondary chain. For simplicity the hydrogen atoms belonging to the monomer and the ligand are omitted. The growing polymer chain and the monomer are represented in green and grey, respectively.

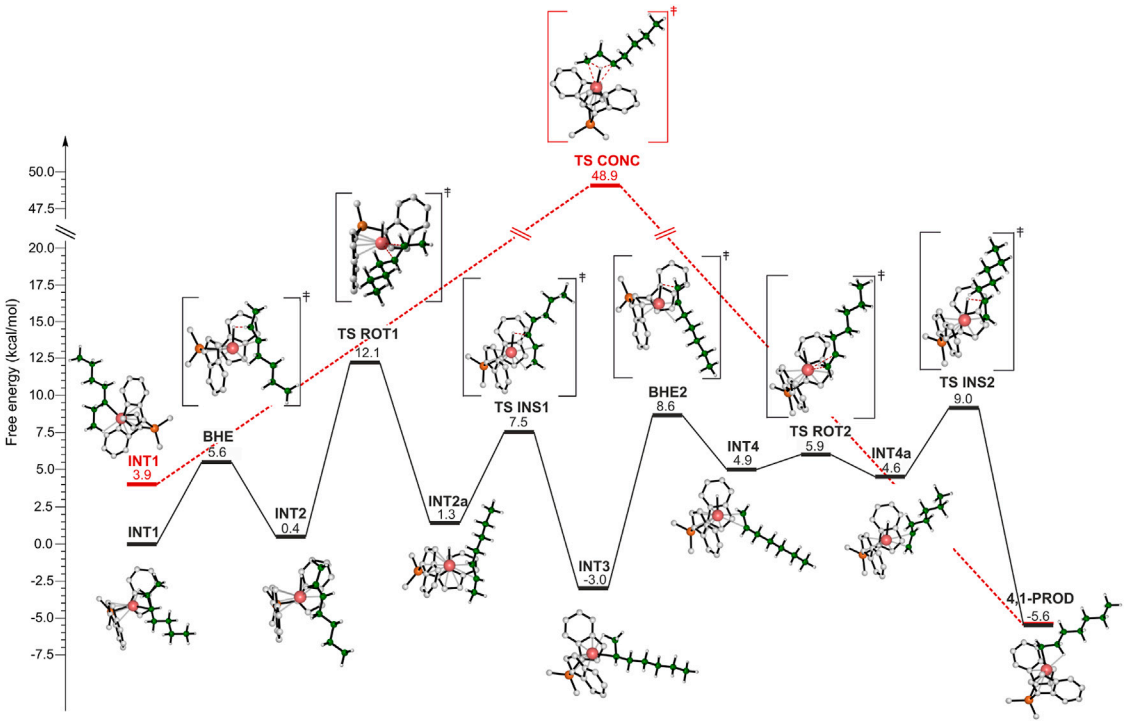

FIGURE 4
DFT calculated energy profile for the stepwise (black) and concerted (red) isomerization mechanisms leading to 4,1 units.

bond occurs. After the rotation, re-insertion of the unsaturated terminal unit into the Zr-H bond takes place and the 4,1 unit is formed.

It is important to highlight that both thermodynamics and kinetics account for the lack of 3,1-units in the main chain of iPB. The 4,1-unit product is more stable than the 3,1-unit and the whole activation energy of the path from 3,1 to 4,1-unit is comparable with the rds energy involved in the formation of the 3,1-unit (Figure 4).

The structures of the species involved in the concerted mechanism are reported for clarity also in Figure 5. The intermediate (Figure 5A) displays a γ-agostic interaction that involves a hydrogen of the methyl group and precedes the TS (Figure 5B), which gives directly the 4,1 product from a 2,1-last inserted unit. The hydrogen belonging to

10.3389/fchem.2024.1377740

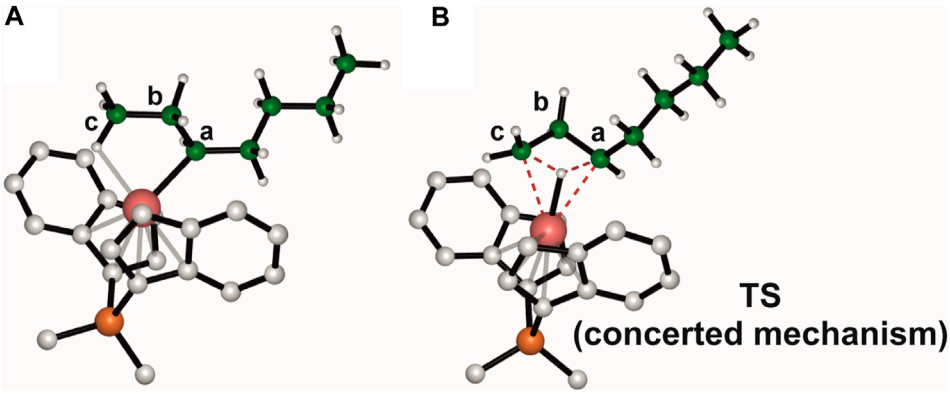

FIGURE 5
DFT optimized geometries for the γ-agostic secondary chain intermediate **(A)** and the TS governing the concerted isomerization mechanism **(B)**.

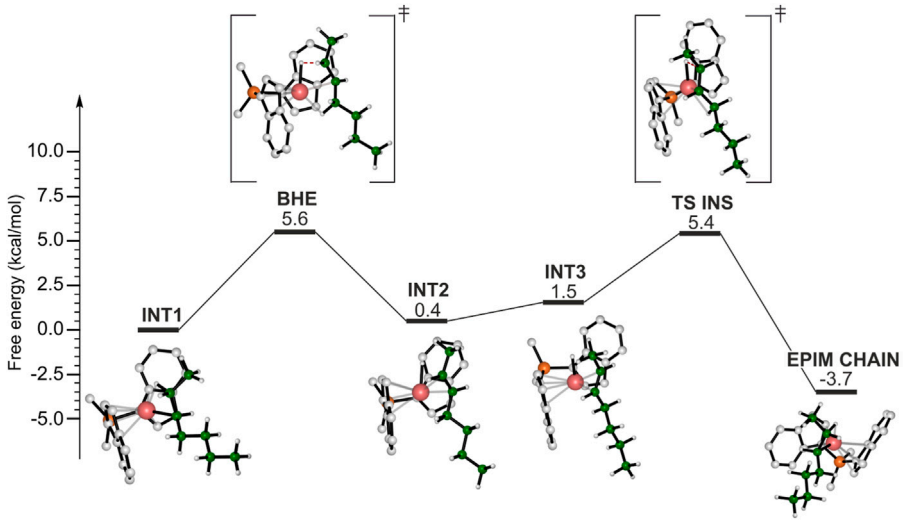

FIGURE 6
DFT calculated energy profile for the epimerization of the secondary chain.

the carbon atom **c** is transferred to the carbon **a**, meanwhile the hydrogen atom interacts with the metal center and the bond between the zirconium and carbon **c** is formed. Although the concerted mechanism seems easier than the stepwise one, DFT calculations indicate that the TS involved in the former is 36.8 kcal/mol higher in free energy than the TS governing the rate limiting step of the latter (TS ROT1).

The 3,1-unit is not observed in the iPB main chain likely due to the kinetics and thermodynamics of the stepwise isomerization path, which result in its transformation in the 4,1-unit, rather than the occurrence of a concerted isomerization mechanism.

Therefore, once a 2,1-unit is inserted, either termination occurs, or a 4,1-unit is formed, and a primary alkyl group linked to the metal center is obtained. In the latter case the propagation can continue and the molecular weight of the achieved PB is slightly higher than what expected from the $\Delta\Delta G^{\#}_{T\text{-}P}$ value.

Finally, we hypothesized that epimerization of the secondary chain may provide an alternative route to isomerization. The calculated DFT energy profile is shown in Figure 6. The reference point is the same as the isomerization and the BHE consists in the H transfer from the methylene of the ethyl side group of the chain leading to the INT2 intermediate, displaying a double bond in *trans* configuration. At this point the epimerization reaction pathway differs from the isomerization one: in the latter the formed double bond rotates around the metal center, instead, in this case the olefin reinserts with the opposite enantioface (TS INS) and a secondary chain characterized by an inversed configuration of the chiral carbon atom is formed (EPIM CHAIN). The epimerization is likely to occur due to its thermodynamic driving force (Figure 6).

Once the epimerization has taken place, termination is still preferred over propagation. In fact, we found that the favored BHT occurring after the epimerization of the secondary chain involves the transfer of the β-H belonging to the methylene of the ethyl group to the 1,2 *re* butene enantioface, exhibits the incoming C=C bond in a *cis* configuration (Figure 3B) and is

3.0 kcal/mol lower in energy with respect to the favored butene insertion TS (see Supplementary Figure S7).

The occurrence of the epimerization of the secondary chain followed by the BHT governed by the aforementioned TS is corroborated by the ^{13}C NMR analysis, which indicates also the presence of *cis*-2,3-pentenyl chain end groups (Resconi et al., 2006). The structures of the relevant BHT TSs from the epimerized chain and their relative energies are reported in Supplementary Figure S8; Supplementary Table S3, respectively.

Conclusion

In this work a comprehensive mechanistic study of 1-butene polymerization promoted by a C_2-symmetric *ansa*-metallocene prototype complex has been carried out by using DFT calculations.

Our findings offer valuable insights into the impact of regioerrors on 1-butene kinetics (Kim et al., 2021), revealing a preference for chain termination from a secondary growing chain over propagation. This observation elucidates the lower molecular weight observed in isotactic polybutene (iPB) samples produced by the *ansa*-metallocene systems.

Upon the insertion of a 2,1 butene unit, our study identifies an alternative route to termination reactions through the isomerization of regioirregular units. Both stepwise and concerted mechanisms, previously proposed in the literature, have been modeled. DFT results consistently support the stepwise mechanism as the most feasible, highlighting the formation of 3,1-units that convert into more thermodynamically stable 4,1-units.

These insights are not confined to the specific C_2-symmetric metallocene system studied herein but are extendable to other analogous systems. The presented findings lay the groundwork for future endeavors focused on enhancing the molecular weight of iPB samples, with the hopes to enlarge the polymer molecular architectures as already reported for iPP (De Rosa et al., 2017; De Rosa et al., 2018; De Rosa et al., 2020b) overcoming the main drawbacks of an "old" but still interesting material (Han et al., 2022).

Data availability statement

The raw data supporting the conclusion of this article will be made available by the authors, without undue reservation.

Author contributions

OD'A: Conceptualization, Investigation, Writing–original draft. CD: Supervision, Writing–review and editing. GT: Conceptualization, Investigation, Supervision, Writing–review and editing.

Funding

The author(s) declare financial support was received for the research, authorship, and/or publication of this article. GT thanks the Italian Ministry of University and Research (PRIN 2022, CUP E53D23008360006) for funding. The authors declare that the funder was not involved in the study design, collection, analysis, interpretation of data, the writing of this article, or the decision to submit it for publication.

Conflict of interest

The authors declare that the research was conducted in the absence of any commercial or financial relationships that could be construed as a potential conflict of interest.

The author(s) declared that they were an editorial board member of Frontiers, at the time of submission. This had no impact on the peer review process and the final decision.

Publisher's note

Supplementary material

The Supplementary Material for this article can be found online at: https://www.frontiersin.org/articles/10.3389/fchem.2024.1377740/full#supplementary-material

References

Becke, A. D. (1988). Density-functional exchange-energy approximation with correct asymptotic behavior. *Phys. Rev. A* 38, 3098–3100. doi:10.1103/physreva.38.3098

Borriello, A., Busico, V., Cipullo, R., Fusco, O., and Chadwick, J. C. (1997). Isotactic 1-butene polymerization promoted by C_2-symmetric metallocene catalysts. *Macromol. Chem. Phys.* 198, 1257–1270. doi:10.1002/macp.1997.021980427

Busico, V., Chadwick, J. C., Cipullo, R., Ronca, S., and Talarico, G. (2004). Propene/Ethene-[1-13C] copolymerization as a tool for investigating catalyst regioselectivity. $MgCl_2$/Internal donor/$TiCl_4$–External donor/AlR_3 systems. *Macromolecules* 37, 7437–7443. doi:10.1021/ma049104a

Busico, V., and Cipullo, R. (1995). Growing chain isomerizations in metallocene-catalyzed Ziegler-Natta 1-alkene polymerization. *J. Organomet. Chem.* 497, 113–118. doi:10.1016/0022-328x(95)00101-u

Busico, V., Cipullo, R., and Borriello, A. (1995). Regiospecificity of 1-butene polymerization catalyzed by C_2-symmetric group IV metallocenes. *Macromol. Rapid Commun.* 16, 269–274. doi:10.1002/marc.1995.030160407

Busico, V., Cipullo, R., Pellecchia, R., Ronca, S., Roviello, G., and Talarico, G. (2006). Design of stereoselective Ziegler–Natta propene polymerization catalysts. *Proc. Natl. Acad. Sci. U.S.A.* 103, 15321–15326. doi:10.1073/pnas.0602856103

Busico, V., Cipullo, R., Romanelli, V., Ronca, S., and Togrou, M. (2005). Reactivity of secondary Metal–Alkyls in catalytic propene polymerization: how dormant are "dormant chains". *J. Am. Chem. Soc.* 127, 1608–1609. doi:10.1021/ja042839a

Busico, V., Cipullo, R., Talarico, G., Segre, A. L., and Caporaso, L. (1998). High-field ^{13}C NMR characterization of ethene-1-^{13}C/propene copolymers prepared with C_s-symmetric *ansa*-metallocene catalysts: a deeper insight into the regio- and

stereoselectivity of syndiotactic propene polymerization. *Macromolecules* 31, 8720–8724. doi:10.1021/ma9810417

Caporaso, L., De Rosa, C., and Talarico, G. (2010). The relationship between catalyst precursors and chain end groups in homogeneous propene polymerization catalysis. *J. Polym. Sci. A Polym. Chem.* 48, 699–708. doi:10.1002/pola.23831

Cavallo, L., and Guerra, G. (1996). A density functional and molecular mechanics study of β-hydrogen transfer in homogeneous Ziegler–Natta catalysis. *Macromolecules* 29, 2729–2737. doi:10.1021/ma9511412

Corradini, P., Barone, V., Fusco, R., and Guerra, G. (1979). Analysis of models for the Ziegler-Natta stereospecific polymerization on the basis of non-bonded interactions at the catalytic site—I. The Cossee model. *Eur. Polym. J.* 15, 1133–1141. doi:10.1016/0014-3057(79)90048-x

Corradini, P., Guerra, G., and Cavallo, L. (2004). Do new century catalysts unravel the mechanism of stereocontrol of old ziegler-natta catalysts? *Acc. Chem. Res.* 37, 231–241. doi:10.1021/ar030165n

Correa, A., Talarico, G., and Cavallo, L. (2007). Regiochemistry of propene insertion with group 4 polymerization catalysts from a theoretical perspective. *J. Organomet. Chem.* 692, 4519–4527. doi:10.1016/j.jorganchem.2007.04.015

Cossi, M., Barone, V., Cammi, R., and Tomasi, J. (1996). *Ab initio* study of solvated molecules: a new implementation of the polarizable continuum model. *Chem. Phys. Lett.* 255, 327–335. doi:10.1016/0009-2614(96)00349-1

De Rosa, C., Auriemma, F., and Resconi, L. (2009a). Metalloorganic polymerization catalysis as a tool to probe crystallization properties of polymers: the case of isotactic poly(1-butene). *Angew. Chem. Int. Ed.* 48, 9871–9874. doi:10.1002/anie.200904300

De Rosa, C., Auriemma, F., Ruiz de Ballesteros, O., Esposito, F., Laguzza, D., Di Girolamo, R., et al. (2009b). Crystallization properties and polymorphic behavior of isotactic poly(1-butene) from metallocene catalysts: the crystallization of form I from the melt. *Macromolecules* 42, 8286–8297. doi:10.1021/ma901453x

De Rosa, C., Auriemma, F., Villani, M., Ruiz de Ballesteros, O., Di Girolamo, R., Tarallo, O., et al. (2014). Mechanical properties and stress-induced phase transformations of metallocene isotactic poly(1-butene): the influence of stereodefects. *Macromolecules* 47, 1053–1064. doi:10.1021/ma402239k

De Rosa, C., Di Girolamo, R., Auriemma, F., Talarico, G., Malafronte, A., Scarica, C., et al. (2017). Controlling size and orientation of lamellar microdomains in crystalline block copolymers. *ACS Appl. Mater. Interfaces* 9, 31252–31259. doi:10.1021/acsami.6b15913

De Rosa, C., Di Girolamo, R., Malafronte, A., Scoti, M., Talarico, G., Auriemma, F., et al. (2020b). Polyolefins based crystalline block copolymers: ordered nanostructures from control of crystallization. *Polymer* 196, 122423. doi:10.1016/j.polymer.2020.122423

De Rosa, C., Ruiz de Ballesteros, O., Auriemma, F., Talarico, G., Scoti, M., Di Girolamo, R., et al. (2019). Crystallization behavior of copolymers of isotactic poly(1-butene) with ethylene from ziegler–natta catalyst: evidence of the blocky molecular structure. *Macromolecules* 52, 9114–9127. doi:10.1021/acs.macromol.9b01570

De Rosa, C., Ruiz de Ballesteros, O., Di Girolamo, R., Malafronte, A., Auriemma, F., Talarico, G., et al. (2020a). The blocky structure of Ziegler–Natta "random" copolymers: myths and experimental evidence. *Polym. Chem.* 11, 34–38. doi:10.1039/c9py01485c

De Rosa, C., Scoti, M., Auriemma, F., Ruiz de Ballesteros, O., Talarico, G., Di Girolamo, R., et al. (2018). Relationships among lamellar morphology parameters, structure and thermal behavior of isotactic propene-pentene copolymers: the role of incorporation of comonomeric units in the crystals. *Eur. Polym. J.* 103, 251–259. doi:10.1016/j.eurpolymj.2018.04.001

Falivene, L., Barone, V., and Talarico, G. (2018). Unraveling the role of entropy in tuning unimolecular *vs.* bimolecular reaction rates: the case of olefin polymerization catalyzed by transition metals. *Mol. Catal.* 452, 138–144. doi:10.1016/j.mcat.2018.04.012

Falivene, L., Cavallo, L., and Talarico, G. (2015). Buried volume analysis for propene polymerization catalysis promoted by group 4 metals: a tool for molecular mass prediction. *ACS Catal.* 5, 6815–6822. doi:10.1021/acscatal.5b01363

Frisch, M. J., Trucks, G. W., Schlegel, H. B., Scuseria, G. E., Robb, M. A., Cheeseman, J. R., et al. (2016). *Gaussian 16 rev. C.01*. Wallingford, CT: Gaussian, Inc.

Gianotti, G., and Capizzi, A. (1969). Butene-1/propylene copolymers. Influence of the comonomerie units on polymorphism. *Makromol. Chem.* 124, 152–159. doi:10.1002/macp.1969.021240116

Grimme, S., Antony, J., Ehrlich, S., and Krieg, H. (2010). A consistent and accurate *ab initio* parametrization of density functional dispersion correction (DFT-D) for the 94 elements H-Pu. *J. Chem- Phys.* 132, 154104. doi:10.1063/1.3382344

Han, J. W., Hollmann, F., Luque, R., Song, I. K., Talarico, G., Tatsumi, T., et al. (2022). Molecular catalysis for the Chemistry of the future: a perspective. *Mol. Catal.* 522, 112233. doi:10.1016/j.mcat.2022.112233

Hay, P. J., and Wadt, W. R. (1985). *Ab initio* effective core potentials for molecular calculations. Potentials for K to Au including the outermost core orbitals. *J. Chem. Phys.* 82, 299–310. doi:10.1063/1.448975

Hutley, T. J., and Ouederni, M. (2016). "Polyolefins—the history and economic impact," in *Polyolefin compounds and materials: fundamentals and industrial applications*. Editors M. Al-Ali Alma'adeed and I. Krupa (Cham: Springer International Publishing).

Jüngling, S., Mülhaupt, R., Stehling, U., Brintzinger, H.-H., Fischer, D., and Langhauser, F. (1995). Propene polymerization using homogeneous MAO-activated metallocene catalysts: $Me_2Si(Benz[e]Indenyl)_2ZrCl_2$/MAO vs. $Me_2Si(2\text{-}Me\text{-}Benz[e]Indenyl)_2ZrCl_2$/MAO. *J. Polym. Sci. Part A Polym. Chem.* 33, 1305–1317. doi:10.1002/pola.1995.080330813

Kim, Y., Samouei, H., and Hilty, C. (2021). Polyolefin catalysis of propene, 1-butene and isobutene monitored using hyperpolarized NMR. *Chem. Sci.* 12, 2823–2828. doi:10.1039/d0sc05408a

Laine, A., Linnolahti, M., Pakkanen, T. A., Severn, J. R., Kokko, E., and Pakkanen, A. (2010). Comparative theoretical study on homopolymerization of α-olefins by bis(cyclopentadienyl) zirconocene and hafnocene: elemental propagation and termination reactions between monomers and metals. *Organometallics* 29, 1541–1550. doi:10.1021/om900843h

Landis, C. R., Sillars, D. R., and Batterton, J. M. (2004). Reactivity of secondary metallocene alkyls and the question of dormant sites in catalytic alkene polymerization. *J. Am. Chem. Soc.* 126, 8890–8891. doi:10.1021/ja047547o

Lee, C., Yang, W., and Parr, R. G. (1988). Development of the Colle-Salvetti correlation-energy formula into a functional of the electron density. *Phys. Rev. B* 37, 785–789. doi:10.1103/physrevb.37.785

Luciani, L., Seppälä, J., and Löfgren, B. (1988). Poly-1-butene: its preparation, properties and challenges. *Prog. Polym. Sci.* 13, 37–62. doi:10.1016/0079-6700(88)90010-x

Makaryan, I. A., and Sedov, I. V. (2020). Analysis of the state and development prospects of the industrial catalysts market for polyolefins production. *Russ. J. Gen. Chem.* 90, 1141–1162. doi:10.1134/s1070363220060304

Mercandelli, P., Sironi, A., Resconi, L., and Camurati, I. (2007). Comparing propene polymerization with 1-butene polymerization catalyzed by MAO-activated C_2- and C_1-symmetric zirconocenes: an experimental and computational study on the influence of olefin size on stereoselectivity. *J. Organomet. Chem.* 692, 4784–4791. doi:10.1016/j.jorganchem.2007.06.021

Nakamura, K., Aoike, T., Usaka, K., and Kanamoto, T. (1999). Phase transformation in poly(1-butene) upon drawing. *Macromolecules* 32, 4975–4982. doi:10.1021/ma981735f

Natta, G., Corradini, P., and Bassi, I. W. (1960). Crystal structure of isotactic poly-alpha-butene. *Nuovo Cimento Suppl.* 15, 52–67. doi:10.1007/bf02731860

Natta, G., Pino, P., Corradini, P., Danusso, F., Mantica, E., Mazzanti, G., et al. (1955). Crystalline high polymers of a-olefins. *J. Am. Chem. Soc.* 77, 1708–1710. doi:10.1021/ja01611a109

Olabisi, O., and Adewale, K. (Eds.). (2016). *Handbook of thermoplastics*. (2nd ed.). Boca Raton: CRC Press. doi:10.1201/b19190

Petraccone, V., Pirozzi, B., Frasci, A., and Corradini, P. (1976). Polymorphism of isotactic poly-α-butene. Conformational analysis of the chain and crystalline structure of form 2. *Eur. Polym. J.* 12, 323–327. doi:10.1016/0014-3057(76)90159-2

Pilme, J., Busico, V., Cossi, M., and Talarico, G. (2007). A possible 2,1→3,1 isomerization mechanism in zirconocene-catalyzed propene polymerization: an application of the density functional theory and combined ONIOM approach. *J. Organomet. Chem.* 692, 4227–4236. doi:10.1016/j.jorganchem.2007.06.048

Qiao, Y., Wang, Q., and Men, Y. (2016). Kinetics of nucleation and growth of form II to I polymorphic transition in polybutene-1 as revealed by stepwise annealing. *Macromolecules* 49, 5126–5136. doi:10.1021/acs.macromol.6b00862

Ratanasak, M., Hasegawa, J.-y., and Parasuk, V. (2021). Design and prediction of high potent ansa-zirconocene catalyst for olefin polymerizations: combined DFT calculations and QSPR approach. *New J. Chem.* 45, 8248–8257. doi:10.1039/d1nj00655j

Resconi, L. (1999). On the mechanisms of growing-chain-end isomerization and transfer reactions in propylene polymerization with isospecific, C_2-symmetric zirconocene catalysts. *J. Mol. Cat. A Chem.* 146, 167–178. doi:10.1016/s1381-1169(99)00101-6

Resconi, L., Camurati, I., and Malizia, F. (2006). Metallocene catalysts for 1-butene polymerization *macromol. Chem. Phys.* 207, 2257–2279. doi:10.1002/macp.200600307

Resconi, L., Cavallo, L., Fait, A., and Piemontesi, F. (2000). Selectivity in propene polymerization with metallocene catalysts. *Chem. Rev.* 100, 1253–1346. doi:10.1021/cr9804691

Sauter, D. W., Taoufik, M., and Boisson, C. (2017). Polyolefins, a success story. *Polymers* 9, 185. doi:10.3390/polym9060185

Schäfer, A., Horn, H., and Ahlrichs, R. (1992). Fully optimized contracted Gaussian basis sets for atoms Li to Kr. *J. Chem- Phys.* 97, 2571–2577. doi:10.1063/1.463096

Schaffhauser, R. J. (1967). On the nature of the form II to from I transformation in isotactic polybutene-1. *J. Polym. Sci. Part B Polym. Lett.* 5, 839–841. doi:10.1002/pol.1967.110050920

Stehling, U., Diebold, J., Kirsten, R., Röll, W., Brintzinger, H. H., Jüngling, S., et al. (1994). Ansa-Zirconocene polymerization catalysts with anelated ring ligands - effects on catalytic activity and polymer chain length. *Organometallics* 13, 964–970. doi:10.1021/om00015a033

Talarico, G., Blok, A. N. J., Woo, T. K., and Cavallo, L. (2002). Comparison of *ab initio* and DFT methods for studying chain propagation and chain termination processes with group 4 polymerization catalysts. 1. The *ansa*-Bis(cyclopentadienyl)zirconium catalyst. *Organometallics* 21, 4939–4949. doi:10.1021/om020315i

Talarico, G., and Budzelaar, P. H. M. (2006). A second transition state for chain transfer to monomer in olefin polymerization promoted by group 4 metal catalysts. *J. Am. Chem. Soc.* 128, 4524–4525. doi:10.1021/ja0586034

Talarico, G., and Budzelaar, P. H. M. (2016). α-Agostic interactions and growing chain orientation for olefin polymerization catalysts. *Organometallics* 35, 47–54. doi:10.1021/acs.organomet.5b00866

Talarico, G., Busico, V., and Cavallo, L. (2003). Origin of the regiochemistry of propene insertion at octahedral column 4 polymerization catalysts: design or serendipity? *J. Am. Chem. Soc.* 125, 7172–7173. doi:10.1021/ja029604o

Talarico, G., De Rosa, C., and Auriemma, F. (2019). "Tacticity, regio and stereoregularity," in *Polypropylene handbook: morphology, blends and composites*. Editors J. Karger-Kocsis and T. Bárány (Cham: Springer International Publishing).

Tashiro, K., Hu, J., Wang, H., Hanesaka, M., and Saiani, A. (2016). Refinement of the crystal structures of forms I and II of isotactic polybutene-1 and a proposal of phase transition mechanism between them. *Macromolecules* 49, 1392–1404. doi:10.1021/acs.macromol.5b02785

Turner-Jones, A. (1963). Polybutene-1 - type II crystalline form. *J. Polym. Sci. Part B Polym. Lett.* 1, 455–456. doi:10.1002/pol.1963.110010815

Wadt, W. R., and Hay, P. J. (1985). *Ab initio* effective core potentials for molecular calculations. Potentials for main group elements Na to Bi. *J. Chem. Phys.* 82, 284–298. doi:10.1063/1.448800

Weigend, F., Furche, F., and Ahlrichs, R. (2003). Gaussian basis sets of quadruple zeta valence quality for atoms H–Kr. *J. Chem. Phys.* 119, 12753–12762. doi:10.1063/1.1627293

frontiers | Frontiers in Chemistry

TYPE Original Research
PUBLISHED 14 March 2024
DOI 10.3389/fchem.2024.1367451

OPEN ACCESS

EDITED BY
Marinos Pitsikalis,
National and Kapodistrian University of Athens, Greece

REVIEWED BY
Junjie Li,
Kyushu University, Japan
Tianyi Liu,
Brewer Science, United States

*CORRESPONDENCE
Baki Hazer,
bkhazer@beun.edu.tr

RECEIVED 01 February 2024
ACCEPTED 01 March 2024
PUBLISHED 14 March 2024

CITATION
Hazer B, Altunordu Kalaycı Ö and Koçak F (2024), Synthesis of fully bio-based poly (3-hydroxybutyrate)-oligo-2-ethyl oxazoline conjugates.
Front. Chem. 12:1367451.
doi: 10.3389/fchem.2024.1367451

Synthesis of fully bio-based poly (3-hydroxybutyrate)-oligo-2-ethyl oxazoline conjugates

Baki Hazer [1,2]*, Özlem Altunordu Kalaycı [3] and Fatma Koçak [2]

[1]Department of Aircraft Airframe Engine Maintenance, Kapadokya University, Ürgüp, Türkiye, [2]Departments of Chemistry/Nano Technology Engineering, Zonguldak Bülent Ecevit University, Zonguldak, Türkiye, [3]Departments of Physics, Zonguldak Bülent Ecevit University, Zonguldak, Türkiye

This work refers to the synthesis and characterization of poly (3-hydroxybutyrate)-b-oligo (2-ethyl oxazoline) (oligoEtOx). Cationic ring-opening polymerization of 2-ethyl oxazoline yielded poly (2-ethyl oxazoline) (oligoEtOx) with a hydroxyl end. Carboxylic acid-terminated PHB was reacted with oligoEtOx via dicyclohexylcarbodiimide chemistry to obtain PHB-b-oligoEtOx conjugates. The obtained PHB-b-oligoEtOx conjugates were successfully characterized by ^{1}H- and ^{13}C NMR, FTIR, DSC, and size exclusion chromatography. PHB-b-oligoEtOx conjugates can be promising biologic active materials.

KEYWORDS

bacterial polyester, PHB, oligo oxazoline, 2-ethyl oxazoline, cationic polymerization, two carboxylic acid-terminated PHB

Introduction

Poly (3-hydroxybutyrate) (PHB) is a microbial aliphatic biopolyester which is accumulated in bacterium cells from some carbon substrates (Ashby and Foglia, 1998; Kocer et al., 2003; Hazer and Steinbüchel, 2007; Chen, 2009; Ashby et al., 2019; Choi et al., 2020; Guzik et al., 2020; Bedade et al., 2021; Kacanski et al., 2023).

PHB is a crystalline polymer with melting transition (Tm) at approximately 170°C. It can also be synthesized by the anionic ring-opening polymerization of beta-butyrolactone (Hazer, 1996; Arkin et al., 2001).

The synthetic PHB is in R, S configuration, while bacterial PHB is only in R configuration (Caputo et al., 2022).

PHB modification reactions are important to prepare new PHB derivatives for some industrial and medical applications (Hazer, 2010; Hazer et al., 2012; Guennec et al., 2021). Some of them are halide derivatives (Arkin and Hazer, 2002; Yalcin et al., 2006; Erol et al., 2020), chitosan derivatives (Arslan et al., 2007), diethanol amine derivatives (Tuzen et al., 2016), trithiocarbonate derivatives (Hazer et al., 2020), methyl salicylate derivatives (Hazer et al., 2021), ricinoleic acid derivatives (Ullah et al., 2024), PEG derivatives (Hazer et al., 1999; Wadhwa et al., 2014), and caffeic acid derivatives (Abdelmalek et al., 2023).

Poly (2-ethyl-2-oxazoline) (oligoEtOx) is obtained by the cationic polymerization of 2-ethyl oxazoline (2-EtOx). OligoEtOx is a water-soluble polymer and is very popular in the field of biomedical and pharmaceutical applications (Vergaelen et al., 2023). Dual initiator techniques, including the carbocationic method and free radical polymerization, can be used to synthesize block copolymers (Hazer, 1991; Christova et al., 1997). In this manner, poly (2-ethyl-2-oxazoline) derivatives were successfully synthesized by polymer chemists

for medical applications (Miyamoto et al., 1989; Christova et al., 2002; Diab et al., 2004; Park et al., 2004; Hoogenboom et al., 2005; Becer et al., 2008; Li et al., 2021; Göppert et al., 2023).

Very recently, Becer et al. reported the synthesis of poly (2-ethyl oxazoline)-b-poly (acrylate) hybrid multiblock copolymers via a click reaction. They evaluate their self-assembly behavior into stomatocyte-like nanoparticles (Hayes et al., 2023). The multiamide structure of polyEtOx makes it a candidate to mimic peptides, and it shows an antibacterial effect against *Staphylococcus aureus* (Hoogenboom, 2009).

Poly (2-ethyl oxazoline) is a new class of functional peptide that mimics with potential in a variety of biological applications (Zhou et al., 2020). PolyEtOx is a thermosensitive polymer with a lower critical solution temperature (LCST), changing the aqueous solution temperature at approximately 62°C (Christova et al., 2003; Park and Kataoka, 2007; Obeid et al., 2009; Hoogenboom and Schlaad, 2011).

Winnik et al. reported the cloud point of aqueous methyl poly(I-propyl oxazoline) with Mn 10 K g/mol. Turbidity decreases with the increasing concentration from ~48°C to ~39°C.

Block copolymers containing hydrophilic and hydrophobic blocks gain the properties of both related blocks. These different polymer blocks can be arranged linearly or as brush-type copolymers (Minoda et al., 1990; Xu et al., 1991; Förster and Antonietti, 1998; Bronstein et al., 1999; Chen et al., 1999; Hu et al., 2008; Mai and Eisenberg, 2012; Kalayci et al., 2013; Glaive et al., 2024; Hosseini et al., 2024; Wang et al., 2024).

The insertion of the hydrophilic polymer in a block copolymer will improve the colloidal stability of the nanoparticles for biomedical applications (Balcı et al., 2010; Kalaycı et al., 2010; Karahaliloğlu et al., 2020; Wen et al., 2023; Kilicay et al., 2024).

PHB is a commercially available biodegradable natural aliphatic polyester for some biomedical applications, such as implant biomaterials, tissue engineering, and food packaging applications (Chen and Zhang, 2018; Mehrpouya et al., 2021; Abdelmalek et al., 2023). PHB derivatives can be used as novel biodegradable adsorbents for analytical applications (Wadhwa et al., 2014; Unsal et al., 2015; Tuzen et al., 2016; Altunay et al., 2020; Ullah et al., 2024; Ali et al., 2024) for drug delivery systems (Bayram et al., 2008; Kılıcay et al., 2011; Kilicay et al., 2024).

In this work, we report the synthesis of poly (3-hydroxybutyrate)-oligo-2-ethyl oxazoline, fully bio-based amphiphilic polymer conjugates. Two carboxyl-terminated PHB were synthesized by refluxing PHB with adipic acid in the presence of Stannous octoate. Then, the carboxyl-terminated PHB was reacted with the hydroxyl end of oligooxazoline, which was obtained by the ring-opening cationic polymerization of 2-ethyl oxazoline. The physicochemical characterization of the PHB-oligo-2-ethyl oxazoline conjugates was carried out in detail.

Experiment

Materials

2-Ethyl oxazoline (2-EtOx) was supplied from Sigma-Aldrich and was passed into the Al_2O_3 column before use. N, N′-Dicyclohexylcarbodiimide (DCC; 99%), dimethylaminopyridine (DMAP; 99%), stannous 2-ethylhexanoate (Sn-oct; ≥92.5%), methyl p-toluene sulfonate (MepTs), and all other chemicals were purchased from Sigma-Aldrich. Poly (3-hydroxybutyrate) (PHB) and microbial polyester (Mn 187,000 g/mol, Mw/Mn 2.5, Biomer Inc.) were supplied from Biomer (Germany) (Neugebauer et al., 2007).

Synthesis of oligo(2-ethyl oxazoline) (oligoEtOx)

2-Ethyl oxazoline was oligomerized by ring-opening cationic polymerization. A mixture of 2-ethyl oxazoline (2.01 g) and MepTs (0.20 g) as the catalyst was dissolved in acetonitrile (AcCN, 2.0 mL) in a reaction bottle. Argon was passed through the solution for 2 min. Polymerization was carried out at 100°C for 70 min. The polymer precipitated in excess diethyl ether. It was dried under vacuum at 40°C for 24 h (yield: 1.98 g, Mn 900 g/mol, and PDI: 1.57).

Synthesis of dicarboxylic acid-terminated PHB, PHB-COOH

A mixture of adipic acid (1.00 g), PHB (0.64 g), and Sn-oct (20 mg) was dissolved in $CHCl_3$ (20 mL). It was refluxed at 85°C for 4 h. After half of the solvent was evaporated, the product was precipitated from excess methanol and dried under vacuum at 40°C for 24 h. The yield was 0.86 g.

Characterization

^{1}H NMR spectra were taken with an Agilent NMR 600 MHz NMR (Agilent, Santa Clara, CA, United States) spectrometer equipped with a 3-mm broadband probe. FT-IR spectra of the substituted polymer samples were recorded using a Bruker Model, Tensor II instrument with the ATR technique in the transmissive mode and a scan rate of 4,000 to 450 cm^{-1}. A Viscotek GPCmax autosampler system, consisting of a pump, three ViscoGEL GPC columns (G2000H HR, G3000H HR, and G4000H HR), and a Viscotek differential refractive index (RI) detector, was used to determine the molecular weights of the polymer products. A calibration curve was generated with five polystyrene (PS) standards of molecular weight 2,960, 8,450, 50,400, 200,000, and 696,500 Da with low polydispersity. Data were analyzed using Viscotek OmniSEC Omni 01 software. Differential scanning calorimetry (DSC) was used in the thermal analysis of the obtained polymers. The DSC analysis was carried out under nitrogen using a TA Q2000 DSC instrument that was calibrated using indium (Tm = 156.6°C) and a Q600 Simultaneous DSC-TGA (SDT) series thermal analysis system. DSC measures the temperatures and heat flows associated with thermal transitions in the polymer samples obtained. The dried polymer samples were heated from −60°C to 220°C under a nitrogen atmosphere. All melting endotherms (Tm) were reported as peak temperatures, while all glass transition temperatures (Tg) were reported as midpoint temperatures. Thermogravimetric analysis (TGA) was

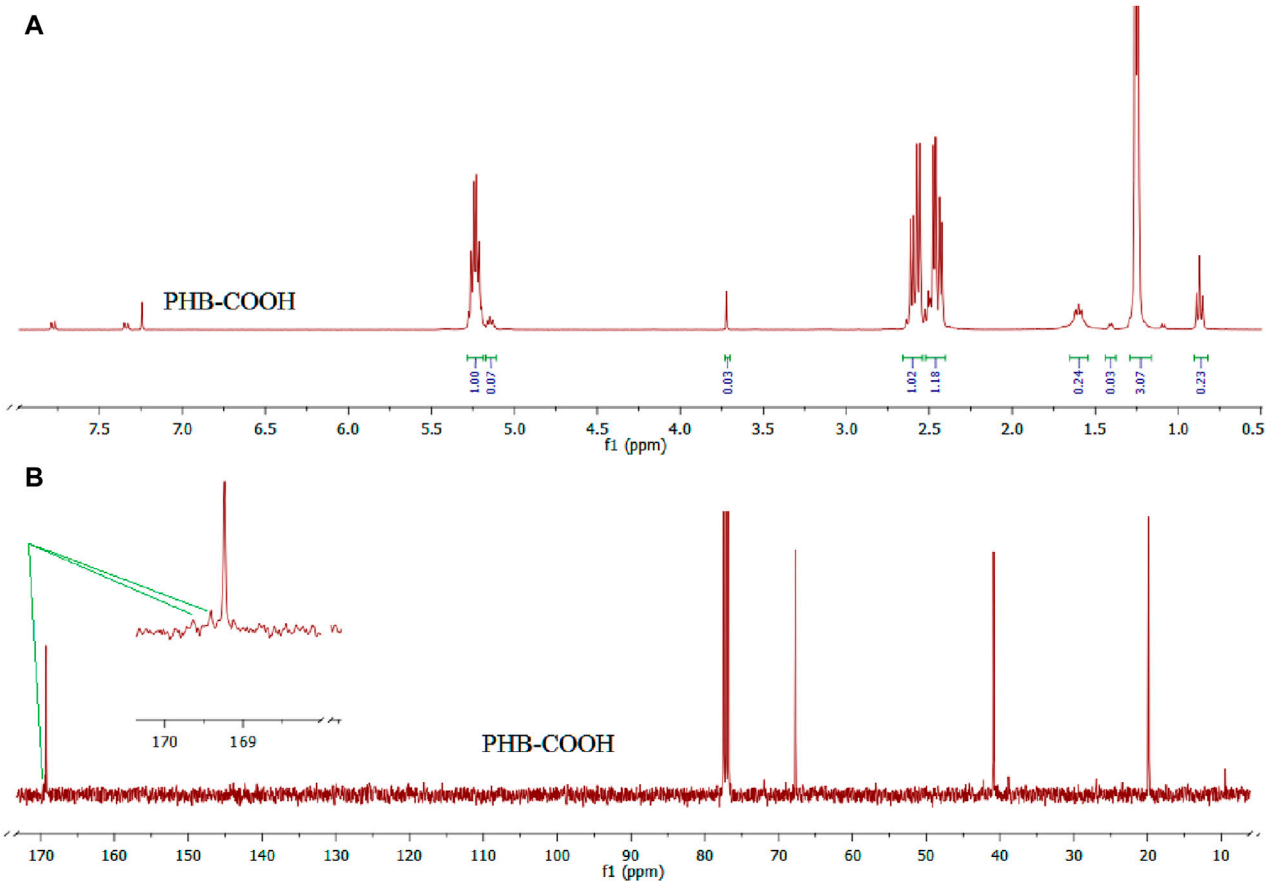

FIGURE 1
1H **(A)** and 13C **(B)** NMR spectra of the PHB-COOH sample.

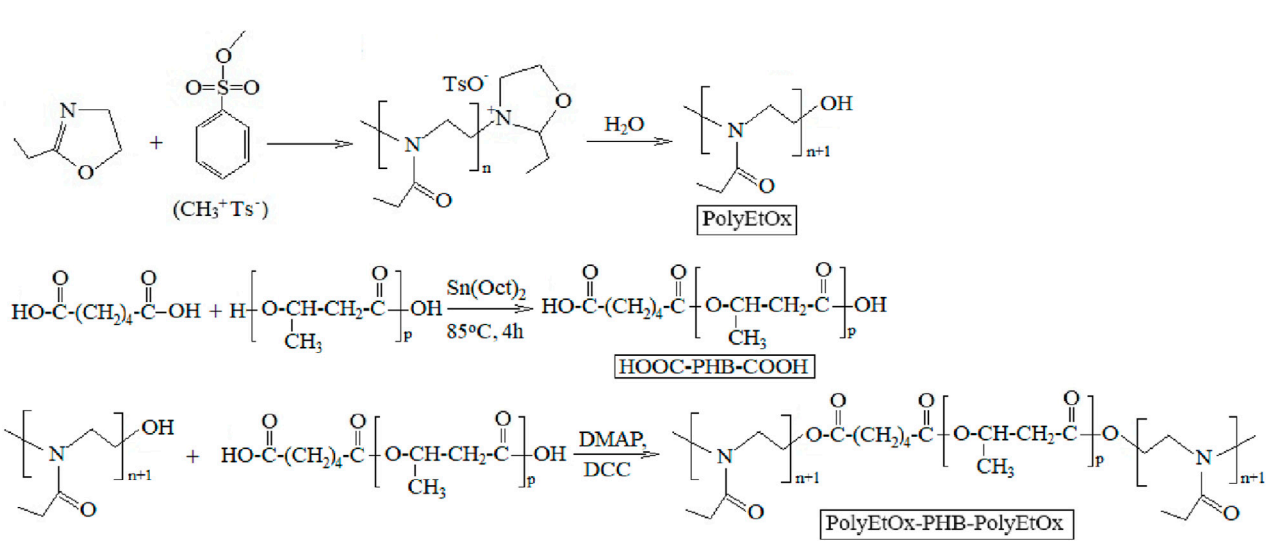

FIGURE 2
Reaction pathways of the synthesis of the oligoEtOx-b-PHB block copolymer.

used to determine the decomposition temperature (T_d) characteristics of the polymers by measuring the weight loss under a nitrogen atmosphere over time. In these analyses, the obtained polymers were heated from 20°C to 600°C at a rate of 10°C/min, and the results were determined based on the first derivative of each curve. Scanning electron microscopy (SEM)

10.3389/fchem.2024.1367451

TABLE 1 Synthesis conditions and results of the PHB-b-oligoEtOx block copolymer at room temperature for 24 h.

Code	PHB(COOH)$_2$ (g)	PolyOx (g) (%)	DMAP (g)	DCC (g)	Yield (g) (%)
PHB-Ox-21	1.08	0.18 14	0.044	0.82	1.04 83
PHB-Ox-23	2.02	0.67 25	0.242	5.03	2.24 83
PHB-Ox-22	1.08	0.56 34	0.092	2.45	1.19 73
PHB-Ox-24	2.02	1.41 41	0.131	3.12	2.34 68

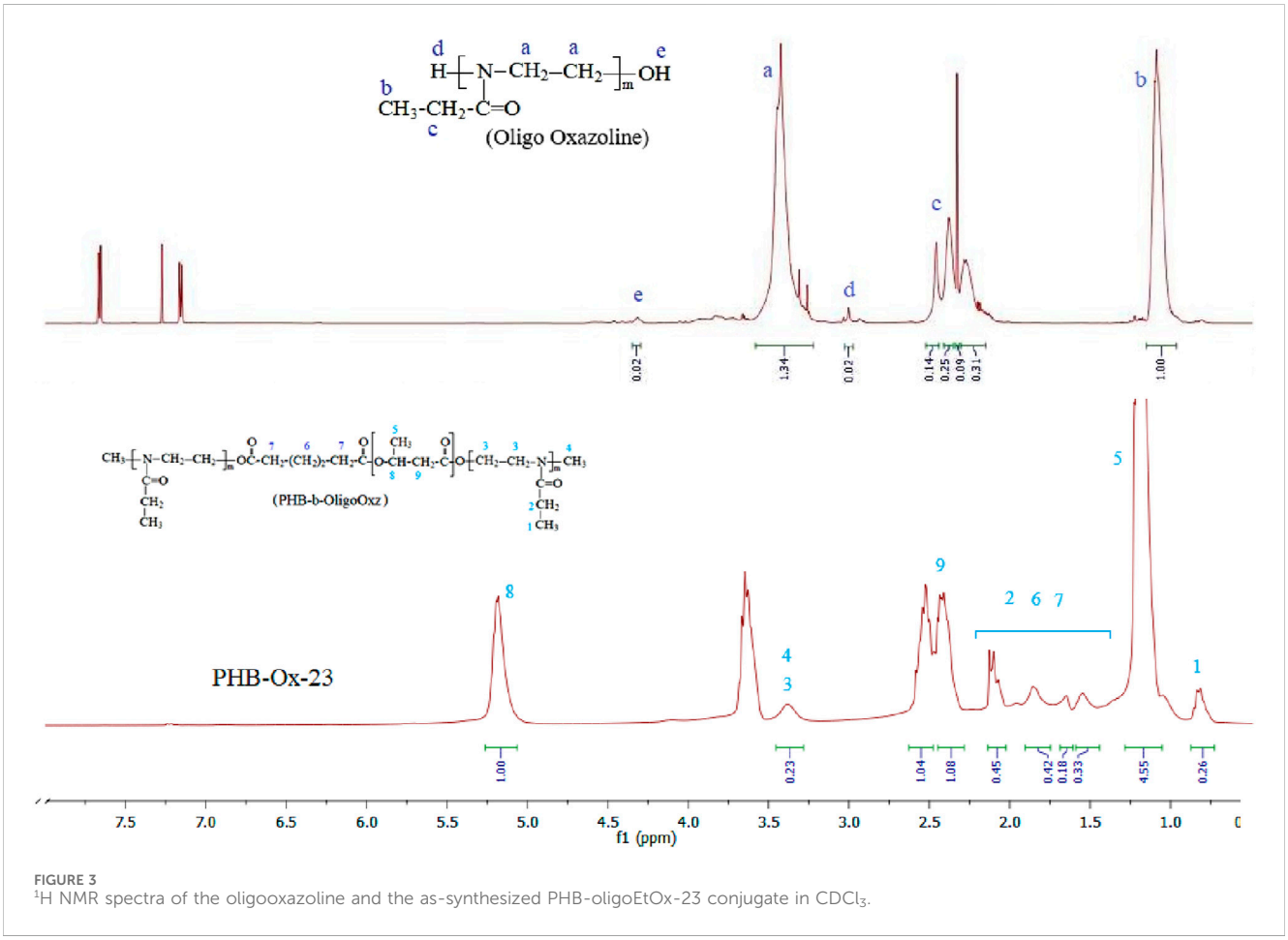

FIGURE 3
^{1}H NMR spectra of the oligooxazoline and the as-synthesized PHB-oligoEtOx-23 conjugate in $CDCl_3$.

imaging (Zeiss EVO lS10) was used for the characterization of the obtained polymers.

Results and discussion

Ring-opening cationic polymerization of 2-ethyl oxazoline, in the presence of MepTs, yielded oligo(2-ethyl oxazoline) (OligoOx). Oxazoline oligomers were obtained in several types, with molar masses changing from 700 to 900 g/mol. Characterization of OligoEtOx confirmed the polymer structure. The FTIR spectrum contained the characteristic signals at 3,462 cm^{-1}, 2,977–2,939 cm^{-1}, 1,624 cm^{-1}, and 1,187 cm^{-1} related to –OH, -C-H, amid carbonyl, and –N-CH_2- groups, respectively. Typical characteristic groups were also observed in the ^{1}H NMR spectrum at chemical shifts at 3.5 ppm (-N-C**H**$_2$-), 2.2–2.5 ppm (-C**H**$_2$-C(O)-), and 1.1 ppm (C**H**$_3$-CH_2-).

PHB with two carboxylic acid terminals was obtained by the reaction of an equimolar amount of adipic acid and PHB under reflux conditions at 85°C. The characteristic signals were observed in the 1H NMR and 13C NMR spectra of the as-synthesized PHB-COOH sample, which is seen in Figure 1, including 1H (a) and 13C (b) NMR spectra. 1H NMR, $\delta_{(ppm)}$: 1.3 ppm for –CH_3, 1.5 ppm for –CH_2-CH_2-, 2.4–2.6 ppm for –CH_2-COO-, 3.7 ppm for CH_2-OC(O)CH_2–, and 5.1–5.3 ppm for–CHO–. 13C NMR, $\delta_{(ppm)}$: 10 (–CH_2-CH_2-), 20 (CH_3-), 40 (-CH_2-C(O)-, 67 (-CH-O-), 169.1, and 169.2 carbonyls for PHB and adipic acid moieties, respectively.

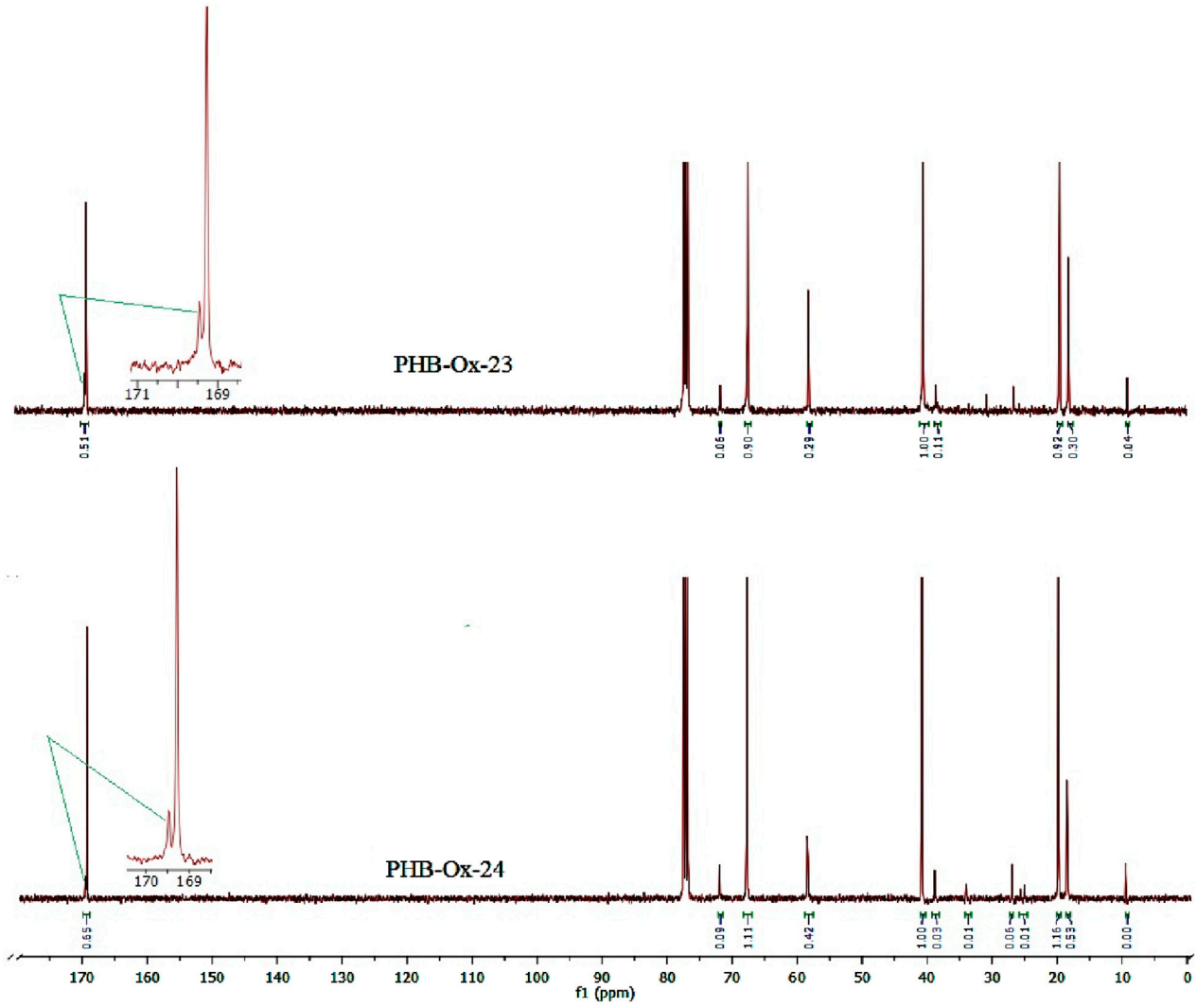

FIGURE 4
13C NMR spectra of the as-synthesized PHB-oligEtOx-23, -24 block copolymers in $CDCl_3$.

Synthesis of PHB-oligoEtOx polymer conjugates

OligoEtOx was capped with the carboxylic acid ends of PHB-COOH to produce the novel PHB-b-oligoEtOx block copolymer. The reaction pathways can be seen in Figure 2.

The reaction conditions and results are listed in Table 1. Changing the feed percentage of oligoEtOx from 14% to 41% against $PHB(COOH)_2$ was reacted at room temperature. The yield of the obtained block copolymer was gravimetrically determined. The polymer obtained was precipitated from the acidified diethyl ether and dried in vacuum. For further purification, it was soaked in distilled water for 24 h in order to remove the unreacted oligoEtOx residue.

Characterization of PHB-oligoEtOx conjugates was carried out by ^1H and ^{13}C NMR, FTIR, differential scanning calorimeter (DSC), and thermo-gravimetric analysis (TGA) techniques. PHB-Ox-21, −22, −23, and −24 samples contained the characteristic samples of oligoEtOx blocks at 3.4 and 3.6 ppm related to the $-CH_2$-N- groups. Chemical shifts at 1.2 ppm (CH_2-CH_2-) and 2.5 ppm (-CH_2-C(O)-) were overlapped with those of PHB blocks. The amount of oligoOx blocks in the obtained PHB-oligoEtOx −21, −22, −23, and −24 conjugates was calculated while comparing them with integral values of the signals at 5.2 ppm (PHB) and 3.5 ppm (oligoOx) 19, 52, 17, and 14%, respectively. Figure 3 shows the ^1H NMR spectra of the comparison of oligoOx with the as-synthesized PHB-oligoOx-23 conjugate in $CDCl_3$.

^{13}C NMR spectra of the PHB-oligoEtOx-23, -24 block copolymers contained the characteristic signals of the PHB and oligoOx blocks. Chemical shifts: 19, 20 ppm (-CH_3, PHB, oligoEtOx), 39, 40 ppm (-CH_2-C(O)-, PHB, oligoEtOx), 58 ppm (-N-CH_2-, oligoEtOx), 67 ppm (-CH-O-, PHB), and 169.1 and 169.2 ppm (-C=O, PHB and oligoOx). Figure 4 shows the ^{13}C NMR spectra of the as-synthesized PHB-oligoEtOx-23 and −24 conjugates in $CDCl_3$.

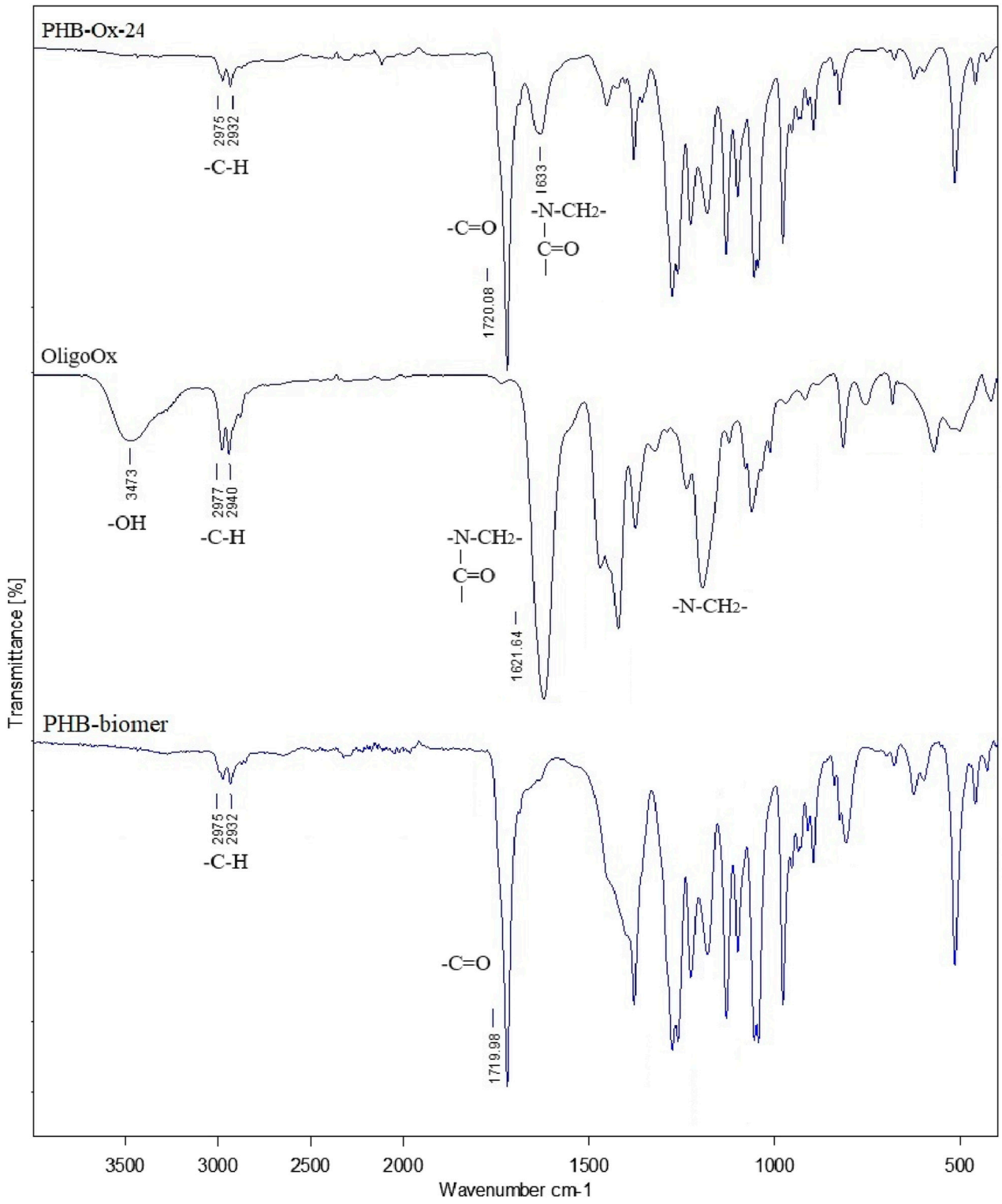

FIGURE 5
FTIR spectrum of PHB-oligEtOx-24 compared with the pristine oligEtOx.

Typical FTIR spectra of PHB-oligoOx-24, oligoOx, and pristine PHB compared with each other are shown in Figure 5. The typical characteristic signal of the oligoEtOx block was observed at 1,633 cm^{-1} related to the –N-C(O) group. The signals of the characteristic groups were marked on the related spectra.

Thermal properties of the block copolymers were measured using a differential scanning calorimeter (DSC). The oligoEtOx sample has a wide glass transition (Tm) between 10 and 76°C and the maximum at 64°C. In the PHB-oligoEtOx polymer conjugate, the same wide melting transition between 6 and

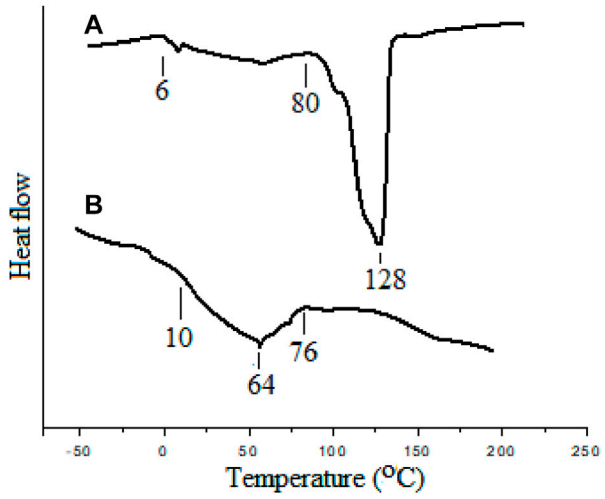

FIGURE 6
DSC curves of **(A)** PHB-oligoOx-21 and **(B)** oligoOx.

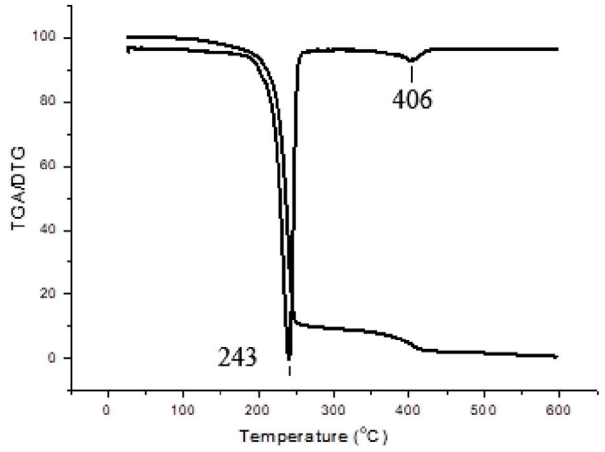

FIGURE 7
TGA/DTA curves of the PHB-oligoEtOx-22 conjugate.

80°C together with that of PHB at 128°C was observed. The PHB homopolymer has a melting transition at 170°C. The lower melting transition of the PHB block in the copolymer shows the plasticizing effect of oligoEtOx. Figure 6 shows the DSC curves of PHB-oligEtOx-21 and homo oligoOx. Homo oligoEtOx showed the glass transition temperature (Tg) at 10°C.

TGA analysis was done in the PHB-oligoEtOx conjugates. The all TGA/DTG curves contained two decomposition temperatures (Td)s: 243 and 406°C (for PHB-oligoOx-22), 249 and 381°C (for PHB-oligoOx-23), and 247 and 381°C (for PHB-oligoEtOx-24). The TGA/DTA curves of the PHB-oligoEtOx-22 conjugate are given in Figure 7. Decomposition of the PHB blocks changes between 243 and 249°C, while that of the oligo oxazoline blocks changes between 386 and 406°C (Bouten et al., 2015).

Conclusion

A fully biodegradable amphiphilic copolymer was obtained in this work. The hydroxyl end of oligoEtOx can easily be reacted with some other reagents to obtain polyoxazoline derivatives. Water-soluble hydrophilic oligoEtOx makes the hydrophobic polymers amphiphilic, which can be useful for medical applications. Combining natural and biodegradable hydrophobic properties of PHB with hydrophilic oligoEtOx yields a novel amphiphilic natural biopolymer.

Block copolymers containing hydrophilic and hydrophobic blocks gain the unique properties of both the related blocks. These different polymer blocks can be arranged linearly or as brush-type copolymers. The insertion of the hydrophilic polymer in a block copolymer can improve the colloidal stability of the biologic active nanoparticles for biomedical applications. Therefore, the PHB-b-oligoEtOx block copolymer can be a promising biopolymer for medical applications.

Data availability statement

The original contributions presented in the study are included in the article/Supplementary material; further inquiries can be directed to the corresponding author.

Author contributions

BH: Conceptualization, Methodology, Project administration, Writing–original draft, and Writing–review and editing. ÖA: Conceptualization, Formal analysis, Writing—review and editing. FK: Formal analysis, Methodology, and Writing–original draft.

Funding

The author(s) declare that financial support was received for the research, authorship, and/or publication of this article. The Kapadokya University Research Funds (#KÜN.2023-BAGP-020) provided funding for this project.

Conflict of interest

The authors declare that the research was conducted in the absence of any commercial or financial relationships that could be construed as a potential conflict of interest.

Publisher's note

References

Abdelmalek, F., Rofeal, M., Pietrasik, J., and Steinbüchel, A. (2023). Novel biodegradable nanoparticulate chain-end functionalized polyhydroxybutyrate–caffeic acid with multifunctionalities for active food coatings. *ACS Sustain. Chem. Eng.* 11 (18), 7123–7135. doi:10.1021/acssuschemeng.3c00389

Ali, J., Tuzen, M., Jatoi, W., Hazer, B., and Feng, X. (2024). A novel block copolymer containing gadolinium oxide nanoparticles in ultrasound assisted-dispersive solid phase microextraction of total arsenic in human foodstuffs: a multivariate optimization methodology. *Food Chem.* 437, 137908. doi:10.1016/j.foodchem.2023.137908

Altunay, N., Tuzen, M., Hazer, B., and Elik, A. (2020). Usage of the newly synthesized Poly(3-hydroxy butyrate)-b-poly(vinyl benzyl xanthate) block copolymer for vortex-assisted solid-phase microextraction of cobalt (II) and nickel (II) in canned foodstuffs. *Food Chem.* 321, 126690. doi:10.1016/j.foodchem.2020.126690

Arkin, A. H., and Hazer, B. (2002). Chemical modification of chlorinated microbial polyesters. *Biomacromolecules* 3 (6), 1327–1335. doi:10.1021/bm020079v

Arkin, A. H., Hazer, B., Adamus, G., Kowalczuk, M., Jedlinski, Z., and Lenz, R. W. (2001). Synthesis of poly(2-methyl-3-hydroxyoctanoate) via anionic polymerization of α-Methyl-β-pentyl-β-propiolactone. *Biomacromolecules* 2 (3), 623–627. doi:10.1021/bm015528q

Arslan, H., Hazer, B., and Yoon, S. C. (2007). Grafting of poly(3-hydroxyalkanoate) and linoleic acid onto chitosan. *J. Appl. Polym. Sci.* 103, 81–89. doi:10.1002/app.24276

Ashby, R. D., and Foglia, T. A. (1998). Poly(hydroxyalkanoate) biosynthesis from triglyceride substrates. *Appl. Microbiol. Biotechnol.* 49, 431–437. doi:10.1007/s002530051194

Ashby, R. D., Solaiman, D. K., and Strahan, G. D. (2019). The Use of Azohydromonas lata DSM 1122 to produce 4-hydroxyvalerate-containing polyhydroxyalkanoate terpolymers, and unique polymer blends from mixed-cultures with Burkholderia sacchari DSM 17165. *J. Polym. Environ.* 27, 198–209. doi:10.1007/s10924-018-1332-2

Balcı, M., Allı, A., Hazer, B., Guven, O., Cavicchi, K., and Cakmak, M. (2010). Synthesis and characterization of novel comb-type amphiphilic graft copolymers containing polypropylene and polyethylene glycol. *Polym. Bull.* 64, 691–705. doi:10.1007/s00289-009-0211-3

Bayram, C., Denkbas, E. B., Kiliçay, E., Hazer, B., Çakmak, H. B., and Noda, I. (2008). Preparation and characterization of triamcinolone acetonide-loaded poly(3-hydroxybutyrate-co-3-hydroxyhexanoate) (PHBHx) microspheres. *J. Bioact. Compat. Polym.* 23, 334–347. doi:10.1177/0883911508092790

Becer, C. R., Paulus, R. M., Hoppener, S., Hoogenboom, R., Fustin, C.-A., Gohy, J.-F., et al. (2008). Synthesis of poly(2-ethyl-2-oxazoline)-b-poly(styrene) copolymers via a dual initiator route combining cationic ring-opening polymerization and atom transfer radical polymerization. *Macromolecules* 41, 5210–5215. doi:10.1021/ma800527h

Bedade, D. K., Edson, C. B., and Gross, R. A. (2021). Emergent approaches to efficient and sustainable polyhydroxyalkanoate production. *Molecules* 26 (11), 3463. doi:10.3390/molecules26113463

Bouten, P. J. M., Lava, K., van Hest, J. C. M., and Hoogenboom, R. (2015). Thermal properties of methyl ester-containing poly(2-oxazoline)s. *Polymers* 7, 1998–2008. doi:10.3390/polym7101494

Bronstein, L., Kramer, E., Berton, B., Burger, C., Forster, S., and Antonietti, M. (1999). Successive use of amphiphilic block copolymers as nanoreactors and templates: preparation of porous silica with metal nanoparticles. *Chem. Mater* 11, 1402–1405. doi:10.1021/cm980762h

Caputo, M. R., Tang, X., Westlie, A. H., Sardon, H., Chen, E. Y.-X., and Müller, A. J. (2022). Effect of chain stereoconfiguration on poly(3-hydroxybutyrate) crystallization kinetics. *Biomacromolecules* 23, 3847–3859. doi:10.1021/acs.biomac.2c00682

Chen, G. Q. (2009). A microbial polyhydroxyalkanoates (PHA) based bio- and materials industry. *Chem. Soc. Rev.* 38 (8), 2434–2446. doi:10.1039/b812677c

Chen, G.-Q., and Zhang, J. (2018). Microbial polyhydroxyalkanoates as medical implant biomaterials. *Artif. Cells Nanomed. Biotechnol.* 46 (1), 1–18. doi:10.1080/21691401.2017.1371185

Chen, M.-Q., Serizawa, T., and Akashi, M. (1999). Graft copolymers having hydrophobic backbone and hydrophilic branches. xvi. Polystyrene microspheres with poly(N-isopropylacrylamide) branches on their surfaces: size control factors and thermosensitive behavior. *Polym. Adv. Technol.* 10, 120–126. doi:10.1002/(sici)1099-1581(199901/02)10:1/2<120::aid-pat781>3.3.co;2-7

Choi, S. Y., Cho, I. J., Lee, Y., Kim, Y. J., Kim, K. J., and Lee, S. Y. (2020). Microbial polyhydroxyalkanoates and nonnatural polyesters. *Adv. Mat.* 32, 1907138. doi:10.1002/adma.201907138

Christova, D., Velichkova, R., and Goethals, E. J. (1997). Bis-macromonomers of 2-alkyl-2-oxazolines - synthesis and polymerization. *Macromol. Rapid Commun.* 18, 1067–1073. doi:10.1002/marc.1997.030181210

Christova, D., Velichkova, R., Goethals, E. J., and Du Prez, F. E. (2002). Amphiphilic segmented polymer networks based on poly(2-alkyl-2-oxazoline) and poly(methyl methacrylate). *Polymer* 43, 4585–4590. doi:10.1016/s0032-3861(02)00313-0

Christova, D., Velichkova, R., Loos, W., Goethals, E. J., and Du Prez, F. (2003). New thermo-responsive polymer materials based on poly(2-ethyl-2-oxazoline) segments. *Polymer* 44, 2255–2261. doi:10.1016/s0032-3861(03)00139-3

Diab, C., Akiyama, Y., Kataoka, K., and Winnik, F. M. (2004). Microcalorimetric study of the temperature-induced phase separation in aqueous solutions of poly(2-isopropyl-2-oxazolines). *Macromolecules* 37, 2556–2562. doi:10.1021/ma0358733

Erol, A., Rosberg, D. B. H., Hazer, B., and Göncü, B. S. (2020). Biodegradable and biocompatible radiopaque iodinated poly-3-hydroxy butyrate. synthesis, characterization and *in vitro/in vivo* x-ray visibility. *Polym. Bull.* 77, 275–289. doi:10.1007/s00289-019-02747-6

Förster, S., and Antonietti, M. (1998). Amphiphilic block copolymers in structure-controlled nanomaterial hybrids. *Adv. Mater.* 10, 195–217. doi:10.1002/(sici)1521-4095(199802)10:3<195::aid-adma195>3.0.co;2-v

Glaive, A.-S., Le Cœur, C., Guigner, J.-M., Amiel, C., and Volet, G. (2024). Amphiphilic heterograft copolymers bearing biocompatible/biodegradable grafts. *Gisèle Volet Langmuir* 40 (4), 2050–2063. doi:10.1021/acs.langmuir.3c02772

Göppert, N. E., Quader, S., Van Guyse, J. F. R., Weber, C., Kataoka, K., and Schubert, U. S. (2023). Amphiphilic poly(2-oxazoline)s with glycine-containing hydrophobic blocks tailored for panobinostat- and imatinib-loaded micelles. *Biomacromolecules* 24, 5915–5925. doi:10.1021/acs.biomac.3c00934

Guennec, A., Brelle, L., Balnois, E., Linossier, I., Renard, E., Langlois, V., et al. (2021). Antifouling properties of amphiphilic poly(3-hydroxyalkanoate): an environmentally-friendly coating. *Biofouling* 37 (8), 894–910. doi:10.1080/08927014.2021.1981298

Guzik, M., Witko, T., Steinbuchel, A., Wojnarowska, M., Soltysik, M., and Wawak, S. (2020). What has been trending in the research of polyhydroxyalkanoates? A systematic review. *Front. Bioengin Biotechnol.* 8, 959. doi:10.3389/fbioe.2020.00959

Hayes, G., Drain, B., Lefley, J., and Becer, C. R. (2023). Hybrid multiblock copolymers of 2-oxazoline and acrylates via Cu-catalyzed Azide–Alkyne cycloaddition step-growth mechanism. *Macromolecules* 56 (1), 271–280. doi:10.1021/acs.macromol.2c01865

Hazer, B. (1991). Synthesis of tetrahydrofuran-styrene (or methyl methacrylate) block copolymers via cationic-to-radical transformation. *Eur. Polym. J.* 27, 775–777. doi:10.1016/0014-3057(91)90007-b

Hazer, B. (1996). Poly(β-hydroxynonanoate) and polystyrene or poly(methyl methacrylate) graft copolymers: microstructure characteristics and mechanical and thermal behavior. *Macromol. Chem. Phys.* 197, 431–441. doi:10.1002/macp.1996.021970202

Hazer, B. (2010). Amphiphilic poly (3-hydroxy Alkanoate)s: potential candidates for medical applications. *Int. J. Polym. Sci.* 2010, 1–8. doi:10.1155/2010/423460

Hazer, B., Eren, M., Senemoğlu, Y., Modjinou, T., Renard, E., and Langlois, V. (2020). Novel poly(3-hydroxy butyrate) macro raft agent. Synthesis and characterization of thermoresponsive block copolymers. *J. Polym. Res.* 27, 147. doi:10.1007/s10965-020-02133-1

Hazer, B., Lenz, R. W., Çakmaklı, B., Borcaklı, M., and Koçer, H. (1999). Preparation of poly(ethylene glycol) grafted poly(3-hydroxyalkanoate) networks. *Macromol. Chem. Phys.* 200, 1903–1907. doi:10.1002/(SICI)1521-3935(19990801)200:8<1903::AID-MACP1903>3.0.CO;2-J

Hazer, B., and Steinbüchel, A. (2007). Increased diversification of polyhydroxyalkanoates by modification reactions for industrial and medical applications. *Appl. Microbiol. Biotechnol.* 74 (1), 1–12. doi:10.1007/s00253-006-0732-8

Hazer, B., Subramaniyan, S., and Zhang, B. (2021). Synthesis of biobased block copolymers using A novel methacrylated methyl salicylate and poly(3-hydroxybutyrate). *ChemistrySelect* 6, 12255–12265. doi:10.1002/slct.202102977

Hazer, D. B., Kilicay, E., and Hazer, B. (2012). Poly(3-hydroxyalkanoate)s: diversification and biomedical applications. *Mater Sci. Eng. C* 32 (4), 637–647. doi:10.1016/j.msec.2012.01.021

Hoogenboom, R. (2009). Poly(2-oxazoline)s: a polymer class with numerous potential applications. *Angew. Chem. Int. Ed.* 48, 7978–7994. doi:10.1002/anie.200901607

Hoogenboom, R., Paulus, R. M., Fıjten, M. W. M., and Schubert, U. S. (2005). Concentration effects in the cationic ring-opening polymerization of 2-ethyl-2-oxazoline in N,N dimethylacetamide. *J. Polym. Sci. Part A Polym. Chem.* 43, 1487–1497. doi:10.1002/pola.20603

Hoogenboom, R., and Schlaad, H. (2011). Bioinspired poly(2-oxazoline)s. *Polymers* 3, 467–488. doi:10.3390/polym3010467

Hosseini, S., Shahrousvand, M., Mohammadi-Rovshandeh, J., Jahanbakhshi, M., Javadi, A., Soleimani, M., et al. (2024). Fabrication of pH-Responsive amphiphilic poly(vinyl alcohol–methyl methacrylate) copolymer nanoparticles for application in cancer drug delivery systems. *Iran. J. Sci.* 48, 99–111. doi:10.1007/s40995-023-01573-w

Hu, Z., Chen, L., Betts, D. E., Pandya, A., Hillmyer, M. A., and DeSimone, J. M. (2008). Optically transparent, amphiphilic networks based on blends of perfluoropolyethers and poly(ethylene glycol). *J. Am. Chem. Soc.* 130, 14244–14252. doi:10.1021/ja803991n

Kacanski, M., Stelzer, F., Walsh, M., Kenny, S., O'Connor, K., and Neureiter, M. (2023). Pilot-scale production of mcl-PHA by Pseudomonas citronellolis using acetic acid as the sole carbon source. *New Biotechnol.* 78 (2023), 68–75. doi:10.1016/j.nbt.2023.10.003

Kalaycı, Ö. A., Cömert, F. B., Hazer, B., Atalay, T., Cavicchi, K., and Cakmak, M. (2010). Synthesis, characterization, and antibacterial activity of metal nanoparticles

embedded into amphiphilic comb-type graft copolymers. *Polym. Bull.* 65, 215–226. doi:10.1007/s00289-009-0196-y

Kalayci, O. A., Duygulu, O., and Hazer, B. (2013). Optical characterization of CdS nanoparticles embedded into the comb-type amphiphilic graft Copolymer. *J. Nanoparticle Res.* 15 (1355), 1355. doi:10.1007/s11051-012-1355-x

Karahaliloğlu, Z., Ilhan, E., Kılıcay, E., Hazer, B., and Denkbas, E. B. (2020). Potent bioactive bone cements impregnated with polystyrene-g-soybean oil-AgNPs foradvanced bonetissue applications. *Mater. Technol.* 35, 179–194. doi:10.1080/10667857.2019.1661157

Kılıcay, E., Demirbilek, M., Turk, M., Guven, E., Hazer, B., and Denkbas, E. B. (2011). Preparation and characterization of poly(3-hydroxybutyrate-co-3-hydroxyhexanoate) (phbhhx) based nanoparticles for targeted cancer therapy. *Eur. J. Pharm. Sci.* 44 (3), 310–320. doi:10.1016/j.ejps.2011.08.013

Kilicay, E., Erdal, E., Elci, P., Hazer, B., and Denkbas, E. B. (2024). Tumour-specific hybrid nanoparticles in therapy of breast cancer. *J. Microencapsul. Micro Nano Carriers* 41, 45–65. doi:10.1080/02652048.2023.2292226

Kocer, H., Borcakli, M., Demirel, S., and Hazer, B. (2003). Production of bacterial polyesters from some various new substrates by Alcaligenes eutrophus and Pseudomonas oleovorans. *Turk J. Chem.* 27 (3), 365–374.

Li, J., Ge, Z., Toh, K., Liu, X., Dirisala, A., Ke, W., et al. (2021). Enzymatically transformable polymersome-based nanotherapeutics to eliminate minimal relapsable cancer. *Adv. Mater.* 33, 2105254. doi:10.1002/adma.202105254

Mai, Y., and Eisenberg, A. (2012). Self-assembly of block copolymers. *Chem. Rev.* 41, 5969–5985. doi:10.1039/c2cs35115c

Mehrpouya, M., Vahabi, H., Barletta, M., Laheurte, P., and Langlois, V. (2021). Additive manufacturing of polyhydroxyalkanoates (PHAs) biopolymers: materials, printing techniques, and applications. *Mater. Sci. Eng. C* 127, 112216. doi:10.1016/j.msec.2021.112216

Minoda, M., Sawamoto, M., and Higashimura, T. (1990). Amphiphilic block copolymers of vinyl ethers by living cationic polymerization. 3. Anionic macromolecular amphiphiles with pendant carboxylate anions. *Macromolecules* 23, 1897–1901. doi:10.1021/ma00209a001

Miyamoto, M., Naka, K., Tokumizu, M., and Saegusa, T. (1989). End capping of growing species of poly(2-oxazoline) with carboxylic acid: a novel and convenient route to prepare vinyl- and carboxy-terminated macromonomers. *Macromolecules* 22, 1604–1607. doi:10.1021/ma00194a016

Neugebauer, D., Rydz, J., Goebel, I., Dacko, P., and Kowalczuk, M. (2007). Synthesis of graft copolymers containing biodegradable poly(3-hydroxybutyrate) chains. *Macromolecules* 40, 1767–1773. doi:10.1021/ma062251j

Obeid, R., Tanaka, F., and Winnik, F. M. (2009). Heat-induced phase transition and crystallization of hydrophobically end-capped poly(2-isopropyl-2-oxazoline)s in water. *Macromolecules* 42, 5818–5828. doi:10.1021/ma900838v

Park, J. S., Akiyama, Y., Winnik, F. M., and Kataoka, K. (2004). Versatile synthesis of end-functionalized thermosensitive poly(2-isopropyl-2-oxazolines). *Macromolecules* 37, 6786–6792. doi:10.1021/ma049677n

Park, J.-S., and Kataoka, K. (2007). Comprehensive and accurate control of thermosensitivity of poly(2-alkyl-2-oxazoline)s via well-defined gradient or random copolymerization. *Macromolecules* 40, 3599–3609. doi:10.1021/ma0701181

Tuzen, M., Sahiner, S., and Hazer, B. (2016). Solid phase extraction of lead, cadmium and zinc on biodegradable polyhydroxybutyrate diethanol amine (PHB-DEA) polymer and their determination in water and food samples. *Food Chem.* 210, 115–120. doi:10.1016/j.foodchem.2016.04.079

Ullah, R., Tuzen, M., Hazer, B., and Saleh, T. A. (2024). Synthesis of poly (3-hydroxy butyrate)-g-poly (ricinoleic acid)-Ag nanocomposite for adsorption of methyl blue with multivariate optimization. *J. Mol. Liq.*, 124369. doi:10.1016/j.molliq.2024.124369

Unsal, Y. E., Soylak, M., Tuzen, M., and Hazer, B. (2015). Determination of lead, copper, and iron in cosmetics, water, soil, and food using polyhydroxybutyrate-b-polydimethyl siloxane preconcentration and flame atomic absorption spectrometry. *Anal. Lett.* 48, 1163–1179. doi:10.1080/00032719.2014.971365

Vergaelen, M., Monnery, B. D., Jerca, V. V., and Hoogenboom, R. (2023). Detailed understanding of solvent effects for the cationic ring-opening polymerization of 2-Ethyl-2-oxazoline. *Macromolecules* 56 (4), 1534–1546. doi:10.1021/acs.macromol.2c01930

Wadhwa, S. K., Tuzen, M., Kazi, T. G., Soylak, M., and Hazer, B. (2014). Polyhydroxybutyrate-b- polyethyleneglycol block copolymer for the solid phase extraction of Lead and copper in water, baby foods, tea and coffee samples. *Food Chem.* 152, 75–80. doi:10.1016/j.foodchem.2013.11.133

Wang, M., Li, Y., Zheng, L., Hu, T., Yan, M., and Wu, C. (2024). Amphiphilic–zwitterionic block polymers. *Polym. Chem.* 15, 622–630. doi:10.1039/d3py01179h

Wen, P., Ke, W., Dirisala, A., Toh, K., Tanaka, M., and Li, J. (2023). Stealth and pseudo-stealth nanocarriers. *Adv. Drug Deliv. Rev.* 198, 114895. doi:10.1016/j.addr.2023.114895

Xu, R., Winnik, M. A., Hallet, F. R., Riess, G., and Croucher, M. D. (1991). Light-scattering study of the association behavior of styrene–ethylene oxide block copolymers in aqueous solution. *Macromolecules* 24, 87–93. doi:10.1021/ma00001a014

Yalcin, B., Cakmak, M., Arkın, A. H., Hazer, B., and Erman, B. (2006). Control of optical anisotropy at large deformations in PMMA/chlorinated-PHB (PHB-Cl) blends: mechano-optical behavior. *Polymer* 47, 8183–8193. doi:10.1016/j.polymer.2006.09.051

Zhou, M., Qian, Y., Xie, J., Zhang, W., Jiang, W., Xiao, X., et al. (2020). Poly(2-Oxazoline)-Based functional peptide mimics: eradicating MRSA infections and persisters while alleviating antimicrobial resistance. *Angew. Chem. Int. Ed.* 59, 6412–6419. doi:10.1002/anie.202000505

frontiers | Frontiers in Chemistry

TYPE Original Research
PUBLISHED 25 March 2024
DOI 10.3389/fchem.2024.1349531

OPEN ACCESS

EDITED BY
Franz Jirsa,
University of Vienna, Austria

REVIEWED BY
Maria Criado,
Spanish National Research Council (CSIC), Spain
Adriano Michael Bernardin,
University of the Extreme South of Santa Catarina, Brazil

*CORRESPONDENCE
Hamid Sepehrian,
hsepehrian@aeoi.org.ir
Mohammad Outokesh,
outokesh@sharif.edu

RECEIVED 04 December 2023
ACCEPTED 12 March 2024
PUBLISHED 25 March 2024

CITATION
Hosseinpour Khanmiri M, Yadollahi A, Samadfam M, Sepehrian H and Outokesh M (2024), Investigation of the leaching behavior of Na and Si in simulated HLW borosilicate glass obtained from the waste of a 1000 MWe class PWR reactor: using the response surface method.
Front. Chem. 12:1349531.
doi: 10.3389/fchem.2024.1349531

Investigation of the leaching behavior of Na and Si in simulated HLW borosilicate glass obtained from the waste of a 1000 MWe class PWR reactor: using the response surface method

Mohammad Hosseinpour Khanmiri[1,2], Ali Yadollahi[2], Mohammad Samadfam[1], Hamid Sepehrian[2]* and Mohammad Outokesh[1]*

[1]Department of Energy Engineering, Sharif University of Technology, Tehran, Iran, [2]Nuclear Fuel Cycle Research School, Nuclear Science and Technology Research Institute, AEOI, Tehran, Iran

The immobilization of high-level nuclear waste (HLW) in glass waste matrices provides the key safety function of slowing down radionuclide emissions from an underground disposal site. This study examines the leaching behavior of two major elements, Na and Si, in HLW borosilicate glass simulated from waste of a 1000 MWe class pressurized water reactor (PWR) using response surface methodology and Box-Behnken Design. The design of the experiment was carried out considering three independent variables: the pH of the solution, the contact time, and the leaching temperature, leading to 17 leaching runs performed using the static product consistency test (PCT). The results of statistical analysis (ANOVA: analysis of variance) indicated that the effects of the individual variables and the interactions between them were statistically significant, and the relative consistency of the data further confirmed the model's applicability. Data obtained from the PCT experiments revealed that the leaching behavior of Na and Si in the evaluated waste glass exhibited similar behavior to previously researched glasses for each condition tested.

KEYWORDS

borosilicate glass, nuclear waste glass, PCT test, leaching rate, HLW immobilization, response surface methodology, modeling

Highlight

- The leaching behavior of Na and Si as a function of time, pH, and temperature in HLW borosilicate glass using the RSM approach was examined.
- The 3D surface plots showed that with the simultaneous increase in pH and temperature over 14 days, the leaching rates of Na and Si increased.
- At 70°C with an increasing pH, the leaching rates of Na and Si increased, but the leaching time had a little negative effect on the rates.
- The pattern of changes in the leaching rates of the elements studied in this work and in other different waste glasses is very similar.

- The experimental validation of the BBD model showed that the actual leaching rates are reasonably close to the predicted values and are located within 95% PI low and 95% PI high intervals.

1 Introduction

The immobilization of high-level radioactive waste (HLW) materials is thought to be the most important step in the final phase of radioactive waste management technology (Ewing et al., 2004; Weber et al., 2009; Ojovan and Lee, 2011; McCloy and Goel, 2017; Hosseinpour Khanmiri and Bogdanov, 2018; Hosseinpour Khanmiri et al., 2018; Rahman and Saleh, 2018; Hyatt and Ojovan, 2019; Ojovan and Yudintsev, 2023; Hosseinpour Khanmiri et al., 2024). Most of the available data is related to the development of materials for the long-term storage or disposal of high-level nuclear waste materials, either from the reprocessing of spent commercial reactor fuels or from a number of defense reprocessing operations. These analyses use a modular strategy to take into account the time-dependent development of technical barriers as well as the dynamic character of biological and hydrological processes in the host environment (Rahman et al., 2014). In order to reduce the likelihood of radioactive transportation or dispersion during the operation and disposal stages of the waste lifecycle, radioactive waste must be immobilized by embedding, solidification, or encapsulation. Waste is immobilized by chemically incorporating it into the framework of a compatible matrix. Its primary safety features are ensuring structural integrity, resisting deterioration, and limiting water infiltration and radioactive leakage. Stabilizing radioactive waste involves using methods like cement, ceramic, polymer, and glass solidification (Yim and Linga Murty, 2000; Lee et al., 2013; Rahman et al., 2013; Ojovan et al., 2019). Out of all of them, vitrified forms are widely accepted as the most feasible and stable form for disposing HLW. According to the obtained laboratory data and due to the special structure and chemical composition, the glass waste matrices have shown acceptable resistance to maintaining their elements in simulated water environments, so these materials provide the key safety function of slowing down radionuclide emissions from an underground disposal site (Ebert and Jerden, 2019).

Despite the fact that a wide variety of ceramic materials and glass have been considered potential candidates for the immobilization of HLW, borosilicate glass is currently the most widely used wasteform. Due to this choice, borosilicate glass is currently being used as the host for the immobilization of HLW in a number of industrial vitrification facilities across the globe (Kaushik et al., 2006; Ojovan and Lee, 2011; Stefanovsky et al., 2017). The borosilicate glass's flexibility in terms of waste loading and capacity to incorporate a variety of waste elements, in addition to its strong glass-forming capabilities, mechanical integrity, chemical resistance, and superior thermal and radiation stability, are the reasons for this decision (Manaktala, 1992; Ojovan et al., 2019). Since water is the most prevalent substance in many environments, borosilicate glass researchers from several fields are very interested in how water interacts with glass. The three phases that make up the interaction between glass and water are the diffusion of water molecules into the glass structure, ion exchange with protons, and hydrolysis of network-modifying species in the glass structure (Wu et al., 2011; Gin et al., 2015a). Whenever waste borosilicate glass is exposed to a natural environment, such as groundwater that is either flowing or still, chemical reactions start at the surface of a waste glass, and then the entire waste glass is affected by these interactions, based on its composition, the pH of the solution, the contact time, and the ambient temperature. As a result, by studying the leaching behavior of the major elements of the numerous borosilicate glasses depending on various factors (temperature, pH, time, etc.) via kinetic models, it is feasible to forecast glass durability and build glasses that adhere to certain leaching requirements based on short-term tests, as well as forecast the long-term dissolution behavior of glasses. In previous work (Kim et al., 2011), the temperature and pH dependences of four glasses created by the KHNP (the Korea Hydro & Nuclear Power Co., Ltd.) on the leaching behavior were discovered by utilizing a collection of pH buffer solutions with a pH range of 4–11 at temperatures of 40, 70, and 90°C over 3 weeks via the MCC-1 leaching standard test (ASTM C1220). When the temperature ranged from 40°C to 90°C and the leachant condition ranged from pH 4 to pH 11, all of the test glasses had a forward dissolve rate of ≤10 [g/(m^2. d)]. In a later paper (Gin et al., 2015b), at pHs of 9.0 and 11.5 thorough static leaching tests on international simple glass (ISG) were conducted and verified the growth of alteration layers on the glass surface as a result of the release of weakly bonded cations like Ca^{2+}, Na^{+}, and boron species. Ebert and Jerden (Ebert and Jerden, 2019) reported results of modified ASTM C1285 tests performed at 90°C using AFCI (Advanced Fuel Cycle Initiative) and LRM (low-activity reference material) glasses to ascertain if dissolving rate dependencies on pH, Al, and Si contents must be taken into account. They came to the conclusion that the pH, Si, and Al concentrations, as well as maybe other facets of the glass composition, are probably what ultimately cause the resumption rate to occur. Here, it is better to briefly mention that the alteration of radioactive waste glass in contact with water can include the following stages: I. Initial diffusion or interdiffusion (exchange between glass network-modifying cations and protons in solution). II. The initial or forward rate (hydrolysis of the glass network). III. The rate drop (saturation of the solution with silicon concentration and formation of gel on the surface of the glass). IV. The residual rate (in a closed system with secondary phase precipitation, the leaching rate remains at a relatively low but approximately constant rate). V. A possible resumption of alteration in particular conditions (precipitation exceeding the pH threshold, self-sustaining precipitation, destabilizing the gel, and the resumption rate of glass alteration) (Frugier et al., 2008). In the study (Neeway et al., 2019), using single-pass flow-through (SPFT) testing at a temperature of 90°C in buffered solutions of pH (RT) 4, 7, 9, and 11 as well as the static product consistency test (PCT), the corrosion behavior of oxyapatite [$Ca_2Nd_8(SiO_4)_6O_2$] and powellite [$(Ca,Sr,Ba)MoO_4$] in glass-ceramic nuclear waste materials was examined. The findings showed that the individual phases' dissolution kinetics varied between pH investigations. According to the material presented above, it can be easily concluded that it is necessary to examine the factors of temperature, pH, and time as leaching criteria to analyze and optimize the resistance of nuclear waste glass. For this purpose, different leaching test methods for waste glasses allow experts in the field of nuclear waste to compare and optimize the resistance of the glass. In the meantime the simultaneous investigation of the effect of several independent variables (temperature, pH, time, and.) on a dependent variable (leaching rate), interesting and promising results will be produced.

In the present study, the dissolving kinetics of non-radioactive high-level waste borosilicate glass simulated from waste of a

TABLE 1 Chemical composition of PWRHLW-BSG-1 simulated waste glass.

Oxide	Weight %	Oxide	Weight %	Oxide	Weight %
Al_2O_3	4.57	Y_2O_3	0.26	Nd_2O_3	3.15
B_2O_3	13.20	ZrO_2	3.15	La_2O_3	1.25
CaO	3.84	MoO_3	2.23	Fe_2O_3	3.68
Li_2O	1.84	MnO_2	0.46	NiO	0.52
Na_2O	5.16	Ag_2O	0.04	Cr_2O_3	0.66
SiO_2	42.78	CdO	0.05	P_2O_5	0.34
ZnO	2.36	SnO_2	0.05	Na_2O	5.25
SeO_2	0.29	BaO	0.79	Total	100
Cs_2O	1.40	Ce_2O_3	1.58		
SrO	0.45	Pr_2O_3	0.66		

1000 MWe class PWR reactor were experimentally investigated. For this purpose, the short-term leaching behavior of Si and Na elements was studied by using a series of pH buffer solutions at different temperatures for various time periods. The leaching process was assessed by conducting a product consistency test method B (PCT-B) (Jantzen et al., 1992; Crawford et al., 2007; Jantzen and Bibler, 2009; Vienna et al., 2013) in accordance with American Society for Testing Materials (ASTM) Standard C1285. To investigate the effect of leaching parameters, including the pH of the solution, the contact time, and the temperature of the environment, Response Surface Methodology (RSM) with a Box-Behnken Design (BBD) implemented in the Design-Expert software was utilized, producing a three-dimensional response surface.

2 Experimental

2.1 Glass specimen

A non-radioactive high-level waste borosilicate glass simulated from waste of a 1000 MWe class PWR reactor (PWRHLW-BSG-1) was employed as a glass specimen in this study. The maximum non-radioactive waste loading in borosilicate glass is 26.25 percent. The corresponding sample was obtained from the Nuclear Fuel Cycle Research School, Nuclear Science and Technology Research Institute, Atomic Energy Organization of Iran. The chemical composition of PWRHLW-BSG-1 is shown in Table 1. The chemical composition of borosilicate glass is similar to the composition of general borosilicate glass and the chemical composition of nuclear waste was simulated from waste of a 1000 MWe class PWR reactor. PWRHLW-BSG-1 was synthesized in a laboratory electric furnace (F11L-1250, Iran) at a temperature of 1,200°C for 2 h. Clean crushed waste glass of a particle size between 149 μm and 74 μm (−100 to +200 mesh) was utilized for the leaching test. The sample was milled under the following conditions: laboratory milling machine: Sanat Ceram, FMSV, 68 kg, 375 W; the volume of mill/jar: 500 cc; characteristics of balls: 5 alumina balls each with a diameter of 3 cm; rotation speed: 400 rpm; time of milling: 1 h; additives: without any additives; the state of the sample during milling: completely dry; homogeneous sample size in the milling process: 4 pieces of approximately 0.8 cm^3; laboratory sieves: 100 and 200 mesh. Specific surface areas of the finely powdered sample, determined by the Brunnauer-Emmett-Teller (BET) method (NOVA 2200e, Quantachrome), were 1.97 10^{-2} m^2/g. To determine the specific surface area in this analysis, 2 g of clean crushed waste glass of a particle size between 149 μm and 74 μm were washed with distilled water to remove any foreign contamination and dried in an oven at 60°C for 24 h. Before determining the specific surface area, the powder sample are degassed at a temperature of about 250°C for 4 h under vacuum. Using the Archimedes technique, the density of the PWRHLW-BSG-1 specimen was measured and found to be 2.737 g cm^{-3}.

2.2 Experimental design for the leaching of simulated waste glass

The Design-Expert software (version 12) from Stat-Ease, Inc. was employed for the experimental design. For this purpose, the investigated parameters were modeled, employing the Box-Behnken Design (BBD) approach in response surface methodology (RSM). To evaluate the leaching behavior of Si and Na elements in the PWRHLW-BSG-1 simulated waste glass, three independent variables, the pH of the solution, the contact time, and the leaching temperature, leading to 17 leaching runs, were generated, as shown in Table 2. Experiments using the PCT leaching test were conducted at three different temperatures of 50, 70, and 90°C (Factor A), under alkaline conditions at pH (Factor B) 8, 10, and 12, and during periods of 7, 14, and 21 days (Factor C). In order to assess the data's statistical significance, analysis of variance (ANOVA) was used, taking into account p[1] < 0.05, Eq. 1 (Rodrigues et al., 2009; Kweinor Tetteh et al., 2021):

1 The F-value in one way ANOVA is a tool to help you answer the question "Is the variance between the means of two populations significantly different?" The F-value in the ANOVA test also determines the p-value; The p-value is the probability of getting a result at least as extreme as the one that was actually observed, given that the null hypothesis is true.

TABLE 2 Experimental design matrix (from BBD) for the leaching of Si and Na in the PWRHLW-BSG-1.

Run	Factor A: Temp°C	Factor B: pH	Factor C: Time, d
1	70	8	21
2	50	8	14
3	70	10	14
4	50	10	21
5	70	12	7
6	70	12	21
7	50	12	14
8	90	10	21
9	70	10	14
10	90	12	14
11	70	10	14
12	90	10	7
13	70	10	14
14	50	10	7
15	90	8	14
16	70	8	7
17	70	10	14

TABLE 3 Excess experiments other than leaching runs of BBD for confirmation of the leaching of Si and Na in the PWRHLW-BSG-1.

Test	Temp°C	pH	Time, d
1	70	8	14
2	70	10	7
3	50	10	14
4	90	10	14
5	70	10	21
6	70	12	14

$$NE = K^2 + K + Cp \quad (1)$$

Here, *NE*, *K*, and *Cp* stand for, respectively, the total number of experiments, the number of factors, and the number of repeated center points. The polynomial quadratic represented in Eq. 2 was used to examine the pivotal relationship between the independent and dependent variables.

$$Y = \beta_0 + \sum_{i=1}^{k}\beta_i x_i + \sum_{i=1}^{k}\beta_{ii} x_i^2 + \sum_{i=1}^{k-1}\sum_{j=2}^{k}\beta_{ij} x_i x_j + \varepsilon \quad (2)$$

Here, Y is a response variable, β_0 is a constant, k is the number of independent variables, β_i is the regression coefficient, x_i and x_j are the independent variables in coded levels and ε is the unidentified error constant that has a mean of zero as a random experimental error.

To provide more experimental data for a wider comparison and to check the accuracy of the results related to the leaching behavior of Si and Na, six additional tests described in Table 3 were performed in parallel with the 17 tests provided in Table 2.

2.3 PCT leaching test

PCT-B on PWRHLW-BSG-1 was carried out using 23 Teflon test containers, each having a capacity of 100 cm^3. The amount of crushed glass in each vessel was precisely 1.5 g. The alkaline buffer solutions at pH 8, 10, and 12 were utilized to control the pH during PCT tests. In order to create buffer solutions with pH values of 8 and 10, determined quantities of the organic tris hydroxymethyl aminomethane buffer (THAM, CAS-No: 77-86-1, Merck KGaA, 64271 Darmstadt, Germany) were added to distilled water, reaching approximately 0.05 M concentration, and adjusted to the required pH at room temperature with 15 M HNO3. A buffer solution with a pH of 12 was created by preparing 0.01 M LiOH and 0.01 M LiCl and adjusting with 0.01 M LiOH. According to the experimental design, a 15 cm^3 buffer solution with different pH values was added to each vessel. The ratio of the waste glass sample surface area to leachate volume (S/V) was 1,970 m^{-1}. The Teflon test containers were kept in ovens set at 50, 70, and 90°C for durations of 7, 14, and 21 days (Figure 1). The containers were taken out of the oven at the conclusion of each test and left to cool. After that, the leachates were filtered to determine the pH values. Table 4 indicates the pH values of the leachate of every sample before and after the leaching test. Finally, the leachate of each waste glass specimen was analyzed to

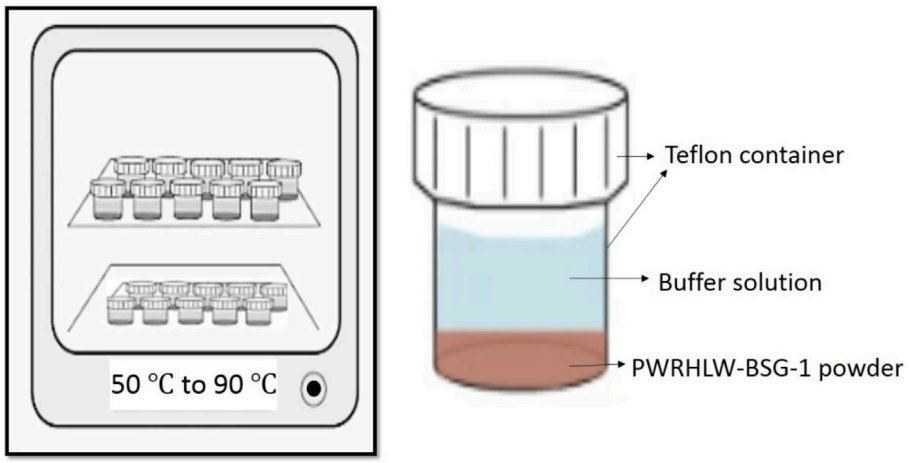

FIGURE 1
PCT-B test in accordance with ASTM—C1285.

TABLE 4 The pH values of the leachates before and after the PCT leaching test for BBD and six excess experiments runs.

Run	Initial pH value	Final pH value	Temp°C	Time, d
1	8	6.29	70	21
2	8	7.79	50	14
3	10	9.68	70	14
4	10	9.44	50	21
5	12	9.80	70	7
6	12	9.66	70	21
7	12	10.90	50	14
8	10	8.45	90	21
9	10	9.71	70	14
10	12	10.30	90	14
11	10	9.66	70	14
12	10	8.51	90	7
13	10	9.65	70	14
14	10	9.56	50	7
15	8	6.07	90	14
16	8	7.74	70	7
17	10	9.69	70	14
1	8	7.75	70	14
2	10	9.46	70	7
3	10	9.68	50	14
4	10	9.67	90	14
5	10	—	70	21
6	12	10.65	70	14

measure values of Si and Na elements using the inductively coupled plasma atomic emission spectrometry technique (ICP-AES) (PerkinElmer OPTIMA 2000).

2.4 Quantitative description of dissolution rates

The effectiveness of the radioactive immobilization approach is assessed by the rate at which radionuclides can escape from the wasteform during long-term storage. Leach rates are the most important factors in determining how efficiently glass can retain radioactive components since water is the most likely means for radiation to enter the biosphere once more. Typically, the amount of each glass constituent released into the solution when the glass comes into contact with it is measured in order to determine the rate of glass dissolution. The characteristics of the contact solution and the chemical makeup of the glass determine the rate at which the constituents are released. The normalized leaching rate (NLR_i) for a specific element (i) from the waste glass has been computed on the basis of the following Eq. 3 (Committee, 2002; Ojovan and Lee, 2011; Inagaki et al., 2012; Thorat et al., 2019):

$$NLR_i = \frac{C_i}{(SA/V)(t)(f_i)} \tag{3}$$

Here, NLR_i [g/(m^2. d)] is the normalized leaching rate of element (i) from the waste glass; C_i (g/m^3) is the concentration of element (i) in the solution; SA (m^2) is the surface area of the specimen; V (m^3) is the leachate volume; t (day) is the leaching time duration; and the mass fraction of element (i) in the initial waste glass is represented by the term f_i (without unit).

As a result, it is possible to determine the leaching rates of elements as a function of time; hence, the leaching rates according to the experimental design method used in this study will be analyzed by producing three-dimensional surface plots with the influence of temperature and pH in different ranges.

3 Results and discussion

3.1 Experimental normalized leaching rates of RSM via BBD design

The BBD matrix produced with randomly selected 17 sets of experimental runs, along with the response and predicted results for the normalized leaching rate of Na (Na-NLR) and the normalized leaching rate of Si (Si-NLR) from the interaction of the three leaching factors, is shown in Table 5. After fitting the experimental data to a reduced quadratic model, the statistical significance and validity of the model were examined using the analysis of variance (ANOVA) method described in Section 3.2. The model Eqs 4, 5 are stated with the experimental values of the input parameters (A, B, and C), their interaction (AB, AC, BC), and quadratic (A^2, B^2, C^2) components as a function of the responses Y_1 and Y_2, where Y_1 is the response of the Na-NLR and Y_2 is the response of the Si-NLR. The Eqs 4, 5 were displayed according to the modified model for the parameters with p-value less than 0.0500 and they expressed in terms of coded factors can be utilized to predict the response at different levels of each factor. By default, the high levels of the factors are coded as +1, and the low levels are coded as −1. The coded equation is useful for identifying the relative impact of the factors by comparing the factor coefficients. The synergistic impact of the term on the response is shown by the positive sign, whereas the antagonistic impact is indicated by the negative sign. To find the best fit, the sequential F-test, lack-of-fit test, and other adequacy metrics were used to analyze the statistical significance of the terms in each regression equation.

The data in Table 5 shows how closely the experimental and predicted normalized leaching rates of Na and Si were related. The relative consistency of the data further confirms the model's applicability (Teimouri, 2020). The statistical parameters (ANOVA) related to confirming the correspondence between the experimental and predicted normalized leaching rates will be further discussed in Section 3.2.

$$\begin{aligned}(Y_1) &= \mathrm{Log}_{10}(\mathrm{Na}-\mathrm{NLR})\\ &= -1.76 + 0.2024A + 0.5373B - 0.1937C + 0.4118B^2\\ &\quad + 0.0688C^2\end{aligned} \tag{4}$$

$$\begin{aligned}(Y_2) &= \mathrm{Log}_{10}(\mathrm{Si}-\mathrm{NLR})\\ &= +4.20230 + 0.005444A - 1.49274B - 0.058357C\\ &\quad - 0.000198AC - 0.003694BC + 0.000069A^2 + 0.090739B^2\\ &\quad + 0.002967C^2\end{aligned} \tag{5}$$

3.2 Variance analysis (ANOVA)

The model accuracy in this work is investigated by the coefficients of determination-R^2 and adjusted-R^2, the results of the analysis for Na-NLR and Si-NLR responses are indicated in Table 6. As seen from Table 6, for the response of Na-NLR, the predicted R^2 of 0.9912 is in reasonable agreement with the adjusted R^2 of 0.9957, i.e., the difference is less than 0.02, and for the response of Si-NLR, the predicted R^2 of 0.9872 is in reasonable agreement with the adjusted R^2 of 0.9976, i.e., in this response as well as Na-NLR, the difference is also less than 0.02. An adequate precision of 82.669 and 94.612 for responses indicates an adequate signal. According to the findings, the model was appropriate for the experimental data (Mahmoudiani et al., 2022). Figure 2 displays the validation of the predicted response values with the actual response values for Na-NLR and Si-NLR.

Tables 7, 8 illustrate the ANOVA results for Na-NLR and Si-NLR, respectively. According to Tables 7, 8, the F-values of 674.12 and 773.27 for Na-NLR and Si-NLR, respectively, imply the models are significant. In both models, there is only a 0.01% chance that an F-value this large could occur due to noise. Also, in Tables 7, 8, significant and insignificant model terms can be seen. It is perfectly clear that p-values less than 0.0500 and greater than 0.0500 indicate that model terms are significant and insignificant, respectively. For the response of Na-NLR, the F-value and p-value for "Lack of Fit" are 5.95 and 0.0589, and for the response of Si-NLR, they are 5.66 and 0.0636, respectively, which reveal that the "Lack of

TABLE 5 Results of BBD with actual and RSM predicted data.

Run	Independent variables			Dependent variables (Responses)			
	Factor A: Temp°C	Factor B: pH	Factor C: Time, d	Na-NLR [g/(m^2.d)]		Si-NLR [g/(m^2.d)]	
				Actual	Predicted	Actual	Predicted
1	70	8	21	1.03E-02	1.02E-02	9.23E-03	9.12E-03
2	50	8	14	8.46E-03	7.94E-03	5.14E-03	5.13E-03
3	70	10	14	1.72E-02	1.74E-02	1.30E-02	1.32E-02
4	50	10	21	7.59E-03	8.13E-03	7.60E-03	7.76E-03
5	70	12	7	2.91E-01	2.95E-01	2.47E-01	2.52E-01
6	70	12	21	1.13E-01	1.09E-01	9.07E-02	8.51E-02
7	50	12	14	1.08E-01	1.05E-01	6.36E-02	6.61E-02
8	90	10	21	2.27E-02	2.24E-02	2.01E-02	2.14E-02
9	70	10	14	1.68E-02	1.74E-02	1.35E-02	1.32E-02
10	90	12	14	2.30E-01	2.42E-01	1.91E-01	1.91E-01
11	70	10	14	1.78E-02	1.74E-02	1.27E-02	1.32E-02
12	90	10	7	5.35E-02	5.01E-02	5.72E-02	5.62E-02
13	70	10	14	1.66E-02	1.74E-02	1.37E-02	1.32E-02
14	50	10	7	2.12E-02	2.14E-02	1.68E-02	1.58E-02
15	90	8	14	2.19E-02	2.24E-02	1.74E-02	1.70E-02
16	70	8	7	2.15E-02	2.24E-02	1.56E-02	1.66E-02
17	70	10	14	1.78E-02	1.74E-02	1.30E-02	1.32E-02

TABLE 6 Variance analysis (ANOVA) results for the response quadratic models.

Parameter	Na-NLR	Si-NLR
Standard deviation	0.0316	0.0236
Mean	−1.53	−1.63
Coefficient of variance (CV, %)	2.06	1.45
Coefficient of determination (R^2)	0.9970	0.9988
Adjusted R^2	0.9957	0.9976
Predicted R^2	0.9912	0.9872
Adequate precision	82.0868	97.5829

Fit" is not significant. It is not far from expected that to have a fitting model, there should be an insignificant lack of fit (Abazarpoor et al., 2013; Astutiningsih et al., 2022; Hamza et al., 2022). The diagnostic plot of residuals vs. run order of experiments for responses is represented in Figure 3, demonstrating that the residuals are random in nature and don't display any pattern with run order and revealing that there is no noticeable pattern or unusual structure associated with the data (Sahoo and Mishra, 2014). Externally studentized residuals based on a deletion method are the default due to being more sensitive for finding problems with the analysis. It is obvious from Figure 3 that all points are inside the red lines (+4.81963 and −4.81963 externally studentized residuals), which ensures that the model fits effectively.

Given that it is an important assumption for statistical data to follow a normal distribution, the Box–Cox transformation was used to analyze the data obtained in this research. Figure 4 indicates the plot of the Box-Cox for Na-NLR and Si-NLR. As can be seen from Figure 4, the values of Lambda, which symbolizes the power applied to the response values obtained for Na-NLR and Si-NLR, are within the 95% confidence interval (Amdoun et al., 2010; Oroumei and Naebe, 2017; Freya and Senthil, 2022). It can be concluded that there is no need to change the response transformation because the models are in the optimum region.

3.3 Effects of the factors on the responses of the Na-NLR and the Si-NLR

The perturbation plots for the Na-NLR (a) and Si-NLR (b) models are shown in Figure 5. These plots provide an outline view of the normalized leaching rates of Na and Si and indicate how these responses alter when any independent variable deviates from the reference value while keeping all other variables constant (Oroumei and Naebe, 2017). It is perfectly evident from Figure 5 that the pH of leachate (factor B) has a negative impact on the durability of PWRHLW-BSG-1simulated waste glass to leaching, and it should also be noted that according to the perturbation plots, the effect of

10.3389/fchem.2024.1349531

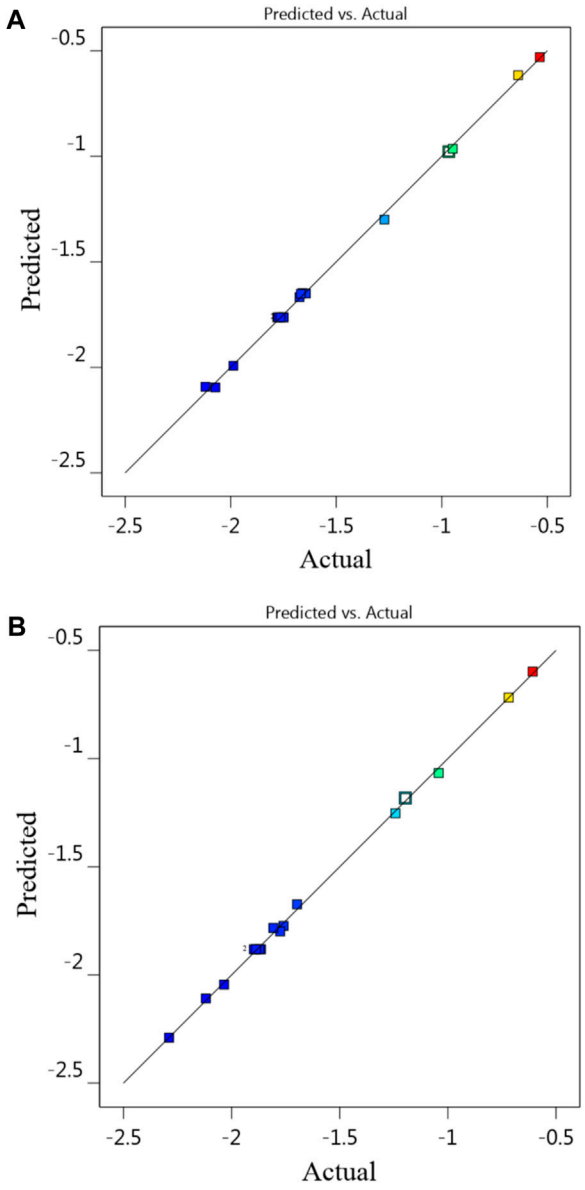

FIGURE 2
The diagnostic plot of predicted vs. actual values for **(A)** Na-NLR and **(B)** Si-NLR.

pH on sodium leaching rate was greater than silicon leaching rate. Factors A (temperature) and C (leaching time) have little positive and negative effects, respectively, on the Na-NLR and Si-NLR. It cannot be ruled out that the pH of leachant produces a higher effect on the investigated responses as compared to temperature and leaching time factors.

Two and three-dimensional surface plots were created using quadratic polynomial model equations (Eqs 4, 5) to visualize the correlation between the Na-NLR and Si-NLR, which are the dependent variables, and the leaching conditions, which are the independent variables (Figures 6, 7). As can be seen from Figure 6, the period of leaching time was set at the center point (14 days), and the Na-NLR (a) and Si-NLR (b) vary with pH and temperature changes. According to the 2D and 3D surface plots in Figure 6, the Na-NLR and Si-NLR increase with increasing pH from 8 to 12. Especially at pH 12, this increase in leaching rates is more severe for both elements. Also, it is worth mentioning that the Na element in PWRHLW-BSG-1 simulated waste glass over a period of 14 days is more sensitive to pH changes and has been leached more than the Si element. As the temperature of the leachate throughout this time period rises from 50°C to 90°C, the normalized leaching rates of Na and Si from the PWRHLW-BSG-1 increase, but they do so slowly. As a result, with the simultaneous increase in pH and temperature, the leaching rates of both elements increase, so, during a period of 14 days, the maximum leaching rates for Na and Si have been calculated at pH 12 and temperature 90°C, that is, Na-NLR is equal to 0.23 g/(m^2. d) and Si-NLR is equal to 0.19 g/(m^2. d). It is also better to mention that the slope of the normalized leaching rate as a function of temperature is therefore less steep than the slope of the normalized leaching rate as a function of pH, i.e., the Na-NLR and Si-NLR are more sensitive to the pH effect compared to the temperature effect.

Due to the sorption of H^+, OH^-, and H_2O on the glass surface, pH plays an important role in the glass dissolving reaction. For usage in acidic, neutral, and alkaline solutions, various parameter values for the pH dependence have been recommended (Köhler et al., 2003; Zapol et al., 2013; Neeway et al., 2018). It is important to keep in mind that a lot of minerals and glasses show a V-shaped dependency in the dissolving rate as a function of pH, meaning that the rate is often high in acidic solutions, approaches a minimum in the range of pH values that are close to neutral, and rises as the alkalinity of the solution's contents rises (Brantley, 2008; Kim et al., 2011; Inagaki et al., 2012). The slope of glass dissolving as a function of pH is not the same for acidic and alkaline solutions, but this known behavior may be approximated by simply altering the pH dependence coefficient (Jeong and Ebert, 2002; Pierce et al., 2008; Vienna et al., 2018), when circumstances shift from alkaline to acidic (Inagaki et al., 2013; Kweinor Tetteh et al., 2021).

The dissociation of H_4SiO_4 into $H_3SiO_4^{1-}$ and $H_2SiO_4^{2-}$ species has been demonstrated to significantly improve the solubility of silica over pH 9. As a result, it may be anticipated that Si release rates and, therefore, alkali ion releases may rise as a result of ion exchange activities (Cassingham et al., 2015). The process of ion exchange is a significant reaction since it enables the disintegration of the glass network into the aqueous phase. This happens as a result of the local pH being raised by the loss of H^+ from the aqueous phase, which in turn produces OH^- ions that can attack the structure of glass directly (McGrail et al., 2001; Pierce et al., 2008). It is generally accepted that this mechanism involves the inter-diffusion of H (as H^+ or H_3O^+) in solution and network-modifying cations in the glass, while the network-forming components' ionic covalent bonds (Si-O-Si, Si-O-Na, etc.) suffer hydrolysis and are attacked by OH^- through nucleophilic nucleation. The breaking of the Si-O bonds and the separation of Si are thought to be the rate-limiting steps in this reaction (Cassingham et al., 2015). Therefore, according to these presented arguments, it is concluded that the leaching mechanism of PWRHLW-BSG-1 simulated waste glass has been affected by the release of $H_3SiO_4^{1-}$ and $H_2SiO_4^{2-}$ during the leaching process. Table 4 confirms this conclusion because all the pHs after leaching are lower than the pHs before leaching. $H_3SiO_4^{1-}$ and $H_2SiO_4^{2-}$ ions increase the H^+ species in the solution and further decrease the pH.

TABLE 7 Variance analysis (ANOVA) for the response of Na-NLR quadratic models.

Source	Sum of squares	df	Mean square	F-value	*p*-value	
Model	3.70	9	0.4107	674.12	< 0.0001	significant
A	0.3278	1	0.3278	538.00	< 0.0001	significant
B	2.31	1	2.31	3,791.48	< 0.0001	significant
C	0.3002	1	0.3002	492.82	< 0.0001	significant
AB	0.0018	1	0.0018	2.95	0.1295	not significant
AC	0.0014	1	0.0014	2.22	0.1795	not significant
BC	0.0022	1	0.0022	3.55	0.1016	not significant
A^2	0.0014	1	0.0014	2.27	0.1754	not significant
B^2	0.7107	1	0.7107	1,166.64	< 0.0001	significant
C^2	0.0194	1	0.0194	31.82	0.0008	significant
Residual	0.0043	7	0.0006			
Lack of fit	0.0035	3	0.0012	5.95	0.0589	not significant
Pure error	0.0008	4	0.0002			
Cor total	3.70	16				

TABLE 8 Variance analysis (ANOVA) for the Response of Si-NLR quadratic models.

Source	Sum of squares	df	Mean square	F-value	*p*-value	
Model	3.78	9	0.4203	773.27	< 0.0001	significant
A	0.4811	1	0.4811	885.15	< 0.0001	significant
B	2.34	1	2.34	4,301.98	< 0.0001	significant
C	0.2669	1	0.2669	490.98	< 0.0001	significant
AB	0.0007	1	0.0007	1.23	0.3043	not significant
AC	0.0031	1	0.0031	5.66	0.0489	significant
BC	0.0107	1	0.0107	19.68	0.0030	significant
A^2	0.0032	1	0.0032	5.82	0.0466	significant
B^2	0.5547	1	0.5547	1,020.48	< 0.0001	significant
C^2	0.0890	1	0.0890	163.72	< 0.0001	significant
Residual	0.0038	7	0.0005			
Lack of fit	0.0031	3	0.0010	5.66	0.0636	not significant
Pure error	0.0007	4	0.0002			
Cor total	3.79	16				

Also, to justify the effect of temperature, as mentioned above, raising the temperature increased each element's normalized dissolution rate. According to the empirical Arrhenius equation (Jeong and Ebert, 2002; Pierce et al., 2008; Neeway et al., 2018; Vienna et al., 2018), a description of the observed temperature dependence on the dissolving rate is provided. It is obvious that, variations in temperature and pH influence the process of glass modification because they vary the activation energies of elements at various pHs (Inagaki et al., 2012; Cassingham et al., 2015).

The leaching behavior of Na and Si with respect to temperature and pH changes in the PWRHLW-BSG-1 simulated waste glass investigated in this study, along with the leaching behavior of Na and Si elements and other important elements involved in the structure of glasses in the matrices of different waste glass, has been compared, so that these matrices with different leaching models in temperature and pH under similar conditions have been tested. The results show that the pattern of changes in the leaching rates of the elements investigated in this research is very similar to the pattern of changes

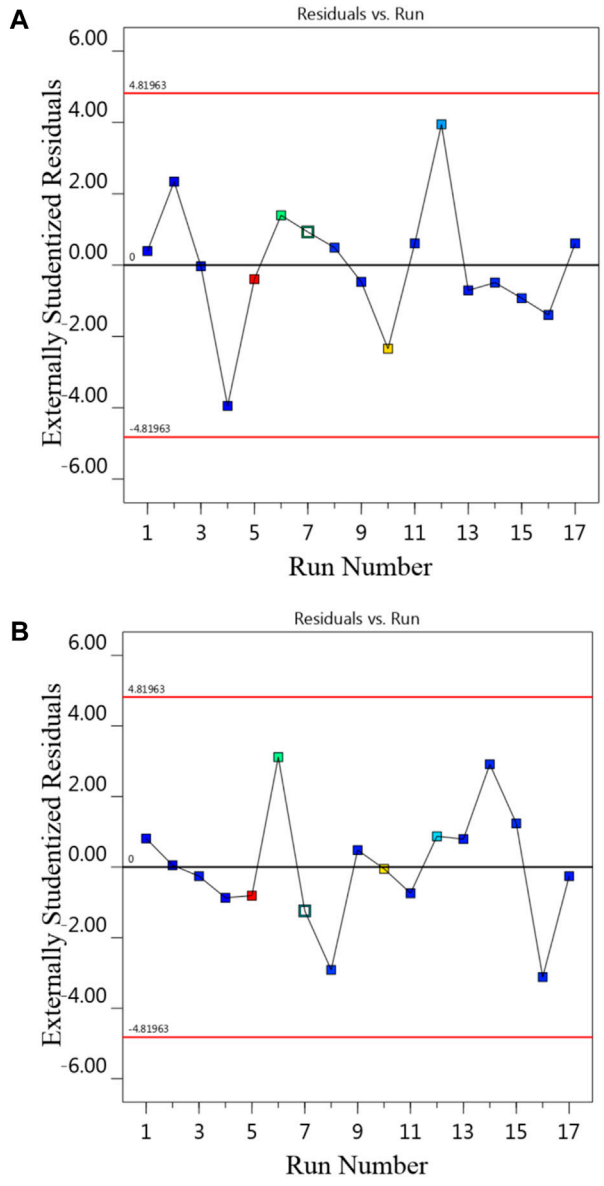

FIGURE 3
The diagnostic plot of residuals vs. run for **(A)** Na-NLR and **(B)** Si-NLR.

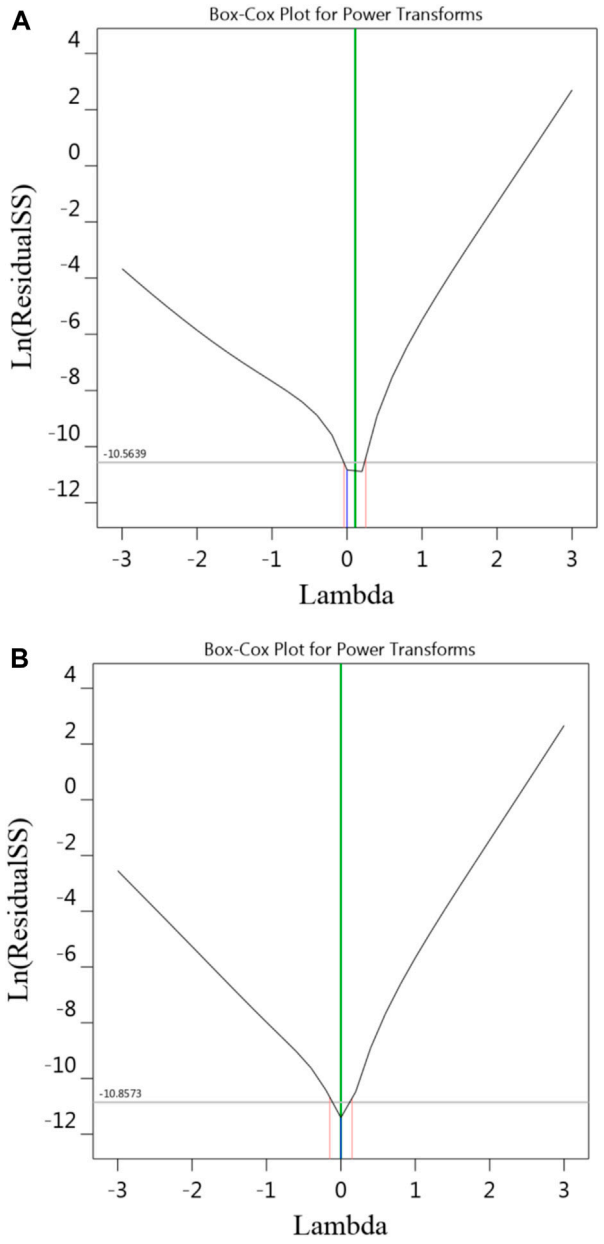

FIGURE 4
The diagnostic plot of Box-Cox for transformation, **(A,B)** are related to Na-NLR and Si-NLR respectively.

in the leaching rates of elements in glasses of AFCI, ISG, SON68 (Neeway et al., 2018), LAWA44, LAWB45, LAWC22, SRL202 (Pierce et al., 2008), MT25, MT30 (Cassingham et al., 2015), a complex borosilicate glass (Abraitis et al., 1997), LD6-5412 (McGrail et al., 1997), P0798 (Inagaki et al., 2012), and ISG (Backhouse et al., 2018).

Figure 7 depicts the interaction effects of pH and leaching time on the (a) Na-NLR and (b) Si-NLR at a fixed center point of temperature (70°C). As can be observed from the 2D and 3D surface plots in Figure 7, at the temperature of 70°C with an increasing pH from 8 to 12, the Na-NLR and Si-NLR increase, but factor C of the leaching time has a little negative effect on the Na-NLR and Si-NLR, so that, after the glass was affected by the leaching process and the Na and Si began to be released, the leaching rates of elements gradually reached an approximately constant value over time. As a result, with the simultaneous increase in pH and leaching time, the leaching rates of both elements increase in general, but this increase has a lower intensity compared to the effect of the simultaneous increase in temperature and pH on the leaching rates.

The comparison of the leaching behavior of Na and Si as a function of time in the PWRHLW-BSG-1 with the leaching behavior of Na and Si elements and other important elements in the various waste glasses, so that these glasses have been tested with different leaching models in pH and leaching time under similar conditions, gave the result that the pattern of changes in the leaching rates of the elements studied in this work is very similar to the pattern of changes in the leaching rates of elements in other different waste glasses. For example, glasses of LD6-5412 (McGrail et al., 1997), a

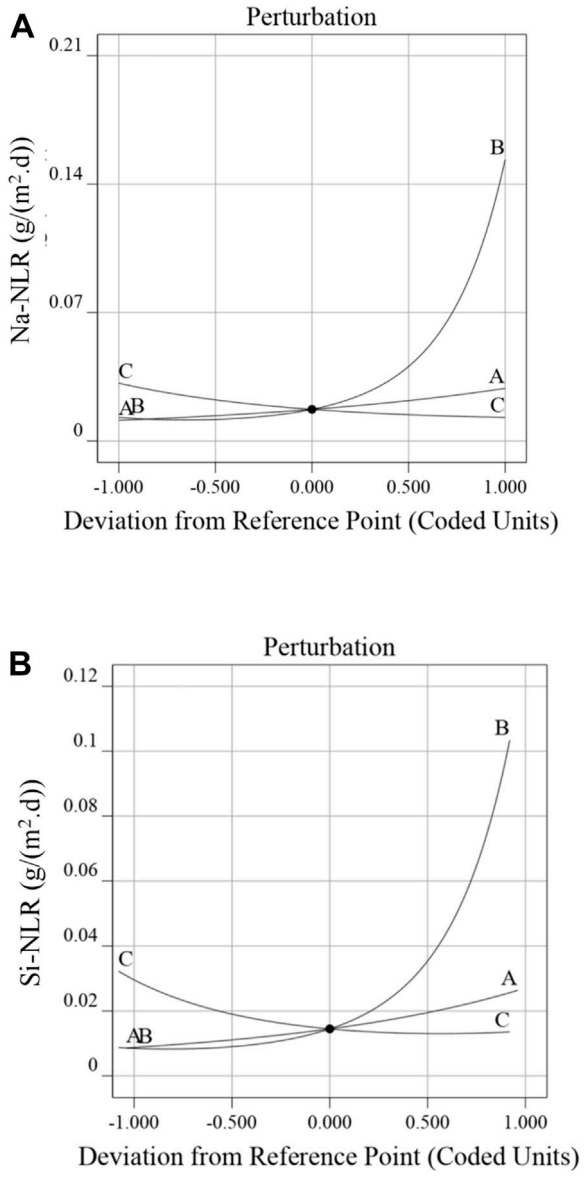

FIGURE 5
Perturbation plot displaying the effect of factors A, B, and C on the **(A)** Na-NLR and **(B)** Si-NLR.

simple five-component borosilicate glass (Knauss et al., 1989), P0798 (Inagaki et al., 2012), LAWA44 (Pierce et al., 2008), DG2B (Kim et al., 2011), P0798 (Inagaki et al., 2006), CSG (Jeong and Ebert, 2002), and a natural glass (Wolff-Boenisch et al., 2004) were compared.

From a kinetic perspective, transport or chemical interactions at the interface control how quickly glasses dissolve. Surface reaction control is indicated by a constant leachate concentration throughout time in the leaching tests. The leached glass is vulnerable to leachant attack, which causes partial glass disintegration and changes to the surface. Some glass constituents leak into the leachate, and other glass and leachate constituents bind to the surface of the glass to produce a precipitated layer. It comprises a crystal and/or amorphous collection with impacts on the progression of the leaching process and corrosion growth. Based on these principles of glass leaching kinetics and considering that the Na-NLR and Si-NLR in the PWRHLW-BSG-1 remain approximately constant over time, and since the PCT test was done in a closed system, it can be considered that the leaching of the PWRHLW-BSG-1 follows four steps: the diffusion of water substances into the glass structure (stage I), ion exchange with protons (stage II), hydrolysis of network-modifying species in the PWRHLW-BSG-1 structure (stage III), and the formation of a precipitated layer on the surface of the glass due to the saturation of the solution with leached species in a closed system (stage IV). For interest, in the work (Luo et al., 1997), the compositional changes in the surface layer, surface layer precipitation, surface layer pitting corrosion, and surface layer break and spallation were detailly examined.

A similar conclusion has been drawn related to stage IV of PWRHLW-BSG-1 leaching in a static test (Frankel et al., 2018). In that test, as time passes, the concentration of components in the leachate rises, and the leach rate progressively falls as the chemical affinity for dissolution decreases. The soluble capacity of secondary phase precipitates, particularly for incongruent dissolution, may have an impact on the pace of dissolution as dissolved components accumulate. The concentration of leachate in solution approaches saturation as a result of a buildup of the dissolved molecules in bulk solution and a consequent reduction in under saturation.

Another of our possible hypotheses regarding the reason for the constant Na-NLR and Si-NLR in the PWRHLW-BSG-1 over time is in accordance with the findings of research work (Inagaki et al., 2012). It is stated that the relatively higher rate of dissolution at the beginning of the test period may have been brought on by the initial glass specimen's larger surface area, which was originally rough due to polishing. As the glass dissolves, the roughness becomes smoother, resulting in a constant dissolution rate for the duration of the test period, which extends above 20 h. Anyway, in order to check the correctness of the proposed hypothesis, it needs future analyses related to PWRHLW-BSG-1 simulated waste glass.

3.4 Experimental validation of the BBD model

To evaluate the employed model to study the leaching behavior of PWRHLW-BSG-1 simulated waste glass in this research, as well as to ensure the accuracy of the results obtained from leaching Na and Si, in addition to the suggested points of the model, six confirmation experiments were conducted in parallel with different parameters other than the points designed by the model. For this purpose, the laboratory results obtained for these 6 tests in the "Post Analysis—Confirmation" section of Design-Expert software, according to Tables 9, 10, for Na-NLR and Si-NLR, respectively, have been compared with statistical data within the predicted range at a 95% confidence level. As can be seen from Tables 9, 10, the actual leaching rates obtained for Na and Si are reasonably close to the predicted values and are located within 95% PI (Prediction Interval) low and 95% PI (Prediction Interval) high intervals (Oroumei and Naebe, 2017; Enyoh et al., 2022; Freya and Senthil, 2022). Hence, it can be concluded that consistency between the data verifies the model's potential for prediction that was employed in this work and reveals that the experimental result is substantially close to the desired value.

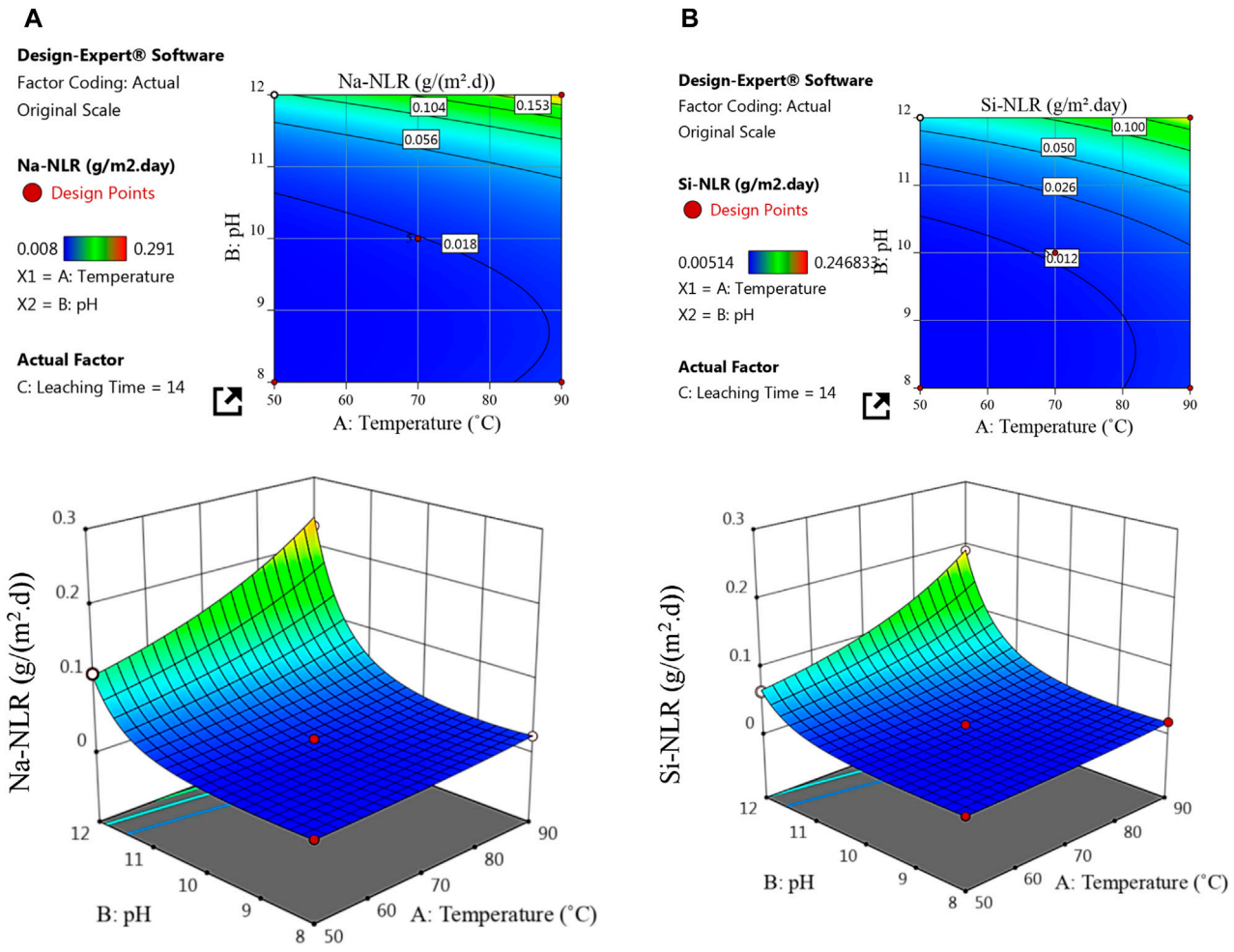

FIGURE 6
2D and 3D response surface plots for the effect of temperature and pH on the **(A)** Na-NLR and **(B)** Si-NLR during period of 14 days.

However, the authors advise that in future research, the PWRHLW-BSG-1 be subjected to experimental and statistical analysis with leaching tests other than PCT and over a wide range of time and temperature intervals, as well as in environments with acidic and alkaline pH with a pH difference of 1. It is also better to be notified that the leaching behavior of two other important elements, boron and strontium, in PWRHLW-BSG-1 is currently being analyzed in another research work. Nevertheless, the results obtained under the new conditions and the comparison with the previous results, as well as the evaluation of the potential of the model under variable circumstances and the comparison of the leaching behavior of B and Sr elements with Na and Si, allow for more decisive decisions to be made regarding the PWRHLW-BSG-1 as a matrix for the immobilization of spent nuclear fuel components.

4 Conclusion

The investigation of the leaching behavior of Na and Si elements as a function of time, pH, and temperature in HLW borosilicate glass simulated from waste of a 1000 MWe class PWR reactor using RSM and BBD leads to the following conclusion:

1. Experiments using the PCT leaching test were conducted at three different temperatures of 50, 70, and 90°C (Factor A), under alkaline conditions at pH (Factor B) 8, 10, and 12, and during periods of 7, 14, and 21 days (Factor C). The experimental and predicted normalized leaching rates of Na and Si obtained through 17 sets of experimental runs produced by BBD were related. The relative consistency of the data further confirmed the model's applicability.
2. The results of statistical analysis (ANOVA) for Na-NLR and Si-NLR indicated that the effects of the individual variables and some of the interactions between the variables were statistically significant. The diagnostic plots of predicted vs. actual values and residuals vs. run for Na-NLR and Si-NLR confirmed the validation of the data and revealed that there is no noticeable pattern or unusual structure associated with the data. The values of Lambda obtained through the Box–Cox transformation are within the 95% confidence interval.
3. According to the 2D and 3D surface plots, while the period of leaching time was set at the center point (14 days), with the simultaneous increase in pH and temperature, the leaching rates of both elements Na and Si increased; nevertheless, the

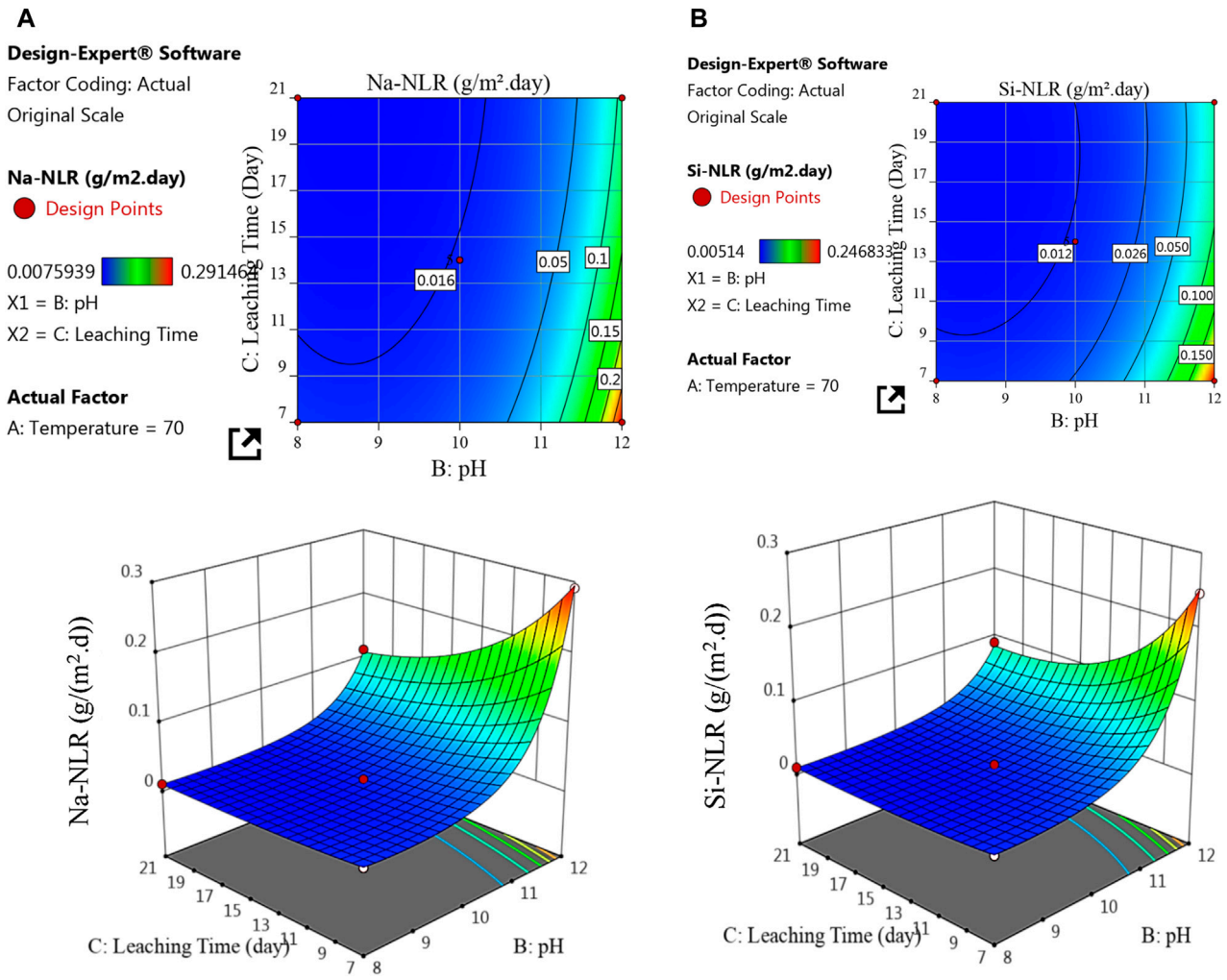

FIGURE 7
2D and 3D response surface plots for the effect of pH and leaching time on the **(A)** Na-NLR and **(B)** Si-NLR at temperature of 70°C.

TABLE 9 Confirmatory values of BBD analysis results for Na-NLR.

Response	Na-NLR [g/(m².d)]					
Number of experiment according to Table 3	1	2	3	4	5	6
Predicted mean	1.29E-02	3.16E-02	1.13E-02	2.87E-02	1.29E-02	1.53E-01
Predicted median	1.29E-02	3.15E-02	1.13E-02	2.87E-02	1.29E-02	1.53E-01
Std Dev	7.34E-04	1.79E-03	6.43E-04	1.63E-03	7.35E-04	8.72E-03
95% PI low	1.10E-02	2.69E-02	9.65E-03	2.45E-02	1.10E-02	1.31E-01
Actual data	1.12E-02	2.96E-02	1.08E-02	2.50E-02	1.13E-02	1.69E-01
95% PI high	1.51E-02	3.69E-02	1.32E-02	3.35E-02	1.51E-02	1.79E-01

slope of the normalized leaching rate as a function of temperature is therefore less steep than the slope of the normalized leaching rate as a function of pH. It is obvious that variations in temperature and pH influence the process of glass modification because they vary the activation energies of elements at various pHs.

4. When the temperature of 70°C was fixed at a center point, the 2D and 3D surface plots indicated that with an increasing pH, the Na-NLR and Si-NLR increased, but factor C of the leaching time had a little negative effect on the rates. So that, after the glass was affected by the leaching process and the Na and Si began to be released, the leaching rates of the elements gradually reached an approximately

TABLE 10 Confirmatory value of BBD analysis results for Si-NLR.

Response	Si-NLR [g/(m^2.d)]					
Number of experiment according to Table 3	1	2	3	4	5	6
Predicted mean	8.74E-03	2.80E-02	7.97E-03	2.47E-02	1.21E-02	1.05E-01
Predicted median	8.73E-03	2.80E-02	7.96E-03	2.46E-02	1.21E-02	1.05E-01
Std Dev	4.70E-04	1.51E-03	4.28E-04	1.32E-03	6.49E-04	5.66E-03
95% PI low	7.53E-03	2.41E-02	6.86E-03	2.12E-02	1.04E-02	9.08E-02
Actual data	8.31E-03	2.49E-02	6.90E-03	2.28E-02	1.08E-02	1.22E-01
95% PI high	1.01E-02	3.24E-02	9.23E-03	2.86E-02	1.40E-02	1.22E-01

constant value over time. Hence, with the simultaneous increase in pH and leaching time, the leaching rates of both elements increase in general, but this increase has a lower intensity compared to the effect of the simultaneous increase in temperature and pH on the leaching rates.

5. The comparison of the leaching behavior of Na and Si in the PWRHLW-BSG-1 with the leaching behavior of the mentioned elements and other important elements in the various waste glasses, so that these glasses have been tested with different leaching models in temperature, pH, and leaching time under similar conditions, gave the result that the pattern of changes in the leaching rates of the elements studied in this work is very similar to the pattern of changes in the leaching rates of elements in other different waste glasses.
6. The experimental validation of the BBD model showed that the actual leaching rates obtained for Na and Si are reasonably close to the predicted values and are located within 95% PI low and 95% PI high intervals.

Data availability statement

The original contributions presented in the study are included in the article/Supplementary material, further inquiries can be directed to the corresponding authors.

Author contributions

MH: Conceptualization, Investigation, Methodology, Software, Writing–original draft, Writing–review and editing. AY: Methodology, Supervision, Validation, Writing–original draft. MS: Methodology, Validation, Writing–original draft. HS: Supervision, Writing–review and editing. MO: Supervision, Writing–review and editing.

Funding

The author(s) declare that no financial support was received for the research, authorship, and/or publication of this article.

Acknowledgments

The Authorities of the Department of Energy Engineering of Sharif University of Technology are thanked and appreciated.

Conflict of interest

The authors declare that the research was conducted in the absence of any commercial or financial relationships that could be construed as a potential conflict of interest.

Publisher's note

References

Abazarpoor, A., Halali, M., Maarefvand, M., and Khatibnczhad, H. (2013). Application of response surface methodology and central composite rotatable design for modeling and optimization of sulfuric leaching of rutile containing slag and ilmenite. *Russ. J. Non-Ferrous Metals* 54, 388–397. doi:10.3103/s1067821213050027

Abraitis, P., Vaughan, D. J., Livens, F. R., Monteith, J., Trivedi, D. P., and Small, J. S. (1997). Dissolution of a complex borosilicate glass at 60°C: the influence of pH and proton adsorption on the congruence of short-term leaching. *MRS Online Proc. Libr. Opl.* 506, 47. doi:10.1557/proc-506-47

Amdoun, R., Khelifi, L., Khelifi-Slaoui, M., Amroune, S., Asch, M., Assaf-Ducrocq, C., et al. (2010). Optimization of the culture medium composition to improve the production of hyoscyamine in elicited Datura stramonium L. hairy roots using the response surface methodology (RSM). *Int. J. Mol. Sci.* 11 (11), 4726–4740. doi:10.3390/ijms11114726

Astutiningsih, F., et al. (2022). Optimization of saffron essential oil nanoparticles using chitosan-Arabic gum complex nanocarrier with ionic gelation method. *Int. J. Food Sci.*, 2022. doi:10.1155/2022/4035033

Backhouse, D. J., Fisher, A. J., Neeway, J. J., Corkhill, C. L., Hyatt, N. C., and Hand, R. J. (2018). Corrosion of the international simple glass under acidic to hyperalkaline conditions. *Npj Mater. Degrad.* 2 (1), 29. doi:10.1038/s41529-018-0050-5

Brantley, S. L. (2008). "Kinetics of mineral dissolution," in *Kinetics of water-rock interaction* (Springer), 151–210.

Cassingham, N., Corkhill, C., Backhouse, D., Hand, R., Ryan, J., Vienna, J., et al. (2015). The initial dissolution rates of simulated UK Magnox–ThORP blend nuclear waste glass as a function of pH, temperature and waste loading. *Mineral. Mag.* 79 (6), 1529–1542. doi:10.1180/minmag.2015.079.6.28

Committee, A. (2002). *Standard test methods for determining chemical durability of nuclear, hazardous, and mixed waste glasses and multiphase glass ceramics: the product consistency test (PCT)*. West Conshohocken: ASTM International.

Crawford, C., Marra, J., and Bibler, N. (2007). Glass fabrication and product consistency testing of lanthanide borosilicate glass for plutonium disposition. *J. alloys Compd.* 444, 569–579. doi:10.1016/j.jallcom.2007.02.164

Ebert, W. L., and Jerden, J. L., Jr (2019). Parameterizing a borosilicate waste glass degradation model. *npj Mater. Degrad.* 3 (1), 31. doi:10.1038/s41529-019-0093-2

Enyoh, C. E., Wang, Q., and Ovuoraye, P. E. (2022). Response surface methodology for modeling the adsorptive uptake of phenol from aqueous solution using adsorbent polyethylene terephthalate microplastics. *Chem. Eng. J. Adv.* 12, 100370. doi:10.1016/j.ceja.2022.100370

Ewing, R. C., Weber, W. J., and Lian, J. (2004). *Nuclear waste disposal—pyrochlore (A2B2O7): Nuclear waste form for the immobilization of plutonium and "minor" actinides. J. Appl. Phys.* 95 (11), 5949–5971. doi:10.1063/1.1707213

Frankel, G. S., Vienna, J. D., Lian, J., Scully, J. R., Gin, S., Ryan, J. V., et al. (2018). A comparative review of the aqueous corrosion of glasses, crystalline ceramics, and metals. *npj Mater. Degrad.* 2 (1), 15. doi:10.1038/s41529-018-0037-2

Freya, R., and Senthil, R. (2022). Optimal evaluation of the rheological parameters for STF dampers in semi-rigid joints of steel structures using response surface method. *Adv. Civ. Eng.*, 2022. doi:10.1155/2022/1769739

Frugier, P., Gin, S., Minet, Y., Chave, T., Bonin, B., Godon, N., et al. (2008). SON68 nuclear glass dissolution kinetics: current state of knowledge and basis of the new GRAAL model. *J. Nucl. Mater.* 380, 8–21. doi:10.1016/j.jnucmat.2008.06.044

Gin, S., Jollivet, P., Fournier, M., Angeli, F., Frugier, P., and Charpentier, T. (2015a). Origin and consequences of silicate glass passivation by surface layers. *Nat. Commun.* 6 (1), 6360. doi:10.1038/ncomms7360

Gin, S., Jollivet, P., Fournier, M., Berthon, C., Wang, Z., Mitroshkov, A., et al. (2015b). The fate of silicon during glass corrosion under alkaline conditions: a mechanistic and kinetic study with the International Simple Glass. *Geochimica Cosmochimica Acta* 151, 68–85. doi:10.1016/j.gca.2014.12.009

Hamza, H., Eterigho-Ikelegbe, O., Jibril, A., and Bada, S. O. (2022). Application of the response surface methodology to optimise the leaching process and recovery of rare earth elements from discard and run of mine coal. *Minerals* 12 (8), 938. doi:10.3390/min12080938

Hosseinpour Khanmiri, M., and Bogdanov, R. (2018). Nuclear chemical effects in the paragenetic mineral association based on polycrase. *Radiochemistry* 60, 79–91. doi:10.1134/s1066362218010137

Hosseinpour Khanmiri, M., Bogdanov, R. V., Titov, A. V., Fomin, E. V., Samadfam, M., and Outokesh, M. (2024). *The tendency towards equalization of the $^{234}U/^{238}U$ isotopic activity ratios in fractions of U(IV) and U(VI) during thermal annealing of metamict polycrase. Appl. Geochem.* 161, 105881. doi:10.1016/j.apgeochem.2023.105881

Hosseinpour Khanmiri, M., Yanson, S. Y., Fomin, E. V., Titov, A. V., Grebeniuk, A. V., Polekhovsky, Y. S., et al. (2018). Uranium as a possible criterion for the hydrochemical alteration of betafite. *Phys. Chem. Minerals* 45, 549–562. doi:10.1007/s00269-018-0941-6

Hyatt, N. C., and Ojovan, M. I. (2019). Materials for nuclear waste immobilization. *MDPI* 12 (21), 3611. doi:10.3390/ma12213611

Inagaki, Y., Kikunaga, T., Idemitsu, K., and Arima, T. (2013). Initial dissolution rate of the international simple glass as a function of pH and temperature measured using microchannel flow-through test method. *Int. J. Appl. Glass Sci.* 4 (4), 317–327. doi:10.1111/ijag.12043

Inagaki, Y., Makigaki, H., Idemitsu, K., Arima, T., Mitsui, S. I., and Noshita, K. (2012). Initial dissolution rate of a Japanese simulated high-level waste glass P0798 as a function of pH and temperature measured by using micro-channel flow-through test method. *J. Nucl. Sci. Technol.* 49 (4), 438–449. doi:10.1080/00223131.2012.669246

Inagaki, Y., Shinkai, A., Idemistu, K., Arima, T., Yoshikawa, H., and Yui, M. (2006). Aqueous alteration of Japanese simulated waste glass P0798: effects of alteration-phase formation on alteration rate and cesium retention. *J. Nucl. Mater.* 354 (1-3), 171–184. doi:10.1016/j.jnucmat.2006.04.002

Jantzen, C. M., and Bibler, N. E. (2009). *Environmental issues and waste management technologies in the materials and nuclear industries XII. The product consistency test (PCT): how and why it was developed*, 155–167.

Jantzen, C. M., et al. (1992). *Nuclear waste glass product consistency test (PCT)*. Aiken, SC (United States): Savannah River Site (SRS). Version 5. 0.

Jeong, S.-Y., and Ebert, W. (2002). *Glass dissolution rates from static and flow-through tests*. IL (US): Argonne National Lab.

Kaushik, C., Mishra, R., Sengupta, P., Kumar, A., Das, D., Kale, G., et al. (2006). Barium borosilicate glass–a potential matrix for immobilization of sulfate bearing high-level radioactive liquid waste. *J. Nucl. Mater.* 358 (2-3), 129–138. doi:10.1016/j.jnucmat.2006.07.004

Kim, C.-W., Park, J.-K., and Hwang, T.-W. (2011). Analysis of leaching behavior of simulated LILW glasses by using the MCC-1 test method. *J. Nucl. Sci. Technol.* 48 (7), 1108–1114. doi:10.3327/jnst.48.1108

Knauss, K. G., Bourcier, W. L., McKeegan, K. D., Merzbacher, C. I., Nguyen, S. N., Ryerson, F. J., et al. (1989). Dissolution kinetics of a simple analogue nuclear waste glass as a function of pH, time and temperature. *MRS Online Proc. Libr.* 176, 176–381. doi:10.1557/proc-176-176

Köhler, S. J., Dufaud, F., and Oelkers, E. H. (2003). An experimental study of illite dissolution kinetics as a function of ph from 1.4 to 12.4 and temperature from 5 to 50°C. *Geochimica Cosmochimica Acta* 67 (19), 3583–3594. doi:10.1016/s0016-7037(03)00163-7

Kweinor Tetteh, E., Obotey Ezugbe, E., Asante-Sackey, D., Armah, E. K., and Rathilal, S. (2021). Response surface methodology: photocatalytic degradation kinetics of basic blue 41 dye using activated carbon with TiO2. *Molecules* 26 (4), 1068. doi:10.3390/molecules26041068

Lee, W. E., Ojovan, M. I., and Jantzen, C. M. (2013). *Radioactive waste management and contaminated site clean-up: processes, technologies and international experience*. Elsevier.

Luo, S., et al. (1997). *Alteration of leached glass surface*.

Mahmoudiani, F., Alamdar Milani, S., Hormozi, F., and Yadollahi, A. (2022). Application of response surface methodology for modeling and optimization of the extraction and separation of Se (IV) and Te (IV) from nitric acid solution by Cyanex 301 extractant. *Prog. Nucl. Energy* 143, 104052. doi:10.1016/j.pnucene.2021.104052

Manaktala, H. (1992). *NRC center for nuclear waste regulatory analysis report rep. No.* CNWRA, 92–017.An assessment of borosilicate glass as a high-level waste form

McCloy, J. S., and Goel, A. (2017). Glass-ceramics for nuclear-waste immobilization. *MRS Bull.* 42 (3), 233–240. doi:10.1557/mrs.2017.8

McGrail, B., Ebert, W., Bakel, A., and Peeler, D. (1997). Measurement of kinetic rate law parameters on a Na[Ca[Al borosilicate glass for low-activity waste. *J. Nucl. Mater.* 249 (2-3), 175–189. doi:10.1016/s0022-3115(97)00213-4

McGrail, B. P., Icenhower, J., Shuh, D., Liu, P., Darab, J., Baer, D., et al. (2001). The structure of Na2O–Al2O3–SiO2 glass: impact on sodium ion exchange in H2O and D2O. *J. Non-Crystalline Solids* 296 (1), 10–26. doi:10.1016/s0022-3093(01)00890-0

Neeway, J. J., Asmussen, R. M., McElroy, E. M., Peterson, J. A., Riley, B. J., and Crum, J. V. (2019). Kinetics of oxyapatite [Ca2Nd8 (SiO4) 6O2] and powellite [(Ca, Sr, Ba) MoO4] dissolution in glass-ceramic nuclear waste forms in acidic, neutral, and alkaline conditions. *J. Nucl. Mater.* 515, 227–237. doi:10.1016/j.jnucmat.2018.12.043

Neeway, J. J., Rieke, P. C., Parruzot, B. P., Ryan, J. V., and Asmussen, R. M. (2018). The dissolution behavior of borosilicate glasses in far-from equilibrium conditions. *Geochimica Cosmochimica Acta* 226, 132–148. doi:10.1016/j.gca.2018.02.001

Ojovan, M. I., and Lee, W. E. (2011). Glassy wasteforms for nuclear waste immobilization. *Metallurgical Mater. Trans. A* 42, 837–851. doi:10.1007/s11661-010-0525-7

Ojovan, M. I., Lee, W. E., and Kalmykov, S. N. (2019). *An introduction to nuclear waste immobilisation*. Elsevier.

Ojovan, M. I., and Yudintsev, S. V. (2023). Glass, ceramic, and glass-crystalline matrices for HLW immobilisation. *Open Ceram.* 14, 100355. doi:10.1016/j.oceram.2023.100355

Oroumei, A., and Naebe, M. (2017). Mechanical property optimization of wet-spun lignin/polyacrylonitrile carbon fiber precursor by response surface methodology. *Fibers Polym.* 18, 2079–2093. doi:10.1007/s12221-017-7363-9

Pierce, E. M., Rodriguez, E. A., Calligan, L., Shaw, W. J., and Pete McGrail, B. (2008). An experimental study of the dissolution rates of simulated aluminoborosilicate waste glasses as a function of pH and temperature under dilute conditions. *Appl. Geochem.* 23 (9), 2559–2573. doi:10.1016/j.apgeochem.2008.05.006

Rahman, R. A., El Abidin, D. Z., and Abou-Shady, H. (2013). Assessment of strontium immobilization in cement–bentonite matrices. *Chem. Eng. J.* 228, 772–780. doi:10.1016/j.cej.2013.05.034

Rahman, R. A., El Abidin, D. Z., and Abou-Shady, H. (2014). Cesium binding and leaching from single and binary contaminant cement–bentonite matrices. *Chem. Eng. J.* 245, 276–287. doi:10.1016/j.cej.2014.02.033

Rahman, R. O. A., and Saleh, H. M. (2018). "Introductory chapter: safety aspects in nuclear engineering," in *Principles and applications in nuclear engineering-radiation effects* (IntechOpen: Thermal Hydraulics, Radionuclide Migration in the Environment).

Rodrigues, C. S., Madeira, L. M., and Boaventura, R. A. (2009). Optimization of the azo dye Procion Red H-EXL degradation by Fenton's reagent using experimental design. *J. Hazard. Mater.* 164 (2-3), 987–994. doi:10.1016/j.jhazmat.2008.08.109

Sahoo, A., and Mishra, P. (2014). A response surface methodology and desirability approach for predictive modeling and optimization of cutting temperature in machining hardened steel. *Int. J. Industrial Eng. Comput.* 5 (3), 407–416. doi:10.5267/j.ijiec.2014.4.002

Stefanovsky, S., Skvortsov, M. V., Stefanovsky, O. I., Nikonov, B. S., Presniakov, I. A., Glazkova, I. S., et al. (2017). Preparation and characterization of borosilicate glass waste

form for immobilization of HLW from WWER spent nuclear fuel reprocessing. *MRS Adv.* 2 (11), 583–589. doi:10.1557/adv.2016.622

Teimouri, S. (2020). *Feasibility study on the use of imidazolium-based ionic liquids in the extraction of gold*. Master of Science in Engineering.

Thorat, V. S., Mishra, R. K., Sudarsan, V., Kumar, A., Tyagi, A. K., and Kaushik, C. P. (2019). Leaching studies on borosilicate glasses for the immobilization of high-level radioactive waste in the pellet form subjected to aggressive test conditions. *Bull. Mater. Sci.* 42, 211–218. doi:10.1007/s12034-019-1900-7

Vienna, J. D., et al. (2013). *Glass property models and constraints for estimating the glass to be produced at Hanford by implementing current advanced glass formulation efforts*. Richland, WA (United States): Pacific Northwest National Lab (PNNL).

Vienna, J. D., Neeway, J. J., Ryan, J. V., and Kerisit, S. N. (2018). Impacts of glass composition, pH, and temperature on glass forward dissolution rate. *npj Mater. Degrad.* 2 (1), 22. doi:10.1038/s41529-018-0042-5

Weber, W. J., Navrotsky, A., Stefanovsky, S., Vance, E. R., and Vernaz, E. (2009). Materials science of high-level nuclear waste immobilization. *MRS Bull.* 34 (1), 46–53. doi:10.1557/mrs2009.12

Wolff-Boenisch, D., Gislason, S. R., Oelkers, E. H., and Putnis, C. V. (2004). The dissolution rates of natural glasses as a function of their composition at pH 4 and 10.6, and temperatures from 25 to 74°C. *Geochimica Cosmochimica Acta* 68 (23), 4843–4858. doi:10.1016/j.gca.2004.05.027

Wu, P. P., Zhang, C., Xu, H. F., Huang, D. X., Xu, B., and Jiang, D. Y. (2011). Corrosion behaviors of borosilicate glasses in various leaching agents. *Adv. Mater. Res.* 177, 466–469. doi:10.4028/www.scientific.net/amr.177.466

Yim, M.-S., and Linga Murty, K. (2000). Materials issues in nuclear-waste management. *Jom* 52, 26–29. doi:10.1007/s11837-000-0183-0

Zapol, P., He, H., Kwon, K. D., and Criscenti, L. J. (2013). First-principles study of hydrolysis reaction barriers in a sodium borosilicate glass. *Int. J. Appl. Glass Sci.* 4 (4), 395–407. doi:10.1111/ijag.12052

frontiers | Frontiers in Chemistry

TYPE Review
PUBLISHED 28 May 2024
DOI 10.3389/fchem.2024.1400375

OPEN ACCESS

EDITED BY
Andreas Rosenkranz,
University of Chile, Chile

REVIEWED BY
Madhurya Chandel,
Warsaw University of Technology, Poland
Chenhui Yang,
Northwestern Polytechnical University, China
Max Marian,
Pontificia Universidad Católica de Chile, Chile

*CORRESPONDENCE
D. Parajuli,
deepenparaj@gmail.com

RECEIVED 13 March 2024
ACCEPTED 04 April 2024
PUBLISHED 28 May 2024

CITATION
Parajuli D (2024), MXenes-polymer nanocomposites for biomedical applications: fundamentals and future perspectives. *Front. Chem.* 12:1400375. doi: 10.3389/fchem.2024.1400375

MXenes-polymer nanocomposites for biomedical applications: fundamentals and future perspectives

D. Parajuli*

Research Center for Applied Science and Technology, Tribhuvan University, Kathmandu, Nepal

The article discusses the promising synergy between MXenes and polymers in developing advanced nanocomposites with diverse applications in biomedicine domains. MXenes, possessing exceptional properties, are integrated into polymer matrices through various synthesis and fabrication methods. These nanocomposites find applications in drug delivery, imaging, diagnostics, and environmental remediation. They offer improved therapeutic efficacy and reduced side effects in drug delivery, enhanced sensitivity and specificity in imaging and diagnostics, and effectiveness in water purification and pollutant removal. The perspective also addresses challenges like biocompatibility and toxicity, while suggesting future research directions. In totality, it highlights the transformative potential of MXenes-polymer nanocomposites in addressing critical issues across various fields.

KEYWORDS

MXene-polymers nanocomposites, biomedical applications, biocompatibility and toxicity, drug delivery and targeting, cost effective

1 Introduction

MXenes are a family of two-dimensional (2D) transition metal carbides, nitrides, or carbonitrides that exhibit a unique combination of properties, making them highly versatile materials (Naguib et al., 2014). MXenes are derived from layered ternary carbide, nitride, or carbonitride precursors known as MAX phases. The structure involves selective etching (Ghidiu et al., 2014) of the "A" element layers (typically aluminum) from the MAX phase, leaving behind a 2D layered structure. The general formula for MXenes is $M_{n+1}X_nT_x$, where M represents a transition metal (e.g., titanium, tantalum, or niobium), X is carbon and/or nitrogen, T represents surface terminations (such as hydroxyl or fluorine), and n is the number of metal layers (Halim et al., 2014). Without the hydroxyl or oxygen termination, they are hydrophilic (Harris et al., 2015; Halim, Cook, et al., 2016). MXenes typically exhibit metallic conductivity, making them suitable for applications in electronics, sensors (Guo et al., 2019), and energy storage devices (Simon and Gogotsi, 2008; Meng et al., 2014; Kurra, Hota, and Alshareef, 2015). The presence of transition metal layers contributes to their excellent electronic conductivity. MXenes possess impressive mechanical properties, including high stiffness and strength, making them suitable for applications where mechanical integrity is crucial (Ling et al., 2014). MXenes are chemically stable in various environments, showing feasibility for oxidation and resistance to corrosion. MXenes and their oxides are promising topological materials that are experimentally and

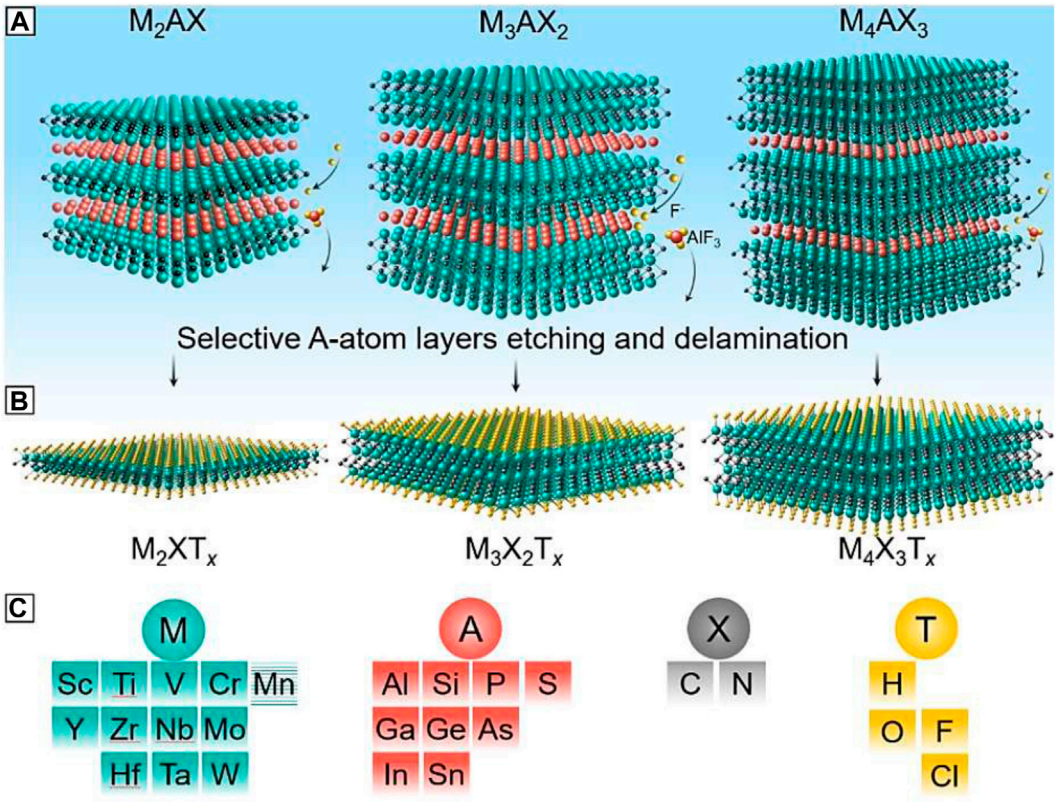

FIGURE 1
Different types of MXenes with different compositions with their precursor MAX phases. **(A)** MAX phases, **(B)** terminated MXenes after etching of MAX phases and **(C)** representation of M, A, X, and T. Adapted with the permission of (Hong et al., 2020)©Springer Nature 2020.

computationally studied (Parajuli and Samatha, 2022; 2019; Parajuli, Kaphle, and Samatha, 2019; Parajuli and Samatha, 2022; Parajuli, Uppugalla, et al., 2023) (S. Huang and Mochalin, 2019)(S. Huang and Mochalin, 2019). This stability contributes to their applicability in a wide range of conditions. The surface of MXenes is rich in functional groups, such as hydroxyl (OH-) and/or fluorine (F-) terminations, providing reactive sites for further functionalization. Surface functionalization enhances their compatibility with other materials and expands their application range (Harris et al., 2015; Halim, Cook, et al., 2016). MXenes typically have a high specific surface area due to their layered structure, which is advantageous for applications such as energy storage, catalysis, and sensing. MXenes exhibit interesting optical properties, including strong light absorption, which can be exploited in various optoelectronic and sensing applications. Their incorporation for energy storage were found more efficient that those we studied earlier (Parajuli, Murali, Samatha, and Veeraiah, 2022; Parajuli, Taddesse, Murali, Veeraiah, et al., 2022). MXenes demonstrate good thermal conductivity, making them promising candidates for applications in thermal management and electronic devices (Forrest, 2004; Y; Shi et al., 2015; Reese et al., 2004). The unique combination of electronic, mechanical, chemical, and optical properties makes MXenes a promising class of materials with diverse applications in fields ranging from electronics and energy storage to catalysis and biomedicine (Z. Liu et al., 2018; C; Dai, Chen, et al., 2017; Lin et al., 2018; X; Han et al., 2018) (C. Dai, Lin, et al., 2017).

The different types of MXenes derived from their precursors through their selective etching processes are shown in Figure 1A, it showcases three categories of mono-M MAX phases: M_2AX, M_3AX_2, and M_4AX_3, along with the selective etching procedure targeting the A-group layers (depicted by red atoms). In Figure 1B, it follows the selective etching process, MXenes emerge, characterized by the formation of surface terminations (depicted by yellow atoms) denoted as T. Figure 1C presents the potential elements for M, A, X, and T in both MAX and MXene phases. Additionally, although MXenes with orders as high as M_5X_4 have been successfully synthesized, they are not included in this table. It's noteworthy that while Mn occupies the M sites in MAX phases, MXenes containing Mn have not been synthesized to date, indicated by the horizontally patterned background of Mn.

MXenes in addition to their exhibiting excellent electrical conductivity, mechanical strength, and chemical stability, often lack certain properties required for specific applications (Bilibana, 2023). By incorporating MXenes into different matrices such as polymers, ceramics, or metals, it can be exploited synergistic effects to achieve desired functionalities. For instance, MXene nanocomposites can offer improved mechanical strength, electrical conductivity, thermal stability, and even functionalities like electromagnetic interference shielding or energy storage (Gao et al., 2020). These nanocomposites find

applications across various fields including energy storage devices like batteries and supercapacitors, electromagnetic shielding materials, sensors, catalysis, and biomedical devices. The versatility and tunability of MXene nanocomposites make them highly desirable for addressing specific needs in diverse technological domains (Perera et al., 2023). MXenes exhibit chemical stability, resisting oxidation and corrosion, contributing to the durability of nanocomposites in various environments (W. Wu et al., 2019a; M; Zhu et al., 2016b). MXenes can be synthesized with different transition metals, providing versatility in tailoring their properties for specific nanocomposite applications (Naguib et al., 2016).

In nanocomposite applications, MXenes are often combined with polymers, ceramics, or other materials to create hybrid materials with enhanced or multifunctional properties. The combination of these MXene properties allows for the development of advanced nanocomposites with diverse applications across various fields.

2 MXene, polymer, and their nanocomposites

MXene nanocomposites, combining the unique properties of MXenes with the versatility of polymers, offer enhanced mechanical, thermal, and electrical properties. These materials hold promise in applications such as flexible electronics and energy storage. Understanding fabrication techniques and interface engineering is crucial for tailoring MXene-polymer nanocomposites to specific needs. The MXene, Polymer, and their classification and nanocomposites are described briefly below.

2.1 MXenes

MXenes possess a distinctive set of properties that make them highly suitable for nanocomposite applications, particularly in the fields of biomedical science. MXenes have a unique 2D layered structure, providing a large surface area for interactions within nanocomposites. MXenes exhibit excellent electrical conductivity (Wang et al., 2019), making them advantageous for applications in electronics, sensors (Guo et al., 2019), and energy storage devices (George and Kandasubramanian, 2020). MXenes demonstrate impressive mechanical strength and stiffness, contributing to enhanced mechanical properties when incorporated into nanocomposites (Jimmy and Kandasubramanian, 2020). The surface of MXenes is rich in functional groups, such as hydroxyl and/or fluorine terminations, enabling easy surface modification and compatibility with other materials (Chen et al., 2020). MXenes typically possess a high specific surface area due to their layered structure, facilitating improved adsorption and reactivity in nanocomposite applications (Oyedotun et al., 2009). MXenes exhibit good thermal conductivity, making them suitable for applications in thermal management and devices requiring efficient heat dissipation. MXenes often demonstrate biocompatibility, a crucial property for their integration into nanocomposites for biomedical applications, such as drug delivery systems and medical implants. Some MXenes, like titanium carbide ($Ti_3C_2T_x$), possess excellent photothermal properties, making them useful in nanocomposites for applications like cancer therapy (Z. Liu et al., 2018; C; Dai, Chen, et al., 2017; Lin et al., 2018; X; Han et al., 2018; C; Dai, Lin, et al., 2017). MXenes are available in various compositions (carbides, nitrides, or carbonitrides), allowing for versatility in tailoring nanocomposites for specific applications. MXenes display interesting optical properties, including strong light absorption, which can be harnessed for applications in sensing and optoelectronics (McKeen, 2017).

2.1.1 Classification of MXenes on different basis

MXenes can be classified based on several different criteria, including composition, synthesis method, structural properties, and applications. The classification of MXenes based on various factors is listed in Table 1.

This classification scheme highlights the diverse nature of MXenes and their potential across multiple fields, from energy storage and electronics to catalysis, sensing, and biomedical applications depending also on the transitional metals.

2.2 Polymer

Polymers are large molecules composed of repeating structural units called monomers. These molecules are characterized by their long chains and versatile properties, making them essential in various industries and everyday products (Painter and Coleman, 2019). They can be natural, such as proteins and DNA, or synthetic, like plastics and rubbers. Synthetic polymers are typically created through polymerization processes, where monomers are chemically bonded together to form long chains or networks (McCrum, Buckley, and Bucknall, 1997). This process allows for the manipulation of properties like strength, flexibility, and durability, making polymers highly customizable for specific applications. Polymers play a vital role in modern society, being used in countless products ranging from packaging materials and textiles to medical devices and electronics. Their versatility, affordability, and ease of manufacturing have led to their widespread adoption across industries, driving innovation and technological advancement. However, concerns about environmental impact and sustainability have prompted efforts to develop biodegradable and eco-friendly alternatives to traditional polymers, reflecting the ongoing evolution of polymer science and engineering (Young and Lovell, 2008).

2.2.1 Classification of polymers

Polymers can be classified into several types based on their structure, origin, properties and applications. Some common types of polymers are listed in Table 2 (Young and Lovell, 2008).

2.3 MXene nanocomposites

MXene nanocomposites are a class of materials that have garnered significant attention due to their unique properties and potential applications. (Parajuli et al., 2022). MXene nanocomposites are formed by incorporating MXene nanosheets into a matrix material, such as polymers, ceramics, or metals, to enhance or impart specific properties. The addition of MXenes can

TABLE 1 Classification of MXenes on different basis.

Class. Basis	Types
Composition (Naguib et al., 2011)	Transitional metal: MXenes are primarily composed of transition metals such as titanium (Ti), vanadium (V), molybdenum (Mo), tungsten (W), niobium (Nb), etc.
	Element X: MXenes contain carbon (C), nitrogen (N), or both (carbonitrides) as the second element
Synthesis (Anasori, Lukatskaya, and Gogotsi, 2017)	Top-down: Involves etching of MAX phases (precursor materials) with strong acids or other chemical treatments to selectively remove the 'A' layer, resulting in the formation of MXenes
	Bottom-up: Involves direct synthesis of MXenes from precursor materials or starting compounds, often through chemical vapor deposition (CVD) or other methods
Structure (Parajuli et al., 2022)	Layered: MXenes typically have a layered structure with transition metal layers sandwiched between 'X' layers
	Surface functionalization: MXenes can be functionalized with various functional groups or ions on their surfaces, altering their properties and applications
Application (Lukatskaya et al., 2013; Lipatov et al., 2016; Shahzad et al., 2016)	Energy storage: MXenes are extensively used in energy storage devices such as batteries, supercapacitors, and fuel cells due to their high conductivity and large surface area
	Electronics: MXenes find applications in electronics, including transparent conductive films, flexible electronics, and electromagnetic interference shielding
	Catalysis: MXenes exhibit catalytic activity in various reactions, including hydrogen evolution, oxygen reduction, and water splitting
	Sensing: MXenes are utilized in gas sensing, biosensing, and electrochemical sensing applications due to their high surface area and conductivity
	Biomedical: Some MXenes show biocompatibility and are explored for drug delivery, photothermal therapy, tissue engineering, and bioimaging applications
Properties (Parajuli, Uppugalla, et al., 2023)	Electrical conductivity: MXenes possess high electrical conductivity, making them suitable for electronic and energy storage applications
	Mechanical properties: MXenes exhibit excellent mechanical strength and flexibility, which is advantageous for applications requiring robust materials
	Chemical stability: MXenes are chemically stable under various conditions, enhancing their suitability for catalytic and environmental applications
Layer thickness	MXenes can have varying layer thicknesses, ranging from a few atomic layers to thicker structures, influencing their properties and applications
Transitional Metals	Titanium: (Ti3C2, Ti2C, etc.): (Naguib et al., 2011)
	• Energy storage devices: Titanium-based MXenes are widely used in supercapacitors and lithium-ion batteries due to their high surface area, excellent electrical conductivity, and ability to intercalate ions
	• Electromagnetic interference (EMI) shielding: Their high electrical conductivity makes them suitable for shielding electromagnetic radiation in various electronic devices
	Vanadium (V2C, V2CTx, etc.): (Naguib et al., 2012)
	• Electrochemical sensors: Vanadium-based MXenes have shown promising applications in electrochemical sensing due to their high surface area and excellent electrical conductivity
	• Catalysis: They are explored as catalysts for various reactions, including hydrogen evolution reaction (HER), oxygen reduction reaction (ORR), and water splitting
	Molybdenum (Mo2CTx, Mo2TiC2Tx, etc.)(Halim, Kota, et al., 2016; Parajuli, Devendra, et al., 2021)
	• Lubrication: Molybdenum-based MXenes exhibit excellent lubricating properties, making them suitable additives in lubricant formulations for reducing friction and wear
	• Gas sensing: They have demonstrated sensitivity towards gases like ammonia and nitrogen dioxide, making them potential candidates for gas sensing applications
	Tungsten (W2CTx, W2TiC2Tx, etc.)(Koc and Kodambaka, 2000)
	• Photothermal therapy: Tungsten-based MXenes have been explored for their photothermal properties, which can be utilized in cancer therapy by converting light energy into heat to ablate cancer cells
	• Water purification: They have shown promise in removing heavy metal ions and organic pollutants from water due to their high adsorption capacity and selectivity

(Continued on following page)

TABLE 1 (*Continued*) Classification of MXenes on different basis.

Class. Basis	Types
	Other (Nb2CTx, Mo2TiC2Tx, etc.)(Khazaei et al., 2019)
	• Flexible electronics: MXenes with suitable properties are being investigated for applications in flexible and transparent electronics, such as flexible electrodes and transparent conductive films
	• Biomedical applications: Some MXenes exhibit biocompatibility and are being explored for biomedical applications such as drug delivery, biosensing, and tissue engineering scaffolds

improve mechanical strength, electrical conductivity, and thermal stability of the composite material. Research in MXene nanocomposites has demonstrated their potential in various fields (Aghamohammadi, Amousa, and Eslami-Farsani, 2021). For instance, MXene/polymer nanocomposites have shown promise in flexible electronics and sensors due to their excellent electrical conductivity and mechanical flexibility. In energy storage applications, MXene-based nanocomposites have been explored for supercapacitors and batteries, where they offer high specific capacitance and stability. One example of a study in MXene nanocomposites is the work by Liu et al. (2021), where they developed MXene/polymer nanocomposites for electromagnetic interference shielding applications. The study demonstrated that the incorporation of MXene nanosheets into the polymer matrix significantly enhanced the electromagnetic interference shielding effectiveness of the composite material (Zhang and Gu, 2022).

2.4 Polymer nanocomposites

Polymer nanocomposites are a class of materials composed of a polymer matrix reinforced with nanoscale fillers or additives. These nanofillers typically have at least one dimension in the nanometer range, providing unique properties and enhanced performance compared to traditional composite materials (Koo, 2019). The incorporation of nanofillers into polymers can result in significant improvements in mechanical, thermal, electrical, and barrier properties (Pinto et al., 2023). Common types of nanofillers used in polymer nanocomposites include nanoparticles such as metal oxides (e.g., silica, alumina), carbon-based materials (e.g., carbon nanotubes, graphene), and clay minerals (e.g., montmorillonite).

Polymer nanocomposites offer numerous advantages over conventional composites, including:

- Enhanced mechanical properties such as increased stiffness, strength, and toughness.
- Improved thermal stability and flame retardancy due to the barrier effect of nanofillers.
- Enhanced electrical conductivity or dielectric properties, making them suitable for electronic and electrical applications.
- Increased gas barrier properties, making them ideal for packaging materials.
- Reduced weight and improved fuel efficiency in transportation applications.

The fabrication of polymer nanocomposites involves various techniques such as melt blending, solution mixing, *in situ* polymerization, and electrospinning. The selection of nanofillers, their dispersion within the polymer matrix, and the processing conditions play crucial roles in determining the properties and performance of the nanocomposite material. Polymer nanocomposites find applications in diverse industries, including automotive, aerospace, electronics, packaging, biomedical, and energy storage. Ongoing research in this field aims to further optimize the properties of nanocomposites and explore novel applications, paving the way for the development of advanced materials with tailored properties and multifunctionality.

2.5 MXene-polymer nanocomposites

By integrating MXenes, renowned for their exceptional conductivity and mechanical properties, into polymer matrices, the resulting nanocomposites exhibit enhanced functionalities such as improved electrical conductivity, mechanical strength, and thermal stability (Gong et al., 2021). These tailored properties make MXene polymer nanocomposites highly promising for a wide array of applications, including flexible electronics, energy storage devices like batteries and supercapacitors, electromagnetic interference shielding materials, and even biomedical applications (Bilibana, 2023). Moreover, the versatility of polymers allows for easy processing and shaping, further expanding the potential applications and manufacturability of MXene polymer nanocomposites. The synthesis of MXene polymer nanocomposites represents a synergistic approach to harnessing the strengths of both materials, paving the way for advancements in numerous fields (Riazi et al., 2021).

From few years back, we have studied the MXenes and Ferrites (Parajuli, Raghavendra, et al., 2021; Parajuli, Murali, Rao, Ramakrishna, et al., 2022; Parajuli, Taddesse, Murali, and Samatha 2022; Parajuli, Murali, Raghavendra, et al., 2023; Parajuli, Murali, Samatha, et al., 2023) separately and their mixtures with the most exploited material in the society polymer in the form of their nanocomposites (Parajuli et al., 2022; Parajuli, Uppugalla, et al., 2023). We found them most efficient combination among the recently developed other nanocomposites which are far efficient than their pristine form.

Nanocomposites represent a cutting-edge technology with transformative potential in biomedical fields. Their ability to address specific challenges and provide tailored solutions underscores their significance in advancing healthcare and promoting environmental sustainability. The need for advanced materials like MXenes-polymer nanocomposites stems from their exceptional properties, versatility, and potential to address challenges in diverse applications, ranging from healthcare

TABLE 2 Common types of polymers.

Classification	Types and properties
Structure (Figure 2)	1. Linear: They have long, straight chains of monomer units. Examples include polyethylene and polypropylene
	2. Branched: They have linear chains with occasional side branches stemming from the main chain. Examples include low-density polyethylene (LDPE) and certain types of polyethylene
	3. Cross-linked: They have covalent bonds between polymer chains, forming a network structure. This type of polymer exhibits high strength and rigidity. Examples include vulcanized rubber and epoxy resins
Origin	1. Natural: These polymers occur naturally and are often derived from renewable resources. e.g., proteins (silk and wool), cellulose, and natural rubber
	2. Synthetic: They are man-made and are typically derived from petrochemicals and extensively used in various industries due to their versatility and controllable properties. e.g. polyethylene, polypropylene, polyvinyl chloride (PVC), and polystyrene
Polymerization	1. Addition: They are formed by the repeated addition of monomer units, typically through a double or triple bond. Examples include polyethylene, polypropylene, and polyvinyl chloride (PVC)
	2. Condensation: They are formed by the condensation reaction between monomer units, often accompanied by the elimination of small molecules such as water or alcohol. Examples include nylon, polyester, and polycarbonate
Molecular forces	1. Thermoplastic: Thermoplastic polymers can be melted and reshaped multiple times without undergoing chemical degradation. They are held together by weak intermolecular forces. Examples include polyethylene, polypropylene, and polystyrene
	2. Thermosetting: They undergo irreversible chemical reactions during curing, forming a network structure that cannot be melted or reshaped. They exhibit high strength and dimensional stability at high temperatures. Examples include epoxy resins and phenolic resins
Applications (Painter and Coleman, 2019)	1. Packaging
	Polyethylene (PE): Widely used for packaging films, bags, and bottles due to its flexibility, toughness, and moisture resistance
	Polyethylene Terephthalate (PET): Commonly used for beverage bottles and food packaging due to its transparency, strength, and barrier properties
	Polypropylene (PP): Suitable for packaging containers, food containers, and flexible packaging due to its heat resistance, stiffness, and chemical resistance
	2. Construction Field
	Polyvinyl chloride (PVC): Utilized in pipes, window frames, flooring, and siding due to its durability, weather resistance, and versatility
	Polystyrene (PS): Used in insulation, packaging, and construction materials due to its lightweight nature and insulation properties
	Polyethylene (PE) and Polypropylene (PP): Employed in geomembranes, roofing membranes, and insulation materials due to their waterproofing and durability
	3. Automotive field
	Polyurethane (PU): Used in car seats, foam cushions, and interior trim due to its comfort, durability, and vibration-dampening properties
	Acrylonitrile Butadiene Styrene (ABS): Utilized in automotive interior and exterior parts, such as dashboard components and body panels, due to its impact resistance and toughness
	Polyethylene (PE) and Polypropylene (PP): Employed in automotive bumpers, fuel tanks, and interior components due to their lightweight nature and impact resistance
	4. Medical field
	Polymethyl Methacrylate (PMMA): Used in medical devices such as intraocular lenses, bone cement, and dental materials due to its optical clarity and biocompatibility
	Polyethylene (PE) and Polypropylene (PP): Utilized in medical packaging, syringes, and implants due to their inertness, stabilizability, and biocompatibility
	Polyvinyl Chloride (PVC): Employed in medical tubing, blood bags, and IV containers due to its flexibility, transparency, and ease of sterilization
	5. Electronics field

(Continued on following page)

TABLE 2 (*Continued*) Common types of polymers.

Classification	Types and properties
	Polyethylene Terephthalate (PET): Used in electronic housings, insulating films, and printed circuit boards due to its dimensional stability and electrical insulation properties
	Polyamides (PI): Utilized in flexible circuits, insulating coatings, and electronic components due to their high-temperature stability, chemical resistance, and electrical insulation properties
	Polyethylene (PE) and Polypropylene (PP): Employed in battery casings, cable insulation, and electronic packaging due to their electrical insulation, thermal stability, and chemical resistance
Conducting polymer (Kurra, Jiang, and Alshareef, 2015)	Polypyrrole (PPy): It is one of the most extensively studied conducting polymers. It exhibits high conductivity, good environmental stability, and processability. Polypyrrole can be synthesized via chemical oxidation of pyrrole monomers, forming a highly conjugated polymer chain
	Polyaniline (PANI): It is another widely researched conducting polymer. It can be synthesized in various oxidation states, each exhibiting different electrical and optical properties. Polyaniline is relatively easy to process and shows good environmental stability, making it suitable for various applications such as sensors, actuators, and energy storage devices
	Polythiophene (PTh): Polythiophene and its derivatives are conducting polymers with high stability and good processability. They can be synthesized with different side chains and substituents to tailor their properties for specific applications. Polythiophenes are commonly used in organic electronic devices, including organic photovoltaics and organic light-emitting diodes (OLEDs)
	Polyacetylene (PA): It was one of the first conducting polymers to be discovered and studied. It exhibits high conductivity when doped with suitable dopants, but it is highly sensitive to oxygen and moisture, limiting its practical applications. However, polyacetylene has paved the way for the development of other conducting polymers with improved stability and performance
	Poly (3, 4-ethylenedioxythiophene (PEDOT): It is a conducting polymer known for its high conductivity, transparency, and flexibility. It is commonly used as a transparent electrode in organic electronics, touchscreens, and electrochromic devices. PEDOT can be synthesized through various methods, including chemical oxidation and electrochemical polymerization

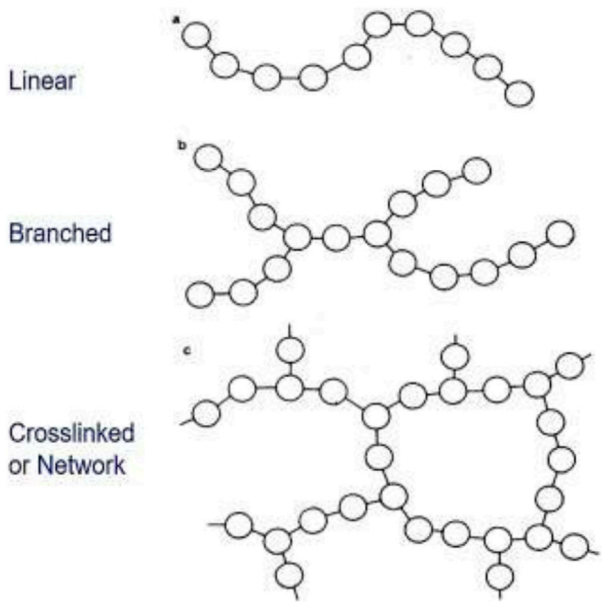

FIGURE 2
Types of Polymers: **(A)** linear, **(B)** branched, and **(C)** cross-linked or network.

protection to energy storage and beyond. Their unique combination of attributes positions them as key players in advancing technological solutions for the future. In this article, the synthesis of MXene Polymer nanocomposites, their biomedical and environmental aspects along with the issues, challenges, and perspectives are discussed. MXenes properties for nanocomposite applications.

2.6 MXenes and polymers compatibility for nanocomposite

The compatibility of MXene with polymers is a crucial aspect in the formation of nanocomposites, determining the effectiveness and performance of the resulting hybrid materials (X. Chen et al., 2020). The compatibilities of MXene with polymers for nanocomposite formation are:

2.6.1 Surface functional groups

MXenes possess surface functional groups, such as hydroxyl (-OH) or fluorine (-F), which enhance their compatibility with polymers. These functional groups provide active sites for bonding and interactions with polymer chains.

2.6.2 Chemical affinity

The surface chemistry of MXene allows for strong interactions with various polymers. The presence of transition metal terminations and surface functional groups promotes chemical compatibility, ensuring a stable interface between MXene and polymer components.

2.6.3 Electrostatic interactions

The charged nature of MXene surfaces facilitates electrostatic interactions with polymers, especially those with opposite

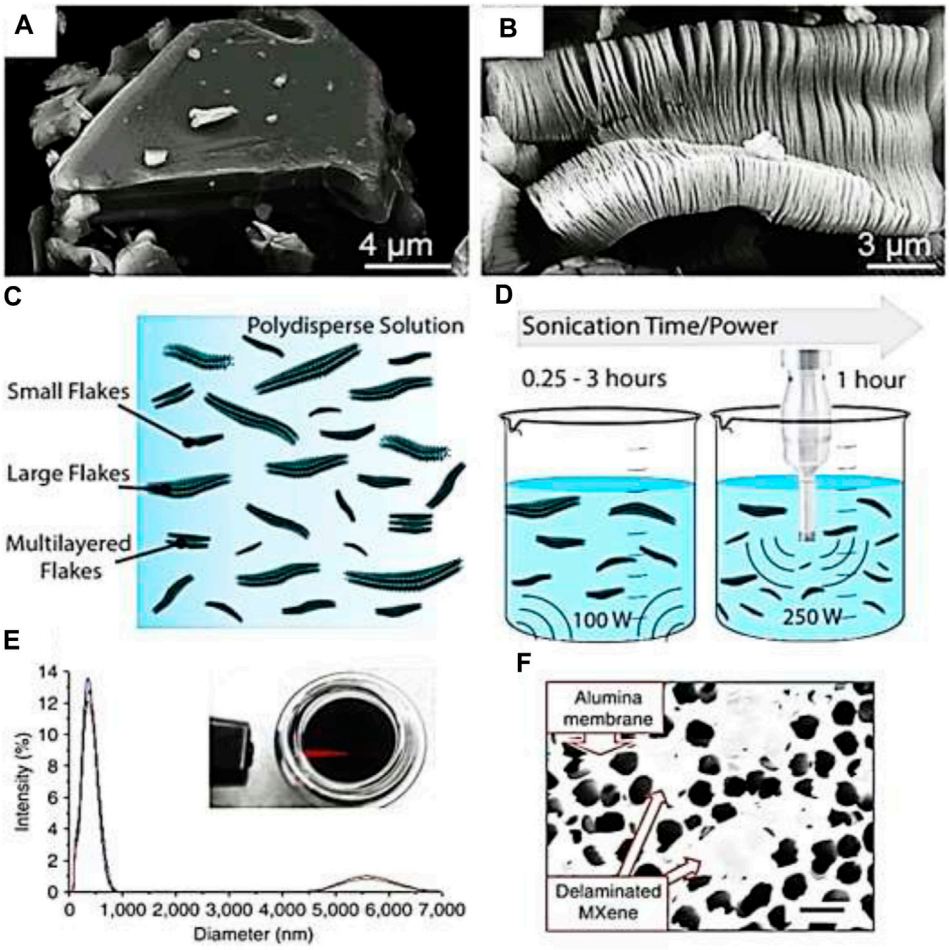

FIGURE 3
(A) Scanning electron microscopy (SEM) depiction of Ti_3AlC_2 particle **(B)** Formation of $Ti_3C_2T_z$ after etching in hydrofluoric acid (HF). **(C)** Diagrammatic representation illustrating MXene suspension exhibiting various flake sizes. **(D)** Representation demonstrating the impact of sonication on dimensions of MXene flakes, with increasing sonication time and power. **(E)** Light scattering analysis of a typical colloidal MXene suspension post-sonication, accompanied by an inset image demonstrating the Tyndall effect. **(F)** SEM micrograph displaying drop-cast colloidal MXene on a porous alumina substrate, showcasing transparent delaminated MXene sheets. **(A, B)** are reproduced from Naguib et al., 2012. **(C, D)** are reproduced from Maleski et al., 2018. **(E, F)** are reproduced from Mashtalir et al., 2013.

charges. This can contribute to improved dispersion and stability of MXene within the polymer matrix.

2.6.4 Enhanced mechanical properties

The mechanical strength of MXene, coupled with its compatibility with polymer matrices, results in nanocomposites with enhanced mechanical properties. This is particularly beneficial in applications requiring increased strength and durability.

2.6.5 Synergistic effects

The combination of MXene and polymers often leads to synergistic effects, where the unique properties of each component complement and enhance the overall performance of the nanocomposite. This synergy can result in improved conductivity, mechanical strength, or other desired characteristics.

2.6.6 Versatility of polymer selection

MXenes can be compatible with a wide range of polymers, including but not limited to, thermoplastics, thermosets, and elastomers. This versatility allows for the tailoring of nanocomposite properties to suit specific applications.

2.6.7 Improved processability

MXene's compatibility with polymers facilitates the processing and fabrication of nanocomposites. Techniques such as solution mixing, melt blending, or *in situ* polymerization can be employed to achieve homogeneous dispersion and integration.

2.6.8 Biocompatibility

MXenes can be engineered to be biocompatible, making them suitable for integration into biopolymer matrices. This opens up opportunities for applications in biomedical nanocomposites, such as drug delivery systems and tissue engineering (K. Chen et al., 2017).

The compatibility of MXene with polymers is a critical factor in the successful formation of nanocomposites. The chemical affinity, surface functional groups, and synergistic effects contribute to creating hybrid materials with tailored properties, expanding the range of applications in various fields.

3 Synthesis of MXene-polymer nanocomposites

Synthesizing MXene-polymer nanocomposites involves various techniques, each with its advantages, limitations, and recent advancements. In most cases, the MXenes are synthesized from etching processes. The layered structures in colloidal solution form obtained from etching can be sonicated and delaminated to get a few layered MXenes (Carey and Barsoum, 2021) as shown in Figure 3. Their synthesis involves integrating MXene nanosheets into a polymer matrix to create materials with enhanced properties. The detail of the synthesis of MXene-Polymer nanocomposites is found in our recently published articles (Parajuli et al., 2022; Parajuli, Uppugalla, et al., 2023).

3.1 Steps of synthesis methods

The synthesis typically involves the following steps.

1 Preparation of MXene Nanosheets: MXene nanosheets are synthesized through methods such as chemical etching of MAX phases or exfoliation of precursor materials. The resulting MXene nanosheets are typically functionalized to improve their dispersion and compatibility with the polymer matrix.
2 Preparation of Polymer Matrix: The polymer matrix is prepared separately, often by dissolving the polymer in a suitable solvent to form a polymer solution. The choice of polymer depends on the desired properties of the nanocomposite and the intended application.
3 Dispersion of MXene in Polymer solution: The MXene nanosheets are then dispersed in the polymer solution using techniques such as sonication or mechanical stirring. Proper dispersion is crucial to ensure uniform distribution of MXene within the polymer matrix and to prevent aggregation.
4 Fabrication of Nanocomposite: The dispersed MXene-polymer solution is then subjected to a suitable fabrication method to form the nanocomposite material. Common techniques include solution casting, spin-coating, or electrospinning, depending on the desired morphology and application of the nanocomposite.
5 Characterization and Optimization: The synthesized MXene-polymer nanocomposite is characterized to evaluate its structural, mechanical, electrical, and thermal properties. Optimization of synthesis parameters may be performed to achieve desired properties such as improved mechanical strength, conductivity, or thermal stability.
6 Application Testing: The MXene-polymer nanocomposite is then evaluated for its performance in specific applications such as energy storage, electromagnetic interference shielding, sensors, or biomedical devices. The nanocomposite's properties are tailored to meet the requirements of the intended application.

The synthesis of MXene-polymer nanocomposites involves careful control of MXene dispersion, polymer compatibility, and fabrication techniques to achieve nanocomposites with enhanced properties suitable for various practical applications.

3.2 Types of synthesis methods

3.2.1 Selective etching

The synthesis of MXenes and hence the MXene Nanocomposites, involves a multistep process, primarily starting with the selective etching of layers from a precursor material known as a MAX phase. The etching of MXene typically refers to a process of selectively removing the "A" layer (typically aluminum) from the MXene structure, leaving behind a porous 2D material with various applications. The etching process is essential because it alters the surface chemistry and structure of MXene, allowing for tuning of its properties and enabling various applications. The etching of MXene can be used to control the surface chemistry, surface area, and interlayer spacing, which are crucial for applications such as energy storage devices (like batteries and supercapacitors), electromagnetic interference shielding, catalysis, sensors, and more. The steps for the synthesis of MXene Polymer nanocomposite by selective etching process are as below.

3.2.1.1 Selective etching

The primary step in MXene synthesis involves the selective etching of the A-element layers from the MAX phase. Common etchants include hydrofluoric acid (HF) or a combination of hydrochloric acid (HCl) and an oxidizing agent. The etching process exposes the MXene layers, creating a 2D structure (Naguib et al., 2012).

3.2.1.2 Washing and delamination

After etching, the resulting MXene flakes are thoroughly washed to remove residual etchants and by-products. This step is crucial for the removal of any remaining A-element residues. Delamination processes, such as intercalation of ions or molecules, may be employed to exfoliate MXene layers and enhance their dispersibility (Ling et al., 2014).

3.2.1.3 Surface functionalization

MXene surfaces often have terminations, such as hydroxyl (-OH) or fluorine (-F), which affect their properties. Surface functionalization can be performed to introduce desired functional groups, enhancing their compatibility with other materials or improving specific characteristics.

MXenes are frequently integrated into polymer matrices to form nanocomposites. This can be achieved through methods like solution mixing, melt blending, or *in situ* polymerization. The choice of polymer and the synthesis method can be tailored to achieve the desired properties for specific applications (Khazaei et al., 2013; Ashton et al., 2016; T; Hu et al., 2015).

3.2.1.4 Drying and powder formation

The resulting MXene dispersion is often dried to produce a powder form for ease of handling and storage. Techniques like

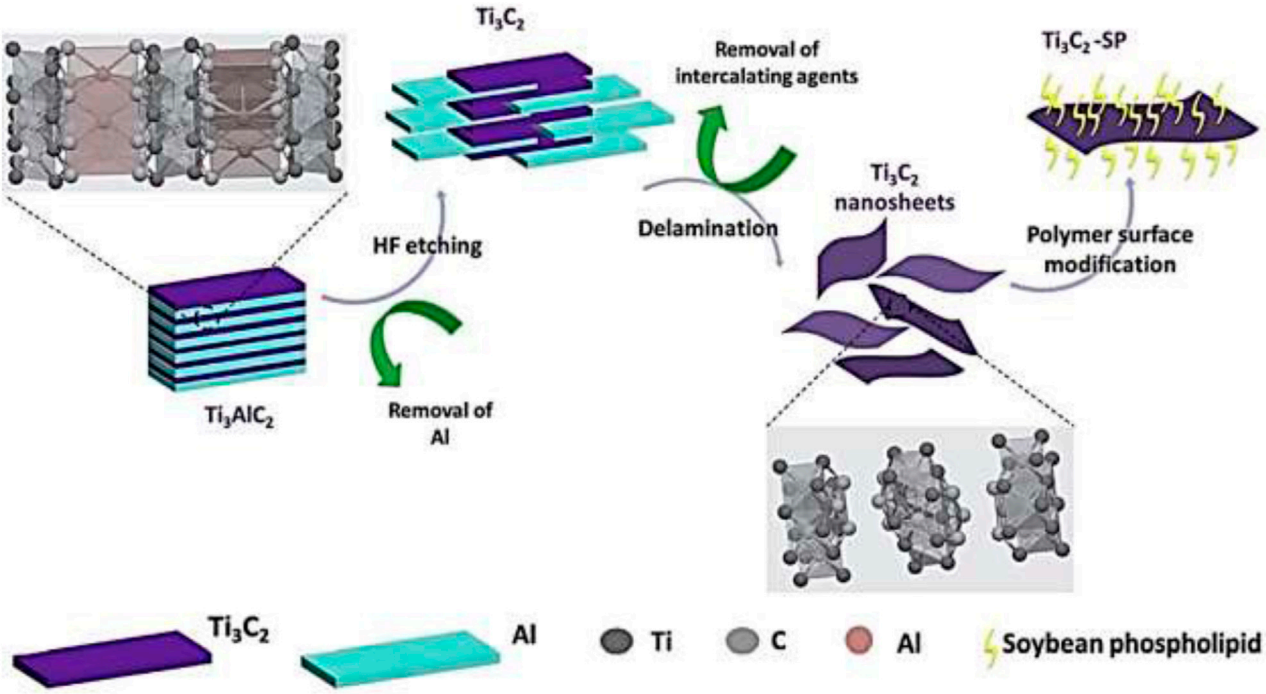

FIGURE 4
Synthesis cycle of Ti_3C_2-SP nanocomposite (Jain et al., 2013).

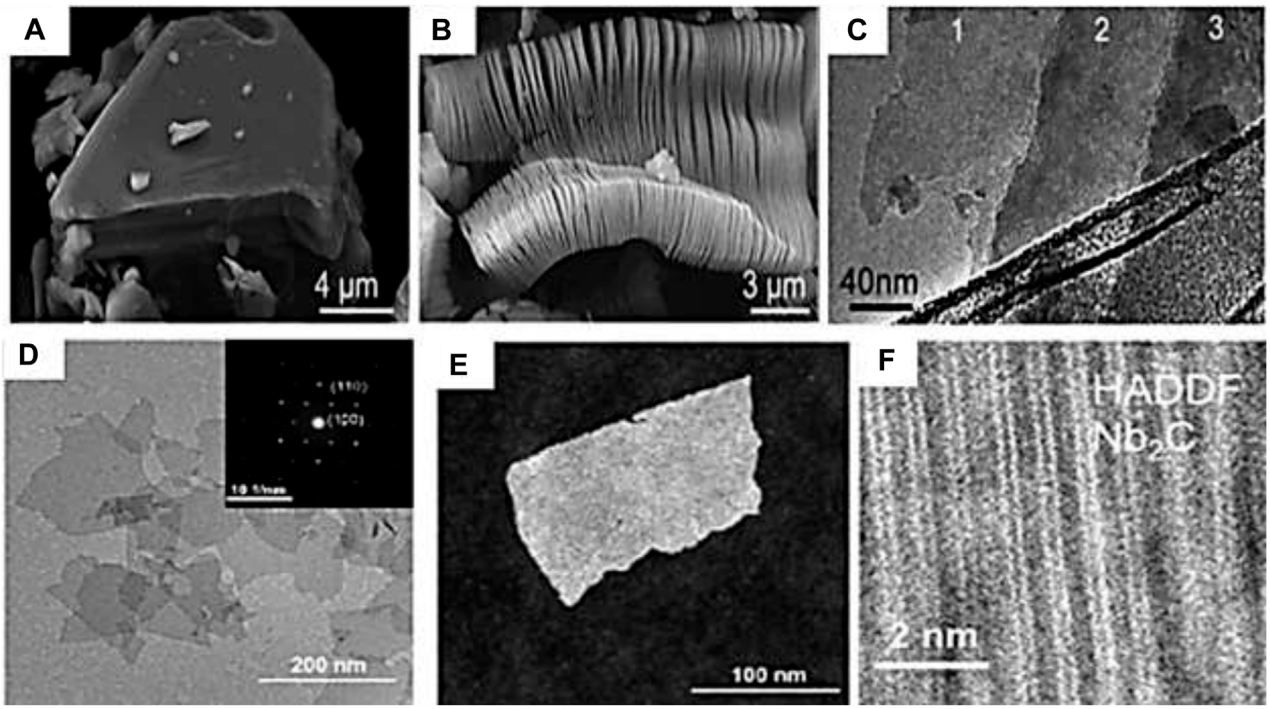

FIGURE 5
(A) SEM micrographs of Ti_3AlC_2 before and **(B)** after etching. **(C)** TEM images of Ti_3C_2 after etching (Naguib et al., 2012) © American Chemical Society (2012). **(D, E)** TEM images (Bright and dark field Nb_2C). **(F)** High resolution HAADF-STEM image. © American Chemical Society (2019).

freeze-drying or spray-drying are commonly employed to preserve the 2D structure.

3.2.1.5 MXene-polymer nanocomposite formation

The schematic representation of the synthesis cycle for the MXene-SP composite is illustrated in Figure 4. The bottom-up methodology can also be employed for MXene synthesis through techniques such as EVD (Manawi et al., 2018).

Figure 5 presents scanning transmission electron microscopy (STEM) images of Ti_3AlC_2 before and after etching, high-resolution transmission electron microscope (HRTEM) of Ti_3C_2 after etching, bright and dark selected area electron diffraction (SAED) of Nb_2C, high angular annular dark field (HAADF) respectively, and showcasing hexagonally layered intercalated nanosheets with a space group of P63/mmc and atomic arrangement dependent on "n," with lateral dimensions ranging from 0.5 to 200 nm and a thickness of a few nanometers (Naguib et al., 2014) (X. Ren et al., 2019).

3.2.2 Solution mixing

They are simple and cost-effective, suitable for a wide range of polymers, and allow for precise control over the composition. However, they are limited to polymers soluble in the chosen solvent and may require additional steps for complete mixing and dispersion. Advanced mixing techniques, such as sonication or high-shear mixing, can be used to improve dispersion. Solution mixing is a common and straightforward method for preparing MXene-polymer nanocomposites (Maleski, Mochalin, and Gogotsi, 2017).

3.2.2.1 Material and method

The MXene of interest, such as titanium carbide ($Ti_3C_2T_x$) or others, is prepared through appropriate synthesis methods. The chosen polymer, compatible with the solvent is used for MXene dispersion. Common polymers include polyvinyl alcohol (PVA), polyethylene glycol (PEG), or others. A solvent in which both MXene and the polymer are soluble. Common solvents include water, N-methyl-2-pyrrolidone (NMP), or dimethyl sulfoxide (DMSO). A sonicator is needed to assist in dispersing MXene and polymer in the solvent. For continuous mixing during the preparation is done by magnetic stirrer or stirring rod. A suitable container is used for mixing and storing the nanocomposite solution.

The MXene is dispersed in the chosen solvent, with uniform dispersion often achieved through sonication. For example, a desired amount of MXene powder is added to the solvent, and the mixture is sonicated for a specific duration until a well-dispersed MXene solution is obtained. The polymer is dissolved in the same solvent used for MXene dispersion, with the solution stirred until the polymer is fully dissolved, forming a clear polymer solution. The MXene solution is slowly added into the polymer solution while continuously stirring, with this process carried out dropwise to ensure a gradual and homogeneous mixture. The combined solution is stirred for an extended period to ensure proper mixing and distribution of MXene within the polymer matrix. Depending on the desired concentration of MXene in the nanocomposite, the ratio of MXene to polymer solutions is adjusted, with this step potentially requiring optimization based on the specific application. The resulting nanocomposite solution is characterized to ensure the desired properties, with techniques such as UV-Vis spectroscopy, Fourier-transform infrared spectroscopy (FTIR), or other relevant methods employed. Depending on the application, the nanocomposite solution can be cast into films or coatings or dried to obtain the final nanocomposite material.

3.2.2.2 Considerations

In this process, some special considerations are needed. The concentration of MXene, polymer, and the ratio between them should be optimized based on the desired properties of the nanocomposite. The choice of solvent is critical, as it affects the solubility of both MXene and the polymer. Consideration should be given to environmental and safety aspects when selecting solvents. Proper sonication is essential to ensure a well-dispersed MXene solution, preventing agglomeration. Sufficient stirring time is crucial for achieving a homogeneous nanocomposite solution.

3.2.3 *In-situ* polymerization

They are a direct synthesis of nanocomposites during polymerization and have good control over the nanocomposite structure. They are suitable for a variety of polymer matrices. However, they are limited to polymers that can undergo *in situ* polymerization, and reaction conditions may affect MXene properties. The development of controlled polymerization methods for better control over nanocomposite structure. *In situ* polymerization is a method for preparing MXene-polymer nanocomposites in which the polymerization of monomers occurs directly in the presence of dispersed MXene sheets.

Due to limited polymerization energy, only certain types of monomers can undergo polymerization on the surface of MXenes through methods such as physical agitation, UV radiation, or electrochemical processes (C. Chen et al., 2017) (J. Chen et al., 2014; Boota et al., 2016). Chen et al. proposed two primary electron transfer mechanisms during the charge-transfer-induced polymerization of 3, 4-ethylenedioxythiophene (EDOT) under agitation. In one mechanism, electrons transition from the high-energy orbits (HOMOs) of the monomer to the lower-energy orbits (LUMOs) of the MXene, while in the other, electrons shift from the HOMOs of the MXene to the LUMOs of the monomer (Figure 6A) (C. Chen et al., 2017). Additionally, proximity between the monomer and MXene surface is crucial for efficient electron transfer during polymerization. Leveraging hydroxyl and fluorine terminations, 2-(dimethylamino) ethyl methacrylate (DMAEMA) was successfully polymerized on the surface of V_2C (Figure 6B) (J. Chen et al., 2014), leading to the formation of PDMAEMA grafted V_2C with demonstrated sensitivity to CO2 and temperature. Furthermore, MXene/polypyrrole (PPy) composites were synthesized via electrochemical polymerization by Zhu et al., involving the electrolysis of a pyrrole-containing solution with a Ti_3C_2-modified electrode. Although *in situ* polymerization ensures a uniform distribution of polymers on the MXene surface, it may alter the properties of MXene materials during the process.

3.2.3.1 Material and method

In this method, the monomers are required for polymerization to make nanocomposite with the MXene of interest, such as titanium carbide ($Ti_3C_2T_x$). Common monomers include acrylic

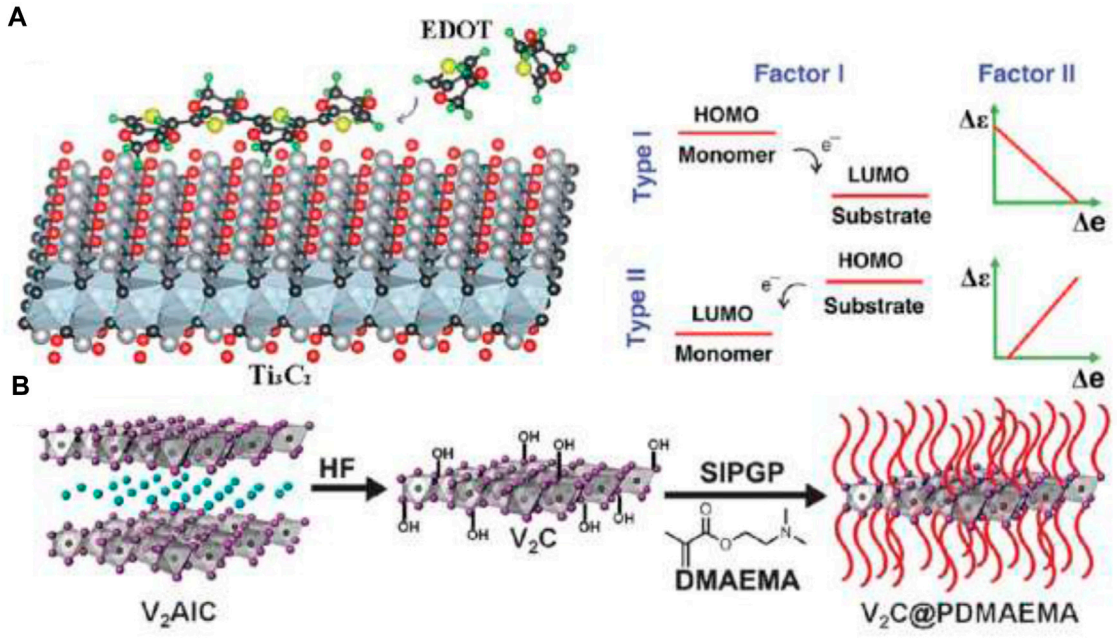

FIGURE 6
Synthesis of MXene/polymer composites through *in situ* polymerization: **(A)** Schematic depiction of the polymerization of EDOT on the surface of MXene and the process of charge transfer during polymerization, adapted from (C. Chen et al., 2017) ©2017 Royal Society of Chemistry and **(B)** Schematic illustration of the preparation of V2C@PDMAEMA composite. **(A)**: Adapted with permission from reference (J. Chen et al., 2014) ©2015 Royal Society of Chemistry.

acid, acrylamide, or other suitable monomers compatible with the polymerization conditions. A suitable initiator to initiate the polymerization reaction. Common initiators include ammonium persulfate (APS), azobisisobutyronitrile (AIBN), or others, depending on the polymerization mechanism. A solvent in which both MXene and the monomers are dispersible. Common solvents include water, N-methyl-2-pyrrolidone (NMP), or dimethyl sulfoxide (DMSO). A suitable reaction vessel equipped with a stirring mechanism and temperature control is needed.

The MXene is dispersed in the chosen solvent to achieve a stable MXene dispersion, potentially involving sonication for uniform dispersion. The desired monomers are dissolved in the solvent to prepare the monomer solution, with the concentration adjusted based on the nanocomposite (NC) properties. e.g., epoxies (Sliozberg et al., 2020; H; Zhang et al., 2016; Zou et al., 2018) and polydimethylsiloxane (PDMS) like polymers are mixed from one side.

The most common reports of *insitu* polymerizations for MXene polymer NCs are of curing systems, such as epoxies (Hatter et al., 2020; Sliozberg et al., 2020) (A. Feng et al., 2020) and PDMS (D. Hu et al., 2020) (X. Wu et al., 2020)(D. Wang et al., 2020) aqueous solutions have been reported in the case of PPy (Zhu et al., 2016a; Boota et al., 2016; Zhang et al., 2020), polyaniline (Vahidmohammadi et al., 2018; Y; Ren et al., 2018; Wei et al., 2019; Vahidmohammadi et al., 2018; Xu et al., 2020), PAM(Zhang et al., 2019), PAM/PVA (Liao et al., 2019) and PEDOT (Chen et al., 2017; Qin et al., 2019), that can be polymerized with acetonitrile (Li et al., 2019).

The initiator is added to the monomer solution, its amount is determined by polymerization kinetics and reaction rate preferences. The MXene dispersion is slowly added into the monomer solution while continuously stirring to uniformly disperse MXene sheets. Polymerization is initiated by raising the temperature or other suitable methods activating the initiator. The polymerization reaction proceeds for the specified duration under controlled conditions. The resulting MXene-polymer nanocomposite is characterized using techniques such as FTIR, SEM, or other relevant methods. The nanocomposite material is isolated from the reaction mixture through filtration or other separation techniques and washed to remove unreacted monomers or by-products. Finally, the nanocomposite material is dried to obtain the final product.

3.2.3.2 Considerations

The polymerization conditions, including temperature, initiator concentration, and reaction time, to achieve the desired properties of the nanocomposite are optimized. Continuous stirring are ensured during the polymerization reaction to promote uniform dispersion of MXene sheets and facilitate homogeneous polymerization. Thorough characterization of the nanocomposite material are done to evaluate its structure, morphology, and properties.

In-situ polymerization offers precise control over the nanocomposite structure and properties, making it a valuable method for preparing MXene-polymer nanocomposites with tailored characteristics for specific applications. Adjustments can be made to this general procedure based on the choice of monomers, initiators, or MXene types.

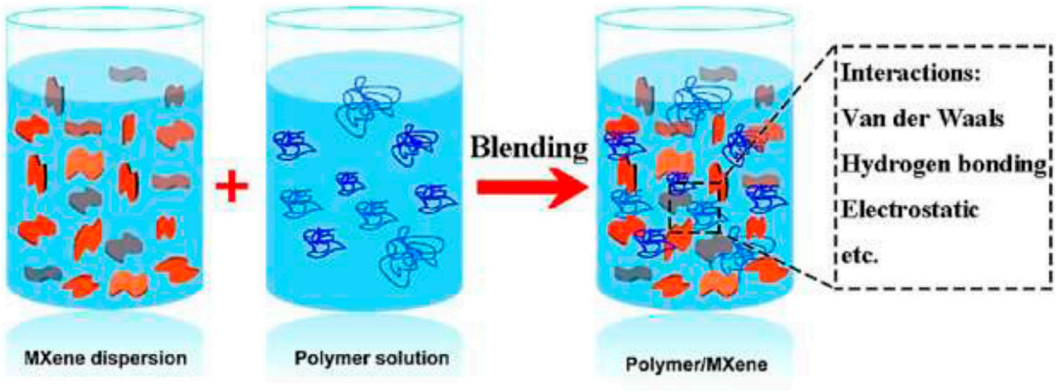

FIGURE 7
Creation of MXene/polymer composites through *ex-situ* solution blending. Reproduced with authorization from reference (Mirkhani et al., 2019). © 2019 American Chemical Society.

3.2.4 Melt blending

Melt blending is a commonly used method for preparing MXene-polymer nanocomposites, particularly when working with thermoplastic polymers (Figure 7). They are scalable and applicable to various polymer matrices, suitable for industrial-scale production, and are simple with cost-effective. However, they are limited to thermoplastic polymers and may require high processing temperatures. The optimization of processing parameters improves dispersion and mechanical properties (Sheng et al., 2019).

Ex-situ blending methods (Figure 7) are frequently utilized due to their ease in regulating the properties of polymer and MXene precursors. Leveraging their relatively modest interactions, such as van der Waals attraction, hydrogen bonding force, and electrostatic interaction, MXene/polymer composites are predominantly produced through solution mixing (Figure 7).

3.2.4.1 Material and method

The MXene of interest, such as titanium carbide ($Ti_3C_2T_x$) or others, is prepared through appropriate synthesis methods. The chosen thermoplastic polymer, is compatible with the processing temperature and MXene dispersion. A twin-screw extruder or internal mixer capable of high-temperature processing and efficient mixing. Additives such as compatibilizers, plasticizers, or stabilizers may be used to improve dispersion or enhance properties.

The MXene powder is properly dried to remove any residual moisture, as moisture can affect processing and properties. The thermoplastic polymer pellets are pre-dried to remove moisture and ensure uniform processing, with any desired additives optionally incorporated into the polymer pellets. The dried MXene powder and polymer pellets are loaded into the mixing equipment in the desired ratios, with the loading ratio adjusted based on the desired properties of the nanocomposite. The mixing equipment is heated to the appropriate processing temperature, typically above the melting point of the polymer. The mixing process is started, allowing the MXene powder and polymer pellets to melt and blend thoroughly, with high shear forces generated during mixing helping to disperse MXene within the polymer matrix. After thorough mixing, the molten mixture is extruded or discharged from the mixing equipment onto a cooling conveyor or casting surface. The mixture is allowed to cool and solidify, forming the MXene-polymer nanocomposite in the desired shape (e.g., pellets, sheets, or films). Further processing steps such as pelletizing, compression molding, or injection molding may be applied to the resulting nanocomposite material depending on the intended application. The nanocomposite material is characterized to evaluate its structure, morphology, and properties, with techniques such as SEM, XRD, or mechanical testing employed.

3.2.4.2 Consideration

The processing temperature should be carefully controlled to ensure proper melting of the polymer and dispersion of MXene while avoiding degradation of either component. Sufficient mixing time is essential to achieve uniform dispersion of MXene within the polymer matrix. Longer mixing times may be required for higher loading levels or less compatible polymer-MXene combinations. The incorporation of additives, such as compatibilizers or plasticizers, may improve the dispersion and compatibility of MXene within the polymer matrix. Melt blending involves high temperatures and mechanical shear forces. Proper safety precautions should be followed to prevent accidents or injuries.

Melt blending offers scalability and versatility, making it suitable for industrial-scale production of MXene-polymer nanocomposites. Adjustments to processing parameters can be made based on the specific polymer-MXene combination and intended application requirements.

3.2.5 Layer-by-layer assembly

This process has precise control over layer arrangement, suitable for a variety of polymers and MXenes. They can be used for thin films and coatings. However, the process is time-consuming and is limited to specific applications due to its layer-to-layer nature. Layer-by-layer (LbL) assembly (Figure 8) is a versatile technique for fabricating MXene-polymer nanocomposites with precise control over layer thickness and composition (Chen et al., 2020).

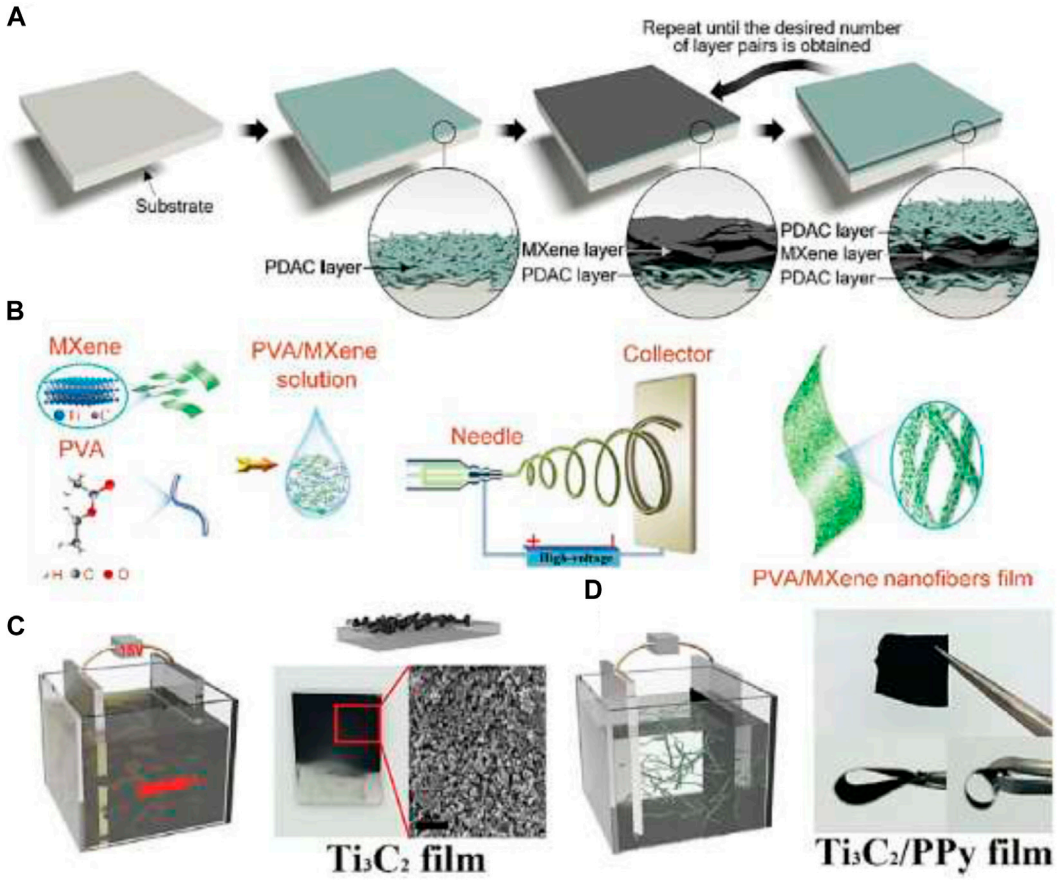

FIGURE 8
(A) Schematic illustration of the synthesis of MXene/PDAC membrane by LbL assembly process. **(B)** Schematic illustration of the fabrication process of MXene/PVA film by electrospinning approach. **(C)** Schematic illustration of the electrophoretic deposition of Ti_3C_2 flakes. **(D)** Schematic illustration of the synthesis of Ti_3C_2/PPy membrane by electrochemical polymerization of PPy on Ti_3C_2 film. Panel a: Reprinted from ref (An et al., 2018) ©2016, The Authors, **(B)**: Reprinted with permission from ref (C. Jiang et al., 2019). ©2019 Elsevier. Panels c and d: Reprinted with permission from ref (M. Zhu et al., 2016a). © 2016 John Wiley and Sons. A step-by-step guide for the LbL assembly is as.

3.2.5.1 Material and method

The MXene of interest, such as titanium carbide ($Ti_3C_2T_x$) or others, is prepared through appropriate synthesis methods. The chosen polymer, typically in the form of a solution or dispersion compatible with the assembly process. Polyelectrolytes like poly (allylamine hydrochloride) (PAH) or poly (sodium 4-styrenesulfonate) (PSS) are commonly used. A solvent suitable for both MXene dispersion and polymer dissolution. Common solvents include water, ethanol, or other polar solvents. A solid substrate on which the LbL assembly will take place. Common substrates include silicon wafers, glass slides, or functionalized surfaces. Additives such as crosslinkers or stabilizers may be used to enhance film stability or modify properties.

The MXene is dispersed in the chosen solvent to create a stable MXene dispersion, with sonication or high-shear mixing possibly utilized to achieve uniform dispersion. The chosen polymer is dissolved in the solvent to generate a polymer solution or dispersion, with the polymer concentration adjustable based on desired film properties. The substrate is thoroughly cleaned to remove any contaminants or residues that may affect film formation, and optionally, the substrate surface is functionalized to promote adhesion or enhance film stability. The process is repeated by immersing the substrate in the polymer solution, allowing the polymer to adsorb onto the MXene-coated substrate surface. The substrate is rinsed with solvent to eliminate any unbound polymer molecules and stabilize the polymer layer. Deposition of MXene and polymer layers is continued alternately until the desired number of layers is achieved, with control over the sequence and thickness of layers by adjusting deposition parameters. Post-treatment steps, such as crosslinking or annealing, may be performed to enhance film stability or modify properties. The assembled MXene-polymer nanocomposite film is characterized to evaluate its structure, morphology, and properties, with techniques such as atomic force microscopy (AFM), ellipsometry, or spectroscopic methods employed.

3.2.5.2 Consideration

The pH and ionic strength of the deposition solutions can influence layer deposition and film properties, so these parameters should be controlled and optimized. Parameters such as immersion time, solution concentration, and drying conditions can affect film thickness and quality and should be carefully optimized. The substrate material and surface properties can influence film adhesion, stability, and performance, so substrate

selection should be based on the desired application. LbL assembly allows for precise control over film composition, enabling the incorporation of multiple materials and functionalities into the nanocomposite film.

Layer-by-layer assembly offers fine control over film thickness, composition, and functionality, making it a versatile technique for fabricating MXene-polymer nanocomposites with tailored properties for various applications. Optimization of deposition parameters and thorough characterization are essential for achieving desired film properties and performance.

3.2.6 Electrospinning

They produce nanofibrous structures for enhanced properties, are suitable for a variety of polymers, and enable the fabrication of nanocomposite mats (Boys, 1887). However, they require specialized equipment and are limited to certain polymers and MXenes. Integration of electrospinning with other techniques for multifunctional nanocomposites may overcome this difficulty. Electrospinning is a versatile and widely used method for fabricating nanofibrous structures, including MXene-polymer nanocomposites (Ziabicki, 1976).

3.2.6.1 Material and method

After the preparation of the MXene of interest, such as titanium carbide ($Ti_3C_2T_x$), through an appropriate synthesis method, a polymer is chosen which is typically in the form of a solution or melt suitable for electrospinning. Common polymers include polyvinyl alcohol (PVA), polyethylene oxide (PEO), or others. A solvent suitable for both MXene dispersion and polymer dissolution. Common solvents include water, dimethylformamide (DMF), or other polar solvents. A grounded collector, typically in the form of a rotating drum or flat plate, collects the electrospun fibers. A high voltage power supply capable of generating electric fields in the range of 1–30 kV. A syringe pump or similar device for controlled delivery of the polymer solution during electrospinning. A spinneret or needle with a fine tip, through which the polymer solution is extruded during electrospinning (D. Li and Xia, 2004).

The MXene is dispersed in the chosen solvent to create a stable MXene dispersion, with sonication or high-shear mixing possibly employed to achieve uniform dispersion. The chosen polymer is dissolved in the solvent to form a polymer solution, with the polymer concentration optimized for electrospinning, typically in the range of 5%–20% w/v. The electrospinning apparatus is set up in a controlled environment to prevent airflow disturbances, and the grounded collector is positioned at an appropriate distance (usually 10–20 cm) from the spinneret. The polymer solution is loaded into a syringe or reservoir connected to the spinneret, ensuring it is free of air bubbles to prevent disruption during electrospinning. A high voltage (typically in the range of 1–30 kV) is applied between the spinneret and the collector to generate an electric field, initiating the electrospinning process by dispensing the polymer solution through the spinneret at a controlled flow rate (typically in the range of 0.1–10 mL/h). The electric field induces a charge on the surface of the polymer solution droplet, leading to the formation of a Taylor cone and subsequent elongation into nanofibers. Simultaneously, the MXene dispersion is introduced into the polymer solution or applied directly onto the collector to incorporate MXene into the electrospun fibers. The electrospun fibers are collected onto the grounded collector, forming a nonwoven mat or membrane, with the rotating drum or flat plate possibly used to facilitate continuous fiber collection. Post-treatment steps, such as drying, crosslinking, or annealing, may be performed to enhance fiber stability or modify properties. The electrospun MXene-polymer nanocomposite fibers are characterized to evaluate their structure, morphology, and properties, with techniques such as SEM, transmission electron microscopy (TEM), or mechanical testing employed (Merritt et al., 2012; Keirouz et al., 2020).

3.2.6.2 Consideration

The polymer concentration and solvent composition are optimized to achieve the desired solution viscosity for electrospinning. Control electrospinning parameters such as voltage, flow rate, and distance between the spinneret and collector to obtain uniform and well-aligned fibers. Uniform dispersion of MXene is ensured within the polymer solution to facilitate its incorporation into the electrospun fibers and enhance their properties. Cautions are exercised when working with high voltages and organic solvents, and follow appropriate safety protocols to prevent accidents or injuries.

Electrospinning offers precise control over fiber diameter, morphology, and composition, making it a valuable technique for fabricating MXene-polymer nanocomposite fibers with tailored properties for various applications such as filtration, tissue engineering, and sensors. Optimization of electrospinning parameters and thorough characterization are essential for achieving desired fiber properties and performance.

3.2.7 Chemical vapor deposition

They allow for direct synthesis on substrates and have uniform coatings on various surfaces along with precise control over film thickness. However, they require specialized equipment and are limited to specific substrates. These days, the scalability is improved, and have control over the CVD process. Chemical vapor deposition (CVD) is a method commonly used for the synthesis of thin films or coatings of MXene-polymer nanocomposites on solid substrates (Shareef et al., 1995; Schropp et al., 2000; Hamzan et al., 2021).

3.2.7.1 Material and method

The MXene of interest, such as titanium carbide ($Ti_3C_2T_x$) or others, is prepared through appropriate synthesis methods. The chosen polymer precursor, typically in the form of a vapor or gas, will react or deposit onto the substrate surface. A solid substrate onto which the MXene-polymer nanocomposite film will be deposited. Common substrates include silicon wafers, glass slides, or functionalized surfaces. A CVD reactor is equipped with the necessary components for gas flow control, temperature control, and vacuum pumping. An inert carrier gas such as nitrogen or argon, is used to transport the polymer precursor vapor to the substrate. Additives such as catalysts or dopants may be used to modify film properties or promote deposition. The substrate is thoroughly cleaned to remove any contaminants or residues that may affect film deposition, with the substrate surface optionally functionalized to promote adhesion or enhance film properties. The MXene powder is loaded onto a substrate holder inside the CVD reactor, ensuring uniform dispersion of MXene particles on the substrate surface. The polymer precursor is prepared in the desired

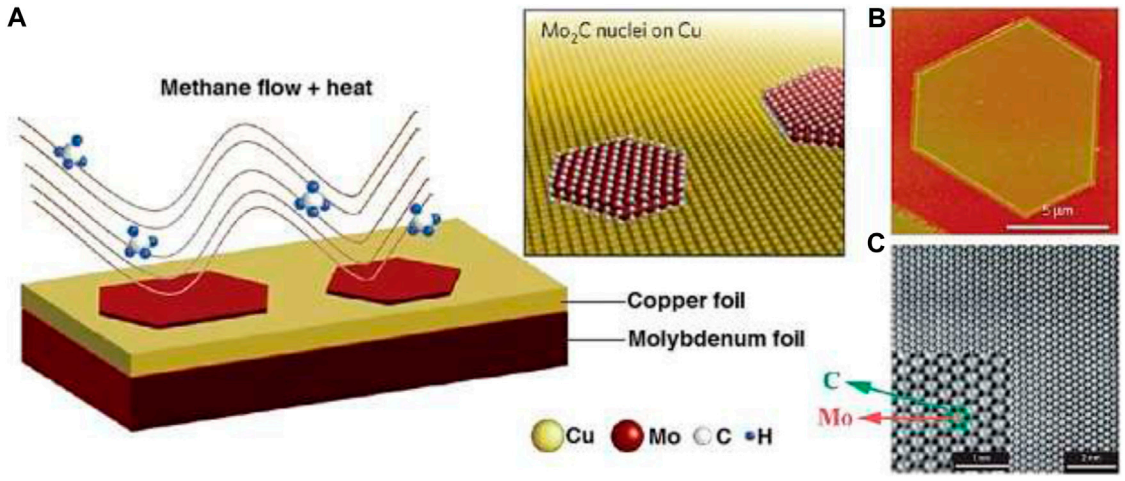

FIGURE 9
(A) The synthesis process of Mo_2C. **(B)** Images depicting hexagonal ultra-thin Mo_2C crystals. **(C)** STEM diagrams (P. Hu et al., 2022; Amu-Darko et al., 2024).

form for CVD deposition, which may involve heating the precursor to its vaporization temperature or introducing it as a gas into the CVD reactor. The CVD reactor is purged with an inert gas (e.g., nitrogen or argon) to remove air and moisture. The polymer precursor vapor or gas is introduced into the CVD reactor at the desired flow rate, and the substrate is heated to the appropriate temperature for polymer deposition, typically in the range of 100°C–300°C. The polymer precursor reacts or deposits onto the substrate surface, forming a thin film or coating. Alternatively, MXene can be simultaneously deposited with the polymer precursor by introducing MXene vapor or gas into the CVD reactor alongside the polymer precursor. Deposition parameters such as temperature, precursor flow rate, and deposition time are controlled to achieve the desired film thickness and properties. Post-treatment steps, such as annealing or surface modification, may be performed to enhance film properties or stability. The deposited MXene-polymer nanocomposite film is characterized to evaluate its structure, morphology, and properties, with techniques such as SEM, X-ray diffraction (XRD), or spectroscopic methods employed.

A novel method utilizing chemical vapor deposition (CVD) has been uncovered for the direct production of ultrathin MXene materials, offering a new avenue for MXene-based material fabrication (Gogotsi, 2015) (C. Xu et al., 2015; Geng et al., 2017). By employing methane as a carbon source over a Cu/Mo alloyed surface at temperatures surpassing 1085°C (Figures 9A–C) (Gogotsi, 2015) (C. Xu et al., 2015) large-area high-quality 2D ultrathin α-Mo_2C crystals (–3 nm) were successfully synthesized. Control over crystal size and thickness was achieved through manipulation of experimental conditions, where growth time influenced lateral size while growth temperature affected nucleation density. The method demonstrated versatility in generating various crystal shapes, including triangles, rectangles, hexagons, octagons, nonagons, and dodecagons, all exhibiting hexagonal packing of Mo atoms. Furthermore, enabling the fabrication of ultrathin β-Mo_2C nanosheets using a rapid and scalable synthesis approach involving MoO_2 nanosheets as templates and Mo sources. Unlike 2D materials obtained from alternative methods, CVD-fabricated MXenes showcased fewer defects and terminations, facilitating comprehensive investigations into their intrinsic properties and domain boundaries' effects. The exploration of bottom-up synthetic approaches is encouraged to prepare other types of monolayered MXenes with diverse functionalities, thereby enabling further investigations into their inherent electronic and optical properties (Gogotsi, 2015; Jeon et al., 2018; Sang et al., 2018)(L. Wang et al., 2016).

3.2.7.2 Consideration

A polymer precursor compatible with the CVD process and suitable for deposition onto the substrate surface is chosen and optimized the substrate temperature and deposition parameters to ensure uniform film growth and adhesion. The flow rates of carrier gas and precursor gas are controlled to achieve desired deposition rates and film properties. The deposition conditions are adjusted to control the composition and stoichiometry of the deposited MXene-polymer nanocomposite film.

CVD offers precise control over film thickness, composition, and properties, making it a valuable technique for fabricating MXene-polymer nanocomposites on solid substrates. Optimization of deposition parameters and thorough characterization are essential for achieving desired film properties and performance.

3.2.8 Hydrothermal/solvothermal methods

It is a method of producing a single crystal under high pressure using a hot mineral water solution that is hydrothermal and producing a chemical compound that is solvothermal (Demazeau, 2008). They have a low-temperature synthesis approach that is scalable applicable to various polymers and enables large-scale production. However, the reaction conditions may affect MXene properties and require careful optimization. They are advanced by using environmentally friendly solvents (like water, limonene, ethyl acetate, ethers, esters, ionic liquids, etc.) and improved reaction control (like catalysis, optimization techniques, etc.). Hydrothermal (Byrappa and Yoshimura, 2013) and

solvothermal methods are commonly used for synthesizing MXene-polymer nanocomposites in a controlled environment (Rabenau, 1985).

3.2.8.1 Material and method

The MXene of interest, such as titanium carbide ($Ti_3C_2T_x$) or others, is prepared through appropriate synthesis methods. The chosen polymer precursor, is typically in the form of a solution or dispersion compatible with the hydrothermal/solvothermal conditions. Common polymers include polyvinyl alcohol (PVA), polyethylene glycol (PEG), or others. A solvent is suitable for both MXene dispersion and polymer dissolution under hydrothermal/solvothermal conditions. Common solvents include water, ethanol, or other polar solvents. A sealed autoclave or reaction vessel capable of withstanding high temperatures and pressures. A heating source capable of providing the required temperature for the hydrothermal/solvothermal reaction. Additives such as surfactants, catalysts, or stabilizers may be used to modify reaction kinetics or improve nanocomposite properties.

The MXene is dispersed in the chosen solvent to create a stable MXene dispersion, with sonication or high-shear mixing potentially employed to achieve uniform dispersion. The chosen polymer is dissolved in the solvent to form a polymer solution or dispersion, with the polymer concentration optimized for the hydrothermal/solvothermal conditions. The MXene dispersion and polymer solution are mixed in the desired ratio to obtain a homogeneous MXene-polymer mixture, ensuring thorough mixing to achieve uniform dispersion of MXene within the polymer matrix. The MXene-polymer mixture is transferred into a sealed autoclave or reaction vessel suitable for hydrothermal/solvothermal reactions, ensuring the vessel is clean and free of contaminants. The autoclave or reaction vessel is heated to the desired temperature for the hydrothermal/solvothermal reaction, typically ranging from 100°C to 250°C, depending on the polymer and MXene used. The reaction temperature is maintained for a specified duration to allow for the synthesis of the MXene-polymer nanocomposite. After the reaction is complete, the autoclave or reaction vessel is cooled to room temperature, and the MXene-polymer nanocomposite product is retrieved. The product may be in the form of a gel, powder, or precipitate, depending on the reaction conditions. Post-treatment steps, such as washing, drying, or annealing, may be performed to remove any unreacted precursors or by-products and to enhance the properties of the nanocomposite material. The synthesized MXene-polymer nanocomposite is characterized to evaluate its structure, morphology, and properties, with techniques such as SEM, XRD, or spectroscopic methods employed.

3.2.8.2 Consideration

The reaction temperature, pressure, and duration to achieve the desired properties of the MXene-polymer nanocomposite are optimized. A solvent suitable (like N-methyl-2-pyrrolidone (NMP) a polar aprotic solvent that has good solubility for a wide range of polymers, including many commonly used ones such as polyvinylidene fluoride (PVDF), polyvinyl alcohol (PVA), and polyethylene oxide (PEO)) for both MXene dispersion and polymer dissolution under hydrothermal/solvothermal conditions are chosen. The additives or surfactants are incorporated to control particle size, and morphology, or to enhance the dispersion of MXene within the polymer matrix. High temperatures and pressures are handled with caution and follow appropriate safety protocols during the hydrothermal/solvothermal reaction.

This method offer controlled conditions for synthesizing MXene-polymer nanocomposites with tailored properties. Optimization of reaction parameters and thorough characterization are essential for achieving desired nanocomposite properties and performance.

3.2.9 Emulsion polymerization

Production of hydrophobic polymers in industrial and academic scales (Hohenstein and Mark, 1946) They are suitable for water-soluble polymers and have good control over particle size and distribution. However, they are limited to specific polymer types and may require additional steps for nanocomposite formation. The novel emulsion systems are developed for improved stability. Emulsion polymerization is a versatile method for preparing polymer-MXene nanocomposites in the form of latex particles dispersed in an aqueous medium (Whitby and Katz, 1933).

3.2.9.1 Material and method

The MXene of interest, such as titanium carbide ($Ti_3C_2T_x$), is prepared through appropriate synthesis methods, and the monomers that are compatible with the emulsion polymerization process are selected for polymerization. Common monomers include styrene, methyl methacrylate, or butyl acrylate. An emulsifier or surfactant stabilizes the emulsion and prevents the coalescence of polymer particles. Common surfactants include sodium dodecyl sulfate (SDS), polyvinyl alcohol (PVA), or cetyltrimethylammonium bromide (CTAB). A water-soluble initiator to initiate the polymerization reaction in the aqueous phase. Common initiators include potassium persulfate (KPS), ammonium persulfate (APS), or hydrogen peroxide. Water is the continuous phase for emulsion polymerization. Optionally, a stabilizer such as polyvinyl alcohol (PVA) or polyethylene glycol (PEG) may be added to improve stability and control particle size.

The MXene is dispersed in water using mechanical agitation or sonication to obtain a stable aqueous dispersion, with the MXene concentration optimized based on the desired loading in the nanocomposite. The emulsion is prepared by mixing the MXene dispersion with the surfactant solution, with the surfactant concentration optimized to ensure the stabilization of the emulsion. The chosen monomer or monomer mixture is dissolved in water-soluble initiators to form the aqueous monomer phase, with the monomer concentration adjustable based on the desired properties of the polymer-MXene nanocomposite. The polymerization reaction is initiated by adding the monomer solution to the emulsion under stirring or agitation, with the addition performed gradually to control the particle size and nucleation rate. The reaction temperature is maintained, and stirring continues until the polymerization is complete, typically controlled below the boiling point of water. During polymerization, MXene particles become embedded within the growing polymer particles, forming a polymer-MXene

nanocomposite. The surfactant molecules at the interface between water and monomer droplets stabilize the growing polymer particles, preventing coalescence. After polymerization, the nanocomposite latex can undergo post-polymerization treatments such as purification, drying, or chemical modification to remove unreacted monomers or improve their properties. The synthesized polymer-MXene nanocomposite is characterized to evaluate its structure, morphology, and properties, with techniques such as dynamic light scattering (DLS), TEM, or mechanical testing employed.

3.2.9.2 Consideration

An appropriate surfactant is selected to stabilize the emulsion and control particle size during polymerization. Select monomers compatible with water-based emulsion polymerization and capable of forming stable latex particles. Water-soluble initiators are used for polymerization in the aqueous phase, ensuring efficient initiation and control of the reaction. Maintain appropriate stirring and temperature conditions throughout the polymerization process to ensure uniform particle formation and polymerization kinetics.

Emulsion polymerization offers advantages such as easy scalability, control over particle size, and compatibility with aqueous systems, making it a promising method for preparing polymer-MXene nanocomposites in latex form. Optimization of parameters and thorough characterization are essential for tailoring the properties of the nanocomposite for specific applications.

Each synthesis method has its own set of considerations, and the choice depends on the specific requirements of the application. Recent advancements often focus on improving scalability, efficiency, and control over the nanocomposite's structure and properties. Exploration is going on innovative approaches to enhance the performance and broaden the applicability of MXene-polymer nanocomposites in diverse fields.

3.2.10 Characterization

Techniques such as XRD and TEM are used to confirm the 2D structure and layer spacing of MXenes. X-ray photoelectron spectroscopy (XPS) and FTIR help analyze the chemical composition and functional groups on the MXene surface. Brunauer-Emmett-Teller (BET) surface area analysis is commonly used to determine the specific surface area of MXenes, providing insights into their porosity.

MXene synthesis methods are continuously evolving, with an exploration of new etchants, delamination techniques, and polymer integration strategies to enhance the properties and applications of these unique materials. The ability to customize MXene structures and incorporate them into nanocomposites opens up a wide range of possibilities for various technological advancements.

4 Biomedical application

There are several fields under the biomedical application of MXene Polymer nanocomposite (George, Tandon, and Kandasubramanian, 2020; Garg and Ahmad, 2022; Parajuli et al., 2022).

4.1 Role in drug delivery systems

MXene-polymer nanocomposites play a significant role in drug delivery systems due to their unique properties of higher photothermal conversion and pH sensitivity, which offer advantages for enhancing therapeutic efficacy and addressing challenges associated with conventional drug delivery methods. A sketch of Nb_2C/PVP used for tumor ablation by *In Vivo* Photothermal irradiated with NIR-I and NIR-II is shown in Figure 10. Here are some key roles of MXene-polymer nanocomposites in drug delivery systems.

4.1.1 Improved drug loading and release

MXene nanosheets provide a high surface area and abundant functional groups, allowing for efficient loading of therapeutic agents such as drugs, proteins, or nucleic acids (Sur et al., 2019). The controlled release of these agents can be achieved by modulating the interaction between the drug molecules and the nanocomposite matrix, leading to sustained or triggered release profiles (P. Zhang et al., 2019). For example: the synergistic effect developed in SP surface modified with Ti_3C_2 destroys the cancerous cells with the help of NIR laser (X. Han et al., 2018) as shown in Figure 11.

4.1.2 Enhanced biocompatibility and stability

Incorporating MXenes into polymer matrices can improve the biocompatibility and stability of drug delivery systems. The polymer coating protects the MXene nanosheets from degradation and minimizes potential cytotoxicity, enhancing the overall biocompatibility of the nanocomposite (Zhao et al., 2021; Cui et al., 2023).

4.1.3 Targeted drug delivery

Surface functionalization of MXene-polymer nanocomposites allows for the introduction of targeting ligands such as antibodies, peptides, or aptamers. These ligands can selectively bind to specific receptors or biomarkers overexpressed on target cells, facilitating targeted drug delivery and minimizing off-target effects (Mohajer et al., 2022) (A. Liu et al., 2022). G. Liu et al. and Z. Li et al. studied MXene nanocomposites for the targeted drug delivery and found efficient for that. (Z. Li et al., 2018).

4.1.4 Responsive drug release

MXene-polymer nanocomposites can be engineered to respond to external stimuli such as pH, redox, temperature, light, electric, magnetic, etc. By incorporating responsive polymers or responsive MXene coatings, drug release from the nanocomposite can be triggered or modulated in a controlled manner, enabling on-demand drug delivery and localized therapy (He et al., 2024).

The pH of cancerous tissues is lower than normal (i.e. below 7.4) dealing with hydrophilic and hydrophilic interaction. (Lopes et al., 2013). In redox response, there is oxidation-reduction in extra and intracellular regions. For example: glutathione (GSH) can be the reducing agent as shown in Figure 12. (Hatakeyama, 2017). (Y. Dai, Chen, and Zhang, 2018). Some of the responsive polymers are Poly acrylic acid (PAA), polyethylene glycol (PEG), poly 2-dimethylamino ethyl methacrylate (PDMAEMA), polyethylene oxide (PEO), poly oligo ethylene methacrylate (POEGMA), etc. In electro-responsive drug release, the electrically conductive

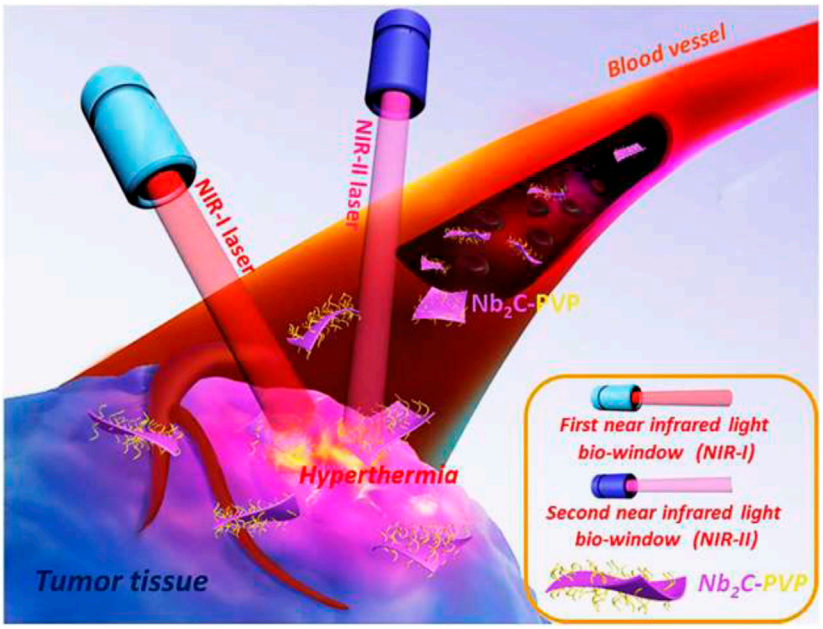

FIGURE 10
A sketch of Nb_2C/PVP used for tumor ablation by *In Vivo* Photothermal irradiated with NIR-I and NIR-II (Reprinted with permission from ref (Lin, Gao, et al., 2017). Copyright 2017 American Chemical Society.

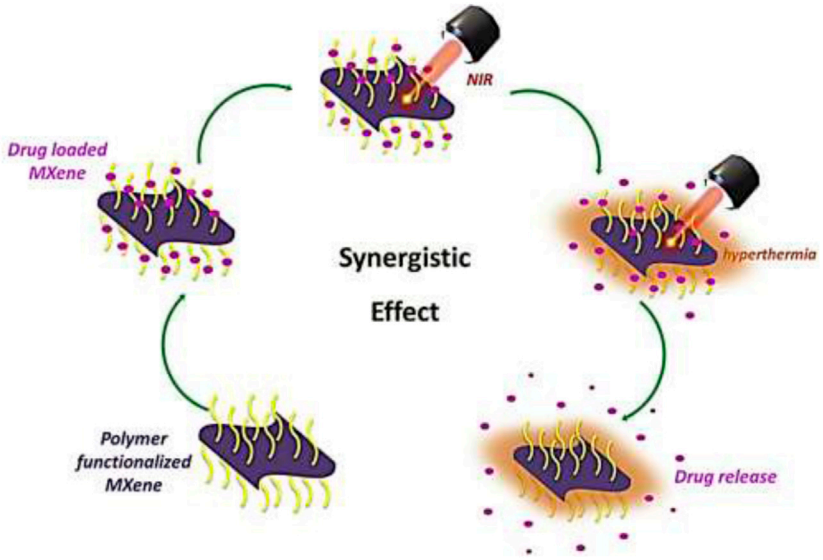

FIGURE 11
The chemo and photothermal therapy process showing synergistic effect.

MXene by using the external electric field (Zavahir et al., 2020). Similarly, the external magnetic field plays the same role in magnetic-responsive drug release (Darroudi et al., 2023).The light-responsive molecules like photochromic compounds stimulated by light of a certain wavelength create structural changes in MXene or its surroundings for light-responsive drug release (Zavahir et al., 2020). In case of temperature-responsive drug release, MXene nanosheets into a polymer matrix with a lower critical solution temperature (LCST), the drug release can be triggered by changes in temperature above or below the LCST can be utilized (Karimi et al., 2016).

4.1.5 Theranostic application

MXene-polymer nanocomposites have shown promise for theranostic applications, combining therapeutic and diagnostic functionalities within a single platform. The efficient breast

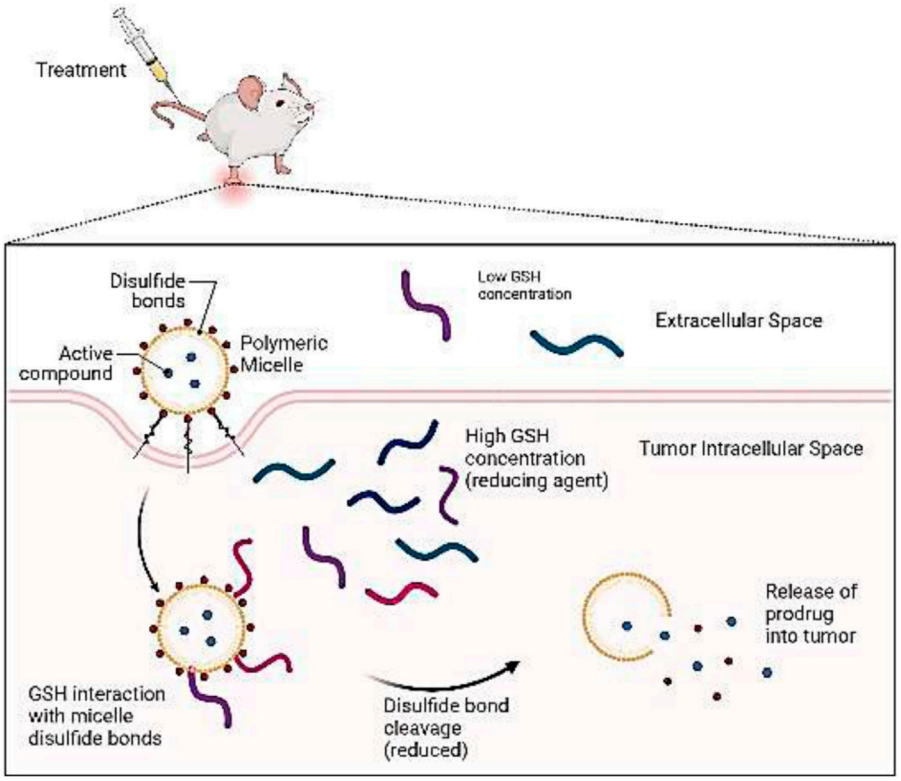

FIGURE 12
Intra-tumoral Redox responsive drug delivery systems activated by GSH.

cancer theranostic was achieved by tantalum carbide MXene composite (Z. Liu et al., 2018; Lin et al., 2018). Polyoxometalate as functionalizing agent for Tantalum carbide was studied by L Zong et al., 2018 for theranostic application. MXene Functionalization with imaging agents or contrast agents enables real-time monitoring of drug distribution and therapeutic response, facilitating personalized medicine and treatment optimization (Sivasankarapillai et al., 2020; Aslam et al., 2023; Nikazar, Mofidi, and Mortazavi, 2023).

4.1.6 Synergistic therapeutic effect

The combination of MXenes with polymers can lead to synergistic therapeutic effects, where the unique properties of each component complement each other. For example, A. Liu et al., 2022, Yang et al., 2022, W Tang et al., 2019 found that MXene's high conductivity and mechanical strength combined with the polymer's biocompatibility and versatility can enhance the overall performance of drug delivery systems, enabling novel therapeutic strategies (A. Liu et al., 2022; Yang et al., 2022)(W. Tang et al., 2019).

4.1.7 Multifunctional platforms

MXene-polymer nanocomposites can serve as multifunctional platforms for combination therapy, allowing for the co-delivery of multiple drugs or therapeutic agents with different mechanisms of action. This approach can overcome drug resistance, improve treatment outcomes, and reduce side effects compared to single-agent therapy. Several studies and experiments have demonstrated the efficacy of MXene-polymer nanocomposites in Drug delivery systems. Wang et al. (2019) developed a pH-responsive drug delivery system based on MXene-polymer nanocomposites for targeted cancer therapy. The nanocomposites exhibited high drug loading capacity, controlled drug release behavior, and enhanced cytotoxicity against cancer cells compared to free drugs (Wang et al., 2019). In another study, Liu et al. (2021) synthesized MXene-polymer nanocomposites for the co-delivery of doxorubicin (DOX) and indocyanine green (ICG) for combined chemotherapy and photothermal therapy. The nanocomposites showed improved therapeutic efficacy and enhanced tumor inhibition in a mouse xenograft model compared to monotherapy (X. Liu et al., 2021).

4.1.8 Anticancer treatment

In cancer treatment, therapeutics such as PLGA/Ti_3C_2 (Lin, Wang, et al., 2017) are employed for photothermal ablation. Additionally, Ti_3C_2/Al has been utilized for cancer treatment under 808 nm laser radiation (Z. Liu et al., 2018). V_2C nanosheets demonstrate efficacy as photothermal agents for photothermal treatment, with applications in photoacoustic (PA) and magnetic resonance imaging (MRI) (Zada et al., 2020). Moreover, AIPH@Nb_2C@mSiO_2 nanocomposites have been employed for thermodynamic therapy targeting cancer cells deficient in oxygen (Xiang et al., 2019). Ti_3C_2-DOX complexes have been demonstrated to generate reactive oxygen species (ROS) during photodynamic therapy, effectively targeting and killing cancerous cells (K. Huang et al., 2018). Additionally, they

find utility in drug delivery applications. Nb_2C/polymer nanocomposites have been utilized to ablate tumors via photothermal processes, particularly in the near-infrared region (Lin, Gao, et al., 2017). Furthermore, MnO_x/Ti_3C_2-SP and MnO_x/Ta_4C_3-SP MXene nanocomposites have been employed for the treatment of acidic tumors (C. Dai, Chen, et al., 2017; Lin, Chen, and Shi, 2018).

Thus, MXene-polymer nanocomposites hold great promise for revolutionizing drug delivery systems by offering tailored properties, enhanced functionality, and improved therapeutic outcomes. Continued research and development in this field are expected to lead to the translation of these nanocomposites into clinically relevant applications for the treatment of various diseases.

4.2 Imaging and diagnostics

MXene-polymer nanocomposites hold significant potential in imaging and diagnostics due to their unique properties and versatile functionalities. For example: They are used for the allocation of affected areas like tumor regions and monitoring the treatment effect by MRI. Here are some key aspects highlighting their potential in this field.

4.2.1 Enhanced contrast agents

MXene nanosheets can be functionalized with imaging agents such as fluorophores, magnetic nanoparticles, or radioisotopes to enhance contrast in various imaging modalities including optical imaging, MRI, and nuclear imaging techniques (e.g., positron emission tomography (PET) or single-photon emission computed tomography (SPECT)). The integration of MXenes into polymer matrices ensures stability and biocompatibility of the contrast agents, enabling their use *in vivo* for non-invasive imaging (Aslam et al., 2023). Ta_4C_3-IONP-SP nanocomposites represent a case employed in MRI applications (Z. Liu et al., 2018) as enhanced contrast agent.

4.2.2 Targeted imaging

Surface modification of MXene-polymer nanocomposites with targeting ligands (e.g., antibodies, peptides, or aptamers) allows for specific binding to molecular targets or biomarkers overexpressed in diseased tissues. This targeted approach improves imaging sensitivity and specificity, enabling early detection and precise localization of pathological lesions (Kumar, Barman, and Singh, 2021).

4.2.3 Multimodal imaging

MXene-polymer nanocomposites can be engineered to exhibit multimodal imaging capabilities by combining different imaging agents within a single platform. For example, integrating fluorescent dyes for optical imaging with magnetic nanoparticles for MRI or radionuclides for PET allows for complementary information acquisition and improved diagnostic accuracy (Z. Liu et al., 2018).

4.2.4 Responsive imaging

MXene-based nanocomposites can respond to external stimuli such as pH, temperature, or specific biomolecules, leading to changes in their imaging properties. C. Dai et al., 2017 used the nanocomposite in pH-guided MRI for hyperthermia treatment of tumors (C. Dai, Lin, et al., 2017). Responsive imaging agents enable dynamic monitoring of physiological processes or disease progression in real-time, providing valuable insights into treatment response and disease mechanisms (X. Han et al., 2018).

4.2.5 Theranostic application

MXene-polymer nanocomposites have the potential for theranostic applications, combining diagnostic and therapeutic functionalities within a single platform. By incorporating both imaging agents and therapeutic agents, these nanocomposites enable image-guided therapy, personalized treatment planning, and monitoring of therapeutic response in real-time (Lin et al., 2018).

4.2.6 Bioimaging

MXene-polymer nanocomposites exhibit excellent biocompatibility and low cytotoxicity, making them suitable for biomedical imaging applications. These nanocomposites can be used for *in vitro* cell imaging, *in vivo* molecular imaging, and bioimaging of tissues and organs, providing valuable information for disease diagnosis, prognosis, and treatment evaluation (Gomez et al., 2018).

4.2.7 Flexible and functional platforms

MXene-polymer nanocomposites offer flexibility in design and functionalization, allowing for the customization of imaging properties based on specific application requirements. Tailoring the composition, size, and surface chemistry of the nanocomposites enables fine-tuning of imaging performance and optimization for different imaging modalities (Ling et al., 2014).

Some additional prominent research was made in Imaging and diagnostics. Xu et al. (2020) developed MXene-polymer nanocomposites as dual-modal contrast agents for both photoacoustic imaging (PAI) and MRI. The nanocomposites exhibited excellent imaging performance with high signal intensity and superior contrast enhancement in tumor imaging (Xu et al., 2020). Kong and Chen in 2022 reported the synthesis of MXene-polymer nanocomposites as theranostic agents for combined photothermal therapy (PTT) and photodynamic therapy (PDT) of cancer (Kong and Chen, 2022). The nanocomposites showed efficient tumor ablation and simultaneous imaging capability for guiding therapy (H. Li et al., 2021).

4.3 Biosensors

Biosensors are employed to identify specific elements within the human body. These devices consist of several components: a sensing element, a transducer, and a data interpreter (Prajapati and Kandasubramanian, 2019). The sensing element, typically an immobilized biomolecule like an enzyme, can detect the concentration of a target analyte in its vicinity, generating a biochemical signal. This signal is then converted into an electrical signal by a transducer and subsequently interpreted by a data interpreter. In a study by Rakhi and colleagues, they developed an enzymatic biosensor (GOx/Au/Ti_3C_2/Nafion/GCE) for detecting glucose (Rakhi et al., 2016). Glucose is converted

into gluconolactone and hydrogen peroxide (H_2O_2) through the action of the enzyme glucose oxidase (GOx). The presence of glucose leads to the production of peroxide, generating a high potential indicative of glucose levels. Nafion facilitates the enzyme's adhesion to the glassy carbon electrode (GCE) (Harper and Anderson, 2010).

In Biosensing and detection, Li et al. (2020) synthesized MXene-polymer nanocomposites for glucose biosensing applications. The nanocomposites exhibited high sensitivity, excellent selectivity, and rapid response toward glucose detection, showing promise for diabetes management and point-of-care testing (X. Li, Zhao, and Wu, 2020). Jiang et al. (2021) developed MXene-polymer nanocomposites for ultrasensitive detection of circulating tumor DNA (ctDNA) in blood samples. The nanocomposites demonstrated high specificity and sensitivity for ctDNA detection, offering potential for early cancer diagnosis and prognosis monitoring (Y. Jiang et al., 2021). The GOx/Au/Ti3C2/Nafion/GCE configuration represents an enzymatic biosensor for glucose detection (Rakhi et al., 2016).

4.4 Tissue engineering

In Tissue engineering and regenerative medicine, Zhu et al. (2020) fabricated MXene-polymer nanocomposite scaffolds for bone tissue engineering applications. The nanocomposite scaffolds exhibited excellent biocompatibility, enhanced mechanical properties, and promoted osteogenic differentiation of mesenchymal stem cells (MSCs) *in vitro* (J. Zhu et al., 2020). In a study by Ma et al. (2021), MXene-polymer hydrogels were developed as injectable scaffolds for cartilage repair. The nanocomposite hydrogels exhibited excellent biocompatibility, controlled drug release, and promoted chondrogenic differentiation of MSCs, showing potential for cartilage regeneration (Ma et al., 2021)

The literature demonstrates the biocompatibility of MXene-polymer nanocomposites for biomedical applications, including tissue engineering, drug delivery, and implantable medical devices. Further research is needed to fully understand the biocompatibility mechanisms and optimize the design of MXene-polymer nanocomposites for safe and effective biomedical applications. The synthesis, application, and properties of MXene-polymer nanocomposites are listed in Table 3.

Overall, MXene-polymer nanocomposites represent a promising platform for advancing imaging and diagnostics, offering enhanced contrast, targeted imaging, multimodal capabilities, responsiveness, and biocompatibility. Continued research and development in this area are expected to lead to the translation of these nanocomposites into clinically relevant imaging agents for early disease detection, precise diagnosis, and personalized medicine.

These studies highlight the diverse applications and promising outcomes of MXene-polymer nanocomposites in biomedical research, ranging from drug delivery systems and imaging diagnostics to tissue engineering and biosensing. Continued exploration and innovation in this field are expected to lead to the development of novel nanocomposite-based technologies for improved healthcare and disease management.

5 Biocompatibility and toxicity

MXene-polymer nanocomposites hold great promise for biomedical applications due to their unique properties and versatile functionalities. Biocompatibility refers to the ability of a material to perform its desired function without eliciting an adverse reaction in living organisms. In the context of MXene-polymer nanocomposites, assessing biocompatibility involves evaluating how these materials interact with biological systems, including cells, tissues, and organs. Several factors influence nanocomposites' biocompatibility, including the materials' physicochemical properties, surface characteristics, and degradation behavior (Parajuli et al., 2022). Toxicity assessment is another critical aspect, focusing on the potential adverse effects of MXene-polymer nanocomposites on biological systems. Toxicity can arise from various sources, such as the release of toxic ions, generation of reactive oxygen species (ROS), or physical damage to cells and tissues. Understanding the toxicity profile of nanocomposites is essential for ensuring their safety in biomedical applications, such as drug delivery, tissue engineering, and medical implants (Vasyukova et al., 2022).

Various techniques are being employed to evaluate the biocompatibility and toxicity of MXene-polymer nanocomposites, including *in vitro* assays using cell cultures, *in vivo* studies using animal models, and computational modeling approaches. These studies assess parameters such as cell viability, proliferation, inflammation, oxidative stress, genotoxicity, and organ function following exposure to nanocomposite materials (Khatri et al., 2013). Additionally, surface modification strategies can be employed to enhance the biocompatibility of MXene-polymer nanocomposites by reducing potential cytotoxicity and improving their interactions with biological systems. Surface functionalization with biocompatible molecules or polymers can mitigate adverse effects and promote desirable biological responses.

Ensuring the biocompatibility of these nanocomposites is crucial for their safe and effective use in biological systems. Ti_3C_2-SP, Ta_4C_3-SP, and MnOx/Ti_3C_2-SP are utilized in a photoacoustic signal approach, leveraging stress waves from tissues irradiated by NIR. Ta_4C_3-IONP-SPs and Ta_4C_3-SP nanocomposites possess the capability to attenuate X-rays, making them suitable for employment in computed tomography (CT) (Z. Liu et al., 2018; C; Dai, Chen, et al., 2017; Lin et al., 2018).

Several studies have investigated the biocompatibility of MXene-polymer nanocomposites, demonstrating their potential for various biomedical applications.

5.1 Biocompatibility assessment

Research by Li et al. (2021) conducted comprehensive biocompatibility assessments of MXene-polymer nanocomposites for biomedical applications. The study evaluated cytotoxicity, hemocompatibility, and *in vivo* biocompatibility, demonstrating minimal adverse effects and high biocompatibility of MXene-polymer nanocomposites (X. Li et al., 2021).

TABLE 3 MXene–polymer composite materials for Biocompatibility and environment remedies with synthesis, application, and properties (adopted from (Parajuli et al., 2022)).

S. N	MXene/polymer	Synthesis	Application and properties	Refs
01	AgNP-$Ti_3C_2T_x$/Fe_3O_4 and PVA	Electrospinning + heat treatment	Wastewater treatment	Huang et al. (2019)
02	Ti_3C_2/PLA	Melt blending	Thermal + mechanical	Xue et al. (2020)
03	$Ti_3C_2T_x$@CS/PU	Dip coating	Pressure sensors	Li et al. (2019)
04	GO_x/Au/$Ti_3C_2T_x$/naflon	Chemical reduction	Biosensors	Rakhi et al. (2016)
05	$Ti_3C_2T_x$/PVDF	Vacuum-assisted filtration	Antibacterial + wastewater treatment	Rasool et al. (2017)
06	$Ti_3C_2T_x$/PDMS	MILD etching	Skin conformal tattoo sensors	Kedambaimoole et al. (2020)
07	$Ti_3C_2T_x$/PEI modified alginate aerogel	Cross-linking reaction	Heavy metal ion absorptions	(Y. Feng et al., 2021)
08	$Ti_3C_2T_x$/PPy	*In situ* depositing	Water Remediation	Shi et al. (2022)
09	$Ti_3C_2T_x$@Au/polydopamine	Polymerization	Photothermal + catalytic activity	Zhang et al. (2022)
10	$Ti_3C_2T_x$/PVDF	MILD etching	Water purification	Jin et al. (2021)
11	$Ti_3C_2T_x$/PA	*In situ* interfacial polymerization	Water desalination	Wang et al. (2020)

5.2 Cell viability and proliferation

Wang et al. (2020) investigated the effect of MXene-polymer nanocomposites on cell viability and proliferation for tissue engineering applications. The study showed that MXene-polymer nanocomposites supported cell attachment, proliferation, and differentiation, indicating their biocompatibility and potential for promoting tissue regeneration (Wang et al., 2020). The colloidal solution of Ti_3C_2 facilitates the proliferation of Gram-negative *E. coli* and Gram-positive *Bacillus subtilis*, demonstrating antibacterial properties (Han et al., 2017). Ag@Ti_3C_2@Cu_2O nanocomposites serve as photocatalysts suitable for antibacterial applications (Feng et al., 2020).

5.3 Inflammatory response

Zhang et al. (2021) evaluated the inflammatory response of MXene-polymer nanocomposites *in vitro* and *in vivo*. The study demonstrated low levels of inflammatory cytokine production and minimal tissue inflammation upon exposure to MXene-polymer nanocomposites, highlighting their biocompatibility and suitability for biomedical applications (Zhang, Y., Wang, S., Liu, X., & Chen, 2021).

5.4 Tissue compatibility

Xu et al. (2019) investigated the tissue compatibility of MXene-polymer nanocomposites for implantable medical devices. The study showed favorable tissue responses, minimal fibrous encapsulation, and enhanced tissue integration with MXene-polymer nanocomposites, suggesting their potential for long-term implantation *in vivo* (Y. Xu et al., 2019). $Ti_3C_2T_z$ combined with PLA and octyltriethoxysilane (OTES) exhibits favorable mechanical properties and biocompatibility, aiding in tissue engineering (Zhang et al., 2018; Zhou et al., 2018).

Conclusively, comprehensive evaluation of biocompatibility and toxicity is essential for advancing the development of MXene-polymer nanocomposites for biomedical applications, ensuring their safe and effective use in various healthcare settings.

6 Challenges, solutions, and outlooks

While MXene-polymer nanocomposites hold immense promise for various applications, several challenges still need to be addressed to fully exploit their potential. The challenges faced by MXenes and their future perspectives are sketched in Figure 13. The challenges are on the outer octagon and the future perspectives in the inner octagon of the Figure. Some of the current challenges in the development and application of MXene-polymer nanocomposites include.

6.1 Challenges and solutions

6.1.1 Scalability of synthesis

One major challenge is scaling up the synthesis of MXene-polymer nanocomposites to meet industrial production demands. Current synthesis methods often involve complex and time-consuming procedures, limiting their scalability and commercial viability.

6.1.1.1 Advanced synthesis techniques

Novel synthesis techniques are being employed that enable the scalable production of MXene-polymer nanocomposites with improved efficiency and reproducibility. Techniques such as aerosol-assisted synthesis, microwave-assisted synthesis, and template-assisted synthesis offer potential solutions for overcoming scalability issues.

6.1.2 Uniform dispersion

Achieving uniform dispersion of MXene nanosheets within polymer matrices is crucial for maintaining the desired properties

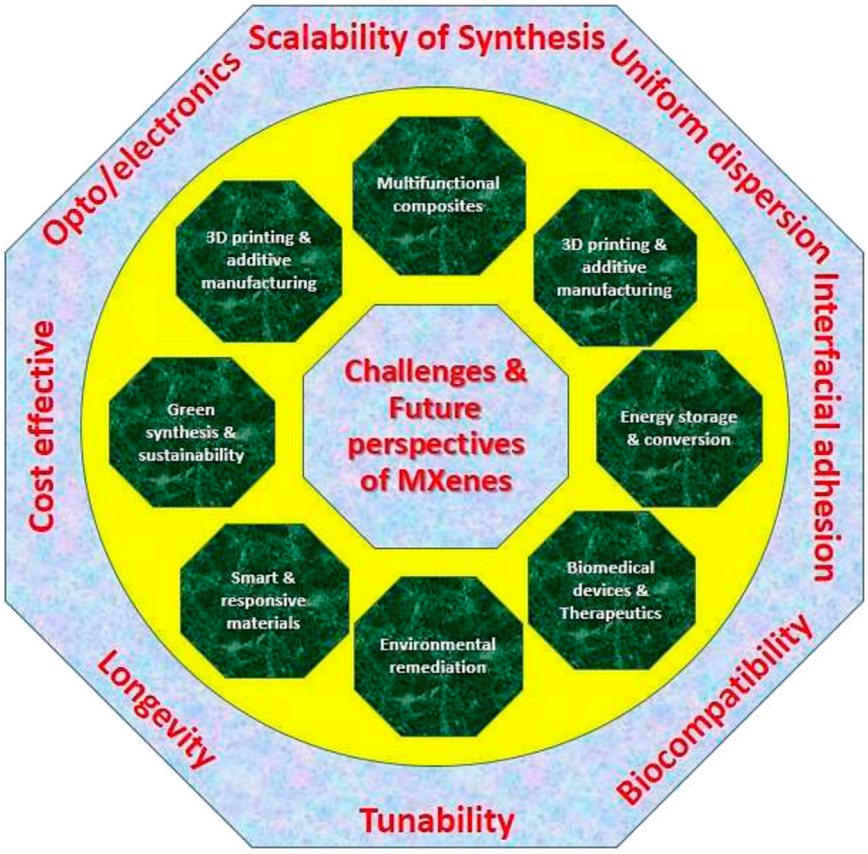

FIGURE 13
Challenges and Future Perspectives of MXene Polymer nanocomposites.

and performance of nanocomposites. However, ensuring uniform dispersion remains a challenge due to the tendency of MXene nanosheets to agglomerate during processing.

6.1.2.1 Surface modification

Surface modification of MXene nanosheets with functional groups or surfactants can enhance their dispersibility within polymer matrices and improve interfacial adhesion. Surface modification techniques such as chemical functionalization, plasma treatment, and surfactant-assisted dispersion are being investigated to address agglomeration and achieve uniform dispersion.

6.1.3 Interfacial adhesion

Achieving strong interfacial adhesion between MXene nanosheets and polymer matrices is essential for enhancing mechanical properties and stability of nanocomposites. However, achieving optimal interfacial adhesion remains challenging due to the inherently different properties of MXenes and polymers.

6.1.3.1 Interfacial engineering

Strategies for optimizing interfacial adhesion between MXene nanosheets and polymer matrices are being explored to enhance the mechanical properties and stability of nanocomposites. Approaches such as compatibilizer incorporation, *in-situ* polymerization, and interfacial coupling agents aim to improve interfacial interactions and enhance nanocomposite performance.

6.1.4 Biocompatibility

While MXene-polymer nanocomposites show great potential for biomedical applications, ensuring their biocompatibility remains a challenge. Further research is needed to comprehensively evaluate the biocompatibility of these nanocomposites and mitigate potential cytotoxicity or immunogenicity issues.

6.1.4.1 Biocompatibility assessment

Ongoing research focuses on comprehensive biocompatibility assessment of MXene-polymer nanocomposites for biomedical applications. Studies involve evaluating cytotoxicity, immunogenicity, and long-term biocompatibility through *in vitro* and *in vivo* experiments, aiming to ensure the safety and efficacy of nanocomposites in biological environments.

6.1.5 Tunable properties

Tailoring the properties of MXene-polymer nanocomposites to meet specific application requirements poses a challenge. Achieving tunable properties such as electrical conductivity, mechanical strength, and thermal stability requires precise control over MXene loading, polymer composition, and processing conditions.

6.1.5.1 Property tuning

Investigations are going on for tuning the properties of MXene-polymer nanocomposites to meet specific application requirements. Strategies such as controlling MXene loading, varying polymer composition, and adjusting processing conditions enable the customization of nanocomposite properties such as electrical conductivity, mechanical strength, and thermal stability.

6.1.6 Longevity

Ensuring the long-term stability of MXene-polymer nanocomposites under various environmental conditions is essential for their practical applications. However, issues such as degradation, leaching, and agglomeration may affect the stability and performance of nanocomposites over time.

6.1.6.1 Stability enhancement

Ongoing research focuses on enhancing the long-term stability of MXene-polymer nanocomposites under various environmental conditions. Strategies such as surface passivation, encapsulation, and cross-linking aim to improve nanocomposite stability, preventing degradation, leaching, and agglomeration over time.

6.1.7 Cost-effectiveness

The cost-effectiveness of MXene-polymer nanocomposites remains a concern, especially for large-scale applications. The high cost of MXene precursors and complex synthesis processes may hinder their widespread adoption in commercial applications. Efforts are underway to develop cost-effective synthesis routes and utilize more affordable precursor materials to reduce the production cost of MXene-polymer nanocomposites. Additionally, process optimization and scale-up strategies aim to streamline production processes and lower overall manufacturing costs.

Since the cost is a major factor in the manufacture of the MXene-polymer nanocomposite on a large scale (Zaed et al., 2024), we have further gone in with the factors of impact as sketched in Figure 14. These factors are.

6.1.7.1 Raw material costs

The cost of raw materials, particularly the precursors needed to produce MXenes, significantly impacts the overall synthesis cost. Precursors may include transition metal carbides, nitrides, or carbonitrides, which can be expensive depending on their source and availability (Rasid et al., 2017).

- Transition metal carbides, nitrides, or carbonitrides: Prices can vary based on factors such as purity, synthesis method, and availability. For example, the cost of titanium carbide powder can range from $50 to $200 per kilogram depending on quality and quantity purchased.
- Precursor chemicals: Prices vary widely depending on the specific chemicals used in the synthesis process. For instance, hydrochloric acid (HCl), a common etchant used in MXene synthesis, costs approximately $0.30 to $1.00 per liter.

6.1.7.2 Synthesis methodology

The choice of synthesis method plays a crucial role in determining costs (Shuck et al., 2021). Some synthesis routes may require expensive equipment, specialized facilities, or energy-intensive processes, increasing production expenses. Optimizing synthesis methods to minimize energy consumption or utilizing simpler techniques can help reduce costs (Jolly, Paranthaman, and Naguib, 2021). High-temperature synthesis methods such as MAX phase etching and exfoliation may require energy-intensive processes, increasing operational costs. For example, the energy cost for heating furnaces or reactors can be significant, ranging from several hundred to thousands of dollars per batch depending on the scale and duration of the synthesis process. Alternatively, low-temperature synthesis methods, such as the use of ionic liquids or mild etchants, may reduce energy consumption but could require specialized equipment or reagents, impacting upfront capital costs (Jolly, Paranthaman, and Naguib, 2021).

6.1.7.3 Process efficiency

The efficiency of the synthesis process affects the yield of desired MXene-polymer nanocomposites per unit of input materials. Low efficiency may result in the wastage of raw materials, energy, and time, driving up production costs. Improving process efficiency through better reaction conditions, catalysts, or purification methods can lower overall costs (Tan et al., 2024).

- Yield of desired MXene product: Efficiency in converting precursor materials into high-quality MXene affects production costs. Higher yields reduce material wastage and associated costs.
- Time required for synthesis: Longer reaction times or complex purification processes can increase labor and energy costs. Optimizing reaction conditions and purification steps can improve process efficiency and reduce overall production time and costs.

6.1.7.4 Labor costs

Skilled labor is essential for synthesizing MXene-polymer nanocomposites, especially in research and development phases where experimentation and optimization are common. Labor costs can significantly impact the overall synthesis cost, particularly if extensive manual intervention is required. Automation and streamlining of processes can help mitigate labor expenses (Islam and Shazali, 2011).

- Skilled labor wages: Labor costs vary widely depending on location, expertise required, and labor market conditions. For example, researchers or technicians involved in MXene synthesis may earn salaries ranging from $40,000 to $100,000 or more annually, depending on experience and qualifications.
- Automation and process optimization: Investments in automation technologies and streamlined processes can reduce labor requirements and associated costs over time.

6.1.7.5 Scale of production

Economies of scale have a significant impact on synthesis costs, as larger production volumes often lead to reduced unit costs (Shuck et al., 2020a). However, expanding production while ensuring consistent quality can be challenging. To achieve cost-effective large-scale production, investments in infrastructure, equipment, and process optimization are essential. The advantages of economies

FIGURE 14
Cost effecting factors of MXene Polymer Nanocomposites.

of scale become apparent as production volumes increase, allowing fixed costs to be spread out over a larger output (Shuck et al., 2020). This typically results in lower unit costs. Nevertheless, the initial investments required to scale up production facilities and equipment can be considerable. For instance, transitioning from laboratory-scale to pilot-scale or industrial-scale production may necessitate investments ranging from thousands to millions of dollars. The magnitude of investment depends on factors such as the complexity of the process and the desired output capacity (Charitidis et al., 2014).

6.1.7.6 Purification and characterization

Purification steps to remove impurities and characterization techniques to assess product quality add to the synthesis cost. These processes require additional materials, equipment, and labor. Developing efficient purification methods and adopting cost-effective characterization techniques can help manage these expenses (H. Tang et al., 2021).

- Cost of purification agents and equipment: Purification processes, such as acid washing or filtration, require chemicals, solvents, and specialized equipment. For example, the cost of membrane filtration systems for removing impurities can range from a few hundred to several thousand dollars depending on capacity and efficiency.
- Analytical techniques: Characterization methods such as SEM, XRD, and atomic force microscopy (AFM) incur costs for instrument purchase, maintenance, and consumables. For example, an SEM instrument may cost anywhere from $100,000 to over $1 million, plus ongoing maintenance and operation expenses.

6.1.7.7 Regulatory compliance

This is to follow with environmental, health, and safety regulations adds to the cost of synthesis (Kumari et al., 2023). Implementing sustainable practices and ensuring compliance with regulations may require investments in waste management, safety measures, and compliance monitoring (Journal and Ondokuzmay 2020). One of the concerns is the environmental and safety regulations. It is compliance with regulations governing chemical handling, waste disposal, and workplace safety may require investments in training, protective equipment, and facility modifications (Foulkes et al., 2020). Costs associated with regulatory compliance can vary widely depending on the jurisdiction and specific requirements (Directorate et al., 2015).

6.1.7.8 Supply chain consideration

The availability and cost of ancillary materials, such as solvents, catalysts, and additives, can impact overall synthesis costs. Fluctuations in prices or supply chain disruptions can affect

production economics. Diversifying supply sources or developing alternative materials can mitigate these risks (Lele, 2023).

- Ancillary materials and consumables: Prices of solvents, catalysts, and other consumables used in the synthesis process can fluctuate based on market conditions and availability. Bulk purchasing or negotiating long-term supply contracts may help stabilize costs.
- Supply chain disruptions: Events such as natural disasters, geopolitical tensions, or trade restrictions can disrupt the availability of raw materials or increase transportation costs. Diversifying supply sources and maintaining contingency plans can mitigate these risks.

Addressing these critical factors through research, innovation, and process optimization is essential for achieving cost-effective synthesis of MXene-polymer nanocomposites on a large scale. Collaboration between academia, industry, and government stakeholders can accelerate progress in this field and facilitate the commercialization of MXene-based materials.

6.1.8 Regulatory approval

Not only is the cost of manufacturing the nanocomposite, but it is also concerned with obtaining regulatory approval for MXene-polymer nanocomposites, particularly for biomedical and environmental applications, poses a challenge. Comprehensive safety assessments and standardized testing protocols are needed to ensure compliance with regulatory requirements.

6.1.8.1 Regulatory compliance

Investigation are going towards obtaining regulatory approval for MXene-polymer nanocomposites by conducting comprehensive safety assessments and adhering to standardized testing protocols. Collaboration with regulatory agencies and compliance with regulatory guidelines ensure the safe and ethical use of nanocomposites in commercial applications.

Addressing these challenges requires interdisciplinary research focusing on developing novel synthesis techniques, optimizing nanocomposite properties, improving scalability, enhancing biocompatibility, and conducting thorough performance evaluations. Collaborative efforts between academia, industry, and regulatory agencies are essential to overcome these challenges and unlock the full potential of MXene-polymer nanocomposites for diverse applications. Ongoing research in MXene-polymer nanocomposites aims to address the existing challenges through innovative solutions, interdisciplinary collaborations, and advancements in synthesis, characterization, and application techniques. These efforts pave the way for the widespread adoption of MXene-polymer nanocomposites across various industries, including electronics, energy, healthcare, and environmental remediation.

6.2 Outlooks

Future directions for the field of MXene-polymer nanocomposites encompass emerging trends and areas for exploration that hold promise for advancing research and applications. Some key future directions include.

6.2.1 Multifunctional nanocomposites

Future research will focus on developing MXene-polymer nanocomposites with multifunctional properties for diverse applications. They are composite materials composed of two or more distinct nanomaterials (such as nanoparticles, nanotubes, or nanosheets) dispersed within a matrix material (polymer, ceramic, or metal). These nanocomposites exhibit a combination of properties not present in the individual components alone. Various synthesis methods are employed to fabricate multifunctional nanocomposites, including solution mixing, *in situ* polymerization, melt blending, electrospinning, and layer-by-layer assembly. Each method offers advantages in terms of control over nanomaterial dispersion, interfacial interactions, and composite structure. These properties can be tailored by adjusting the composition, size, shape, and distribution of the nanomaterials within the matrix. These nanocomposites may integrate functionalities such as conductivity, mechanical strength, electrical conductivity, thermal stability, optical transparency, magnetic response, chemical reactivity, magnetism, biocompatibility, and stimuli-responsiveness, enabling their use in advanced electronics, sensors, actuators, biomedical devices electronics, aerospace, energy storage, sensing, catalysis, and environmental remediation (Yadav, 2023).

Despite their potential, multifunctional nanocomposites face challenges related to scalability, reproducibility, stability, and environmental impact. Future research aims to address these challenges by developing novel synthesis techniques, optimizing composite properties, and exploring new applications in emerging fields.

6.2.2 3D printing and additive manufacturing

The integration of MXene-polymer nanocomposites into additive manufacturing processes, such as 3D printing, will be explored for fabricating complex structures and functional devices with tailored properties. This approach offers opportunities for rapid prototyping, customization, and on-demand manufacturing of MXene-based products.

There are several techniques for 3D printing, including fused deposition modeling (FDM), stereolithography (SLA), selective laser sintering (SLS), binder jetting, and directed energy deposition (DED). Each technique has its advantages and is suitable for different materials and applications (Jiménez et al., 2019). 3D printing has diverse applications across industries such as aerospace, automotive, healthcare, architecture, consumer goods, and education. It is used for prototyping, rapid manufacturing, custom production, tooling, and even creating complex biological structures in biomedical engineering. Some key advantages of 3D printing include rapid prototyping, customization, reduced material waste, design freedom, and the ability to create intricate and lightweight structures. It also allows for on-demand production and decentralized manufacturing.

Despite its numerous advantages, 3D printing still faces challenges related to material limitations, surface quality, printing speed, scalability, and regulatory considerations, particularly in highly regulated industries such as healthcare.

6.2.3 Energy storage and conversion

Future research will focus on leveraging the unique properties of MXene-polymer nanocomposites for energy storage and conversion applications. These nanocomposites may be used as electrode materials in batteries, supercapacitors, and fuel cells, offering high energy density, fast charge-discharge rates, and long-term stability.

MXene-polymer nanocomposites offer several advantages that make them attractive for energy storage and conversion applications (Qiu et al., 2021). These include high surface area, excellent electrical conductivity, mechanical flexibility, and chemical stability. These properties enable them to serve as efficient electrode materials in various energy storage and conversion devices. Furthermore, MXene-polymer nanocomposites have shown promise in enhancing the performance of lithium-ion batteries, fuel cells, and other energy storage devices. Research in this area is ongoing, focusing on optimizing the composition, structure, and processing techniques of MXene-based materials to improve their energy storage and conversion properties (Parajuli et al., 2022).

By leveraging the unique properties of MXene-polymer nanocomposites, future research endeavors seek to develop next-generation energy storage and conversion technologies that offer high energy density, rapid charge-discharge rates, and long-term stability, contributing to the advancement of renewable energy integration and sustainable energy solutions.

6.2.4 Biomedical devices and therapeutics

The development of MXene-polymer nanocomposites for biomedical devices and therapeutics will be explored further. These nanocomposites may find applications in drug delivery systems, tissue engineering scaffolds, biosensors (Guo et al., 2019), and medical implants, offering biocompatibility, bioactivity, and controlled release properties.

The field of biomedical devices and therapeutics is rapidly evolving, driven by technological advancements and innovative research. Here are some future perspectives along.

6.2.4.1 Personalized medicine

Future biomedical devices and therapeutics will increasingly focus on personalized medicine approaches, tailoring treatments to individual patients based on their genetic makeup, lifestyle factors, and disease characteristics. This includes the development of biomarker-based diagnostics, targeted therapies, and precision drug delivery systems (Foroutan, 2015).

6.2.4.2 Implantable medical devices

Advances in materials science, microelectronics, and biocompatible coatings will lead to the development of smarter, more functional implantable devices for monitoring and treating various medical conditions. These devices may incorporate sensors, actuators, and wireless communication capabilities to provide real-time data and therapeutic interventions (Wodlinger, Dweiri, and Durand, 2015).

6.2.4.3 Biomedical devices

Nanomedicine will continue to revolutionize biomedical applications by enabling targeted drug delivery, enhanced imaging, and regenerative therapies. Nanoparticle-based drug carriers, nanofiber scaffolds for tissue engineering, and nanoscale imaging agents hold great potential for improving diagnosis and treatment outcomes (Bai et al., 2006).

6.2.4.4 Bioelectronics and wearable devices

The integration of biology with electronics will lead to the development of advanced wearable devices for continuous health monitoring, disease management, and drug delivery. Flexible and stretchable electronics, bio-compatible materials, and miniaturized sensors will enable seamless integration with the human body (Manjushree et al. 2022).

6.2.4.5 Gene editing and cell therapies

Advances in gene editing technologies such as CRISPR-Cas9 will revolutionize the development of gene therapies for treating genetic disorders and cancer (Jiang and Doudna, 2017). Cell-based therapies, including CAR-T cell immunotherapy and stem cell transplantation, hold promise for regenerative medicine and personalized cancer treatments (H. Wang, La Russa, and Qi, 2016).

In conclusion, the future of biomedical devices and therapeutics holds great promise, with ongoing research and innovation focusing on personalized medicine, implantable devices, nanotechnology, bioelectronics, and gene editing technologies, all aimed at revolutionizing healthcare delivery and improving patient outcomes.

6.2.5 Environmental remediation

Future research will focus on harnessing MXene-polymer nanocomposites for environmental remediation and pollution control. These nanocomposites may be used for water purification, air filtration, soil remediation, and wastewater treatment, offering high adsorption capacity, catalytic activity, and selectivity towards pollutants. One significant future direction involves the integration of emerging technologies such as artificial intelligence, machine learning, and remote sensing into environmental monitoring and remediation strategies. These technologies can improve the efficiency and effectiveness of pollution detection, site characterization, and remediation efforts by providing real-time data, predictive modeling, and automated decision-making capabilities (Shah, Rodriguez-Couto, and Sengor, 2020).

Furthermore, there is growing interest in the development of nature-based solutions and green infrastructure for environmental remediation. These approaches harness natural processes and ecosystems to restore habitats, purify water, and sequester carbon, offering cost-effective and sustainable alternatives to conventional remediation techniques.

6.2.6 Smart and responsive materials

The development of smart and responsive MXene-polymer nanocomposites that can sense and respond to external stimuli, such as light, temperature, pH, and mechanical stress, will be explored. These materials may find applications in smart textiles, adaptive coatings, drug delivery systems, and biomedical implants.

One significant future direction is the enhancement of the stimuli-responsive properties of MXene-polymer nanocomposites through precise control over their composition, structure, and interface interactions. This may involve the incorporation of stimuli-responsive polymers or functionalization of MXene nanosheets with responsive molecules to achieve tunable and reversible responses to environmental changes. Furthermore, research efforts are focused on integrating MXene-polymer nanocomposites into multifunctional

devices and systems for diverse applications. These may include smart coatings for corrosion protection, stimuli-responsive drug delivery systems for targeted therapies, and adaptive materials for shape-shifting structures or wearable electronics (Parajuli et al., 2022).

6.2.7 Green synthesis and sustainability

Future research will focus on developing green synthesis routes and sustainable manufacturing processes for MXene-polymer nanocomposites. These efforts aim to reduce environmental impact, minimize resource consumption, and enhance the eco-friendliness of nanocomposite production. The future research in this direction involves the following.

6.2.7.1 Environmentally benign synthesis routes

One focal point of future research involves exploring synthesis pathways that minimize or eliminate hazardous chemicals, volatile organic compounds (VOCs), and other environmentally detrimental substances. Green synthesis methodologies, such as aqueous-based processes or solvent-free techniques, are gaining traction for their reduced environmental footprint and improved safety profiles.

6.2.7.2 Renewable feedstock utilization

Another pivotal aspect revolves around harnessing renewable feedstock and sustainable raw materials for MXene synthesis. By shifting away from fossil fuel-derived precursors towards bio-based or recycled materials, researchers aim to lessen dependence on finite resources and promote circular economy principles.

6.2.7.3 Energy-efficient production process

Efficiency improvements in energy consumption during the synthesis and processing stages represent a crucial avenue for sustainable manufacturing. Integration of energy-saving technologies, waste heat recovery systems, and renewable energy sources can contribute to lowering carbon emissions and enhancing overall energy sustainability.

6.2.7.4 Waste minimization and recycling strategies

Addressing waste generation throughout the production lifecycle is paramount. Implementation of waste minimization techniques, recycling initiatives, and closed-loop manufacturing systems can help reduce environmental burden and optimize resource utilization, thereby fostering a more sustainable nanocomposite manufacturing ecosystem.

6.2.7.5 Life cycle assessment and environmental impact analysis

Comprehensive life cycle assessments and environmental impact analyses play a pivotal role in quantifying the ecological footprint of MXene-polymer nanocomposites. By systematically evaluating the environmental consequences of different production pathways, researchers can identify areas for improvement and guide decision-making towards more sustainable practices (F. Zhang et al., 2022).

6.2.7.6 Regulatory compliance and green certification

Adherence to stringent environmental regulations and attainment of green certifications signify essential benchmarks for sustainable nanocomposite production. Compliance with eco-labeling schemes, such as the EU Ecolabel or Green Seal, can validate adherence to environmental standards and enhance market acceptance of green products.

6.2.7.7 Collaborative research and knowledge sharing

Collaboration among academia, industry, and regulatory bodies is instrumental in advancing green synthesis initiatives and fostering knowledge exchange. Interdisciplinary research consortia, public-private partnerships, and collaborative platforms facilitate innovation, accelerate technology transfer, and drive collective progress towards sustainability goals (Payumo et al., 2020).

By prioritizing green synthesis principles and sustainability-driven manufacturing paradigms, the research community aims to usher in a new era of environmentally responsible MXene-polymer nanocomposite production, thereby harmonizing technological progress with ecological stewardship.

6.2.8 Computational modeling and design

The integration of computational modeling and simulation techniques will play a significant role in the rational design and optimization of MXene-polymer nanocomposites. Computational approaches enable predictive modeling of nanocomposite properties, structure-property relationships, and performance under different conditions.

One significant aspect of computational modeling is its ability to explore the effects of different parameters, such as MXene concentration, polymer morphology, and processing conditions, on the final properties of nanocomposites. This predictive capability allows researchers to optimize material composition and processing parameters to achieve desired performance metrics, such as mechanical strength, electrical conductivity, and thermal stability. Moreover, computational modeling facilitates the exploration of novel MXene-polymer combinations and architectures, guiding experimental efforts toward the synthesis of materials with unprecedented properties or functionalities. By simulating the behavior of nanocomposites at the atomic or molecular level, researchers can uncover underlying mechanisms and design principles that govern their performance, leading to informed decision-making and accelerated materials development cycles (Ohno, Esfarjani, and Kawazoe, 2018).

Overall, future research in the field of MXene-polymer nanocomposites will be characterized by interdisciplinary collaborations, innovative approaches, and transformative applications across various industries. By addressing emerging challenges and exploring new frontiers, researchers aim to unlock the full potential of MXene-based materials for addressing societal needs and advancing technological innovation.

7 Conclusion

In conclusion, MXene-polymer nanocomposites hold significant promise in both biomedical fields. These advanced materials offer multifunctional properties, including biocompatibility, tunable surface chemistry, and high adsorption capacity, making them suitable for diverse applications. In biomedicine, MXene-polymer nanocomposites show potential for drug delivery, tissue engineering, biosensors, and medical implants. Ongoing research and development efforts focus on addressing challenges and exploring

new frontiers, paving the way for the widespread adoption of MXene-polymer nanocomposites and their transformative impact on healthcare sustainability. In light of the promising potential of MXene-polymer nanocomposites in biomedical applications, it is imperative to emphasize the importance of continued research in this area. By addressing existing challenges, exploring emerging trends, and pushing the boundaries of innovation, researchers can unlock the full capabilities of MXene-polymer nanocomposites. The cost-effectiveness is studied deeply. Therefore, commitment is needed to enhance ongoing collaboration, investment, and exploration in MXene-polymer nanocomposites, as we strive to harness their transformative impact on our society and pave the way for a brighter, more sustainable future.

Data availability statement

The raw data supporting the conclusion of this article will be made available by the authors, without undue reservation.

Author contributions

DP: Writing–review and editing, Writing–original draft, Visualization, Validation, Supervision, Software, Resources, Project administration, Methodology, Investigation, Funding acquisition, Formal Analysis, Data curation, Conceptualization.

Funding

The author(s) declare that no financial support was received for the research, authorship, and/or publication of this article.

Conflict of interest

The author declares that the research was conducted in the absence of any commercial or financial relationships that could be construed as a potential conflict of interest.

Publisher's note

All claims expressed in this article are solely those of the authors and do not necessarily represent those of their affiliated organizations, or those of the publisher, the editors and the reviewers. Any product that may be evaluated in this article, or claim that may be made by its manufacturer, is not guaranteed or endorsed by the publisher.

References

Aghamohammadi, H., Amousa, N., and Eslami-Farsani, R. (2021). Recent advances in developing the MXene/polymer nanocomposites with multiple properties: a review study. *Synth. Met.* 273 (March), 116695. doi:10.1016/J.SYNTHMET.2020.116695

Amu-Darko, Jesse Nii OkaiHussain, S., Wang, M., Lei, S., Alothman, A. A., Mohammad, S., Qiao, G., et al. (2024). Advanced 2D nanosheet-based gas sensor for sensitive detection of low concentration NO2 gas using In2O3/Ti3C2 layers. *Sensors Actuators B Chem.* 407 (May), 135464. doi:10.1016/J.SNB.2024.135464

An, H., Habib, T., Shah, S., Gao, H., Radovic, M., Green, M. J., et al. (2018). Surface-agnostic highly stretchable and bendable conductive MXene multilayers. *Sci. Adv.* 4 (3), eaaq0118. doi:10.1126/sciadv.aaq0118

Anasori, B., Lukatskaya, M. R., and Gogotsi, Y. (2017). 2D metal carbides and nitrides (MXenes) for energy storage. *Nat. Rev. Mater.* 2 (2), 16098–16117. doi:10.1038/natrevmats.2016.98

Ashton, M., Mathew, K., Hennig, R. G., and Sinnott, S. B. (2016). Predicted surface composition and thermodynamic stability of MXenes in solution. *J. Phys. Chem. C* 120 (6), 3550–3556. doi:10.1021/acs.jpcc.5b11887

Aslam, M., Ahmad, T., Husnain Manzoor, M., Verpoort, F., and Verpoort, F. (2023). MXenes as theranostics: diagnosis and therapy including *in vitro* and *in vivo* applications. *Appl. Mater. Today* 35 (December), 102002. doi:10.1016/J.APMT.2023.102002

Bilibana, M. P. (2023). Electrochemical properties of MXenes and applications. *Adv. Sens. Energy Mater.* 2 (4), 100080. doi:10.1016/J.ASEMS.2023.100080

Boota, M., Anasori, B., Voigt, C., Zhao, M. Q., Barsoum, M. W., and Gogotsi, Y. (2016). Pseudocapacitive electrodes produced by oxidant-free polymerization of pyrrole between the layers of 2D titanium carbide (MXene). *Adv. Mater.* 28 (7), 1517–1522. doi:10.1002/ADMA.201504705

Boys, C. V. (1887). On the production, properties, and some suggested uses of the finest threads. *Proc. Phys. Soc. Lond.* 9 (1), 8–19. doi:10.1088/1478-7814/9/1/303

Byrappa, K., and Yoshimura, M. (2013). *Handbook of hydrothermal technology | 978-0-8155-1445-9*. Elsevier, 779. Available at: https://books.google.com/books/about/Handbook_of_Hydrothermal_Technology.html?id=vA5tXzLsHioC.

Carey, M., and Barsoum, M. W. (2021). MXene polymer nanocomposites: a review. *Mater. Today Adv.* 9 (March), 100120. doi:10.1016/J.MTADV.2020.100120

Charitidis, C. A., Georgiou, P., Koklioti, M. A., Trompeta, A. F., and Markakis, V. (2014). Manufacturing nanomaterials: from research to industry. *Manuf. Rev.* 1, 11. doi:10.1051/MFREVIEW/2014009

Chen, C., Boota, M., Xie, X., Zhao, M., Anasori, B., Ren, C. E., et al. (2017). Charge transfer induced polymerization of EDOT confined between 2D titanium carbide layers. *J. Mater. Chem. A* 5 (11), 5260–5265. doi:10.1039/c7ta00149e

Chen, J., Chen, Ke, Tong, D., Huang, Y., Zhang, J., Xue, J., et al. (2014). CO2 and temperature dual responsive 'smart' MXene phases. *Chem. Commun.* 51 (2), 314–317. doi:10.1039/C4CC07220K

Chen, Ke, Qiu, N., Deng, Q., Kang, M.Ho, Yang, H., Baek, J.Uk, et al. (2017). Cytocompatibility of Ti3AlC2, Ti3SiC2, and Ti2AlN: *in vitro* tests and first-principles calculations. *ACS Biomaterials Sci. Eng.* 3 (10), 2293–2301. doi:10.1021/ACSBIOMATERIALS.7B00432

Chen, X., Zhao, Y., Li, L., Wang, Y., Wang, J., Xiong, J., et al. (2020). MXene/polymer nanocomposites: preparation, properties, and applications. *Polym. Rev.* 0 (0), 80–115. doi:10.1080/15583724.2020.1729179

Cui, T., Cai, W., Zheng, Y., Wang, J., Lin, B., Zhou, G., et al. (2023). Unlocking interfacial dynamics of biocompatible MXene/polyurethane-based nanocomposites for photothermal de-icing and thermal safety. *Chem. Eng. J.* 473 (October), 145357. doi:10.1016/J.CEJ.2023.145357

Dai, C., Chen, Yu, Jing, X., Xiang, L., Yang, D., Lin, H., et al. (2017). Two-dimensional tantalum carbide (MXenes) composite nanosheets for multiple imaging-guided photothermal tumor ablation. *ACS Nano* 11 (12), 12696–12712. doi:10.1021/acsnano.7b07241

Dai, C., Lin, H., Xu, G., Liu, Z., Wu, R., and Chen, Yu (2017). Biocompatible 2D titanium carbide (MXenes) composite nanosheets for PH-responsive MRI-guided tumor hyperthermia. *Chem. Mater.* 29 (20), 8637–8652. doi:10.1021/acs.chemmater.7b02441

Dai, Yu, Chen, X., and Zhang, X. (2018). Recent advances in stimuli-responsive polymeric micelles via click chemistry. *Polym. Chem.* 10 (1), 34–44. doi:10.1039/C8PY01174E

Darroudi, M., Elnaz Nazari, S., Karimzadeh, M., Asgharzadeh, F., Zahra Asghari, S., Khalili-Tanha, N., et al. (2023). Fabrication of magnetic nanocomposite as responsive drug delivery vehicle for cervical cancer therapy. *Appl. Organomet. Chem.* 37 (6), e7068. doi:10.1002/AOC.7068

Demazeau, G. (2008). Solvothermal reactions: an original route for the synthesis of novel materials. *J. Mater. Sci.* 43 (7), 2104–2114. doi:10.1007/s10853-007-2024-9

Directorate, E., Meeting, J., and The, O. F. (2015). *Chemicals committee, T H E working, party on, current developments, I N delegations, O N the, and safety of* 2015. 12. Oecd_–60. United States.

Feng, A., Hou, T., Jia, Z., Zhang, Yi, Zhang, F., and Wu, G. (2020). Preparation and characterization of epoxy resin filled with Ti3C2Tx MXene nanosheets with excellent electric conductivity. *Nanomaterials* 10 (1), 162. doi:10.3390/NANO10010162

Feng, H., Wang, W., Zhang, M., Zhu, S., and Wang, Q. (2020). 2D titanium carbide-based nanocomposites for photocatalytic bacteriostatic applications. in *Applied catalysis B*. Elsevier.

Feng, Y., Wang, H., Xu, J., Du, X., Cheng, Xu, Du, Z., et al. (2021). Fabrication of MXene/PEI functionalized sodium alginate aerogel and its excellent adsorption behavior for Cr(VI) and Congo red from aqueous solution. *J. Hazard. Mater.* 416 (August), 125777. doi:10.1016/J.JHAZMAT.2021.125777

Foroutan, B. (2015). Personalized medicine: a review with regard to biomarkers. *J. Bioequivalence Bioavailab.* 7 (6), 0. doi:10.4172/JBB.1000248

Forrest, S. R. (2004). *The path to ubiquitous and low-cost organic electronic appliances on plastic*.

Foulkes, R., Man, E., Thind, J., Yeung, S., Joy, A., and Hoskins, C. (2020). The regulation of nanomaterials and nanomedicines for clinical application: current and future perspectives. *Biomaterials Sci.* 8 (17), 4653–4664. doi:10.1039/D0BM00558D

Gao, L., Li, C., Huang, W., Mei, S., Lin, H., Qi, Ou, et al. (2020). MXene/polymer membranes: synthesis, properties, and emerging applications. *Chem. Mater.* 32 (5), 1703–1747. doi:10.1021/acs.chemmater.9b04408

Garg, N., and Ahmad, F. J. (2022). Biomedical applications of MXene/polymer nanocomposites. *MXene-Filled Polym. Nanocomposites*, 247–258. doi:10.1201/9781003164975-13

Geng, De C., Zhao, X.Xu, Chen, Z. X., Sun, W. W., Fu, W., Chen, J.Yi, et al. (2017). Direct synthesis of large-area 2D Mo2 C on *in situ* grown graphene. *Adv. Mater. Deerf. Beach, Fla.* 29 (35). doi:10.1002/ADMA.201700072

George, S. M., and Kandasubramanian, B. (2020). Advancements in MXene-polymer composites for various biomedical applications. *Ceram. Int.* 46, 8522–8535. doi:10.1016/j.ceramint.2019.12.257

George, S. M., Tandon, S., and Kandasubramanian, B. (2020). Advancements in hydrogel-functionalized immunosensing platforms. *ACS Omega* 5 (5), 2060–2068. doi:10.1021/acsomega.9b03816

Ghidiu, M., Lukatskaya, M. R., Zhao, M.-Q., Gogotsi, Y., and Barsoum, M. W. (2014). *Conductive two-dimensional titanium carbide 'clay' with high volumetric capacitance*. doi:10.1038/nature13970

Gogotsi, Y. (2015). Transition metal carbides go 2D. *Nat. Mater.* 14 (11), 1079–1080. doi:10.1038/nmat4386

Gomez, I. J., Arnaiz, B., Cacioppo, M., Arcudi, F., and Prato, M. (2018). Nitrogen-doped carbon nanodots for bioimaging and delivery of paclitaxel. *J. Mater. Chem. B* 6 (35), 5540–5548. doi:10.1039/c8tb01796d

Gong, K., Zhou, K., Qian, X., Shi, C., and Yu, B. (2021). MXene as emerging nanofillers for high-performance polymer composites: a review. *Compos. Part B Eng.* 217 (July), 108867. doi:10.1016/J.COMPOSITESB.2021.108867

Guo, Y., Zhong, M., Fang, Z., Wan, P., and Yu, G. (2019). A wearable transient pressure sensor made with MXene nanosheets for sensitive broad-range human-machine interfacing. *Nano Lett.* 19 (2), 1143–1150. doi:10.1021/ACS.NANOLETT.8B04514

Halim, J., Cook, K. M., Naguib, M., Gogotsi, Y., Rosén, J., Barsoum, M., et al. (2016). X-ray photoelectron spectroscopy of select multi-layered transition metal carbides (MXenes). *Appl. Surf. Sci.* 362, 406–417. doi:10.1016/j.apsusc.2015.11.089

Halim, J., Kota, S., Lukatskaya, M. R., Naguib, M., Zhao, M. Q., Ju Moon, E., et al. (2016). Synthesis and characterization of 2D molybdenum carbide (MXene). *Adv. Funct. Mater.* 26 (18), 3118–3127. doi:10.1002/adfm.201505328

Halim, J., Lukatskaya, M. R., Cook, K. M., Lu, J., Smith, C. R., Åke Näslund, L.-Å., et al. (2014). Transparent conductive two-dimensional titanium carbide epitaxial thin films. *Chem. Mater.* 7 (26), 2374–2381. doi:10.1021/cm500641a

Hamzan, N. binti, Yi Bin Ng, C., Rad, S., Lee, M. K., Chang, L. J., Tripathi, M., et al. (2021). Controlled physical properties and growth mechanism of manganese silicide nanorods. *J. Alloys Compd.* 851 (January), 156693. doi:10.1016/J.JALLCOM.2020.156693

Han, R., Ma, X., Xie, Y., Teng, Da, and Zhang, S. (2017). Preparation of a new 2D MXene/PES composite membrane with excellent hydrophilicity and high flux. *RSC Adv.* 7 (89), 56204–56210. doi:10.1039/C7RA10318B

Han, X., Huang, Ju, Lin, H., Wang, Z., Pan, Li, and Chen, Yu (2018). 2D ultrathin MXene-based drug-delivery nanoplatform for synergistic photothermal ablation and chemotherapy of cancer. *Adv. Healthc. Mat.* 7 (9), 1701394. doi:10.1002/adhm.201701394

Harper, A., and Anderson, M. R. (2010). Electrochemical glucose sensors—developments using electrostatic assembly and carbon nanotubes for biosensor construction. *Sensors* 10 (9), 8248–8274. doi:10.3390/s100908248

Harris, K. J., Bugnet, M., Naguib, M., Barsoum, M. W., and Goward, G. R. (2015). Direct measurement of surface termination groups and their connectivity in the 2D MXene V_2CT_x using NMR spectroscopy. *J. Phys. Chem. C* 119 (24), 13713–13720. doi:10.1021/acs.jpcc.5b03038

Hatakeyama, H. (2017). Recent advances in endogenous and exogenous stimuli-responsive nanocarriers for drug delivery and therapeutics. *Chem. Pharm. Bull.* 65 (7), 612–617. doi:10.1248/CPB.C17-00068

Hatter, C. B., Shah, J., Anasori, B., and Gogotsi, Y. (2020). Micromechanical response of two-dimensional transition metal carbonitride (MXene) reinforced epoxy composites. *Compos. Part B Eng.* 182 (February), 107603. doi:10.1016/J.COMPOSITESB.2019.107603

He, J., Zou, H., Zhou, J., and Deng, C. (2024). Thermoresponsive MXene-based hydrogel for controlled anticancer drug release. *J. Drug Deliv. Sci. Technol.* 91 (January), 105207. doi:10.1016/J.JDDST.2023.105207

Hohenstein, W. P., and Mark, H. (1946). Polymerization of olefins and diolefins in suspension and emulsion. Part I. *J. Polym. Sci.* 1 (2), 127–145. doi:10.1002/POL.1946.120010207

Hong, W., Wyatt, B. C., Nemani, S. K., and Anasori, B. (2020). Double transition-metal MXenes: atomistic design of two-dimensional carbides and nitrides. *MRS Bull.* 45 (10), 850–861. doi:10.1557/mrs.2020.251

Hu, D., Huang, X., Li, S., and Jiang, P. (2020). Flexible and durable cellulose/MXene nanocomposite paper for efficient electromagnetic interference shielding. *Compos. Sci. Technol.* 188 (March), 107995. doi:10.1016/J.COMPSCITECH.2020.107995

Hu, Po, Li, J., Jin, J., Lin, X., and Tan, X. (2022). Highly sensitive photopolymer for holographic data storage containing methacryl polyhedral oligomeric silsesquioxane. *ACS Appl. Mater. Interfaces* 14, 21544–21554. doi:10.1021/acsami.2c04011

Hu, T., Wang, J., Zhang, H., Li, Z., Hu, M., and Wang, X. (2015). Vibrational properties of Ti3C2 and Ti3C2T2 (T = O, F, OH) monosheets by first-principles calculations: a comparative study. *Phys. Chem. Chem. Phys.* 17 (15), 9997–10003. doi:10.1039/c4cp05666c

Huang, K., Li, Z., Lin, J., Han, G., and Huang, P. (2018). Two-dimensional transition metal carbides and nitrides (MXenes) for biomedical applications. *Chem. Soc. Rev.* 47, 5109–5124. doi:10.1039/c7cs00838d

Huang, S., and Mochalin, V. N. (2019). Hydrolysis of 2D transition-metal carbides (MXenes) in colloidal solutions. *Inorg. Chem.* 58 (3), 1958–1966. doi:10.1021/acs.inorgchem.8b02890

Huang, X., Wang, R., Jiao, T., Zou, G., Zhan, F., Yin, J., et al. (2019). Facile preparation of hierarchical AgNP-loaded MXene/Fe3O4 polymer nanocomposites by electrospinning with enhanced catalytic performance for wastewater treatment. *ACS Omega* 4 (1), 1897–1906. doi:10.1021/acsomega.8b03615

Islam, S., and Syed Shazali, S. T. (2011). Determinants of manufacturing productivity: pilot study on labor-intensive industries. *Int. J. Prod. Perform. Manag.* 60 (6), 567–582. doi:10.1108/17410401111150751

Jain, A., Ong, S. P., Hautier, G., Chen, W., Richards, W. D., Dacek, S., et al. (2013). Commentary: the materials Project: a materials genome approach to accelerating materials innovation. *Apl. Mater.* 1 (1). doi:10.1063/1.4812323

Jeon, J., Park, Y., Choi, S., Lee, J., Lim, S. S., Lee, B. H., et al. (2018). Epitaxial synthesis of molybdenum carbide and Formation of a Mo2C/MoS2 hybrid structure via chemical conversion of molybdenum disulfide. *ACS Nano* 12 (1), 338–346. doi:10.1021/acsnano.7b06417

Jiang, F., and Doudna, J. A. (2017). CRISPR-Cas9 structures and mechanisms. *Annu. Rev. Biophys.* 46, 505–529. doi:10.1146/annurev-biophys-062215-010822

Jiang, C., Wu, C., Li, X., Yao, Y., Lan, L., Zhao, F., et al. (2019). All-electrospun flexible triboelectric nanogenerator based on metallic MXene nanosheets. *Nano Energy* 59 (May), 268–276. doi:10.1016/J.NANOEN.2019.02.052

Jiang, Y., Zhang, L., Wang, S., and Chen, Y. (2021). MXene-polymer nanocomposites for ultrasensitive detection of circulating tumor DNA in blood samples. *J. Nanobiotechnology* 19 (1), 191. doi:10.1186/s12951-021-00955-2

Jiménez, M., Romero, L., Domínguez, I. A., Del Mar Espinosa, M., and Domínguez, M. (2019). Additive manufacturing technologies: an overview about 3D printing methods and future prospects. *Complexity* 2019, 1–30. doi:10.1155/2019/9656938

Jimmy, J., and Kandasubramanian, B. (2020). Mxene functionalized polymer composites: synthesis and applications. *Eur. Polym. J.* 122 (January), 109367. doi:10.1016/j.eurpolymj.2019.109367

Jin, Y., Fan, Y., Meng, X., Li, J., Li, C., Sunarso, J., et al. (2021). Modeling of hydrated cations transport through 2D MXene (Ti3C2Tx) membranes for water purification. *J. Membr. Sci.* 631 (August), 119346. doi:10.1016/J.MEMSCI.2021.119346

Jolly, S., Paranthaman, M. P., and Naguib, M. (2021). Synthesis of Ti3C2Tz MXene from low-cost and environmentally friendly precursors. *Mater. Today Adv.* 10, 100139. doi:10.1016/j.mtadv.2021.100139

Journal, O., and Ondokuzmay, M. E. (2020). *Regulatory policies for safety of nanomaterials nanomalzemelerin guvenligi ile*, 1–16.

Karimi, M., Zangabad, P. S., Ghasemi, A., Amiri, M., Bahrami, M., Malekzad, H., et al. (2016). Temperature-responsive smart nanocarriers for delivery of therapeutic agents: applications and recent advances. *ACS Appl. Mater. Interfaces* 8 (33), 21107–21133. doi:10.1021/acsami.6b00371

Kedambaimoole, V., Kumar, N., Shirhatti, V., Nuthalapati, S., Sen, P., Nayak, M. M., et al. (2020). Laser-induced direct patterning of free-standing Ti3C2-MXene films for

skin conformal tattoo sensors. *ACS Sensors* 5 (7), 2086–2095. doi:10.1021/acssensors.0c00647

Keirouz, A., Radacsi, N., Ren, Q., Dommann, A., Beldi, G., Maniura-Weber, K., et al. (2020). Nylon-6/Chitosan core/shell antimicrobial nanofibers for the prevention of mesh-associated surgical site infection. *J. Nanobiotechnology* 18 (1), 51–17. doi:10.1186/s12951-020-00602-9

Khatri, M., Bello, D., Pal, A. K., Cohen, J. M., Woskie, S., Gassert, T., et al. (2013). Evaluation of cytotoxic, genotoxic and inflammatory responses of nanoparticles from photocopiers in three human cell lines. *Part. Fibre Toxicol.* 10 (1), 42–22. doi:10.1186/1743-8977-10-42

Khazaei, M., Arai, M., Sasaki, T., Chung, C. Y., Venkataramanan, N. S., Estili, M., et al. (2013). Novel electronic and magnetic properties of two-dimensional transition metal carbides and nitrides. *Adv. Funct. Mater.* 23 (17), 2185–2192. doi:10.1002/adfm.201202502

Khazaei, M., Mishra, A., Venkataramanan, N. S., Singh, A. K., and Yunoki, S. (2019). Recent advances in MXenes: from fundamentals to applications. *Curr. Opin. Solid State Mater. Sci.* 23 (3), 164–178. doi:10.1016/J.COSSMS.2019.01.002

Koc, R., and Kodambaka, S. K. (2000). Tungsten carbide (WC) synthesis from novel precursors. *J. Eur. Ceram. Soc.* 20 (11), 1859–1869. doi:10.1016/S0955-2219(00)00038-8

Kong, C., and Chen, X. (2022). Combined photodynamic and photothermal therapy and immunotherapy for cancer treatment: a review. *Int. J. Nanomedicine* 17, 6427–6446. doi:10.2147/IJN.S388996

Koo, J. H. (2019). *Polymer nanocomposites: processing, characterization, and applications*. Second Edi. Access Engineering - York University. United States: McGraw Hill.

Kumar, R., Barman, P. B., and Singh, R. R. (2021). An innovative direct non-aqueous method for the development of Co doped Ni-Zn ferrite nanoparticles. *Mater. Today Commun.* 27 (June), 102238. doi:10.1016/J.MTCOMM.2021.102238

Kumari, R., Suman, K., Karmakar, S., Mishra, V., Lakra, S. G., Saurav, G. K., et al. (2023). Regulation and safety measures for nanotechnology-based agri-products. *Front. Genome Ed.* 5 (June), 1–12. doi:10.3389/fgeed.2023.1200987

Kurra, N., Hota, M. K., and Alshareef, H. N. (2015). Conducting polymer micro-supercapacitors for flexible energy storage and Ac line-filtering. *Nano Energy* 13 (April), 500–508. doi:10.1016/j.nanoen.2015.03.018

Kurra, N., Jiang, Q., and Alshareef, H. N. (2015). A general strategy for the fabrication of high performance microsupercapacitors. *Nano Energy* 16 (September), 1–9. doi:10.1016/j.nanoen.2015.05.031

Lele, V. P. (2023). Influence of supply chain factors on material science and its developments. *Int. J. Industrial Eng.* 10 (2), 1–7. doi:10.14445/23499362/IJIE-V10I2P101

Li, D., and Xia, Y. (2004). Electrospinning of nanofibers: reinventing the wheel? *Adv. Mater.* 16 (14), 1151–1170. doi:10.1002/ADMA.200400719

Li, H., Li, T., Wu, Q., Wang, R., Hong, R., and Li, Y. (2021). Super stable water-based magnetic fluid as a dual-mode contrast agent. *Nanotechnol. Rev.* 10 (1), 1031–1045. doi:10.1515/ntrev-2021-0068

Li, J., Levitt, A., Kurra, N., Juan, K., Noriega, N., Xiao, Xu, et al. (2019). MXene-conducting polymer electrochromic microsupercapacitors. *Energy Storage Mater.* 20 (July), 455–461. doi:10.1016/J.ENSM.2019.04.028

Li, X., Wang, Y., Zhang, L., and Chen, Z. (2021). Comprehensive biocompatibility assessments of MXene-polymer nanocomposites for biomedical applications. *ACS Appl. Mater. Interfaces* 13 (17), 19607–19617. doi:10.1021/acsami.1c03192

Li, X., Zhao, Y., Wu, L., Li, G., Xu, L., and Ye, B. (2020). Highly ordered 3D electrochemical DNA biosensor based on dual orientation controlled rolling motor and graftable tetrahedron DNA. *Biosens. Bioelectron.* 147, 111759. doi:10.1016/j.bios.2019.111759

Li, X. P., Yue, Li, Li, X., Song, D., Peng, M., Hu, C., et al. (2019). Highly sensitive, reliable and flexible piezoresistive pressure sensors featuring polyurethane sponge coated with MXene sheets. *J. Colloid Interface Sci.* 542 (April), 54–62. doi:10.1016/J.JCIS.2019.01.123

Li, Z., Zhang, H., Han, J., Chen, Yu, Lin, H., and Yang, T. (2018). Surface nanopore engineering of 2D MXenes for targeted and synergistic multitherapies of hepatocellular carcinoma. *Adv. Mater.* 30 (25), 1706981. doi:10.1002/adma.201706981

Liao, H., Guo, X., Wan, P., and Yu, G. (2019). Conductive MXene nanocomposite organohydrogel for flexible, healable, low-temperature tolerant strain sensors. *Adv. Funct. Mater.* 29 (39), 1904507. doi:10.1002/ADFM.201904507

Lin, H., Chen, Yu, and Shi, J. (2018). Insights into 2D MXenes for versatile biomedical applications: current advances and challenges ahead. *Adv. Sci.* 5 (10), 1800518. doi:10.1002/advs.201800518

Lin, H., Gao, S., Chen, D., Chen, Yu, and Shi, J. (2017). A two-dimensional biodegradable niobium carbide (MXene) for photothermal tumor eradication in NIR-I and NIR-II biowindows. *J. Am. Chem. Soc.* 139 (45), 16235–16247. doi:10.1021/jacs.7b07818

Lin, H., Wang, X., Yu, L., Chen, Yu, and Shi, J. (2017). Two-dimensional ultrathin MXene ceramic nanosheets for photothermal conversion. *Nano Lett.* 17 (1), 384–391. doi:10.1021/acs.nanolett.6b04339

Lin, H., Wang, Y., Gao, S., Chen, Yu, and Shi, J. (2018). Theranostic 2D tantalum carbide (MXene). *Adv. Mater.* 30 (4), 1703284. doi:10.1002/adma.201703284

Ling, Z., Ren, C. E., Zhao, M. Q., Yang, J., Giammarco, J. M., Qiu, J., et al. (2014). Flexible and conductive MXene films and nanocomposites with high capacitance. *Proc. Natl. Acad. Sci. U. S. A.* 111 (47), 16676–16681. doi:10.1073/pnas.1414215111

Lipatov, A., Mohamed, A., Lukatskaya, M. R., Boson, A., Gogotsi, Y., and Sinitskii, A. (2016). Effect of synthesis on quality, electronic properties and environmental stability of individual monolayer Ti3C2 MXene flakes. *Adv. Electron. Mater.* 2 (12), 1600255. doi:10.1002/AELM.201600255

Liu, A., Liu, Y., Liu, G., Zhang, A., Cheng, Y., Li, Y., et al. (2022). Engineering of surface modified Ti3C2Tx MXene based dually controlled drug release system for synergistic multitherapies of cancer. *Chem. Eng. J.* 448 (November), 137691. doi:10.1016/J.CEJ.2022.137691

Liu, X., Feng, Y., Xu, J., Shi, Y., Yang, J., Zhang, R., et al. (2021). Combination of MAPK inhibition with photothermal therapy synergistically augments the anti-tumor efficacy of immune checkpoint blockade. *J. Control. Release* 332 (April), 194–209. doi:10.1016/J.JCONREL.2021.02.020

Liu, Z., Lin, H., Zhao, M., Chen, D., Zhang, S., Peng, W., et al. (2018). 2D superparamagnetic tantalum carbide composite MXenes for efficient breast-cancer theranostics. *Theranostics* 8 (6), 1648–1664. doi:10.7150/thno.23369

Lopes, J. R., Santos, G., Barata, P., Oliveira, R., and Lopes, C. M. (2013). Physical and chemical stimuli-responsive drug delivery systems: targeted delivery and main routes of administration. *Curr. Pharm. Des.* 19 (14): 7169–7184. doi:10.2174/13816128113199990698

Lukatskaya, M. R., Mashtalir, O., Ren, C. E., Dall'Agnese, Y., Rozier, P., Louis Taberna, P., et al. (2013). Cation intercalation and high volumetric capacitance of two-dimensional titanium carbide. *Science* 341 (6153), 1502–1505. doi:10.1126/science.1241488

Ma, L., Zhu, C., Chen, C., Meng, X., Chen, L., and Wang, H. (2021). MXene-polymer hydrogels as injectable scaffolds for cartilage repair. *Biomaterials Sci.* 9 (14): 4948–4958. doi:10.1039/D1BM00349G

Maleski, K., Mochalin, V. N., and Gogotsi, Y. (2017). Dispersions of two-dimensional titanium carbide MXene in organic solvents. *Chem. Mater.* 29 (4), 1632–1640. doi:10.1021/acs.chemmater.6b04830

Maleski, K., Ren, C. E., Zhao, M. Q., Anasori, B., and Gogotsi, Y. (2018). Size-dependent physical and electrochemical properties of two-dimensional MXene flakes. *ACS Appl. Mater. Interfaces* 10 (29), 24491–24498. doi:10.1021/acsami.8b04662

Manawi, Y., Ihsanullah, A. S., Al-Ansari, T., Atieh, M., and Atieh, M. (2018). A review of carbon nanomaterials' synthesis via the chemical vapor deposition (CVD) method. *Materials* 11 (5), 822. doi:10.3390/ma11050822

Manjushree, S. G., Prashanth, S., Adarakatti, P. S., Almalki, A. S. A., and Alhadhrami, A. (2022). "MXenes-based polymer composites for bioelectronics," in *Bioelectronics*, 237–250. doi:10.1201/9781003263265-15

Mashtalir, O., Naguib, M., Mochalin, V. N., Dall'Agnese, Y., Heon, M., Barsoum, M. W., et al. (2013). Intercalation and delamination of layered carbides and carbonitrides. *Nat. Commun.* 4, 1716–1717. doi:10.1038/ncomms2664

McCrum, N. G., Buckley, C. P., and Bucknall, C. B. (1997). The elastic properties of rubber. *Princ. Polym. Eng.*, 84–116.

McKeen, L. W. (2017). "High-temperature/high-performance polymers," in *Film properties of plastics and elastomers* (Elsevier), 389–417. doi:10.1016/b978-0-12-813292-0.00012-5

Meng, C., Maeng, J., John, S. W. M., and Irazoqui, P. P. (2014). Ultrasmall integrated 3D micro-supercapacitors solve energy storage for miniature devices. *Adv. Energy Mater.* 4 (7), 1301269. doi:10.1002/aenm.201301269

Merritt, S. R., Exner, A. A., Lee, Z., and Von Recum, H. A. (2012). Electrospinning and imaging. *Adv. Eng. Mater.* 14 (5), B266–B278. doi:10.1002/ADEM.201180010

Mirkhani, S. A., Zeraati, A. S., Aliabadian, E., Naguib, M., and Sundararaj, U. (2019). High dielectric constant and low dielectric loss via poly(vinyl alcohol)/$Ti_3C_2T_x$ MXene nanocomposites. *ACS Appl. Mater. Interfaces* 11 (20), 18599–18608. doi:10.1021/acsami.9b00393

Mohajer, F., Mohammadi Ziarani, G., Badiei, A., Iravani, S., and Varma, R. S. (2022). Advanced MXene-based micro- and nanosystems for targeted drug delivery in cancer therapy. *Micromachines* 13 (10), 1773. doi:10.3390/MI13101773

Naguib, M., Kurtoglu, M., Presser, V., Lu, J., Niu, J., Heon, M., et al. (2011). Two-dimensional nanocrystals produced by exfoliation of Ti 3AlC 2. *Adv. Mater.* 23 (37), 4248–4253. doi:10.1002/adma.201102306

Naguib, M., Mashtalir, O., Carle, J., Presser, V., Lu, J., Hultman, L., et al. (2012). Two-dimensional transition metal carbides. *ACS Nano* 6 (2), 1322–1331. doi:10.1021/nn204153h

Naguib, M., Mochalin, V. N., Barsoum, M. W., and Gogotsi, Y. (2014). 25th anniversary article: MXenes: a new family of two-dimensional materials. *Adv. Mater.* 26 (7), 992–1005. doi:10.1002/adma.201304138

Naguib, M., Saito, T., Lai, S., Rager, M. S., Aytug, T., Parans Paranthaman, M., et al. (2016). Ti3C2Tx (MXene)–Polyacrylamide nanocomposite films. *RSC Adv.* 6 (76), 72069–72073. doi:10.1039/C6RA10384G

Nikazar, S., Mofidi, Z., and Mortazavi, M. (2023). Cancer theranostic applications of MXenes. *ACS Symp. Ser.* 1443 (September), 19–46. doi:10.1021/BK-2023-1443.CH002

Ohno, K., Esfarjani, K., and Kawazoe, Y. (2018). Computational materials science. *Comput. Mater. Sci.* doi:10.1007/978-3-662-56542-1

Oyedotun, K. O., Madito, M. J., Momodu, D. Y., Mirghni, A. A., Masikhwa, T. M., and Manyala, N. (2009). Synthesis of ternary NiCo-MnO2 nanocomposite and its application as a novel high energy supercapattery device. *Chem. Eng. J.* 335 (March), 416–433. doi:10.1016/J.CEJ.2017.10.169

Painter, P. C., and Coleman, M. M. (2019). Fundamentals of polymer science: an introductory text. *Fundam. Polym. Sci.* doi:10.1201/9780203755211

Parajuli, D., Devendra, K. C., Reda, T. G., Sravani, G. M., Murali, N., and Samatha, K. (2021). RHEED analysis of the oxidized M′2M″xXyene sheets by ablated plasma thrust method in pulsed laser deposition chamber. *AIP Adv.* 11 (11), 115019. doi:10.1063/5.0068659

Parajuli, D., Kaphle, G. C., and Samatha, K. (2019). First-principles study of electronic and magnetic properties of anatase and its role in anatase-mxene nanocomposite. *J. Nepal Phys. Soc.* 5 (1), 42–53. doi:10.3126/JNPHYSSOC.V5I1.26940

Parajuli, D., Murali, N., Devendra, K. C., Karki, B., Samatha, K., Kim, A. A., et al. (2022). Advancements in MXene-polymer nanocomposites in energy storage and biomedical applications. *Polymers* 14 (16), 3433. doi:10.3390/POLYM14163433

Parajuli, D., Murali, N., Raghavendra, V., Suryanarayana, B., Batoo, K. M., and Samatha, K. (2023). Investigation of structural, morphological and magnetic study of Ni–Cu-substituted Li0.5Fe2.5O4 Ferrites. *Appl. Phys. A* 129 (7), 502–512. doi:10.1007/S00339-023-06772-1

Parajuli, D., Murali, N., Samatha, K., Shah, N. L., and Sharma, B. R. (2023). Structural, morphological, and textural properties of coprecipitated CaTiO3 for anion exchange in the electrolyzer. *J. Nepal Phys. Soc.* 9 (1), 137–142. doi:10.3126/JNPHYSSOC.V9I1.57751

Parajuli, D., Murali, N., Samatha, K., and Veeraiah, V. (2022). Thermal, structural, morphological, functional group and first cycle charge/discharge study of Co substituted LiNi1−x-0.02Mg0.02CoxO2 (x = 0.00, 0.02, 0.04, 0.06, and 0.08) cathode material for LIBs. *AIP Adv.* 12 (8), 085010. doi:10.1063/5.0096297

Parajuli, D., Murali, N., Venkateswara Rao, A., Ramakrishna, A., Yonatan, M. S., and Samatha, K. (2022). Structural, dc electrical resistivity and magnetic investigation of Mg, Ni, and Zn substituted Co-Cu nano spinel Ferrites. *South Afr. J. Chem. Eng.* 42 (October), 106–114. doi:10.1016/J.SAJCE.2022.07.009

Parajuli, D., Raghavendra, V., Suryanarayana, B., Rao, P. A., Murali, N., Phanidhar Varma, P. V. S. K., et al. (2021). Corrigendum to 'cadmium substitution effect on structural, electrical and magnetic properties of Ni-Zn nano Ferrites. *Phys* 19 (2020), 2211–2379. doi:10.1016/J.RINP.2021.103947

Parajuli, D., and Samatha, K. (2019). MXene as topological insulator. *JETIR* 6 (4), 689–706. doi:10.1729/Journal.23872

Parajuli, D., and Samatha, K. (2022). "Topological properties of MXenes," in *MXenes and their composites* (Elsevier). doi:10.1016/B978-0-12-823361-0.00015-0

Parajuli, D., Taddesse, P., Murali, N., and Samatha, K. (2022). Correlation between the structural, magnetic, and dc resistivity properties of Co0.5m0.5-XCuxFe2O4 (M = Mg, and Zn) nano Ferrites. *Appl. Phys. A Mater. Sci. Process.* 128 (1), 58–59. doi:10.1007/s00339-021-05211-3

Parajuli, D., Taddesse, P., Murali, N., Veeraiah, V., and Samatha, K. (2022). Effect of Zn2+ doping on thermal, structural, morphological, functional group, and electrochemical properties of layered LiNi0.8Co0.1Mn0.1O2 cathode material. *AIP Adv.* 12 (12), 125012. doi:10.1063/5.0122976

Parajuli, D., Uppugalla, S., Murali, N., Ramakrishna, A., Suryanarayana, B., and Samatha, K. (2023). Synthesis and characterization MXene-ferrite nanocomposites and its application for dying and shielding. *Inorg. Chem. Commun.* 148 (February), 110319. doi:10.1016/J.INOCHE.2022.110319

Payumo, J., He, G., Chintamani Manjunatha, A., Higgins, D., and Calvert, S. (2020). Mapping collaborations and partnerships in SDG research. *Front. Res. Metrics Anal.* 5 (February), 612442. doi:10.3389/frma.2020.612442

Perera, A. A. P. R., Madhushani, K. A. U., Punchihewa, B. T., Kumar, A., and Gupta, R. K. (2023). MXene-based nanomaterials for multifunctional applications. *Materials* 16 (3), 1138. *Page 1138* 16. doi:10.3390/MA16031138

Pinto, G. M., Cremonezzi, J. M. O., Ribeiro, H., Andrade, R. J. E., Demarquette, N. R., and Fechine, G. J. M. (2023). From two-dimensional materials to polymer nanocomposites with emerging multifunctional applications: a critical review. *Polym. Compos.* 44 (3), 1438–1470. doi:10.1002/PC.27213

Prajapati, D. G., and Balasubramanian, K. (2019). Progress in the development of intrinsically conducting polymer composites as biosensors. *Macromol. Chem. Phys.* 220 (10), 1800561. doi:10.1002/macp.201800561

Qin, L., Tao, Q., Liu, X., Fahlman, M., Halim, J., Persson, P. O. Å., et al. (2019). Polymer-MXene composite films formed by MXene-facilitated electrochemical polymerization for flexible solid-state microsupercapacitors. *Nano Energy* 60 (April), 734–742. doi:10.1016/j.nanoen.2019.04.002

Qiu, Zi M., Yang, B., Gao, Yi D., Liu, C.Li, Yue, Ru, Pi, Ye C., et al. (2021). MXenes nanocomposites for energy storage and conversion. *Rare Met.* 41 (4), 1101–1128. doi:10.1007/S12598-021-01876-0

Rabenau, A. (1985). The role of hydrothermal synthesis in preparative chemistry. *Angewandte Chemie Int. Ed. Engl.* 24 (12), 1026–1040. doi:10.1002/ANIE.198510261

Rakhi, R. B., Nayuk, P., Xia, C., and Alshareef, H. N. (2016). Novel amperometric glucose biosensor based on MXene nanocomposite. *Sci. Rep.* 6 (1), 1–10. doi:10.1038/srep36422

Rasid, Z. A. M., Omar, M. F., Nazeri, M. F. M., A'Ziz, M. A. A., and Szota, M. (2017). Low cost synthesis method of two-dimensional titanium carbide MXene. *IOP Conf. Ser. Mater. Sci. Eng.* 209 (1), 012001. doi:10.1088/1757-899X/209/1/012001

Rasool, K., Mahmoud, K. A., Johnson, D. J., Helal, M., Berdiyorov, G. R., and Gogotsi, Y. (2017). Efficient antibacterial membrane based on two-dimensional Ti3C2Tx (MXene) nanosheets. *Sci. Rep. 2017* 7 (1), 1–11. doi:10.1038/s41598-017-01714-3

Reese, C., Roberts, M., Ling, M. M., and Bao, Z. (2004). Organic thin film transistors. *Mater. Today* 7 (9), 20–27. doi:10.1016/S1369-7021(04)00398-0

Ren, X., Huo, M., Wang, M., Lin, H., Zhang, X., Yin, J., et al. (2019). Highly catalytic niobium carbide (MXene) promotes hematopoietic recovery after radiation by free radical scavenging. *ACS Nano* 13, 6438–6454. doi:10.1021/acsnano.8b09327

Ren, Y., Zhu, J., Wang, L., Liu, H., Liu, Yi, Wu, W., et al. (2018). Synthesis of polyaniline nanoparticles deposited on two-dimensional titanium carbide for high-performance supercapacitors. *Mater. Lett.* 214 (March), 84–87. doi:10.1016/J.MATLET.2017.11.060

Riazi, H., Nemani, S. K., Grady, M. C., Anasori, B., and Soroush, M. (2021). Ti3C2 MXene–polymer nanocomposites and their applications. *J. Mater. Chem. A* 9 (13), 8051–8098. doi:10.1039/D0TA08023C

Sang, X., Xie, Yu, Yilmaz, D. E., Lotfi, R., Mohamed, A., Ostadhossein, A., et al. (2018). *In situ* atomistic insight into the growth mechanisms of single layer 2D transition metal carbides. *Nat. Commun.* 9 (1), 2266–2269. doi:10.1038/s41467-018-04610-0

Schropp, R. E. I., Stannowski, B., Brockhoff, A. M., van Veenendaal, P. A. T. T., and Rath, J. K. (2000). Hot wire CVD of heterogeneous and polycrystalline silicon semiconducting thin films for applications in thin film transistors and solar cells. *Mater. Phys. Mech.* 2 (2), 73–82.

Shah, M., Rodriguez-Couto, S., and Sevinc Sengor, S. (2020). Emerging technologies in environmental bioremediation. in *Emerging technologies in environmental bioremediation*. Elsevier. doi:10.1016/B978-0-12-819860-5.00021-3

Shahzad, F., Mohamed, A., Hatter, C. B., Anasori, B., Hong, S. M., Koo, C. M., et al. (2016). Electromagnetic interference shielding with 2D transition metal carbides (MXenes). *Science* 353 (6304), 1137–1140. doi:10.1126/science.aag2421

Shareef, I. A., Rubloff, G. W., Anderle, M., Gill, W. N., Cotte, J., and Kim, D. H. (1995). Subatmospheric chemical vapor deposition ozone/TEOS process for SiO2 trench filling. *J. Vac. Sci. Technol. B Microelectron. Nanom. Struct. Process. Meas. Phenom.* 13 (4), 1888–1892. doi:10.1116/1.587830

Sheng, X., Zhao, Y., Zhang, Li, and Xiang, Lu (2019). Properties of two-dimensional Ti3C2 MXene/thermoplastic polyurethane nanocomposites with effective reinforcement via melt blending. *Compos. Sci. Technol.* 181 (September), 107710. doi:10.1016/J.COMPSCITECH.2019.107710

Shi, X. ying, Gao, M. hang, Wen, wen Hu, Luo, D., Shao, zhong Hu, Huang, T., et al. (2022). Largely enhanced adsorption performance and stability of MXene through *in-situ* depositing polypyrrole nanoparticles. *Sep. Purif. Technol.* 287 (April), 120596. doi:10.1016/J.SEPPUR.2022.120596

Shi, Ye, Peng, L., Ding, Yu, Zhao, Yu, and Yu, G. (2015). Nanostructured conductive polymers for advanced energy storage. *Chem. Soc. Rev.* 44 (19), 6684–6696. doi:10.1039/c5cs00362h

Shuck, C. E., Sarycheva, A., Anayee, M., Levitt, A., Zhu, Y., Uzun, S., et al. (2020a). Scalable synthesis of $Ti_3C_2T_x$ MXene. *Adv. Eng. Mater.* 22 (3), 1901241. doi:10.1002/ADEM.201901241

Shuck, C. E., Ventura-Martinez, K., Goad, A., Uzun, S., Shekhirev, M., and Gogotsi, Y. (2021). Safe synthesis of MAX and MXene: guidelines to reduce risk during synthesis. *ACS Chem. Health Saf.* 28 (5), 326–338. doi:10.1021/acs.chas.1c00051

Simon, P., and Gogotsi, Y. (2008). "Materials for electrochemical capacitors," in *Nature materials* (United States, Germany, UK; Nature Publishing Group). doi:10.1038/nmat2297

Sivasankarapillai, V. S., Kumar Somakumar, A., Joseph, J., Nikazar, S., Rahdar, A., and Kyzas, G. Z. (2020). Cancer theranostic applications of MXene nanomaterials: recent updates. *Nano-Structures Nano-Objects* 22 (April), 100457. doi:10.1016/J.NANOSO.2020.100457

Sliozberg, Y., Jan, A., Hatter, C. B., Anasori, B., Gogotsi, Y., and Hall, A. (2020). Interface binding and mechanical properties of MXene-epoxy nanocomposites. *Compos. Sci. Technol.* 192 (May), 108124. doi:10.1016/J.COMPSCITECH.2020.108124

Sur, S., Rathore, A., Dave, V., Reddy, K. R., Singh Chouhan, R., and Sadhu, V. (2019). "Recent developments in functionalized polymer nanoparticles for efficient drug delivery system," in *Nano-structures and nano-objects* (Elsevier B.V). doi:10.1016/j.nanoso.2019.100397

Tan, K. H., Abu Zaed, Md, Saidur, R., Abdullah, N., Ishak, N. A. I.Md, and Cherusseri, J. (2024). Strategic insights for bulk production of MXene: a review. *E3S Web Conf.* 488 (February), 01003. doi:10.1051/E3SCONF/202448801003

Tang, H., Wang, R., Shi, L., Sheremet, E., Rodriguez, R. D., and Sun, J. (2021). Post-processing strategies for improving the electrical and mechanical properties of MXenes. *Chem. Eng. J.* 425 (December), 131472. doi:10.1016/J.CEJ.2021.131472

Tang, W., Dong, Z., Zhang, R., Yi, X., Yang, K., Jin, M., et al. (2019). Multifunctional two-dimensional core-shell MXene@Gold nanocomposites for enhanced photo-radio combined therapy in the second biological window. *ACS Nano* 13 (1), 284–294. doi:10.1021/acsnano.8b05982

Vahidmohammadi, A., Moncada, J., Chen, H., Kayali, E., Orangi, J., Carrero, C. A., et al. (2018). Thick and freestanding MXene/PANI pseudocapacitive electrodes with ultrahigh specific capacitance. *J. Mater. Chem. A* 6 (44), 22123–22133. doi:10.1039/C8TA05807E

Vasyukova, I. A., Zakharova, O. V., Kuznetsov, D. V., and Gusev, A. A. (2022). Synthesis, toxicity assessment, environmental and biomedical applications of MXenes: a review. *Nanomaterials* 12 (11), 1797. doi:10.3390/NANO12111797

Wang, D., Lin, Y., Hu, D., Jiang, P., and Huang, X. (2020). Multifunctional 3D-MXene/PDMS nanocomposites for electrical, thermal and triboelectric applications. *Compos. Part A Appl. Sci. Manuf.* 130 (March), 105754. doi:10.1016/J.COMPOSITESA.2019.105754

Wang, H., Russa, M.La, and Qi, L. S. (2016). CRISPR/Cas9 in genome editing and beyond. *Annu. Rev. Biochem.* 85 (June), 227–264. doi:10.1146/ANNUREV-BIOCHEM-060815-014607

Wang, J., Liu, Y., Zhang, H., and Chen, W. (2020). Effect of MXene-polymer nanocomposites on cell viability and proliferation for tissue engineering applications. *Biomaterials Sci.* 8 (15), 4170–4181. doi:10.1039/D0BM00682H

Wang, L., Xu, C., Liu, Z., Chen, L., Ma, X., Cheng, H. M., et al. (2016). Magnetotransport properties in high-quality ultrathin two-dimensional superconducting Mo2C crystals. *ACS Nano* 10 (4), 4504–4510. doi:10.1021/acsnano.6b00270

Wang, Qi W., Zhang, H. B., Liu, Ji, Zhao, S., Xie, Xi, Liu, L., et al. (2019). Multifunctional and water-resistant MXene-decorated polyester textiles with outstanding electromagnetic interference shielding and joule heating performances. *Adv. Funct. Mater.* 29 (7), 1806819. doi:10.1002/ADFM.201806819

Wang, X., Li, Q., Zhang, J., Huang, H., Wu, S., and Yang, Y. (2020). Novel thin-film reverse osmosis membrane with MXene Ti3C2T embedded in polyamide to enhance the water flux, anti-fouling and chlorine resistance for water desalination. *J. Membr. Sci.* 603 (May), 118036. doi:10.1016/J.MEMSCI.2020.118036

Wang, Y., Bai, F., Luo, Q., Wu, M., Song, G., Zhang, H., et al. (2019). Lycium barbarum polysaccharides grafted with doxorubicin: an efficient PH-responsive anticancer drug delivery system. *Int. J. Biol. Macromol.* 121 (January), 964–970. doi:10.1016/J.IJBIOMAC.2018.10.103

Wei, H., Dong, J., Fang, X., Zheng, W., Sun, Y., Qian, Y., et al. (2019). Ti3C2Tx MXene/polyaniline (PANI) sandwich intercalation structure composites constructed for microwave absorption. *Compos. Sci. Technol.* 169 (January), 52–59. doi:10.1016/J.COMPSCITECH.2018.10.016

Whitby, G. S., and Katz, M. (1933). Synthetic rubber. *Industrial Eng. Chem.* 25 (12), 1338–1348. doi:10.1021/ie50288a012

Wodlinger, B., Dweiri, Y., and Durand, D. M. (2015). *Chapter 9 - biochips*. Implantable Biomedical Microsystems. Oxford: William Andrew Publishing, 203–214. doi:10.1016/B978-0-323-26208-8.00009-1

Wu, W., Wei, D., Zhu, J., Niu, D., Wang, F., Wang, L., et al. (2019a). Enhanced electrochemical performances of organ-like Ti 3 C 2 MXenes/polypyrrole composites as supercapacitors electrode materials. *Ceram. Int.* 45 (6), 7328–7337. doi:10.1016/J.CERAMINT.2019.01.016

Wu, X., Han, B., Zhang, H. B., Xie, Xi, Tu, T., Zhang, Yu, et al. (2020). Compressible, durable and conductive polydimethylsiloxane-coated MXene foams for high-performance electromagnetic interference shielding. *Chem. Eng. J.* 381 (February), 122622. doi:10.1016/J.CEJ.2019.122622

Xiang, H., Lin, H., Yu, L., and Chen, Yu (2019). Hypoxia-irrelevant photonic thermodynamic cancer nanomedicine. *ACS Nano* 13 (2), 2223–2235. doi:10.1021/ACSNANO.8B08910

Xu, C., Wang, L., Liu, Z., Chen, L., Guo, J., Kang, N., et al. (2015). Large-area high-quality 2D ultrathin Mo2C superconducting crystals. *Nat. Mater.* 14 (11), 1135–1141. doi:10.1038/nmat4374

Xu, H., Zheng, D., Liu, F., Li, W., and Lin, J. (2020). Synthesis of an MXene/polyaniline composite with excellent electrochemical properties. *J. Mater. Chem. A* 8 (12), 5853–5858. doi:10.1039/D0TA00572J

Xu, Yu, Sun, G., Middha, E., Liu, Yu H., Chan, K. C., Liu, B., et al. (2020). Organic nanoparticle-doped microdroplets as dual-modality contrast agents for ultrasound microvascular flow and photoacoustic imaging. *Sci. Rep.* 10 (1), 17009–17012. doi:10.1038/s41598-020-72795-w

Xu, Y., Zhang, H., Li, Y., and Wang, L. (2019). Tissue compatibility of MXene-polymer nanocomposites for implantable medical devices. *Acta Biomater.* 97, 602–612. doi:10.1016/j.actbio.2019.08.028

Xue, Y., Feng, J., Huo, S., Song, P., Yu, B., Liu, L., et al. (2020). Polyphosphoramide-intercalated MXene for simultaneously enhancing thermal stability, flame retardancy and mechanical properties of polylactide. *Chem. Eng. J.* 397 (October), 125336. doi:10.1016/J.CEJ.2020.125336

Yadav, R. S. (2023). Multifunctional nanomaterials: synthesis, properties, and applications 2.0. *Int. J. Mol. Sci.* 24 (8), 7619. doi:10.3390/IJMS24087619

Yang, L., Chen, S., Wei, H., Luo, Y., Cong, F., Li, W., et al. (2022). Low-temperature photothermal therapy based on borneol-containing polymer-modified MXene nanosheets. *ACS Appl. Mater. Interfaces* 14 (40), 45178–45188. doi:10.1021/acsami.2c12839

Young, R. J., and Lovell, P. A. (2008). "Introduction to polymers," in *Food materials science: principles and practice*. 3rd Editio (United States: CRC Press, Taylor and Francis Group). doi:10.1007/978-0-387-71947-4_4

Zada, S., Dai, W., Kai, Z., Lu, H., Zhang, Y., Meng, X., et al. (2020). Algae extraction controllable delamination of vanadium carbide nanosheets with enhanced near-infrared photothermal performance. *Angew. Chem. Wiley Online Libr.* 59 (16), 6601–6606. doi:10.1002/anie.201916748

Zaed, Md A., Tan, K. H., Norulsamani, A., Saidur, R., Pandey, A. K., and Ahmed, M. S. (2024). Cost analysis of MXene for low-cost production, and pinpointing of its economic footprint. *Open Ceram.* 17 (March), 100526. doi:10.1016/J.OCERAM.2023.100526

Zavahir, S., Sobolčiak, P., Krupa, I., Han, D. S., Tkac, J., and Kasak, P. (2020). Ti3C2Tx MXene-based light-responsive hydrogel composite for bendable bilayer photoactuator. *Nanomaterials* 10 (7), 1419. doi:10.3390/NANO10071419

Zhang, C., Xu, S., Cai, D., Cao, J., Wang, L., and Han, W. (2020). Planar supercapacitor with high areal capacitance based on Ti3C2/polypyrrole composite film. *Electrochimica Acta* 330 (January), 135277. doi:10.1016/J.ELECTACTA.2019.135277

Zhang, F., Wang, F., Wei, X., Yang, Y., Xu, S., Deng, D., et al. (2022). From trash to treasure: chemical recycling and upcycling of commodity plastic waste to fuels, high-valued chemicals and advanced materials. *J. Energy Chem.* 69 (June), 369–388. doi:10.1016/J.JECHEM.2021.12.052

Zhang, H., Wang, L., Zhou, A., Shen, C., Dai, Y., Liu, F., et al. (2016). Effects of 2-D transition metal carbide Ti 2 CT x on properties of epoxy composites. *RSC Adv.* 6 (90), 87341–87352. doi:10.1039/C6RA14560D

Zhang, J., Zeng, B., Li, D., Cui, Y., Wang, J., Duan, X., et al. (2022). Boron nitride-Au (Ag) loaded eggshell membrane with enhanced photothermal property. *Colloids Surfaces A Physicochem. Eng. Aspects* 642 (June), 128726. doi:10.1016/J.COLSURFA.2022.128726

Zhang, P., Yang, X. J., Peng, Li, Zhao, Y., and Niu, Q. J. (2019). Fabrication of novel MXene (Ti 3 C 2)/Polyacrylamide nanocomposite hydrogels with enhanced mechanical and drug release properties. *Soft Matter* 16 (1), 162–169. doi:10.1039/C9SM01985E

Zhang, Y., and Gu, J. (2022). A perspective for developing polymer-based electromagnetic interference shielding composites. *Nano-Micro Lett.* 14 (1), 89–9. doi:10.1007/s40820-022-00843-3

Zhang, Y., Wang, L., Zhang, N., and Zhou, Z. (2018). Adsorptive environmental applications of MXene nanomaterials: a review. *RSC Adv.* 8 (36), 19895–19905. doi:10.1039/C8RA03077D

Zhang, Y., Wang, S., Liu, X., and Chen, Z. 2021. "Evaluation of the inflammatory response of MXene-polymer nanocomposites *in vitro* and *in vivo*." *J. Biomed. Mater. Res. Part A* 109 (9): 1875–1886. doi:10.1002/jbm.a.37199

Zhao, L., Wang, L., Zheng, Y., Zhao, S., Wei, W., Zhang, D., et al. (2021). Highly-stable polymer-crosslinked 2D MXene-based flexible biocompatible electronic skins for *in vivo* biomonitoring. *Nano Energy* 84 (June), 105921. doi:10.1016/J.NANOEN.2021.105921

Zhou, Z., Panatdasirisuk, W., Mathis, T. S., Anasori, B., Lu, C., Zhang, X., et al. (2018). Layer-by-Layer assembly of MXene and carbon nanotubes on electrospun polymer films for flexible energy storage. *Nanoscale* 10 (13), 6005–6013. doi:10.1039/C8NR00313K

Zhu, J., Tang, Y., Zhu, X., Zhang, B., Wang, Y., Xu, W., et al. (2020). MXene-polymer nanocomposite scaffolds for bone tissue engineering applications. *Tissue Eng. Part A* 26 (5–6), 292–301. doi:10.1089/ten.TEA.2019.0301

Zhu, M., Huang, Y., Deng, Q., Zhou, J., Pei, Z., Qi, X., et al. (2016a). Highly flexible, freestanding supercapacitor electrode with enhanced performance obtained by hybridizing polypyrrole chains with MXene. *Adv. Energy Mater.* 6 (21), 1600969. doi:10.1002/AENM.201600969

Zhu, M., Huang, Y., Deng, Q., Zhou, J., Pei, Z., Qi, X., et al. (2016b). Highly flexible, freestanding supercapacitor electrode with enhanced performance obtained by hybridizing polypyrrole chains with MXene. *Adv. Energy Mater.* 6 (21), 1600969. doi:10.1002/aenm.201600969

Ziabicki, A. (1976). *Fundamentals of fiber formation*. W Książce. United States: Wiley, University of Minnesota.

Zong, L., Wu, H., Lin, H., and Chen, Yu (2018). A polyoxometalate-functionalized two-dimensional titanium carbide composite MXene for effective cancer theranostics. *Cancer Theranostics* 11 (8), 4149–4168. doi:10.1007/s12274-018-2002-3

Zou, Y., Fang, L., Chen, T., Sun, M., Lu, C., and Xu, Z. (2018). Near-infrared light and solar light activated self-healing epoxy coating having enhanced properties using MXene flakes as multifunctional fillers. *Polymers* 10 (5), 474. doi:10.3390/POLYM10050474

frontiers | Frontiers in Chemistry

TYPE Original Research
PUBLISHED 19 June 2024
DOI 10.3389/fchem.2024.1353524

OPEN ACCESS

EDITED BY
Xinfeng Wei,
Stockholm University, Sweden

REVIEWED BY
Nabil Ibrahim,
National Research Centre, Egypt
Tianyi Liu,
Brewer Science, United States

*CORRESPONDENCE
Ahmed Barhoum,
ahmed.barhoum@science.helwan.edu.eg

RECEIVED 10 December 2023
ACCEPTED 23 May 2024
PUBLISHED 19 June 2024

CITATION
Hemmami H, Ben Amor I, Zeghoud S, Ben Amor A, Laouini SE, Alsalme A, Cornu D, Bechelany M and Barhoum A (2024), Chitosan extraction from *Amanita phalloides*: yield, crystallinity, degree of deacetylation, azo dye removal and antibacterial properties. *Front. Chem.* 12:1353524. doi: 10.3389/fchem.2024.1353524

Chitosan extraction from *Amanita phalloides*: yield, crystallinity, degree of deacetylation, azo dye removal and antibacterial properties

Hadia Hemmami[1,2], Ilham Ben Amor[1,2], Soumeia Zeghoud[1,2], Asma Ben Amor[1,2], Salah Eddine Laouini[1,3], Ali Alsalme[4], David Cornu[5], Mikhael Bechelany[5,6] and Ahmed Barhoum[7]*

[1]Department of Process Engineering and Petrochemical, Faculty of Technology, University of El Oued, El Oued, Algeria, [2]Renewable Energy Development Unit in Arid Zones (UDERZA), University of El Oued, El Oued, Algeria, [3]Laboratory of Biotechnology Biomaterials and Condensed Materials, Faculty of Technology, University of El Oued, El Oued, Algeria, [4]Department of Chemistry, College of Science, King Saud University, Riyadh, Saudi Arabia, [5]Institut Européen des Membranes (IEM), UMR 5635, University Montpellier, ENSCM, CNRS, Montpellier, France, [6]Gulf University for Science and Technology, GUST, Mubarak Al-Abdullah, Kuwait, [7]NanoStruc Research Group, Chemistry Department, Faculty of Science, Helwan University, Cairo, Egypt

Chitosan, a biopolymer obtained from chitin, is known for its remarkable adsorption abilities for dyes, drugs, and fats, and its diverse array of antibacterial characteristics. This study explores the extraction and characterization of chitosan from the mycelium of *Amanita phalloides*. The moisture content, ash content, water binding capacity, fat binding capacity, and degree of deacetylation of the extracted chitosan were determined. The chitosan exhibited a high yield of 70%, crystallinity of 49.07%, a degree of deacetylation of 86%, and potent antimicrobial properties against both Gram-negative and Gram-positive bacteria. The study also examined the adsorption capabilities of chitosan to remove methylene blue (MB) dye by analysing specific factors like pH, reaction time, and MB concentration using the response surface model. The highest degree of MB dye removal was 91.6% at a pH of 6, a reaction time of around 60 min and an initial dye concentration of 16 ppm. This experimental design can be applied for chitosan adsorption of other organic compounds such as dyes, proteins, drugs, and fats.

KEYWORDS

***Amanita phalloids*, chitosan extraction, degree of deacetylation, methylene blue dye removal, response surface model, adsorption optimization, antibacterial activity**

1 Introduction

Chitosan, comprised of N-acetyl-D-glucosamine and D-linked D-glucosamine units arranged in a linear polysaccharide structure, boasts several advantageous traits. These characteristics encompass its impressive adsorption properties, increased bioavailability, biodegradability, and lack of toxicity (Torres et al., 2019; Thambiliyagodage et al., 2023). As a derivative of chitin, chitosan emerges through the process of deacetylation, presenting with varying levels of deacetylation. Chitosan is derived from the deacetylation process of chitin found in a variety of organisms such as fungi, crabs, shrimp, squid pens, crawfish, and

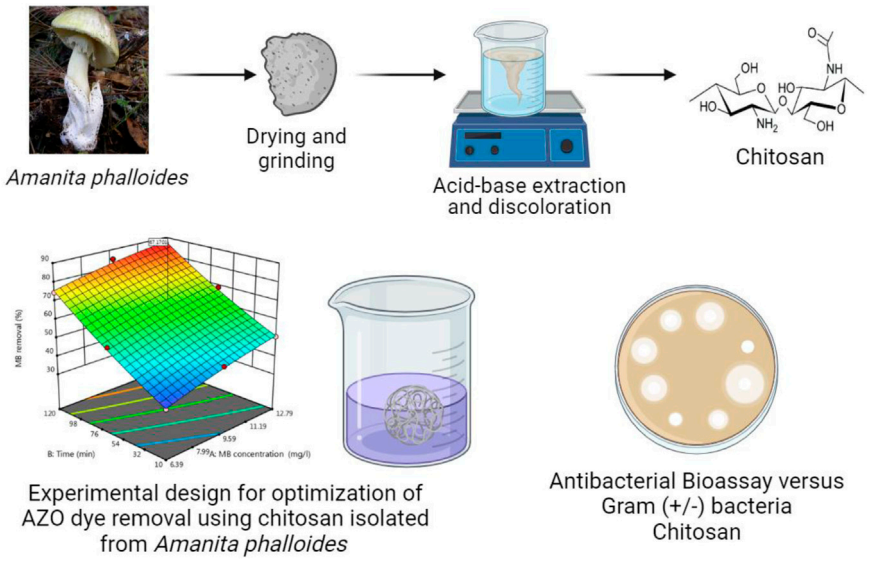

GRAPHICAL ABSTRACT

insects and it demonstrates limited solubility in acidic solutions (Ibrahim and Eid, 2017; Amor et al., 2023). The hydroxyl (-OH) groups present at the C-3 and C-6 positions of chitosan play a key role in its capability to engage with other molecules, improve its solubility in water, and facilitate chemical alterations. The crystallinity, molecular weight, and degree of deacetylation of chitosan are notably affected by the ratio of the two monomer units. This interplay significantly influences chitosan's antibacterial activity. Chitosan's versatility, marked by its attributes of biodegradability, biocompatibility, non-toxicity, and absorbency, facilitates its broad utilization across various industries. Its applications span medicine, water treatment, food packaging, wound care, drug delivery systems, textiles, agriculture, and beauty care products (Ibrahim and Eid, 2016; Reshad et al., 2021; Fatullayeva et al., 2022; Thambiliyagodage et al., 2023).

Chitosan exhibits exceptional antimicrobial effectiveness against a wide spectrum of algae, yeasts, bacteria, and fungi. This is attributed to the interaction between the positively charged amino groups of chitosan and the negatively charged molecules present on the surface of bacterial cell membranes (Yilmaz Atay, 2019; Yan et al., 2021). Subsequently, chitosan interferes with DNA replication, leading to cell demise. The chemical modifications of chitosan, such as salinization, ammonium sulfonation, carboxylation, phosphorylation, and quaternization, hold significant potential to alter its antibacterial properties (Ke et al., 2021). Moreover, chitosan's application extends to dye removal from aqueous solutions, effectively eliminating various cationic and anionic dyes (Li et al., 2021; Nayl et al., 2022). Chitosan and its derivatives boast high absorption capabilities for heavy metal ions and organic dyes, thanks to the abundant presence of -OH and -NH_2 groups within their polymeric structure. For cationic dyes, chitosan's negatively charged nature allows it to attract and bond with these dyes through electrostatic interactions. Likewise, with anionic dyes, chitosan's positive charge enables effective adsorption by attracting and binding with the negatively charged anionic dyes. This adsorption capacity is valuable in various applications such as water treatment, purification processes, and the removal of pollutants from different industrial and environmental settings (Ibrahim and Eid, 2018; Alnemari et al., 2023; Goci et al., 2023).

This study involved the extraction of chitosan from *Amanita phalloides*, followed by several physical characterization techniques to assess its properties, including the extraction yield and degree of deacetylation (DD). Various analysis methods (FTIR, UV-vis, SEM, and XRD) were employed to characterize the chitosan obtained. Various physical characterization techniques including extraction yield, deacetylation degree (DD), moisture content (MC), ash content (AC) measurement, fat binding capacity (FBC) and water binding capacity (WBC) were performed for the synthesized chitosan. The antibacterial efficacy of the chitosan was evaluated against both Gram-positive (e.g., *Staphylococcus aureus*, *Bacillus subtilis*, *Listeria innocuous*) and Gram-negative bacteria (e.g., *Salmonella Typhimurium*, *Pseudomonas aeruginosa*). Notably, the study focused on optimizing treatment conditions using Response Surface Methodology (RSM) to efficiently remove MB dye from wastewater. This optimization process involved adjusting variables like pH, MB concentration, and time to achieve the most effective MB removal. The innovative aspect of this research lies in its use of RSM, a powerful tool for systematic exploration of different parameters and their interactions, thereby enhancing the process optimization. Moreover, the utilization of chitosan derived from mushrooms as an absorbent for removing MB dye not only demonstrates an eco-friendly approach but also introduces a sustainable and renewable source of chitosan.

2 Materials and methods

2.1 Materials

Hydrochloric acid (HCl, 99%), sodium hydroxide (NaOH, 97%), hydrogen peroxide (H_2O_2, 98%), acetic acid (CH_3COOH,

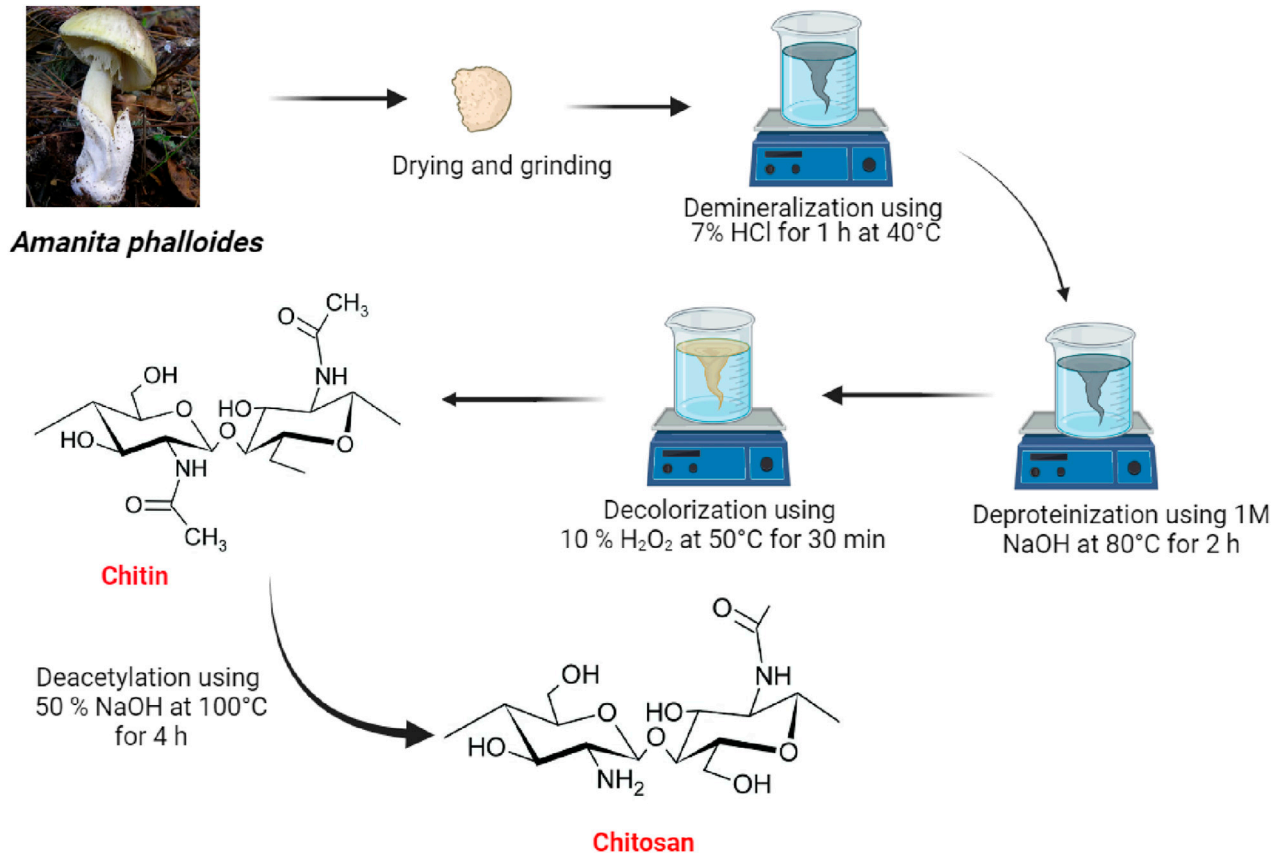

FIGURE 1
Diagram illustrating the methods involved in extracting chitin and chitosan from *Amanita phalloides*.

99.5%), and methylene blue ($C_{16}H_{18}ClN_3S$, 82%) dye was purchased from Biochem Chemophara. Bioscan Industrie Algeria gave the Mueller-Hinton agar. *Amanita phalloides* sourced from the local market of El Oued, Algeria (6°52′03″E, 33°22′06″N), was utilized for the extraction of chitin and chitosan. Bacterial samples were obtained from the Algerian Culture Center of Microorganisms.

2.2 Extraction of chitin and chitosan from *Amanita phalloides*

Chitin and subsequently chitosan were produced from 40 g of powdered *A. phalloides* through a series of treatments (see Figure 1). Initially, the sample underwent an hour-long treatment with a 7% HCl solution at 40°C to eliminate metals. Subsequently, a 1 M NaOH solution was applied at 80°C for 2 hours, using a solution ratio of 1: 10 (w/v), to remove proteins as a step in the deproteinization process. Following a decolorization process using H_2O_2 at 50°C for 30 min, the resulting precipitate led to the production of chitin. This chitin was further processed to create chitosan through a deacetylation method, exposing it to a 50% NaOH solution for 4 h at 100°C. The final chitosan was obtained by washing the precipitate repeatedly with distilled water until a neutral pH was achieved.

2.3 Physicochemical characterization

FTIR spectra were obtained using a total reflection (ATR) spectrometer (Thermo Scientific-Nicolet iS5) within the range of 400–4,000 cm^{-1}. To determine the degree of deacetylation (DD) in chitin and chitosan, FTIR spectroscopy was applied utilizing the formula Eq. 1:

$$DD(\%) = 100 - [100^{*}(A_{1655}/A_{3450})/1.33] \quad (1)$$

Where: A_{1655} and A_{3450} cm^{-1} represent the heights of absorption bands for the amide and hydroxyl groups at 1,655 and 3,450 cm^{-1}, respectively. X-ray diffraction (XRD, Rigaku Miniflex 600) was used to examine the crystalline structure of chitosan, employing CuK radiation (40 kV and 30 mA). The crystalline index (CrI) values were calculated using the equation Eq. 2 (Teli and Sheikh, 2012; Ibitoye et al., 2018; Olafadehan et al., 2021b):

$$CrI = [I_{110} - I_{am}]/I_{110} \quad (2)$$

Where: I_{110} is the intensity of the crystalline peak at around 2 θ ≅ 20° (002 reflection), and I_{am} is the intensity of amorphous diffraction at 2 θ ≅ 10°–15° (Zhu et al., 2020).

The morphology of chitosan and chitin was examined using a scanning electron microscope (FESEM, Leo Supra 55-Zeiss Inc., Germany). Ultraviolet spectroscopy (UV-2450, Shimadzu,

TABLE 1 Design matrix for various factor values and experimental responses.

Run no.	Experimental factors			Response (MB removal)	
	pH	MB conc. (ppm)	Time (min)	Actual value	Predicted value
1	10	15.99	35	57.1	56.65
2	2	12.79	60	57.38	57.77
3	6	12.79	35	87.52	85.52
4	2	12.79	10	49.34	49.25
5	6	15.99	60	91.23	91.60
6	6	12.79	35	84.52	85.52
7	2	9.59	35	45.36	45.82
8	6	9.59	60	82.65	81.80
9	6	15.99	10	89.14	89.99
10	6	9.59	10	79.92	79.55
11	6	12.79	35	84.52	85.52
12	2	15.99	35	61.28	60.52
13	10	12.79	60	51.81	51.90
14	10	12.79	10	56.95	56.56
15	10	9.59	35	50.36	51.12
Factors and levels for experimental design					
Factors	Codes	−1.0	0.0	1.0	
pH	A	2	6	10	
MB concentration (ppm)	B	9.59	12.79	15.99	
Time (min)	C	10	35	60	

TABLE 2 Characteristics of the chitosan extract.

Characteristics	Value (%)
Yield (Y)	70
Ash contents (AC)	6.7
Moisture content (MC)	13.9
Fat binding capacity (FBC)	253
Water binding capacity (WBC)	671
Crystallinity Index (CrI)	49.07

Germany) was employed to record dye absorption spectra in the water treatment experiments.

The chitosan's ash content was determined through the combustion of the sample in an air atmosphere at 550°C for 3 h. The percentage ash content in a chitosan sample was calculated using Eq. 3:

$$\text{Ash}\,\% = (W2/W1)\,x\,100 \tag{3}$$

where W1 represents the original weight of the chitosan sample, and W2 represents the weight of the residue in grams. The moisture content of the chitosan sample was assessed by vacuum drying it at 110°C for 24 h. The Eq. 4 for determining moisture content (MC, %) is expressed as:

$$MC\% = (W1 - W2/W1) \times 100 \tag{4}$$

where W1 is the weight of the wet sample, and W2 is the weight of the oven-dried sample (Marei et al., 2016).

To measure fat binding capacity (FBC) and water binding capacity (WBC), a centrifuge tube containing 0.5 g of chitosan was initially weighed. For WBC, 10 mL of water was added, while for FBC, soybean oil was used. After combining these substances with chitosan in the centrifuge tube and vortex mixing for 1 min, the mixture stood at 25°C for 30 min. Stirring occurred every 10 min for 5 s, followed by centrifugation at 3,200 rpm for 25 min. After separating the liquid fraction from the solid sediment, the tube was reweighed. WBC and FBC were calculated using the Eqs 5, 6 (Nouri et al., 2016):

$$WBC\% = (\text{weight of water} - \text{bound chitosan}/\text{initial weight of chitosan}) \times 100 \tag{5}$$

$$FBC\,\% = (\text{weight of lipid} - \text{bound chitosan}/\text{initial weight of chitosan}) \times 100 \tag{6}$$

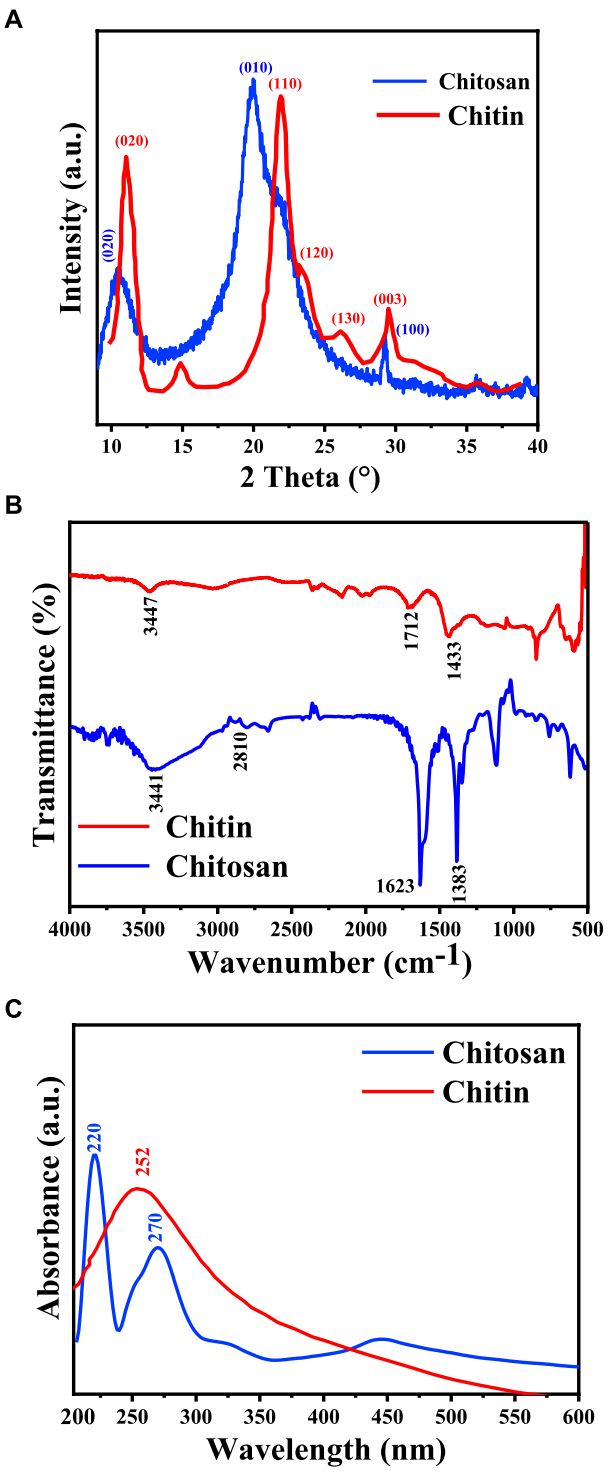

FIGURE 2
Chemical analysis of chitosan and chitin extracted from *Amanita phalloides*: **(A)** XRD diffraction; **(B)** FTIR spectra; and **(C)** UV-vis spectra.

2.4 Antibacterial bioassay of chitosan

The antibacterial effectiveness of chitosan against various bacterial species, including *Pseudomonas Aeruginosa* (ATCC9027), *Bacillus Subtiliis* (ATCC6633), *Listeria Innocua* (CLIP74915), *Staphylococcus Aureus* (ATCC6538), and *Salmonella Typhimurium* (ATCC14028), was assessed using the agar well diffusion technique. Wells of 6 mm in diameter were created on agar plates using a sterile stainless steel cork borer. The culture plates were then prepared and inoculated with 100 µL of a 24-hour-old bacterial broth culture. Chitosan's bactericidal activity was examined at various concentrations (1%, 4%, and 8%) in acetic acid, with ciprofloxacin (CIP-5) used as the reference standard for comparison. The plates were calibrated using a 5 µL solution of chitosan. Following a 24-h incubation period at 37°C, inhibitory zones were observed.

2.5 Adsorption studies on chitosan

The experiment was designed using the Box Behnken design and the statistical program Design Expert ver.15 by Response Surface Methodology. Table 1 outlines the factors considered in this research. Chitosan was added to 0.5 g flasks containing 30 mL of dye solution at varying concentrations (ranging from 9.59 to 15.99 ppm) and across predetermined pH values (ranging from 2 to 10) for different durations (from 10 to 60 min) to achieve equilibrium. The mixture was agitated in an orbital shaker at 150 rpm and maintained at a temperature of 25°C. Subsequently, the solid phase was separated by centrifugation at 6,000 rpm. A UV-vis spectrophotometer was utilized to compare the concentration of the MB dye before and after the adsorption procedures. Additionally, 0.1 M NaOH and 0.1 M HCl were employed to adjust the solution's pH during the experiment. The percentage of dye removal capacity was calculated using the Eq. 7 provided below (Ben Amor et al., 2022).

$$Dye\ removal\,(\%) = \frac{(C_0 - C_e)}{C_0} \times 100 \tag{7}$$

Co and Ce in the formula represent the initial (starting) and equilibrium dye concentrations in $mg.L^{-1}$ (ppm), respectively.

The quadratic Eq. 8 can be stated as follows in the Box-Behnken Design, with 03 factors (Ben Amor et al., 2023):

$$Y = \beta_0 + \sum_{j=1}^{m} \beta_j x_j + \sum_{j=1}^{m} \beta_{jj} x_j^{\,2} + \sum \sum_{i<j=2}^{m} \beta_{ij} x_i x_j + \varepsilon \tag{8}$$

Where ε represents the error, x_i and x_j represent variables. The linear, binominal, and combination effects are represented by the coefficients β_i, β_{ii}, and β_{ij}, respectively. β_0 is a constant coefficient, and m denotes the total of the factors under study (Mondal and Purkait, 2018).

3 Results and discussion

3.1 Characteristics of chitosan

The production of chitosan extracted from *A. phalloides* is a critical metric that indicates the efficiency of the extraction process. In several studies it has been reported that the chitosan content extracted from different insects ranges from 2% to 79% (Mohan et al., 2020; Zainol Abidin et al., 2020). In the course of this study, the

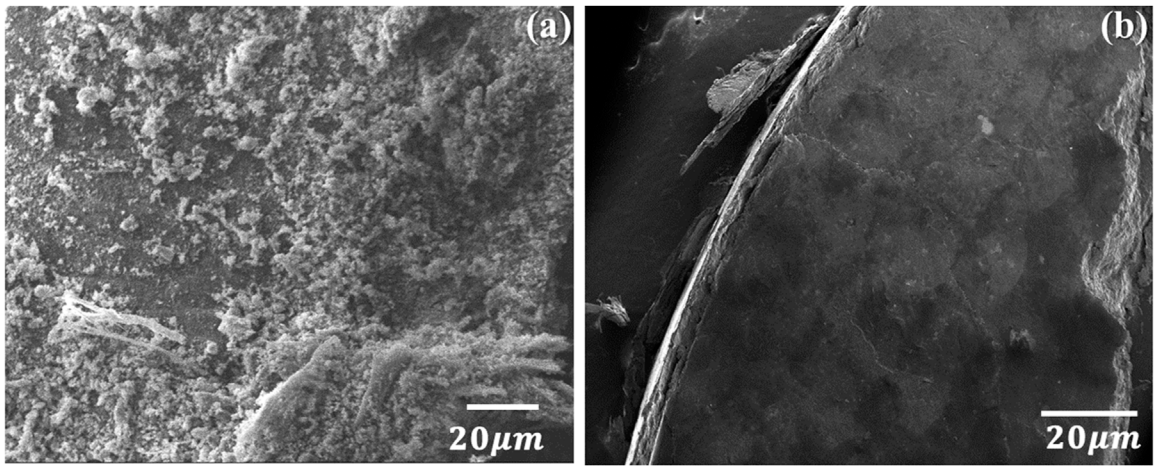

FIGURE 3
SEM images of **(A)** chitin and **(B)** chitosan extracted from *Amanita phalloides*.

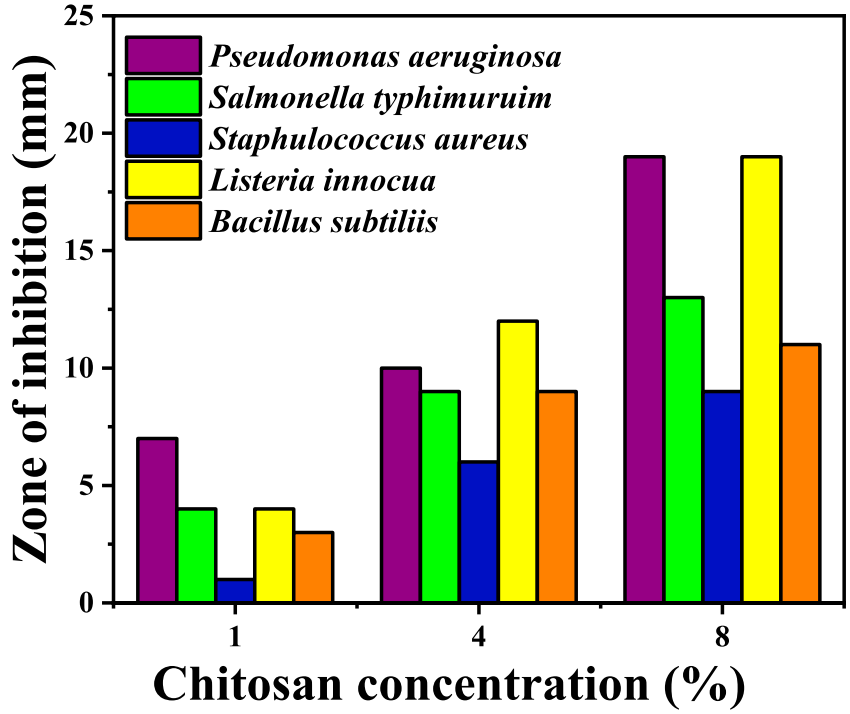

FIGURE 4
Antibacterial activity of chitosan at various concentrations against different bacteria. The values of the chitosan solutions were subtracted from the inhibition zone of acetic acid. (Every test was carried out in triplicate. The values were expressed as means ± standard deviation (SD) (n = 3).

extraction yield of chitin and chitosan from *A. phalloides* was determined to be 52.5% and 70%, respectively. The yield of chitosan from *A. phalloides* indicates a relatively efficient and productive extraction process. Achieving a higher yield in the extraction process is generally favourable because it ensures a greater amount of chitosan, which can be used in different applications across different industries.

Amanita phalloides chitosan exhibits notable Water Binding Capacity (WBC) at approximately 671% and a considerable Fat Binding Capacity (FBC) of around 253%. In comparison, commercial chitosan shows WBC capabilities similar to extracted chitosan but tends to have lower FBC. Many commercially available chitosan display WBC and FBC capacities ranging between 458%–805% and 314%–535%, respectively (Kumari et al., 2017). The term "ash contents" refers to the inorganic residue resulting from the complete decomposition of chitosan when subjected to heating in the presence of air. The concentration of chitosan ash is a crucial

TABLE 3 Zone of inhibition of the extracted chitosan.

Sample	Conc	Zone of inhibition[a] (mm)				
		Gram-negative bacteria		Gram-positive bacteria		
		Pseudomonas aeruginosa	*Salmonella typhimuruim*	*Staphulococcus aureus*	*Listeria innocua*	*Bacillus subtiliis*
Chitosan (is dissolved in acetic acid)[b]	1 wt%	7 ± 0.1	4 ± 0.3	1 ± 0.1	4 ± 0.1	3 ± 0.2
	4 wt%	10 ± 0.1	9 ± 0.1	6 ± 0.25	12 ± 0.1	9 ± 0.1
	8 wt%	19 ± 0.3	13 ± 0.25	9 ± 0.15	19 ± 0.17	11 ± 0.25
Ciprofloxacin (CIP-5)	50 µg	24 ± 0.4	16 ± 0.15	16.5 ± 0.2	24 ± 0.3	24 ± 0.3

[a]The value of three measurements was used to calculate the zone of inhibition.
[b]The values of the chitosan solutions were subtracted from the inhibition zone of acetic acid.

TABLE 4 Adsorption using ANOVA variance analysis.

Source	Sum of squares	Degree of freedom	Mean square	F -value	*p*-value
Model	4,087.90	9	454.21	236.59	< 0.0001
A	1.02	1	1.02	0.5326	0.4983
B	204.63	1	204.63	106.58	0.0001
C	7.45	1	7.45	3.88	0.1059
AB	21.07	1	21.07	10.97	0.0212
AC	43.43	1	43.43	22.62	0.0051
BC	0.1024	1	0.1024	0.0533	0.8265
A^2	3,764.40	1	3,764.40	1960.77	< 0.0001
B^2	0.0156	1	0.0156	0.0081	0.9317
C^2	0.2895	1	0.2895	0.1508	0.7138
Residual	9.60	5	1.92		
Lack of fit	3.60	3	1.20	0.3999	0.7704
Pure error	6.00	2	3.00		
Total	4,097.50	14			
R^2	0.9977				
R^2 Adjusted	0.9934				

factor in assessing the efficacy of calcium carbonate removal during the demineralization phase. High-quality chitosan typically maintains an ash concentration of less than 1% (Ibitoye et al., 2018). In Table 2, the chitosan isolated from *A. phalloides* is reported to have an ash concentration of 6.7%, indicating that chitosan from *A. phalloides* possesses superior quality. Additionally, chitosan derived from *A. phalloides* is found to have a moisture content of 13.9%.

3.2 Crystallinity of chitin and chitosan

XRD spectra of chitin and chitosan, depicted in Figure 2A, unveil intricate patterns indicative of their crystalline and semi-crystalline nature. Chitin's XRD pattern showcases distinctive boundary peaks at 11.04°, 14.89°, 21.94°, 23.16°, 26.18°, and 29.26°, consistent with prior studies (Kaya et al., 2015a; Raut et al., 2016; Olafadehan et al., 2021b). Conversely, XRD pattern of chitosan shows three peaks at 10.57°, 20.30°, and 29.26°, with a notably lower intensity observed at 10.57°. This reduction in peak intensity is attributed to the formation of intramolecular hydrogen bonds post-deacetylation, a phenomenon well-documented in the literature (Kaya et al., 2015b). Crystalline reflections characteristic of chitin and semi-crystalline features indicative of chitosan are discerned at $2\theta = 20.30°$ and $2\theta = 10.57°$, respectively. CrI values were calculated using Eq. 2, as described by Olafadehan et al. (2021b), Ibitoye et al. (2018), and Teli and Sheikh (2012). In this study, CrI values for chitin and chitosan stand at 70.01% and 49.07%, respectively. These findings align with previous research, which reported CrI

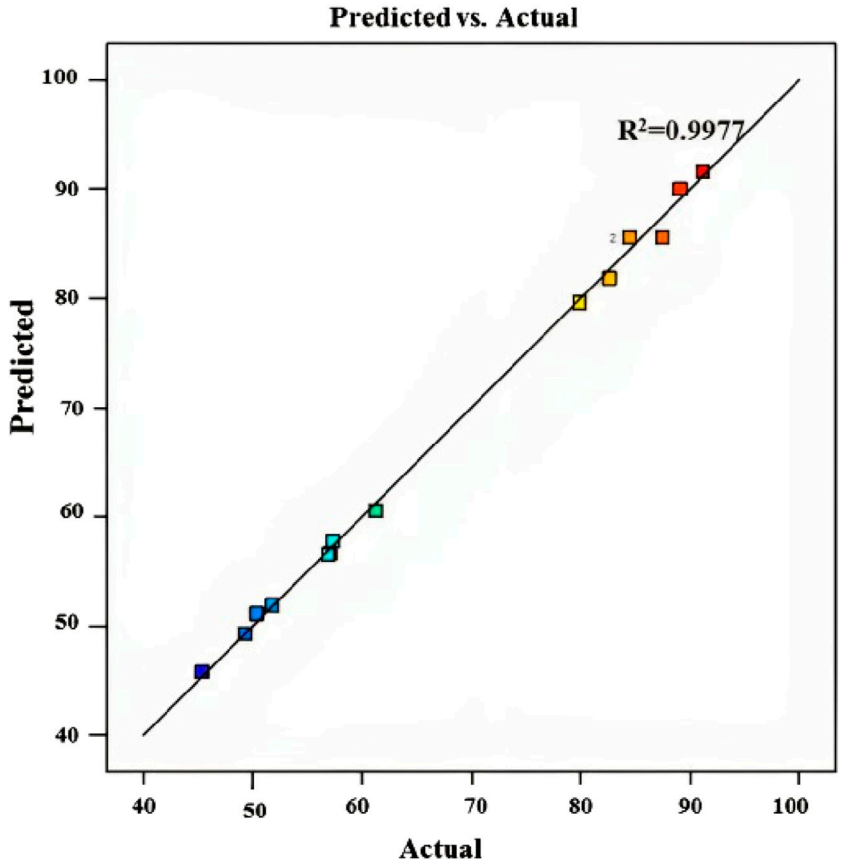

FIGURE 5
Predicted vs. experimental values for MB dye removal using chitosan extracted from *Amanita phalloides*.

values for chitin ranging between 50% and 90% and for chitosan between 20% and 70%, underscoring the inherent variability in crystallinity within these polymers (Ibitoye et al., 2018; Mohan et al., 2020).

In a study by Kaya et al. (2015c), CrI values for wasp-extracted chitin were reported to be 50% for Vespula germanica, 69.88% for Vespa crabro, and 53.92% for Vespa orientalis, highlighting variability in crystallinity among different chitin sources. Similarly, Hajji et al. (2014) found that chitin prepared from shrimp and crab shells exhibited crystallinity rates of 64.1% and 67.8%, respectively, while chitosan derived from the same sources displayed crystallization rates of 31.9% and 35.2%. These findings indicate the influence of source material on the crystalline properties of chitin and chitosan. Structural modifications introduced during the deacetylation process contribute to chitosan's lower CrI, characterized by disrupted polymer chain organization, increased hydrophilicity, and enhanced flexibility, factors that influence the formation of crystalline domains. Furthermore, it's important to note that processing parameters such as temperature, pH, and solvent choice play crucial roles in determining the final crystalline structure of chitosan, adding additional layers of complexity to its crystallinity behaviour and emphasizing the need for meticulous control in manufacturing processes.

3.3 Degree of deacetylation of chitin and chitosan

Utilizing FTIR spectroscopy, the degree of deacetylation in chitosan was assessed (Figure 2B). Notably, the peaks at 3,460 cm^{-1} in both chitin and chitosan spectra are attributed to the stretching vibrations and hydrogen bonding among NH_2 and -OH groups (Amor et al., 2023). Specific characteristics observed in the chitin spectrum include the band at 1,712 cm^{-1}, indicating the expansion of the C=O hydrogen group bonded to N-H, and the band at 1,433 cm^{-1}, suggesting a distinct hydrogen bond between the C=O and the hydroxyl-methyl group of the chitin residue [19]. Conversely, the chitosan spectrum displays distinctive peaks, such as the band at 2,810 cm^{-1} (stretching of H-C polysaccharide bonds), 1,623 cm^{-1} (amide I indicating the removal of the acetyl group), and 1,338 cm^{-1} (amide II representing bending -NH_2) (Qiao et al., 2021). The degree of deacetylation (DD) calculated via FTIR analysis was 16% for chitin and 86% for chitosan. It's important to note that the value of deacetylation can varying sample preparation methods, and chitosan resources.

3.4 UV-Vis spectra of chitin and chitosan

In Figure 2C, the UV-Vis spectra of chitin and chitosan obtained from *A. phalloides* are presented. Notably, each spectrum exhibits

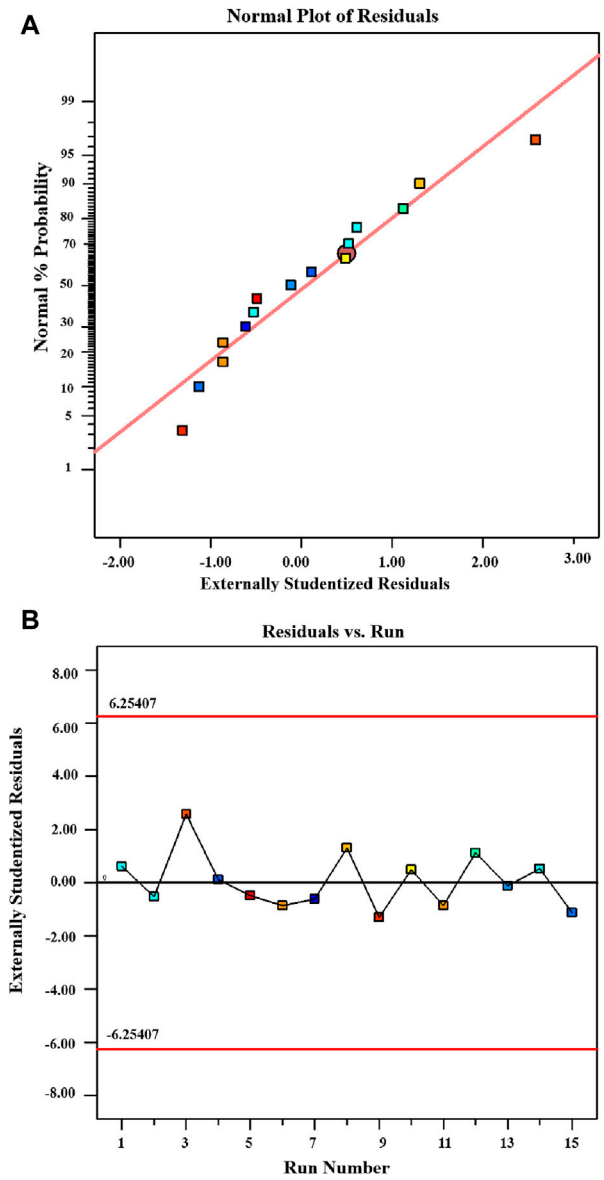

FIGURE 6
Experimental design for dye removal **(A)** Polt displaying the externally studentized residual along with normal probability. **(B)** Polt depicting the predicted value against the externally studentized residuals for MB dye removal utilizing chitosan.

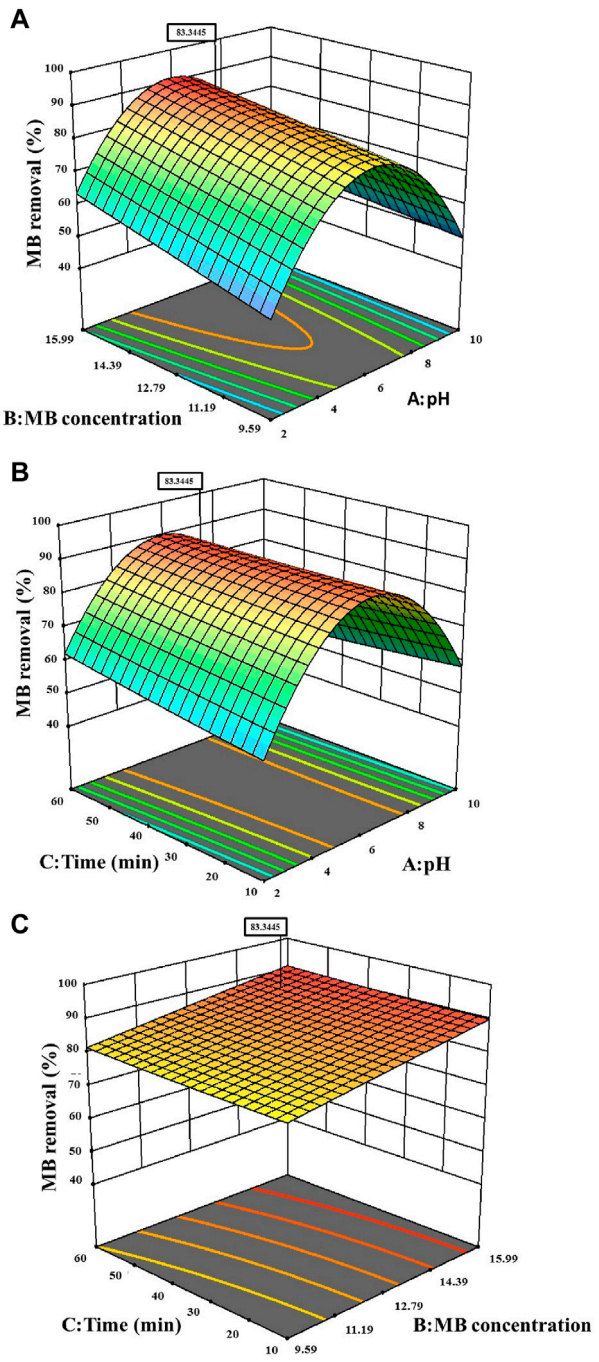

FIGURE 7
3-D Surface contour plot for the effects on MB dye removal **(A)** MB concentration versus pH, **(B)** Time versus pH **(C)** Time versus MB concentration.

unique absorption bands: specifically, chitosan displays a prominent absorption band at 252 nm, while chitin exhibits absorption bands at 220 nm and 270 nm. These absorption peaks correspond to π-π* transitions of electrons within the ring system and n-π* transitions of electrons in the oxygen or nitrogen atoms attached to the ring system, respectively, following the removal of the acetyl group. These findings align with prior research in the field (Fatullayeva et al., 2022; Tarique et al., 2023). The difference in the UV-Vis absorption patterns between chitin and chitosan, particularly in the observed wavelengths, highlights the alteration in the molecular structure due to the deacetylation process and changing of the chemical structure from chitin to chitosan.

3.5 Morphological analysis of chitin and chitosan

The morphological analysis of chitin (Figure 3A) and chitosan (Figure 3B), observed through a scanning electron microscope (SEM) reveals distinct differences in their structures. Chitin demonstrates an irregular structure, characterized by a rough surface, whereas chitosan showcases a transformed surface,

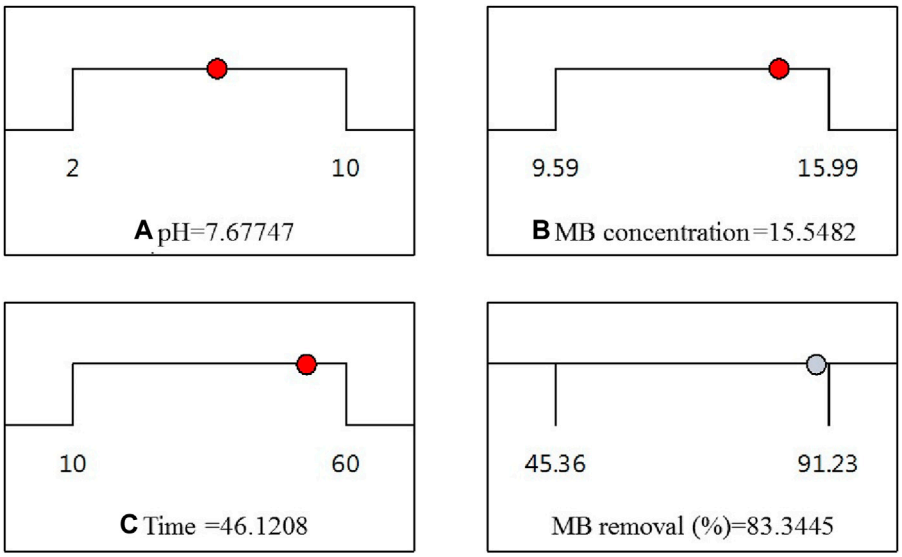

FIGURE 8
Desirability ramp for optimization.

TABLE 5 Comparing the outcomes of MB dye removal efficiency of chitosan prepared from various sources with other studies.

Source of chitosan	Extraction conditions	MB removal (%)	Ref.
Fenneropenaeus indicus	Chitosan mass: 4 g; MB concentration: 10 ppm, pH = 7, time: 24 h	93.2	Arunachalam (2021)
Blaps lethifera	Chitosan mass 1 g; MB concentration 12.79 ppm; pH 7, volume 30 mL, time: 120 min	88.7	Ben Amor et al. (2023)
Pimelia fernandezlopezi		47.1	
Musca domestica		29.0	
Amanita phalloides	Chitosan mass 0.5 g, MB concentration 15.99 ppm; volume: 30 mL, pH 6; time 60 min	91.6	This work

displaying a smoother polymer structure. This observation aligns with findings from multiple earlier studies (Olafadehan et al., 2021a; Son et al., 2021; Piekarska et al., 2023). In contrast, chitosan, derived from chitin through deacetylation, presents a modified structure with a smoother surface, indicative of its altered polymer nature. This difference in morphology between chitin and chitosan serves as a visual confirmation of the structural changes brought about by the deacetylation process, which are consistent with previous research findings.

3.6 Antibacterial activities of chitosan

Antibacterial activity of chitosan against both Gram-positive (Gram+) and Gram-negative (Gram -) bacteria is illustrated in Figure 4; Table 3, revealing an increase in the zone of inhibition as the concentration of chitosan rises. For Gram-negative bacteria, such as *P. aeruginosa* and *Salmonella typhimurium*, the zone of inhibition increased with higher chitosan concentrations. For instance, at a chitosan concentration of 1 wt%, the zones of inhibition were 7 ± 0.1 mm and 4 ± 0.3 mm against *P. aeruginosa* and *S. typhimurium*, respectively. However, at 8 wt% concentration, these values increased to 19 ± 0.3 mm and 13 ± 0.25 mm, indicating a notable increase in the inhibitory effect against these Gram-negative bacteria. Similarly, for Gram-positive bacteria, higher chitosan concentrations resulted in more substantial zones of inhibition. *Pseudomonas aeruginosa* and *Listeria innocua* demonstrated higher sensitivity to chitosan, especially at higher concentrations. At 8 wt% chitosan concentration, the zone of inhibition against *P. aeruginosa* and *L. innocua* was measured at 19 ± 0.3 mm and 19 ± 0.17 mm, respectively.

Chitosan primarily exerts its antibacterial effect through electrostatic interactions with the surface of bacterial cells, inducing increased permeability in the bacterial membrane (Alhamad et al., 2023). This interaction occurs between the positively charged protonated amino group of chitosan and the negatively charged molecules on the bacterial cell membrane (Ardean et al., 2021). Research by Zeinab Abedian and colleagues (Abedian et al., 2020) assessed the antibacterial activity of commercial chitosan with a high degree of deacetylation (94%) and low molecular weight against various spoilage pathogens. The study demonstrated notable variations in sensitivity between Gram-positive and Gram-negative bacteria when exposed to chitosan. Multiple factors are crucial in determining the antibacterial activity of chitosan, such as the bacterial strain, growth stage, molecular weight, concentration, environmental temperature, and

pH level (Ardean et al., 2021). Chitosan exhibits an affinity for the surfaces of negatively charged cells, like Gram-negative bacteria, when present in low quantities, reducing cell membrane permeability, resulting in cell death. The positively charged amino groups of chitosan create a protective coating on the cell surface, impeding the entry of intracellular components (Ibitoye et al., 2018). In contrast, for Gram-positive bacteria, the electrostatic repulsion between the positively charged chitosan and bacterial cells impedes agglutination (Abedian et al., 2020; Ke et al., 2021). In a study investigation into the fractional weight and concentration of chitosan against *E. coli* demonstrated that high concentrations (>200 ppm) exhibited effective antibacterial properties, while low concentrations (20 ppm) displayed a weaker effect (Ardean et al., 2021). At higher concentrations, the bactericidal effects may be due to bacterial flocculation, whereas low concentrations may Favor bacterial proliferation, promoting survival (Antaby et al., 2021). This difference in effect might be linked to the antibacterial mechanisms associated with varying chitosan concentrations.

3.7 Experimental design for dye removal

Table 1 displays the experimental outcomes related to the removal of MB dye and provides a comprehensive comparison between anticipated and actual results. Each row in this table outlines a specific experimental setup, detailing the values assigned to key parameters such as pH, MB concentration (ppm), and time (min). Moreover, the table encompasses both the anticipated and observed MB removal percentages under these set conditions. Notably, the comparison between the predicted and actual values demonstrates a remarkable consistency, affirming the accuracy of the proposed model. Experimental setups 5 and 9 exhibit notably high MB removal percentages, aligning closely with the predicted values of 91.60% and 89.99%, respectively. Conversely, setups 2, 4, and 13 demonstrate lower MB removal percentages, corresponding to the expected values of 57.38%, 49.34%, and 51.81%, respectively. This congruence between the predicted and observed responses emphasizes the reliability of the model in estimating MB removal efficiency across diverse experimental conditions.

The analysis of variance (ANOVA) conducted for MB dye removal using chitosan has resulted in a highly accurate quadratic polynomial model equation. This equation effectively correlates the responses with the variables being investigated (as detailed in Table 4). The exceptionally high coefficient of determination (R^2 = 0.9977) indicates an almost perfect alignment between the predicted and actual values, while the adjusted R^2 value (0.9934) further underscores the model's exceptional accuracy. The significant F-value (236.59, $p < 0.0001$) highlights the overall reliability and importance of the model. In the ANOVA, each factor (pH, MB concentration, and time) and their interactions were thoroughly examined. Factors A (pH), B (MB concentration), AB (interaction between pH and MB concentration), AC (interaction between pH and time), and A^2 (pH square term) exhibited substantial impact with p-values <0.05. However, factors C (time) and BC (interaction between MB concentration and time) displayed slightly higher p-values, though still within a reasonably acceptable range (0.1059 and 0.8265, respectively). The coefficients within the quadratic polynomial model equation further elucidate the magnitude and direction of influence each factor holds over the MB removal response.

The analysis has shown that a quadratic polynomial model's equation, which expresses the responses in coded factors, links the responses with the factors under study. This model is given below in Eq. 9. The terms "sign" (positive or negative) and "coefficient" (representing the kind and strength of the influence on the response) are used in the equation to accurately characterize the effect of each element.

$$\text{MB removal (\%)} = 85.52 + 0.3575\,\mathbf{A} + 5.06\,\mathbf{B} + 0.9650\,\mathbf{C} - 31.93\,\mathbf{A^2} - 0.0650\,\mathbf{B^2} + 0.2800\,\mathbf{C^2} - 2.29\,\mathbf{AB} - 3.29\,\mathbf{AC} - 0.1600\,\mathbf{BC} \quad (9)$$

A is pH, B is MB concentration (ppm), and C is the Time (min).

Figure 5 displays the expected versus actual values for the MB dye removal reaction, yielding an R^2 value of 0.9977 (Table 4), revealing that the predicted values align closely with the experimental values, affirming the accuracy of the model's predictions. This suggests that the model developed is effective in estimating the efficiency of chitosan in removing MB dye under various conditions, providing insights into optimizing the removal process for enhanced effectiveness.

Figure 6A presents a normal probability plot that is particularly useful in determining the distribution pattern of the data (Moria et al., 2022). The lack of conspicuous deviations in the plot signifies that the data aligns well with the assumptions of the statistical model. In Figure 6B, the residuals are displayed along with the run numbers in what's known as an outlier t-plot. The red lines at the top (6.25407) and bottom of the figure (−6.25407) indicate the 95% confidence interval for the control range. Remarkably, all data points fall within this allowed range (from 6.25407 to−6.25407), demonstrating consistency with expectations. Additionally, the histogram of the residual data shows a lack of any discernible structure or pattern, suggesting a random and normal distribution of residuals. The absence of a specific shape or structure in the distribution implies that there is no systematic connection or pattern among the residuals.

Process parameters (pH, MB concentration, and time) are intentionally varied according to a pre-established plan, often utilizing a response surface design, to assess their influence on the targeted response variable. Figure 7 portrays 3D plots of the response surfaces, illustrating the individual impacts of the three independent parameters (pH, MB concentration, and time) on MB removal. Analysing the response surface aids in comprehending the singular and combined influences of these input factors on the outcomes. The curves derived from the plots demonstrate that the efficiency of MB removal increases with a rise in the initial concentration of MB from 12.79 to 15.99 ppm, and within a pH range of 4.5–6.5. The peak MB removal efficiency reached 83.34% at a pH of 7.67%, an MB concentration of 15.54 ppm, and a contact time of 46.12 min.

Throughout this study, all factor ranges were confined between their minimum (1) and maximum (+1) values, aiming to optimize

the maximization of MB elimination. The graphical representation in Figure 8 demonstrated a maximum desirability of 1.00 using the preset optimization criteria. With these established conditions, the observed maximum MB Removal (%) of 83.34% corresponded to a pH (A) of approximately 7.67, an MB concentration (B) around 15.54 ppm, and a reaction time (C) close to 46.12 min. Under the optimized Response Surface Methodology conditions, the highest degree of MB dye removal was found to be 91.6%. This occurred at a pH of 6, a MB concentration of approximately 15.99 ppm, and a reaction time of around 60 min.

3.8 Evaluation of the previous research

Chitosan is acknowledged for its efficacy as an adsorbent, adept at the removal of diverse pollutants including heavy metals, organic dyes, and microbial contaminants. Its reusability stands out as a key advantage in wastewater treatment, promising cost-effectiveness and sustainability (da Silva Alves et al., 2021). Numerous studies have delved into the reusability of chitosan-based adsorbents, consistently showing that chitosan can be regenerated and reused multiple times without compromising its adsorption capacity or performance (Dago-Serry et al., 2024; Kaczorowska and Bożejewicz, 2024). Typically, the regeneration process involves desorbing the adsorbed contaminants from the chitosan matrix using appropriate desorbing agents, followed by washing and drying for subsequent reuse (Soares et al., 2021). However, handling contaminated chitosan, especially when loaded with basic dyes, requires careful consideration to ensure safe and effective management of the material and its associated contaminants. Here are some key considerations.

(1) Storage: Contaminated chitosan should be stored in designated containers or areas clearly labelled to indicate the presence of hazardous substances. Storage facilities must be secure and inaccessible to unauthorized individuals to prevent accidental exposure (Moder et al., 2007).
(2) Disposal: Disposing of contaminated chitosan should adhere to local regulations and guidelines for handling hazardous waste. This typically involves segregating contaminated materials, proper packaging, and transportation to authorized disposal facilities equipped to handle hazardous waste (Goel, 2017).
(3) Treatment: Depending on the contamination's nature and extent, treatment options like chemical or thermal treatment, incineration, or biological degradation may be considered to deactivate or remove contaminants from the chitosan matrix before disposal. These methods should be chosen for their effectiveness in decontaminating the material while minimizing environmental impact (González-Martínez et al., 2019).
(4) Recycling: Contaminated chitosan may undergo regeneration or recycling processes to recover valuable components or resources. This often entails desorbing contaminants, followed by purification or regeneration of the chitosan matrix for reuse in subsequent applications (Bhatt et al., 2023).

In Table 5, a comparative analysis of the efficiency in removing MB dye by chitosan derived from various sources is presented, shedding light on the absorption rates achieved across different experimental conditions. The findings suggest that chitosan extracted from *Fenneropenaeus indicus* demonstrated a relatively higher MB removal percentage, reaching 93.2% at a low MB concentration of 10 ppm, with a pH of 7, a reaction volume of 50 mL, and a 24-h reaction time. In contrast, the chitosan extracted from *A. phalloides*, the focus of this study, displayed a high MB removal percentage of 91.6% at a higher MB concentration of 15.99 ppm, a pH of 6, and a shorter reaction time of 1 h, with a reaction volume of 30 mL. However, chitosan obtained from other sources, namely, *Blaps lethifera*, *Pimelia fernandezlopezi*, and *Musca domestica*, exhibited lower MB removal percentages. They achieved 88.7%, 47.1%, and 29.0% removal rates, respectively, at a low MB dye concentration of 12.79 ppm, a pH of 7, and a reaction time of 2 h. Our results showed that the extracted chitosan showed high adsorption capacity for the pollutant present in wastewater. The unique physicochemical properties of chitosan, such as its positively charged functional groups, enable it to effectively adsorb diverse contaminants through various mechanisms, including electrostatic interactions, hydrogen bonding, and surface complexation (da Silva Alves et al., 2021).

4 Conclusion

Extraction of chitin and chitosan from *A. phalloides* exhibited a yield of 52.5% and 70%, respectively. Several parameters were investigated, encompassing the degree of deacetylation (DD), fat binding capacity (FBC), water binding capacity (WBC), as well as moisture content and ash content. Notably, the antibacterial activity of chitosan revealed higher efficacy against Gram-positive bacteria compared to Gram-negative strains. Employing Response Surface Methodology based on the Box-Behnken design, the impact of specific conditions (time, pH, methyl blue concentration) on the removal of MB was rigorously examined. The high R value (R^2 = 0.99) underscores the model's relevance in MB dye removal. Under the optimized Response Surface Methodology conditions, the highest degree of MB dye removal was found to be 91.6%. This occurred at a pH of 6, a MB concentration of approximately 15.99 ppm, and a reaction time of around 60 min. These findings suggest that the procedure for chitosan extraction from *A. phalloides* is a cost-effective, eco-friendly, and biodegradable approach for wastewater treatment. Response Surface Methodology emerges as a valuable statistical tool for enhancing chitosan's efficacy in removing diverse organic pollutants. Overall, the study highlights the potential of chitosan sourced from this fungal origin in addressing azo dye removal from wastewater and exploring its antibacterial applications. The study's successful demonstration of chitosan's prowess in dye removal and antibacterial properties promises significant environmental and health benefits by offering an eco-conscious solution for wastewater treatment.

Data availability statement

The original contributions presented in the study are included in the article/Supplementary material, further inquiries can be directed to the corresponding author.

Author contributions

HH: Conceptualization, Data curation, Formal Analysis, Investigation, Methodology, Writing–original draft. IB: Conceptualization, Data curation, Formal Analysis, Investigation, Methodology, Writing–original draft, Software, Validation, Visualization. SZ: Conceptualization, Data curation, Formal Analysis, Investigation, Methodology, Validation, Writing–original draft. AB: Conceptualization, Data curation, Formal Analysis, Investigation, Methodology, Writing–original draft. SL: Conceptualization, Data curation, Formal Analysis, Investigation, Methodology, Writing–original draft, Validation. AA: Formal Analysis, Validation, Writing–original draft, Project administration. DC: Funding acquisition, Investigation, Project administration, Validation, Writing–review and editing. MB: Formal Analysis, Project administration, Validation, Writing–original draft, Data curation. AB: Data curation, Formal Analysis, Project administration, Validation, Writing–original draft, Conceptualization, Funding acquisition, Investigation, Methodology, Resources, Software, Supervision, Visualization, Writing–review and editing.

Funding

The authors declare that financial support was received for the research, authorship, and/or publication of this article. Consortium Author AB and AlA were financially supported by the Science, Technology and Innovation Funding Authority (Project ID 42811) and Researchers Supporting Project number (RSP-2024R78), King Saud University, Riyadh, Saudi Arabia.

Conflict of interest

The authors declare that the research was conducted in the absence of any commercial or financial relationships that could be construed as a potential conflict of interest.

The author(s) declared that they were an editorial board member of Frontiers, at the time of submission. This had no impact on the peer review process and the final decision.

Publisher's note

References

Abedian, Z., Jenabian, N., Moghadamnia, A., Zabihi, E., Pourbagher, R., and Rajabnia, M. (2020). Antibacterial activity of high-molecular-weight and low-molecular-weight chitosan upon oral pathogens. *Int. J. Infect. Dis.* 101, 46–47. doi:10.1016/j.ijid.2020.09.154

Alhamad, A. A., Zeghoud, S., Amor, I. B., and Hemmami, H. (2023). Chitosan-based hydrogels for wound healing: correspondence. *Int. J. Surg.* 109, 1821–1822. doi:10.1097/js9.0000000000000414

Alnemari, A. M., Moustapha, M. E., Hassan, A. A., and Salah, D. (2023). Chitosan nano-composites applications for water remediation. *Cogent Eng.* 10, 2220498. doi:10.1080/23311916.2023.2220498

Amor, I. B., Hemmami, H., Laouini, S. E., Abdelaziz, A. G., and Barhoum, A. (2023). Influence of chitosan source and degree of deacetylation on antibacterial activity and adsorption of AZO dye from water. *Biomass Convers. Biorefinery*, 1–11. doi:10.1007/s13399-023-03741-9

Antaby, E., Klinkhammer, K., and Sabantina, L. (2021). Electrospinning of chitosan for antibacterial applications—current trends. *Appl. Sci.* 11, 11937. doi:10.3390/app112411937

Ardean, C., Davidescu, C. M., Nemeş, N. S., Negrea, A., Ciopec, M., Duteanu, N., et al. (2021). Factors influencing the antibacterial activity of chitosan and chitosan modified by functionalization. *Int. J. Mol. Sci.* 22, 7449. doi:10.3390/ijms22147449

Arunachalam, K. (2021). Bio-adsorption of methylene blue dye using chitosan-extracted from Fenneropenaeus indicus shrimp shell waste. *J. Aquac. Mar. Biol.* 10, 146–150. doi:10.15406/jamb.2021.10.00316

Ben Amor, I., Hemmami, H., Laouini, S. E., Mahboub, M. S., and Barhoum, A. (2022). Sol-gel synthesis of ZnO nanoparticles using different chitosan sources: effects on antibacterial activity and photocatalytic degradation of AZO Dye. *Catalysts* 12, 1611. doi:10.3390/catal12121611

Ben Amor, I., Hemmami, H., Laouini, S., Zeghoud, S., Benzina, M., Achour, S., et al. (2023). Use of insect-derived chitosan for the removal of methylene blue dye from wastewater: process optimization using a central composite design. *Materials* 16, 5049. doi:10.3390/ma16145049

Bhatt, P., Joshi, S., Bayram, G. M. U., Khati, P., and Simsek, H. (2023). Developments and application of chitosan-based adsorbents for wastewater treatments. *Environ. Res.* 226, 115530. doi:10.1016/j.envres.2023.115530

Dago-Serry, Y., Maroulas, K. N., Tolkou, A. K., Kokkinos, N. K., and Kyzas, G. Z. (2024). How the chitosan structure can affect the adsorption of pharmaceuticals from wastewaters: an overview. *Carbohydr. Polym. Technol. Appl.* 7, 100466. doi:10.1016/j.carpta.2024.100466

Da Silva Alves, D. C., Healy, B., Pinto, L. A. D. A., Cadaval JR, T. R. S. A., and Breslin, C. B. (2021). Recent developments in chitosan-based adsorbents for the removal of pollutants from aqueous environments. *Molecules* 26, 594. doi:10.3390/molecules26030594

Fatullayeva, S., Tagiyev, D., Zeynalov, N., Mammadova, S., and Aliyeva, E. (2022). Recent advances of chitosan-based polymers in biomedical applications and environmental protection. *J. Polym. Res.* 29, 259. doi:10.1007/s10965-022-03121-3

Goci, M. C., Leudjo Taka, A., Martin, L., and Klink, M. J. (2023). Chitosan-based polymer nanocomposites for environmental remediation of mercury pollution. *Polymers* 15, 482. doi:10.3390/polym15030482

Goel, S. (2017). Solid and hazardous waste management: an introduction. *Adv. Solid Hazard. Waste Manag.*, 1–27. doi:10.1007/978-3-319-57076-1_1

González-Martínez, A., De Simón-Martín, M., López, R., Táboas-Fernández, R., and Bernardo-Sánchez, A. (2019). Remediation of potential toxic elements from wastes and soils: analysis and energy prospects. *Sustainability* 11, 3307. doi:10.3390/su11123307

Hajji, S., Younes, I., Ghorbel-Bellaaj, O., Hajji, R., Rinaudo, M., Nasri, M., et al. (2014). Structural differences between chitin and chitosan extracted from three different marine sources. *Int. J. Biol. Macromol.* 65, 298–306. doi:10.1016/j.ijbiomac.2014.01.045

Ibitoye, E., Lokman, I., Hezmee, M., Goh, Y., Zuki, A., and Jimoh, A. (2018). Extraction and physicochemical characterization of chitin and chitosan isolated from house cricket. *Biomed. Mater.* 13, 025009. doi:10.1088/1748-605x/aa9dde

Ibrahim, N. A., and Eid, B. M. (2016). Potential applications of sustainable polymers in functionalization of cellulosic textile materials. *Handb. Sustain Polym. Process Appl.* 6, 215–264. doi:10.1002/9781119441632.ch44

Ibrahim, N. A., and Eid, B. M. (2017). "Chitosan-based composite materials: fabrication and characterization," in *Handbook of composites from renewable materials*. Editors V. K. Thakur, M. K. Thakur, and M. R. Kessler, 103–136.

Ibrahim, N., and Eid, B. (2018). "Emerging technologies for source reduction and end-of-pipe treatments of the cotton-based textile industry," in *Handbook of textile effluent remediation*. New York: Pan Stanford Publishing, Taylor and Francis Group, 185–202.

Kaczorowska, M. A., and Bożejewicz, D. (2024). The application of chitosan-based adsorbents for the removal of hazardous pollutants from aqueous solutions—a review. *Sustainability* 16, 2615. doi:10.3390/su16072615

Kaya, M., BağrıAÇıK, N., Seyyar, O., and Baran, T. (2015a). Comparison of chitin structures derived from three common wasp species (Vespa crabro Linnaeus, 1758, Vespa orientalis Linnaeus, 1771 and Vespula germanica (Fabricius, 1793)). *Archives insect Biochem. physiology* 89, 204–217. doi:10.1002/arch.21237

Kaya, M., Baran, T., Asan-Ozusaglam, M., Cakmak, Y. S., Tozak, K. O., Mol, A., et al. (2015b). Extraction and characterization of chitin and chitosan with antimicrobial and antioxidant activities from cosmopolitan Orthoptera species (Insecta). *Biotechnol. Bioprocess Eng.* 20, 168–179. doi:10.1007/s12257-014-0391-z

Kaya, M., Bitim, B., Mujtaba, M., and Koyuncu, T. (2015c). Surface morphology of chitin highly related with the isolated body part of butterfly (Argynnis pandora). *Int. J. Biol. Macromol.* 81, 443–449. doi:10.1016/j.ijbiomac.2015.08.021

Ke, C.-L., Deng, F.-S., Chuang, C.-Y., and Lin, C.-H. (2021). Antimicrobial actions and applications of chitosan. *Polymers* 13, 904. doi:10.3390/polym13060904

Kumari, S., Annamareddy, S. H. K., Abanti, S., and Rath, P. K. (2017). Physicochemical properties and characterization of chitosan synthesized from fish scales, crab and shrimp shells. *Int. J. Biol. Macromol.* 104, 1697–1705. doi:10.1016/j.ijbiomac.2017.04.119

Li, M., Li, X., Wang, L., Pei, Y., An, M., Liu, J., et al. (2021). Highly efficient and selective removal of anionic dyes from water using a cellulose nanofibril/chitosan sponge prepared by dehydrothermal treatment. *J. Environ. Chem. Eng.* 9, 105745. doi:10.1016/j.jece.2021.105745

Marei, N. H., Abd El-Samie, E., Salah, T., Saad, G. R., and Elwahy, A. H. (2016). Isolation and characterization of chitosan from different local insects in Egypt. *Int. J. Biol. Macromol.* 82, 871–877. doi:10.1016/j.ijbiomac.2015.10.024

Moder, K. P., Russo, J. P., Justiniano, F., Marshall, W. F., Mcghee, T. H., Stankovich, R., et al. (2007). Development of a hazardous material compatibility storage guideline and tool. *Process Saf. Prog.* 26, 114–122. doi:10.1002/prs.10186

Mohan, K., Ganesan, A. R., Muralisankar, T., Jayakumar, R., Sathishkumar, P., Uthayakumar, V., et al. (2020). Recent insights into the extraction, characterization, and bioactivities of chitin and chitosan from insects. *Trends food Sci. Technol.* 105, 17–42. doi:10.1016/j.tifs.2020.08.016

Mondal, P., and Purkait, M. K. (2018). Green synthesized iron nanoparticles supported on pH responsive polymeric membrane for nitrobenzene reduction and fluoride rejection study: optimization approach. *J. Clean. Prod.* 170, 1111–1123. doi:10.1016/j.jclepro.2017.09.222

Moria, K. M., Khurshid, H., Mustafa, M. R. U., Alhothali, A., and Bamasag, O. O. (2022). Application of the response surface methodology (RSM) in the optimization of acenaphthene (ACN) removal from wastewater by activated carbon. *Sustainability* 14, 8581. doi:10.3390/su14148581

Nayl, A. A., Abd-Elhamid, A. I., Arafa, W. A., Ahmed, I. M., El-Shanshory, A. A., Abu-Saied, M. A., et al. (2022). Chitosan-functionalized-graphene oxide (GO@ CS) beads as an effective adsorbent to remove cationic dye from wastewater. *Polymers* 14, 4236. doi:10.3390/polym14194236

Nouri, M., Khodaiyan, F., Razavi, S. H., and Mousavi, M. A. (2016). The effect of different chemical and physical processing on the physicochemical and functional characterization of chitosan extracted from shrimp waste species of indian white shrimp. *Prog. Rubber Plastics Recycl. Technol.* 32, 39–54. doi:10.1177/147776061603200103

Olafadehan, O. A., Amoo, K. O., Ajayi, T. O., and Bello, V. E. (2021a). Extraction and characterization of chitin and chitosan from Callinectes amnicola and Penaeus notialis shell wastes. *J. Chem. Eng. Material Sci.* 12, 1–30. doi:10.5897/jcems2020.0353

Olafadehan, O. A., Amoo, K. O., Ajayi, T. O., and Bello, V. E. (2021b). Extraction and characterization of chitin and chitosan from Callinectes amnicola and Penaeus notialis shell wastes. *J. Chem. Eng. Mater Sci.* 12, 1–30. doi:10.5897/jcems2020.0353

Piekarska, K., Sikora, M., Owczarek, M., Jóźwik-Pruska, J., and Wiśniewska-Wrona, M. (2023). Chitin and chitosan as polymers of the future—obtaining, modification, life cycle assessment and main directions of application. *Polymers* 15, 793. doi:10.3390/polym15040793

Qiao, C., Ma, X., Wang, X., and Liu, L. (2021). Structure and properties of chitosan films: effect of the type of solvent acid. *Lwt* 135, 109984. doi:10.1016/j.lwt.2020.109984

Raut, A., Satvekar, R., Rohiwal, S., Tiwari, A., Gnanamani, A., Pushpavanam, S., et al. (2016). *In vitro* biocompatibility and antimicrobial activity of chitin monomer obtain from hollow fiber membrane. *Des. Monomers Polym.* 19, 445–455. doi:10.1080/15685551.2016.1169379

Reshad, R. A. I., Jishan, T. A., and Chowdhury, N. N. (2021). *Chitosan and its broad applications: a brief review. Available at SSRN 3842055*.

Soares, S. F., Amorim, C. O., Amaral, J. S., Trindade, T., and Daniel-Da-Silva, A. L. (2021). On the efficient removal, regeneration and reuse of quaternary chitosan magnetite nanosorbents for glyphosate herbicide in water. *J. Environ. Chem. Eng.* 9, 105189. doi:10.1016/j.jece.2021.105189

Son, Y.-J., Hwang, I.-K., Nho, C. W., Kim, S. M., and Kim, S. H. (2021). Determination of carbohydrate composition in mealworm (*Tenebrio molitor* L.) larvae and characterization of mealworm chitin and chitosan. *Foods* 10, 640. doi:10.3390/foods10030640

Tarique, J., Sapuan, S., Aqil, N., Farhan, A., Faiz, J., and Shahrizan, S. (2023). A comprehensive review based on chitin and chitosan composites. *Compos. Aquatic Environ.*, 15–66. doi:10.1007/978-981-19-5327-9_1

Teli, M., and Sheikh, J. (2012). Extraction of chitosan from shrimp shells waste and application in antibacterial finishing of bamboo rayon. *Int. J. Biol. Macromol.* 50, 1195–1200. doi:10.1016/j.ijbiomac.2012.04.003

Thambiliyagodage, C., Jayanetti, M., Mendis, A., Ekanayake, G., Liyanaarachchi, H., and Vigneswaran, S. (2023). Recent advances in chitosan-based applications—a review. *Materials* 16, 2073. doi:10.3390/ma16052073

Torres, F. G., Troncoso, O. P., Pisani, A., Gatto, F., and Bardi, G. (2019). Natural polysaccharide nanomaterials: an overview of their immunological properties. *Int. J. Mol. Sci.* 20, 5092. doi:10.3390/ijms20205092

Yan, D., Li, Y., Liu, Y., Li, N., Zhang, X., and Yan, C. (2021). Antimicrobial properties of chitosan and chitosan derivatives in the treatment of enteric infections. *Molecules* 26, 7136. doi:10.3390/molecules26237136

Yilmaz Atay, H. (2019). Antibacterial activity of chitosan-based systems. *Funct. chitosan drug Deliv. Biomed. Appl.*, 457–489. doi:10.1007/978-981-15-0263-7_15

Zainol Abidin, N. A., Kormin, F., Zainol Abidin, N. A., Mohamed Anuar, N. A. F., and Abu Bakar, M. F. (2020). The potential of insects as alternative sources of chitin: an overview on the chemical method of extraction from various sources. *Int. J. Mol. Sci.* 21, 4978. doi:10.3390/ijms21144978

Zhu, L. F., Chen, X., Wu, Z., Wang, G., Ahmad, Z., and Chang, M. W. (2020). Optimization conversion of chitosan from Ganoderma lucidum spore powder using ultrasound-assisted deacetylation: influence of processing parameters. *J. Food Process. Preserv.* 44, e14297. doi:10.1111/jfpp.14297

frontiers | Frontiers in Chemistry

TYPE Original Research
PUBLISHED 30 August 2024
DOI 10.3389/fchem.2024.1433004

OPEN ACCESS

EDITED BY
Cristina Leonelli,
University of Modena and Reggio Emilia, Italy

REVIEWED BY
Kazi Hanium Maria,
University of Dhaka, Bangladesh
Omer Kaygili,
Firat University, Türkiye

*CORRESPONDENCE
Hafeez Anwar,
hafeez.anwar@gmail.com
Karim Khan,
karim_khan_niazi@yahoo.com

RECEIVED 15 May 2024
ACCEPTED 06 August 2024
PUBLISHED 30 August 2024

CITATION
Hameed A, Asghar A, Shabbir S, Ahmed I, Tareen AK, Khan K, Hussain G, Awaji MY and Anwar H (2024) A detailed investigation of rare earth lanthanum substitution effects on the structural, morphological, vibrational, optical, dielectric and magnetic properties of Co-Zn spinel ferrites.
Front. Chem. 12:1433004.
doi: 10.3389/fchem.2024.1433004

A detailed investigation of rare earth lanthanum substitution effects on the structural, morphological, vibrational, optical, dielectric and magnetic properties of Co-Zn spinel ferrites

Anam Hameed[1], Ali Asghar[2], Saqib Shabbir[1], Ishfaq Ahmed[1,3], Ayesha Khan Tareen[4], Karim Khan[2]*, Gulzar Hussain[1], Majed Yousef Awaji[5,6] and Hafeez Anwar[1]*

[1]Department of Physics, University of Agriculture Faisalabad, Faisalabad, Pakistan, [2]Shenzhen University, Shenzhen, China, [3]School of Materials Science and Engineering, Harbin Institute of Technology, Harbin, China, [4]Dongguan University of Technology, Dongguan, Saudi Arabia, [5]Department of Physics, Faculty of Science, Jazan University, Jazan, Saudi Arabia, [6]Institute Jean Lamour, University of Lorraine, Nancy, France

In this work, $Co_{0.5}Zn_{0.5}La_xFe_{2-x}O_4$ ($0.00 \leq x \leq 0.10$) spinel ferrites were synthesized using the sol-gel auto-combustion method. X-ray diffraction (XRD) analysis and Rietveld refinement confirmed the presence of a cubic spinel structure. The crystallite size was estimated to be between 17.5 nm and 26.5 nm using Scherrer's method and 31.27 nm–54.52 nm using the Williamson–Hall (W-H) method. Lattice constants determined from XRD and Rietveld refinement ranged from (8.440 to 8.433 Å and 8.442 to 8.431 Å), respectively. Scanning electron microscopy (SEM) revealed a non-uniform distribution of morphology with a decrease in particle size. The bandgap values decreased from 2.0 eV to 1.68 eV with increasing rare earth (La^{3+}) doping concentration. Fourier-transform infrared (FT-IR) spectroscopy confirmed the presence of functional groups and M-O vibrations. The dielectric constant and dielectric loss exhibited similar behavior across all samples. The maximum tan δ value obtained at lower frequencies. Regarding magnetic behavior, there was a decrease in magnetization from 55.84 emu/g to 22.08 emu/g and an increase in coercivity from 25.63 Oe to 33.88 Oe with higher doping concentrations. Based on these results, these materials exhibit promising properties for applications in microwave and energy storage devices.

KEYWORDS

sol-gel auto combustion, rare earth spinel ferrites, optical bandgap, dielectric materials, conductivity, magnetization

1 Introduction

Nanocrystalline spinel ferrites have garnered significant attention in the scientific community due to their distinctive structural, optical, dielectric and magnetic characteristics. These ferrites are found in applications such as sensors, supercapacitors, magnetic substances, magneto-thermal energy storage systems, magnetic drug delivery and

hypothermia therapy specifically for cancer patients (Nikam et al., 2014; Kiani et al., 2022). Among spinel ferrites, cobalt ferrite has garnered considerable research interest for medical and secondary storage device applications (Asghar et al., 2022; Mısırlıoğlu et al., 2022). With a moderate saturation magnetization, cobalt ferrite exhibits notable coercivity. The introduction of non-magnetic Zn^{2+} ions allowed tailoring of ferrite properties for various purposes (Andhare et al., 2020). Dielectric and magnetic properties of ferrites can be enhanced by incorporating trivalent rare-earth ions (Li et al., 2021). Even a modest amount of RE substitution can lead to improved dielectric and magnetic attributes in ferrites (Tanbir et al., 2020; Suo et al., 2021). For instance, replacing nanocrystalline $CoFe_2O_4$ with La, Gd, Sm, or Nd reduces the dielectric constant (ε′) with increasing RE ion concentration (Nikumbh et al., 2014). Substituting larger radius RE ions effectively has altered the ferrite's Curie temperature. Nd^{3+} ion substitution enhanced the coercivity of cobalt ferrite (Muskan et al., 2024; Reddy et al., 2022). This substitution reduced the ferrite's dielectric loss and enhanced usability. Ni ferrite's structural and magnetic traits improved significantly with rare-earth substitution (Lumina et al., 2018).

Within the lanthanides group, lanthanum (La^{3+}) stands out due to its significant atomic size, despite being non-magnetic (Mariño-Castellanos et al., 2021). The advantage of La for substitution in $Co_{0.5}Zn_{0.5}La_xFe_{2-x}O_4$ spinel ferrites is due to its relatively suitable ionic radius, chemical stability, and impact on magnetic interactions. La also has the potential to modify the electronic structure and enhance dielectric and microwave absorption properties. These factors collectively make La an ideal choice for advancing the understanding and application of rare earth-substituted ferrites. The substitution of RE with Fe^{3+} cations introduced strain into the lattice ferrites, thereby altering the crystal size. Given its singular +3 valence state, La^{3+} readily occupies octahedral [B] lattice sites within the ferrite structure, consequently modifying magneto-structural characteristics. The impact of the structure of La^{3+} ions on the magneto-structural, dielectric, and magnetic properties has been studied deeply. In La-substituted Cu-Zn ferrites, it has been observed that the dielectric constant and loss tangent increase as temperature rises (Patil et al., 2023). Furthermore, the addition of La^{3+} to Co ferrite results in alterations to the super-exchange interactions between Fe^{3+} and Fe^{2+} ions (Haque et al., 2017). The replacement of larger La^{3+} cations in Mn-Cr ferrites leads to lattice deformation, which in turn influences magnetic properties and structural characteristics (Abdellatif et al., 2018). In the case of Ni-Co ferrites, the substitution of Sm^{3+} ions diminish their magnetic features, rendering them suitable for use in recording and memory devices (Kokare et al., 2019). Lastly, the introduction of La^{3+} ions into Co ferrites results in a reduction of its magnetic attributes, rendering it superparamagnetic in nature (Gaba et al., 2018).

This research investigates the effect of rare earth element La^{3+} on the morphological, optical, dielectric and magnetic properties of $Co_{0.5}Zn_{0.5}La_xFe_{2-x}O_4$ (x = 0.00, 0.025, 0.050, 0.075, 0.10), synthesized using the auto-combustion technique. The amount of Zn concentration is fixed at 0.5 for several reasons such as maintaining a constant Zn level allowed us to systematically explore the effects of La substitution on Co-Zn ferrite. This approach ensured that any observed changes in properties were directly attributable to La substitution, yielding more consistent and comparable results. The substitution of La results in a decrease in the band gap of the prepared samples from 2.0 to 1.68 eV, making these materials promising candidates for photocatalysis. Additionally, the replacement of Fe^{3+} with non-magnetic rare earth cations weakens Fe^{3+}-Fe^{3+} interactions, affecting not only the magnetic properties but also inducing changes in the microstructures. The peak values of the loss tangent (tanδ) indicate an enhancement in both microwave absorption and dielectric properties (Ren and Xu, 2014).

2 Materials and method

2.1 Reagents

The synthesis of $Co_{0.5}Zn_{0.5}La_xFe_{2-x}O_4$ (x = 0.00, 0.025, 0.050, 0.075, 0.10) involves the utilization of the following components in their respective forms: ferric nitrate non-ahydrate $[Fe(NO_3)_3{\cdot}9H_2O]$, cobalt nitrate hexahydrate $[Co(NO_3)_2{\cdot}6H_2O]$, ammonium hydroxide (NH_4OH), zinc nitrate hexahydrate $[Zn(NO_3)_2{\cdot}6H_2O]$, lanthanum nitrate hexahydrate $[La(NO_3)_3{\cdot}6H_2O]$ and citric acid ($C_6H_8O_7$). The solutions are prepared using deionized water. All compounds are directly used without any additional processing.

2.2 Experimental section

The $Co_{0.5}Zn_{0.5}La_xFe_{2-x}O_4$ (x = 0.00, 0.025, 0.050, 0.075, 0.10) spinel ferrites were prepared using the sol-gel auto combustion technique, as illustrated in Figure 1. The sol-gel auto-combustion method is distinguished by its versatility and efficiency in synthesizing spinel ferrites, allowing for precise control over composition, morphology, and uniformity. The synthesis involved the use of $La(NO_3)_3{\cdot}6H_2O$, $Zn(NO_3)_2{\cdot}6H_2O$, $Fe(NO_3)_3{\cdot}9H_2O$ and $Co(NO_3)_2{\cdot}6H_2O$ based on stoichiometric calculations. These salts were mixed in distilled water (DI) in accordance with stoichiometric ratios and then subjected to agitation to achieve a homogeneous solution. The prepared solution was placed on a magnetic stirrer and citric acid was added to the solution to act as a fuel agent alongside the nitrates.

The solution's pH was sustained at 7 through the gradual addition of ammonia solution. Subsequently, the temperature was raised from 100°C to 110°C until the sample transformed into a gel-like state. Stirring was sustained until combustion took place. A comparison of the synthesis conditions and parameters for the present study with those from prior literature is presented in Table 1. The resulting ash was obtained and the prepared samples were sintered at 750°C for 4 h in a furnace to remove volatile substances like moisture and other undesirable elements. The sintered powders were then subjected to analysis using various procedures, including X-ray diffraction, scanning electron microscopy, energy-dispersive X-ray analysis, Fourier-transform infrared spectroscopy, UV-visible spectroscopy, LCR measurements and vibrating sample magnetometry to characterize their properties.

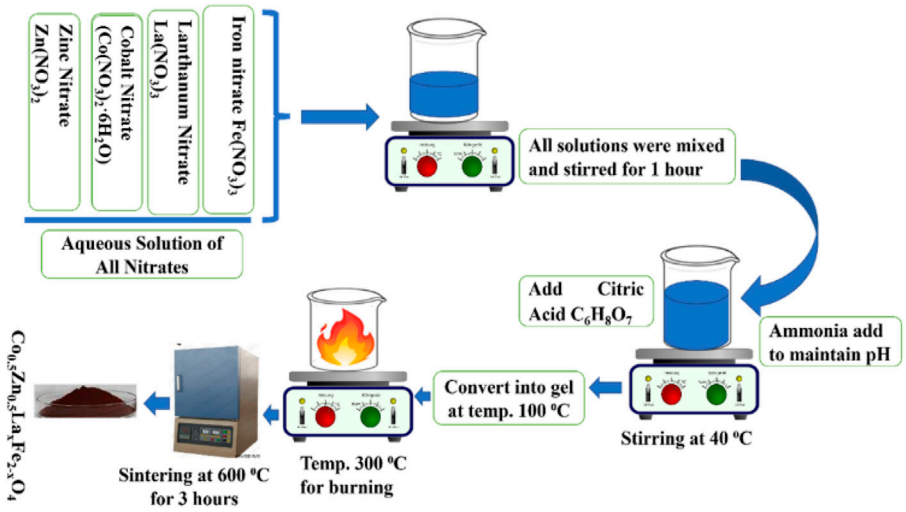

FIGURE 1
Preparation of Lanthanum substitution cobalt zinc spinel ferrites.

TABLE 1 Comparison of synthesis conditions/parameters for current work with previous literature.

Material	Method of preparation	Dissolving media	Sintering temperature (°C)	Time of sintering (h)	Ref
$Co_{0.5}Zn_{0.5}La_xFe_{2-x}O_4$	Sol-gel	Distilled water	—	—	Gilani et al. (2020)
$Zn_{0.5}Co_{0.5}La_xFe_{2-x}O_4$	Co-precipitation	De-ionized water	750	—	Aslam et al. (2021)
$Co_{0.1}Zn_{0.9}La_xFe_{2-x}O_4$	Citrate gel auto-combustion	Double-distilled water	500	4	Sumalatha et al. (2022)
La-substituted Zn–Co–La ferrite	sol-gel	—	1,400	5	Dippong and Mereu (2024)
$Co_{0.5}Zn_{0.5}La_xFe_{2-x}O_4$	sol-gel auto combustion	Distilled water	600	4	Kulkarni and Rathod (2016)
$Co_{0.7}Zn_{0.3}La_xFe_{2-2x}O_4$	Sol-gel route	Deionized water	400	—	Mugutkar et al. (2022)
$Co_{0.65}Zn_{0.35}La_xFe_{2-x}O_4$	Flash method	—	800	—	Altarawneh et al. (2023)
$Co_{0.7}Zn_{0.3}La_xFe_{2-x}O_4$	Sol gel auto ignition route	Aqueous solutions	450	—	Mugutkar et al. (2020)
$Co_{0.5}Zn_{0.5}La_xFe_{2-x}O_4$	Auto-combustion	Distilled water	750	1	Current work

2.3 Characterization

The X-ray diffractometer (XRD), which operated with a precise wavelength (λ) of 0.154 nm and covered a 2θ range spanning from 20° to 80°, was utilized for capturing diffraction patterns. The scanning electron microscope played a pivotal role in elucidating external appearance and crystallographic structure. FTIR spectroscopy, specifically using a Perkin instrument, was employed to validate the absorption bands (ν_1, ν_2) within the wavenumber range of 4,000 to 400 cm^{-1}. The samples' absorption spectra were documented employing the UV-Vis spectrophotometer PG (Model T-80). Dielectric measurements were performed at room temperature (RT) using the IM-3536 series LCR Meter and Impedance Analyzer. Lastly, a VSM investigation was conducted to ascertain the M-H hysteresis loops of $Co_{0.5}Zn_{0.5}La_xFe_{2-x}O_4$.

3 Results and discussion

3.1 Structural analysis

Figure 2A displays the X-ray diffraction pattern of as-prepared spinel ferrites synthesized through the auto-combustion process. The discernible peaks (220), (110), (311), (400), (422), (511), (440), (533) and (622) significantly confirmed the existence of a single-phase cubic structure, corresponding to the JCPDS file no: 22-1086 (Guo et al., 2022). In Figure 2B, the peak (311) exhibited a shift towards a higher angle. It is worth noting that the preparation of this material is reproducible, as it prepared many times for other investigations. To further investigate crystal structures, Rietveld refinement plots were generated for synthesized spinel ferrites, refer to Figures 3A–E. These findings align with prior data,

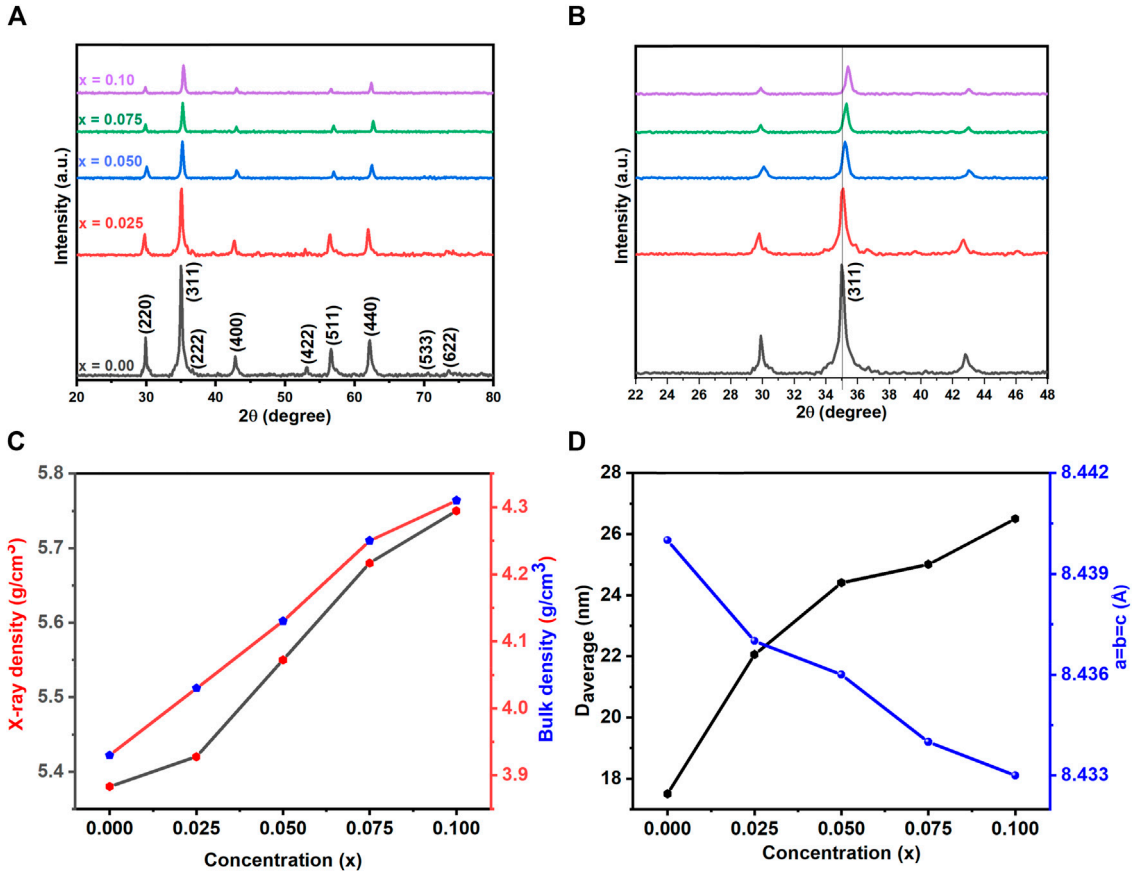

FIGURE 2
(A) XRD pattern **(B)** enlarged view of XRD **(C)** effect of La concentration on $D_{average}$, Lattice constant (a = b = c) **(D)** $\rho_{x\text{-}ray}$ and bulk density of $Co_{0.5}Zn_{0.5}La_xFe_{2-x}O_4$ (x = 0.00, 0.025, 0.050, 0.075, 0.10) spinel ferrites.

providing further assurance of the nanocomposites' composition and crystal structures. For the Rietveld refinement process, the FULLPROF software was utilized, and the Thompson-Cox-Hastings pseudo-Voigt function was employed to model the Bragg peaks (Abbas et al., 2023; Ahmed et al., 2023; Shabbir et al., 2024). A polynomial function with six coefficients was utilized for background calculation. The parameters used for fitting, including weighted profile R-factor (R_{wp}), unweighted profile R-factor (R_{exp}), GoF and chi-square (χ^2), have been recorded in Table 2.

The weighted profile R-factor (R_{wp}) in the provided data ranges from 20.4 to 25.6, indicating a trend of improvement in the fit between observed and calculated diffraction patterns as the concentration of Co-Zn spinel ferrites increases. Correspondingly, the expected R-factor (R_{exp}) values decrease from 10.5 to 8.2, supporting the notion of enhanced fit with higher concentrations. The chi-square (χ^2) values, ranging from 1.23 to 1.58, are relatively close to 1, suggesting good agreement between observed and calculated data. Notably, the lowest R_{wp}, R_{exp}, and χ^2 values are observed at a concentration of 0.025, indicating that the crystal structure refinement at this specific concentration yields the best agreement with experimental data. This concentration appears to be optimal for achieving an improved fit in the context of the investigated Co-Zn spinel ferrites.

Notably, at x = 0.05, a relatively low-intensity peak (110) appears around 33°, indicating the presence of the α-Fe_2O_3 phase. This might be associated with the dissimilarity in ionic radius between the substituted rare earth cations and the original Fe^{3+}. The XRD graphs affirmed the development of a solitary geometric cubic pattern for lanthanum-substituted cobalt spinel ferrites, without any secondary phase. Scherrer equation (mentioned as Equation 1) was utilized to determine the crystallite size (D) of the synthesized samples (Ahmed et al., 2022; Hussain et al., 2022):

$$D = \frac{K\lambda}{\beta Cos\,\theta} \quad (1)$$

where k, λ, β and θ represent shape factor, wavelength 1.54 (Å), peak broadening, and diffraction angle, respectively. The values of crystallite size increase with increasing the lanthanum substitution as shown in Figure 2C. With increasing RE (La) doping concentration, the crystallite size generally increases, signifying potential effects on magnetic and electrical properties, and suggesting alterations in synthesis or annealing conditions. The following Equation 2 is used to measure micro-strain:

$$\beta = 4 \times \varepsilon \times \tan\theta \quad (2)$$

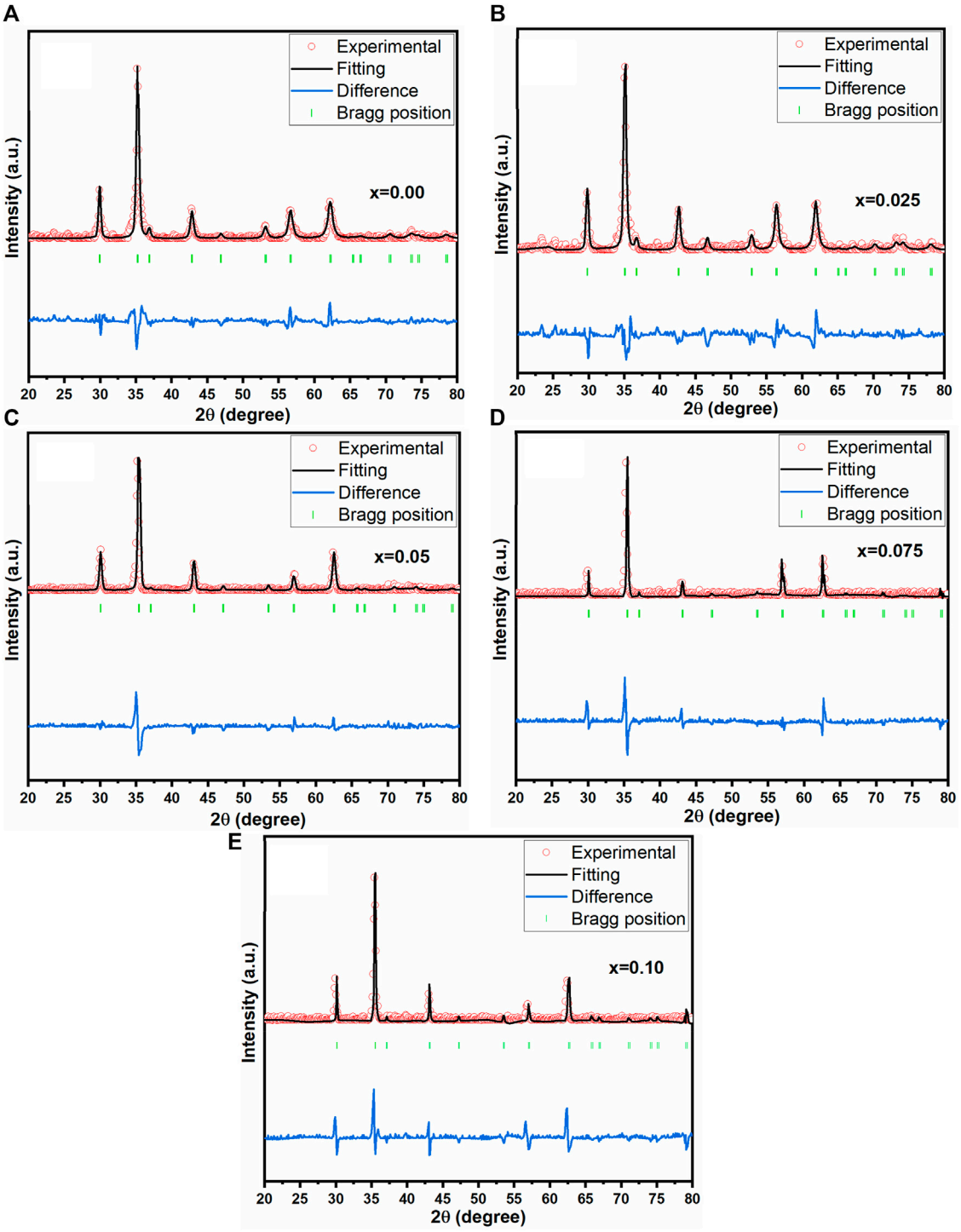

FIGURE 3
Rietveld refined pattern of the $Co_{0.5}Zn_{0.5}La_xFe_{2-x}O_4$ **(A)** x = 0.00 **(B)** x = 0.025 **(C)** x = 0.05 **(D)** x = 0.075 **(E)** x = 0.10.

The observed peak broadening in Williamson–Hall analysis results from the summation of Equations 1, 2, as expressed by the following formulation (Equation 3):

$$\beta \times \cos\theta = (0.9\lambda/D) + (4 \times \text{Strain} \times \sin\theta) \quad (3)$$

The straight line represents the slope value obtained from the relationship between β × cosθ and 4sinθ. Micro-strain is then calculated based on the slope values Figures 4A–E. The lattice constant of prepared samples was calculated by the following Equation 4:

$$\frac{1}{d^2} = \frac{h^2}{a^2} + \frac{k^2}{b^2} + \frac{l^2}{c^2} \quad (4)$$

In the equation, where h, k, l, and d denote the Miller indices and d-spacing, respectively. The lattice constant's trend is observed to

TABLE 2 Data was obtained through Rietveld refinement for prepared samples.

Concentration	R_{wp} (%)	R_{exp} (%)	χ^2	GoF	a = b = c (Å)	Volume (Å)^3
0.00	25.6	10.5	2.43	15.2	8.442	601.639
0.025	20.4	8.2	2.48	13.7	8.438	600.784
0.05	23.3	9.7	2.40	17.5	8.436	600.357
0.075	24.1	9.9	2.43	19.1	8.435	600.143
0.10	22.2	8.6	2.58	16.8	8.431	599.290

decrease with increasing lanthanum substitution, as depicted in Figure 2C.

This phenomenon can be ascribed to the existence of larger RE cations, which have an ionic radius of (1.061 Å), in contrast to the smaller ionic radius of Fe^{3+} ions (0.67 Å) (Mahmood and Maqsood, 2021). The unit cell volume (V_{cell}) of the synthesized samples was calculated using the following Equation 5:

$$V = a^3 \tag{5}$$

An observable trend emerged as lanthanum substitution increased, resulting in a decrease in the unit cell volume (V_{cell}) values from 605 (Å)^3 to 570 (Å)^3 at x = 0.00 to 0.10, as detailed in Table 3.

The X-ray density (ρ_x) and bulk density of the synthesized samples were computed using the following Equations 6, 7 (Shoba and Kaleemulla, 2017; Kalam et al., 2018):

$$\rho_x = \frac{nA}{VN_A} \tag{6}$$

$$\rho_b = \frac{m}{\pi r^2 h} \tag{7}$$

where n, A, N_A, and V represent the number of atoms in the unit cell volume, molar mass, Avogadro's number, and unit cell volume, respectively, of the spinel lattice.

X-ray density and bulk density show a rise with La doping, attributed to the increased atomic mass of La relative to Co and Zn, influencing the overall density and consequently, structural and material properties, as illustrated in Figure 2D.

The specific values for X-ray density and bulk density for the prepared samples are indicated in Table 3. Additionally, porosity and specific surface area (S) can be calculated employing Equations 8, 9:

$$P = \left[1 - \frac{\rho_b}{\rho_x}\right] \times 100 \tag{8}$$

$$S = \frac{6000}{\rho_x \times D} \tag{9}$$

A slight reduction in porosity is noted, potentially contributing to enhanced mechanical strength and density, though careful consideration of doping levels is essential. Strain values (see Table 3) indicated the changes in lattice structure, impacting electrical and magnetic properties. Moreover, the decrease in specific surface area with increased La doping suggests reduced reactivity, a factor of significance in applications where surface properties, such as catalysis, play a crucial role. The arrangement of cations within the [A] and [B] sites significantly influenced the magnetic, structural and dielectric characteristics of ferrites (Gore et al., 2017; Islam et al., 2022). The cation distribution within ferrites can be determined using XRD data, with analysis conducted on planes such as (2 2 0), (4 0 0), (4 2 2) and (4 4 0) (Sanchez-Lievanos et al., 2021; Hasan and Azhdar, 2022). Structural factors for these (hkl) planes were computed using established equations (Gómez et al., 2018; Guo et al., 2022). Within the lattice, Zn^{2+} ions prefer occupying the (A) site, rare earth cations favour the [B] site, while both Co^{2+} and Fe^{3+} ions can occupy either [A] or [B] sites (Andhare et al., 2020; Mugutkar et al., 2020; Sanchez-Lievanos et al., 2021). Cation distribution results for $Co_{0.5}Zn_{0.5}La_x\ Fe_{2-x}O_4$ spinel ferrites are presented in Table 4.

The distribution of cations was determined through Rietveld refinement, aligning closely with the estimated values. Introducing rare earth cations at the [B] site led to a migration of Co^{2+} ions to the [A] site, accompanied by a slight shift of Fe^{3+} ions from the [A] to the [B] site. As RE (La^{3+}) substitution increased in $Co_{0.5}Zn_{0.5}La_x\ Fe_{2-x}O_4$ spinel ferrites, there was a gradual rise in the proportion of Fe^{3+} ions at the [B] site, diminishing their presence at the [A] site. Utilizing equations from established sources (Gómez et al., 2018), we calculated parameters such as a_{th}, r_A, and r_B for [A] and [B], as detailed in Table 5. The values of a_{th} closely align with the experimentally calculated "a", validating the predicted cation distribution.

As the RE (La^{3+}) substitution increased at the [B] site, the ionic radii at that site also increased. Similarly, at the [A] site, the ionic radii rise with increasing small concentrations of Co^{2+}. Consequently, both the [A] and [B] sites experience lattice expansion. An oxygen parameter, represented by "u", helps distinguish between the expansions at [B] and [A] sites. Ideally, both sub-lattices should expand in the same ratio, with u = 3/8 = 0.375 being the expected value. In the current $Co_{0.5}Zn_{0.5}La_xFe_{2-x}O_4$ spinel ferrites, a value of u = 0.375 indicates significant expansion in the tetrahedral lattice, signifying the movement of oxygen ions from their ideal locations along the body diagonal of the cubic lattice (Aslam et al., 2021).

The addition of RE (La^{3+}) ions into Co-Zn spinel ferrites does lead to a redistribution of cations among the 8 tetrahedral and 16 octahedral sites. The proposed cation arrangement is detailed in Table 5. In this configuration, both [A] and [B] sites are occupied by Co^{2+} and Fe^{3+} ions, while Zn^{2+} ions are specifically situated at the tetrahedral sites. Notably, due to their larger ionic radii, RE (La^{3+}) ions exclusively occupy positions r_A and r_B at the [A] and [B] sites, respectively. As the RE (La^{3+}) concentration increases, the value of r_B also increases, implying an expansion at the [B] site. The calculated a_{th} values show an increase from 8.493 to 8.550 with La^{3+} ion

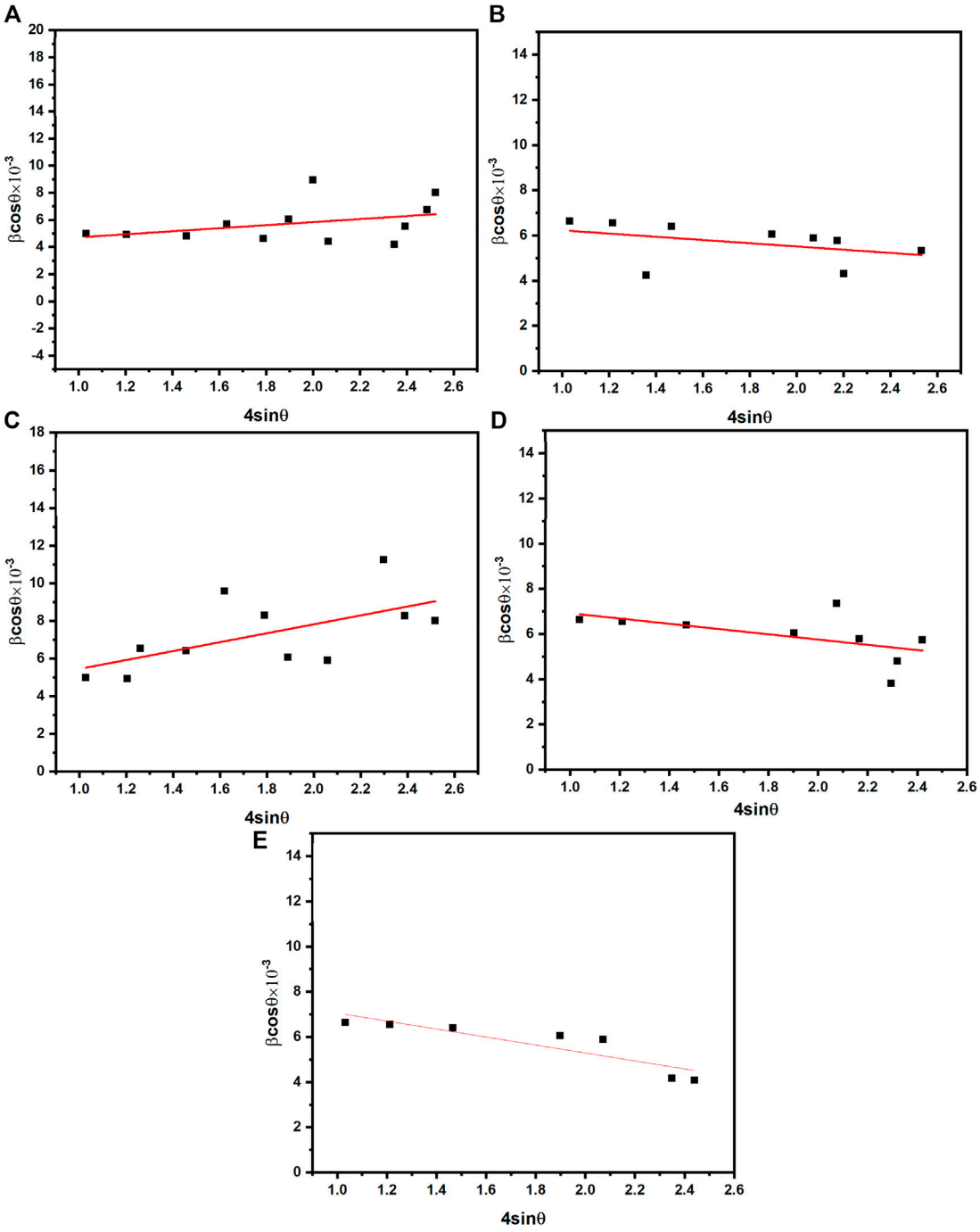

FIGURE 4
(A–E) The W-H plots of $Co_{0.5}Zn_{0.5}La_x Fe_{2-x}O_4$ (x = 0.00, 0.025, 0.05, 0.075, 0.10).

substitution (as seen in Table 5). This increase can be linked to the challenge of replacing smaller ferric ions with larger RE (La^{3+}) ions within the lattice sites. Consequently, only a limited number of rare earth cations are retained in proximity to the grain boundaries.

This discrepancy may stem from disparities between experimental and theoretical lattice parameters. The oxygen parameter (u) was calculated using established formulas based on prior research (Gómez et al., 2018; Islam et al., 2022; Xue et al., 2022). As a result, metal ions face a more significant challenge in occupying the [A] site as opposed to the [B] site. The shifting of oxygen ions contributed to the expansion of the [A] site and the contraction of the [B] site, a phenomenon that is demonstrated by variations in the oxygen positional parameter (u). With an increase in RE (La^{3+}) substitution, both the calculated u and inversion parameters experience an increase. The shifts in the calculated R_A and R_B values are contingent on the a_{th} parameter, as detailed in Table 5. Varied magnetic interactions, denoted as (A-A), (A-B) and (B-B) as explained later, result from differences in cation-cation and cation-anion bond lengths (Islam et al., 2022). The

TABLE 3 Different parameters of $Co_{0.5}Zn_{0.5}La_x Fe_{2-x}O_4$ (x = 0.00, 0.025, 0.05, 0.075, 0.10) spinel ferrites calculated from XRD data.

Concentration	0.00	0.025	0.05	0.075	0.10
Crystallite size D (nm)	17.5	22.06	24.41	25.01	26.5
Crystallite size from W-H plot	31.27	32.16	37.13	45.4	54.52
a = b = c (Å)	8.440	8.437	8.436	8.434	8.433
Unit cell Volume V $(Å)^3$	601.211	600.570	600.357	599.930	599.716
X-ray density (ρ) g/cm^3	5.38	5.42	5.55	5.68	5.75
Bulk density (ρB) g/cm^3	3.93	4.03	4.13	4.25	4.31
Porosity (%)	26.96	25.65	25.59	25.18	25.05
Strain ε	26.60	27.87	28.14	31.28	32.67
Specific surface area S (m^2/g)	63.72	50.18	44.29	42.24	39.38

TABLE 4 Cation distribution from XRD and Rietveld refinement of $Co_{0.5}Zn_{0.5}La_xFe_{2-x}O_4$ (x = 0.00, 0.025, 0.05, 0.075, 0.10) spinel ferrites.

Concentration	XRD	Rietveld refinement
0.00	$(Zn_{0.4}Fe_{0.6})$ $[Co_{0.8}Fe_{1.2}]$	$(Zn_{0.3999}Fe_{0.6})$ $[Co_{0.7999}Fe_{1.2}$
0.025	$(Zn_{0.4}Co_{0.1}Fe_{0.5})$ $[Co_{0.7}Fe_{1.275}La_{0.025}]$	$(Zn_{0.3998}Co_{0.0999}Fe_{0.4998})$ $[Co_{0.6998}Fe_{1.2749}La_{0.0249}]$
0.05	$(Zn_{0.4}Co_{0.2}Fe_{0.4})$ $[Co_{0.6}Fe_{1.35}La_{0.05}]$	$(Zn_{0.3998}Co_{0.1997}Fe_{0.3999})$ $[Co_{0.5998}Fe_{1.349}La_{0.0499}]$
0.075	$(Zn_{0.4}Co_{0.3}Fe_{0.3})$ $[Co_{0.5}Fe_{1.425}La_{0.075}]$	$(Zn_{0.3999}Co_{0.2998}Fe_{0.2999})$ $[Co_{0.4999}Fe_{1.4249}La_{0.0749}]$
0.10	$(Zn_{0.4}Co_{0.4}Fe_{0.2})$ $[Co_{0.4}Fe_{1.5}La_{0.10}]$	$(Zn_{0.3998}Co_{0.3999}Fe_{0.1999})$ $[Co_{0.3998}Fe_{1.4499}La_{0.0999}]$

TABLE 5 Theoretical parameters of $Co_{0.5}Zn_{0.5}La_x Fe_{2-x}O_4$ (x = 0.00, 0.025, 0.05, 0.075, 0.10).

Concentration	0.00	0.025	0.05	0.075	0.10
r_A (Å)	0.698	0.705	0.713	0.720	0.728
r_B (Å)	0.700	0.701	0.702	0.703	0.704
a_{th} (Å)	8.493	8.507	8.522	8.536	8.550
u (Å)	0.3872	0.3875	0.3877	0.3881	0.3883
δ (Å)	0.0122	0.0125	0.0127	0.0131	0.0133
R_A (Å)	1.8613	1.8648	1.8684	1.8723	1.8758
R_B (Å)	2.0242	2.0257	2.0292	2.0308	2.0360
R (Å)	6.2894	6.3037	6.3231	6.3398	6.3592
R' (Å)	5.7028	5.7103	5.7150	5.7206	5.7280
R" (Å)	3.0076	3.0124	3.0194	3.0230	3.0313

TABLE 6 Cation-anion and cation-cation distances for $Co_{0.5}Zn_{0.5}La_x Fe_{2-x}O_4$ (x = 0.00, 0.025, 0.05, 0.075, 0.10).

Concentration	0.0	0.025	0.05	0.075	0.10
p (Å)	2.0189	2.0189	2.0217	2.0257	2.0297
q (Å)	2.0175	2.0243	2.0320	2.0403	2.0480
r (Å)	3.8632	3.8763	3.8910	3.9069	3.9217
s (Å)	3.7350	3.7409	3.7517	3.7580	3.7679
b (Å)	3.0016	3.0052	3.0087	3.0158	3.0228
c (Å)	3.5197	3.5239	3.5280	3.5363	3.5446
d (Å)	3.6762	3.6806	3.6849	3.6935	3.7022
e (Å)	5.5144	5.5209	5.5274	5.5403	5.5533
f (Å)	5.1990	5.52051	5.2112	5.2235	5.2357

measurements of R, R′ and R″ were determined using the subsequent equation (Gore et al., 2017; Islam et al., 2022). The values of R, R′ and R″ increased by increasing the concentration of La^{3+} ion and the value of a_{th}. The intensity of magnetic interactions is mostly determined by interionic distances and bond angles (Gore et al., 2017).

The calculations of the distances between cation-anion and cation-cation ions were performed using the following mathematical expressions (Gómez et al., 2018; Islam et al., 2022). When the concentration of La^{3+} ion increases the value of interionic distances also increases as given in Table 6. The bond angles θ_1, θ_2, θ_3, θ_4, and θ_5 were determined from the equations referenced in Islam et al. (2022) and Gómez et al. (2018). A rise in the concentration of RE (La) was seen to result in decreased values for θ_1, θ_2, and θ_5, indicating a reduction in the intensity of A-A and A-B interactions. Conversely, B-B interactions appeared to strengthen, as indicated by the increased values of θ_3 and θ_4 (refer to Table 7). The hopping lengths L_A and L_B at the A and B sites were calculated using the relationships provided in Anwar et al. (2020), and Table 7 presents the corresponding values for

TABLE 7 Values of bond angles for $Co_{0.5}Zn_{0.5}La_x Fe_{2-x}O_4$ (x = 0.00, 0.025, 0.05, 0.075, 0.10).

Concentration	0.00	0.025	0.05	0.075	0.10
θ_1	121.3657	121.2786	120.9774	120.8505	120.7437
θ_2	136.9870	136.6271	136.0379	135.6923	135.4223
θ_3	127.2216	127.3945	127.4305	127.4594	127.4733
θ_4	126.3630	126.4841	126.5126	126.6481	126.6767
θ_5	69.4209	69.1881	68.9120	68.7277	68.5801
L_A (Å)	3.6759	3.6794	3.6806	3.6915	3.6997
L_B (Å)	3.0014	3.0045	3.0118	3.0148	3.0217

L_A and L_B. Notably, in Co-ferrite, both L_A and L_B exhibited significant increases with the rising concentration of La^{3+}.

3.2 Morphological and elemental analysis

In Figures 5A–C, the microstructures of the prepared samples with concentrations x = 0.0, 0.05 and 0.10 are presented. The micrographs revealed a uniform distribution of grains on the surface and a noticeable trend of reduction in grain size with increased lanthanum substitution. This size reduction can be attributed to the larger ionic radius of lanthanum in comparison to iron, resulting in a notable increase in particle size as the lanthanum content increased. Additionally, particle agglomeration becomes more prominent as lanthanum concentration increases (Thakur et al., 2019; Kadam et al., 2020). Energy-dispersive X-ray analysis was conducted to evaluate the elemental composition of $Co_{0.5}Zn_{0.5}La_{0.05}Fe_{1.95}O_4$, as depicted in Figure 5D. The analysis confirmed the absence of contaminants in the prepared sample. Consequently, the current synthesis method has yielded mixed ferrites with a high degree of purity and excellent stoichiometry.

3.3 FT-IR and UV visible spectroscopy analysis

In Figure 6A, the FTIR spectra of $Co_{0.5}Zn_{0.5}La_xFe_{2-x}O_4$ (x = 0.00, 0.05 and 0.10) spinel ferrites are displayed and analyzed within the range of 400–4,000 cm^{-1}. Notably, two distinctive bands are observed in ferrite materials, both with widths of less than 1,000 cm^{-1}, corresponding to the vibrations of the M-O bond. Upon the substitution of RE (La^{3+}), the frequency bands ν_1 and ν_2 undergo shifts in their positions, indicating a redistribution of cations. The equation found in Mohamed and Wahba (2014), Jeevanantham et al. (2021), Ahmed et al. (2022) is utilized for the computation of the force constant (K) of ions at both tetrahedral and octahedral sites. Table 8 displays the calculated K_o and K_t values for the [B] and [A] sites, respectively. As the RE (La^{3+}) substitution increased, the force constants K_t and K_o also experienced an increase, changing from 22.52 N/m to 23.26 N/m at the [A] site and from 26.62 N/m to 25.70 N/m at the [B] site (Ahmed et al., 2022).

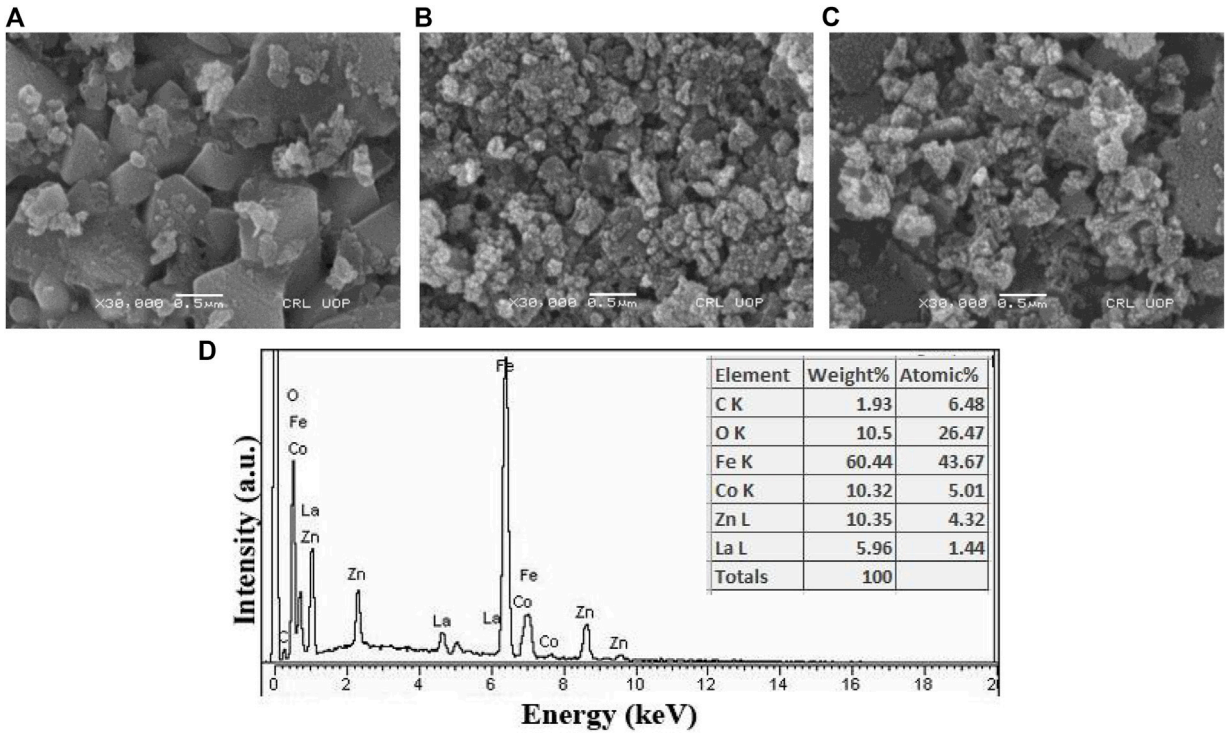

FIGURE 5
SEM images of $Co_{0.5}$ $Zn_{0.5}$ $La_xFe_{2-x}O_4$ at **(A)** x = 0.00 **(B)** x = 0.05 **(C)** x = 0.10 **(D)** EDX spectrum (x = 0.05).

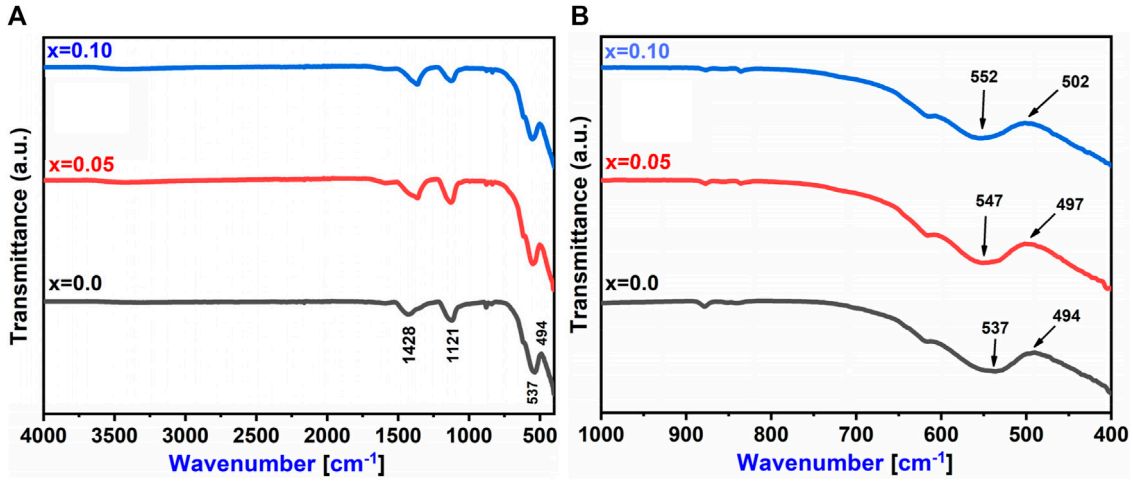

FIGURE 6
(A) FTIR spectra **(B)** Metal oxide bond of $Co_{0.5}Zn_{0.5}La_xFe_{2-x}O_4$ (x = 0.00, 0.05, 0.10).

TABLE 8 The values of vibrational mode frequencies (ν_1 and ν_2) and 'Force constants (K_t, K_o and K)' for $Co_{0.5}Zn_{0.5}La_xFe_{2-x}O_4$ (x = 0.00, 0.05, and 0.10) spinel ferrites.

Concentration	0.00	0.05	0.10
ν_1 (cm^{-1})	494	497	502
ν_2 (cm^{-1})	537	547	552
K_t (N/m)	22.52	22.80	23.26
K_o (N/m)	26.62	27.23	28.13
K	24.57	25.01	25.70

Figure 6B further confirmed the presence of spinel ferrite structure within the synthesized samples, as the M-O bonds are detected under 1,000 cm^{-1}. Notably, the absence of hydroxyl groups signifies that the prepared samples are fully dried (Hussain et al., 2022). In the ultraviolet-visible spectrum analysis of prepared samples, scanning of the ultraviolet-visible spectrum was conducted across the range of 200–800 nm illustrated in Figure 7A. It is observed that the optical energy band gap diminished as the lanthanum content in the system increased. This behavior aligns with findings from Sati et al. (2014), which indicate that the optical band gap in nano ferrites is influenced by factors such as dopant concentration, structural parameters, particle size, surface effects, lattice stresses, and contaminants. The value of the optical band gap ($E_{g,}$) for the prepared samples was determined using a Tauc plot. As shown in Figures 7B–D, the energy bandgap ($E_{g,}$) decreased with the rise in lanthanum substitution, ranging from 2.0 eV to 1.68 eV as x varies from 0.00 to 0.10 (Cyriac et al., 2020; Ahilandeswari et al., 2022).

The bandgap in spinel ferrites critically determines their electrical and magnetic characteristics, serving as the energy gap between the valence and conduction bands in their electronic structure. A reduced bandgap enhances electrical conductivity in these semiconducting materials, rendering them suitable for specific electronic applications. This modulation also affects the alignment of electrons, influencing magnetic properties such as magnetic moment and susceptibility, making the material more responsive to external magnetic fields. In electronic devices like magnetic sensors and microwave devices, tuning the bandgap customizes the electrical and magnetic properties of spinel ferrites to meet specific application requirements.

Furthermore, spinel ferrites with adjusted bandgaps can exhibit multifunctional behaviour, combining magnetic and semiconducting features in a single material, advantageous for advanced electronic and spintronic devices. The thermoelectric performance of spinel ferrites is impacted by bandgap modulation, suggesting potential applications in thermoelectric devices for energy conversion.

3.4 Dielectric analysis

Figure 8A illustrates the behavior of the real component of the dielectric constant (ε′) for $Co_{0.5}Zn_{0.5}La_xFe_{2-x}O_4$ (x = 0.00, 0.05, 0.10) across a frequency range from 10 kHz to 8 MHz. The real component of the dielectric constant (ε′) is indicative of the material's ability to store electric energy. The graph reveals that at lower frequencies, the dielectric constant (ε′) showed maximum value. Conversely, at higher frequencies, all samples exhibited a consistent behavior that remains unaffected by the applied field. This behavior is in line with the typical conduct of normal ferrites (Maksoud et al., 2020; Ansari et al., 2021; Mahmood and Maqsood, 2021). The experimental results for the dielectric constant were compared with the theoretically calculated results obtained using Shah's function depicted in Figures 8B–D.

The relaxation phenomenon is rooted in the exchange of ions between Fe^{2+} and Fe^{3+} as well as space charge polarization. Within ferrites, the conduction mechanism of grain and grain boundaries is explained by the Maxwell-Wagner model and Koop's hypothesis (Jnaneshwara et al., 2014; Kumari et al., 2014). Specifically, at lower frequencies, the obvious peak value of ε′ can be attributed to the impact of grain boundaries. As frequency increases, this behavior

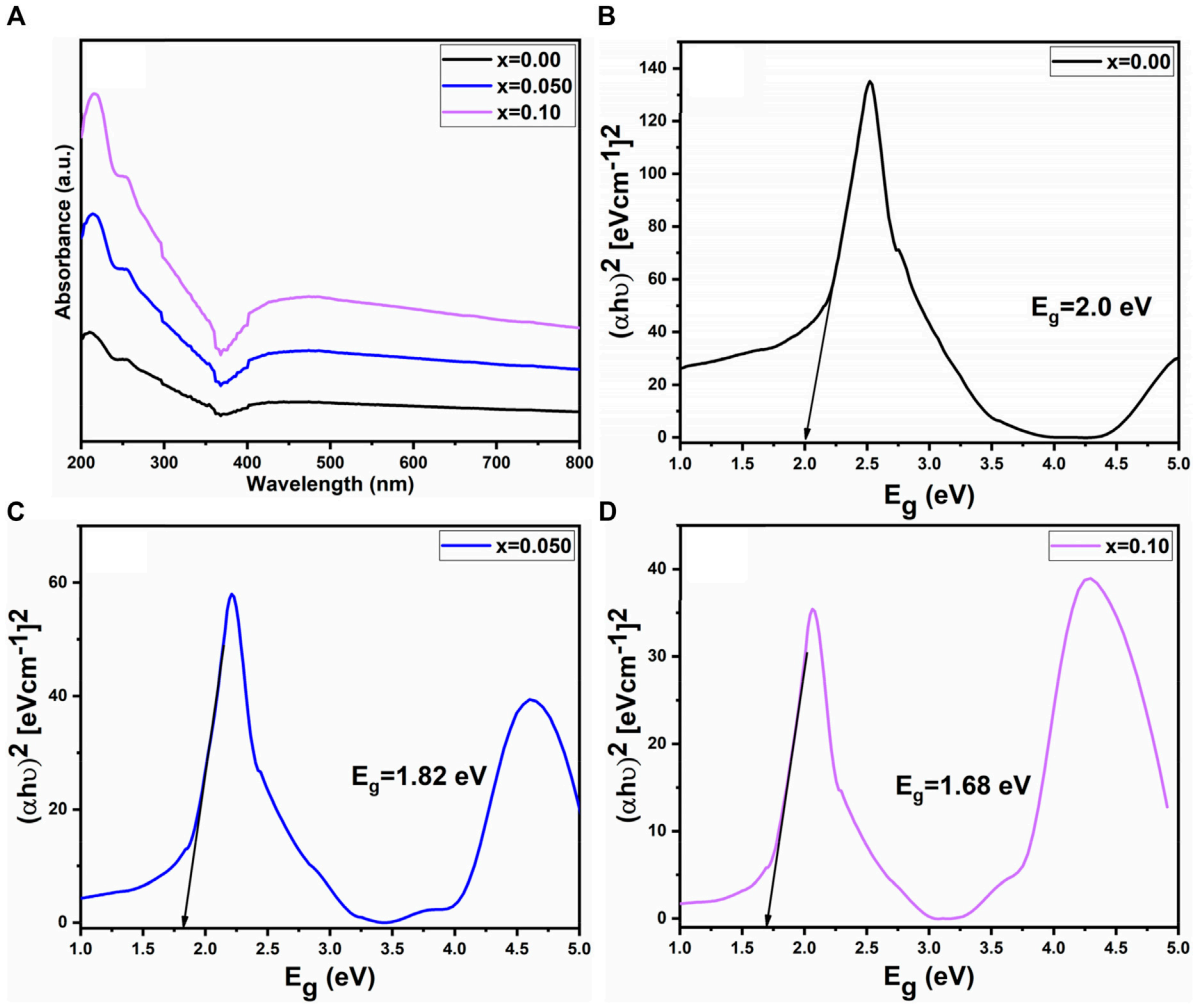

FIGURE 7
(A) UV visible spectra **(B–D)** Tauc plots of $Co_{0.5}Zn_{0.5}La_xFe_{2-x}O_4$ (x = 0.00, 0.05, 0.10).

becomes independent of frequency and stabilized. The concept of space charge polarization primarily arises from the exchange of electrons between ions of the same element but with varying valence states, particularly at the B sites (Phor and Kumar, 2019). At lower frequencies, electrons within the grains may have sufficient time to move toward the grain boundaries, leading to polarization and hence higher ε′ at lower frequencies. However, with increasing frequency, the exchange of ions between Fe^{2+} and Fe^{3+} ions face challenges in keeping pace with the rapid oscillations of the applied field. This is due to the fact that electrons can only migrate over a fraction of a second before the field undergoes a reversal. Consequently, the window of opening for electrons to reach the grain boundary diminishes, leading to a reduced influence on polarization (Iqbal et al., 2014).

Figures 9A, B depicts the dielectric loss (ε″) and tangent loss of prepared spinel ferrites, respectively. The loss factor of a dielectric material is defined by Equation 10:

$$\varepsilon'' = \mathrm{Tan}\delta\varepsilon^0 \quad (10)$$

Here, ε₀ represents the dielectric constant, and ε′′ denotes the dielectric loss factor. This tangent loss is contingent on the polarization arising from grain conduction, which is stimulated by the electron transfer occurring within the grain between Fe^{3+} and Fe^{2+} as well as Co^{2+} and Co^{3+}.

In ferrites, the presence of electrons at grain boundaries impede inter-grain conduction. As the accumulation of electrons at boundaries intensifies, the quantity of space charge accumulates, resulting in a more pronounced potential barrier. The high surface area of nanostructured particles in cobalt zinc spinel ferrites offers a favorable environment for this phenomenon. Lower potential barriers at the grain boundaries lead to a decrease in space charge polarization when grain boundary conduction is active. Hence, inter-grain conduction prevails due to the reduced potential barrier at the grain boundary (Iqbal et al., 2014). This alteration results in a reduction in grain boundary polarizability, which is reflected as a dielectric loss. It is worth noting that tanδ demonstrates a higher value at lower frequencies and a lower value at higher frequencies, primarily due to the increased responsiveness of space charge polarization at lower frequencies (as shown in Figure 9B). Spinel ferrites are a distinct class of magnetic materials renowned for their interesting magnetic and dielectric behavior. This comprehension is important for varied applications,

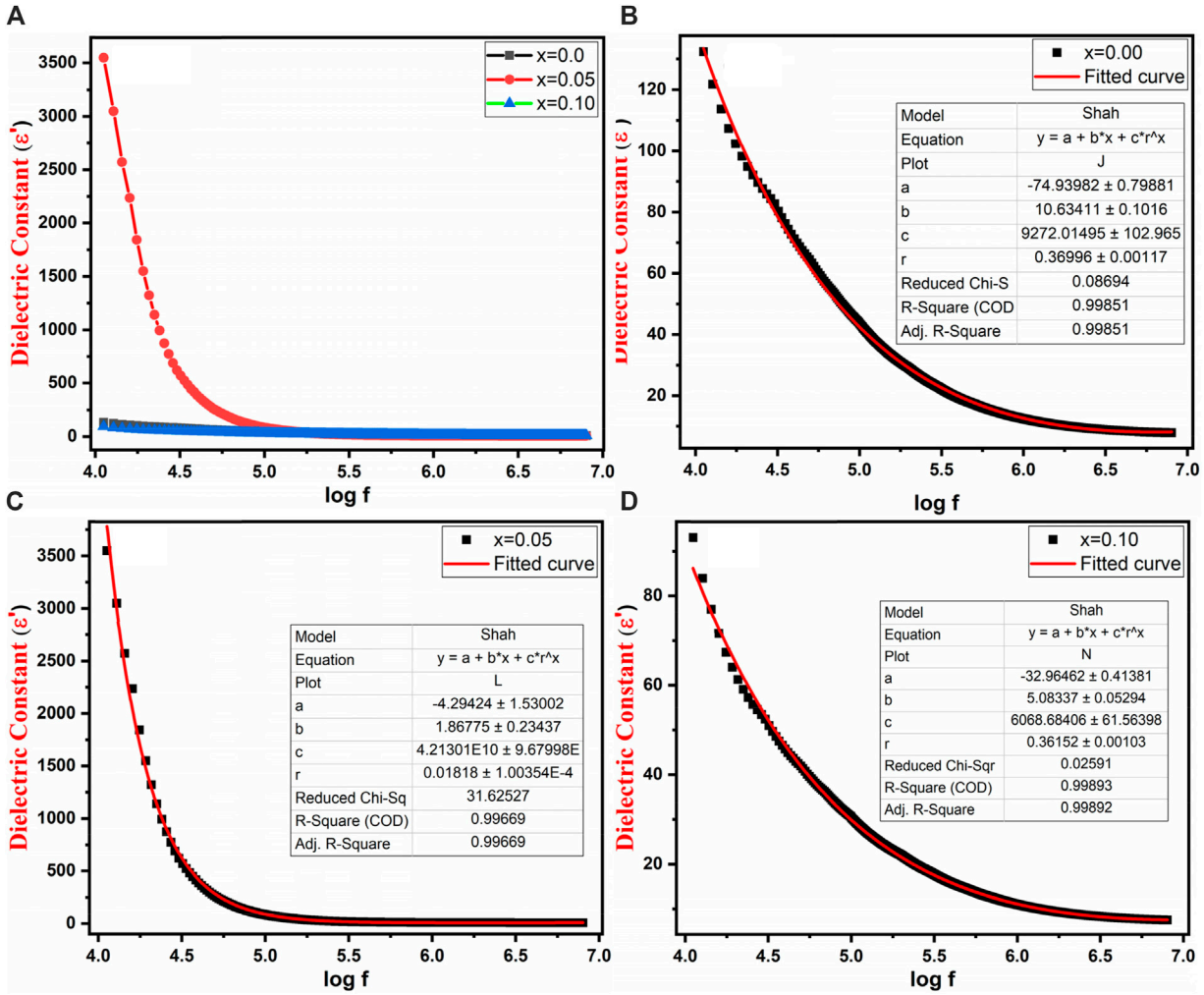

FIGURE 8
(A) Variation of dielectric constant with log frequency **(B–D)** Variation of dielectric constant with log frequency and Shah fitting of $Co_{0.5}Zn_{0.5}La_xFe_{2-x}O_4$ (x = 0.00, 0.05, 0.10).

particularly within electronics and telecommunications. The tangent loss, also known as the dissipation factor or loss tangent, measures the amount of energy converted into heat during each cycle of an electric field within a dielectric material. Its expression as the ratio of the imaginary to the real part of complex permittivity underscores its sensitivity to distinct material phenomena or transitions, thereby contributing to a better understanding of spinel ferrites' behavior.

Figure 10A investigated the influence of frequency range from 10 kHz to 8 MHz on conductivity (σ_{ac}) for $Co_{0.5}$ $Zn_{0.5}$ $La_xFe_{2-x}O_4$ (x = 0.00, 0.05, 0.10). The power of conduction within the material can be assessed through its conductivity (σ_{ac}). Figure 10A shows that AC conductivity exhibits a low value at low frequencies but rises rapidly at higher frequencies. This behavior aligns with the Double-Layer Maxwell and Wagner model, which suggests that at low frequencies, grain boundaries mainly influence conductivity, whereas at higher frequencies, grain activity becomes more distinct, facilitating electron hopping processes. In the present study, at higher frequencies, conductivity significantly increases due to the involvement of bounded charge carriers in the conductivity mechanism (Iqbal et al., 2014). Additionally, Figure 10A reveals two distinct frequency regimes: a plateau region corresponding to low frequencies, where conductivity remains independent of frequency, and a dispersion region corresponding to high frequencies, where conductivity escalates with increasing frequency (Chahar et al., 2022). The experimental findings regarding the conductivity (σ_{ac}) were contrasted with the theoretically computed outcomes derived from Langevin Mod's function, as illustrated in Figures 10B–D. The exponent "n" can be computed using the given relation (Equation 11) by plotting graphs between log σ_{ac} and log ω shown in Figure 10E:

$$\sigma(\omega) = B \times \omega^n \tag{11}$$

The relationship between log σ_{ac} and log ω shows a consistent pattern for x = 0.0, where the slope corresponds to the exponent "n" and the intercept aligns with log B at log ω = 0. Importantly, it is notable that "n" falls within the range of 0–1. When "n" equals 0, electrical conduction remains unaffected by frequency, whereas "n" values less than or equal to 1 signify frequency-dependent electrical conduction. In this study, "n" ranges from

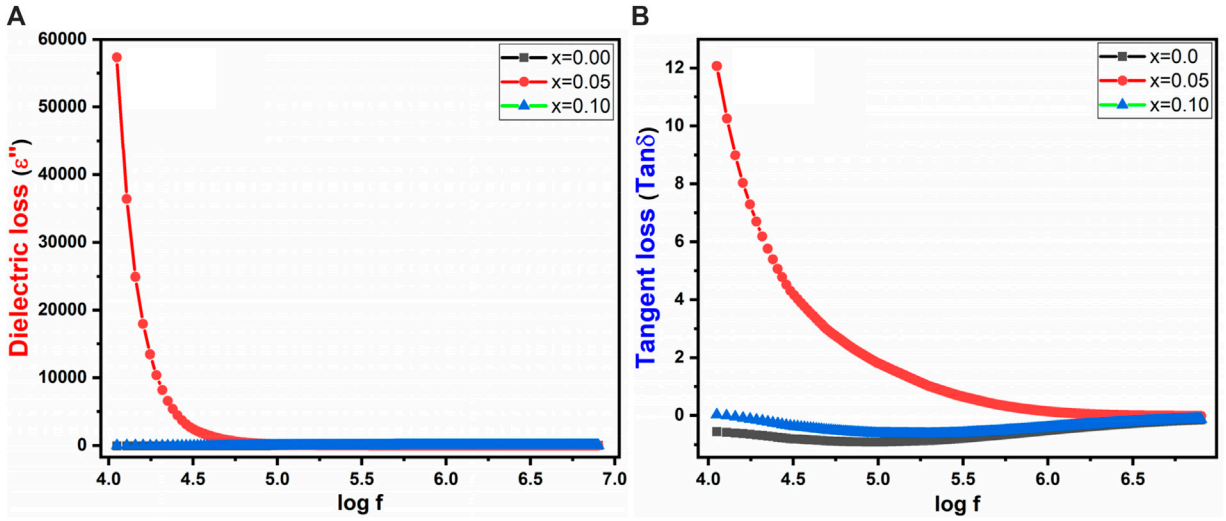

FIGURE 9
(A) ε″ **(B)** tan δ vs. log frequency of $Co_{0.5}Zn_{0.5}La_xFe_{2-x}O_4$ (x = 0.00, 0.05, 0.10).

0.79 to 0.84, indicating that the samples exhibit frequency-dependent behavior.

The graph in Figure 11A illustrates the variation of electric modulus (M′) with the log of frequency across all samples. The total electrical modulus "M" comprises contributions from both the real and complex moduli, represented by the following Equation 12:

$$M_{total} = M' + jM'' \tag{12}$$

In the above Equation 12, the first factor, M′, can be determined using the following expression (Equation 13):

$$M' = \frac{\varepsilon'}{\varepsilon'^2 + \varepsilon''^2} \tag{13}$$

Similarly, the second factor in Equation 12, M″, can be calculated using Equation 14:

$$M'' = \frac{\varepsilon''}{\varepsilon'^2 + \varepsilon''^2} \tag{14}$$

The electrical modulus exhibits exciting behavior with changing frequency. Figure 11A reveals that at lower frequencies, the electric modulus maintains a constant value, attributed to electrode effects or ionic polarization. However, at higher frequencies, all samples (with x = 0.00, 0.05 and 0.10) demonstrated significant asymmetric behavior, indicative of space charge polarization in the high-frequency region.

Figure 11B displays the behavior of the complex modulus, M″, against the log of frequency. At high frequencies, a distinct sharp peak is observed across all samples, reflecting maximum asymmetric tendencies.

This peak signifies relaxation behavior and is associated with the single polarization phenomenon of grain boundaries. Moreover, with the substitution of La^{3+}, the peak intensity increases, and there is a slight shift towards higher frequencies, indicating the presence of dielectric relaxation within the material. Furthermore, the trend observed in the M″ graph at low frequencies suggests that charge carriers undergo significant displacement over larger distances, whereas at high frequencies, their mobility is constrained to shorter distances. This alteration in charge carrier behavior with frequency variations across all samples suggests a shift from small to longer-range mobility, revealing insights into the material's conductivity properties (Mustafa et al., 2022).

3.4.1 Cole-Cole

Figure 12 depicts the Cole-Cole plot representing the complex modulus plane (M′ vs. M″). The Cole-Cole plot serves as a valuable tool for investigating the conduction mechanisms within both grains and grain boundaries.

M′ and M″ were chosen for the Cole-Cole plot as alternative methods did not yield suitable results (Dhabekar and Kant, 2021). The semicircles evident in the Cole-Cole plots provide valuable insights into the material's conducting capacity. Figure 12 demonstrates that only one semicircle is consistently observed in all samples within the Cole-Cole plot. This observation elucidates the reason for the low grain boundary resistance in the high-frequency region (Pandit et al., 2014). The La^{3+} substitution has different effects on grain and grain boundary resistance, as seen by the shift in the radius of the semicircle. According to Dewi et al. (2023), the change in radius might be caused by the distortion of the lattice that occurs because of increasing La^{3+} substitution and attributed to the fluctuation in the relaxation frequency. It can be seen that at x = 0.05 to x = 0.10, the hight of the semicircle changes due to polarization relaxation processes that are caused by the change of field in the ferrites (Junaid et al., 2016).

3.5 Magnetic properties

The M-H loops of $Co_{0.5}Zn_{0.5}La_xFe_{2-x}O_4$ (x = 0.0, 0.050, 0.10) ferrite powders at room temperature were recorded using a VSM (see Figure 13A). The loops in Figure 13A illustrate that the as-synthesized samples exhibit small areas (narrow loops), indicating

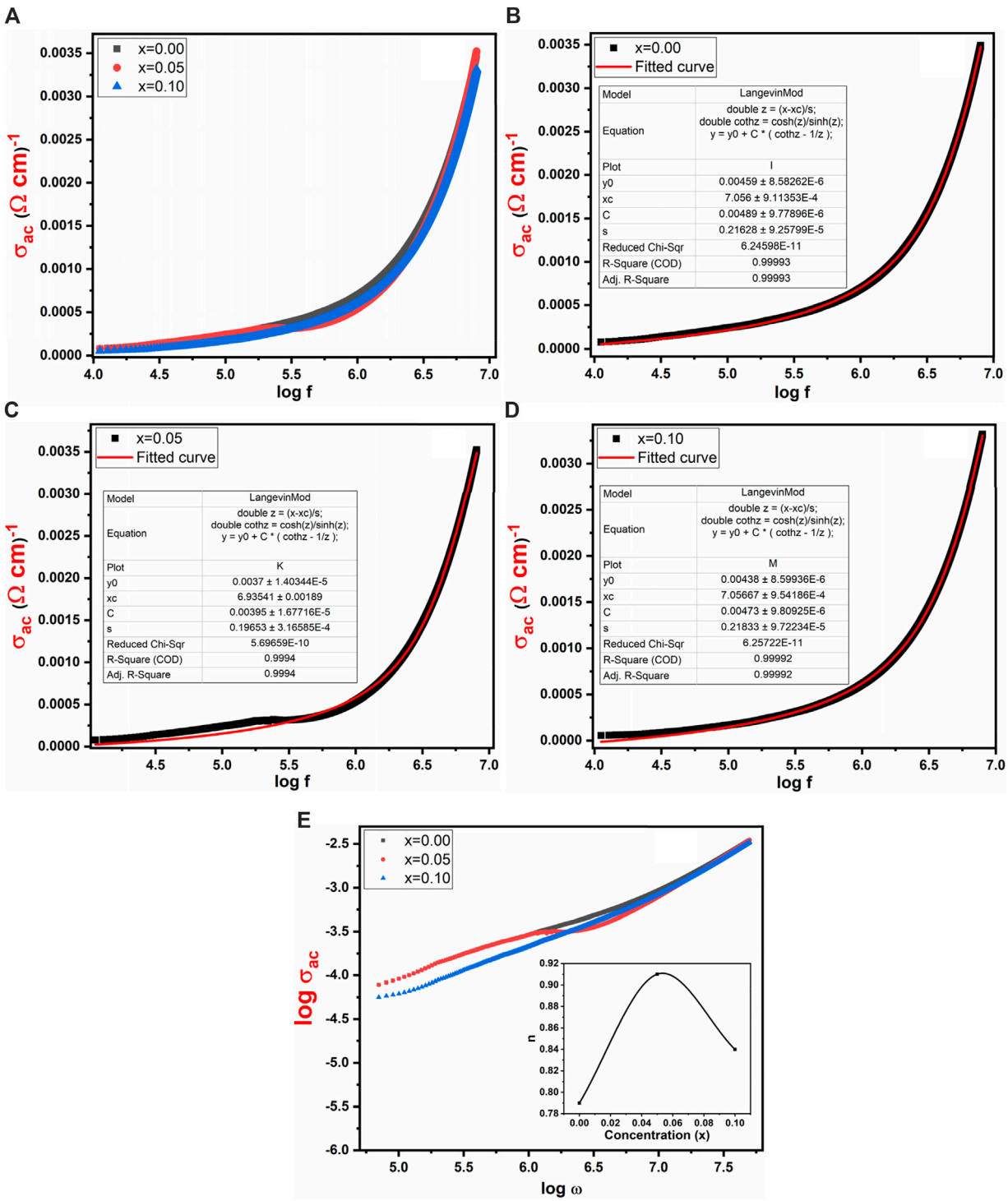

FIGURE 10
Frequency verses **(A)** σ_{ac} **(B–D)** AC conductivity with curve fitting by using Langevin Mod fitting **(E)** log σ_{ac} vs. log ω of $Co_{0.5}Zn_{0.5}La_xFe_{2-x}O_4$ (x = 0.00, 0.05, 0.10), inset: frequency exponent "n" vs. concentration.

soft magnetic behavior (Datta et al., 2023). The saturation magnetization (Ms) values for the $Co_{0.5}Zn_{0.5}La_xFe_{2-x}O_4$ ferrite samples were observed to decrease from 55.84 emu/g to 22.08 emu/g as the concentration of La_{3+} ion increased. From Table 9, it is evident that the saturation magnetization (M_S) decreases with the doping of La^{3+} rare earth ions. Typically, when Fe^{3+} ions in ferrites are replaced by RE^{3+} ions with smaller magnetic moments, the magnetization of RE^{3+}-doped ferrites decreases. Conversely, if the magnetic moment of the RE^{3+} ion exceeds that of Fe^{3+}, the magnetization increases. However, this behavior is not consistent across all RE-doped ferrites. It is reported that rare earth ions, when doped in ferrites, prefer to occupy the

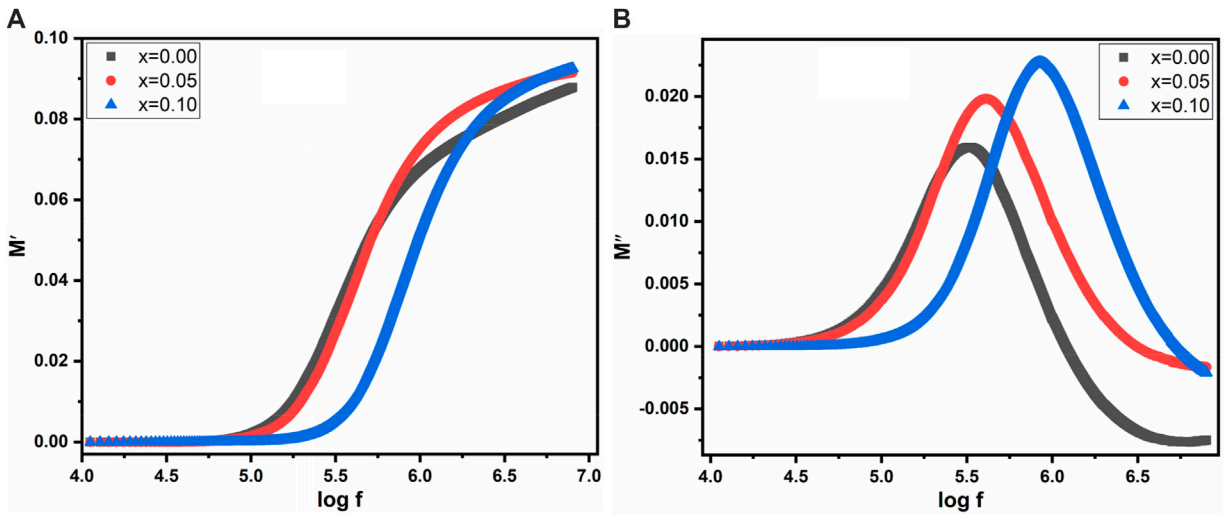

FIGURE 11
Frequency verses **(A)** M′ **(B)** M″ for $Co_{0.5}Zn_{0.5}La_xFe_{2-x}O_4$ (x = 0.00, 0.05, 0.10).

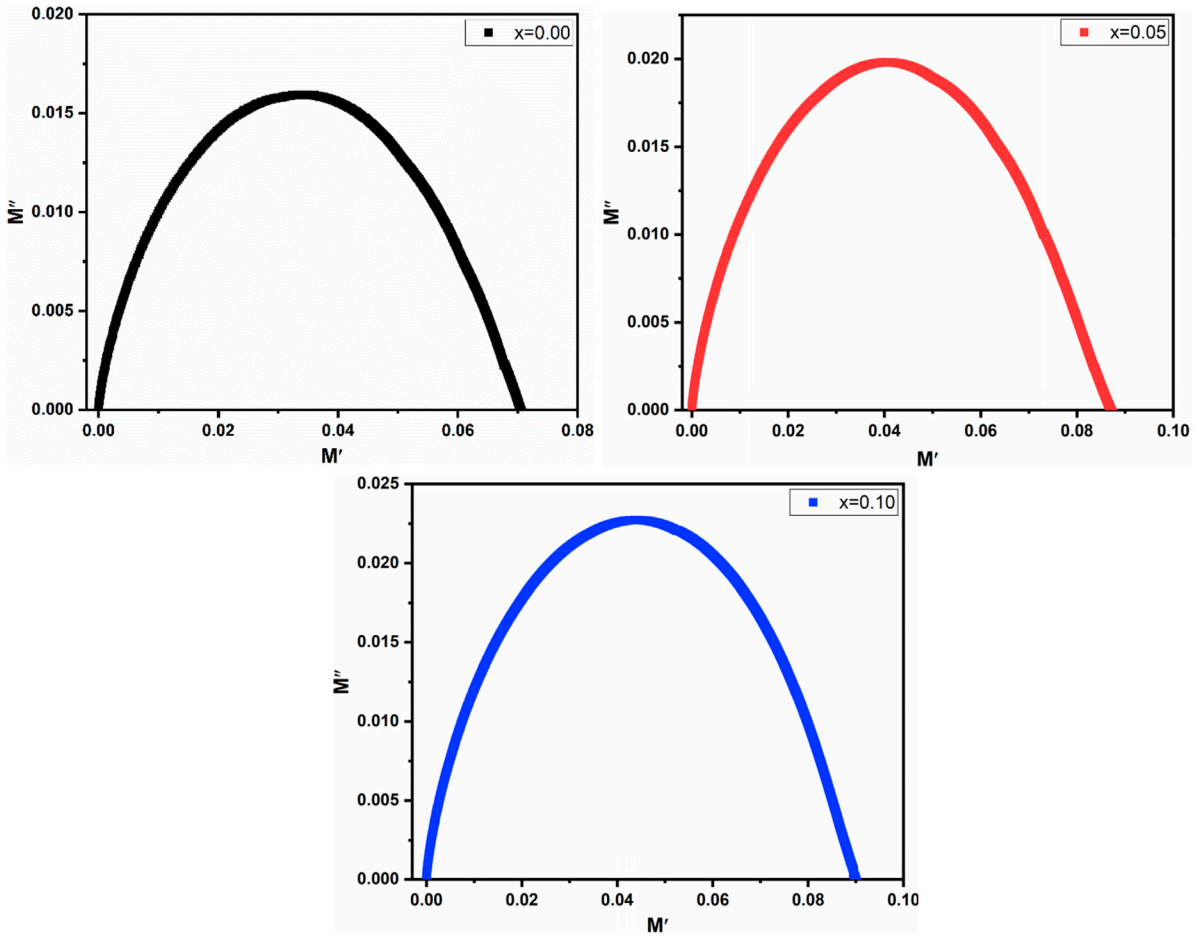

FIGURE 12
Cole-Cole plot of $Co_{0.5}$ $Zn_{0.5}$ $La_xFe_{2-x}O_4$ (x = 0.00, 0.05, 0.10).

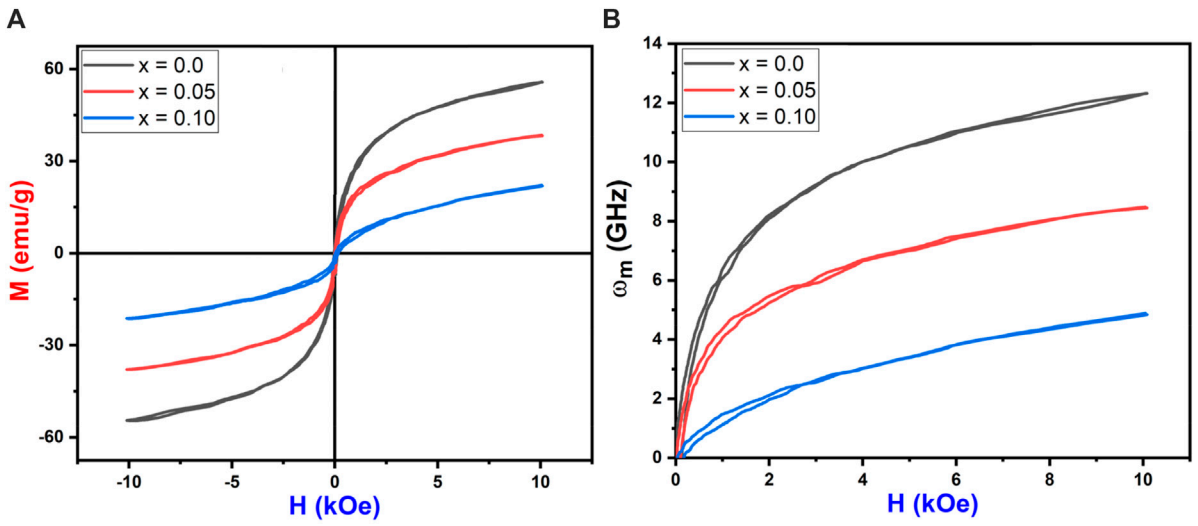

FIGURE 13
(A) M-H loops **(B)** Applied field vs. microwave frequency of $Co_{0.5}Zn_{0.5}La_xFe_{2-x}O_4$ (x = 0.00, 0.05, 0.10).

TABLE 9 Magnetic parameters and cation distribution of $Co_{0.5}Zn_{0.5}La_xFe_{2-x}O_4$ (x = 0.00, 0.05, 0.10).

x	0.00	0.05	0.10
Ms (emu/g)	55.84	38.31	22.08
Mr (emu/g)	2.08	0.75	0.795
Hc (Oe)	25.63	13.33	33.88
SQ (Mr/Ms)	0.037	0.019	0.036
ω_m (GHz)	12.3	8.5	4.9
K (erg/cm^3)	1,490	531	799
n_B	0.442	0.429	0.414
μ_i	36.6	67.3	16.6
μ_B	2.3779	2.3809	2.3805
Cation distribution	$(Zn_{0.3}Fe_{0.7})$ $[Co_{0.5}Fe_{1.5}]$	$(Zn_{0.3}Co_{0.2}Fe_{0.5})$ $[Co_{0.3}Fe_{1.65}La_{0.05}]$	$(Zn_{0.3}Co_{0.4}Fe_{0.3})$ $[Co_{0.1}Fe_{1.8}La_{0.10}]$

octahedral B site (Nikumbh et al., 2014; Ghosh et al., 2020; Ahmed et al., 2022). The Bohr magnetron and magnetic moment of prepared NPs were calculated from the following Equations 15, 16:

$$\mu_B = \frac{M_s \times M_w}{5585 \times dx} \quad (15)$$

$$n_B = \frac{M_s \times M_w}{5585} \quad (16)$$

where (Ms) is magnetization saturation, (d_x) is X-ray density and (M_w) is molecular mass. It is observed that the magneton number value decreased with increasing concentration (x) presented in Table 9.

The decrease in magnetic moment results from the reduction in Ms. The incorporation of non-magnetic La^{3+} ions into the ferrite lattice reduces the number of magnetic ions, leading to a smaller magnetic moment. The A-B superexchange interaction, which is much stronger than the A-A and B-B interactions, exists among these interstitial sites (Dipesh et al., 2016). The remanence magnetization (M_r) and coercivity field (H_c) were measured from each sample's M-H loop, as shown in Table 9. The irregular trends in M_r and H_c are due to the complex magnetic interactions in the ferrite structure influenced by the addition of La^{3+} ions. The competition between exchange interactions and anisotropy effects leads to non-linear behavior. This irregularity in coercivity and remanence magnetization indicates the material's potential for use in magnetic recording media, where precise control of coercivity is crucial for data storage (Alzoubi, 2022).

Further more, the substitution of paramagnetic rare earth cations lead to the formation of a non-magnetic spinel structure. The magnetic moments for Zn^{2+} (0 μB), Co^{2+} (3 μB), Fe^{3+} (5 μB) (Aguilera-Del-Toro et al., 2021) and La^{3+} (0 μB) (Zhang et al., 2019) were considered in this analysis. In the case of Zn–Co ferrites doped with RE (La^{3+}), La^{3+} (0 μB) replaces Fe^{3+} (5 μB) cations at the B sublattice, reducing the octahedral sublattice magnetization (M_B). However, the tetrahedral sublattice magnetization (M_A) remains

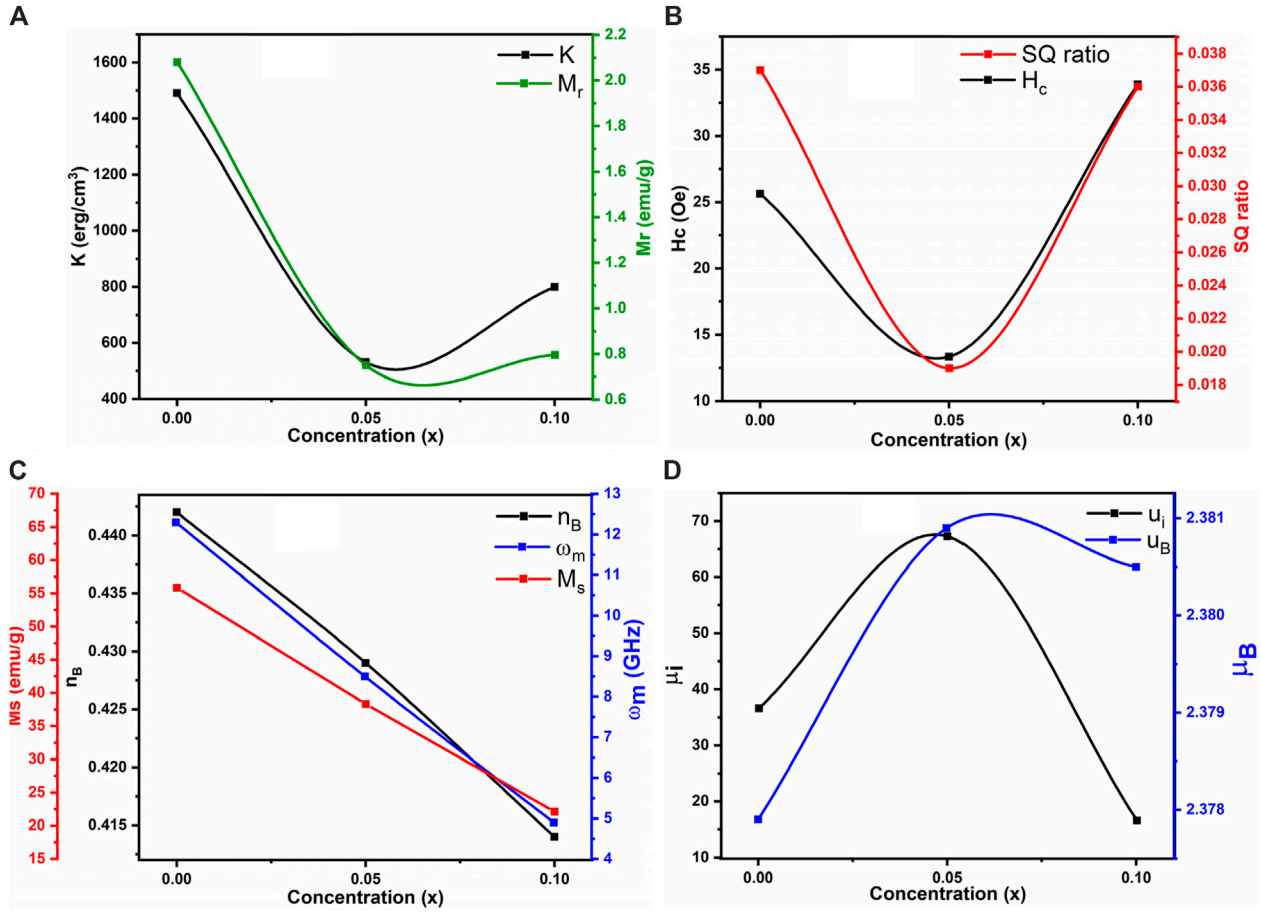

FIGURE 14
Concentration (x) vs. **(A)** Anisotropy constant and retentivity **(B)** Coercivity and remanent ratio **(C)** Saturation magnetization, Bohr magnetron and microwave frequency **(D)** Initial permeability and magnetic moment of all the samples.

unchanged due to the consistent cation distribution at the A-site, resulting in a decrease in the net magnetic moment (n_B). The crystallite size (D) increases with decreasing magnetization saturation (Ms), indicating a superparamagnetic behavior. Notably, $Co_{0.5}Zn_{0.5}La_{0.1}Fe_{1.9}O_4$ contains impurities such as $LaFeO_3$ at grain boundaries, causing internal stress that affects the magnitude of saturation magnetization (Bharti et al., 2021).

The squareness ratio (R_{sq}) was evaluated by the formula (Equation 17):

$$R_{sq} = \frac{M_r}{M_s} \tag{17}$$

All prepared samples exhibited R_{sq} values below 1, indicating super-paramagnetic behavior. This suggests that the magnetic moments within the samples are unaligned, switching rapidly and randomly under an external magnetic field. Such behavior is typical in nanoscale materials, likely due to the small particle size and compositional variations in the ferrite samples (Suo et al., 2020). This super-paramagnetism makes these materials suitable for targeted drug delivery using magnetic nanoparticles, as the rapid switching allows the controlled release of therapeutic agents. Additionally, spinel ferrites can be used in magnetic sensors for detecting weak magnetic fields, valuable for geophysical exploration and non-destructive testing. The anisotropy constant (K) was calculated using the relation (Equation 18):

$$K = \frac{H_c \times M_s}{0.96} \tag{18}$$

The smaller anisotropy constant was 531 for x = 0.05. The anisotropy constant (K) values for varying La^{3+} ion concentrations in ferrite samples were found to be 1,490, 531, and 799 erg/cm^3 for x = 0.0, 0.05, and 0.10, respectively. This irregular trend in K is due to changes in structural and compositional features as La^{3+} is incorporated. Anisotropy in magnetic materials depends on factors such as crystallographic orientation and domain structure, which are affected by La^{3+} concentration. These variations in K can influence the materials' effectiveness as microwave absorbers for electromagnetic interference (EMI) shielding, making them suitable for use in electronics and telecommunications. The tunable magnetic properties of these spinel ferrites provide versatility for various technological applications (Algarou et al., 2020; Bilal et al., 2024). The initial permeability (μ_i) was estimated using Equation 19 and is reported in Table 9.

$$\mu_i = \frac{M_s^2 \times D}{K} \quad (19)$$

The initial permeability (μ_i) exhibited an irregular trend with increasing La^{3+} ion concentration, showing values of 36.6, 67.3 and 16.6 for La^{3+} concentrations of x = 0.0, 0.05 and 0.1, respectively.

This non-linear behavior can be attributed to the complex interplay of magnetic interactions within the ferrite structure, influenced by the addition of La^{3+} ions. The competition between exchange interactions and anisotropy effects contributes to this trend. The microwave frequency (ω_m) is determined using the formula $\omega_m = 8\pi 2M_s\gamma$, where γ is the gyromagnetic ratio (2.8 MHz/Oe). This indicates that higher saturation magnetization (M_s) results in a higher microwave frequency. Figure 13B shows the relationship between the applied magnetic field and microwave frequency. High resistivity and low-loss ferrites are suitable for microwave devices (Ansari et al., 2020). The calculated operating microwave frequencies (ω_m) for samples with x = 0.00, 0.05 and 0.1 falls within the 12–4 GHz range, making them ideal for X-band microwave applications, as detailed in Table 9. The graphical representation of La^{3+} concentration (x) versus magnetic parameters is depicted in Figures 14A–D.

4 Conclusion

Rare earth (La) substituted Co-Zn spinel ferrites were successfully prepared by the sol-gel auto-combustion method. The X-ray diffraction (XRD) pattern demonstrated that the synthesized spinel ferrites possess a single-phase cubic structure which was also confirmed by Rietveld refinement having crystallite size ranging from 17.5 to 26.5 nm. The substitution of lanthanum indicated a decreased behavior in lattice constant from 8.440 (Å) to 8.433 (Å), decreased in volume from 601.2 $(Å)^3$ to 599.7 $(Å)^3$ and increased in X-ray density from 5.38 to 5.75 g/cm^3. Two vibrational bands, a low band (490 cm^{-1}) and a high band (540 cm^{-1}) confirmed by FTIR spectra. UV–vis revealed that the minimum value of the optical band gap observed was 1.68 eV for composition x = 0.10. Dielectric constant and Dielectric loss showed the same behaviour for all samples and raised with doping. AC conductivity's value increased with doping. The dielectric tangent loss showed constant behaviour at higher frequencies for all prepared samples and had a maximum value of 12 at lower frequencies. The VSM results showed that magnetization saturation decreased from 55.84 emu/g to 22.08 emu/g and the value of coercivity increased as rare earth (La) doping increased. The microwave frequency was 4.9 GHz for x = 0.10. Therefore, such materials can be suitable for use in microwave and energy storage devices.

Data availability statement

The raw data supporting the conclusions of this article will be made available by the authors, without undue reservation.

Author contributions

AH: Formal analysis, Investigation, Writing–original draft, AA: Writing–review and editing, SS: Validation, Writing–review and editing, IA: Writing–review and editing, AKT: Funding acquisition, Resources, Writing–review and editing, KK: Funding acquisition, Resources, Writing–review and editing, GH: Writing–review and editing, MYA: Resources, Writing–review and editing, HA: Writing–review and editing, Conceptualization, Project administration, Supervision, Resources, Visualization.

Funding

The authors declare that no financial support was received for the research, authorship, and/or publication of this article.

Conflict of interest

The authors declare that the research was conducted in the absence of any commercial or financial relationships that could be construed as a potential conflict of interest.

Publisher's note

All claims expressed in this article are solely those of the authors and do not necessarily represent those of their affiliated organizations, or those of the publisher, the editors and the reviewers. Any product that may be evaluated in this article, or claim that may be made by its manufacturer, is not guaranteed or endorsed by the publisher.

References

Abbas, B., Ahmad, A. u., Shabbir, S., Shahid, M., Ahmad, T., Braga, M. H., et al. (2023). Enhancing photocatalytic and antibacterial performance through compositional optimization of NiO-CdO heterogeneous nanocomposites. *Ceram. Int.* 49, 33525–33536. doi:10.1016/j.ceramint.2023.07.250

Abdellatif, M. H., El-Komy, G. M., Azab, A. A., and Salerno, M. (2018). Crystal field distortion of La^{3+} ion-doped Mn-Cr ferrite. *J. Magn. Magn. Mat.* 447, 15–20. doi:10.1016/j.jmmm.2017.09.040

Aguilera-Del-Toro, R. H., Aguilera-Granja, F., Torres, M. B., and Vega, A. (2021). Relation between structural patterns and magnetism in small iron oxide clusters: reentrance of the magnetic moment at high oxidation ratios. *Phys. Chem. Chem. Phys.* 23, 246–272. doi:10.1039/d0cp03795h

Ahilandeswari, E., Sakthipandi, K., Kanna, R. R., Hubálovská, M., and Vigneswaran, D. (2022). Lanthanum substitution effect on the structural, optical, and dielectrical properties of nanocrystalline $BaFe_2O_4$ ferrites. *Phys. B Condens. Matter.* 635, 413849. doi:10.1016/j.physb.2022.413849

Ahmed, I., Mustafa, G., Umair Subhani, M., Hussain, G., Ismail, A. G., and Anwar, H. (2022). A detailed investigation of lanthanum substituted bismuth ferrite for enhanced structural, optical, dielectric, magnetic and ferroelectric properties. *Results Phys.* 38, 105584. doi:10.1016/j.rinp.2022.105584

Ahmed, I., Naz, I., Morley, N., Shabbir, S., Maraj, M., Ismail, A. G., et al. (2023). Experimental and DFT investigation of structural and optical properties of lanthanum substituted bismuth ferrites. *Phys. B Condens. Matter.* 661, 414927. doi:10.1016/j.physb.2023.414927

Algarou, N. A., Slimani, Y., Almessiere, M., Alahmari, F., Vakhitov, M., Klygach, D., et al. (2020). Magnetic and microwave properties of $SrFe_{12}O_{19}/MCe_{0.04}Fe_{1.96}O_4$ (M = Cu, Ni, Mn, Co and Zn) hard/soft nanocomposites. *J. Mat. Res. Technol.* 9, 5858–5870. doi:10.1016/j.jmrt.2020.03.113

Altarawneh, A. M., Arrasheed, E. A., Ajlouni, A. W., Ghazy, R., Hemeda, O., Henaish, A., et al. (2023). Correlation between structural, cation distribution with dielectric spectra and magnetic properties for Co–Zn ferrite doped with La^{3+} ions. *Ceram. Int.* 49, 14215–14224. doi:10.1016/j.ceramint.2023.01.008

Alzoubi, G. M. (2022). The effect of Co-doping on the structural and magnetic properties of single-domain crystalline copper ferrite nanoparticles. *Magnetochemistry* 8, 164–169. doi:10.3390/magnetochemistry8120164

Andhare, D. D., Patade, S. R., Kounsalye, J. S., and Jadhav, K. M. (2020). Effect of Zn doping on structural, magnetic and optical properties of cobalt ferrite nanoparticles synthesized via. Co-precipitation method. *Phys. B Condens. Matter.* 583, 412051. doi:10.1016/j.physb.2020.412051

Ansari, A. A., Abushad, M., Arshad, M., Naseem, S., Ahmed, H., Husain, S., et al. (2021). Microstructure, optical and dielectric properties of cobalt-doped zinc ferrite nanostructures. *J. Mat. Sci. Mat. Electron.* 32, 21988–22002. doi:10.1007/s10854-021-06647-2

Ansari, M. M. N., Khan, S., and Ahmad, N. (2020). Structural, electrical transport and magnetic properties of Nd^{3+} substituted Mn–Cu nanoferrites. *J. Alloys Compd.* 831, 154778. doi:10.1016/j.jallcom.2020.154778

Anwar, A., Zulfiqar, S., Yousuf, M. A., Ragab, S. A., Khan, M. A., Shakir, I., et al. (2020). Impact of rare earth Dy^{3+} cations on the various parameters of nanocrystalline nickel spinel ferrite. *J. Mat. Res. Technol.* 9, 5313–5325. doi:10.1016/j.jmrt.2020.03.057

Asghar, Yousaf, M. I., Shad, N. A., Sajid, M. M., Afzal, A. M., Javed, Y., et al. (2022). Enhanced electrochemical performance of hydrothermally synthesized NiS/ZnS composites as an electrode for super-capacitors. *J. Clust. Sci.* 33, 2325–2335. doi:10.1007/s10876-021-02157-7

Aslam, A., Rehman, A. U., Amin, N., Ajaz un Nabi, M., Abdullah, Q. u. a., Morley, N., et al. (2021). Lanthanum doped $Zn_{0.5}Co_{0.5}La_xFe_{2-x}O_4$ spinel ferrites synthesized via co-precipitation route to evaluate structural, vibrational, electrical, optical, dielectric and thermoelectric properties. *J. Phys. Chem. Solids.* 154, 110080. doi:10.1016/j.jpcs.2021.110080

Bharti, M. K., Chalia, S., Thakur, P., and Thakur, A. (2021). Effect of lanthanum doping on microstructural, dielectric and magnetic properties of $Mn_{0.4}Zn_{0.6}Cd_{0.2}La_xFe_{1.8-x}O_4$ ($0.0 \leq x \leq 0.4$). *J. Supercond. Nov. Magn.* 34, 2591–2600. doi:10.1007/s10948-021-05908-9

Bilal, M., Ahmed, I., Shabbir, S., Subhani, M. U., Maraj, M., Anwar, H., et al. (2024). Structural, optical, dielectric and magnetic properties of Cd substituted copper strontium W-type hexaferrite. *Ceram. Int.* 50, 17228–17241. doi:10.1016/j.ceramint.2024.02.198

Chahar, D., Thakur, P., Kumar, R., and Thakur, A. (2022). Influence of Mg doping on the structural, electrical and dielectric properties of Co-Zn nanoferrites. *J. Magn. Magn. Mat.* 544, 168726. doi:10.1016/j.jmmm.2021.168726

Cyriac, J., Augustine, S., Kalarikkal, N., Mukherjee, S., Ahmed, M., and Nambissan, P. M. G. (2020). Dysprosium-substitution-induced structural changes of multiferroic nanocrystalline bismuth ferrite and the investigation through positron annihilation and other studies. *Phys. B Condens. Matter.* 599, 412431. doi:10.1016/j.physb.2020.412431

Datta, S., Manglam, M. K., Panda, S. K., Shukla, A., and Kar, M. (2023). Investigation of crystal structure and magnetic properties in magnetic composite of soft magnetic alloy and hard magnetic ferrite. *Phys. B Condens. Matter.* 653, 414675. doi:10.1016/j.physb.2023.414675

Dewi, S. H., Mulyawan, A., Sarwanto, Y., Winatapura, D. S., and Adi, W. A. (2023). Effect of La^{3+} substitution on structural, microstructure, magnetic properties, and microwave absorbing ability of yttrium iron garnet. *J. Rare Earth.* 41, 578–587. doi:10.1016/j.jre.2022.03.003

Dhabekar, K., and Kant, K. M. (2021). Structural and dielectric properties of cobalt ferrite based nanocomposites. *Phys. B Condens. Matter.* 603, 412752. doi:10.1016/j.physb.2020.412752

Dipesh, D. N., Wang, L., Adhikari, H., Alam, J., and Mishra, S. R. (2016). Influence of Al^{3+} doping on structural and magnetic properties of $CoFe_{2-x}Al_xO_4$ Ferrite nanoparticles. *J. Alloys Compd.* 688, 413–421. doi:10.1016/j.jallcom.2016.07.030

Dippong, T., and Mereu, R. A. (2024). Effect of La^{3+} on thermal, structural and morphological properties of Zn–Co ferrite spinel-based pigments. *Ceram. Int.* 50, 10314–10324. doi:10.1016/j.ceramint.2023.12.343

Gaba, S., Kumar, A., Rana, P. S., and Arora, M. (2018). Influence of La^{3+} ion doping on physical properties of magnesium nanoferrites for microwave absorption application. *J. Magn. Magn. Mat.* 460, 69–77. doi:10.1016/j.jmmm.2018.03.035

Ghosh, M. P., Sharma, S., Satyapal, H. K., Tanbir, K., Singh, R. K., and Mukherjee, S. (2020). Tuning the microstructural, optical and superexchange interactions with rare earth Eu doping in nickel ferrite nanoparticles. *Mat. Chem. Phys.* 241, 122383. doi:10.1016/j.matchemphys.2019.122383

Gilani, Z. A., Farooq, A., Asghar, N. H. K., and Khalid, M. (2020). Synthesis and characterization of lanthanum doped Co-Zn spinel ferrites nanoparticles by sol-gel auto combustion method. *J. Mat. Phys. Sci.* 1, 1–11. doi:10.52131/jmps.2020.0101.0001

Gómez, C. A. P., Meneses, C. A. B., and Matute, A. (2018). Structural parameters and cation distributions in solid state synthesized Ni-Zn ferrites. *Mat. Sci. Eng. B Solid-State Mat. Adv. Technol.* 236-237, 48–55. doi:10.1016/j.mseb.2018.12.003

Gore, S. K., Jadhav, S. S., Tumberphale, U. B., Shaikh, S. M., Naushad, M., and Mane, R. S. (2017). Cation distribution, magnetic properties and cubic-perovskite phase transition in bismuth-doped nickel ferrite. *Solid State Sci.* 74, 88–94. doi:10.1016/j.solidstatesciences.2017.10.009

Guo, H. S., Zhang, L., Yan, Y. L., Zhang, J., Wang, J., Wang, S. Y., et al. (2022). Effect of lanthanum substitution on structural, magnetic, and electric properties of Ni–Zn–Co ferrites for radio frequency and microwave devices. *Ceram. Int.* 48, 22516–22522. doi:10.1016/j.ceramint.2022.04.275

Haque, S. U., Saikia, K. K., Murugesan, G., and Kalainathan, S. (2017). A study on dielectric and magnetic properties of lanthanum substituted cobalt ferrite. *J. Alloys Compd.* 701, 612–618. doi:10.1016/j.jallcom.2016.11.309

Hasan, S., and Azhdar, B. (2022). Synthesis of nickel-zinc ferrite nanoparticles by the sol-gel auto-combustion method: study of crystal structural, cation distribution, and magnetic properties. *Adv. Condens. Matter Phys.* 1, 1–14. doi:10.1155/2022/4603855

Hussain, G., Ahmed, I., Rehman, A. U., Subhani, M. U., Morley, N., Akhtar, M., et al. (2022). Study of the role of dysprosium substitution in tuning structural, optical, electrical, dielectric, ferroelectric, and magnetic properties of bismuth ferrite multiferroic. *J. Alloys Compd.* 919, 165743. doi:10.1016/j.jallcom.2022.165743

Iqbal, M. A., Islam, M. U., Ali, I., Khan, M. A., Sadiq, I., and Ali, I. (2014). High frequency dielectric properties of Eu^{3+}-substituted Li-Mg ferrites synthesized by sol-gel auto-combustion method. *J. Alloys Compd.* 586, 404–410. doi:10.1016/j.jallcom.2013.10.066

Islam, M. A., Hossain, A. K. M. A., Ahsan, M. Z., Bally, M. A. A., Ullah, M. S., Hoque, S. M., et al. (2022). Structural characteristics, cation distribution, and elastic properties of Cr^{3+} substituted stoichiometric and non-stoichiometric cobalt ferrites. *RSC Adv.* 12, 8502–8519. doi:10.1039/d1ra09090a

Jeevanantham, B., Song, Y., Choe, H., and Shobana, M. K. (2021). Structural and optical characteristics of cobalt ferrite nanoparticles. *Mat. Lett. x.* 12, 100105. doi:10.1016/j.mlblux.2021.100105

Jnaneshwara, D. M., Avadhani, D., Daruka Prasad, B., Nagabhushana, B., Nagabhushana, H., Sharma, S., et al. (2014). Effect of zinc substitution on the nanocobalt ferrite powders for nanoelectronic devices. *J. Alloys Compd.* 587, 50–58. doi:10.1016/j.jallcom.2013.10.146

Junaid, M., Khan, M. A., Iqbal, F., Murtaza, G., Akhtar, M. N., Ahmad, M., et al. (2016). Structural, spectral, dielectric and magnetic properties of Tb–Dy doped Li-Ni nano-ferrites synthesized via micro-emulsion route. *J. Magn. Magn. Mat.* 419, 338–344. doi:10.1016/j.jmmm.2016.06.043

Kadam, A. B., Mande, V. K., Kadam, S. B., Kadam, R. H., Shirsath, S. E., and Borade, R. B. (2020). Influence of gadolinium (Gd^{3+}) ion substitution on structural, magnetic and electrical properties of cobalt ferrites. *J. Alloys Compd.* 840, 155669. doi:10.1016/j.jallcom.2020.155669

Kalam, A., Al-Sehemi, A. G., Assiri, M., Du, G., Ahmad, T., Ahmad, I., et al. (2018). Modified solvothermal synthesis of cobalt ferrite ($CoFe_2O_4$) magnetic nanoparticles photocatalysts for degradation of methylene blue with H_2O_2/visible light. *Results Phys.* 8, 1046–1053. doi:10.1016/j.rinp.2018.01.045

Kiani, M. N., Butt, M. S., Gul, I. H., Saleem, M., Irfan, M., Baluch, A. H., et al. (2022). Synthesis and characterization of cobalt-doped ferrites for biomedical applications. *ACS Omega* 8, 3755–3761. doi:10.1021/acsomega.2c05226

Kokare, M. K., Jadhav, N. A., Singh, V., and Rathod, S. M. (2019). Effect of Sm^{3+} substitution on the structural and magnetic properties of Ni-Co nanoferrites. *Opt. Laser Technol.* 112, 107–116. doi:10.1016/j.optlastec.2018.10.045

Kulkarni, V. D., and Rathod, S. M. (2016). Structural, morphological and optical properties of La^{3+} doped Co-Zn nanoferrite. *IJSR* 5.

Kumari, N., Kumar, V., and Singh, S. K. (2014). Synthesis, structural and dielectric properties of Cr^{3+} substituted Fe_3O_4 nano-particles. *Ceram. Int.* 40, 12199–12205. doi:10.1016/j.ceramint.2014.04.061

Li, S., Pan, J., Gao, F., Zeng, D., Qin, F., He, C., et al. (2021). Structure and magnetic properties of coprecipitated nickel-zinc ferrite-doped rare earth elements of Sc, Dy, and Gd. *J. Mat. Sci. Mat. Electron.* 32, 13511–13526. doi:10.1007/s10854-021-05928-0

Lumina, M. M., Anand, S., Vinosel, V. M., Janifer, M. A., Pauline, S., and Manikandan, A. (2018). Effect of lattice strain on structure, morphology and magneto-dielectric properties of spinel $NiGd_xFe_{2-x}O_4$ ferrite nano-crystallites synthesized by sol-gel route. *J. Magn. Magn. Mat.* 466, 238–251. doi:10.1016/j.jmmm.2018.07.017

Mahmood, A., and Maqsood, A. (2021). Physical properties, magnetic measurements, dielectric relaxation, and complex impedance studies of cobalt-doped zinc ferrite nanoparticles. *Appl. Nanosci.* 11, 2311–2336. doi:10.1007/s13204-021-02007-y

Maksoud, M. I. A. A., El-Ghandour, A., El-Sayyad, G. S., Fahim, R. A., El-Hanbaly, A. H., Bekhit, M., et al. (2020). Unveiling the effect of Zn^{2+} substitution in enrichment of

structural, magnetic, and dielectric properties of cobalt ferrite. *J. Inorg. Organomet. Polym. Mat.* 30, 3709–3721. doi:10.1007/s10904-020-01523-8

Mariño-Castellanos, P., Guerrero, F., Romaguera-Barcelay, Y., Goveia-Alcaide, E., Cotta, E., Leyet, Y., et al. (2021). Effect of La^{3+} cation solubility on the structural, magnetic and electrical properties of barium hexaferrite. *Ceram. Int.* 47, 8236–8247. doi:10.1016/j.ceramint.2020.11.183

Mısırlıoğlu, B. S., Çakır, Ö., Calik, H., and Cakir-Koc, R. (2022). Assessment of structural and cytotoxic properties of cobalt ferrite nanoparticles for biomedical applications. *Inorg. Nano-Metal Chem.* 52, 57–62. doi:10.1080/24701556.2020.1862216

Mohamed, M. B., and Wahba, A. M. (2014). Structural, magnetic, and elastic properties of nanocrystalline Al-substituted $Mn_{0.5}Zn_{0.5}Fe_2O_4$ ferrite. *Ceram. Int.* 40, 11773–11780. doi:10.1016/j.ceramint.2014.04.006

Mugutkar, A. B., Gore, S. K., Patange, S. M., Mane, R. S., Raut, S. D., Shaikh, S. F., et al. (2022). Ammonia gas sensing and magnetic permeability of enhanced surface area and high porosity lanthanum substituted Co–Zn nano ferrites. *Ceram. Int.* 48, 15043–15055. doi:10.1016/j.ceramint.2022.02.033

Mugutkar, A. B., Gore, S. K., Tumberphale, U. B., Jadhav, V. V., Mane, R. S., Patange, S. M., et al. (2020). The role of La^{3+} substitution in modification of the magnetic and dielectric properties of the nanocrystalline Co-Zn ferrites. *J. Magn. Magn. Mat.* 502, 166490. doi:10.1016/j.jmmm.2020.166490

Muskan, A., Kumar, N., Singh, R. K., Kumar, P., and Siddique, M. M. H. (2024). Rare earth (Nd^{3+}) mediated structural, magnetic, ferroelectric properties of cobalt ferrite Nanomaterials for its varied applications. *J. Indian Chem. Soc.* 101, 101214. doi:10.1016/j.jics.2024.101214

Mustafa, G., Khalid, M., Chandio, A. D., Shahzadi, K., Uddin, Z., Khan, J. K., et al. (2022). Dielectric, impedance, and modulus spectroscopic studies of lanthanum-doped nickel spinel ferrites $NiLa_xFe_{2-x}O_4$ nanoparticles. *J. Sol-Gel Sci. Technol.* 101, 596–605. doi:10.1007/s10971-020-05359-z

Nikam, D. S., Jadhav, S. V., Khot, V. M., Ningthoujam, R. S., Hong, C. K., Mali, S. S., et al. (2014). Colloidal stability of polyethylene glycol functionalized $Co_{0.5}Zn_{0.5}Fe_2O_4$ nanoparticles: effect of pH, sample and salt concentration for hyperthermia application. *RSC Adv.* 4, 12662–12671. doi:10.1039/c3ra47319h

Nikumbh, A. K., Pawar, R., Nighot, D., Gugale, G., Sangale, M., Khanvilkar, M., et al. (2014). Structural, electrical, magnetic and dielectric properties of rare-earth substituted cobalt ferrites nanoparticles synthesized by the co-precipitation method. *J. Magn. Magn. Mat.* 355, 201–209. doi:10.1016/j.jmmm.2013.11.052

Pandit, R., Sharma, K. K., Kaur, P., and Kumar, R. (2014). Cation distribution controlled dielectric, electrical and magnetic behavior of In^{3+} substituted cobalt ferrites synthesized via solid-state reaction technique. *Mat. Chem. Phys.* 148, 988–999. doi:10.1016/j.matchemphys.2014.09.009

Patil, B. B., Pawar, A. D., Barate, S. S., Ghodake, J. S., Thorat, J. B., and Shinde, T. J. (2023). Impact of La^{3+} substitution on electrical, magnetic, dielectric and optical properties of $Ni_{0.7}Cu_{0.1}Zn_{0.2}La_xFe_{2-x}O_4$ ($0 < x < 0.035$) system. *J. Rare Earth.* 41, 740–746. doi:10.1016/j.jre.2022.03.023

Phor, L., and Kumar, V. (2019). Structural, magnetic and dielectric properties of lanthanum substituted $Mn_{0.5}Zn_{0.5}Fe_2O_4$. *Ceram. Int.* 45, 22972–22980. doi:10.1016/j.ceramint.2019.07.341

Reddy, R. A., Rao, K. R., Rajesh Babu, B., Kumar, G. K., Rajesh, C., Chatterjee, A., et al. (2022). Structural, electrical and magnetic properties of cobalt ferrite with Nd^{3+} doping. *Rare Met.* 41, 240–245. doi:10.1007/s12598-019-01285-4

Ren, X., and Xu, G. (2014). Electromagnetic and microwave absorbing properties of NiCoZn-ferrites doped with La^{3+}. *J. Magn. Magn. Mat.* 354, 44–48. doi:10.1016/j.jmmm.2013.10.056

Sanchez-Lievanos, K. R., Stair, J. L., and Knowles, K. E. (2021). Cation distribution in spinel ferrite nanocrystals: characterization, impact on their physical properties, and opportunities for synthetic control. *Inorg. Chem.* 60, 4291–4305. doi:10.1021/acs.inorgchem.1c00040

Sati, P. C., Arora, M., Chauhan, S., Kumar, M., and Chhoker, S. (2014). Effect of Dy substitution on structural, magnetic and optical properties of $BiFeO_3$ ceramics. *J. Phys. Chem. Solids.* 75, 105–108. doi:10.1016/j.jpcs.2013.09.003

Shabbir, S., Khalid, B., Sehrish, H., Iqbal, M. T., Morley, N., and Anwar, H. (2024). Exploring the structural, morphological, optical, and dielectric properties, along with photocatalytic performance of La-doped $SrFeO_3$ nanofibers. *Mat. Res. Bull.* 179, 112970. doi:10.1016/j.materresbull.2024.112970

Shoba, M., and Kaleemulla, S. (2017). Structural, optical and dielectric studies of Er substituted zinc ferrite nanospheres. *J. Phys. Chem. Solids* 111, 447–457. doi:10.1016/j.jpcs.2017.08.028

Sumalatha, E., Kumar, N. H., Edukondalu, A., and Ravinder, D. (2022). Effect of La^{3+} ion doped Co-Zn nano ferrites: structural, optical, electrical and magnetic properties. *Inorg. Chem. Commun.* 146, 110200. doi:10.1016/j.inoche.2022.110200

Suo, N., Sun, A., Yu, L., Zuo, Z., Pan, X., Zhang, W., et al. (2021). Effect of different rare earth (RE = Y^{3+}, Sm^{3+}, La^{3+}, and Yb^{3+}) ions doped on the magnetic properties of Ni–Cu–Co ferrite nanomagnetic materials. *J. Mat. Sci. Mat. Electron.* 32, 246–264. doi:10.1007/s10854-020-04762-0

Suo, N., Sun, A., Yu, L., Zuo, Z., Zhao, X., Zhang, W., et al. (2020). Effect of Al^{3+} ion-substituted Ni–Mg–Co ferrite prepared by sol–gel auto-combustion on lattice structure and magnetic properties. *Appl. Phys. A Mat. Sci. Process.* 126, 183. doi:10.1007/s00339-020-3361-7

Tanbir, K., Ghosh, M. P., Singh, R. K., Kar, M., and Mukherjee, S. (2020). Effect of doping different rare earth ions on microstructural, optical, and magnetic properties of nickel–cobalt ferrite nanoparticles. *J. Mat. Sci. Mat. Electron.* 31, 435–443. doi:10.1007/s10854-019-02546-9

Thakur, P., Sharma, R., Kumar, M., Katyal, S., Barman, P., Sharma, V., et al. (2019). Structural, morphological, magnetic and optical study of co-precipitated Nd^{3+} doped Mn-Zn ferrite nanoparticles. *J. Magn. Magn. Mat.* 479, 317–325. doi:10.1016/j.jmmm.2019.02.048

Xue, Z., Hou, Z., Ju, J., Gao, L., Zhang, J., and Peng, Y. (2022). The cation distributions of Zn-doped normal spinel $MgFe_2O_4$ ferrite and its magnetic properties. *Materials* 15, 2422. doi:10.3390/ma15072422

Zhang, W., Sun, A., Zhao, X., Suo, N., Yu, L., and Zuo, Z. (2019). Structural and magnetic properties of La^{3+} ion doped Ni–Cu–Co nano ferrites prepared by sol–gel auto-combustion method. *J. Sol-Gel Sci. Technol.* 90, 599–610. doi:10.1007/s10971-019-04941-4

frontiers | Frontiers in Chemistry

TYPE Original Research
PUBLISHED 18 October 2024
DOI 10.3389/fchem.2024.1455838

OPEN ACCESS

EDITED BY
Chris D. Malliakas,
Northwestern University, United States

REVIEWED BY
Rachid Hsissou,
Chouaïb Doukkali University, Morocco
Mohammadi Ahrouch,
Universidad de Cadiz, Spain

*CORRESPONDENCE
Mostafa Abukhadra,
Abukhadra89@Science.bsu.edu.eg
Ashour M. Ahmed,
asmmohamed@imamu.edu.sa

RECEIVED 01 July 2024
ACCEPTED 09 September 2024
PUBLISHED 18 October 2024

CITATION
Ali SM, Mohamed RA, Abdel-Khalek AA, Ahmed AM and Abukhadra M (2024) Physicochemical, steric, and energetic characterization of kaolinite based silicate nano-sheets as potential adsorbents for safranin basic dye: effect of exfoliation reagent and techniques.
Front. Chem. 12:1455838.
doi: 10.3389/fchem.2024.1455838

Physicochemical, steric, and energetic characterization of kaolinite based silicate nano-sheets as potential adsorbents for safranin basic dye: effect of exfoliation reagent and techniques

Samar Mohamed Ali[1,2], Reham A. Mohamed[1], Ahmed A. Abdel-Khalek[1], Ashour M. Ahmed[3]* and Mostafa Abukhadra[2,4]*

[1]Department of Chemistry, Faculty of Science, Beni-Suef University, Beni-Suef, Egypt, [2]Materials Technologies and their Applications Lab, Geology Department, Faculty of Science, Beni-Suef University, Beni-Suef, Egypt, [3]Physics Department, College of Science, Imam Mohammad Ibn Saud Islamic University (IMSIU), Riyadh, Saudi Arabia, [4]Geology Department, Faculty of Science, Beni-Suef University, Beni-Suef, Egypt

Kaolinite was subjected to advanced exfoliation processes to form separated nano-silicate sheets (EXK) with enhanced physicochemical properties as adsorbents. This involved the incorporation of different exfoliating agents, urea (U/EXK), KNO_3 (N/EXK), and CTAB (C/EXK), highlighting their impacts on their textural and surficial properties as adsorbents for safranin dye. The applied characterization techniques confirmed the higher exfoliating degree of C/EXK, followed by N/EXK and U/EXK. This appeared significantly in the determined surface area (55.7 m^2/g (C/EXK), 36.7 m^2/g (U/EXK), and 47.1 m^2/g (N/EXK)) and adsorption performances. The C/EXK structure displayed a better safranin uptake capacity (273.2 mg/g) than N/EXK (231 mg/g) and U/EXK (178.4 mg/g). Beside the remarkable differences in textural properties, the advanced mathematical modeling and the corresponding steric and energetic parameters illustrate the mentioned uptake properties. The interface of C/EXK is highly saturated by active uptake sites (Nm = 158.8 mg/g) as compared to N/EXK (109.3 mg/g) and U/EXK (93.4 mg/g), which is in agreement with the characterization findings and the expected higher exposure of siloxane groups. Each of these sites can be filled with four dye molecules using C/EXK and N/EXK, which implies the vertical orientation of these adsorbed ions and the effective operation of multi-molecular mechanisms. The energetic ($\Delta E < 40$ kJ/mol) and thermodynamic investigations indicate the spontaneous, physical, and exothermic uptake of safranin molecules by EXK particulates. These mechanisms might involve dipole bonding (2–29 kJ/mol), electrostatic attraction (2–50 kJ/mol), van der Waals forces (4–10 kJ/mol), and hydrogen bonding (<30 kJ/mol).

KEYWORDS

kaolinite, exfoliation, intercalating agent, safranin, adsorption, advanced equilibrium

1 Introduction

The primary peril facing the contemporary world is the pollution of potable water as well as the safeguarding of its populace (Yang et al., 2022; Zourou et al., 2022). The World Health Organization (WHO) issued a dire warning, predicting that by 2025, almost half of the world's population would experience substantial water scarcity (Zourou et al., 2022; Arab et al., 2022). The exponential growth of the industrial sector within the past century has resulted in significant environmental issues, such as water contamination, which has had adverse impacts on human beings alongside aquatic ecosystems (Yang et al., 2022; Jawad et al., 2022). Industrial activities release several water pollutants, including bacteria, pesticides, hazardous metals, pharmaceutical residuals, fertilizers, and dyes (Hassan et al., 2022; Prajapati and Mondal, 2022). Synthetic dyes are a varied range of aromatic compounds that are extensively used as crucial coloring agents for numerous industries, including plastic, leather, paper, and textiles (Amri et al., 2023; Bensalah et al., 2023). As a result, an estimated amount exceeding 700,000 tons of the synthesized dyes gets released annually into the surrounding areas and aquatic ecosystems (Kadiri et al., 2021).

The majority of chemically synthesized dyes are toxic and resistant to biological degradation, leading to harmful impacts on both ecosystems and human health (Arab et al., 2022; Kadiri et al., 2021). Safranin dye (SF) is a type of water-soluble basic azine dye that is commonly used in textiles for coloring applications (Laskar and Kumar, 2023; El-Sherbeeny et al., 2021). It is also utilized in various other applications, such as stains, recognizing microorganisms, the healthcare sector, and the packaging of foods (de Araujo et al., 2023; Sarkar et al., 2024). The complex structure and stability of SFR provide difficulties during its biological degradation (de Araujo et al., 2023). This dye has the ability to destroy the nucleic acid of bacteria as well as exhibit tumor-promoting and mutagenic properties. Prolonged or short-term contact with SFR may result in a variety of negative health effects, including irritation of the lips, eyes, stomach, and tongue, as well as itching and redness of skin surfaces. Additional symptoms associated with SFR exposure involve nausea, emesis, and gastrointestinal distress (Shaltout et al., 2022; El-Sherbeeny et al., 2021).

Therefore, the concentrations of SFR, as most synthetic dyes recommend, should be lower than 1 mg/L in the drinking water. Consequently, many techniques have been developed for eliminating dye contaminants, considering the aforementioned concerns about human wellbeing and the environment. The techniques involve ozonation (Le et al., 2022), photocatalytic oxidation (Roy and Chakraborty, 2021), flocculation/coagulation (Basaleh et al., 2021), co-precipitation (Ashrafi et al., 2022), adsorption (Jebli et al., 2023), and ion exchange (Lahiri et al., 2022). The adsorbing method is widely supported as an effective and affordable method to eliminate dyes. This technique has numerous advantages, including high elimination efficiency, a wide variety of applications, simple reuse and recycling abilities, and cost-effective production methods (Lebkiri et al., 2023; Pandey et al., 2022). Hence, researchers have investigated several mono and hybrid structures to provide efficient potential adsorbents for dyes (Zourou et al., 2022; Arab et al., 2022; Kenawy et al., 2022). However, the selection of suitable adsorbents is controlled by several factors, including availability, synthesis cost, adsorption efficiency, adsorption selectivity, recovery, and recyclability (Abukhadra et al., 2022a).

Therefore, the newest research investigation tested and developed several synthetic adsorbents derived from the earth's resources. These types of adsorbents have proven to be remarkably effective and favorable in removing various types of organic contaminants, including dyes, from water, whether in their pure form or in blend with other materials (Ahrouch et al., 2019). Recent investigations focused on innovative modified types of synthesized clay minerals as cost-effective, efficient, and environmentally friendly solutions for decontaminating both organic and inorganic soluble chemicals (Ahrouch et al., 2022; Salam et al., 2020). The majority of recognized clay minerals exhibit adaptable and reacting layered aluminosilicate chemical frameworks that possess notable ion exchange characteristics, chemical reactivity, biological compatibility, active surface, excellent adsorption capacities, natural abundance, nontoxic nature, and thermal resistance (Ahrouch et al., 2020; Dardir et al., 2018). Kaolinite is a naturally occurring mineral with a framework composed of hydrous aluminum silicate layers. These layers are composed of layered tetrahedron/octahedron subunits at a 1:1 ratio (Tian et al., 2020; Shaban et al., 2018). Nevertheless, despite its abundant deposits, accessibility, and cost-effectiveness in comparison to other frequently utilized clay minerals, kaolinite has limited uses in both environmental and commercial industries (Tian et al., 2020; Carretero and Pozo, 2010). Some of the reported limitations for the application of kaolinite include its relatively small surface area and poor ion exchange ability in comparison to frequently employed clay minerals such as halloysite and montmorillonite (Abukhadra and Allah, 2019).

Consequently, various approaches were employed to improve the physicochemical characteristics of kaolinite, including organic and inorganic modifications, exfoliation, and scrolling (Tian et al., 2020; Shaban et al., 2018; Abukhadra and Allah, 2019). Throughout the past few years, there has been notable advancement in the modification and kaolinite conversion methods, which involve exfoliating the layered clay into separated silicate sheets that have two-dimensional morphologies (Zhang et al., 2017; Allah et al., 2023). The implementation of this technique resulted in the development of new nanostructures comprised of clay units, which possess significant characteristics such as impressive biological safety, adsorption capability, surface area, oxidation characteristics, reacting surface features, anti-cancer activity, and dispersion characteristics (Tian et al., 2020; Abukhadra M. R. et al., 2020; Zuo et al., 2017). Common exfoliation techniques comprise high-pressure extrusion, sonication, chemical intercalation, physical grinding, and others (Zuo et al., 2017; Alqahtani et al., 2023). Chemical intercalation methods have been recognized as the best and most efficient method to accomplish the peeling and exfoliation of kaolinite (Zhang et al., 2017; Zuo et al., 2017). The intercalated exfoliating chemicals included N-methylformamide, dimethylsulfoxide, urea, alkylamines, potassium acetate, formamide, fatty acids, quaternary ammonium salts, and hydrazine hydrate (Zuo et al., 2017; Makó et al., 2019). Prior research has shown that various organic guest types, whenever inserted between the kaolinite layers, not only significantly

expand the dimension of the interlayer gap but additionally substantially destruct the hydrogen bonding within the kaolinite-layered units. Enhanced exfoliating of kaolinite-layered units is facilitated by reduced interfacial adhesion (Makó et al., 2019; Abdo et al., 2022).

The structural, morphological, textural and physicochemical characteristics of the exfoliated kaolinite as well as the exfoliation efficiency are strongly influenced by the intercalating chemical agents used (Makó et al., 2019; Abdo et al., 2022; Shawky et al., 2019) Unfortunately, few studies and, to our knowledge, no previous studies have highlighted the impact of the applied exfoliating agents and techniques on the efficiency of the obtained separated silicate sheets as well as their physicochemical and adsorption properties. It was expected that the exfoliating techniques would significantly affect the morphological, textural, physicochemical, and adsorption properties of the end product. This strongly endorses the conduct of extensive comparative studies that highlight the impact of the exfoliation methodologies and the used agents on the separated silicate sheets, particularly as adsorbents, considering the interaction at the adsorbate/adsorbent interface. Therefore, the presented study aims to evaluate the impact of three intercalating agents (CTAB, potassium nitrate, and urea) or their exfoliation techniques on the physicochemical and adsorption properties of exfoliated kaolinite (C/EXK, N/EXK, and U/EXK) as potential adsorbents for safranin-O synthetic dye. These involved experimental investigation of the affecting factors in addition to extensive equilibrium modeling, either by classic models or advanced models. The advanced models were designed based on statistical physics theory, and the main parameters involved existing effective site density, capacity of each uptake site, saturation capacity, and energetic and thermodynamic factors.

2 Experimental work

2.1 Materials

The kaolinite powder (KA) used to produce the exfoliating layers (EXK) was obtained from the Central Metallurgical and Development Institute in Egypt. Chemically, the KA sample composed of SiO_2 (47.83%), Al_2O_3 (35.74%), Fe_2O_3 (0.89%), MgO (0.12%), CaO (0.53%), TiO_2 (0.82%), Na_2O (0.28%), K_2O (0.08%), and loss of ignition (14%). The initial exfoliating approach involved using dimethyl sulfoxide (DMSO) (CAS: 67-68-5) that had a quality exceeding 99.5%, CTAB (cetyltrimethylammonium bromide) (CAS: 57-09-0) with a quality over 98%, and methanol of a quality exceeding 99.9% (CAS: 67-56-1; Sigma-Aldrich). Urea (U) with a purity of 99% from Sigma-Aldrich and potassium nitrate (KNO_3) with a purity of 98% have been employed during the exfoliating processes. NaOH, HNO_3, and N_4OH solutions having particular concentrations were implemented in a variety of processing and adjustment approaches without undergoing purification. The adsorption experiment was conducted employing safranin-O synthetic dye (≥85%; CAS: 477-73-6; Sigma-Aldrich) as the main source of synthesized dye pollutants.

2.2 Exfoliation of kaolinite

2.2.1 Exfoliation by CTAB induced technique (C/EXK)

The kaolinite-layered subunits were exfoliated by a simple chemical-based expansion approach. The original kaolinite sample underwent a pulverizing step for 6 h inside a ball mill, leading to the development of kaolinite granules with particle diameters ranging between 20 and 100 μm. The pulverized kaolinite (15 g) was then thoroughly mixed with 50 mL of DMSO (8 DMSO: 1 water) over a period of 5 h using a conventional magnetic stirrer device. The step described earlier is essential for the destruction of the existing hydrogen bonding connecting the layered silicate units. The kaolinite, which had been immersed in DMSO, was thereafter exposed to a series of washings using methanol for an interval of 20 min each. The process as described was iterated five runs to remove the encapsulated DMSO molecules and replace them with methanol. Consequently, a methoxy-modified kaolinite (Mth/K) had been developed. The Mth/K suspended particulates underwent a homogenizing step with CTAB solution (20 g CTAB + 50 mL distilled water). This step continued over 48 h and encompassed intricate mixing apparatus, which comprises a magnetic stirrer along with an ultrasound generator (240 W). This process resulted in the development of exfoliating or separated kaolinite flakes (EXK). Subsequently, the resultant EXK particulates underwent extensive washing implementing distilled water and then underwent a slow drying step at a temperature of 65°C for an interval of 12 h (Figure 1). The dried particulates were identified as C/EXK and preserved for further characterization and application procedures.

2.2.2 Exfoliation by urea (U/EXK) and KNO_3 (N/EXK)

The exfoliating processes employing the two chemicals were performed according to the methodology described by Shawky et al. (2019). A total of 3 g of finely powdered kaolinite was combined with 1.5 g of urea by utilizing an agate mortar over a duration of 15 min. The mixture was then subjected to thermal treatment for 48 h employing an electric computerized muffle furnace at a temperature of 95°C. For the KNO_3-prepared product, 3 g of the powdered KA precursor had been homogeneously dispersed throughout a water-based solution of KNO_3 (60 mL) over 48 h at 90°C employing a magnetic stirring device (500 rpm). The KA particulates, which had been embedded with the urea alongside KNO_3, were then separated by filtering, underwent a thorough washing process utilizing distilled water through three cycles (each extending 10 min), and subsequently rinsed with ethanol. The washed materials were then subjected to a mild drying procedure for 24 h at a temperature of 60°C. In order to accomplish the successful splitting of the KA particulates into independent layers, the embedded materials thereafter underwent an extra heat-treatment process for a duration of 60 min at a temperature of 120°C. Lastly, the exfoliating products were designated as U/EXK and N/EXK after applying urea and KNO_3, respectively (Figure 11), and preserved for the subsequent characterization and examination stages.

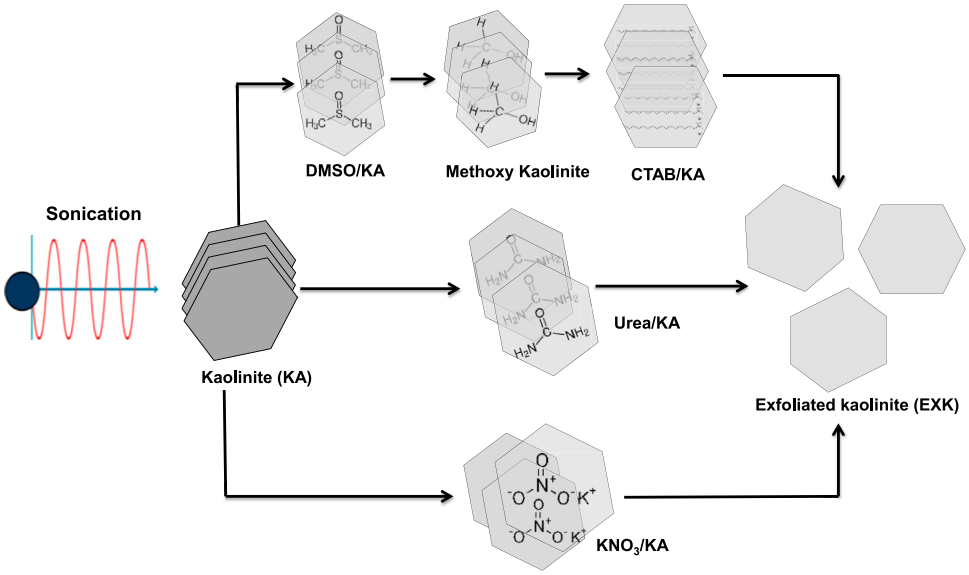

FIGURE 1
Schematic diagram for the synthesis of exfoliated kaolinite using different intercalating agents.

2.3 Analytical techniques

The PANalytical-Empyrean X-ray diffractometer was used to ascertain the degree of crystallization and the corresponding crystalline varieties. The diffraction patterns were determined across the range of 0°–70°. The chemical structures of C/EXK, U/EXK, and N/EXK were determined with a Fourier transform infrared spectrometer (FTIR8400S; Shimadzu) through a range of frequencies from 400 cm^{-1} to 4,000 cm^{-1}. The Gemini Zeiss Ultra 55 scanning electron microscope was used to obtain the SEM photos of the evaluated structures after depositing slim gold covers over their surfaces. These photos were used to track the expected changes in morphology resulting from the three exfoliating techniques. In addition, the interior features of C/EXK, U/EXK, and N/EXK have been further investigated using high-resolution HRTEM photos obtained from a JEOL-JEM2100 transmission electron microscope operating at an accelerated voltage equal to approximately 200 kV. The surface area and porosity of C/EXK, U/EXK, and N/EXK were evaluated using a Beckman Coulter SA3100 analyzer in conjunction with the relevant N_2 adsorption/desorption isotherms.

2.4 Adsorption studies

2.4.1 Batch adsorption studies

The adsorption capacities of C/EXK, U/EXK, and N/EXK as adsorption agents towards safranin-O dye (SFR) were successfully investigated by a series of batch uptake tests. The investigation comprised several influential factors, such as pH values spanning from 3 to 8, starting dye concentrations that varied from 25 to 300 mg/L, and uptake periods varying from 15 to 1,440 min. The overall volumes of contaminated solutions and the amounts of C/EXK, U/EXK, and N/EXK were kept consistent at 100 mL and 0.2 g/L, respectively. Nevertheless, the temperature at which the adsorption occurred varied from 303 K to 323 K for the whole investigation. The mixing process during the adsorption was performed using orbital shaker incubator swathe digital temperature controller. Following the end of all assessments, the residual dye was measured using a UV-Vis spectrophotometer at a detection wavelength of 521 nm. The dye levels were monitored to determine the adsorption capacities of C/EXK, U/EXK, and N/EXK. Equation 1 was used to calculate the result, implementing the treated volume (V), dosage (m), initial level (C_o), and leftover level (C_e).

$$Q_{e\,(mg/g)} = \frac{(C_O - C_e)V}{m} \tag{1}$$

2.4.2 Theoretical traditional and advanced equilibrium studies

The simulation of adsorption behaviors has been accomplished using classic kinetic, normal isotherm, and advanced forms of equilibrium models based on statistical physics hypotheses (Supplementary Table S1). Nonlinear fitting methods were used to fulfill the kinetic and classic equilibrium simulations, utilizing the mathematical formulations for these models. The obtained results of the correlation coefficient (R^2) (Equation 2) together with Chi-squared (χ^2) (Equation 3) were subsequently used to detect the fitting degrees. The compatibility of the adsorption activities with the evaluated advanced equilibrium theories has been verified by implementing the coefficient of correlation (R^2) and the root mean square error (RMSE) (Equation 4). The symbols m′, p, Qi_{cal}, and Qi_{exp} represent the actual observations, investigated variables, expected SFR adsorption, and proved adsorption effectiveness, respectively.

$$R^2 = 1 - \frac{\sum\left(Q_{e,exp} - Q_{e,cal}\right)^2}{\sum\left(Q_{e,exp} - Q_{e,mean}\right)^2} \tag{2}$$

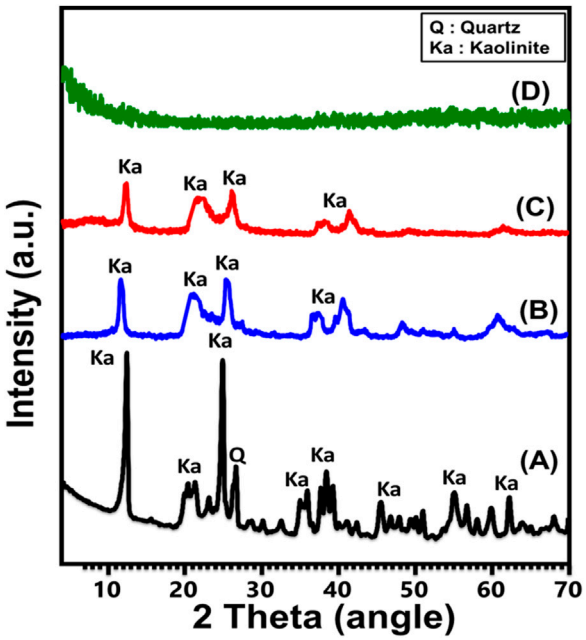

FIGURE 2
XRD patterns of raw kaolinite **(A)**, U/EXK **(B)**, N/EXK **(C)**, and C/EXK **(D)**.

$$\chi^2 = \sum \frac{\left(Q_{e,exp} - Q_{e,cal}\right)^2}{Q_{e,cal}} \quad (3)$$

$$RMSE = \sqrt{\frac{\sum_{i=1}^{m}\left(Qi_{cal} - Qi_{exp}\right)^2}{m' - p}} \quad (4)$$

3 Results and discussion

3.1 Characterization of the adsorbent

3.1.1 XRD analysis

The crystalline modifications that occur throughout the transformation of KA mineral into individual and exfoliated nano-KA layers (EXK) by various intercalating agents have been monitored utilizing their XRD patterns (Figure 1). The well-defined peaks around angles of 12.33° (001) and 24.87° (002) (Figure 2A) identify the triclinic, highly crystalline KA mineral as the initially implemented crystallized component. The kaolinite's crystallization index (HI) is described by its less intense peaks occurring inside the Hinckley range (H), which extends from 12.33° to 24.87°. The basal-spacing distance correlating with these diffraction peaks was detected at 0.72 nm. Regarding the prepared EXK utilizing urea (U/EXK) (Figure 2B) and KNO_3 (N/EXK) (Figure 2C) as intercalating agents, the obtained patterns demonstrate significant structural changes but without extensive destruction of the crystalline structure. The patterns of U/EXK and N/EXK display a notable reduction of the essential peaks of KA and extensive declination in the strengths of Hinckley index peaks, indicating the successful exfoliation of the layered units without extensive destruction of the crystalline structure or its partial exfoliating impacts. Moreover, considering the reduction degress in the main peaks as well as the Hinckley index peaks, it suggests the higher efficiency of the KNO_3-based exfoliating process than the urea-based processes. Finally, the patterns reflected no indication about the intercalated compound, i.e., the structure is free of the used exfoliating agents.

The diffraction pattern obtained after the sonication-supported exfoliation process employing CTAB (C/EXK) displayed a total elimination of the strength of all remaining peaks, suggesting that the resulting material had an amorphous or semi-crystalline structure (Figure 2D). This confirms the complete destruction of the crystal system and the extensive exfolation of the KA-layered units into separated and distinct silicate layers. The previous findings declared the higher performances of the CTAB intercalating method on the exfolaiting efficacy of the kaolinite as compared to the application of the other two methods.

3.1.2 SEM and HRTEM analyses

To follow the morphological and geometrical impacts of the applied exfollation techniques in correlatin with used intercalating agents, the SEM and HRTEM images of the raw KA as well as C/EXK, U/EXK, and N/EXK were inspceted (Figure 3). The starting precursor displays the known geometries and morphology of the highly crystalined KA mineral as flakes or plate-like grains of pesudo-hexagonal outlines that are stacked above each other in aggeragtes or agglomerated form, either in the SEM (Figure 3A) or HRTEM (Figure 3B) photos. Regarding the exfolaikted KA based on CTAB intercalation (C/EXK), the recognized photos demonstrate very effective stripping and splitting of the structural KA layered units into discrete and separated sheets (Figures 3C–E). The sperated sheets still exhibit relict pseudo-hexagonl geometry, but with notable smooth outlines or borders in contrast to the raw particulates (Figure 3D). Some inspected exfolaited grains show batches of a milder gray shade in contrast to the general gray shade of KA flake, suggesting distortion in the ordering properties of the structural silicate units of KA (Figure 3E).

The analyzed photos of both U/EXK and N/EXK also demonstrate the successful separation of the kaolinite units into discrete sheets, but with a lower degree as compared to C/EXK, which is in agreement with the XRD indications. The exfoliation was observed by the reduction in the stacking degree of the KA layers and the declination in the dimension of the present falke-like grains. Moreover, the application of KNO_3 as an intercalating agent during the exfoliating process (N/EXK) (Figures 3F,G) appeared to be more effective than urea (U/EXK) (Figures 3H,I). The recognized particulates of N/EXK shower lower stacking degrees and more discerer sheets than U/EXK particulates. Furthermore, milder gray batches can be detected in the KNO_3-based exfolaited particles, in addition to the noticeable changes in the pseudo-hexagonal outlines. Such obsrevation reflected higher dsirtorytion in the structure of the KA after its modification with KNO_3 during the exfoliation as compared to urea, as concluded by the XRD investigation.

3.1.3 FT-IR analysis

The FT-IR spectra have been employed to assess the impact of the employed intercalating agents or exfoliation techniques on

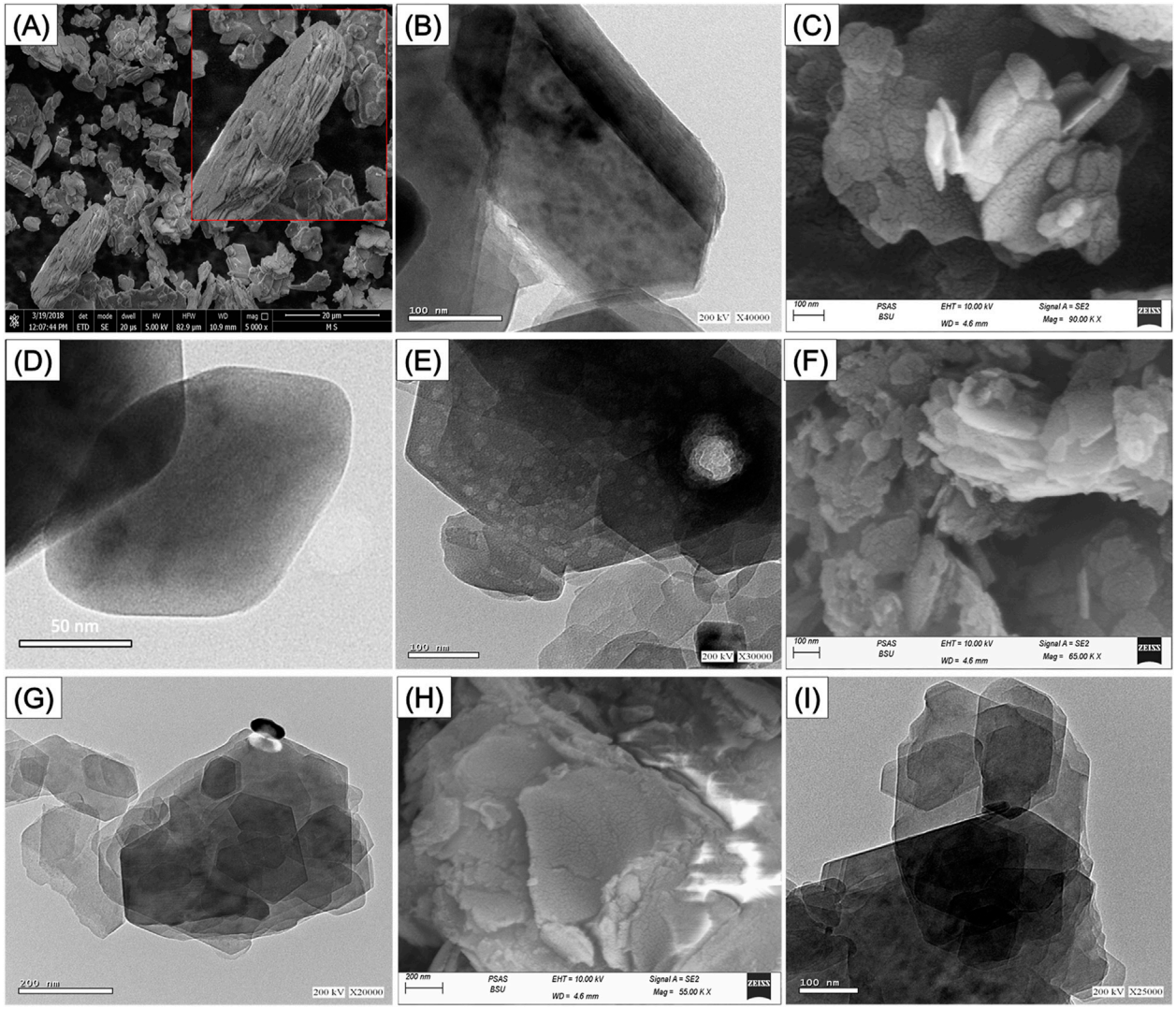

FIGURE 3
SEM of raw kaolinte **(A)**, HRTEM of raw kaolinite **(B)**, SEM of synthetic C/EXK **(C)**, HRTEM images of C/EXK **(D, E)**, SEM image of N/EXK **(F)**, HRTEM image of N/EXK **(G)**, SEM of U/EXK **(H)**, and HRTEM image of U/EXK **(I)**.

existing functional chemical groups. The spectrum of KA displays clearly identifiable bands that correlate to the distinctive functional units detected throughout its aluminosilicate framework as a clay mineral (Figure 4). These involve Si-O (787 and 456 cm^{-1}), Si-O-Al (526 and 680 cm^{-1}), Si-O-Si (1,020 cm^{-1}), Al-OH (912 and 3,500 cm^{-1}), O-H (1,641 cm^{-1}), and Si-OH (3,689 cm^{-1}) (Figure 4A) (Tian et al., 2020; Adly et al., 2022). The spectra of U/EXK (Figure 4B), N/EXK (Figure 4C), and N/EXK (Figure 4D) display absorbing bands which are similar to those observed for untreated KA. However, there are notable differences in their positions, reductions in their intensity, and the splitting of the distinct bands centered at 900 cm^{-1} and 1,000 cm^{-1}. This signifies the effective separation of the KA forming aluminosilicate sheets, leading to the development of single-layered structures or separate nanosheets. Furthermore, the exfoliating processes induce considerably the distortions of both the octahedron and tetrahedron layered units (Abukhadra and Allah, 2019; Shawky et al., 2019). The investigated samples exhibit shifts in the positions of the bands caused by the breakdown of hydrogen bonding within successive KA layers. Additionally, there were variations in strength and widening of the inspected bands, which can be attributed to the development of newly formed hydrogen bonds among KA interlayers together with the functionalities of embedded inercalating chemicals. These findings provide evidence that the interior OH groups of KA are reactive and not inert (Zsirka et al., 2016). Additionally, the remerakable intensification of the coresponding bands of the active siloxane groups demonstrates the effective impact of the exfaolaition processes in inducing and enhancing the exposure of such active groups.

3.1.4 Textural analysis

The N_2 adsorption/desorption isotherms were applied to assess the KA, C/EXK, U/EXK, and N/EXK exterior textural characteristics. The isotherm curves for C/EXK, U/EXK, and N/EXK have been identified as IV-type curves that include

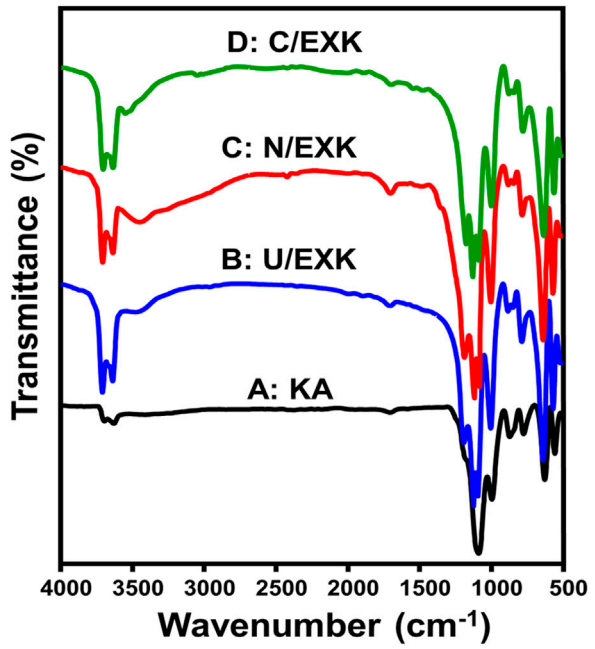

FIGURE 4
FT-IR spectra of raw kaolinite **(A)**, U/EXK **(B)**, N/EXK **(C)**, and C/EXK **(D)**.

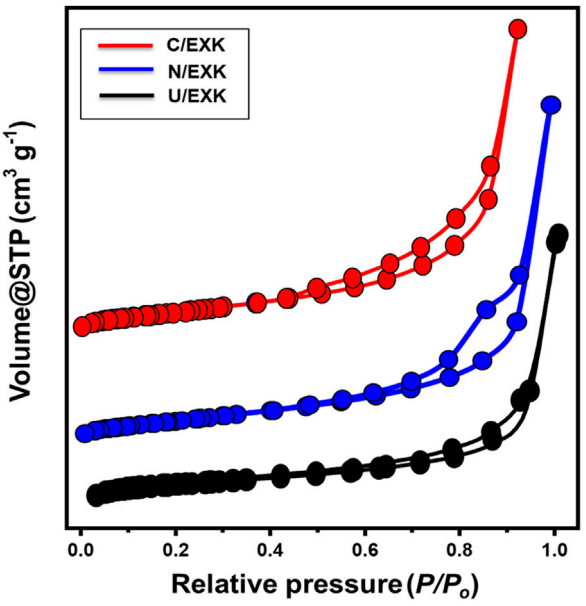

FIGURE 5
The N_2 adsorption/desorption isotherm curves of U/EXK, N/EXK, and C/EXK.

detectable H3 hysteresis loops. This kind was often described in relation to the potential capillary condensation-induced evacuating or filling of mesopores exhibiting tabular or cylindrical geometries (Figure 5). The observed surface area clearly improved using the various exefoliation techniques, as seen by the derived curves. The measured surface areas are 10 m^2/g, 36.7 m^2/g, 47.1 m^2/g, and 55.7 m^2/g for the KA, U/EXK, N/EXK, and C/EXK, respectively. Such values are in agreement with the previously obtained results from the XRD and SEM investigations. The exfoliating modifications based on the CTAB-induced sonication techniques resulted in effective separations of the kaolinite units into monosheets or nano-silicate layers as compared to the applied techniques based on the application of urea and KNO_3 as intercalating agents. Regarding the impact of the applied techniques on the porous properties of the obtained exfoliated products, the determined average pore volumes for KA, U/EXK, N/EXK, and C/EXK are 0.052 cm^3/g, 0.106 cm^3/g, 0.248 cm^3/g, and 0.32 cm^3/g, respectively. This increase in the pore volumes suggested a significant impact for the intercalating agent, inducing basal spascing, the exspour of structural hexagol molecular pores within the silicate tetrahedron sheets, and the expected bending of the silicate sheets during the expansion effect of the intercalating agents, which can be detected clearly in the C/EXK particles. Such changes are also associated with considerable changes in the pore size and dirtibution properties. The pore diameter for all the samples spanned from 2 nm up to about 11 nm, with the average diemater equal to 6.4 nm for U/EXK, 5.5 nm for N/EXK, and 5.12 nm for C/EXK. Such values declare the exfoliation of the keolinite as a mesoporous material, which is favorable during adsorption applications.

3.2 Adsorption results

3.2.1 Effect of the pH

As it affects the adsorbent's external charges alongside the ionization behavior of dissolved pollutants in water-based solutions, the pH factor has significance during the adsorption reaction. The adsorption characteristics of U/EXK, N/EXK, and C/EXK towards the removal of SFR were investigated in terms of the changes in pH. The study comprised a pH range of 2–8 and maintained other specified values at 100 mL for the beginning volume, 100 mg/L for the SFR concentration, 120 min for the study's duration, 0.4 g/L for the dosage, and 20°C for the assessment temperature. The adsorption results were computed as averaged values using the results from three separate tests, and the standard deviations are below 4.2% for all the tests. As can be determined by the findings of determining the amounts of SFR adsorbed using U/EXK, N/EXK, and C/EXK, the results showed a noticeable rise in SFR uptake as frequently the pH value of the analyzed polluted solutions progressed over pH 3 (Figure 6). From 6.6 mg/g (U/EXK), 12.6 mg/g (N/EXK), and 17.2 mg/g (C/EXK) at pH 2–58.9 mg/g (U/EXK), 80.2 mg/g (N/EXK), and 92.4 mg/g (C/EXK) at pH 8, retention qualities improved (Figure 6). In accordance with the pH specifications for industrial wastewater remediation established by the US EPA (pH 6–9), together with the measured efficacy of the evaluated structures throughout various pH levels, the examined structures could therefore be deemed adequate to be employed as reliable adsorbents during realistic treatment for SFR (Vivas and Cho, 2021). This included the elimination of SFR from the industrial wastewater corresponding to staining industries as well as the healthcare sector and the packaging of foods. The uptake activities can be illustrated based on the ionizing activity of SFR as a basic dye in conjunction with the dominant surface charges throughout the U/EXK, N/EXK, and C/EXK structures.

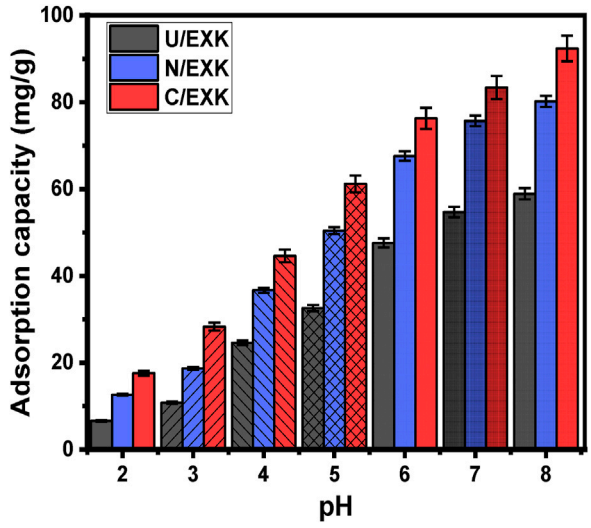

FIGURE 6
The influence of pH on the adsorption of SFR by U/EXK, N/EXK, and C/EXK.

In terms of SFR's ionizing characteristics, the SFR molecules possess positive electrical charges as a result of its protonation behavior at pH < 11 for its pKa value (pKa = 11). Therefore, the soluble SFR molecules at the highest level of studied pH values (pH 8) display powerful electrostatic attractive forces with the deprotonated and negative-charged functionalities of U/EXK, N/EXK, and C/EXK at this pH level (basic environment) (Adly et al., 2022; Vivas and Cho, 2021; Sriram et al., 2024). Moreover, at a significantly low pH, the structural amino group (-NH_2) of safranin undergoes protonation as a result of the high level of hydrogen ions that exist inside the dye solution. This protonation hinders the development of hydrogen-bonding between the SFR molecules and the interface of adsorbents (Ghosh et al., 2021). Also, this induces the formation of electrostatic repulsive forces between the dye molecules with the protonated and positively charged surfaces of EXK particles (Ghosh et al., 2021). By analyzing the optimal pH value in comparison with the values of pH_{PZC} that were measured for the adsorbents (6.8 (U/EXK), 6.6 (N/EXK), and 7.3 (C/EXK), the adsorptive elimination of SFR provided higher efficiency beyond the pH_{PZC}. In general, the EXK structures possess negative surface charges when the pH is higher than pH_{PZC}, but they turn positive when the pH is lower than pH_{PZC}.

3.2.2 Kinetic studies

3.2.2.1 Effect of contact time

An investigation had been performed to follow the adsorption properties of U/EXK, N/EXK, and C/EXK in terms of the duration of SFR elimination. The duration of the test ranged between 15 and 1,440 min. Following the maintenance of the other crucial parameters, like the SFR content (100 mg/L), pH (8), volume (100 mL), temperature (20°C), and dosage (0.4 g/L), the designated influence of time intervals was assessed. The efficacy of U/EXK, N/EXK, and C/EXK throughout the SFR retention processes reveals a substantial rise in both the determined amount of SFR captured and the experimental elimination rates. Furthermore, it is necessary to understand that the duration of the tests plays a major regulating role in the verified increases in the previously mentioned uptake characteristics (Figure 7A). Using U/EXK and C/EXK for 720 min and N/EXK for 480 min results in dramatically enhanced SFR uptake properties. However, there weren't any discernible changes or enhancements in the speed of SFR removal or the quantities of SFR maintained after the specified interacting durations. Based on earlier research, it can be hypothesized that the U/EXK, N/EXK, and C/EXK adsorbents attained their stable states after the aforementioned periods, which signifies the periods of their equilibrium states during the SFR uptake (Figure 7A). It has been determined that SFR has equilibrium retaining capacities of 115.2 mg/g, 154.3 mg/g, and 182.2 mg/g using U/EXK, N/EXK, and C/EXK, respectively. Powerful enhancements and rises in the extent of SFR elimination and the quantities of SFR retained were observed in the early stages of examination related to the abundance of a substantial quantity of reacting and unbound receptors across the structures of U/EXK, N/EXK, and C/EXK (El-Sherbeeny et al., 2021). The number of vacant receptors drops significantly with longer testing times. This is primarily attributable to the prolonged binding of SFR, which eventually occupies the aforementioned receptors and decreases the total number of unfilled receptors. As a result, after a certain period of time, the speed of SFR binding demonstrated a significant decline. Moreover, the uptake of SFR using U/EXK, N/EXK, and C/EXK showed limited improvement or stable characteristics. By occupying all the binding receptors, the equilibrium stages of U/EXK, N/EXK, and C/EXK can be recognized, and no additional SFR molecules can be adsorbed on their surfaces (Alhalili and Abdelrahman, 2024).

3.2.2.2 Intra-particle diffusion behavior

The analysis of SFR uptake behaviors using U/EXK, N/EXK, and C/EXK might potentially be illustrated by examining their intra-particle diffusion tendencies. The presented curves show three distinctive segments with varying slopes (Figure 7B). The ongoing analysis suggests that the evaluated curves deviate from their original positions, suggesting the existence of many adsorption processes alongside the diffusion pathway of SFR (Abdel Salam et al., 2022; Qada, 2020). The operational processes usually comprise three major phases: 1) the interactions among SFR and the unfilled receptors existing across the exterior interfaces of U/EXK, N/EXK, and C/EXK (boundary); 2) the layered capture of SFR alongside the diffusion characteristics of the SFR; and 3) the impact of saturation level and stabilizing conditions (Lin et al., 2021). The first results derived from these analyses suggest that the main processes that are accountable for binding SFR onto the outside layers of U/EXK, N/EXK, and C/EXK (external adsorption) comprised the most significant pathways identified throughout the whole process (Figure 7B). The efficacy of SFR adsorption at this stage relies on the overall quantities of receptors present at the contact interfaces of U/EXK, N/EXK, and C/EXK (Albukhari et al., 2021). Prolonging the time improved the detection of the new mechanistic step and highlighted the effectiveness of extra-layered adsorption reactions immediately after the entirety of external receptors were completely filled up (Figure 7B) (Lin et al., 2021; Abukhadra et al., 2022b). Furthermore, these additional processes involve the consequences of SFR diffusion

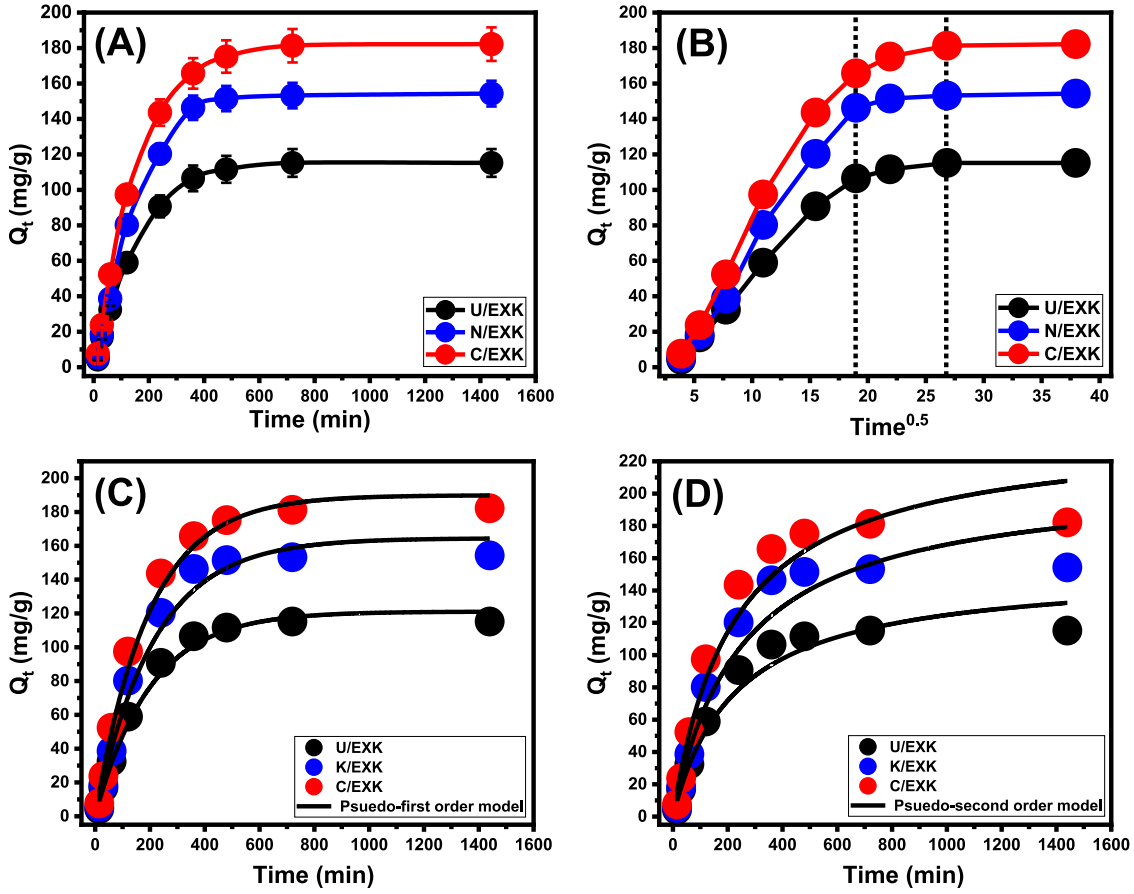

FIGURE 7
The influence of time frame on the adsorption of SFR by U/EXK, N/EXK, and C/EXK **(A)**, Intra-particle diffusion curves **(B)**, fitting of the SFR uptake with Pseudo-First order model **(C)**, and fitting of the SFR uptake with Pseudo-second order model **(D)**.

behaviors. Upon establishing the equilibrium states, the last SFR uptake mechanistic actions of U/EXK, N/EXK, and C/EXK demonstrate a significant effect. This suggests that all the SFR molecules that were successfully retained have filled up all the accessible binding sites (Abdel Salam et al., 2022; Wang et al., 2024). The removal of SFR during this stage is achieved by molecular interactions and interionic attraction mechanisms (Jiang et al., 2020).

3.2.2.3 Kinetic modeling

The use of adsorption-kinetic models is essential for investigating the effects of time as well as determining whether the adsorption process is controlled by physical processes, mainly mass transfer pathways or chemical pathways (Neolaka et al., 2020). The conventional kinetic principles of pseudo-first order (P.F.) and pseudo-second order (P.S.) mathematical models were used for analyzing the kinetic aspects of SFR-eliminating events using U/EXK, N/EXK, and C/EXK. The PFO model is used to analyze the kinetics of uptake activities across the equilibrium operation in order to clarify the relationship between the rate at which the binding sites get saturated by the analyte and the quantity of empty sites. The PSO model is used to illustrate the relationship between the adsorption capacities of assessed adsorbents as time progresses. By using nonlinear fitting parameters in accordance with the corresponding formulas, the agreement levels of the SFR retention procedures and kinetic principles in relation to the two different hypotheses were assessed. The coefficients of determination (R^2) and Chi-squared (χ^2) were used to determine the fitting degrees (Table 1; Figures 7C,D).

The R^2 values, together with the χ^2 statistics, indicate that the kinetic properties and principles of the P.F. theory donate a better fit for the adsorption actions of SFR using U/EXK, N/EXK, and C/EXK compared to the assessed P.S. assumption. The measured equilibrium uptake quantities (115.2 mg/g (U/EXK), 154.3 mg/g (N/EXK), and 182.2 mg/g (C/EXK)) closely matched the results obtained from mathematical calculations using the P.F. model (121.1 mg/g (U/EXK), 164.5 mg/g (N/EXK), and 190 mg/g (C/EXK)). The observed consistency provides further confirmation of the previously demonstrated results, which were highlighted during the kinetic assessments regarding the better compatibility of the P.F. model (Table 1). The P.F. theory suggests that the capture of SFR by U/EXK, N/EXK, and C/EXK is mainly controlled by physical mechanisms such as van der Waals forces or electrostatic attraction (Sherlala et al., 2019; Huang et al., 2018). The observed uptake characteristics likewise demonstrate substantial conformance to the P.S. theory, yet the P.F. modeling provides a higher level of agreement. Prior research has shown that common chemical effects such as hydrogen bonds, complexing, and

TABLE 1 The mathematical parameters of the addressed kinetic models.

Models	Parameters	U/EXK	N/EXK	C/EXK
Pseudo-First-order	K_1 (1/min)	0.995	0.995	0.005
	Qe $_{(Cal)}$ (mg/g)	121.1	164.5	189.9
	R (Zourou et al., 2022)	0.98	0.98	0.97
	X (Zourou et al., 2022)	0.90	1.50	1.18
Pseudo-Second-order	k_2 (mg/g min)	2.88×10^{-6}	1.92×10^{-5}	1.90×10^{-5}
	Qe $_{(Cal)}$ (mg/g)	153.1	210.1	239.5
	R (Zourou et al., 2022)	0.96	0.96	0.97
	X (Zourou et al., 2022)	1.92	3.09	2.71

hydrophobic bonds can either enhance or possess a negligible effect on the reduction of SFR by U/EXK, N/EXK, and C/EXK (Abdel Salam et al., 2022; Sherlala et al., 2019). The previously produced chemically bonded SFR layer may serve as the basis for the development of subsequent SFR adsorbing layers by physical processes (Jasper et al., 2020).

3.2.3 Equilibrium studies

3.2.3.1 Effect of concentrations

By analyzing the effects of starting SFR concentrations, the study intended to determine the highest ranges of the SFR removal qualities by U/EXK, N/EXK, and C/EXK as well as corresponding equilibrium situations throughout the assessed range of 25–300 mg/L. The other factors influencing the reduction of SFR were kept constant at defined levels, comprising a total volume of 100 mL, a duration of 24 h, a dosage of 0.4 g/L, and temperatures ranging between 293 K and 313 K. There may be a correlation between the higher SFR levels and the observed increase in the quantities of SFR retained by U/EXK, N/EXK, and C/EXK (Figures 8A–C). The increase in the extent of SFR within a certain volume led to a significant enhancement in the dispersal, driving forces, and migration characteristics of dissolved SFR. This facilitated interactions with a larger number of the functional uptake receptors that are present across U/EXK, N/EXK, and C/EXK surfaces. Hence, the SFR retaining processes conducted by U/EXK, N/EXK, and C/EXK exhibited noteworthy improvements in efficacy with respect to the assessed SFR contents (Ashraf et al., 2022). However, this relationship is only visible within specific constraints on SFR concentrations. Beyond that, increasing the initial concentration of SFR seems to have minimal impact on its uptake by U/EXK, N/EXK, and C/EXK. The identification of the equilibrium stages enables the determination of the accurate maximum retaining effectiveness of SFR. The SFR retaining capacities of U/EXK were 172.2 mg/g at 293 K, 150.8 mg/g at 303 K, and 125.3 mg/g at 313 K (Figure 8A). The equilibrium adsorption qualities with N/EXK were 220.2 mg/g at 293 K, 181.3 mg/g at 303 K, and 145.8 mg/g at 313 K (Figure 8B). The SFR adsorption qualities of C/EXK at various temperatures were 260.2 mg/g at 293 K, 225.6 mg/g at 303 K, and 190 mg/g at 313 K (Figure 8C). The improved uptake properties revealed by C/EXK can be explained by the following reasons: 1) the augmented surface area; 2) the notable improvement in surface reactivity; and 3) a significant rise in the total quantity of binding sites resulting from the enhanced exposure of the active siloxane groups. The reduction in SFR retention encountered by employing U/EXK, N/EXK, and C/EXK at different temperatures indicates that the processes are exothermic.

3.2.3.2 Giles's classification

The isotherm-based trends for SFR adsorption, employing U/EXK, N/EXK, and C/EXK, have been categorized in accordance with the criteria outlined in Giles' classification. The investigation revealed that the analyzed curves demonstrated an L-type class. Throughout the elimination operations of SFR utilizing U/EXK, N/EXK, and C/EXK, the isotherm aspects of this class reflect the significant impacts caused by intermolecular attractive reactions (Figures 7A–C). The described activities are intensified by the forceful interaction of SFR, which occurs at the highly reactive surfaces of U/EXK, N/EXK, and C/EXK (Abukhadra et al., 2018). According to the criteria of the L-type class, it was believed that U/EXK, N/EXK, and C/EXK particles would have complete layers of retained SFR developed on their surfaces (Shaban et al., 2017a). Furthermore, the recognized isothermal situations imply that the U/EXK, N/EXK, and C/EXK particulates possess a wide range of vital and effective sites for binding. Moreover, those binding sites exhibit notable affinity towards the SFR molecules, particularly when the starting SFR contents are low.

3.2.3.3 Classic isotherm models

Conventional isotherm studies of adsorption reactions may be used to assess the distribution of dissolved pollutants across the water solution and the particles of adsorbent materials at equilibrium. The clarification of adsorption mechanisms heavily depends on the implementation of traditional equilibrium modeling. The traditional isotherm behaviors offer valuable information about (a) the sorbate's affinities for the reacting surfaces of adsorbents, (b) the quantities of water-soluble molecules that can potentially be adsorbed by them, and (c) the greatest potential for adsorption. The Langmuir (Figures 8C–E), Freundlich (Figures 8G–I), and Dubinin-Radushkevich (D-R) (Figures 8J–L) equilibrium concepts were used to evaluate the isotherm characteristics of SFR sequestered characteristics utilizing U/EXK, N/EXK, and C/EXK. The non-linear equations corresponding to the aforementioned theories have been provided in Table 2. The level of agreement among

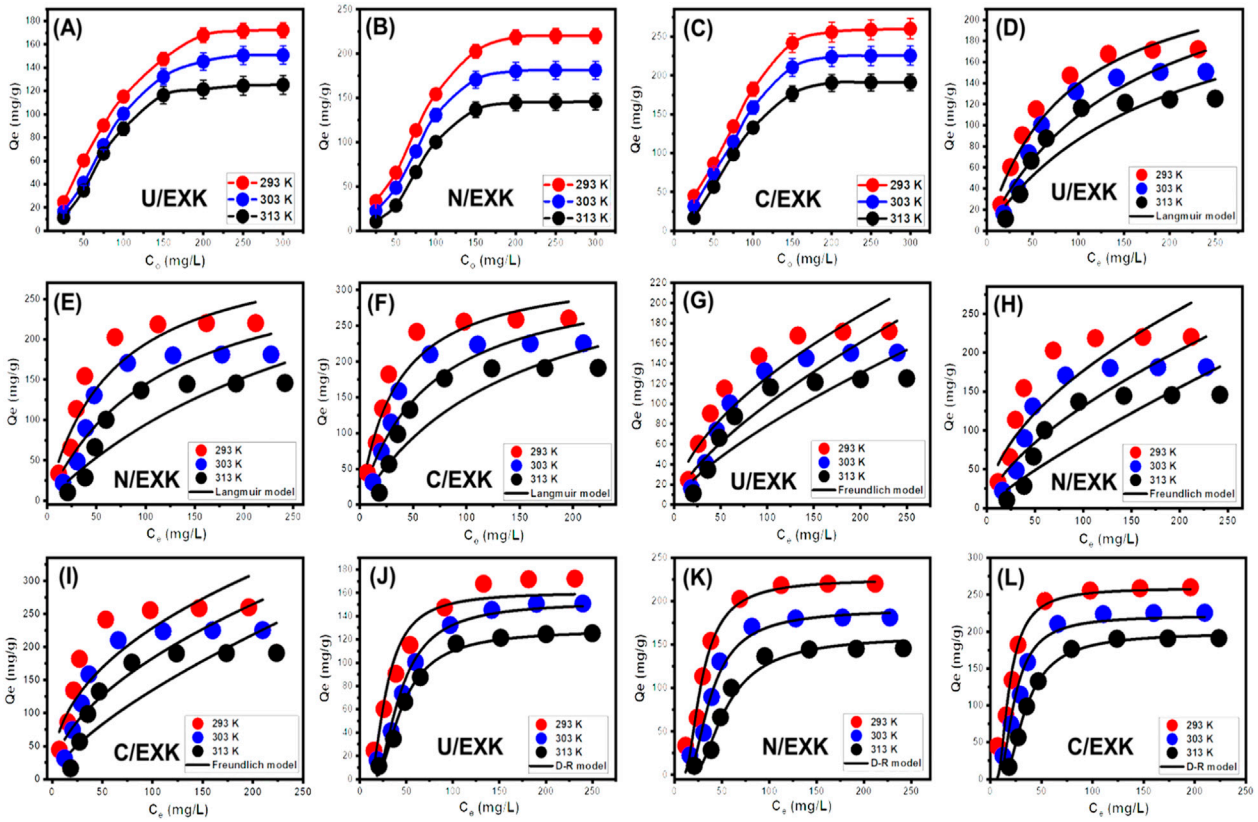

FIGURE 8
The influence of SFR concetration on its uptake capacity (U/EXK **(A)**, N/EXK **(B)**, and C/EXK **(C)**), fitting of the SFR uptake with Langmuir model (U/EXK **(D)**, N/EXK **(E)**, and C/EXK **(F)**), fitting of the SFR uptake with Freundlich model (U/EXK **(G)**, N/EXK **(H)**, and C/EXK **(I)**), and fitting of the SFR uptake with Langmuir model (U/EXK **(J)**, N/EXK **(K)**, and C/EXK **(L)**).

the stated equilibrium assumptions of the previously stated models and the practically measured SFR sequestration tendencies was evaluated using non-linear fitting approaches with the respective formulations for these mathematical models. The assessment involved investigating the correlation coefficient (R^2) in conjunction with the Chi-squared (χ^2) findings. The examination of R^2 and χ^2 indicates that the U/EXK, N/EXK, and C/EXK particulates have SFR adsorbing qualities that correlate more closely with Langmuir's principles than the Freundlich assumption. This equilibrium behavior (Langmuir isotherm) indicates that the binding affinity of SFR is homogeneous and uniformly distributed throughout the free and activated sites of U/EXK, N/EXK, and C/EXK particulates, forming a single or a monolayer of retained SFR (Sherlala et al., 2019; Huang et al., 2018). However, the Freundlich assumption donates the heterogeneous uptake of the dye molecules in multilayered form. Additionally, investigation proved that U/EXK, N/EXK, and C/EXK particles possess favorable SFR-retaining properties, as evidenced by RL values less than 1 (Albukhari et al., 2021; Wang et al., 2024). The highest adsorption capacities (Q_{max}) of SFR by U/EXK, were 287.3 mg/g at 293 K, 262.23 mg/g at 303 K, and 257.2 mg/g at 313 K (Table 2). The calculated values for N/EXK were 331.3 mg/g at 293 K, 323 mg/g at 303 K, and 312.8 mg/g at 313 K (Table 2). The outcomes obtained for C/EXK were 364.4 mg/g at 293 K, 332.7 mg/g at 303 K, and 329 mg/g at 313 K.

The equilibrium features of the D-R theory provide a thorough comprehension of the energy fluctuations displayed by U/EXK, N/EXK, and C/EXK particulates during SFR scavenging operations, regardless of the particle's level of homogeneity or heterogeneity (Dawodu and Akpomie, 2012). Analyzing the D-R simulation outcomes has significance for calculating the Gaussian energy (E) and understanding the fundamental mechanisms (chemical or physical). The adsorption reactions exhibit energy levels below 8 kJ/mol, within 8–16 kJ/mol, and above 16 kJ/mol, which mainly correspond to strong physical, predominantly diminished chemical-based, or a mix of chemical alongside physical and predominantly strong chemical-based mechanisms, respectively (Wang et al., 2024). The measured values of E corresponding to SFR-retaining reactions by U/EXK, N/EXK, and C/EXK are inside the specified energy range (8–16 kJ/mol) for co-operated chemical and physical activities.

3.2.3.4 Advanced isotherm modeling

The classic isotherm models as Langmuir model give no remarkable physical significance about the adsorption processes and cannot describe the relation between the different physicochemical parameters during the adsorption process (Dhaouadi et al., 2021). Therefore, the advanced isotherm models based on the basic s of statistical physics theories were recommended in the later periods. Utilizing statistical physics

TABLE 2 The mathematical parameters of the addressed classic isotherm models.

Models	Parameters	U/EXK			N/EXK			C/EXK		
		293 K	303 K	313 K	293 K	303 K	313 K	293 K	303 K	313 K
Langmuir	Q_{max} (mg/g)	287.3	262.2	257.2	331.3	323.0	312.8	364.4	332.7	329.1
	b (L/mg)	0.006	0.011	0.005	0.003	0.015	0.008	0.007	0.029	0.015
	R (Zourou et al., 2022)	0.92	0.95	0.90	0.87	0.92	0.89	0.88	0.95	0.91
	X (Zourou et al., 2022)	3.18	2.52	4.01	4.13	2.89	3.55	4.38	2.63	3.12
Freundlich	1/n	0.572	0.693	0.733	0.535	0.635	0.836	0.437	0.533	0.698
	k_F (mg/g)	9.03	4.07	2.68	15.02	7.01	1.85	30.50	15.70	5.41
	R (Zourou et al., 2022)	0.88	0.87	0.84	0.83	0.82	0.82	0.84	0.82	0.90
	X (Zourou et al., 2022)	4.30	4.67	5.17	5.27	5.92	6.18	5.33	5.67	3.42
Dubinin-Radushkevich	β (mol (Zourou et al., 2022)/KJ (Zourou et al., 2022))	0.0055	0.0058	0.0061	0.0072	0.0073	0.0074	0.0060	0.0064	0.0066
	Q_m (mg/g)	160.6	152.1	128.1	225.6	190.6	160.2	259.3	221.9	198.5
	R (Zourou et al., 2022)	0.96	0.97	0.98	0.92	0.94	0.96	0.90	0.96	0.99
	X (Zourou et al., 2022)	2.37	1.99	1.03	2.04	1.53	1.38	3.94	2.25	0.11
	E (KJ/mol)	9.51	9.22	8.90	8.30	8.26	8.19	9.12	8.80	8.65

approaches to simulate the equilibrium of adsorption activities may provide an in-depth analysis of the specific qualities of adsorption processes. These mathematical simulations evaluate the interactions between soluble contaminants and exterior active functionalities as reacting receptors across the interfaces of solid materials as adsorbing agents. The mathematical models used in this study comprise a number of computation variables that successfully depict the fundamental mechanisms that involve both energetic and steric factors. The models develop steric aspects such as the receptor site occupation (n) by SFR individually, the overall number of sites occupied by SFR throughout the U/EXK, N/EXK, and C/EXK interfaces (N_m), and the maximum uptake effectiveness of SFR by U/EXK, N/EXK, and C/EXK when they are totally saturated (Q_{sat}). The energetic characteristics consist of internal energy (E_{int}), entropy (Sa), retaining energy (E), and free enthalpy (G). The evaluation of these theories included the application of non-linear regression analyses using the represented equations derived for the relevant models. The earlier investigation was effectively performed by employing multivariable nonlinear regression analyses in combination with the Levenberg-Marquardt iterative method. The obtained levels of fitness were subsequently utilized to assess and characterize the adsorption tendencies of SFR via U/EXK, N/EXK, and C/EXK employing the highly fitted model (monolayer model of a single energetic site (Figures 9A–C)). Table 3 provides the computed parameters along with the fitting factors.

3.2.3.4.1 Steric properties.

3.2.3.4.1.1 Number of adsorbed SFR (n) per each site. The numerical findings of the $n_{(SFR)}$ factor provide adequate proof of the arrangement behavior of the adsorbed SFR ions occupying the exterior surfaces of U/EXK, N/EXK, and C/EXK. This includes both the vertical as well as the horizontal orientations. Additionally, these outcomes are significant in understanding the mechanisms that regulate the reactions, such as multi-docking or multi-interactions. The capture of one SFR ion via multiple uptake sites is one of the reactions that are most significantly impacted by multi-anchorage or multi-docking operations. The retention reactions with values less than one are associated with the ions' horizontal orientation. Conversely, activities that display values above 1 indicate the retaining of SFR within non-parallel geometries together with a vertical orientation. The uptake processes in such systems are mainly mediated by multi-molecular pathways, whereby a single site captures several dye ions (Wang et al., 2024; Mobarak et al., 2021). The determined values of n, which represent the number of bound SFR by a single site of U/EXK, range from 1.91 to 2.37 (Figure 9D). The quantity of SFR molecules maintained by a single site throughout the interfaces of N/EXK (with a range of $n_{(SFR)}$ = 2.11–3.8) (Figure 9E) and C/EXK (with a range of $n_{(SFR)}$ = 1.7–3.4) (Figure 9F) was found to be consistently greater than 1 as determined for U/EXK. As a result, the SFR dye was adsorbed by multi-molecular mechanisms. Each retaining site within the U/EXK, N/EXK, and C/EXK particulates had the ability to accommodate multiple ions that were organized in vertical configurations with distinct non-parallel characteristics. The individual receptors within the exterior surface of U/EXK can hold up to 3 SFR ions; however, each binding site through the external surfaces of N/EXK and C/EXK is capable of holding 4 ions. This suggests considerable changes in the exterior properties of scrubbed kaolinite depending on the used methods and the specific interspersed reagent. The $n_{(SFR)}$ computations for U/EXK, N/EXK, and C/EXK show a significant rise via temperature from 293 K to 313 K. The behavior that has been noticed may be attributed to the presumed increase in the SFR's aggregation qualities during its adsorption by U/EXK, N/EXK, and C/EXK at elevated temperatures (Ashraf et al., 2022). This also indicates the

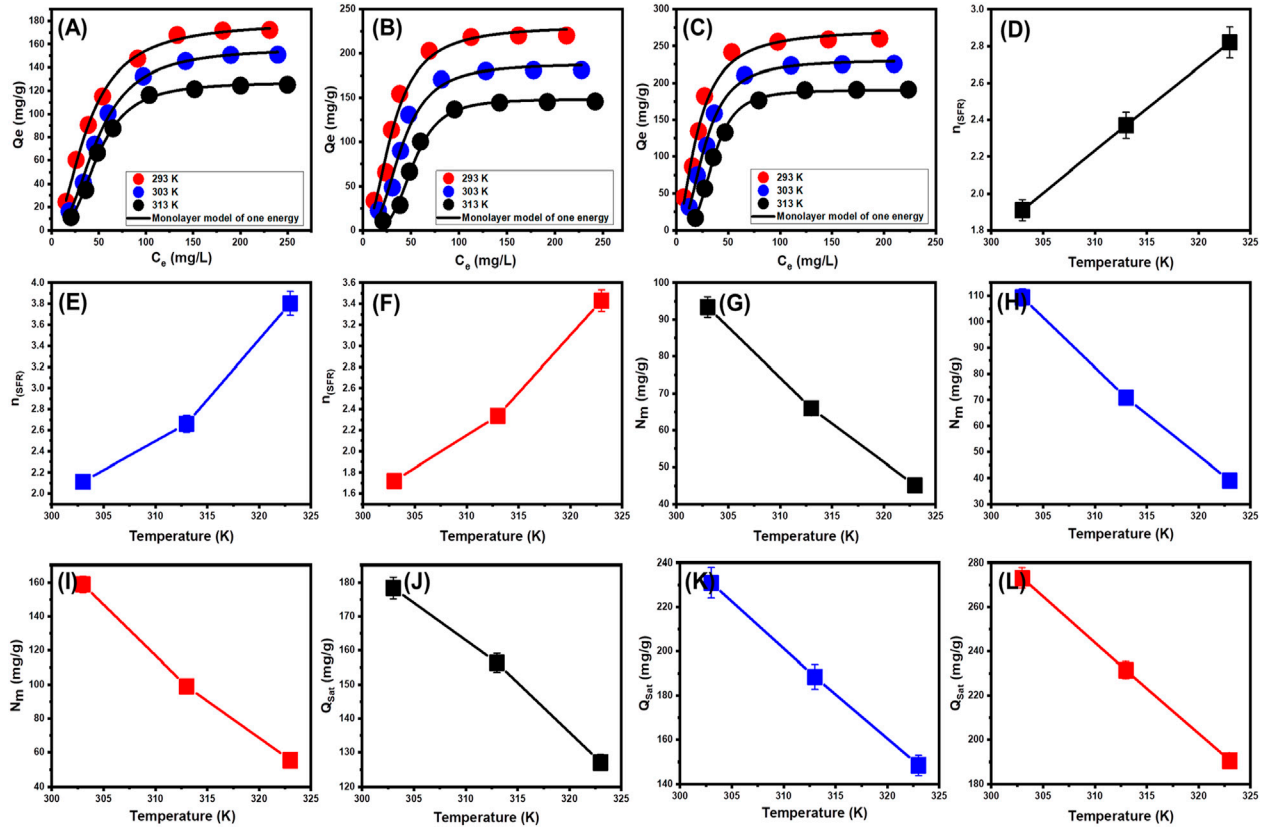

FIGURE 9
Fitting of the SFR uptake with Monolayer model of single energy site (U/EXK **(A)**, N/EXK **(B)**, and C/EXK **(C)**), changes in the number of adsorbed SFR molecules per each site (U/EXK **(D)**, N/EXK **(E)**, and C/EXK **(F)**), changes in the uptake sites density (U/EXK **(G)**, N/EXK **(H)**, and C/EXK **(I)**), and changes in the saturation uptake capacities (U/EXK **(J)**, N/EXK **(K)**, and C/EXK **(L)**).

presence of thermal activation mechanisms prior to the retention of SFR utilizing U/EXK, N/EXK, and C/EXK (Yang et al., 2022; Dhaouadi et al., 2021).

3.2.3.4.1.2 Occupied active sites density (N_m). The density of SFR-occupied sites (Nm $_{(SFR)}$) of U/EXK, N/EXK, and C/EXK may accurately indicate the total amount of free and functional binding receptors onto the exteriors of their particles across the overall reaction (Figures 8E–H; Table 4). U/EXK's estimate indicates that the amounts of Nm $_{(SFR)}$ at various temperatures are 93.4 mg/g (293 K), 65.9 mg/g (303 K), and 45.1 mg/g (313 K) (Figure 9G; Table 3). The quantities showed a notable rise after the exfoliating process employing KNO_3 (N/EXK), reaching 109.3 mg/g at 293 K, 70.8 mg/g at 303 K, and 39.4 mg/g at 313 K (Figure 9H; Table 3). The degree of improvement increased greatly following the exfoliation process employing the CTAB embedding agent, resulting in quantities of 158.8 mg/g (293 K), 99 mg/g (303 K), and 55.5 mg/g (313 K) (Figure 9I; Table 3). The results presented provide reliable proof of a significant increase in the number of existing receptors after exfoliating with CTAB (C/EXK) in comparison with U/EXK and N/EXK. The increase in surface area, coupled with the improved surficial reactivity and the greater exposure for the influential siloxane groups, leads to an improved contact and interaction interface among SFR ions and the C/EXK surface. Regarding their temperature responses, the Nm $_{(SFR)}$ values for U/EXK, N/EXK, and C/EXK reveal temperature-dependent reversible changes. This aligns with the tracked responses of n $_{(SFR)}$, as the higher aggregation affinities of SFR dye result in a decrease in the overall number of occupied receptors as well. Furthermore, the temperature significantly affects the activity degrees of the existing receptors that were involved in the reaction (Yang et al., 2022; Sellaoui et al., 2020).

3.2.3.4.1.3 Adsorption capacity at the saturation state of (Q_{sat}). The saturation adsorption properties of U/EXK, N/EXK, and C/EXK (Q_{sat}) demonstrate the predicted maximum quantities of sequestered SFR with the greatest level of tolerance. The values of Q_{sat} are controlled by two main variables: the specified density of the loaded sites (Nm) and the total number of SFR ions captured by a single receptor (n). U/EXK, a potential adsorbent for SFR, demonstrates Q_{sat} values of 178.4 mg/g at 293 K, 156.4 mg/g at 303 K, and 127.1 mg/g at 313 K (Figure 9J; Table 3). The utilization of N/EXK exhibits hypothesized maximum capacities of 231 mg/g (at 293 K), 188.4 mg/g (at 303 K), and 148.4 mg/g (at 313 K) (Figure 9K; Table 3). The application of C/EXK demonstrated improved effectiveness, exhibiting values of 273.2 mg/g at 293 K, 231.4 mg/g at 303 K, and 190.5 mg/g at 313 K (Figure 9L; Table 3). The exothermic properties of SFR retaining operations using U/EXK, N/EXK, and C/EXK can potentially be noticed by the adverse effect of temperature. This implies that the effect of thermal collisions rises with retaining temperature and reduces the effectiveness of SFR binding (Mobarak et al., 2021).

TABLE 3 The mathematical parameters of the studied advanced isotherm model.

		293 K	303 K	313 K
U.EXK	R (Zourou et al., 2022)	0.99	0.99	0.99
	X (Zourou et al., 2022)	0.09	0.19	0.14
	n	1.91	2.37	2.82
	Nm (mg/g)	93.40	65.98	45.07
	Q_{Sat} (mg/g)	178.4	156.4	127.1
	C1/2 (mg/L)	38.4	48.6	48.8
	ΔE (kJ/mol)	−8.88	−9.78	−10.10
N.EXK	R (Zourou et al., 2022)	0.98	0.98	0.98
	X (Zourou et al., 2022)	1.75	1.61	1.20
	n	2.11	2.66	3.80
	N_m (mg/g)	109.3	70.8	39.0
	Q_{Sat} (mg/g)	231.0	188.4	148.4
	C1/2 (mg/L)	31.2	40.4	52.3
	ΔE (kJ/mol)	−8.38	−9.31	−10.29
C.EXK	R (Zourou et al., 2022)	0.98	0.99	0.99
	X (Zourou et al., 2022)	1.34	0.23	0.10
	n	1.72	2.33	3.43
	N_m (mg/g)	158.8	99.0	55.5
	Q_{Sat} (mg/g)	273.2	231.4	190.5
	C1/2 (mg/L)	20.9	27.7	35.4
	ΔE (kJ/mol)	−7.40	−8.36	−9.29

Furthermore, the observed characteristics of Q_{sat} associated with temperature fluctuations suggest a resemblance to the specified tendencies of Nm instead of n. This proves that the effectiveness of SFR adsorption depends on the quantities of the binding receptors instead of the capacity of every single binding site.

3.2.3.4.2 Energetic properties.

3.2.3.4.2.1 Adsorption energy. The energy variations (ΔE) encountered throughout the uptake activities of SFR may accurately reveal the underlying mechanisms, whether they are related to physical or chemical behaviors. The physical processes exhibit energy beneath 40 kJ/mol, while the chemical paths have energy exceeding 80 kJ/mol. Adsorption energy can be utilized to categorize a variety of physically occurring mechanistic processes. The physical interactions reported include coordinating exchange (40 kJ/mol), bonding of hydrogen (<30 kJ/mol), dipole bonding (2–29 kJ/mol), electrostatic attractions (2–50 kJ/mol), van der Waals forces (4–10 kJ/mol), and hydrophobic bonding (5 kJ/mol) (Ashraf et al., 2022; Ali et al., 2021). The theoretical determination of the SFR elimination energies (ΔE) was accomplished using Equation 5, considering the soluble state of SFR inside water (S), gas constant (R = 0.008314 kJ/mol.K), SFR contents throughout half saturation situations of U/EXK, N/EXK, and C/EXK, and actual temperature (T) (Dhaouadi et al., 2020).

TABLE 4 Comparison between the adsorption properties of EXK structures and other studied structures in literature.

Adsorbent	q_{max} (mg/g)	Reference
Ppy NF/Zn-Fe LDH	63.4	Mohamed et al. (2018)
Glass-MCM-48	62.5	Abukhadra and Shaban (2019)
Activated carbon	576	Kumar and Sivanesan (2005)
MCM-41	68.8	Kaur et al. (2015)
MgO-FLG-FE	201.1	Reddy et al. (2018)
CuO-NP	189.5	Vidovix et al. (2021)
N/porous graphite	20.66	Shaban et al. (2017b)
Sepiolite	233.81	Barhdadi et al. (2024)
Ferruginous kaolinite	59.3	Debnath et al. (2017)
Magnetic clay	18.48	Abukhadra et al. (2020b)
Raw kaolinite	14.37	This study
U/EXK	178.4	This study
N/EXK	231	This study
C/EXK	273.2	This study

$$\Delta E = RT\,ln\left(\frac{S}{C}\right) \tag{5}$$

The energy measurements for SFR retention, as determined for U/EXK and N/EXK, vary from −8.8 and −8.38 kJ/mol to −10.11 and −10.29 kJ/mol, respectively (Table 3). The estimated values for C/EXK varied between −7.4 and −9.29 kJ/mol (Table 4). Hence, the key mechanisms responsible for the uptake of SFR via U/EXK, N/EXK, and C/EXK were physical processes, including dipole bonding (2–29 kJ/mol), van der Waals forces (4–10 kJ/mol), electrostatic attractions (2–50 kJ/mol), and hydrogen bonding (<30 kJ/mol). Additionally, the observed negative indications of the expected E values during the capture of SFR are consistent with the prior experimental results describing the exothermic characteristics of these reactions.

3.2.3.4.3 Thermodynamic functions.

3.2.3.4.3.1 Entropy. The entropy (Sa) corresponding to the SFR retention processes by U/EXK, N/EXK, and C/EXK provides an obvious illustration of the order and disorder characteristics of the outermost surfaces of their nanostructures when subjected to different levels of dye ions, in addition to the specified reaction temperature. The Sa characteristics were illustrated by implementing the results obtained from Equation 6, including the previously established measurements of Nm and n, in addition to the predicted contents of SFR throughout the half-saturation states of U/EXK, N/EXK, and C/EXK (C1/2).

$$\frac{S_a}{K_B} = Nm\left\{ ln\left(1+\left(\frac{C}{C_{\frac{1}{2}}}\right)^n\right) - n\left(\frac{C}{C_{\frac{1}{2}}}\right)^n \frac{ln\left(\frac{C}{C_{\frac{1}{2}}}\right)}{1+\left(\frac{C}{C_{\frac{1}{2}}}\right)^n} \right\} \tag{6}$$

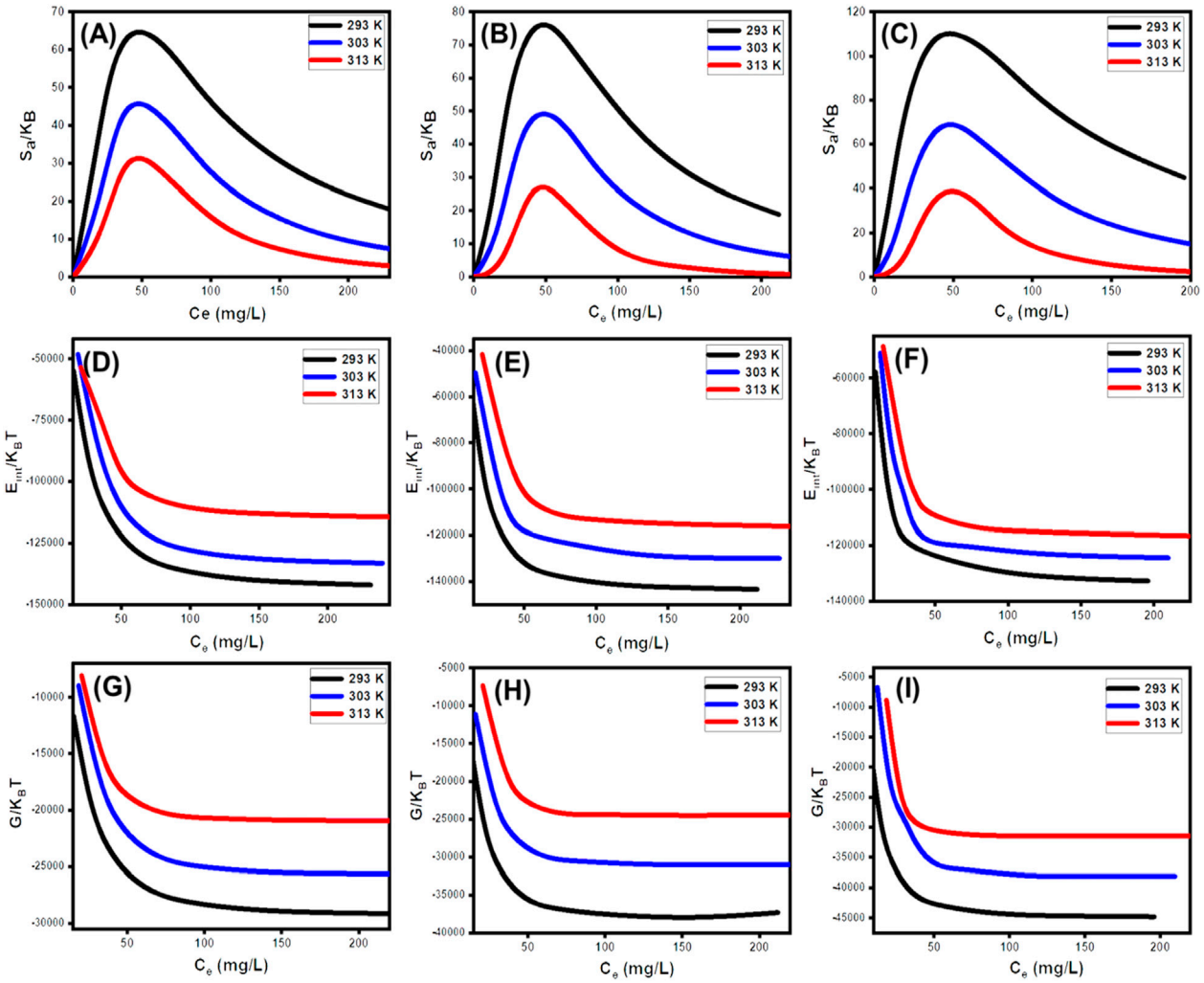

FIGURE 10
Changes in the thermodynamic functions during the upatke of SFR including entropy (U/EXK **(A)**, N/EXK **(B)**, and C/EXK **(C)**), internal energy (U/EXK **(D)**, N/EXK **(E)**, and C/EXK **(F)**), and enthalpy (U/EXK **(G)**, N/EXK **(H)**, and C/EXK **(I)**).

From the observed curves, it is evident that the entropy levels (Sa) experience a significant drop when SFR gets captured by U/EXK, N/EXK, and C/EXK, especially at elevated SFR concentrations (Figures 10A–C). This trend indicates a notable decrease in the disorder characteristics that characterize the interfaces of U/EXK, N/EXK, and C/EXK with increasing examined SFR extents. The entropy characteristics also facilitate the successful docking of SFR onto the unoccupied and influential interacting sites of U/EXK, N/EXK, and C/EXK, regardless of the presence of small concentrations of SFR (Sellaoui et al., 2020; Dhaouadi et al., 2020). The maximum magnitudes of entropy were noted when SFR was captured by U/EXK at equilibrium levels of 38.8 mg/L (293 K), 45.6 mg/L (303 K), and 48.4 mg/L (313 K) (Figure 10A). The equilibrium values for the greatest entropy during the elimination of SFR using N/EXK are 38.3 mg/L at a temperature of 293 K, 47.7 mg/L at a temperature of 303 K, and 48.4 mg/L at a temperature of 313 K (Figure 10B). The employing of C/EXK demonstrates the highest degree of entropy at SFR concentrations of 27.2 mg/L (at 293 K), 36.5 mg/L (at 303 K), and 46.8 mg/L (at 313 K) (Figure 10C). The equilibrium levels closely approximate the concentrations estimated for the half-saturation stages of U/EXK, N/EXK, and C/EXK. As a result, additional SFR ions are unable to dock with the remaining accessible binding receptors. Additionally, the considerable decreases in the assessed entropy degrees suggest an extensive decrease in the quantity of accessible sites, as well as a noticeable decrease in the mobility and diffuse characteristics of the SFR ions (Sellaoui et al., 2016).

3.2.3.4.3.2 Internal energy and free enthalpy. The study assessed the internal energy (E_{int}) correlated with the binding reactions of U/EXK, N/EXK, and C/EXK, alongside the qualities of free enthalpy (G) and the manner in which they are affected by changes in dye contents and operating temperature. The evaluation was conducted using values obtained from Equations 7, 8, which were computed using the earlier established Nm, n, and C1/2, along with the translation partition (Zv) (Dhaouadi et al., 2021).

$$\frac{E_{int}}{K_B T} = n N_m \left[\left(\frac{\left(\frac{C}{C_{1/2}}\right)^n ln\left(\frac{C}{Z_v}\right)}{1+\left(\frac{C}{C_{1/2}}\right)^n} \right) - \left(\frac{n ln\left(\frac{C}{C_{1/2}}\right)\left(\frac{C}{C_{1/2}}\right)^n}{1+\left(\frac{C}{C_{1/2}}\right)^n} \right) \right] \quad (7)$$

$$\frac{G}{K_B T} = n N_m \left(\frac{ln\left(\frac{C}{Z_v}\right)}{1+\left(\frac{C_{1/2}}{C}\right)^n} \right) \quad (8)$$

The calculated values of E_{int} with respect to SFR retention processes via U/EXK, N/EXK, and C/EXK possess negative signs, and these findings reveal a significant decrease whenever the temperature is increased from 293 K to 313 K (Figures 1D–F). This validates the spontaneous alongside exothermic characteristics of the SFR elimination processes via U/EXK, N/EXK, and C/EXK. Similar behaviors and properties have been identified for the described levels and behaviors of enthalpy (Figures 10G–I). The G results have negative signs and demonstrate a reversible correlation with the practical retention temperature. This suggests a decrease in the feasibility features and confirms the spontaneity and exothermic behaviors of the SFR sequestration using U/EXK, N/EXK, and C/EXK (Figures 10K,L).

3.2.4 Recyclability

The efficacy of U/EXK, N/EXK, and C/EXK as adsorption agents for SFR has been investigated, with a focus on their recycling potential, a crucial factor in assessing their feasibility for industrial and realistic uses. The U/EXK, N/EXK, and C/EXK structures underwent thorough rinsing with distilled water throughout a period of 10 min, and this process had been repeated multiple times. The U/EXK, N/EXK, and C/EXK had been subsequently dried at a temperature of 60°C for a period of 10 h to enhance their suitability for use in further SFR purification cycles. The recyclability experiments were carried out under controlled conditions, including a pH of 8, a dosage of 0.40 g/L, a duration of 24 h, a volume of 100 mL, SFR levels of 100 mg/L, and a temperature of 293 K. The outcomes of the five experimental iterations performed to evaluate the utilization of U/EXK, N/EXK, and C/EXK as adsorbents exhibit steady and impressive effectiveness in capturing SFR, together with notable stability and satisfactory reusability characteristics (Figure 11). The U/EXK material exhibited notable recyclability, achieving removal effectiveness of 172.2 mg/g (Run 1), 170.1 mg/g (Run 2), 161.3 mg/g (Run 3), 145.4 mg/g (Run 4), and 140.3 mg/g (Run 5). The purification process of SFR resulted in elimination capacities of 220.2 mg/g (Run 1), 216.4 mg/g (Run 2), 210.3 mg/g (Run 3), 201.4 mg/g (Run 4), and 197.4 mg/g (Run 5) while recycling N/EXK. The results obtained by employing C/EXK during the recycling experiments are as follows: 260.2 mg/g (Run 1), 256.4 mg/g (Run 2), 253.4 mg/g (Run 3), 247.6 mg/g (Run 4), and 235.2 mg/g (Run 5).

3.2.5 Comparison study

The recognized adsorption capacities of the three forms of exfoliated kaolinite (U/EXK, N/EXK, and C/EXK) were compared with the reported adsorption capacities of other investigated adsorbents in the literature (Table. 4). The exfoliated products displayed higher adsorption properties for safranin dye as compared to raw kaolinite and other different species of clay-based adsorbents, including ferruginous kaolinite, magnetic clay, and sepiolite, in addition to other species of adsorbents such as LDH, mesoporous silica, graphite, CuO, MgO, and activated carbon.

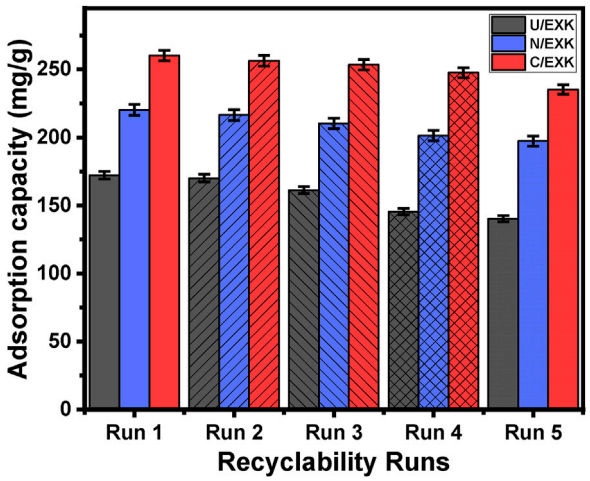

FIGURE 11
The recyclability properties of the synthetic exfoliated products during the adsorption of SFR.

4 Conclusion

Kaolinite mineral was exfoliated successfully into monolayer using three different intercalating agents (urea (U/EXK), KNO_3 (N/EXK), and CTAB (C/EXK)). The applied characterization techniques confirmed effective impact for the applied agent and exfoliation technique on the properties of the obtained monolayers. The structural, morphological, and textural results reflected the highest exfoliation degree of C/EXK as compared to U/EXK and N/EXK. C/EXK also exhibits the best uptake performance of SFR (273.2 mg/g) as compared to 231 mg/g for N/EXK and 178.4 mg/g for U/EXK. This is correlated with its highest surface area (55.7 m^2/g) and effective sites density ($Nm_{(SFR)}$ = 158.8 mg/g) in contrast to U/EXK and N/EXK. The three products display no significant variation in the controlling mechanism based on the adsorption energy ($\Delta E < 40$ kJ/mol). The regulating mechanisms are mainly physical, spontaneous, and exothermic reactions involving dipole bonding, van der Waals forces, and hydrogen bonding. Based on the optimization conditions, the determined adsorption capacities, and recyclability values, the synthetic structures can be effectively applied as reliable adsorbents during the realistic removal of safranin-O dye from industrial wastewater that is related to the discharges of staining industries as well as the healthcare sector and the packaging of foods.

Data availability statement

The original contributions presented in the study are included in the article/Supplementary Material, further inquiries can be directed to the corresponding authors.

Author contributions

SA: Writing–review and editing, Writing–original draft, Visualization, Software, Resources, Methodology, Formal Analysis, Data curation, Conceptualization RM: Writing–review and editing, Writing–original draft, Validation, Supervision AA-K: Writing–review and editing, Writing–original draft, Validation, Supervision AA: Writing–review and editing, Writing–original draft, Validation, Project administration, Methodology, Investigation, Funding acquisition, Formal Analysis, Data curation, Conceptualization MA: Writing–review and editing, Writing–original draft, Visualization, Validation, Supervision, Software, Resources, Methodology, Investigation, Formal Analysis, Data curation, Conceptualization

Funding

The author(s) declare that financial support was received for the research, authorship, and/or publication of this article. This work was supported and funded by the Deanship of Scientific Research at Imam Mohammad Ibn Saud Islamic University (IMSIU) (grant number IMSIU-RPP2023125).

Conflict of interest

The authors declare that the research was conducted in the absence of any commercial or financial relationships that could be construed as a potential conflict of interest.

Publisher's note

All claims expressed in this article are solely those of the authors and do not necessarily represent those of their affiliated organizations, or those of the publisher, the editors and the reviewers. Any product that may be evaluated in this article, or claim that may be made by its manufacturer, is not guaranteed or endorsed by the publisher.

Supplementary material

The Supplementary Material for this article can be found online at: https://www.frontiersin.org/articles/10.3389/fchem.2024.1455838/full#supplementary-material

References

Abdel Salam, M., Mokhtar, M., Albukhari, S. M., Baamer, D. F., Palmisano, L., Jaremko, M., et al. (2022). Synthesis and characterization of green ZnO@ polynaniline/bentonite tripartite structure (G. Zn@ PN/BE) as adsorbent for as (V) ions: integration, steric, and energetic properties. *Polymers* 14 (12), 2329. doi:10.3390/polym14122329

Abdo, S. M., El-Hout, S. I., Shawky, A., Rashed, M. N., and El-Sheikh, S. M. (2022). Visible-light-driven photodegradation of organic pollutants by simply exfoliated kaolinite nanolayers with enhanced activity and recyclability. *Environ. Res.* 214, 113960. doi:10.1016/j.envres.2022.113960

Abukhadra, M. R., and Allah, A. F. (2019). Synthesis and characterization of kaolinite nanotubes (KNTs) as a novel carrier for 5-fluorouracil of high encapsulation properties and controlled release. *Inorg. Chem. Commun.* 103, 30–36. doi:10.1016/j.inoche.2019.03.005

Abukhadra, M. R., Dardir, F. M., Shaban, M., Ahmed, E. A., and Soliman, M. F. (2018). Superior removal of Co2+, Cu2+ and Zn2+ contaminants from water utilizing spongy Ni/Fe carbonate–fluorapatite; preparation, application and mechanism. *Ecotoxicol. Environ. Saf.* 157, 358–368. doi:10.1016/j.ecoenv.2018.03.085

Abukhadra, M. R., El-Meligy, M. A., and El-Sherbeeny, A. M. (2020b). Evaluation and characterization of Egyptian ferruginous kaolinite as adsorbent and heterogeneous catalyst for effective removal of safranin-O cationic dye from water. *Arabian J. Geosciences* 13, 169. doi:10.1007/s12517-020-5182-6

Abukhadra, M. R., Mohamed, A. S., El-Sherbeeny, A. M., and A Soliman, A. T. (2020a). Enhanced adsorption of toxic and biologically active levofloxacin residuals from wastewater using clay nanotubes as a novel fixed bed: column performance and optimization. *ACS Omega* 5 (40), 26195–26205. doi:10.1021/acsomega.0c03785

Abukhadra, M. R., Mostafa, M., Jumah, M. N. B., Al Khalawi, N., Alruhaimi, R. S., Salama, Y. F., et al. (2022b). Correction: insight into the adsorption properties of chitosan/zeolite A hybrid structure for effective decontamination of toxic Cd (II) and as (V) ions from the aqueous environments. *J. Polym. Environ.* 30, 4500. doi:10.1007/s10924-022-02525-y

Abukhadra, M. R., Saad, I., Othman, S. I., Katowah, D. F., Ajarem, J. S., Alqarni, S. A., et al. (2022a). Characterization of Fe0@Chitosan/Cellulose structure as effective green adsorbent for methyl Parathion, malachite Green, and levofloxacin Removal: experimental and theoretical studies. *J. Mol. Liq.* 368, 120730. doi:10.1016/j.molliq.2022.120730

Abukhadra, M. R., and Shaban, M. (2019). Recycling of different solid wastes in synthesis of high-order mesoporous silica as adsorbent for safranin dye. *Int. J. Environ. Sci. Technol.* 16, 7573–7582. doi:10.1007/s13762-019-02231-8

Adly, E. R., Shaban, M. S., El-Sherbeeny, A. M., Al Zoubi, W., and Abukhadra, M. R. (2022). Enhanced Congo red adsorption and photo-fenton oxidation over an iron-impeded geopolymer from ferruginous kaolinite: steric, energetic, oxidation, and synergetic studies. *ACS Omega* 7, 31218–31232. doi:10.1021/acsomega.2c03365

Ahrouch, M., Gatica, J. M., Draoui, K., Bellido, D., and Vidal, H. (2020). Honeycomb filters as an alternative to powders in the use of clays to remove cadmium from water. *Chemosphere* 259, 127526. doi:10.1016/j.chemosphere.2020.127526

Ahrouch, M., Gatica, J. M., Draoui, K., Bellido-Milla, D., and Vidal, H. (2022). Clay honeycomb monoliths for the simultaneous retention of lead and cadmium in water. *Environ. Technol. and Innovation* 27, 102765. doi:10.1016/j.eti.2022.102765

Ahrouch, M., Gatica, J. M., Draoui, K., and Vidal, H. (2019). Adding value to natural clays as low-cost adsorbents of methylene blue in polluted water through honeycomb monoliths manufacture. *SN Appl. Sci.* 1, 1595. doi:10.1007/s42452-019-1636-4

Albukhari, S. M., Salam, M. A., and Abukhadra, M. R. (2021). Effective retention of inorganic Selenium ions (Se (VI) and Se (IV)) using novel sodalite structures from muscovite; characterization and mechanism. *J. Taiwan Inst. Chem. Eng.* 120, 116–126. doi:10.1016/j.jtice.2021.02.026

Alhalili, Z., and Abdelrahman, E. A. (2024). Facile synthesis and characterization of manganese ferrite nanoparticles for the successful removal of safranine T dye from aqueous solutions. *Inorganics* 12 (1), 30. doi:10.3390/inorganics12010030

Ali, R. A., Mobarak, M., Badawy, A. M., Lima, E. C., Seliem, M. K., and Ramadan, H. (2021). New insights into the surface oxidation role in enhancing Congo red dye uptake by Egyptian ilmenite ore: experiments and physicochemical interpretations. *Surfaces Interfaces* 26, 101316. doi:10.1016/j.surfin.2021.101316

Allah, A. F., Abdel-Khalek, A. A., El-Sherbeeny, A. M., Al Zoubi, W., and Abukhadra, M. R. (2023). Synthesis and characterization of iron-rich glauconite nanorods by a facile sonochemical method for instantaneous and eco-friendly elimination of malachite green dye from aquatic environments. *ACS omega* 8 (51), 49347–49361. doi:10.1021/acsomega.3c07870

Alqahtani, M. D., Nasser, N., Bin Jumah, M. N., AlZahrani, S. A., Allam, A. A., Abukhadra, M. R., et al. (2023). Insight into the morphological properties of nano-kaolinite (nanoscrolls and nanosheets) on its qualification as delivery structure of oxaliplatin: loading, release, and kinetic studies. *Molecules* 28 (13), 5158. doi:10.3390/molecules28135158

Amri, A. E., Kadiri, L., Hsissou, R., Lebkiri, A., Wardighi, Z., Rifi, E. H., et al. (2023). Investigation of Typha Latifolia (TL) as potential biosorbent for removal of the methyl orange anionic dye in the aqueous solution. Kinetic and DFT approaches. *J. Mol. Struct.* 1272, 134098. doi:10.1016/j.molstruc.2022.134098

Arab, A., El Kurdi, R., and Patra, D. (2022). Zinc curcumin oxide nanoparticles for enhanced adsorption of Congo red: kinetics and adsorption isotherms study. *Mater. Today Chem.* 23, 100701. doi:10.1016/j.mtchem.2021.100701

Ashraf, M.-T., AlHammadi, A. A., El-Sherbeeny, A. M., Alhammadi, S., Al Zoubi, W., Ko, Y. G., et al. (2022). Synthesis of cellulose fibers/Zeolite-A nanocomposite as an environmental adsorbent for organic and inorganic selenium ions; Characterization and advanced equilibrium studies. *J. Mol. Liq.* 360, 119573. doi:10.1016/j.molliq.2022.119573

Ashrafi, G., Nasrollahzadeh, M., Jaleh, B., Sajjadi, M., and Ghafuri, H. (2022). Biowaste- and nature-derived (nano)materials: biosynthesis, stability and

environmental applications. *Adv. Colloid Interface Sci.* 301, 102599. doi:10.1016/j.cis.2022.102599

Barhdadi, I., Seddik, N. B., Allaoui, I., Boumhidi, B., Kharim, Y. E., Hadri, M., et al. (2024). Detailed study of safranin-O adsorption on sepiolite clay: kinetics, thermodynamics, isotherms and theoretical calculations for optimal water treatment efficiency. *J. Mol. Struct.* 1308, 138130. doi:10.1016/j.molstruc.2024.138130

Basaleh, A. A., Al-Malack, M. H., and Saleh, T. A. (2021). Poly(acrylamide acrylic acid) grafted on steel slag as an efficient magnetic adsorbent for cationic and anionic dyes. *J. Environ. Chem. Eng.* 9, 105126. doi:10.1016/j.jece.2021.105126

Bensalah, J., Idrissi, A., Faydy, M. E., Doumane, G., Staoui, A., Hsissou, R., et al. (2023). Investigation of the cationic resin as a potential adsorbent to remove MR and CV dyes: kinetic, equilibrium isotherms studies and DFT calculations. *J. Mol. Struct.* 1278, 134849. doi:10.1016/j.molstruc.2022.134849

Carretero, M. I., and Pozo, M. (2010). Clay and non-clay minerals in the pharmaceutical and cosmetic industries Part II. Active ingredients. *Appl. Clay Sci.* 47 (3-4), 171–181. doi:10.1016/j.clay.2009.10.016

Dardir, F. M., Mohamed, A. S., Abukhadra, M. R., Ahmed, E. A., and Soliman, M. F. (2018). Cosmetic and pharmaceutical qualifications of Egyptian bentonite and its suitability as drug carrier for praziquantel drug. *Eur. J. Pharm. Sci.* 115, 320–329. doi:10.1016/j.ejps.2018.01.041

Dawodu, G., and Akpomie, M. (2012). Abuh, equilibrium isotherm studies on the batch sorption of copper (II) ions from aqueous solution unto nsu clay. *Int. J. Sci. Eng. Res.* 3 (12), 1–7. doi:10.1016/j.jmrt.2014.03.002

de Araujo, C. M. B., Wernke, G., Ghislandi, M. G., Diório, A., Vieira, M. F., Bergamasco, R., et al. (2023). Continuous removal of pharmaceutical drug chloroquine and Safranin-O dye from water using agar-graphene oxide hydrogel: selective adsorption in batch and fixed-bed experiments. *Environ. Res.* 216, 114425. doi:10.1016/j.envres.2022.114425

Debnath, S., Parashar, K., and Pillay, K. (2017). Ultrasound assisted adsorptive removal of hazardous dye Safranin O from aqueous solution using crosslinked graphene oxide-chitosan (GO CH) composite and optimization by response surface methodology (RSM) approach. *Carbohydr. Polym.* 175, 509–517. doi:10.1016/j.carbpol.2017.07.088

Dhaouadi, F., Sellaoui, L., Badawi, M., Reynel-Ávila, H. E., Mendoza-Castillo, D. I., Jaime-Leal, J. E., et al. (2020). Statistical physics interpretation of the adsorption mechanism of Pb^{2+}, Cd^{2+} and Ni^{2+} on chicken feathers. *J. Mol. Liq.* 319, 114168. doi:10.1016/j.molliq.2020.114168

Dhaouadi, F., Sellaoui, L., Reynel-Ávila, H. E., Landín-Sandoval, V., Mendoza-Castillo, D. I., Jaime-Leal, J. E., et al. (2021). Adsorption mechanism of Zn2+, Ni2+, Cd2+, and Cu2+ ions by carbon-based adsorbents: interpretation of the adsorption isotherms via physical modelling. *Environ. Sci. Pollut. Res.* 28 (24), 30943–30954. doi:10.1007/s11356-021-12832-x

El-Sherbeeny, A. M., Ibrahim, S. M., AlHammadi, A. A., Soliman, A. T. A., Shim, J. J., and Abukhadra, M. R. (2021). Effective retention of radioactive Cs+ and Ba^{2+} ions using β-cyclodextrin functionalized diatomite (β-CD/D) as environmental adsorbent; characterization, application, and safety. *Surf. Interfaces* 26, 101434. doi:10.1016/j.surfin.2021.101434

Ghosh, I., Kar, S., Chatterjee, T., Bar, N., and Das, S. K. (2021). Adsorptive removal of Safranin-O dye from aqueous medium using coconut coir and its acid-treated forms: adsorption study, scale-up design, MPR and GA-ANN modeling. *Sustain. Chem. Pharm.* 19, 100374. doi:10.1016/j.scp.2021.100374

Hassan, H. M. A., El-Aassar, M. R., El-Hashemy, M. A., Betiha, M. A., Alzaid, M., Alqhobisi, A. N., et al. (2022). Sulfanilic acid-functionalized magnetic GO as a robust adsorbent for the efficient adsorption of methylene blue from aqueous solution. *J. Mol. Liq.* 361, 119603. doi:10.1016/j.molliq.2022.119603

Huang, Y., Zeng, X., Guo, L., Lan, J., Zhang, L., and Cao, D. (2018). Heavy metal ion removal of wastewater by zeolite-imidazolate frameworks. *Sep. Purif. Technol.* 194, 462–469. doi:10.1016/j.seppur.2017.11.068

Jasper, E. E., Ajibola, V. O., and Onwuka, J. C. (2020). Nonlinear regression analysis of the sorption of crystal violet and methylene blue from aqueous solutions onto an agro-waste derived activated carbon. *Appl. Water Sci.* 10 (6), 132–211. doi:10.1007/s13201-020-01218-y

Jawad, A. H., Malek, N. N. A., Khadiran, T., Alothman, Z. A., and Yaseen, Z. M. (2022). Mesoporous high-surface-area activated carbon from biomass waste via microwave-assisted-H3PO4 activation for methylene blue dye adsorption: an optimized process. *Diam. Relat. Mater.* 128, 109288. doi:10.1016/j.diamond.2022.109288

Jebli, A., Amri, A. E., Hsissou, R., Lebkiri, A., Zarrik, B., Bouhassane, F. Z., et al. (2023). Synthesis of a chitosan@hydroxyapatite composite hybrid using a new approach for high-performance removal of crystal violet dye in aqueous solution, equilibrium isotherms and process optimization. *J. Taiwan Inst. Chem. Eng.* 149, 105006. doi:10.1016/j.jtice.2023.105006

Jiang, Y., Abukhadra, M. R., Refay, N. M., Sharaf, M. F., El-Meligy, M. A., and Awwad, E. M. (2020). Synthesis of chitosan/MCM-48 and β-cyclodextrin/MCM-48 composites as bio-adsorbents for environmental removal of Cd2+ ions; kinetic and equilibrium studies. *React. Funct. Polym.* 154, 104675. doi:10.1016/j.reactfunctpolym.2020.104675

Kadiri, L., Ouass, A., Hsissou, R., Safi, Z., Wazzan, N., Essaadaoui, Y., et al. (2021). Adsorption properties of coriander seeds: spectroscopic kinetic thermodynamic and computational approaches. *J. Mol. Liq.* 343, 116971. doi:10.1016/j.molliq.2021.116971

Kaur, S., Rani, S., Mahajan, R. K., Asif, M., and Gupta, V. K. (2015). Synthesis and adsorption properties of mesoporous material for the removal of dye safranin: kinetics, equilibrium, and thermodynamics. *J. Industrial Eng. Chem.* 22, 19–27. doi:10.1016/j.jiec.2014.06.019

Kenawy, E.-R., Tenhu, H., Khattab, S. A., Eldeeb, A. A., and Azaam, M. M. (2022). Highly efficient adsorbent material for removal of methylene blue dye based on functionalized polyacrylonitrile. *Eur. Polym. J.* 169, 111138. doi:10.1016/j.eurpolymj.2022.111138

Kumar, K. V., and Sivanesan, S. (2005). Comparison of linear and non-linear method in estimating the sorption isotherm parameters for safranin onto activated carbon. *J. Hazard. Mater.* 123, 288–292. doi:10.1016/j.jhazmat.2005.03.040

Lahiri, S. K., Zhang, C., Sillanpää, M., and Liu, L. (2022). Nanoporous NiO@SiO2 photo-catalyst prepared by ion-exchange method for fast elimination of reactive dyes from wastewater. *Mater. Today Chem.* 23, 100677. doi:10.1016/j.mtchem.2021.100677

Laskar, N., and Kumar, U. (2023). Adsorption of Safranin dye, an emerging contaminant from wastewater by modified bamboo (Bambusa Tulda): characterization and column model analysis. *Environ. Qual. Manag.* 33 (2), 193–204. doi:10.1002/tqem.21940

Le, T. M. H., Nuisin, R., Mongkolnavin, R., Painmanakul, P., and Sairiam, S. (2022). Enhancing dye wastewater treatment efficiency in ozonation membrane contactors by chloro- and fluoro-organosilanes' functionality on hydrophobic pvdf membrane modification. *SSRN Electron. J.* 288, 120711. doi:10.1016/j.seppur.2022.120711

Lebkiri, I., Abbou, B., Hsissou, R., Safi, Z., Sadiku, M., Berisha, A., et al. (2023). Investigation of the anionic polyacrylamide as a potential adsorbent of crystal violet dye from aqueous solution: equilibrium, kinetic, thermodynamic, DFT, MC and MD approaches. *J. Mol. Liq.* 372, 121220. doi:10.1016/j.molliq.2023.121220

Lin, X., Xie, Y., Lu, H., Xin, Y., Altaf, R., Zhu, S., et al. (2021). Facile preparation of dual La-Zr modified magnetite adsorbents for efficient and selective phosphorus recovery. *Chem. Eng. J.* 413, 127530. doi:10.1016/j.cej.2020.127530

Makó, É., Kovács, A., and Kristóf, T. (2019). Influencing parameters of direct homogenization intercalation of kaolinite with urea, dimethyl sulfoxide, formamide, and N-methylformamide. *Appl. Clay Sci.* 182, 105287. doi:10.1016/j.clay.2019.105287

Mobarak, M., Ali, R. A., and Seliem, M. K. (2021). Chitosan/activated coal composite as an effective adsorbent for Mn (VII): modeling and interpretation of physicochemical parameters. *Int. J. Biol. Macromol.* 186, 750–758. doi:10.1016/j.ijbiomac.2021.07.089

Mohamed, F., Abukhadra, M. R., and Shaban, M. (2018). Removal of safranin dye from water using polypyrrole nanofiber/Zn-Fe layered double hydroxide nanocomposite (Ppy NF/Zn-Fe LDH) of enhanced adsorption and photocatalytic properties. *Sci. Total Environ.* 640–641, 352–363. doi:10.1016/j.scitotenv.2018.05.316

Neolaka, Y. A., Lawa, Y., Naat, J. N., Riwu, A. A., Iqbal, M., Darmokoesoemo, H., et al. (2020). The adsorption of Cr (VI) from water samples using graphene oxide-magnetic (GO-Fe3O4) synthesized from natural cellulose-based graphite (kusambi wood or Schleichera oleosa): study of kinetics, isotherms and thermodynamics. *J. Mater. Res. Technol.* 9 (3), 6544–6556. doi:10.1016/j.jmrt.2020.04.040

Pandey, C., Daverey, A., Dutta, K., Yata, V. K., and Arunachalam, K. (2022). Valorization of waste pine needle biomass into biosorbents for the removal of methylene blue dye from water: kinetics, equilibrium and thermodynamics study. *Environ. Technol. and Innovation.* 25, 102200. doi:10.1016/j.eti.2021.102200

Prajapati, A. K., and Mondal, M. K. (2022). Green synthesis of Fe3O4-onion peel biochar nanocomposites for adsorption of Cr (VI), methylene blue and Congo red dye from aqueous solutions. *J. Mol. Liq.* 3499, 118161. doi:10.1016/j.molliq.2021.118161

Qada, El (2020). Kinetic behavior of the adsorption of malachite green using Jordanian diatomite as adsorbent. *Jordanian J. Eng. Chem. Industries (JJECI) Res. Pap.* 3 (1), 1–10. doi:10.48103/jjeci3120220

Reddy, Y. S., Magdalane, C. M., Kaviyarasu, K., Mola, G. T., Kennedy, J., and Maaza, M. (2018). Equilibrium and kinetic studies of the adsorption of acid blue 9 and Safranin O from aqueous solutions by MgO decked FLG coated Fuller's earth. *J. Phys. Chem. Solids* 123, 43–51. doi:10.1016/j.jpcs.2018.07.009

Roy, N., and Chakraborty, S. (2021). ZnO as photocatalyst: an approach to waste water treatment. *Mater. Today Proc.* 46, 6399–6403. doi:10.1016/j.matpr.2020.06.264

Salam, M. A., Abukhadra, M. R., and Mostafa, M. (2020). Effective decontamination of as (V), Hg (II), and U (VI) toxic ions from water using novel muscovite/zeolite aluminosilicate composite: adsorption behavior and mechanism. *Environ. Sci. Pollut. Res.* 27 (12), 13247–13260. doi:10.1007/s11356-020-07945-8

Sarkar, S., Chakraborty, P., and Das, P. (2024). Synthesis of nano-silica-coated peanut shell-derived bio-char composite for removal of safranin dye present in aqueous solution: batch and optimization using response surface methodology. *Biomass Convers. Biorefinery*, 1–16. doi:10.1007/s13399-024-05389-5

Sellaoui, L., Ali, J., Badawi, M., Bonilla-Petriciolet, A., and Chen, Z. (2020). Understanding the adsorption mechanism of Ag+ and Hg2+ on functionalized layered double hydroxide via statistical physics modeling. *Appl. Clay Sci.* 198, 105828. doi:10.1016/j.clay.2020.105828

Sellaoui, L., Guedidi, H., Reinert, L., Knani, S., Duclaux, L., Lamine, A. B., et al. (2016). Experimental and theoretical studies of adsorption of ibuprofen on raw and two chemically modified activated carbons: new physicochemical interpretations. *RSC Adv.* 6 (15), 12363–12373. doi:10.1039/c5ra22302d

Shaban, M., Abukhadra, M. R., Mohamed, A. S., Shahien, M. G., and Ibrahim, S. S. (2017b). Synthesis of mesoporous graphite functionalized by nitrogen for efficient removal of safranin dye utilizing rice husk ash; equilibrium studies and response surface optimization. *J. Inorg. Organomet. Polym. Mater.* 28, 279–294. doi:10.1007/s10904-017-0726-2

Shaban, M., Abukhadra, M. R., Shahien, M. G., and Khan, A. A. P. (2017a). Upgraded modified forms of bituminous coal for the removal of safranin-T dye from aqueous solution. *Environ. Sci. Pollut. Res.* 24 (22), 18135–18151. doi:10.1007/s11356-017-9424-4

Shaban, M., Sayed, M. I., Shahien, M. G., Abukhadra, M. R., and Ahmed, Z. M. (2018). Adsorption behavior of inorganic-and organic-modified kaolinite for Congo red dye from water, kinetic modeling, and equilibrium studies. *J. Sol-Gel Sci. Technol.* 87 (2), 427–441. doi:10.1007/s10971-018-4719-6

Shaltout, W. A., El-Naggar, G. A., Esmail, G., and Hassan, A. F. (2022). Synthesis and characterization of ferric@ nanocellulose/nanohydroxyapatite bio-composite based on sea scallop shells and cotton stalks: adsorption of Safranin-O dye. *Biomass Convers. Biorefinery* 14, 4759–4776. doi:10.1007/s13399-022-02753-1

Shawky, A., El-Sheikh, S. M., Rashed, M. N., Abdo, S. M., and El-Dosoqy, T. I. (2019). Exfoliated kaolinite nanolayers as an alternative photocatalyst with superb activity. *J. Environ. Chem. Eng.* 7 (3), 103174. doi:10.1016/j.jece.2019.103174

Sherlala, A., Raman, A., Bello, M. M., and Buthiyappan, A. (2019). Adsorption of arsenic using chitosan magnetic graphene oxide nanocomposite. *J. Environ. Manag.* 246, 547–556. doi:10.1016/j.jenvman.2019.05.117

Sriram, G., Thangarasu, S., Selvakumar, K., Kurkuri, M., Dhineshbabu, N. R., and Oh, T. H. (2024). Effective removal of Rose Bengal using Ni-Co-Zn layered triple hydroxide: studies on batch adsorption, mechanism, selectivity, co-ions, and reusability. *Colloids Surfaces A Physicochem. Eng. Aspects* 685, 133199. doi:10.1016/j.colsurfa.2024.133199

Tian, L., Abukhadra, M. R., Mohamed, A. S., Nadeem, A., Ahmad, S. F., and Ibrahim, K. E. (2020). Insight into the loading and release properties of an exfoliated kaolinite/cellulose fiber (EXK/CF) composite as a carrier for oxaliplatin drug: cytotoxicity and release kinetics. *ACS Omega* 5 (30), 19165–19173. doi:10.1021/acsomega.0c02529

Vidovix, T. B., Quesada, H. B., Bergamasco, R., Vieira, M. F., and Vieira, A. M. S. (2021). Adsorption of Safranin-O dye by copper oxide nanoparticles synthesized from Punica granatum leaf extract. *Environ. Technol.* 43, 3047–3063. doi:10.1080/09593330.2021.1914180

Vivas, E. L., and Cho, K. (2021). Efficient adsorptive removal of Cobalt (II) ions from water by dicalcium phosphate dihydrate. *J. Environ. Manag.* 283, 111990. doi:10.1016/j.jenvman.2021.111990

Wang, M., Yan, R., Shan, M., Liu, S., and Tang, H. (2024). Fabrication of crown ether-containing copolymer porous membrane and their enhanced adsorption performance for cationic dyes: experimental and DFT investigations. *Chemosphere* 352, 141363. doi:10.1016/j.chemosphere.2024.141363

Yang, X., Wang, J., El-Sherbeeny, A. M., AlHammadi, A. A., Park, W.-H., and Abukhadra, M. R. (2022). Insight into the adsorption and oxidation activity of a ZnO/piezoelectric quartz core-shell for enhanced decontamination of ibuprofen: steric, energetic, and oxidation studies. *Chem. Eng. J.* 431, 134312. doi:10.1016/j.cej.2021.134312

Zhang, X., Liu, H., Xing, H., Li, H., Hu, H., Li, A., et al. (2017). Improved sodium adsorption by modified kaolinite at high temperature using intercalation-exfoliation method. *Fuel* 191, 198–203. doi:10.1016/j.fuel.2016.11.067

Zourou, A. N., Adamopoulos, N., Roman, T., Zhang, F., Terrones, M., Kordatos, K., et al. (2022). Graphene oxide-CuFe2O4 nanohybrid material as an adsorbent of Congo red dye. *Carbon Trends* 7, 100147. doi:10.1016/j.cartre.2022.100147

Zsirka, B., Horváth, E., Járvás, Z., Dallos, A., Makó, É., and Kristóf, J. (2016). Structural and energetical characterization of exfoliated kaolinite surfaces. *Appl. Clay Sci.* 124, 54–61. doi:10.1016/j.clay.2016.01.035

Zuo, X., Wang, D., Zhang, S., Liu, Q., and Yang, H. (2017). Effect of intercalation agents on morphology of exfoliated kaolinite. *Minerals* 7 (12), 249. doi:10.3390/min7120249

Frontiers in Chemistry

Explores all fields of chemical science across the periodic table

Advances our understanding of how atoms, ions, and molecules come together and come apart. It explores the role of chemistry in our everyday lives - from electronic devices to health and wellbeing.

Discover the latest Research Topics

See more →

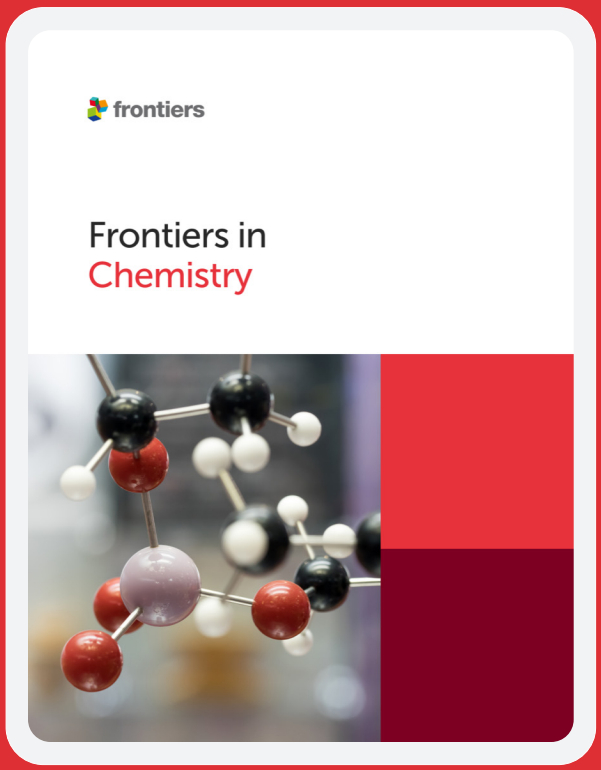

Frontiers

Avenue du Tribunal-Fédéral 34
1005 Lausanne, Switzerland
frontiersin.org

Contact us

+41 (0)21 510 17 00
frontiersin.org/about/contact